

**Hf-B-Li-Mg isotope systematics of late Cenozoic
volcanic rocks from the Chugoku district,
Southwest Japan: Implications for the property and
transport mechanism of slab-derived fluids in the
subduction zone**

2023, March

ZHANG WEI

**The Graduate School of Natural Science and
Technology**

(Doctor's Course)

OKAYAMA UNIVERSITY

Table of contents

Table of contents	I
List of Figures	VII
List of Tables	XIII
Abstract	XV
Acknowledgements	XVII
Chapter 1. Introduction and geological background	1
1. Introduction.....	1
2. Tectonic-geological background and geophysical observation in SW Japan	6
3. Volcanic history of the Chugoku district	8
3.1 <i>Stage-I volcanic activity: 25–17 Ma</i>	11
3.2 <i>Stage-II volcanic activity: 17–12 Ma</i>	11
3.3 <i>Episode 1 in Stage-III/IV volcanic activity: 12–8 Ma</i>	12
3.4 <i>Episode 2 in Stage-III/IV volcanic activity: 8–4 Ma</i>	12
3.5 <i>Episode 3 in Stage-III/IV volcanic activity: 4–0 Ma</i>	12
4. Previous studies on volcanic rocks in the Chugoku district	13
4.1 <i>High-Mg andesites in Setouchi during Miocene</i>	13
4.2 <i>High-Sr andesites and dacites in the San-in zone during Pliocene–Holocene</i>	14
4.3 <i>Monogenetic basalts in the entire Chugoku region during Miocene–Holocene</i>	18
5. References.....	26
Chapter 2. Evolution of slab-derived fluids beneath the SW Japan arc: Perspectives from Hf isotope compositions of volcanic rocks	35
Abstract	35

1. Introduction.....	36
2. Global adakites.....	37
3. Rock type	38
4. Methods.....	41
5. Results.....	43
5.1 Isotope variations in the Chugoku volcanic rocks.....	43
5.2 Comparison of Hf isotope compositions with the other arcs.....	46
6. Discussion.....	49
6.1 Characteristics of basalt-magma sources.....	49
6.2 Modelling parameters for slab contribution in Hf isotopic perspective.....	52
6.3 The change of the fluid property from oceanic crust.....	53
6.4 Temporal evolution of sediment contribution.....	58
6.5 Lateral structural variation in the subducting sediments.....	59
6.6 Implication for the evolution of the subducting lithosphere and island-arc volcanism in Southwest Japan	62
7. Conclusions.....	64
References.....	64
Tables.....	76

Chapter 3. Slab melting beneath the Southwest Japan Arc driven by dehydration of altered oceanic serpentinite: Evidence from Boron isotopes 131

Abstract.....	131
1. Introduction.....	132
2. Analytical methods	134
3. Results.....	135
4. Discussion.....	141

4.1. Potential sources of boron in arc magmas	142
4.2. Parameters for B isotopic fractionation during the dehydration modeling	143
4.3 Dehydration of the upper slab (AOC + sediments)	146
4.4 Dehydration of the serpentized peridotite	148
4.5 Implications for slab melting	152
5. Conclusions.....	154
References.....	154
Tables.....	167
Chapter 4. A rapid method of simultaneous chromatographic purification of Li and Mg for isotopic analyses using MC-ICP-MS.....	169
Abstract.....	169
1. Introduction.....	170
2. Experimental Methods	171
2.1 Reagents and materials.....	171
2.2 Sample and standard preparation	173
2.3 Column chromatography.....	174
2.4 Mass spectrometry	176
3. Results and discussion	180
3.1 Sample-standard concentration matching.....	180
3.2 Recovery yields and blanks of lithium and magnesium	182
3.3 Evaluation of the interfering elements removal procedure	182
3.4 Li and Mg isotopic compositions of reference materials.....	185
4. Conclusions.....	191
References.....	191

Chapter 5. Lithium isotope constraints on slab and mantle contribution to arc magmas

in SW Japan.....	201
Abstract.....	201
1. Introduction.....	201
2. Results.....	204
3. Discussion.....	209
3.1 Processes responsible for $^7\text{Li}/^6\text{Li}$ variation	210
3.2 Processes responsible for heterogeneity of Li isotope compositions of the Chugoku magmas	221
3.3 Modeling of Li-isotope fractionation during subduction.....	227
3.4 Mantle buffering of the slab-derived Li-isotope signature	241
3.5 Implications for Li isotope variation in global arc magmas	249
4. Conclusions.....	250
References.....	251
Tables.....	268

Chapter 6. Mg isotope fractionation and modification of slab-derived melt: Perspective from Mg isotopic compositions of volcanic rocks from the Southwest Japan.....

Abstract.....	277
1. Introduction.....	277
2. Results.....	281
2.1 Temporal variation	281
2.2 Spatial variation	282
2.3 Correlation of Mg isotope with $^{87}\text{Sr}/^{86}\text{Sr}$, $^{143}\text{Nd}/^{144}\text{Nd}$, $^{177}\text{Hf}/^{178}\text{Hf}$, and $^{206}\text{Pb}/^{204}\text{Pb}$	282
2.4 Correlation of Mg isotope with trace element ratios	283

3. Discussion.....	284
3.1 <i>The contribution of altered oceanic basalts</i>	284
3.2 <i>Sediment contribution</i>	287
3.3 <i>The contribution of slab serpentinite</i>	291
3.4 <i>Mantle peridotite contribution</i>	292
4. Conclusions.....	293
References.....	294
Tables.....	303
Chapter 7. Summary and future vision	308

List of Figures

Figure 1-1. A map showing the tectonic setting of southwest Japan and spatial distributions of late Cenozoic volcanic fields in the Chugoku district.2

Figure 1-2. Cenozoic volcanic activity in the SW Japan arc in the last 25 Myrs, subdivided into Stages I (25–17 Ma), II (17–12 Ma), III (12–4 Ma) and IV (4–0 Ma). 10

Figure 1-3. Spatial and temporal distribution of volcanic rocks in the Chugoku district (12 Ma to recent; Nguyen et al., 2020). 11

Figure 1-4. Schematic model for production of high-Mg andesites (HMA) and associated basalts in Setouchi volcanic belt by Kawamoto et al. (2012). 14

Figure 1-5. Schematic model for the productions of porphyritic and aphyric andesites in Daisen volcano. 15

Figure 1-6. A model of transporting siliceous slab melts to surface in the Chugoku district.. 18

Figure 1-7. Schematic model for the genesis of alkaline basalts in SW Japan.20

Figure 1-8. Schematic model of magma productions in the Chugoku district21

Figure 1-9. Schematic model for the volcanic and tectonic evolution of SW Japan22

Figure 1-10. Schematic models for the evolution of late Cenozoic volcanic activity in the Chugoku and the morphology of subducting PHS plate in relation to plate configuration25

Figure 2-1. ($^{143}\text{Nd}/^{144}\text{Nd}$)_i versus ($^{87}\text{Sr}/^{86}\text{Sr}$)_i of global adakites (high-Sr andesites and dacites).38

Figure 2-2. Total alkali (Na₂O + K₂O) abundance plotted against SiO₂ abundance.40

Figure 2-4. Temporal changes in ($^{176}\text{Hf}/^{177}\text{Hf}$) _i , ($^{143}\text{Nd}/^{144}\text{Nd}$) _i , ($^{87}\text{Sr}/^{86}\text{Sr}$) _i and ($^{206}\text{Pb}/^{204}\text{Pb}$) _i of volcanic rocks in Chugoku and Setouchi.....	45
Figure 2-5. Longitudinal changes in ($^{176}\text{Hf}/^{177}\text{Hf}$) _i , ($^{143}\text{Nd}/^{144}\text{Nd}$) _i , ($^{87}\text{Sr}/^{86}\text{Sr}$) _i and ($^{206}\text{Pb}/^{204}\text{Pb}$) _i of volcanic rocks in Chugoku.	46
Figure 2-6. Hf, Sr, Nd and Pb isotope compositions of ADK, OIB and IAB in Chugoku, SW Japan in comparison with SVB HMA and the other arc volcanic rocks	48
Figure 2-7. Variations in Sr-Nd-Pb-Hf isotopic compositions of OIB-type lavas in the Chugoku district, SW Japan, in comparison with Cenozoic basalts in East Asia, seafloor basalts of Pacific Plate (near Japan trench) and Philippine Sea Plate (in Shikoku Basin), and sediments.....	51
Figure 2-8. Mixing models between two components from oceanic crust basalts and sediments.	57
Figure 2-9. Temporal variations in (A) Sr/Y and (B) $\delta^7\text{Li}$ of volcanic rocks from Chugoku and Setouchi.....	58
Figure 2-10. Longitudinal variations in Sr-Nd-Pb-Hf isotopic compositions of high-Sr andesites and dacites in the Chugoku district, southwest Japan.	61
Figure 2-11. A conceptual model for the evolution of the Chugoku volcanism.....	63
Figure 3-1. Boron isotope ($\delta^{11}\text{B}$) compositions of some arc volcanic rocks, back-arc volcanic rocks, serpentinite (Serp.), altered oceanic crust (AOC), mid-ocean ridge basalts (MORB), and sediment.	134
Figure 3-2. $\delta^{11}\text{B}$ (‰) versus boron concentrations and B/Nb ratios obtained for ADK from the Chugoku district and HMA from the Setouchi district in SW Japan.....	137

Figure 3-3. $\delta^{11}\text{B}$ (‰) plotted against longitudes of collection sites of the volcanic rocks from the Chugoku district in SW Japan.....	138
Figure 3-4. Plots of $\delta^{11}\text{B}$ values versus Sr-Nd-Pb isotopic compositions of the Chugoku ADK and the Setouchi HMA.....	139
Figure 3-5. Plots of $\delta^{11}\text{B}$ values against (A) SiO_2 abundance and (B) MgO abundance of ADK.	140
Figure 3-6. Plots of $\delta^{11}\text{B}$ in ADK of the Chugoku district in SW Japan versus LOI (Loss on ignition).....	141
Figure 3-7. (A) Slab temperature change ($^{\circ}\text{C}$) and (B) dehydration water loss (wt. %) as a function of slab depth (km) of the slab sediment, oceanic crust (AOC), mantle wedge peridotite and slab lithosphere peridotite in the Chugoku subduction zone,	146
Figure 3-8. Dehydration model showing the variation of $\delta^{11}\text{B}$ and B concentrations of the slab sediment (SED), oceanic crust (AOC), mantle wedge peridotite (MWP) and slab lithosphere peridotite (SLP) as well as their dehydration fluids with subduction depth from 30 km until 110 km with 10 km intervals.	148
Figure 3-9. Plot of $\delta^{11}\text{B}$ in volcanic rocks from the Chugoku district in SW Japan versus (A) $(^{87}\text{Sr}/^{86}\text{Sr})_t$, (B) $(^{143}\text{Nd}/^{144}\text{Nd})_t$, (C) $(^{206}\text{Pb}/^{204}\text{Pb})_t$, and (D) $(^{207}\text{Pb}/^{204}\text{Pb})_t$	152
Figure 4-1. Elution curves for separation of Li and Mg from various sample matrices (reference standard silicate rocks).....	175
Figure 4-3. $\delta^7\text{Li}$ values of LSVEC (A) and $\delta^{26}\text{Mg}$ values of DSM-3 (B) at varying sample/standard concentration ratios.	181
Figure 4-4. Effect of contaminant matrix elements on (A) $\delta^7\text{Li}$ values of LSVEC and (B) $\delta^{26}\text{Mg}$ values of DSM-3.	182

Figure 4-5. $\delta^7\text{Li}$ values for the reference geological samples analyzed in this study in comparison with literature data.....	186
Figure 4-6. $\delta^{26}\text{Mg}$ values for the reference geological samples analyzed in this study in comparison with literature data.....	187
Figure 5-1. $\delta^7\text{Li}$ values in volcanic rocks from the Chugoku district in SW Japan (ADK: green dots; IAB: blue dots; HMA: purple dots) compared to published values for mafic-intermediate volcanic rocks ($\text{SiO}_2 \leq 63$ wt%, except for rocks classified as ‘adakite’) in other arcs.	206
Figure 5-2. Plot of $\delta^7\text{Li}$ in volcanic rocks from the Chugoku district in SW Japan versus (a) ($^{87}\text{Sr}/^{86}\text{Sr}$) _t , (b) ($^{143}\text{Nd}/^{144}\text{Nd}$) _t , (c) ($^{176}\text{Hf}/^{177}\text{Hf}$) _t , and (d) ($^{206}\text{Pb}/^{204}\text{Pb}$) _t	208
Figure 5-3. Temporal variations in (a) $\delta^7\text{Li}$ value, (b) Sr/Nd ratio, and (c) Th/U ratios of the Chugoku volcanic rocks.....	209
Figure 5-4. Comparison of Li contents ([Li] in $\mu\text{g}\cdot\text{g}^{-1}$) and $\delta^7\text{Li}$ values of volcanic rocks in each volcanic field of the Chugoku district in SW Japan.	212
Figure 5-5. Plots of $\delta^7\text{Li}$ in ADK and IAB of the Chugoku district in SW Japan against (a) CIA and (b) MgO.....	213
Figure 5-6. Comparison of CIA (chemical index of alteration) and $\delta^7\text{Li}$ values of volcanic rocks in each volcanic field of the Chugoku district in SW Japan.	214
Figure 5-7. Comparison of $\delta^7\text{Li}$ values with (a) Cs/Rb ratio and (b) Li/Y ratios of volcanic rocks of IAB and ADK types.....	215
Figure 5-8. Comparison of MgO contents (wt. %) and $\delta^7\text{Li}$ values of volcanic rocks in each volcanic field of the Chugoku district in SW Japan.	218

Figure 5-9. Results of the modeling of [Li] and $\delta^7\text{Li}$ of subducting AOC using the Rayleigh distillation equation.....231

Figure 5-10. The changes in [Li] (blue lines) and $\delta^7\text{Li}$ values (red lines) of (a) AOC (Shikoku Basin basalt) and (b) sediment (Nankai sediment) in the subducted oceanic lithosphere at the depth from *c.* 20 km to 90 km beneath the Chugoku district.....241

Figure 5-11. Diffusion modeling for temporal and spatial changes in Li concentration and $\delta^7\text{Li}$ values of a slab melt diapir with the radius of 3000 m (initial [Li] = 20 $\mu\text{g}\cdot\text{g}^{-1}$ and initial $\delta^7\text{Li}$ = +7 ‰), having been preserved in the mantle ([Li] = 1.3 $\mu\text{g}\cdot\text{g}^{-1}$ and $\delta^7\text{Li}$ = +3.5‰) during 320 kyrs.....248

Figure 6-1. $\delta^{26}\text{Mg}$ (‰) plotted against sample age of volcanic rocks from the Chugoku district in SW Japan.282

Figure 6-2. $\delta^{26}\text{Mg}$ (‰) plotted against Longitude of volcanic rocks from the Chugoku district in SW Japan.282

Figure 6-3. Plot of $\delta^{26}\text{Mg}$ in volcanic rocks from the Chugoku district in SW Japan versus (A) $(^{87}\text{Sr}/^{86}\text{Sr})_t$, (B) $(^{143}\text{Nd}/^{144}\text{Nd})_t$, (C) $(^{206}\text{Pb}/^{204}\text{Pb})_t$, and (D) $(^{176}\text{Hf}/^{177}\text{Hf})_t$283

Figure 6-4. Plot of $\delta^{26}\text{Mg}$ in volcanic rocks from the Chugoku district in SW Japan versus (A) Sr/Nd, (B) La/Yb, (C) Th/U, and (D) Pb/Ce.284

Figure 6-5. The diagram of $\delta^{26}\text{Mg}$ vs MgO for predicted pristine slab-derived melts.....293

List of Tables

Table 2-1: Hf, Sr, Nd and Pb isotopic compositions of late Cenozoic volcanic rocks in the Chugoku district, SW Japan.....	76
Table 2-2: Hf, Sr, Nd and Pb isotopic composition of hot and cold subduction zones in Pacific margins. (Reference therein).....	79
Table 2-3. Parameters used for the two-component mixing model.....	123
Table 2-4: Hf, Sr, Nd and Pb isotopic composition of OIB lavas from eastern China, the Korean Peninsula. (Reference therein).....	124
Table 3-1. [B] and $\delta^{11}\text{B}$ data of studied samples from the Chugoku district of Southwest Japan.....	167
Table 3-2. [B] and $\delta^{11}\text{B}$ of different endmembers for the mixing model in Figure 3-9	167
Table 3-3. Parameters of Sr-Nd-Pb contents and isotopic ratios for mixing models	168
Table 4-1. Loaded masses on column for calibration seen in Figure 4-1.....	173
Table 4-2. Elution protocol for single-step separation of Li and Mg from sample matrices.	176
Table 4-3. Instrumental parameters for the analysis of Li and Mg isotopes on the NEPTUNE Plus.....	179
Table 4-4. $\delta^7\text{Li}$ values of reference standards.....	187
Table 4-5. $\delta^{25}\text{Mg}$ and $\delta^{26}\text{Mg}$ values of reference standards.....	189

Table 5-1. Li isotopic compositions of late Cenozoic volcanic rocks on the Chugoku district, SW Japan	268
Table 5-2. Results of the incremental dehydration modeling for the altered oceanic crust beneath the Chugoku district, SW Japan	271
Table 5-3. Results of the incremental dehydration modeling for the sediment beneath the Chugoku district, SW Japan.....	273
Table 6-1. Mg isotopic compositions of Late Cenozoic volcanic rocks in the Chugoku district, SW Japan and metasedimentary rocks (shales) from Shimanto zone.....	303
Table 6-2. The calculated $\delta^{26}\text{Mg}$ of AOC melts and residue under P and T conditions beneath the Chugoku district.....	305
Table 6-3. The calculated $\delta^{26}\text{Mg}$ of sediment melts and residue under P and T conditions beneath the Chugoku district, SW Japan.	306

Abstract

Fluids released from subducting lithosphere play an essential role in the production of island-arc magmas. However, the sources, properties, and transfer of subduction-zone fluids remain poorly constrained by studies of island-arc magmas, yet experimental studies have demonstrated that variable types of fluids (aqueous solution, supercritical liquid or melt) can be produced from subducted oceanic lithosphere (slab) consisting of various lithologies (sediment, oceanic crust, or slab mantle). In this study, I investigated the Hf, B, Li, and Mg isotope compositions of late Cenozoic volcanic rocks, well characterized by geochronological and geochemical analyses, from the Chugoku district in SW Japan to trace the evolution and variation of fluids beneath this region.

The dissertation first investigated the Hf isotope compositions in the Chugoku volcanic rocks (Chapter 2). The Hf isotope compositions show a clear temporal variation, from lower ($\epsilon_{\text{Hf}} = +2.0$ to $+5.0$) values in early-stage (12–5 Ma) samples to higher and more variable values (-0.6 to $+12.5$) in late-stage samples, suggesting sediment contribution occurred through all episodes but the relative proportion of AOC component gradually increased with time. Our modeling also suggests that subducted basalt-derived fluids may be supercritical fluids in the early stage and transitioned to hydrous melt in the later stage, owing to the shallowing of the oceanic lithosphere. The next chapter (Chapter 3) reported the systematic B isotopic data of the adakitic lavas. The adakitic lavas have $\delta^{11}\text{B}$ of $-7.2\text{‰} \sim +0.3\text{‰}$, which roughly correlated with Sr-Nd-Pb isotopic ratios. Results from slab dehydration modeling and mixing calculations suggest that the boron isotope signature points to the involvement of inputs from (1) a high- $\delta^{11}\text{B}$ hybrid component composed of a serpentinite-derived fluid from slab mantle and a melt from dehydrated oceanic crust, (2) a low- $\delta^{11}\text{B}$ melt from the dehydrated sediments. Our modeling shows that, in the hotter subduction zone, fluids were released from the deeper

serpentinites. Those fluids migrate upward and facilitate the melting of the upper slab, which was dehydrated at shallower depths. The fourth chapter introduced the chemical purification methods of Li and Mg and the optimization of instrumental analysis in MC-ICP-MS, which is applied to the discussion of the fourth and fifth chapters. The fifth chapter aims to study the process responsible for Li-isotope variation in arc magmas. The Chugoku volcanic rocks show large $\delta^7\text{Li}$ variation (-1.9 to $+7.4\%$), and thus are ideal candidates. The models for slab dehydration and a diffusive exchange between slab-derived melt and mantle demonstrate that slab-derived $\delta^7\text{Li}$ features in arc magmas can be preserved if slab-derived fluids/melts have distinct $\delta^7\text{Li}$ values from mantle and ascend rapidly. The sixth chapter investigated Mg isotope fractionation during slab melting, a garnet-bearing source. The Chugoku volcanic rocks have homogeneous Mg isotopic compositions, with an average $\delta^{26}\text{Mg}$ of $-0.23 \pm 0.08\%$, within the range of mantle peridotite. Our modeling shows that slab-derived melts may have $\delta^{26}\text{Mg}$ higher than their sources by up to $+0.31\%$, however, the heavy Mg isotopic features can be easily erased by later melt-mantle interaction. In this regard, Mg isotopes may be not a powerful tracer of slab melting.

Collectively, this dissertation reaffirms the temporal variation of slab-released fluids beneath the Chugoku district, highlights the importance of serpentinite-derived fluids to promote the hydrous melting of subducted slab, confirms the potential of Li isotopes to trace the slab signals, and clarifies the role of Mg isotope fractionation during slab melting and subsequent melt-mantle interaction. The results from this dissertation contribute to the overall development of using fluid-mobile and -immobile isotopic system to trace crustal recycling and fluid properties in the subduction zones.

Acknowledgements

On the 6-hour flight to visit a remote village “Misasa” in Japan, I started the first sentence of my PhD dissertation. It is a completely new experience for me. I was challenged by loneliness, inconvenience, and COVID-19, but finally, I received growth in my research career, the expansion of international sight, and, surprisingly, the protection of the isolated but clean environment away from the virus in Misasa.

I would like to express my honest appreciation and deepest gratitude to my academic supervisors; Prof. Eizo Nakamura, Prof. Ryoji Tanaka, Prof. Katsura Kobayashi, and Assistant Prof. Hiroshi Kitagawa for their academic supervision, scientific guidance and all their constant encouragement. My PhD work will not be possible without the help from my supervisors. Back in that time, I know little knowledge about a clean laboratory or geochemistry. Therefore, I would like to express my deepest gratitude to my advisor Assistant Prof. Hiroshi Kitagawa, for the frequent and fruitful discussions with him, for his careful revision of my manuscript, and for his supervision of the design proceeding, and completion of my PhD study. I would like to thank Prof. Ryoji Tanaka, for his expertise on both instrumental analysis and isotope geochemistry, and for his great favor on my first publication in my PhD career. The development of a new method on mass spectrometers and column chemistry is rather difficult, but it gave me a completely distinct experience and a sense of achievement. He gave me encouragement that I could add a different thing to my resume and even manage a laboratory in the future. I am grateful to Prof. Eizo Nakamura, for sharing his interests in rocks, minerals, meteorites, and the philosophy of science, for his thoughtful advice on my research, and for his constant support during various meetings. His passion for teaching always motivates me to be a good scientist. I would also like to recognize Prof. Katsura Kobayashi, for his constructive input and for raising thoughtful questions about my research, and for his kind instruction on

my daily living and research in Japan.

My PhD work has also been benefited greatly from interactions with all my colleagues. I would like to express my thanks to our laboratory technician Miss Chie Sakaguchi, for maintaining the instrument and clean laboratory with extreme care, patience, and enthusiasm, and for her technical, academic, and life support. I would like to especially thank Assistant Prof. Christian Postizil for his careful handling and polishing of my manuscript with bad grammar. I also thank Dr. Madeleine Bohlin from University of Cambridge, for teaching me how to optimize the column chromatography method and tune the Neptune MC-ICPMS. In addition, I would like to bring my gratefulness to Assistant Prof. Christian Postizil and Associate Profs. Takuya Kunihiro, and Dr. Tsutomu Ota for all their productive guidance and encouragement. I am deeply grateful to Dr. Masahiro Yamanaka, and Ms. Kayo Tanaka for their teaching, training, and help in my laboratory work, analytical guidance, and valuable discussions.

My special thanks to my mates Dr. Ivan Pineda-Velasco, Dr. Nghiem Van Dao, Dr. Xiaoyu Zhou, Dr. Yanqing Li, Dr. Yunchao Shu, Mr. Dilan Ratnayake, Ms. Nurcan Kucukarslan, Mr. Havishk Tripathi, Mr. Rahul Kumar, Ms., Mr. Noah Miklusicak, Mr. Wei Li, Ms. Tulibako Mwaisuba Tulibonwya, Ms. Maya-Liliana Avramescu and Mrs. Yukari Shimizu for their lovely friendship, encouragement, and continuous support.

I would like to bring my gratitude to all the academic and administrative staff members of the Pheasant Memorial Laboratory (PML) and the Institute for Planetary Materials (IPM). Especially, I am deeply grateful to Masako Uyama san for taking care of students with great patience. I am sincerely grateful for the financial support from the IPM and OU scholarship. Finally, my special thanks go to my family and my wife, Mrs. Yu Min, whose love and encouragement are meaningful in my life.

Chapter 1. Introduction and geological background

1. Introduction

Fluids liberated from subducting slab play an essential role in island-arc magma production; they lower the solidus of and induce melting of magma sources in the mantle wedge (Kushiro et al., 1968; Ringwood, 1974; Tatsumi and Eggins, 1995). These fluids are considered to have variable physical and chemical properties (Manning, 2004), owing to the variation in pressure (P)-temperature (T) paths taken (Peacock and Wang, 1999) and the lithology of the slab (Christensen, 1978; Walowski et al., 2015). Morphology of subducting slab may have a strong impact on the volume and composition of magmas produced in island-arcs, as it causes intra-slab P - T variations (Yogodzinski et al., 2001; Liu and Stegman, 2011).

Southwest Japan is a subduction zone where the Philippine Sea (PHS) plate is sinking into the trench. The volcanism occurs in two districts, Chugoku and Kyushu (Figure 1-1). These regions show uneven distributions of volcanoes (Japan Meteorological Agency, 2013); Kyushu has 13 active (Holocene) volcanoes while Chugoku has only two active examples (Figure 1-1A). Tatsumi et al. (2020) attributed biased volcanic distribution in these districts to subduction of differently-aged oceanic crust; subduction of PHS plate with a younger crust (< 25 Ma) beneath Chugoku and that with older crust (>50 Ma) beneath Kyushu.

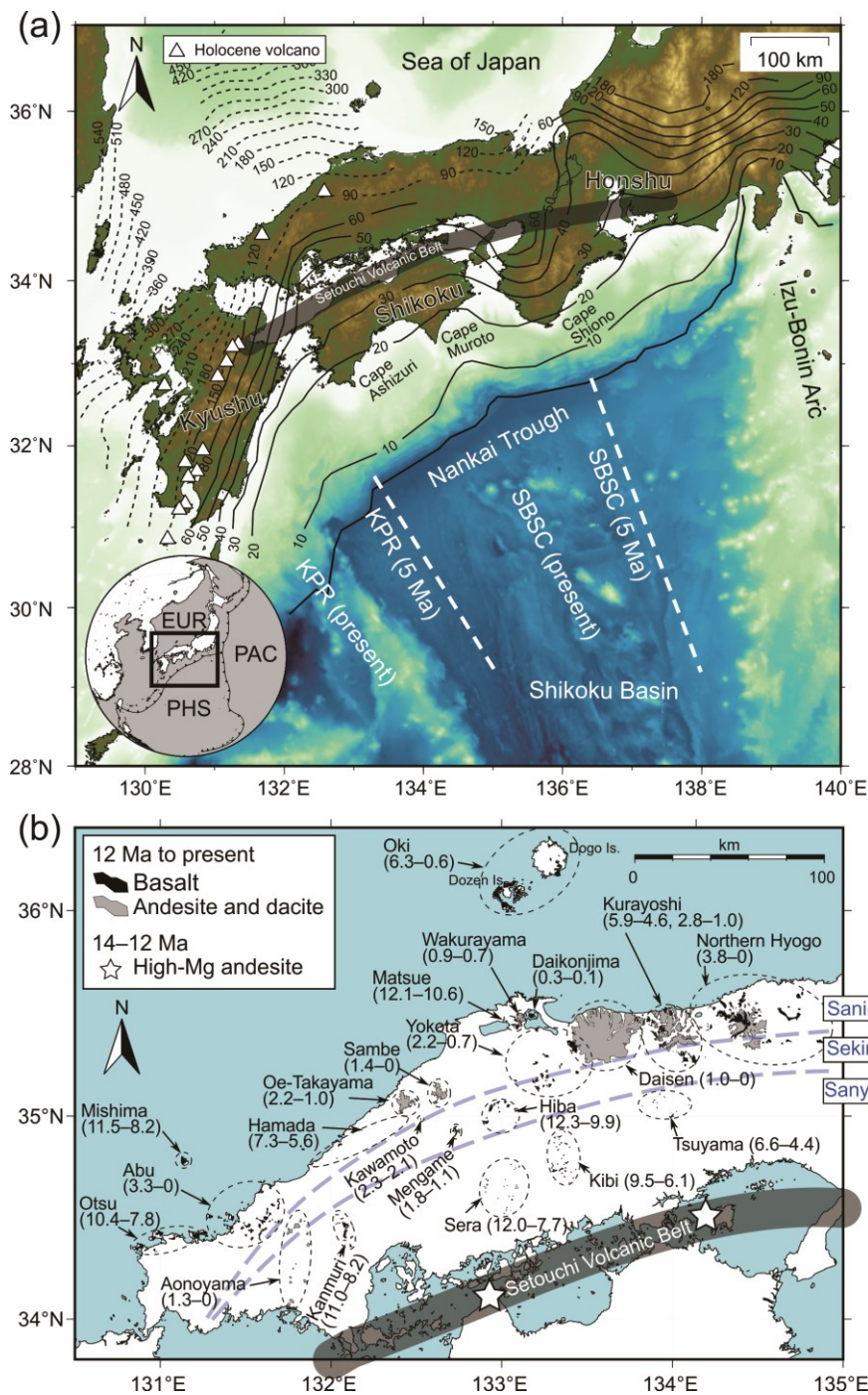


Figure 1-1. A map showing the tectonic setting of southwest Japan and spatial distributions of late Cenozoic volcanic fields in the Chugoku district.

(A): A map showing the tectonic setting of southwest Japan. Present and past (5 Ma) positions of the Shikoku Basin spreading center (SBSC) and Kyushu-Palau ridge (KPR) are after Mahony et al. (2011). Depth (in km) of the top of the subducting slab is shown with contour lines (dotted line, the aseismic slab; solid line, seismic slab; Asamori and Zhao, 2015). Locations of Holocene volcanoes in the Chugoku and Kyushu districts are after Japan Meteorological Agency (2013). An inset map shows

the plate configuration around SW Japan (PHS, Philippine Sea Plate; PAC, Pacific Plate; EUR, Eurasian Plate). **(B)**: Spatial distributions of late Cenozoic volcanic fields in the Chugoku district. Each volcanic field is circled by dotted line (age [in Ma] of volcanic activity shown in parenthesis). The locality of high-Mg andesites in Setouchi Volcanic Belt are shown as open stars (Tatsumi et al., 2003). The borders of trench-parallel zones (San-yo, Seki-ryo, and San-in) are after Iwamori (1991).

It is also noted that the PHS plate beneath Chugoku exhibits a complex morphology with laterally various subduction angles and intra-slab discontinuities (Zhao et al., 2012, 2018), ascribed to subduction of an extinct spreading center and aseismic ridges formed in a marginal basin (Shikoku Basin; Pineda-Velasco et al., 2018). Subduction is shallower ($<30^\circ$) beneath central Chugoku, and becomes steeper ($>50^\circ$) to northern coastal region and western Chugoku.

The previous studies on basalts and high-Sr andesites and dacites in the Chugoku district gives an insight on secular change in the physical and chemical properties of slab-derived fluids. Feineman et al. (2013) proposed that high-Sr andesites and dacites were significantly affected by the contribution of subducted sediments through the Nankai trench. Pineda-Velasco et al. (2018) revealed the parental magmas of high-Sr andesites and dacites are formed by the mixing of partial melts from oceanic crust and sediment in various proportion and suggested the shallowing and flattening of the subducted PHS plate over time. Nguyen et al. (2020) further advocated that slab-derived components varied from those dominated by aqueous fluids to hydrous melt. The change in fluid type is due to morphological change of the PHS slab; it subducted at a steeper angle in the older period (12–5 Ma) and got shallower with bending in the younger period (5 Ma to present). The change in subduction angle resulted in tearing of the PHS slab as was suggested by Pineda-Velasco et al. (2018) and Nguyen et al. (2020). Pineda-Velasco et al. (2018) also speculated that, in the greater depth, the fluids can be released from serpentinite in the mantle section of the subducting slab. However, the precise sources and properties of subduction-zone fluids remain poorly constrained by those studies of SW Japan

island-arc magmas, although experimental studies have demonstrated that various fluids (aqueous solution, supercritical liquid or melt) can be produced from various lithologies in the slab (sediment, oceanic crust, or slab mantle).

Given that Hf preferentially resides in specific phases (e.g., garnet, zircon and rutile), it can be a useful tracer to examine the involvement of sediments (Patchett et al., 1984; Blichert-Toft and Frei, 2001; Tollstrup and Gill, 2005). Another important feature of Hf is that it is less mobile with aqueous fluids, while Pb, Sr and Nd are highly to moderately fluid-mobile elements (e.g., Keppler, 1996; Kogiso et al., 1997). Therefore, aqueous fluids may strongly affect Sr-Nd-Pb isotopic composition of wedge mantle and its derived melts, but it is not the case for Hf isotope (Keppler, 1996; Kogiso et al., 1997). Therefore, Hf isotope composition is an ideal tracer for the physical and chemical properties of slab-derived fluid (Kessel et al., 2005).

Pineda-Velasco et al. (2018) noted that parental magmas of high-Sr andesites and dacites should have significant amount of water. Pre-eruptive abundance of H₂O would be 2 wt% or greater, as indicated by the presence of hornblende phenocrysts in high-Sr andesites and dacites (Eggler, 1972; Green, 1972; Krawczynski et al., 2012). Thus, the magma source region, located beneath high-Sr andesite and dacite volcanoes, should be intensively hydrated. By contrast, the studies of mafic volcanic rocks suggested relatively anhydrous feature of their magma source regions within mantle wedge (Zellmer et al., 2012; Kimura et al., 2014). Numerical experiments of slab thermal structure also demonstrate low fluid fluxing from the PHS slab beneath the Quaternary volcanoes, owing to intensive dehydration at shallower depth (40 km) via transformation of basaltic crust of the slab to eclogite-facies rock (Peacock and Wang, 1999; Tatsumi et al., 2020). Thus, Pineda-Velasco et al. (2018) ascribed the supplier of water to serpentinized mantle section of the PHS slab. The slab tearing allows the exposure of mantle

section of the PHS slab to asthenospheric mantle, resulting dehydration by serpentinite breakdown.

It has been considered that serpentinitized mantle section in the subducting oceanic lithosphere is an important reservoir of delivering water to sub-arc mantle (Tenthorey and Hermann, 2004). Dehydration of serpentine, a major mineral in serpentinite, show strong temperature dependency but this phase is fairly stable under elevating pressure conditions (Ulmer and Trommsdorft, 1995). Several studies pointed out the role of serpentinite breakdown that triggers the production of island-arc magmas (Walowski et al., 2015; Konrad-Schmolke et al., 2016; Yogodzinski et al., 2017), although the role of slab serpentinite in magma productions beneath the other arcs is poorly constrained. This is partly due to difficulty of detecting serpentinite contribution by geochemical analysis of volcanic rocks, given that serpentinite contains little amounts of Sr, Nd, Hf, and Pb, hence the tracers of these isotopes are not sensitive to this lithology within the slab. Recent studies argued the utilities of “non-traditional” isotope tracers for detecting the contribution of serpentinitized mantle in the slab to subduction zone fluids; those include hydrogen (Walowski et al., 2015), lithium (Tian et al., 2019; Liu et al., 2020), boron (Konrad-Schmolke et al., 2016), and magnesium (Hu et al., 2020; Teng et al., 2016).

To further constrain the properties of slab-derived fluids, it is essential to understand element transfer via fluids using isotope tracers with different element mobilities. Given that the above two studies on SW Japan utilized Sr, Nd and Pb isotope analyses, the applications of (1) isotope tracers of “fluid-immobile” elements, such as Hf and (2) isotope tracers of “more fluid-mobile” elements, such as Li, Mg and B may provide further constraints on this issue.

Below, the objective and the approaches in my works are described.

1. Chapter 2: Investigation of Hf isotopes to decipher temporal and spatial of slab-derived fluids properties.
2. Chapter 3: Investigation of B isotopes to explore the role of fluids released from the slab serpentinites during the slab melting processes.
3. Chapter 4: Development of chemical purification methods of Mg and Li, and optimization of instrumental analysis (MC-ICP-MS) for the discussion of Li and Mg isotopic data in Chugoku volcanic rocks.
4. Chapter 5: Investigation of Li isotopes aiming to discuss whether Li isotopes can be used to trace the slab-derived signals.
5. Chapter 6: Investigation of Mg isotopes to clarify the role of Mg isotope fractionation during slab melting and subsequent melt-mantle interaction.

2. Tectonic-geological background and geophysical observation in SW Japan

Southwest Japan is a volcanic island arc formed by subduction of the Philippine Sea (PHS) plate via the Nankai trench (**Figure 1-1a**). The magmatism in this arc has been active during the last 12 Myr and has produced various volcanic rocks distributed in the Kyushu and Chugoku districts (Feineman et al., 2013; Iwamori, 1991; Kimura, 2005, 2014; Mahony et al., 2011; Morris, 1995; Nakamura et al., 1985, 1990; Pineda-Velasco et al., 2018; Sakuyama et al., 2014, 2009; Tatsumi et al., 2003, 2006).

The PHS plate has topographic prominences consisting of seamounts, island chains and an extinct spreading center, which are located within or at the periphery of a marginal basin (Shikoku Basin) formed between 26 and 15 Myr ago or Ma (Okino et al., 1994). The prominences, consisting of the Izu-Bonin arc in the east, Kinan Seamounts and Shikoku Basin spreading center (SBSC) in the center, and Kyushu-Palau ridge (KPR) in the west, are currently

colliding with the Nankai trench (Kodaira et al., 2004; Toda et al., 2008).

The PHS plate has been subducting into Nankai Trough with a velocity of 3 to 5 cm/yr since 15 Ma (Sdrolias et al., 2004). Continuous subduction has induced a number of large earthquakes (Nakajima and Hasegawa, 2007), including 1944 Tonankai ($M_s = 8.2$), 1946 Nankai ($M_s = 8.3$), 1995 Kobe ($M_s = 7.2$), 2000 western Tottori ($M_s = 7.3$), and 2001 Geiyo ($M_s = 6.4$). Subduction of PHS plate also plays a major role in volcanic activity in SW Japan. Since this oceanic plate is young and warmer, thermodynamic model predicts that intensive dehydration occurs as shallow as 60 km (Peacock, 2003). Trench-parallel narrow seismic zone is clearly observed at the slab depth of *c.* 50 km (Seno et al., 2001; Zhao et al., 2012), that is the zone of low-frequency tremors (LFT) of non-volcanic origin (Obara, 2002; Shelly et al., 2006). The LFT is considered to have been formed by dehydration of PHS slab, consistent with thermodynamic prediction (Peacock, 2003). Fluids released by slab dehydration led to fracturing of the desiccated slab and hydration of the base of wedge mantle (Seno and Yamasaki, 2003; Wang et al., 2006). As a result, shear slips occur along the interface of subducting slab and wedge mantle (Shelly et al., 2007). Prominent LFT formation in SW Japan demonstrates intensive dehydration in shallower depths (40–50 km) owing to its high T/P gradient during subduction (Wang et al., 2006).

Using numerous high-resolution seismic data, lateral and vertical variation of seismic tomography of PHS slab have been observed (Okada et al., 2004; Obara et al., 2005). The PHS slab exhibits seismicity in > 60 km depth beneath Kannabe-Oki Island or the Abu-Tsushima Island areas and is traced to the depth of 400 km beneath the Sea of Japan (Zhao et al., 2012; Huang et al., 2013). These discontinuities are interpreted as tears of the PHS slab, probably caused by the subducted Kyushu-Palau Ridge and Kinan Seamount Chain (Zhao et al., 2012; Huang et al., 2013; Pineda-Velasco et al., 2018). Heat flow measurements in Nankai Trough

revealed on-going subduction of these ridges (Yamano et al., 1984).

Seismic tomography also reveals thermal structure of wedge mantle and crust beneath the SW Japan (Utsu, 1967; Katsumata, 2010; Salah and Zhao, 2004; Yamane et al., 2012). An inclined high-velocity (V) and low-attenuation (i.e., high- Q) region corresponding to the Wadati-Benioff zone, is surrounded by low- V and low- Q zones that correspond to hotter regions within the mantle wedge (Sato et al., 1988, 1989). This V - Q distribution is interpreted as deep-mantle-rooted active upwelling that is intruded by subducting slab.

The Moho depth (crust thickness) beneath Chugoku was estimated to be *c.* 30 km, the depth corresponding to the location of seismic wave deflections (Salah and Zhao, 2004; Katsumata, 2010). Katsumata (2010) noted that the Moho depth beneath Chugoku is significantly shallower than the adjacent regions (central Honshu and Kyushu where the Moho depths are *c.* 40 km) and considered that the Chugoku district have experienced crustal extension and thinning related to the opening of Sea of Japan during Miocene (Otofujii et al., 1991).

3. Volcanic history of the Chugoku district

The Chugoku district is located in the westernmost part of Honshu. This district is subdivided into trench-parallel zones, namely San-yo zone and San-in zone, respectively (Figure 1-2). In some studies, transitional zone between San-yo and San-in zones is referred to as Seki-ryo zone (Iwamori, 1991). In the south of the Chugoku district, two trench-parallel zones are defined as Outer zone and Setouchi zone; the former is located in southern part of Shikoku, and the latter straddle the region between northern Shikoku and southern Chugoku including islets in Seto Inland Sea.

The volcanism in the Chugoku district began at 25 Ma and continues to present (Kimura et al., 2005). Based on temporal distribution and petrologic types of erupted products in the

Chugoku, Setouchi and Outer zones, Kimura et al. (2005) subdivided into volcanic activity into 4 stages. The Stage I volcanism is related to the rifting of Sea of Japan during 25–17 Ma (Poucllet et al., 1994). The Stage II volcanism occurred after cessation of the rifting of Sea of Japan and is related to incipient subduction of PHS during 17–12 Ma (Tatsumi, 2006). The Stage III volcanism occurred during 12–4 Ma and mainly produced intra-plate type basaltic volcanoes (Nakamura et al., 1989; Iwamori, 1991). The Stage IV volcanism has occurred since 4 Ma and is characterized by voluminous emplacements of high-Sr andesites and dacites (Morris, 1995; Feineman et al., 2013; Kimura et al., 2014; Pineda-Velasco et al., 2018). Nguyen et al. (2020) refined three episodes of volcanism in Stages III and IV by Kimura et al. (2005) as (1) episode 1 from 12 to 8 Ma, (2) episode 2 from 8 to 4 Ma, and (3) episode 3 from 4 Ma to recent (**Figure 1-3**). Below, the volcanic activities in each stage/episode are overviewed. We follow the trace-element-based nomenclature of these volcanic rocks following the previous studies (Tatsumi & Ishizaka, 1982; Kimura et al., 2014; Pineda-Velasco et al., 2018; Nguyen et al., 2020); Mafic volcanic rocks referred to as OIB and IAB are discriminated based on trace-element abundance patterns. The OIB has trace-element abundance patterns similar to intraplate basalts while the IAB has trace-element abundance patterns similar to island-arc basalts (Kimura et al., 2005, 2014; Pineda-Velasco et al., 2018; Nguyen et al., 2020). The HMA are primitive andesitic rocks with FeO^*/MgO ratios < 1 [where FeO^* is total Fe as FeO ; Tatsumi and Ishizaka (1982)]. The classification for andesites and dacites is based on the extent of Sr enrichment and Y depletion; ADK shows marked enrichment of Sr and depletion of Y (hence high Sr/Y ratio), while IAA does not exhibit such an anomaly.

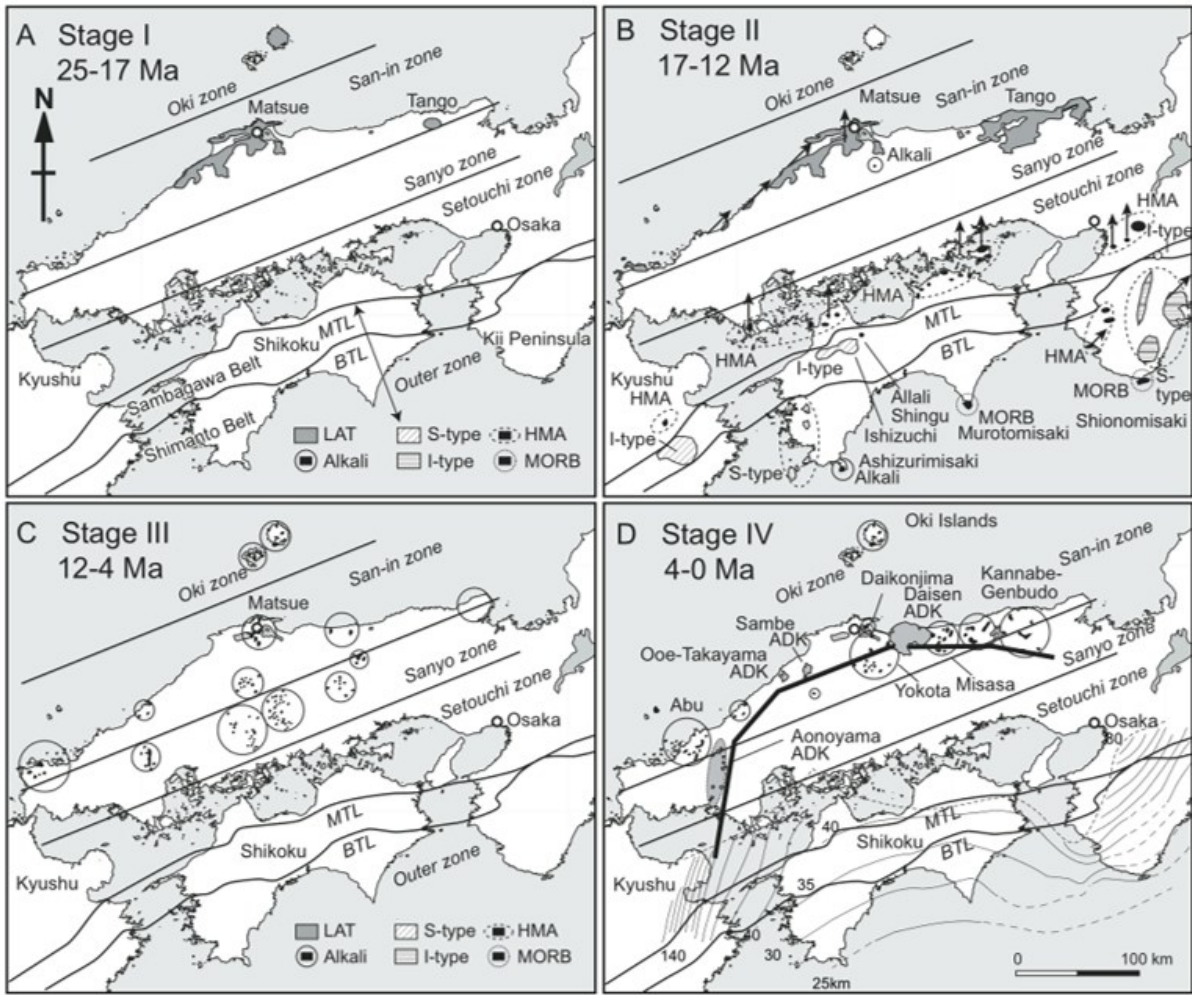


Figure 1-2. Cenozoic volcanic activity in the SW Japan arc in the last 25 Myrs, subdivided into Stages I (25–17 Ma), II (17–12 Ma), III (12–4 Ma) and IV (4–0 Ma).

The figure is modified from [Kimura et al. \(2005\)](#). Abbreviations in the Figure 1-2 are as follows: MTL, Median Tectonic Line; BTL, Butsuzo Tectonic Line; LAT, low-alkali tholeiite basalt; Alkali, alkali basalt; HMA, high-magnesium andesite; ADK, adakitic andesite and dacite; MORB, gabbroic intrusions with trace-element abundance similar to mid-oceanic-ridge basalt.

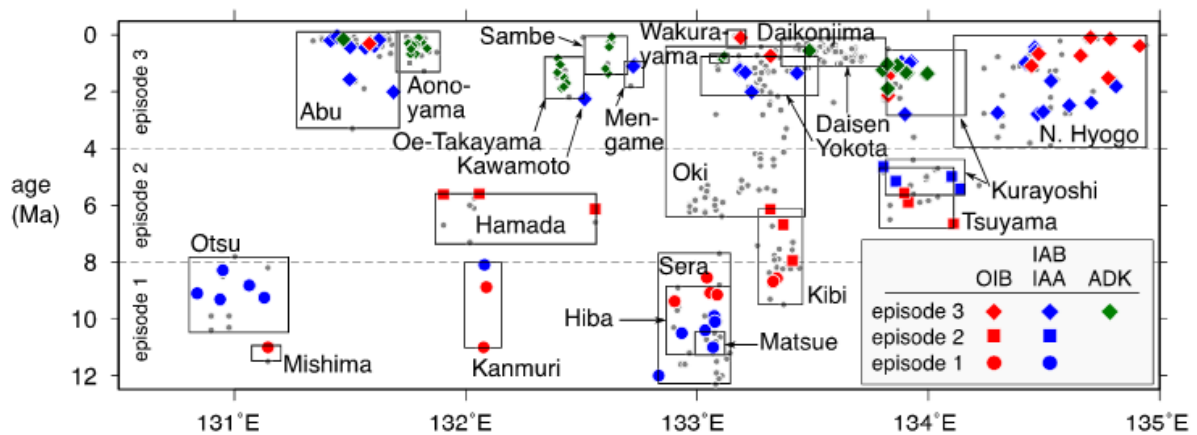


Figure 1-3. Spatial and temporal distribution of volcanic rocks in the Chugoku district (12 Ma to recent; modified from Nguyen et al., 2020).

3.1 Stage-I volcanic activity: 25–17 Ma

At 25–17 Ma, the volcanism was confined to the San-in zone (Matsue and northern Hyogo) and an island in Sea of Japan (Oki-Dogo). This activity is characterized by eruptions of sub-alkaline mafic to felsic magmas (**Figure 1-2**). Asthenospheric injection induced by the rifting of back-arc basin (Sea of Japan) is suggested as trigger for the volcanic activity (Pouquet et al., 1994).

3.2 Stage-II volcanic activity: 17–12 Ma

At 17–12 Ma, the volcanism spread across the entire Chugoku zone (Kimura et al., 2005; **Figure 1-2**). Paleomagnetic and geochronological studies of the volcanic rocks in this stage revealed a rapid clockwise deflection of the SW Japan arc, caused by the opening of Sea of Japan, during 16–14 Ma (Otofujii et al., 1991). In the San-in zone, the eruptions of sub-alkaline mafic to felsic magmas continued, while in the fore-arc region (Setouchi zone) high-magnesia andesite (HMA) had erupted (Shimoda et al., 1998; Kimura et al., 2005; Tatsumi, 2006). Mafic intrusions in Cape Ashizuri, Cape Muroto, and Cape Shiono, located in the Outer zone, are also regarded as products of the fore-arc magmatism during this stage (Murakami et al., 1983; Miyake, 1985; Hamamoto and Sato, 1987; Miyake and Hisatomi, 1985; Kimura et al., 2005).

3.3 Episode 1 in Stage-III/IV volcanic activity: 12–8 Ma

Volcanic activity in Episode 1 occurred in seven volcanic fields including Otsu, Mishima, Kanmuri, Sera, Hiba, Matsue, and Kibi, from west to east (**Figures 1-1 and 1-3**). The oldest activities occurred in the central to western regions in the Chugoku district. Eruptions of mafic lavas began at 12–11 Ma in the Mishima, Kanmuri, Sera, Hiba, and Matsue volcanic fields, and at 10–9 Ma in the Otsu and Kibi volcanic fields ([Nguyen et al., 2020](#)). The volcanism during 12–9 Ma produced both the OIB and IAB. Except for the Kanmuri and Sera volcanic fields, OIB and IAB lavas do not coexist in individual volcanic regions. In general, IAB lavas occur in the San-in region (closer to rear-arc; Otsu, Hiba, and Matsue volcanic fields), whereas OIB lavas occur in the San-yo region (closer to fore-arc; Kanmuri, Sera, and Kibi), except for Mishima in the Sea of Japan.

3.4 Episode 2 in Stage-III/IV volcanic activity: 8–4 Ma

Mafic lavas formed in Episode 2 are distributed in five volcanic fields, the Hamada, Oki, Kibi, Tsuyama, and Kurayoshi fields (denoted as old Kurayoshi volcanic activity; **Figures 1-1 and 1-3**). Volcanic activity in this period is dominated by eruptions of OIB, and IAB activity is confined in the eastern part of the Chugoku district (Kurayoshi volcanic field) in the latter quarter of Episode 2 (5–4 Ma).

3.5 Episode 3 in Stage-III/IV volcanic activity: 4–0 Ma

Since 3 Ma, the volcanic activities have been dominated by eruptions of high-Sr (adakitic) andesites and dacites (**Figures 1-2 and 1-3**; [Tamura et al., 2000](#); [Feineman et al., 2013](#); [Kimura et al., 2014](#); [Pineda-Velasco et al., 2018](#)). These high-Sr andesites and dacites comprise volcanic complexes in association with monogenetic basalt volcanoes (both IAB and OIB) in temporal and spatial proximities. The Episode-3 volcanisms have been confined to the San-in regions and Oki-Dogo Island in Sea of Japan.

4. Previous studies on volcanic rocks in the Chugoku district

Petrologic and geochemical studies of volcanic rocks in the Chugoku district have been conducted in the last four decades. These studies were attempted to constrain the sources and generation processes of parental magmas of (1) high-Mg andesites in Setouchi during Miocene, (2) high-Sr andesites and dacites in the San-in zone during Pliocene–Holocene, and (3) basalts which form monogenetic volcanoes in the entire Chugoku region during Miocene–Holocene.

4.1 High-Mg andesites in Setouchi during Miocene

The Miocene volcanism in the Setouchi region (termed Setouchi Volcanic Belt or SVB) is characterized by eruptions of high-Mg andesites in association with high-Mg sub-alkaline basalts (Tatsumi, 2006). Tatsumi and co-workers have conducted numerous geologic, petrologic, geochronologic and geochemical studies of SVB volcanic rocks (e.g., Tatsumi and Ishizaka, 1982; Tatsumi, 2003; Shimoda et al., 1998; Hanyu et al., 2002; Tatsumi et al., 2001, 2002, 2008; Tatsumi and Hanyu, 2003; Tatsumi, 2006). The volcanic activity occurred in short period of time during 14.7 to 12.7 Ma. The HMA and basalts in SVB contain rocks with major-element compositions (Fe/Mg ratio and Ni abundance) in equilibrium with mantle peridotite (Tatsumi, 1982; Tatsumi and Ishizaka, 1982) under hydrous condition (Kushiro, 1974; Hirose, 1997). Isotopic studies indicate the involvements of significant amounts of sediments (Shimoda et al., 1998; Hanyu et al., 2002; Tatsumi and Hanyu, 2003), leading them to conclude that HMA was produced by melting of PHS slab (basaltic crust + sediment) and subsequent equilibration with mantle peridotite.

Kawamoto et al. (2011) proposed an alternative idea for HMA production based on in-situ X-ray observation of high-pressure experiments on analogues of sediment-derived melts under water-saturated condition (Figure 1-4). They demonstrated that sediments on PHS slab would have released supercritical fluids (SCF) at the depth greater than 80 km, and upward-migrating

two different petrologic types; aphyric and porphyritic types (Tsukui, 1985). Tamura et al. (2003) considered that aphyric nature of high-Sr andesites and dacites from Daisen volcano indicate superheating condition of these magmas just before eruptions (Figure 1-5). They explained superheating condition for aphyric magmas by melting of precursor andesite bodies solidified in shallow crustal level. In contrast, Pineda-Velasco et al. (2018) explained the coexistence of aphyric and porphyritic types by tapping magmas with different crystallinity in a chamber. The margin of a magma chamber should be mushy given that this part is cooled by surrounding wall rocks (Kuritani, 1998), while an interior part is essentially aphyric as this part has temperature higher than solidus of phenocryst phases. Differentiated feature of aphyric andesites can be attained by mixing of differentiated interstitial melts expelled from crystal mush layer and a main magma body (Kuritani, 1998).

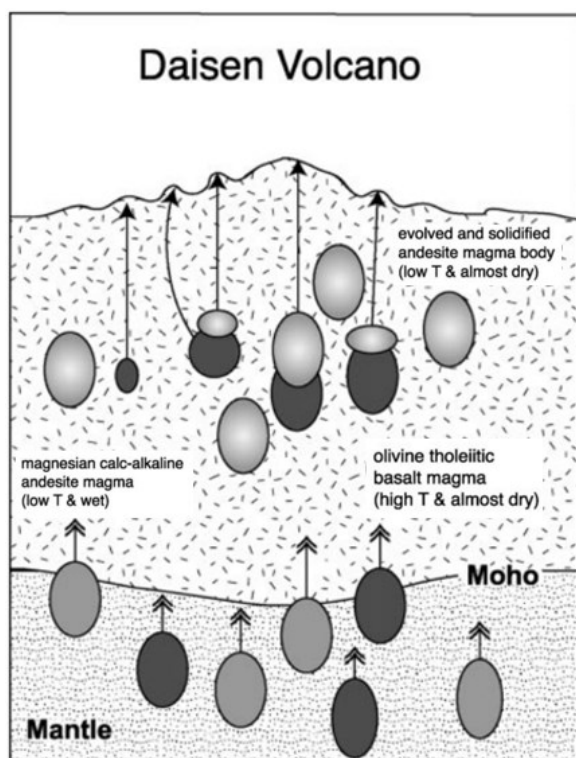


Figure 1-5. Schematic model for the productions of porphyritic and aphyric andesites in Daisen volcano.

The figure is modified from Tamura et al. (2003). Pre-existing andesite body in the crust was remelted

by heat supplied from emplacement of basalt (Yokota).

The other alternative idea for the genesis of high-Sr andesites and dacites was proposed by Zellmer et al. (2012). They found that H₂O abundances in primitive basalts decrease from those in Kyushu (3.5–6.5 wt%) to those in Chugoku (2 wt% or lower), based on plagioclase hygrometer (Lange et al., 2009). They noted that garnet can be stable if basaltic magma is anhydrous under lower crustal depth (Müntener & Ulmer, 2006); that is, high-Sr andesites and dacites could be produced by from anhydrous basalt magmas by fractional crystallization of garnet-bearing phase assemblage in lower crustal depth. However, this scenario cannot account for the difference in isotopic compositions of high-Sr andesites and dacites and associated basalts (Feineman et al., 2013; Pineda-Velasco et al., 2018). Also, this scenario could not provide an explanation about the occurrence of high-Sr andesites and dacites; it is confined to San-in zone, yet the crustal depth is relatively constant at 30 km in the entire Chugoku district (Salah and Zhao, 2004; Katsumata, 2010).

The slab-melting origin of high-Sr andesites and dacites in the Chugoku district, first proposed by Morris (1995), was reaffirmed by Feineman et al. (2013), Kimura et al. (2014), and Pineda-Velasco et al. (2018). Feineman et al. (2013) applied U-Th isotopic analysis of high-Sr andesites and dacites of Daisen volcano together with major- and trace-element and Sr-Nd-Pb isotope analyses. The Daisen intermediate magmas show trace element and isotopic evidence for interaction with garnet, consistent with partial melting of the hot, young (~20 Ma) Philippine Sea Plate. Isotopic similarities between Nankai Trough sediments and Miocene volcanics in the forearc of the modern Southwest Japan arc suggest that significant sediment was added to the mantle at the time of initiation of Shikoku Basin subduction at ~20 Ma [Ishikawa and Nakamura, 1994]. They speculated that remnants of this past sediment

subduction may have been relaminated at the base of the arc crust and/or contributed to a broadly sediment-contaminated mantle wedge.

[Kimura et al. \(2014\)](#) extended geochemical and isotopic investigations to high-Sr andesites and dacites from the other volcanoes in the Chugoku district; Aonoyama, Oe-Takayama, Sambe, and Kurayoshi volcanic fields (**Figure 1-1**). They reached the conclusion for the genesis of high-Sr andesites and dacites essentially identical to [Feineman et al. \(2013\)](#). They also argued that high-Sr andesites and dacites experienced significant crustal assimilation during their ascent for the following observations: (1) Pb-isotopic linear array formed by high-Sr andesites and dacites points toward the composition distinctly different from subducted crustal rocks (basalt and sediment), and (2) amphibole phenocryst in high-Sr dacites from Daisen shows the compositional zonation; high Sr/Y ratio in its core and low Sr/Y ratio in its margin. However, the observation (1) was suggested to be due to analytical artifact ([Pineda-Velasco et al., 2015](#)), and the observation (2) may be explained by cotectic crystallization of amphibole and plagioclase, the latter largely consumes Sr in a residual magma and thus later-formed amphibole rim is depleted in Sr (low Sr/Y).

[Pineda-Velasco et al. \(2018\)](#) conducted detailed geochronological (K-Ar) and geochemical (major and trace element concentrations, and Sr-Nd-Pb isotope analyses) investigations of high-Sr andesites and dacites in the entire Chugoku (Aonoyama, Oe-Takayama, Sambe, Wakurayama, Daisen and Kurayoshi volcanic fields; see **Figures 1-1 and 1-2**). They found spatial coincidence of high-Sr andesite and dacite volcanoes and discontinuities of aseismic slab of PHS plate (**Figure 1-1**). They demonstrated that geochemical signature of high-Sr andesites and dacites in the Chugoku district is best explained by melting of subducted PHS slab (sediment + basaltic crust) as was proposed by [Feineman et al. \(2013\)](#). In addition, they explained that basaltic magmas erupted in the vicinities of high-Sr andesites and dacites were

derived by melting of wedge mantle peridotite metasomatized by slab-derived melts (i.e., parental magmas of high-Sr andesites and dacites). This study first provides the causal link of basalts and high-Sr andesites and dacites as; a warm mantle upwelled through tears and induced dehydration of slab-mantle section and flux melting of crustal section of PHS slab, leading to evolution of parental magmas of high-Sr andesites and dacites. Siliceous slab melts react with surrounding mantle while the reaction mantle regime decompressed as its ascent. Thus, siliceous slab melts could reach the surface without solidification (**Figure 1-6**).

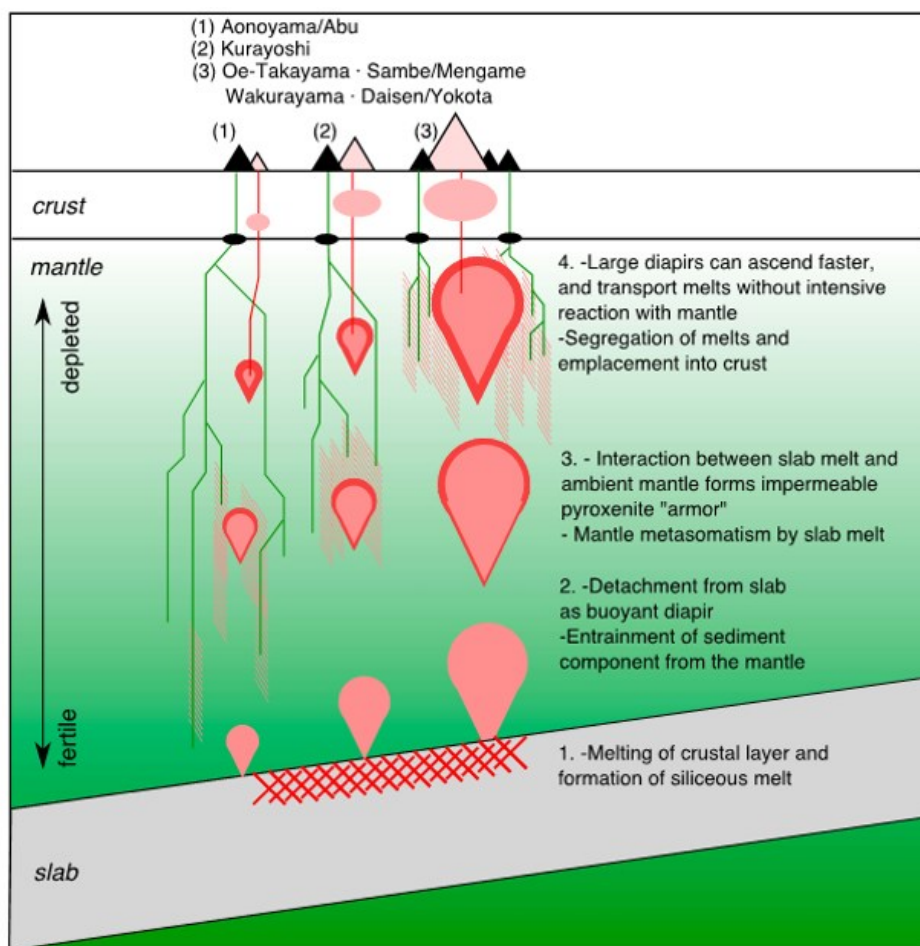


Figure 1-6. A model of transporting siliceous slab melts to surface in the Chugoku district.
The figure is modified from [Pineda-Velasco et al. \(2018\)](#).

4.3 Monogenetic basalts in the entire Chugoku region during Miocene–Holocene

Basaltic volcanism has occurred during Episode 1 to Episode 3. [Nakamura et al. \(1985\)](#)

first presented Pb-isotope and trace-element geochemistry of alkali basalts in the Chugoku district together with trace-element analyses of alkali basalts in Kyushu, Northeast China and Korean Peninsula. They revealed lateral variations in the extents of depletions in Ta, Nb and Ti; basalts in Chugoku and Kyushu show slight depletions of these elements relative to elements with similar incompatibilities (K, Rb, and Pb), while basalts in Northeast China and Korean Peninsula do not show such elemental depletions. They attributed the lateral geochemical variation to decreasing contributions of fluids from the subducting Pacific plate to the upper mantle in the western Pacific margin. [Nakamura et al. \(1989, 1990\)](#) extended this idea using the analyses of geochemical and Nd-Sr isotopic compositions of Cenozoic basalts in these regions. Contributions from two different reservoirs (components) were identified from isotopic analyses; these reservoirs should reside in isolated mantle domains with different extents of long-term trace-element depletion. They considered that these mantle domains are located in different depths in the mantle; a depleted source is in the upper mantle, while a fertile source is in the lower mantle derived by a hot and buoyant upwelling flow (i.e., mantle plume). Given that aseismic slab of Philippine Sea plate could not be detected in 1980's, [Nakamura et al. \(1985, 1989, 1990\)](#) ascribed the “island-arc”-like geochemical feature of mafic volcanic rocks in SW Japan to subduction of Pacific plate (**Figure 1-7**).

[Iwamori \(1991, 1992\)](#) investigated across-arc variations in major and trace element compositions of basalts in the Chugoku district; at a given value of differentiation index (e.g., $Mg^{\#}$), whole-rock SiO_2 and Al_2O_3 abundances increase, while whole-rock FeO, MgO and CaO abundances decrease from San-yo to San-in. He attributed lateral variations in major element compositions to different depths of melt segregation from wedge mantle. [Iwamori \(1991\)](#) conducted melting experiments on magnesian basalts in the Chugoku district. From the experimental results, he estimated melt segregation depths to be 50–60 km (1.7–1.9 GPa)

beneath the San-yo zone and 20–30 km (*c.* 0.8 GPa) beneath the San-in zone, respectively.

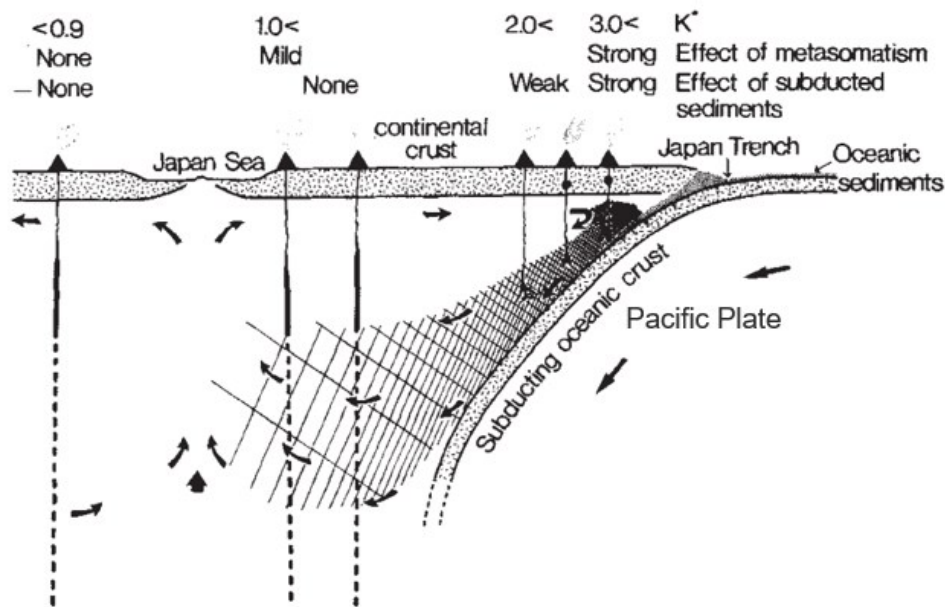


Figure 1-7. Schematic model for the genesis of alkaline basalts in SW Japan

The figure is modified from Nakamura et al. (1985). As a function of distance from Japan trench, the contribution from subducting oceanic crust to wedge mantle decreases, while the root of mantle upwelling flows become deeper.

With the occurrence of alkaline basalts in Oki islands with major element compositions similar those in the San-yo zone, he proposed an axisymmetric change of melting depth about the San-in region in a single mantle flow centered on the San-in zone (Figure 1-8). In his model, the role of Philippine Sea plate subduction is not considered. Also, temporal variation in tectonic background is not taken into account.

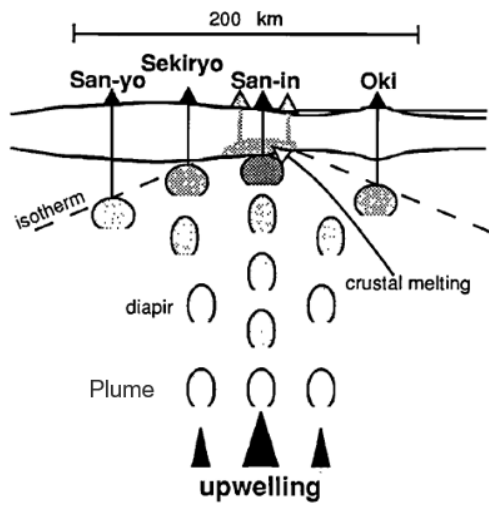


Figure 1-8. Schematic model of magma productions in the Chugoku district

The figure is modified from [Iwamori \(1991\)](#). An upwelling flow of asthenospheric mantle was centered on the San-in zone where melt segregation depth is shallower. With distance from San-in, melt segregation depths become deeper.

[Kimura et al. \(2003, 2005\)](#) conducted K-Ar dating on 108 samples and compiled the existing 334 dates, and examined the geologic and tectonic background of late Cenozoic volcanism in the Chugoku district. They proposed four stages of tectonic background. Stage I. At 25–17 Ma, PHS plate did not subduct into the trench. Arc-like magmatism in San-in zone is due to melting of mantle metasomatized by subducted Pacific plate. Stage II. At 17–11 Ma, PHS plate began to subduct. Its leading edge was melted due to its own intra-slab heat and produced high-Mg andesites in Setouchi volcanic belt. Stage III. The PHS slab continued to subduct, but its leading edge did not reach beneath the Chugoku. Basaltic magmatism in the Chugoku district is assumed to have been caused by asthenospheric upwelling from rear-arc side. The leading edge of PHS slab reached beneath the San-in zone where the interaction between PHS slab and a hot asthenospheric mantle led to melting of PHS slab and production of high-Sr andesites and dacites (ADK). They attributed the IAB magmas in Stage II erupted

in Sanin zone to melting of continental lithosphere metasomatized prior to this episode by fluids, probably released from the PAC Plate (**Figure 1-9**). However, later published data supported that IAB have a geochemical and isotopic composition consistent with the influence of PHS rather than that of PAC.

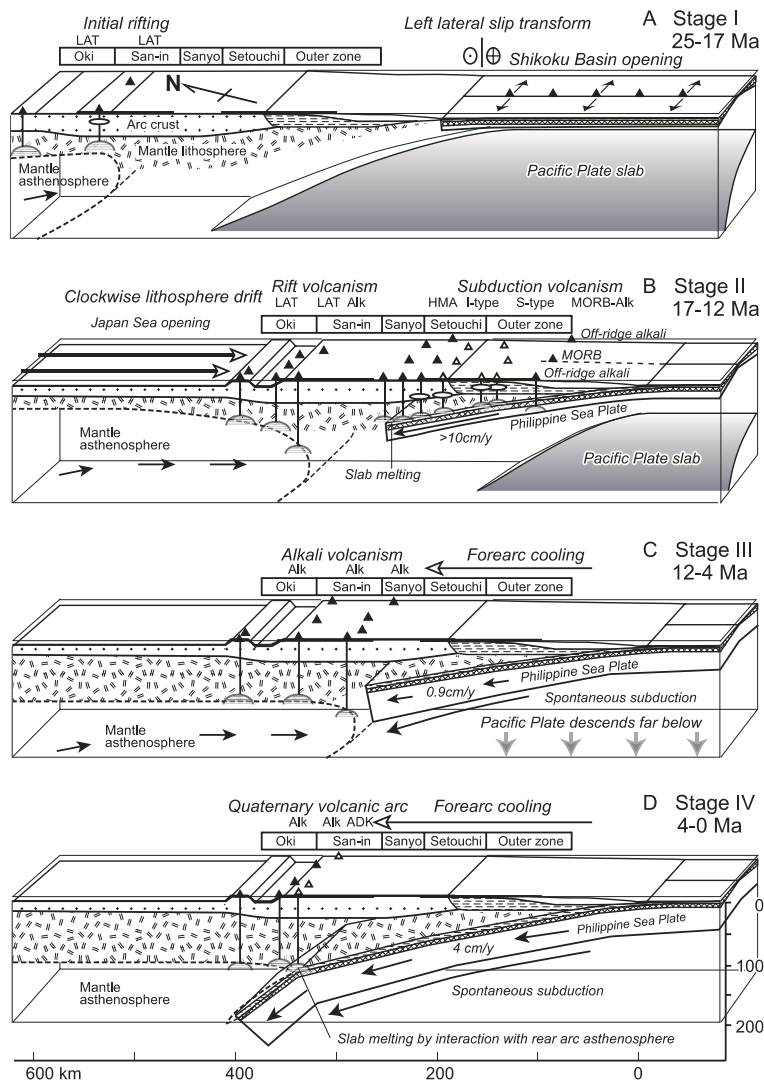


Figure 1-9. Schematic model for the volcanic and tectonic evolution of SW Japan

The figure is cited from [Kimura et al. \(2005\)](#). A: Stage I. At 25–17 Ma, PHS plate did not subduct into the trench. Arc-like magmatism in San-in zone is due to melting of mantle metasomatized by subducted Pacific plate. B: Stage II. At 17–11 Ma, PHS plate began to subduct. Its leading edge was melted due to its own intra-slab heat and produced high-Mg andesites in Setouchi volcanic belt. C: Stage III. The PHS slab continued to subduct, but its leading edge did not reach beneath the Chugoku.

Basaltic magmatism in the Chugoku district is assumed to have been caused by asthenospheric upwelling from rear-arc side. D: The leading edge of PHS slab reached beneath the San-in zone where the interaction between PHS slab and a hot asthenospheric mantle led to melting of PHS slab and production of high-Sr andesites and dacites (ADK).

[Feineman et al. \(2013\)](#) determined alkaline basalts from Southwest Japan and suggested that the basalts erupted at the Daisen volcanic field are not parental to the intermediate magmas and contain a small contribution of EM1-like mantle common in Sea of Japan alkali basalts. The regional alkali basalts have previously been attributed to a mantle plume rising beneath the Sea of Japan ([Nakamura et al., 1985, 1989, 1990](#)). [Pineda-Velasco et al. \(2018\)](#) proposed that small amount (1–4 wt %) of slab melt is mixed with a mantle, then the hybrid source is melted at degree of 1 to 15% to produce IAB in Episode 3. Two types of IAB lavas were identified; one shows strong negative anomalies of Nb and Ta (low-Nb lava), whereas another shows weak negative anomalies for these elements (high-Nb lava). The high-Nb type occurs in Abu and Kurayoshi, while Mengame and Yokota regions yield the low-Nb type. Trace element patterns of low-Nb lavas are reproduced well by 5% melting of the metasomatized mantle consisting of 96% DMM (depleted MORB mantle) and 4% slab melt in the spinel-stability field. Instead, the melting of PUM (primitive upper mantle) source can reproduce the pattern of these high-Nb basalts with $f = 4\%$ and degree of melting at 5% in the garnet-stability field. Those studies supplied a modern comprehensive geochemistry to volcanoes in the southwest Japan, however, it is still poorly understood how the subduction system in the southwest Japan has evolved and those studies could not control the slab morphology back to 12 Ma when the slab had already subducted.

[Kimura et al. \(2014\)](#) analyzed ocean island basalt (OIB), shoshonite (SHO), arc-type alkali basalt (AB), typical subalkalic arc basalt (SAB), high-Mg andesite (HMA), and adakite (ADK)

from the Chugoku district and suggested that those magmas originated from slab melts that induced flux melting of mantle peridotite. They proposed that the suites differ mostly in the mass fraction of slab-melt flux, increasing from SHO through AB, SAB, HMA, to ADK. The pressure and temperature of mantle melting decreases in the same order. The sediment component is most prominent in Setouchi HMA, followed by Abu SAB, Abu HMA, Yokota ABL/ABH, and Daisen AA/ADK, with the least in Aonoyama ADK and Abu SHO. The atypical suites associated with hot subduction result from unusually large mass fractions of slab melt and unusually cool mantle temperatures.

Nguyen et al. (2020) conducted detailed investigations of the geochemistry and geochronology of late Cenozoic (12 Myrs or younger) volcanic rocks, mainly on two types of mafic rocks (OIB and IAB), from the entire volcanic field in Chugoku (**Figure 1-1**). The mafic magmas would have been extracted from the upwelling mantle at different depths (80- to 40-km depth for OIB and 60- to 30-km depth for IAB). Production of IAB parental magmas was assisted by addition of fluids released from the subducting slab, which lowers the solidus of refractory mantle by progressive melt extraction. Secular variation in the geochemistry of IAB reveals the transition of slab-derived fluid from that dominated by an aqueous component to that with a melt component (**Figure 1-10**). The variation in fluid composition is interpreted as a change in the thermal conditions within the subducting slab, which most likely resulted from shallowing of subduction angle (**Figure 1-10**). They interpret the change as a consequence of the interaction between the asthenospheric mantle upwelling from the back-arc side and the oceanic lithosphere sinking from the trench side (**Figure 1-10**). However, the properties of slab-derived fluids (aqueous solution, supercritical liquid or melt) are still not precisely constrained.

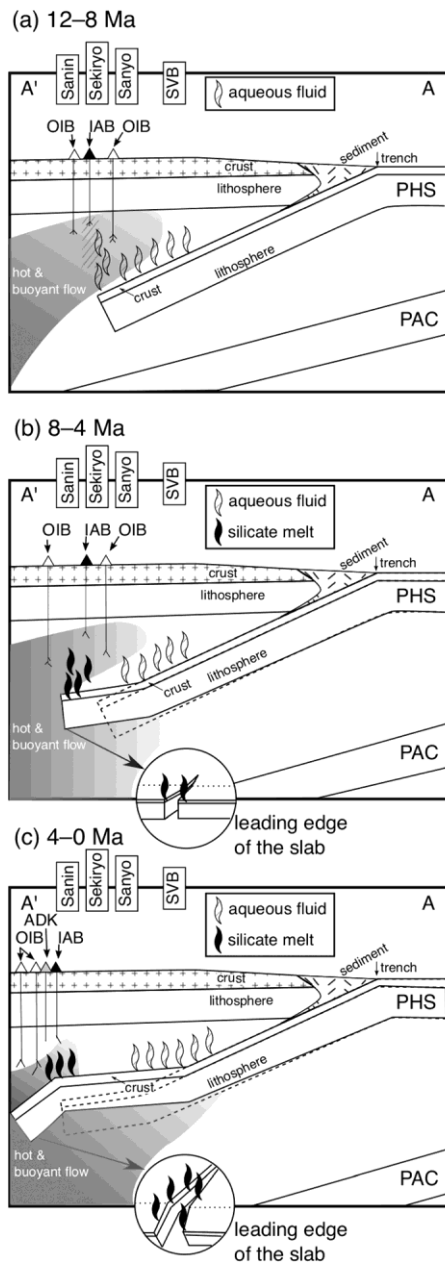


Figure 1-10. Schematic models for the evolution of late Cenozoic volcanic activity in the Chugoku and the morphology of subducting PHS plate in relation to plate configuration

The figure is cited from [Nguyen et al. \(2020\)](#). (a): In 12–8 Ma, the PHS slab subducted at steeper angle. Relatively cooler PHS slab released fluids dominated by aqueous solution; (b) The PHS slab began to be bent by collision with asthenospheric flow and its leading edge started to be torn apart. (c) Further interaction between the PHS slab and mantle led to propagation of slab tears, dehydration of the slab (mantle section) and melting of its crustal layer. Hydrous melts produced ascent with buoyant mantle and erupted as high-Sr andesites and dacites.

5. References

- Asamori K. and Zhao D. (2015) Teleseismic shear wave tomography of the Japan subduction zone. *Geophys. J. Int.* **203**, 1752-1772.
- Blichert-Toft J. and Frei R. (2001) Complex Sm-Nd and Lu-Hf isotope systematics in metamorphic garnets from the Isua supracrustal belt, West Greenland. *Geochim. Cosmochim. Ac.* **65**, 3177-3189.
- Christensen N. I. (1978) Ophiolites, seismic velocities and oceanic crustal structure. *Tectonophysics* **47**, 131-157.
- Eggler D. H. (1972) Amphibole stability in H₂O-undersaturated calc-alkaline melts. *Earth Planet. Sc. Lett.* **15**, 28-34.
- Green T. H. (1972) Crystallization of calc-alkaline andesite under controlled high-pressure hydrous conditions. *Contrib. Mineral. Petr.* **34**, 150-166.
- Hamamoto R. (1987) Rb-Sr age of granophyre associated with the Cape Muroto gabbroic complex. *Kyushu Univ. Sci. Rep.(Geol.)* **15**, 1-5.
- Hirose K. and Kawamoto T. (1995) Hydrous partial melting of lherzolite at 1 GPa: The effect of H₂O on the genesis of basaltic magmas. *Earth Planet. Sc. Lett.* **133**, 463-473.
- Hu Y., Teng F. and Ionov D. A. (2020) Magnesium isotopic composition of metasomatized upper sub-arc mantle and its implications to Mg cycling in subduction zones. *Geochim. Cosmochim. Ac.* **278**, 219-234.
- Huang Z., Zhao D., Hasegawa A., Umino N., Park J. and Kang I. (2013) Aseismic deep subduction of the Philippine Sea plate and slab window. *J. Asian Earth Sci.* **75**, 82-94.
- Iwamori H. (1991) Zonal structure of Cenozoic basalts related to mantle upwelling in southwest Japan. *Journal of Geophysical Research: Solid Earth* **96**, 6157-6170.
- Kano K., Kaneko N., Ishizuka O., Tiba T. and Yanagisawa Y. (2014) The beginning of lifetime

- of Dozen Volcano, Oki Islands, SW Japan. *Bull Volcanol Soc Japan* **59**, 77-88.
- Katsumata A. (2010) Depth of the Moho discontinuity beneath the Japanese islands estimated by travelttime analysis. *Journal of Geophysical Research: Solid Earth* **115**.
- Keppler H. (1996) Constraints from partitioning experiments on the composition of subduction-zone fluids. *Nature* **380**, 237-240.
- Kessel R., Schmidt M. W., Ulmer P. and Pettke T. (2005) Trace element signature of subduction-zone fluids, melts and supercritical liquids at 120–180 km depth. *Nature* **437**, 724-727.
- Kimura J. I., Stern R. J. and Yoshida T. (2005) Reinitiation of subduction and magmatic responses in SW Japan during Neogene time. *Geol. Soc. Am. Bull.* **117**, 969-986.
- Kimura J. I., Kunikiyo T., Osaka I., Nagao T., Yamauchi S. and Kakubuchi S., et al. (2003) Late Cenozoic volcanic activity in the Chugoku area, southwest Japan arc during back-arc basin opening and reinitiation of subduction. *Isl. Arc* **12**, 22-45.
- Kodaira S., Iidaka T., Kato A., Park J., Iwasaki T. and Kaneda Y. (2004) High pore fluid pressure may cause silent slip in the Nankai Trough. *Science* **304**, 1295-1298.
- Kogiso T., Omori S. and Maruyama S. (2009) Magma genesis beneath Northeast Japan arc: a new perspective on subduction zone magmatism. *Gondwana Res.* **16**, 446-457.
- Konrad-Schmolke M., Halama R. and Manea V. C. (2016) Slab mantle dehydrates beneath Kamchatka-Yet recycles water into the deep mantle. *Geochemistry, Geophysics, Geosystems* **17**, 2987-3007.
- Krawczynski M. J., Grove T. L. and Behrens H. (2012) Amphibole stability in primitive arc magmas: effects of temperature, H₂O content, and oxygen fugacity. *Contrib. Mineral. Petr.* **164**, 317-339.
- Kuritani T. (1998) Boundary layer crystallization in a basaltic magma chamber: evidence from

- Rishiri Volcano, northern Japan. *J. Petrol.* **39**, 1619-1640.
- Kushiro I. (1974) Melting of hydrous upper mantle and possible generation of andesitic magma: an approach from synthetic systems. *Earth Planet. Sc. Lett.* **22**, 294-299.
- Kushiro I., Syono Y. and Akimoto S. I. (1968) Melting of a peridotite nodule at high pressures and high water pressures. *Journal of Geophysical Research* **73**, 6023-6029.
- Lange R. A., Frey H. M. and Hector J. (2009) A thermodynamic model for the plagioclase-liquid hygrometer/thermometer. *Am. Mineral.* **94**, 494-506.
- Liu H., Sun H., Xiao Y., Wang Y., Zeng L. and Li W., et al. (2019) Lithium isotope systematics of the Sumdo Eclogite, Tibet: Tracing fluid/rock interaction of subducted low-T altered oceanic crust. *Geochim. Cosmochim. Ac.* **246**, 385-405.
- Liu L. and Stegman D. R. (2011) Segmentation of the Farallon slab. *Earth Planet. Sc. Lett.* **311**, 1-10.
- Mahony S. H., Wallace L. M., Miyoshi M., Villamor P., Sparks R. S. J. and Hasenaka T. (2011) Volcano-tectonic interactions during rapid plate-boundary evolution in the Kyushu region, SW Japan. *Geol. Soc. Am. Bull.* **123**, 2201-2223.
- Manning C. E. (2004a) The chemistry of subduction-zone fluids. *Earth Planet. Sc. Lett.* **223**, 1-16.
- Manning C. E. (2004b) The chemistry of subduction-zone fluids. *Earth Planet. Sc. Lett.* **223**, 1-16.
- Miyake Y. (1985) A Miocene forearc magmatism at Shionomisaki, southwest Japan. *Formation of Active Ocean Margins*, 411-422.
- Miyake Y. (1985) MORB-like tholeiites formed within the Miocene forearc basin, southwest Japan. *Lithos* **18**, 23-34.
- Morris P. A. (1995) Slab melting as an explanation of Quaternary volcanism and aseismicity in

- southwest Japan. *Geology* **23**, 395.
- Müntener O. and Ulmer P. (2006) Experimentally derived high-pressure cumulates from hydrous arc magmas and consequences for the seismic velocity structure of lower arc crust. *Geophys. Res. Lett.* **33**.
- Murakami N., Kanisawa S. and Ishikawa K. (1983) High fluorine content of Tertiary igneous rocks from Cape of Ashizuri, Kochi Prefecture, Southwest Japan. *The Journal of the Japanese Association of Mineralogists, Petrologists and Economic Geologists* **78**, 497-504.
- Nakajima J. and Hasegawa A. (2007) Subduction of the Philippine Sea plate beneath southwestern Japan: Slab geometry and its relationship to arc magmatism. *Journal of Geophysical Research: Solid Earth* **112**.
- Nakamura E., Campbell I. H., Mcculloch M. T. and Sun S. S. (1989) Chemical geodynamics in a back arc region around the Sea of Japan: Implications for the genesis of alkaline basalts in Japan, Korea, and China. *Journal of Geophysical Research: Solid Earth* **94**, 4634-4654.
- Nakamura E., Campbell I. H. and Sun S. (1985) The influence of subduction processes on the geochemistry of Japanese alkaline basalts. *Nature* **316**, 55-58.
- Nakamura E., Mcculloch M. T. and Campbell I. H. (1990) Chemical geodynamics in the back-arc region of Japan based on the trace element and Sr⁸⁷/Nd isotopic compositions. *Tectonophysics* **174**, 207-233.
- Nguyen T. T., Kitagawa H., Pineda Velasco I. and Nakamura E. (2020) Feedback of Slab Distortion on Volcanic Arc Evolution: Geochemical Perspective From Late Cenozoic Volcanism in SW Japan. *Journal of Geophysical Research: Solid Earth* **125**.
- Obara K. (2002) Nonvolcanic deep tremor associated with subduction in southwest Japan. *Science* **296**, 1679-1681.
- Obara K. and Ito Y. (2005) Very low frequency earthquakes excited by the 2004 off the Kii

- peninsula earthquakes: A dynamic deformation process in the large accretionary prism. *Earth, Planets and Space* **57**, 321-326.
- Okada Y., Kasahara K., Hori S., Obara K., Sekiguchi S. and Fujiwara H., et al. (2004) Recent progress of seismic observation networks in Japan—Hi-net, F-net, K-NET and KiK-net—. *Earth, Planets and Space* **56**, xv-xxviii.
- Okino K., Shimakawa Y. and Nagaoka S. (1994) Evolution of the Shikoku Basin. *Journal of geomagnetism and geoelectricity* **46**, 463-479.
- Otofuji Y., Itaya T. and Matsuda T. (1991) Rapid rotation of southwest Japan— palaeomagnetism and K-Ar ages of Miocene volcanic rocks of southwest Japan. *Geophys. J. Int.* **105**, 397-405.
- Patchett P. J., White W. M., Feldmann H., Kielinczuk S. and Hofmann A. W. (1984) Hafnium/rare earth element fractionation in the sedimentary system and crustal recycling into the Earth's mantle. *Earth Planet. Sc. Lett.* **69**, 365-378.
- Peacock S. M. (2003) Thermal structure and metamorphic evolution of subducting slabs. *Geophysical Monograph-American Geophysical Union* **138**, 7-22.
- Peacock S. M. and Wang K. (1999) Seismic Consequences of Warm versus Cool Subduction Metamorphism: Examples from Southwest and Northeast Japan. *Science* **286**, 937-939.
- Pineda-Velasco I., Kitagawa H., Nguyen T. T., Kobayashi K. and Nakamura E. (2018) Production of High-Sr Andesite and Dacite Magmas by Melting of Subducting Oceanic Lithosphere at Propagating Slab Tears. *Journal of Geophysical Research: Solid Earth* **123**, 3698-3728.
- Pouclet A., Lee J., Vidal P., Cousens B. and Bellon H. (1994) Cretaceous to Cenozoic volcanism in South Korea and in the Sea of Japan: magmatic constraints on the opening of the back-arc basin. *Geological Society, London, Special Publications* **81**, 169-191.

- Ringwood A. E. (1974) The petrological evolution of island arc systems: Twenty-seventh William Smith Lecture. *J. Geol. Soc. London*. **130**, 183-204.
- Sakuyama T., Nakai S., Yoshikawa M., Shibata T. and Ozawa K. (2014) Progressive Interaction between Dry and Wet Mantle during High-temperature Diapiric Upwelling: Constraints from Cenozoic Kita-Matsuura Intraplate Basalt Province, Northwestern Kyushu, Japan. *J. Petrol.* **55**, 1083-1128.
- Sakuyama T., Ozawa K., Sumino H. and Nagao K. (2009) Progressive Melt Extraction from Upwelling Mantle Constrained by the Kita-Matsuura Basalts in NW Kyushu, SW Japan. *J. Petrol.* **50**, 725-779.
- Salah M. K. and Zhao D. (2004) Mapping the crustal thickness in southwest Japan using Moho-reflected waves. *Phys. Earth Planet. In.* **141**, 79-94.
- Sato H., Sacks I. S., Murase T., Muncill G. and Fukuyama H. (1989) Qp-melting temperature relation in peridotite at high pressure and temperature: Attenuation mechanism and implications for the mechanical properties of the upper mantle. *Journal of Geophysical Research: Solid Earth* **94**, 10647-10661.
- Sato H., Sacks I. S., Murase T. and Scarfe C. M. (1988) Thermal structure of the low velocity zone derived from laboratory and seismic investigations. *Geophys. Res. Lett.* **15**, 1227-1230.
- Sdrolias M., Roest W. R. and Müller R. D. (2004) An expression of Philippine Sea plate rotation: the Parece Vela and Shikoku basins. *Tectonophysics* **394**, 69-86.
- Seno T. and Yamasaki T. (2003) Low-frequency tremors, intraslab and interplate earthquakes in Southwest Japan—from a viewpoint of slab dehydration. *Geophys. Res. Lett.* **30**.
- Seno T., Zhao D., Kobayashi Y. and Nakamura M. (2001) Dehydration of serpentized slab mantle: Seismic evidence from southwest Japan. *Earth, planets and space* **53**, 861-871.
- Shelly D. R., Beroza G. C., Ide S. and Nakamura S. (2006) Low-frequency earthquakes in

- Shikoku, Japan, and their relationship to episodic tremor and slip. *Nature* **442**, 188-191.
- Shimoda G., Tatsumi Y., Nohda S., Ishizaka K. and Jahn B. M. (1998) Setouchi high-Mg andesites revisited: geochemical evidence for melting of subducting sediments. *Earth Planet. Sc. Lett.* **160**, 479-492.
- Tamura Y., Yuhara M. and Ishii T. (2000) Primary arc basalts from Daisen volcano, Japan: equilibrium crystal fractionation versus disequilibrium fractionation during supercooling. *J. Petrol.* **41**, 431-448.
- Tamura Y., Yuhara M., Ishii T., Irino N. and Shukuno H. (2003) Andesites and dacites from Daisen volcano, Japan: partial-to-total remelting of an andesite magma body. *J. Petrol.* **44**, 2243-2260.
- Tatsumi Y., Takahashi T., Hirahara Y., Chang Q., Miyazaki T. and Kimura J. I., et al. (2008) New Insights into Andesite Genesis: the Role of Mantle-derived Calc-alkalic and Crust-derived Tholeiitic Melts in Magma Differentiation beneath Zao Volcano, NE Japan. *J. Petrol.* **49**, 1971-2008.
- Tatsumi Y. and Eggins S. (1995) *Subduction zone magmatism*. Wiley.
- Tatsumi Y. (2006) High-Mg Andesites in the Setouchi Volcanic Belt, Southwestern Japan: Analogy to Archean Magmatism and Continental Crust Formation? *Annu. Rev. Earth Pl. Sc.* **34**, 467-499.
- Tatsumi Y., Nakashima T. and Tamura Y. (2002) The petrology and geochemistry of calc-alkaline andesites on Shodo-Shima Island, SW Japan. *J. Petrol.* **43**, 3-16.
- Tatsumi Y., Suenaga N., Yoshioka S., Kaneko K. and Matsumoto T. (2020) Contrasting volcano spacing along SW Japan arc caused by difference in age of subducting lithosphere. *Sci. Rep.-Uk* **10**.
- Teng F., Hu Y. and Chauvel C. (2016) Magnesium isotope geochemistry in arc volcanism.

Proceedings of the National Academy of Sciences **113**, 7082-7087.

- Tenthorey E. and Hermann J. (2004) Composition of fluids during serpentinite breakdown in subduction zones: evidence for limited boron mobility. *Geology* **32**, 865-868.
- Tian Y., Xiao Y., Chen Y., Sun H., Liu H. and Tong F., et al. (2019) Serpentinite-derived low $\delta^{7}\text{Li}$ fluids in continental subduction zones: Constraints from the fluid metasomatic rocks (whiteschist) from the Dora-Maira Massif, Western Alps. *Lithos* **348-349**, 105177.
- Toda S., Stein R. S., Kirby S. H. and Bozkurt S. B. (2008) A slab fragment wedged under Tokyo and its tectonic and seismic implications. *Nat. Geosci.* **1**, 771-776.
- Tollstrup D. L. and Gill J. B. (2005) Hafnium systematics of the Mariana arc: Evidence for sediment melt and residual phases. *Geology* **33**, 737-740.
- Tsukui M. (1985) Temporal variation in chemical composition of phenocrysts and magmatic temperature at Daisen volcano, southwest Japan. *J. Volcanol. Geoth. Res.* **26**, 317-336.
- Ulmer P. and Trommsdorff V. (1995) Serpentine stability to mantle depths and subduction-related magmatism. *Science* **268**, 858-861.
- Utsu T. (1967) Anomalies in seismic wave velocity and attenuation associated with a deep earthquake zone (1). *Journal of the Faculty of Science, Hokkaido University. Series 7, Geophysics* **3**, 1-25.
- Walowski K. J., Wallace P. J., Hauri E. H., Wada I. and Clynne M. A. (2015) Slab melting beneath the Cascade Arc driven by dehydration of altered oceanic peridotite. *Nat. Geosci.* **8**, 404-408.
- Yamane N., Kanagawa K. and Ito T. (2012) Contrasting seismic reflectivity of the lower crust and uppermost mantle between NE Japan and SW Japan as illustrated by petrophysical analyses of mafic and ultramafic xenoliths. *Journal of Geophysical Research: Solid Earth* **117**.

- Yamano M., Honda S. and Uyeda S. (1984) Nankai Trough: A hot trench? *Marine Geophysical Researches* **6**, 187-203.
- Yogodzinski G. M., Lees J. M., Churikova T. G., Dorendorf F., Wöerner G. and Volynets O. N. (2001) Geochemical evidence for the melting of subducting oceanic lithosphere at plate edges. *Nature* **409**, 500-504.
- Yogodzinski G. M., Kelemen P. B., Hoernle K., Brown S. T., Bindeman I. and Vervoort J. D., et al. (2017) Sr and O isotopes in western Aleutian seafloor lavas: Implications for the source of fluids and trace element character of arc volcanic rocks. *Earth Planet. Sc. Lett.* **475**, 169-180.
- Zellmer G. F., Iizuka Y., Miyoshi M., Tamura Y. and Tatsumi Y. (2012) Lower crustal H₂O controls on the formation of adakitic melts. *Geology* **40**, 487-490.
- Zhao D. P., Liu X. and Hua Y. Y. (2018) Tottori earthquakes and Daisen volcano: Effects of fluids, slab melting and hot mantle upwelling. *Earth Planet. Sc. Lett.* **485**, 121-129.
- Zhao D., Yanada T., Hasegawa A., Umino N. and Wei W. (2012) Imaging the subducting slabs and mantle upwelling under the Japan Islands. *Geophys. J. Int.* **190**, 816-828.

Chapter 2. Evolution of slab-derived fluids beneath the SW Japan arc: Perspectives from Hf isotope compositions of volcanic rocks

Abstract

Fluids released from subducted oceanic lithosphere (slab) play an essential role in the production of island-arc magmas. However, how the compositions and properties of subduction-zone fluids are affected by the variation of slab morphology remain poorly constrained. It is known that the PHS plate beneath Southwest Japan exhibits complex morphology, thus leading to the tempo-spatial variation of subducted-derived fluids. We investigated Hf, Sr and Nd isotope compositions of well-dated volcanic rocks from the Chugoku district in SW Japan, whose ages range between 12 Ma to the present. New Hf isotope analyses show the Hf isotope compositions show a clear temporal variation, from lower ($\epsilon_{\text{Hf}} = +2.0$ to $+5.0$) values in early-stage [12–5 million years (Myr) ago] samples to higher and more variable values (-0.6 to $+12.5$) in late-stage samples, suggesting sediment contribution occurred through all episodes but the relative proportion of AOC component gradually increased with time. Our modeling also suggests that the of AOC-release component is unlikely to be aqueous fluids and bulk *mélange* in the early stage. The early-stage rocks also do not exhibit clear “slab-melt” signatures (e.g., high Sr/Y) like late-stage rocks, therefore, subducted basalt-derived fluids may be supercritical fluids in the early stage and transitioned to hydrous melt in the later stage. We suggest that the transition of slab-derived component in the last 12 Myr can be attributed to the shallowing and morphological distortion of subducted slab. Our data also show sediment contribution varies among the volcanoes in Chugoku district in the later

stage; magmas erupted in the western part, received a smaller contribution than those of the other volcanic regions. Lateral variation in sediment contribution may be attributed to lateral variation in accumulated sediment. Our study suggests the contribution of sediments is largely affected by surface morphology of the slab.

Keywords: SW Japan, island arcs; Hf isotope; slab-derived fluids; slab morphology

1. Introduction

Fluids liberated from subducting slab play an essential role in island-arc magma production; they lower the solidus of and induce melting of magma sources in the mantle wedge (Ishikawa and Nakamura, 1994). These fluids are considered to have variable physical and chemical properties, owing to the variation in pressure (P)-temperature (T) paths taken (Peacock and Wang, 1999) and the lithology of the slab (Walowski et al., 2015). However, it is still unclear how slab morphology, which causes intra-slab P-T variations, affects the evolution of island-arc volcanism.

Southwest Japan is a subduction zone where the Philippine Sea (PHS) plate is sinking into the trench. The volcanism occurs in two districts, Chugoku and Kyushu (Fig. 1). Subduction is shallower ($<30^\circ$) beneath central Chugoku and becomes steeper ($>40^\circ$) to Kyushu region and western Chugoku. Moreover, the subduction angle is also steeper ($>50^\circ$) to the north of Chugoku district. It is noted that the PHS plate beneath Chugoku exhibits complex surface morphology, owing to the topographic prominence (Izu-Bonin Arc, Kinan Seamounts, and Kyushu-Palau Ridge) within or in periphery of Shikoku Basin. Thus, the extent to which the lithospheric materials metamorphose should be variable within the slab, making SW Japan an ideal place to study the relationship between fluid composition and slab morphology.

Our companion studies (Pineda-Velasco et al., 2018; Nguyen et al., 2020) suggested that the PHS slab became shallower and flatter over time, and slab-derived components varied from

those dominated by aqueous fluids to slab melt. In this study, Hf isotope analysis has been applied to the Chugoku volcanic rocks. Since Hf exhibits variable solubility within different types of fluids, its isotope composition is an ideal tracer for the physical and chemical properties of slab-derived fluid (Kessel et al., 2005). Through integrating Hf isotope data with the published geochemical analyses, the evolution of the subducting lithosphere and the mechanism responsible for the production of chemically variable magmas are examined.

2. Global adakites

The high-Sr andesites and dacites (adakites) from subduction zones are generally attributed to be partial melts of subducted oceanic crust (Kay, 1978; Drummond & Defant, 1990), the inference is supported by Sr-Nd isotopic compositions of some high-Sr andesites and dacites akin to those of subducted oceanic crust (Figure 2-1; Group 1; e.g., Yogodzinski et al., 1995). The high-Sr andesites and dacites from some subduction zones have isotopic compositions slightly different from subducted oceanic crust (Figure 2-1; Group 2; e.g., Stern & Kilian, 1996). It is however noted that SW Japan (Figure 2-1; Chugoku and Kyushu district) also the volcanic field which yields high-Sr andesites and dacites with isotopic compositions distinctly different from subducted oceanic crusts. Such an “enriched” isotopic feature is considered to have been resulted from melting of a source with significant amounts of subducted sediments (Feineman et al., 2013; Pineda-Velasco et al., 2018).

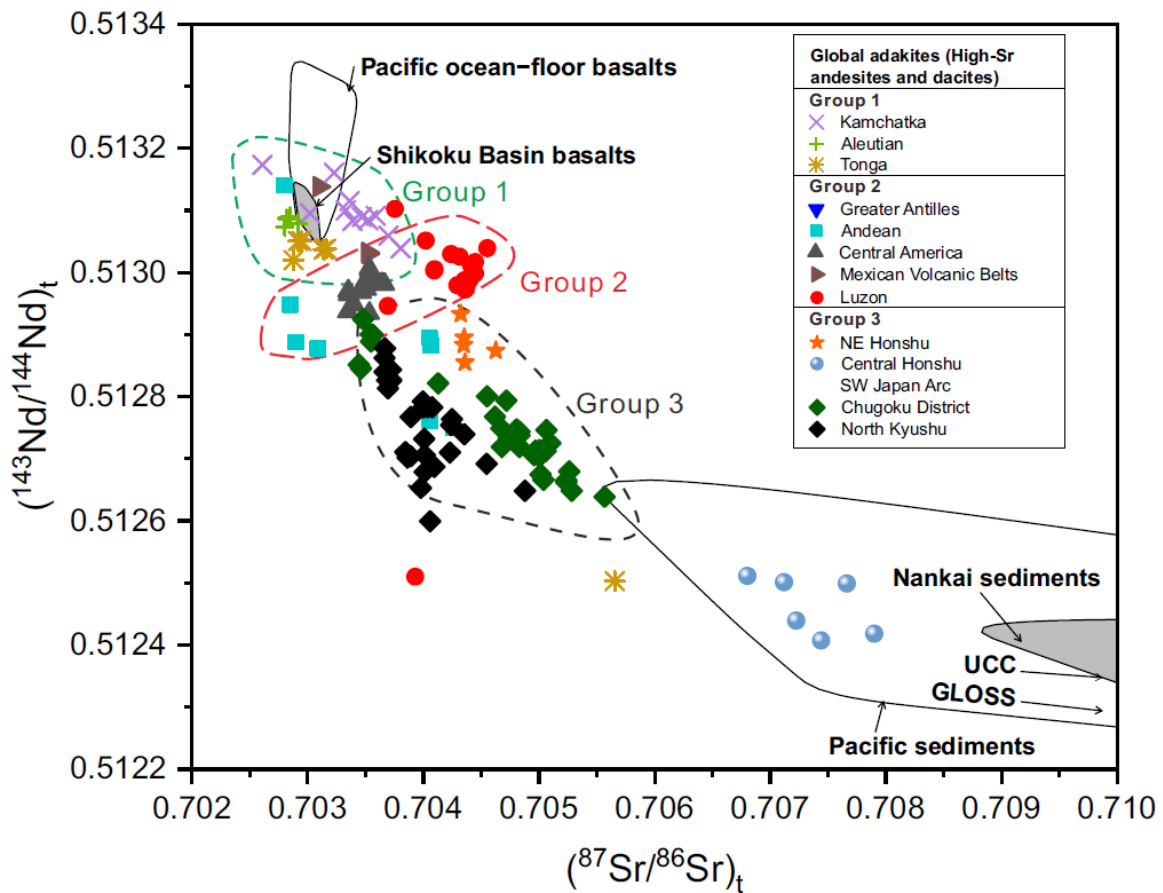


Figure 2-1. $(^{143}\text{Nd}/^{144}\text{Nd})_i$ versus $(^{87}\text{Sr}/^{86}\text{Sr})_i$ of global adakites (high-Sr andesites and dacites).

Data are from GeoRoc dataset (<https://georoc.eu>), Feineman et al., 2013; Pineda-Velasco et al., 2018.

3. Rock type

Volcanic rocks (12 Ma to recent) in the Chugoku district consist of basalts, basaltic andesites, andesites, and dacites, which are classified either sub-alkaline or alkaline series (Figure 2-2). We follow the trace-element-based nomenclature of the volcanic rocks in the Chugoku district used in the previous studies (Kimura et al., 2014; Nguyen et al., 2020); OIB (ocean-island basalt), IAB (island-arc basalt), IAA (island-arc andesite), ADK (adakite, i.e., high-Sr andesite and dacite), and HMA (high magnesium andesite). The OIB and IAB classification for mafic rocks is the extent of Nb and Ta depletions; the latter type shows marked depletions of Nb and Ta in trace-element abundance patterns, while the former type does not exhibit such anomaly (Figure 2-3). Kimura et al. (2014) subdivided IAB type into three sub-

types, normal IAB (arc-type basalt, either alkaline or subalkaline rock series), shoshonite (high-K IAB) and high-Mg andesite (in a strict sense, they are mostly basaltic andesite). Given that the compositions of these types of IAB are transitional, we do not separately discuss these subtypes. The IAA and ADK are andesites or dacites; the former show trace-element abundance patterns typical to andesites occurring in island arcs (Pineda-Velasco et al., 2018 and reference therein), whereas the latter exhibit marked enrichments of Ba (280–1120 $\mu\text{g g}^{-1}$) and Sr (590–2190 $\mu\text{g g}^{-1}$) and depletions of heavy rare-earth elements, although patterns of the other trace-element abundances are similar to IAA. Such features are commonly found in andesitic and dacitic rocks referred to as adakites (Defant & Drummond, 1990). The HMA in the Setouchi Volcanic Belt consists of phyric andesites which contain olivine, clinopyroxene and orthopyroxene (bronzite) with minor hornblende (Tatsumi, 2006). The HMA rocks are geochemically characterized by whole-rock $\text{FeO}^{\text{T}}/\text{MgO} < 1$ (where FeO^{T} denotes total Fe as FeO), and trace-element abundance patterns with marked depletions of Nb and Ta and enrichments of Cs, Rb and Pb (Tatsumi, 2006).

For this study, eighty-eight samples, consisting of OIB, IAB, IAA, and ADK types, were selected from the sample set ($n = 199$) collected by Feineman et al. (2013), Pineda-Velasco et al. (2015, 2018) and Nguyen et al. (2020). Data for HMA are referred from Hanyu et al. (2002) and Shimoda et al. (1998) for comparison of the Chugoku volcanism and the preceding activity in Setouchi. The selected OIB and IAB samples have SiO_2 abundance of 45–57 wt% (anhydrous basis, see **Figure 2-2**) except for high- P_2O_5 basalt (HYO-15 with $[\text{SiO}_2] = 41$ wt%, where bracket denotes element abundance). The IAA and ADK rocks are classified into andesites and dacites with $[\text{SiO}_2] = 59$ –68 wt%. Major element compositions of these samples largely overlap with the major-element data of the samples studied by Kimura et al. (2014), hence geochemical and isotopic data of these studies are thought to be comparable.

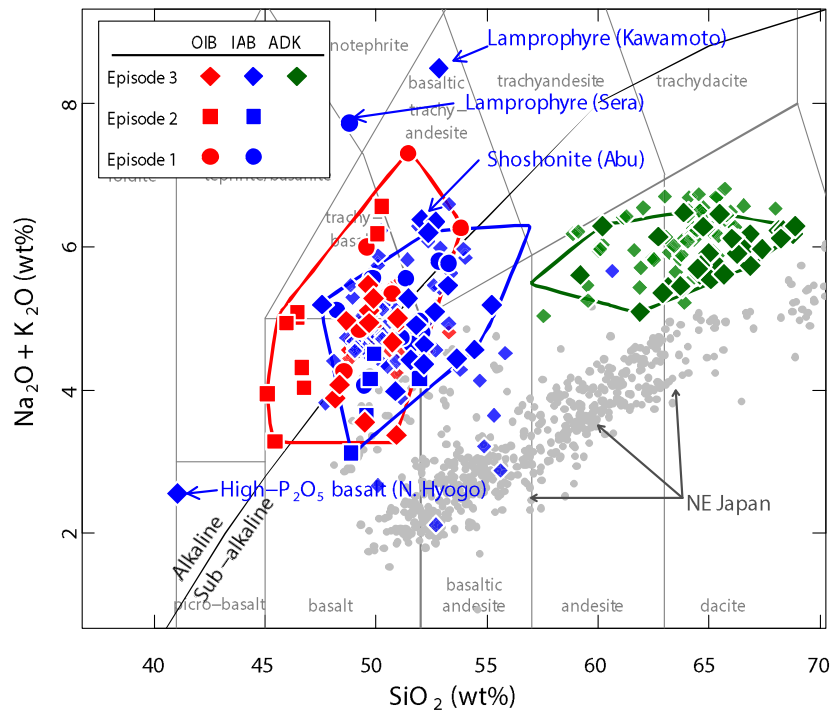


Figure 2-2. Total alkali ($\text{Na}_2\text{O} + \text{K}_2\text{O}$) abundance plotted against SiO_2 abundance.

Compositional fields of each rock types are after [Le Bas et al. \(1986\)](#) and the border of alkaline and sub-alkaline rocks is after [Irvine & Baragar \(1971\)](#), respectively. Larger symbols represent data by this study and smaller, pale-colored symbols represent data for the same types of volcanic rocks used for isotopic analysis in [Kimura et al. \(2014\)](#). Data for Quaternary volcanic rocks from northeast Japan arc are from the compilation by [Pineda-Velasco et al. \(2018\)](#).

performed by an inductively coupled plasma mass spectrometry (ICPMS) in static multicollection mode using Thermo Fisher Neptune plus. Instrumental mass bias was corrected using $^{179}\text{Hf}/^{177}\text{Hf} = 0.7325$. The epsilon Hf values (ϵ_{Hf}) were calculated using $(^{176}\text{Hf}/^{177}\text{Hf})_{\text{CHUR}} = 0.282785$ and $(^{176}\text{Lu}/^{177}\text{Hf})_{\text{CHUR}} = 0.0336$ [CHUR, chondritic uniform reservoir (Bouvier *et al.*, 2008)] after normalization to $^{176}\text{Hf}/^{177}\text{Hf} = 0.282160$ for the JMC 475 standard solution, equivalent to $^{176}\text{Hf}/^{177}\text{Hf} = 0.282192$ for JMC 14374 standard solution (Lu *et al.*, 2007). External reproducibility is estimated to be 40 ppm from repeated analysis of JMC 14374 (25 ng mL⁻¹, $n = 38$).

For Sr and Nd analysis, powdered samples (0.1 g) were leached in 6 M HCl at 100 °C for 1 hour, then digested in solutions of 30 M HF–12 M HClO₄, followed by dissolution into 4 M HCl (Yokoyama *et al.*, 1999). The procedures of Yoshikawa & Nakamura (1993) and Nakamura *et al.* (2003) were employed for chromatographic separation and mass spectrometry. Isotopic measurements were performed by a thermal ionization mass spectrometry (TIMS) in static multicollection mode using Thermo Fisher TRITON plus. Instrumental mass bias was corrected using $^{86}\text{Sr}/^{88}\text{Sr} = 0.1194$ and $^{146}\text{Nd}/^{144}\text{Nd} = 0.7219$. The standard materials yielded the following values: $^{87}\text{Sr}/^{86}\text{Sr} = 0.710253 \pm 0.000005$ (2σ , $n = 5$) for NIST SRM 987; $^{143}\text{Nd}/^{144}\text{Nd} = 0.511709 \pm 0.000012$ (2σ , $n = 4$) for the in-house standard PML-Nd, which are equivalent to $^{143}\text{Nd}/^{144}\text{Nd}$ of 0.511845 for La Jolla (conversion factor 1.000266; Makishima *et al.*, 2008). All the data are adjusted relative to $^{87}\text{Sr}/^{86}\text{Sr} = 0.710240$ for NIST SRM 987 and $^{143}\text{Nd}/^{144}\text{Nd} = 0.511860$ for La Jolla. The epsilon Nd values (ϵ_{Nd}) were calculated using $(^{143}\text{Nd}/^{144}\text{Nd})_{\text{CHUR}} = 0.512630$ and $(^{147}\text{Sm}/^{144}\text{Nd})_{\text{CHUR}} = 0.1960$ (Bouvier *et al.*, 2008).

Results are presented in **Table 2-1**. Age corrections were made using the decay constants of $^{87}\text{Rb} = 1.393 \times 10^{-11} \text{ year}^{-1}$ (Nebel *et al.*, 2011), $^{147}\text{Sm} = 6.539 \times 10^{-12} \text{ year}^{-1}$ (Begemann *et al.*, 2001) $^{176}\text{Lu} = 1.867 \times 10^{-11} \text{ year}^{-1}$ (Söderlund *et al.*, 2004), respectively. Pb isotopic data

by [Nguyen et al. \(2020\)](#) for the samples used in Hf isotope analysis were age-corrected using $^{235}\text{U} = 9.8485 \times 10^{-10} \text{ year}^{-1}$, $^{238}\text{U} = 1.55125 \times 10^{-10} \text{ year}^{-1}$ and $^{232}\text{Th} = 4.9475 \times 10^{-11} \text{ year}^{-1}$, respectively ([Steiger and Jäger, 1977](#)). Compiled isotopic data for the volcanic rocks in the other island arcs were also age-corrected using these decay constants (**Table 2-2**).

5. Results

5.1 Isotope variations in the Chugoku volcanic rocks

It has been known that the Chugoku volcanic rocks have considerable isotopic variations (**Figs. 4–6**; [Kimura et al., 2014](#); [Pineda-Velasco et al., 2015, 2018](#); [Nguyen et al., 2020](#)); $(^{87}\text{Sr}/^{86}\text{Sr})_i = 0.7033\text{--}0.7080$, $(^{143}\text{Nd}/^{144}\text{Nd})_i = 0.51237\text{--}0.51295$, $(^{176}\text{Hf}/^{177}\text{Hf})_i = 0.28275\text{--}0.28316$, $(^{206}\text{Pb}/^{204}\text{Pb})_i = 17.67\text{--}18.39$, $(^{207}\text{Pb}/^{204}\text{Pb})_i = 15.484\text{--}15.609$, and $(^{208}\text{Pb}/^{204}\text{Pb})_i = 37.97\text{--}38.69$, where subscript i denotes initial isotopic ratio. Temporal variations in Sr, Nd, Hf and Pb isotopic compositions of the IAB rocks (**Figure 2-4**) are summarized as follows; (1) Episode-3 IAB rocks exhibit greater isotopic variations than those of Episode-1 and -2 IAB rocks, due to the occurrence of the rocks with less radiogenic Sr-Pb and more radiogenic Nd-Hf isotopic compositions (e.g., Abu shoshonite), and (2) IAB and ADK in Episode 3 show isotopic variations largely overlapped with each other.

The OIB rocks (**Figure 2-4**) show distinct temporal variations; (1) Episode-1 and -2 OIB have Sr and Pb isotopic compositions which are more variable and less radiogenic compositions, and Nd isotopic compositions which are more radiogenic compositions than those of IAB in these episodes. And, their Hf isotopic composition are largely overlapped, (2) Episode 3 OIB have Sr-Nd-Hf-Pb isotopic compositions largely overlapping with the variations in Episode-3 IAB, (3) Episode-3 OIB include rocks (Kannabe and Kurayoshi) with more radiogenic Sr-Pb and less radiogenic Nd-Hf isotopic compositions.

It is noted that Episode-3 IAB and ADK also exhibits significant isotopic variations among

volcanic fields (**Figure 2-5**). These types of rocks with more radiogenic Nd and Hf isotopic compositions is confined to occur in the western part of the Chugoku district (Aonoyama and Abu), as was noted by [Pineda-Velasco et al. \(2018\)](#). Such spatial variations are not observed in Episode-1 and Episode 2 IAB rocks and OIB rocks in all episodes. Also noted is that ADK rocks in the entire Chugoku tend to have more radiogenic Nd and Hf isotopic compositions and less radiogenic Sr and Pb isotopic compositions than those of IAB rocks in close proximity (**Figure 2-5**).

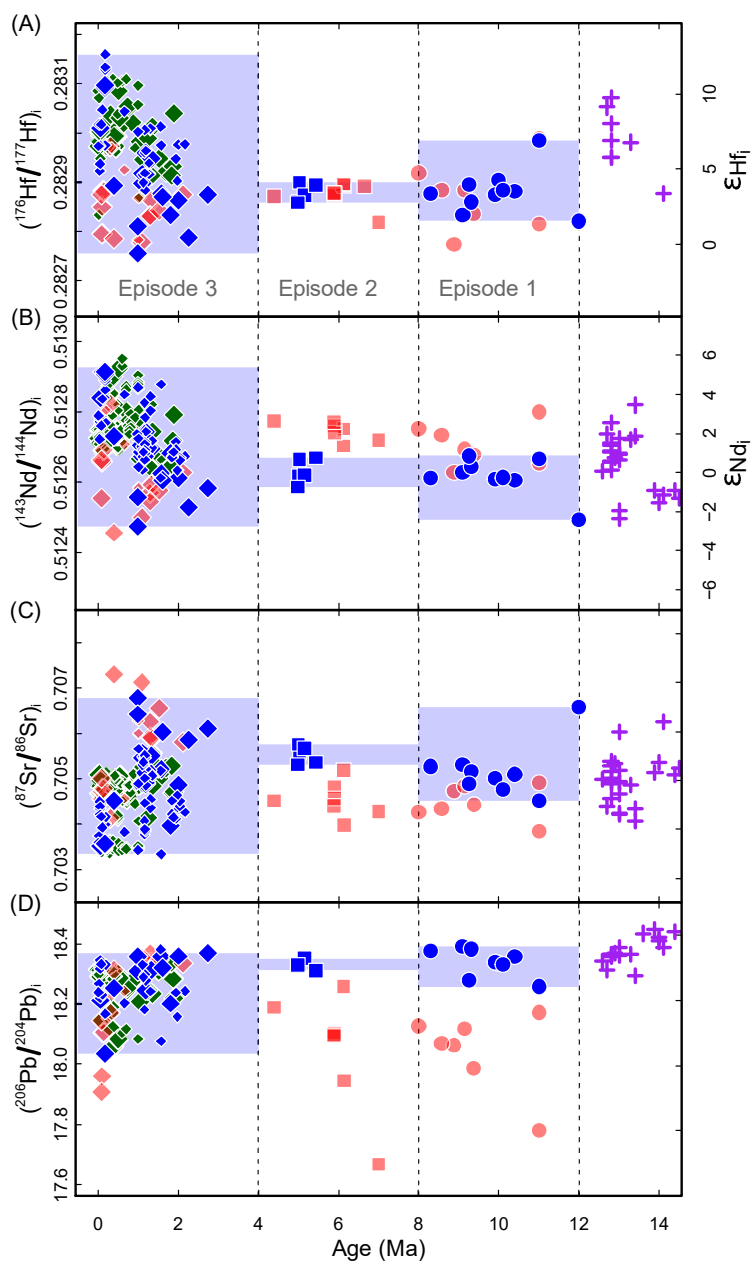


Figure 2-4. Temporal changes in $(^{176}\text{Hf}/^{177}\text{Hf})_i$, $(^{143}\text{Nd}/^{144}\text{Nd})_i$, $(^{87}\text{Sr}/^{86}\text{Sr})_i$ and $(^{206}\text{Pb}/^{204}\text{Pb})_i$ of volcanic rocks in Chugoku and Setouchi.

Temporal changes in $(^{176}\text{Hf}/^{177}\text{Hf})_i$, $(^{143}\text{Nd}/^{144}\text{Nd})_i$, $(^{87}\text{Sr}/^{86}\text{Sr})_i$ and $(^{206}\text{Pb}/^{204}\text{Pb})_i$ of volcanic rocks (subscript i denotes an age-corrected composition) in Chugoku [IAB, ADK, and OIB; this study and [Kimura et al. \(2014\)](#) for $(^{176}\text{Hf}/^{177}\text{Hf})_i$, $(^{143}\text{Nd}/^{144}\text{Nd})_i$ and $(^{87}\text{Sr}/^{86}\text{Sr})_i$] and the Setouchi volcanic belt (HMA; [Table 2-2](#) and reference therein). Pale-blue rectangles indicate isotopic variations in IAB of Episode 1, Episode 2 and Episode 3.

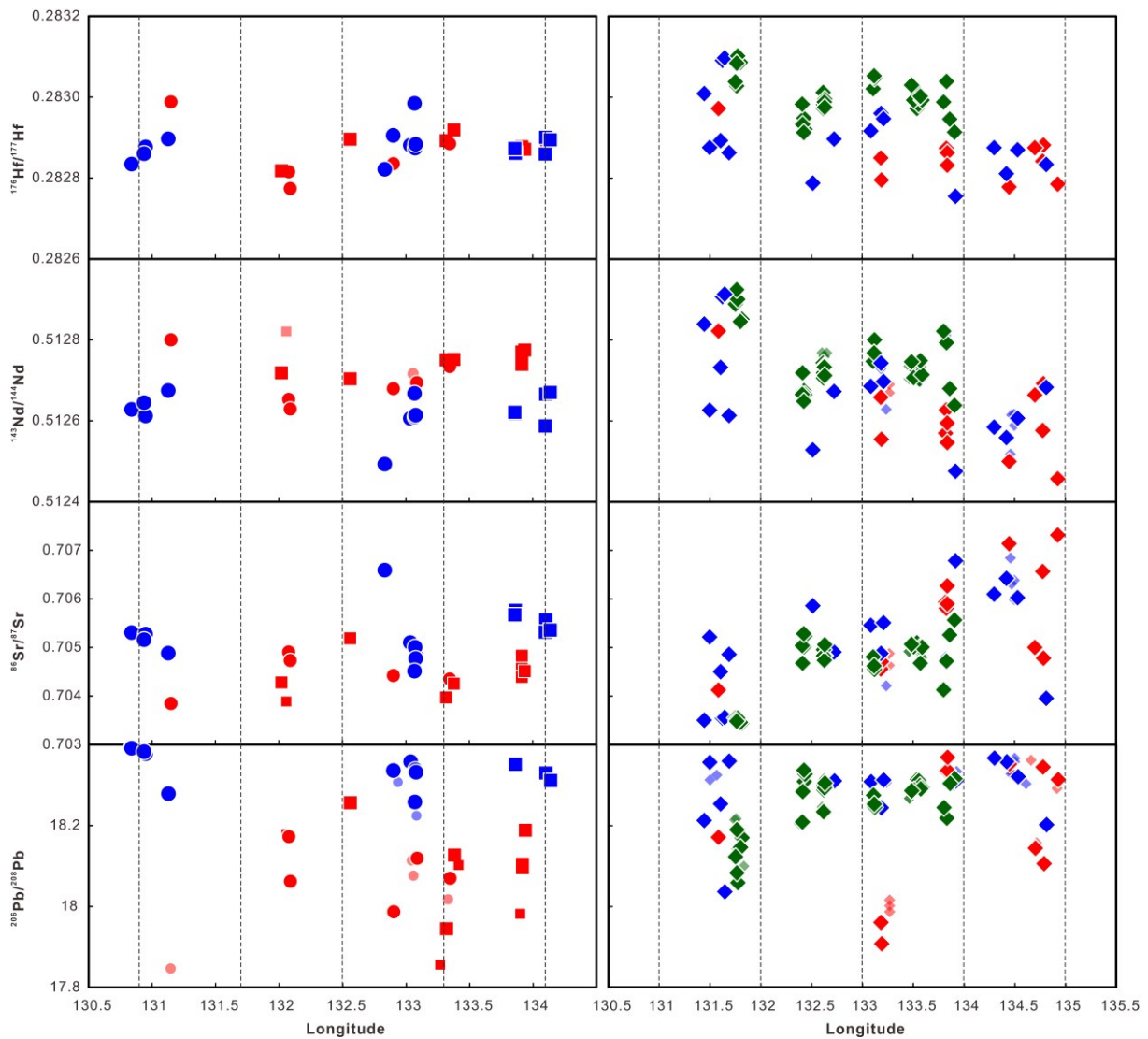


Figure 2-5. Longitudinal changes in $(^{176}\text{Hf}/^{177}\text{Hf})_i$, $(^{143}\text{Nd}/^{144}\text{Nd})_i$, $(^{87}\text{Sr}/^{86}\text{Sr})_i$ and $(^{206}\text{Pb}/^{204}\text{Pb})_i$ of volcanic rocks in Chugoku.

Longitudinal changes in $(^{176}\text{Hf}/^{177}\text{Hf})_i$, $(^{143}\text{Nd}/^{144}\text{Nd})_i$, $(^{87}\text{Sr}/^{86}\text{Sr})_i$ and $(^{206}\text{Pb}/^{204}\text{Pb})_i$ of volcanic rocks (subscript i denotes an age-corrected composition) in Chugoku [IAB, ADK, and OIB; this study and [Kimura et al. \(2014\)](#) for $(^{176}\text{Hf}/^{177}\text{Hf})_i$, $(^{143}\text{Nd}/^{144}\text{Nd})_i$ and $(^{87}\text{Sr}/^{86}\text{Sr})_i$]. Pale-blue rectangles indicate isotopic variations in IAB of Episode 1, Episode 2 and Episode 3. The left part shows the IAB of Episode 1 and Episode 2, whereas the right part shows the IAB and ADK of Episode 3.

5.2 Comparison of Hf isotope compositions with the other arcs

Large variations in Sr-Nd-Hf isotopic compositions of the Chugoku volcanic rocks differ from relatively homogeneous compositions of volcanic rocks from the Kamchatka-Aleutian, NE Japan, Izu-Bonin, Mariana and Tonga-Kermadec arcs (**Figure 2-6**). Magmas in these arcs

are generally attributed to melting of wedge mantle influxed by aqueous fluid largely from subducted oceanic crust (Ishikawa and Nakamura, 1994; Woodhead *et al.*, 2012). It is noted that the Kamchatka-Aleutian, NE Japan, Izu-Bonin, Mariana and Tonga-Kermadec arcs are subduction zones of old (hence cold) oceanic lithosphere (Pacific Plate, >100 Ma; Syracuse *et al.*, 2010). By contrast, Sr-Nd-Hf isotope compositions of the Chugoku volcanic rocks are similar to those of volcanic rocks in the Luzon-Philippine and Sunda-Banda arcs and SVB in SW Japan (**Figure 2-6**). Production of magmas in these arcs are generally attributed to the involvement of sediment melt (Woodhead *et al.*, 2001, 2012; Tatsumi & Hanyu, 2003). Subducting slabs beneath these arcs show a higher T/P gradient (Syracuse *et al.*, 2010), attributed to either subduction of young oceanic lithosphere (e.g., SW Japan; Peacock and Wang, 1999) or slab tearing (e.g., Sunda-Banda; Widiyantoro & van der Hilst, 1996).

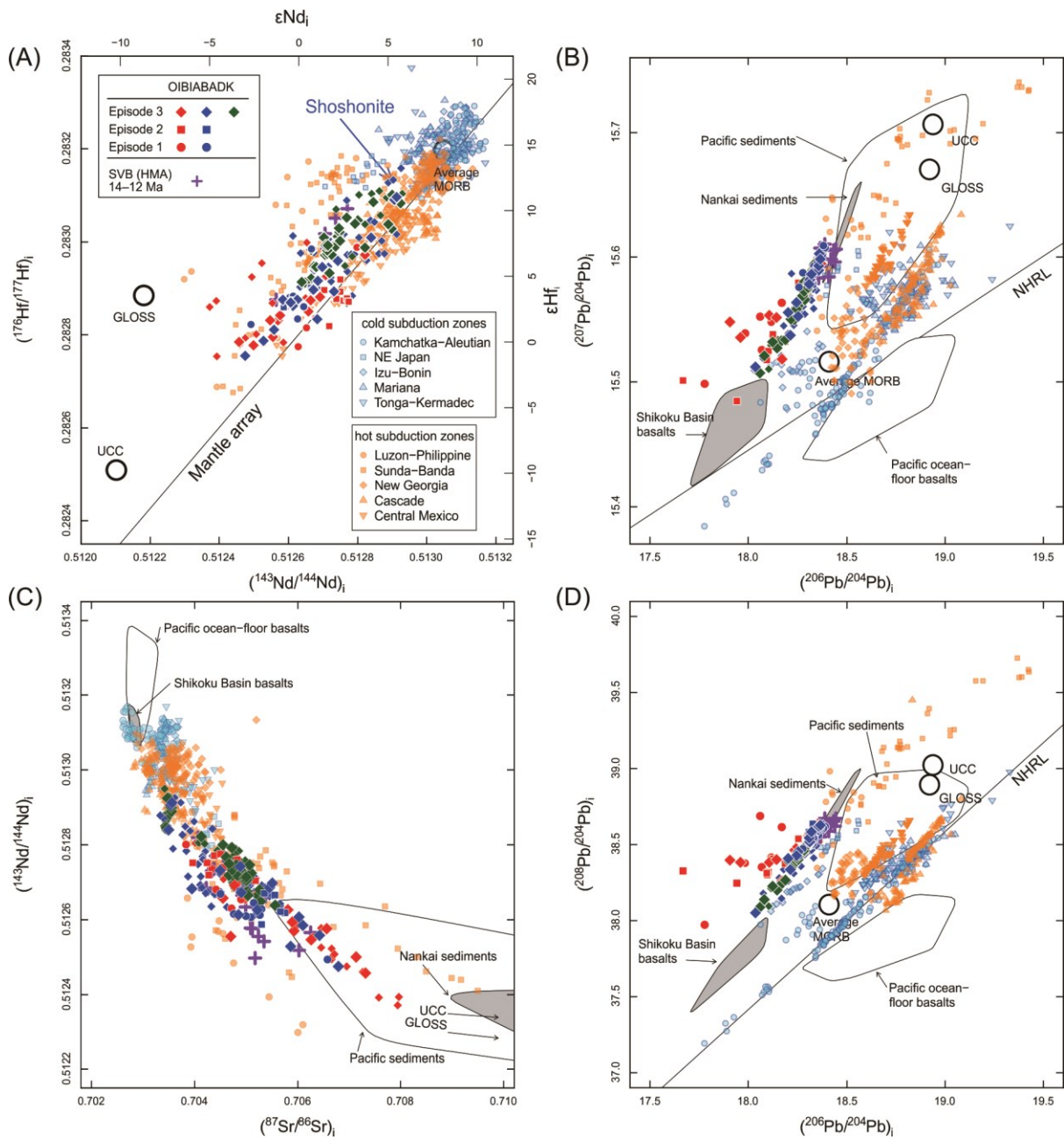


Figure 2-6. Hf, Sr, Nd and Pb isotope compositions of ADK, OIB and IAB in Chugoku, SW Japan in comparison with SVB HMA and the other arc volcanic rocks

Hf, Sr, Nd and Pb isotope compositions of ADK, OIB and IAB in Chugoku, SW Japan (12 Ma to recent, subscript i denotes an age-corrected composition) in comparison with high magnesium andesites in Setouchi Volcanic Belt [SVB (HMA)] and the other arc volcanic rocks (Table 2-2). The Sr and Nd isotopic data by Kimura et al. (2014) for ADK, OIB and IAB in the same district are also included in the plots (same but smaller symbols). Data sources for volcanic rocks (high-Mg andesites, HMA) from Setouchi Volcanic Belt (SVB) and the other island arcs are the same as in Figure 2-2 and summarized in Table 2-2. Data for Pacific Ocean-floor basalts, Shikoku Basin basalts, Pacific sediments and Nankai

sediments are those compiled by [Pineda-Velasco et al. \(2018, reference therein\)](#) and [Nguyen et al. \(2020, reference therein\)](#). Mean compositions of mid-ocean ridge basalts (Average MORB), [Gale et al. \(2013\)](#) and [Chauvel et al. \(2014\)](#); global subducted sediments (GLOSS), [Plank and Langmuir \(1998\)](#) and [Chauvel et al. \(2008\)](#); upper continental crusts (UCC), [McCulloch and Wasserburg \(1978\)](#), [Millot et al. \(2004\)](#), and [Chauvel et al. \(2014\)](#). The $^{87}\text{Sr}/^{86}\text{Sr}$ of GLOSS and UCC are 0.7173 and 0.7421, respectively, hence fall on the extensions of arrows outside plots. The NHRL is after [Hart \(1984\)](#).

6. Discussion

6.1 Characteristics of basalt-magma sources

Previous studies suggested that OIB and IAB parental magmas in the Chugoku district were extracted from the continuously upwelled mantle ([Kimura et al., 2014; Nguyen et al., 2020](#)). The melting depth of OIB sources is greater (60–100 km) than that of the IAB sources (30–60 km). Therefore, the geochemistry of OIB rocks largely reflect the magma sources in asthenospheric mantle and insignificant lithospheric or crustal assimilation. [Nguyen et al. \(2020\)](#) noted that OIB in the Chugoku district shows Sr-Nd-Pb isotopic composition similar to the Cenozoic basalts in the East Asia and ascribed the isotopic variation in Chugoku OIB to the involvement of two different magma sources in the asthenospheric mantle (C1 and C2). Combined with Cenozoic basalts in East Asia ([Choi et al., 2006, 2008, 2014; Sakuyama et al., 2013; Sun et al., 2014; Wang et al., 2017; Guo et al., 2016; Zeng et al., 2013; Zhang et al., 2009, 2012](#)), the Sr-Nd-Pb isotopic composition of C1 and C2 endmember had been estimated ([Nguyen et al., 2020](#)).

In order to further constrain the origins of C1 and C2 end-member components, their Hf isotopic compositions are estimated using the correlations of $^{176}\text{Hf}/^{177}\text{Hf}$ with published $^{87}\text{Sr}/^{86}\text{Sr}$, $^{143}\text{Nd}/^{144}\text{Nd}$, $^{206}\text{Pb}/^{204}\text{Pb}$, $^{207}\text{Pb}/^{204}\text{Pb}$ and $^{208}\text{Pb}/^{204}\text{Pb}$ (**Figure 2-7**) ([Nguyen et al., 2020 and reference therein](#)). In $^{176}\text{Hf}/^{177}\text{Hf}$ versus $^{143}\text{Nd}/^{144}\text{Nd}$ plot (**Figure 2-7A**), most of samples from the Chugoku OIB plot along the mantle array ([Willig et al., 2020](#)), therefore C1 and C2 composition may also plot close to this array. We obtain $^{176}\text{Hf}/^{177}\text{Hf}$ ratios of 0.28275

for the C1 end-member component and of 0.28245 for the C2 end-member component, respectively. Also, we integrated isotopic composition of the Chugoku OIB with that of the other Cenozoic basalts in East Asia to estimate the Hf isotopic composition of C1 and C2 endmember. Similar composition has been estimated (**Figure 2-7**). [Nguyen et al. \(2020\)](#) inferred that the C1 component is a crustal material of seamount on subducted oceanic lithosphere. Our estimate for $^{176}\text{Hf}/^{177}\text{Hf}$ of the C1 end-member component falls within the compositions of Pitcairn basalts ([Wang et al., 2017](#)), consistent with the seamount origin of this component. As suggested by [Nguyen et al. \(2020\)](#), this end-member component also contributed to the formation of late Cenozoic basalts in other regions from East Asia, including eastern China, the Korean Peninsula, and northern Kyushu.

The isotopic feature of estimated C2 end-member component resembles to EM1 (enriched mantle 1) isotopic end-member component (**Figure 2-7**; [Zindler & Hart, 1986](#); [Eisele et al., 2002](#); [Delavault et al., 2015](#); [Wang et al., 2017](#)). [Kuritani et al. \(2011, 2013\)](#) argued that the EM1 component is inferred to be upwelling of asthenosphere from the mantle transition zone hydrated by fluids from ancient sediments, and largely contributed to Cenozoic basalts in North China. Ancient pelagic sediments (~1.9 Ga) have low μ ($^{238}\text{U}/^{204}\text{Pb}$) values and K-hollandite primarily retains the incompatible element characteristics of its host rock. Therefore, mobile elements (such as K, Sr and Pb) released by the K-hollandite breakdown could produce lower $^{87}\text{Sr}/^{86}\text{Sr}$ and $^{206}\text{Pb}/^{204}\text{Pb}$ of C2 component than that of modern sediments ([Kuritani et al., 2011](#)). The C2 end-member component has similar $^{176}\text{Hf}/^{177}\text{Hf}$ to modern Nankai sediments, probably because Hf and Lu serve as moderately incompatible elements and less mobile elements ([Wang et al., 2017](#)). Therefore, our Hf isotopic data support C2 components are likely melts or supercritical fluids derived from ancient, subducted sediments in the mantle transition zone ([Sun et al., 2014](#); [Wang et al., 2017](#)). In our samples, the OIB rocks from Mishima, Hamada,

and Oki volcanic fields, which are located in the back-arc side, have relatively large contribution from the C2 component.

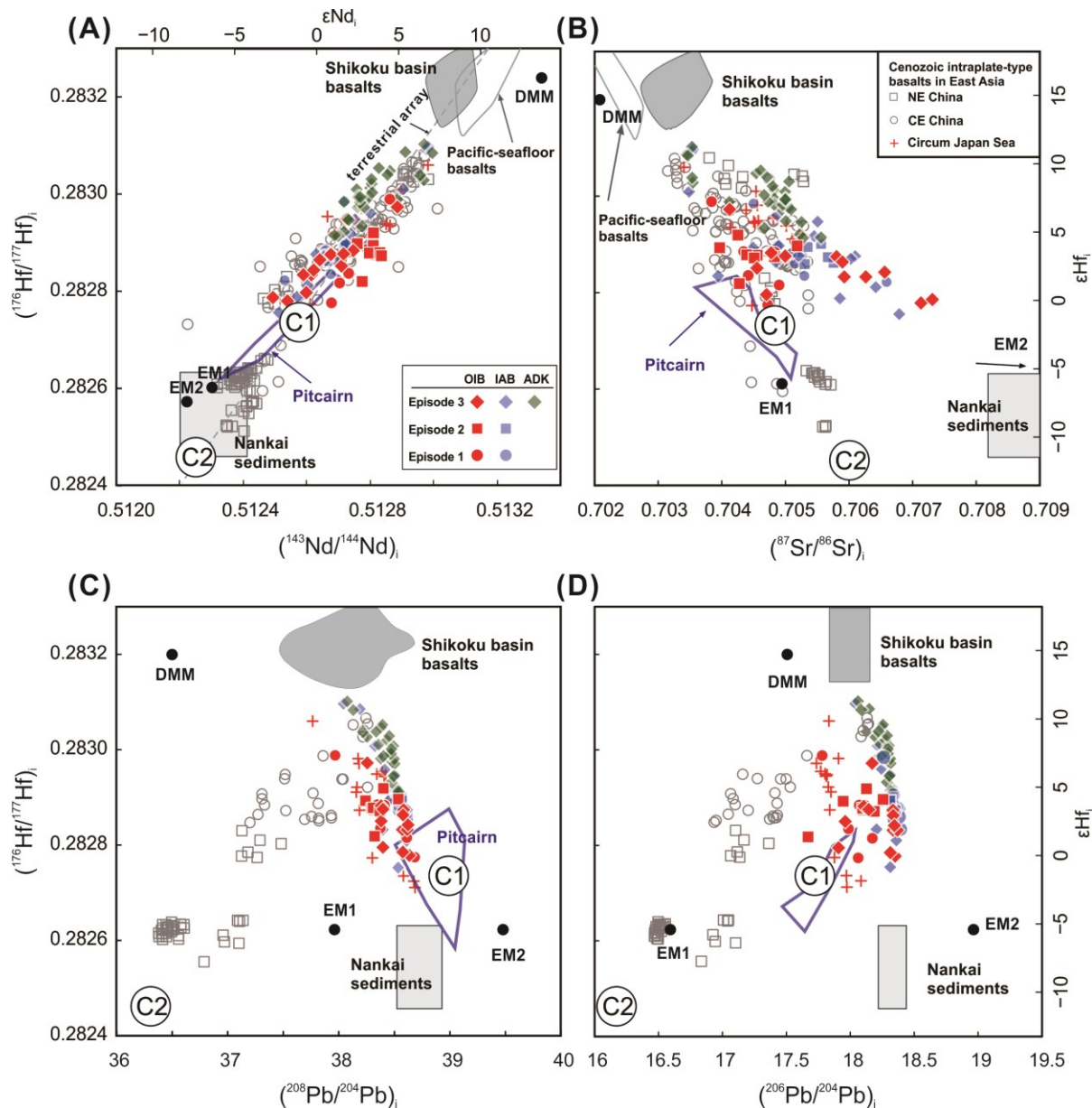


Figure 2-7. Variations in Sr-Nd-Pb-Hf isotopic compositions of OIB-type lavas in the Chugoku district, SW Japan, in comparison with Cenozoic basalts in East Asia, seafloor basalts of Pacific Plate (near Japan trench) and Philippine Sea Plate (in Shikoku Basin), and sediments.

(A) $(^{176}\text{Hf}/^{177}\text{Hf})_i$ versus $(^{143}\text{Nd}/^{144}\text{Nd})_i$, (B) $(^{176}\text{Hf}/^{177}\text{Hf})_i$ versus $(^{87}\text{Sr}/^{86}\text{Sr})_i$, (C) $(^{176}\text{Hf}/^{177}\text{Hf})_i$ versus $(^{208}\text{Pb}/^{204}\text{Pb})_i$, (D) $(^{176}\text{Hf}/^{177}\text{Hf})_i$ versus $(^{206}\text{Pb}/^{204}\text{Pb})_i$. Subscript *i* denotes age-corrected compositions. The circles denoted as “1” and “2” show the compositions of end-member components postulated for the sources of parental magmas of OIB in the Chugoku district. The mantle end-member components

DMM, EM1, and EM2 are from [Zindler and Hart \(1986\)](#). Sources for literature data: Quaternary ADK (adakitic high-Sr andesites and dacites) in the Chugoku district ([Feineman et al., 2013](#); [Kimura et al., 2014](#); [Kimura et al., 2015](#); [Pineda-Velasco et al., 2015, 2018](#)), Cenozoic basalts in East Asia ([Choi et al., 2006, 2008, 2014](#); [Sakuyama et al., 2013](#); [Sun et al., 2014](#); [Wang et al., 2017](#); [Guo et al., 2016](#); [Zeng et al., 2013](#); [Zhang et al., 2009, 2012](#)), seafloor basalts from Pacific and Shikoku Basin ([Pineda-Velasco et al., 2018, references therein](#)), sediments ([Pineda-Velasco et al., 2018, references therein](#); [Vervoort et al., 2011](#)) and Pitcairn islands ([Eisele et al., 2001](#)).

6.2 Modelling parameters for slab contribution in Hf isotopic perspective

Recent work has credited ADK (high-Sr andesite and dacite) occurred in Episode 3 in SW Japan was formed by melting of the subducted oceanic crust of Shikoku Basin Plate with a component of melted sediment from Nankai trench ([Feineman et al., 2013](#); [Kimura et al., 2014](#); [Pineda-Velasco et al., 2018](#)). Episode-3 IAB show a co-genetic relationship with ADK and both IAB and HMA was interpreted to be produced by the interaction of slab melt with mantle ([Tatsumi, 2006](#); [Feineman et al., 2013](#); [Pineda-Velasco et al., 2018](#); [Nguyen et al., 2020](#)). To further examine the role of mixing of altered oceanic crust (AOC) component with sediment component in Hf isotopic systematics, we apply a mixing model that employs two end members (AOC, sediment) and calculation parameters in **Table 2-3**.

The Sr-Nd-Pb-Hf isotopic composition of subducted basalt of altered oceanic crust (AOC) is taken from sea-floor basalt in Shikoku Basin ([Hickey-Vargas, 1991, 1998](#); [Ishizuka et al., 2009](#); [Straub et al., 2010](#); [Shu et al., 2017](#)), and that of subducted sediment is that from Nankai Trough ([Ishikawa & Nakamura, 1994](#); [Plank & Langmuir, 1998](#); [Shimoda et al., 1998](#); [Terakado et al., 1988](#); [Shu et al., 2017](#)). Sr-Nd-Pb-Hf elemental concentrations for bulk AOC and sediment are from elemental values of [Ishizuka et al. \(2009\)](#) and [Plank and Langmuir \(1998\)](#), respectively.

In the modeling presented here, partition coefficients of AOC melt and sediment melt are from [Johnson & Plank, 1999](#) and [Kessel et al. \(2005\)](#), respectively. The F for sediment melt is

estimated to be 30% following [Kimura et al. \(2014\)](#) and [Feineman et al. \(2013\)](#), whereas that for subducting basalt is estimated to be 10% following [Pineda-Velasco et al. \(2018\)](#). The trace element composition of AOC-derived aqueous fluid was calculated by using the mobility data of [Kessel et al. \(2005\)](#) for eclogite (altered oceanic crust). For the modeling, 5 wt.% H₂O in the AOC was assumed.

6.3 The change of the fluid property from oceanic crust

The slab depth in the central and eastern SVB is 40–60 km, whereas the western terminus of SVB in Kyushu is located 90-km above the slab (**Figure 2-1A**, [Asamori and Zhao et al., 2015](#)), consistent with most of other arc systems ([Syracuse et al., 2010](#)). Hence, the discrepancy of slab depths from two regions implies that the PHS slab may have been located at 80–90 km depth beneath the whole SVB at 14–12 Ma, but then become shallower over time ([Nguyen et al., 2020](#)) in the central and eastern section. If this is the case, the depth of the slab beneath Chugoku should have been deeper than at present (90–100 km), possibly 120–140 km beneath Sekiryō and Sanin in Episode 1 (12–8 Ma), which is shortly after 14–12 Ma. Steeper subduction in this period is also supported by the occurrence of OIB beneath Sanyo; the melting depth for its sources was as deep as 80 km ([Nguyen et al., 2020](#)), which is significantly deeper than the current depth of wedge mantle (50–70 km; **Figure 2-1A**).

Given that Hf preferentially resides in specific phases (e.g., garnet, zircon and rutile), it can be a useful tracer to examine the involvement of sediments ([Patchett et al., 1984](#); [Blichert-Toft and Frei, 2001](#); [Tollstrup and Gill, 2005](#)). Another important feature of Hf is that it is less mobile with aqueous fluids, while Pb, Sr and Nd are highly to moderately fluid-mobile elements (e.g., [Keppler, 1996](#); [Kogiso et al., 1997](#)). Therefore, aqueous fluids may strongly affect Sr-Nd-Pb isotopic composition of wedge mantle and its derived melts, but it is not the case for Hf isotope ([Keppler, 1996](#); [Kogiso et al., 1997](#)). This inference is supported by global

variability of Hf-Nd isotopic compositions of island arc lavas, being classified into two groups (e.g., [Tatsumi, 2006](#); **Figure 2-7A**). Volcanic rocks from Izu-Mariana, Kermadec and New Britain arcs have isotopic compositions close to MORB and show relatively small variation. The other group, including the Lesser Antilles and Sunda arcs as well as Setouchi HMA, show different isotopic signatures. They have larger variations in $^{143}\text{Nd}/^{144}\text{Nd}$ and $^{176}\text{Hf}/^{177}\text{Hf}$ ratios, extending to the compositions of sediments (**Figure 2-7A**), suggesting the contribution of significant sediment material, rather than aqueous fluid. Most ADK and IAB samples from the Chugoku plot close to the latter group (**Figure 2-7A**). Therefore, sediment melts or bulk sediments, rather than aqueous fluid, is likely to contribute to the source of Chugoku ADK and IAB. Similar to Hf, rare-earth elements (REE) and Th are less mobile relative to alkali and alkali-earth elements, Pb and U in aqueous fluids ([Kessel et al., 2005](#)). Previous studies have documented higher abundances of Th (relative to U) and REE (relative to Pb) in the Chugoku IAB than volcanic rocks in the northeastern Japan and Izu arcs (**Figure 2-3**), which is indicative of the addition of sediment-derived hydrous melts or bulk sediments from the subducted slab to wedge mantle ([Pineda-Velasco et al., 2018](#); [Nguyen et al., 2020](#)).

Many past studies of subduction zone processes infer a metasomatized mantle model is the primary vector to explain material transfer between the slab and the mantle (e.g., [Ryan and Chauvel, 2014](#); [Schmidt and Poli, 2014](#)). The metasomatized agent is a combination of partial melting of subducted sediments and metamorphic dehydration of altered oceanic crust (AOC). Owing to different abundances of Sr, Nd, Hf and Pb in subducted basalt and sediment, as well as the different affinities of these elements for partitioning into fluids/melts, mixing of their-derived components may form hyperbolic lines approximated by various curvature functions ([Langmuir et al., 1978](#)). The hyperbolic lines (gray lines) calculated from the mixed compositions of AOC-derived fluids and sediment-derived melts does not reproduce arrays of

data for IAB and ADK of different episodes in plots of ($^{176}\text{Hf}/^{177}\text{Hf}$)_i versus ($^{208}\text{Pb}/^{204}\text{Pb}$)_i, (d) ($^{176}\text{Hf}/^{177}\text{Hf}$)_i versus ($^{206}\text{Pb}/^{204}\text{Pb}$)_i because Hf and Pb have distinct mobilities during slab dehydration (**Figure 2-8C and D**).

Recently, numerical experiments predicted that subducted sediments could detach from the subducting lithosphere and form buoyant diapirs (Currie et al., 2007; Behn et al., 2011). These buoyant flows probably entrain the other lithologies (e.g. AOC and hydrated mantle) from the slab surface, and are termed *mélange* diapirs (Marschall and Schumacher, 2012; Nielsen and Marschall, 2017). Given that the wedge mantle generally has an inverted thermal gradient (Peacock and Wang, 1999), these *mélange* diapirs must be heated up during decompression and likely melt partially (Kelemen et al., 1993). **Figure 2-8** shows mixing lines between bulk compositions of subducted sediment and basalts (in dash lines) to examine this model in SW Japan. The IAB and ADK in the Chugoku district plot off those mixing lines, suggesting *mélange* diapir is unlikely the main mechanism to produce isotopic signatures in our study lavas.

Therefore, the of AOC-release component is unlikely to be aqueous fluids and bulk *mélange*. Moreover, regardless of the episodes in question, the compositions of IAB samples plot on the isotopic arrays formed by ADK samples, whose parental magmas are considered to have been produced by mixing of hydrous melts from subducted basalts and sediment (Pineda-Velasco et al., 2018). This indicates that the component, which was derived from subducted basalts and that was incorporated into IAB, would have had elemental solubilities similar to a hydrous melt through Episode 1 to Episode 3. Nevertheless, the geochemistry of IAB shows clear temporal variations (**Figure 2-4**). Nguyen et al. (2020) also noted a temporal increase of variability in the Sr/Nd ratio of IAB and attributed it to the production of hydrous melt from subducted basalt since Episode 2. The occurrence of ADK suggests Sr, Nd, Hf and Pb isotopic

compositions in Episode-3 IAB arise from the melting of sources by oceanic crust melts; However, episode-1 IAB can be hardly explained by the contribution of oceanic crust melts due to the lack of high Sr/Nd features and adakites.

An alternative model suggests the transition from an aqueous fluid to a melt may occur with prograde metamorphic reactions in the subducting oceanic lithosphere. At a certain P-T range, slab-derived fluids would be less viscous like aqueous solution (Audétat and Keppler, 2004; Hack and Thompson, 2011) but have melt-like element solubility (Kessel et al., 2005). Such fluids are referred to as “supercritical fluids” (SCF; Manning, 2004; Hack et al., 2007; Sanchez-Valle, 2013), which thus may be an effective media to deliver slab geochemical signature to the wedge mantle beneath the Chugoku district. As aforementioned, the depth of the slab beneath Chugoku should have been deeper than at present (90–100 km), possibly 120–140 km beneath Sekiryō and Sanin in Episode 1 (12–8 Ma). Mibe et al. (2011) proposed that the fluid released from subducting oceanic crust at depths greater than 100–120 km under volcanic arcs (3.4 GPa and 770 °C) is supercritical fluid rather than aqueous fluid and/or hydrous melts. According to their model, it would be easier to generate hydrous melt (i.e., adakites) below 3.4 GPa because a relatively high T is required to produce melt above 3.4 GPa. Above 3.4 GPa, relatively low-T, water-rich SCF could become the source of water that generates “normal” basaltic magmas by the hydrous melting of mantle wedge peridotite, instead of forming adakites. Therefore, the fluid released from oceanic crust might be supercritical fluid beneath Chugoku region at episode-1 IAB lavas and change to hydrous melt after 4 Ma.

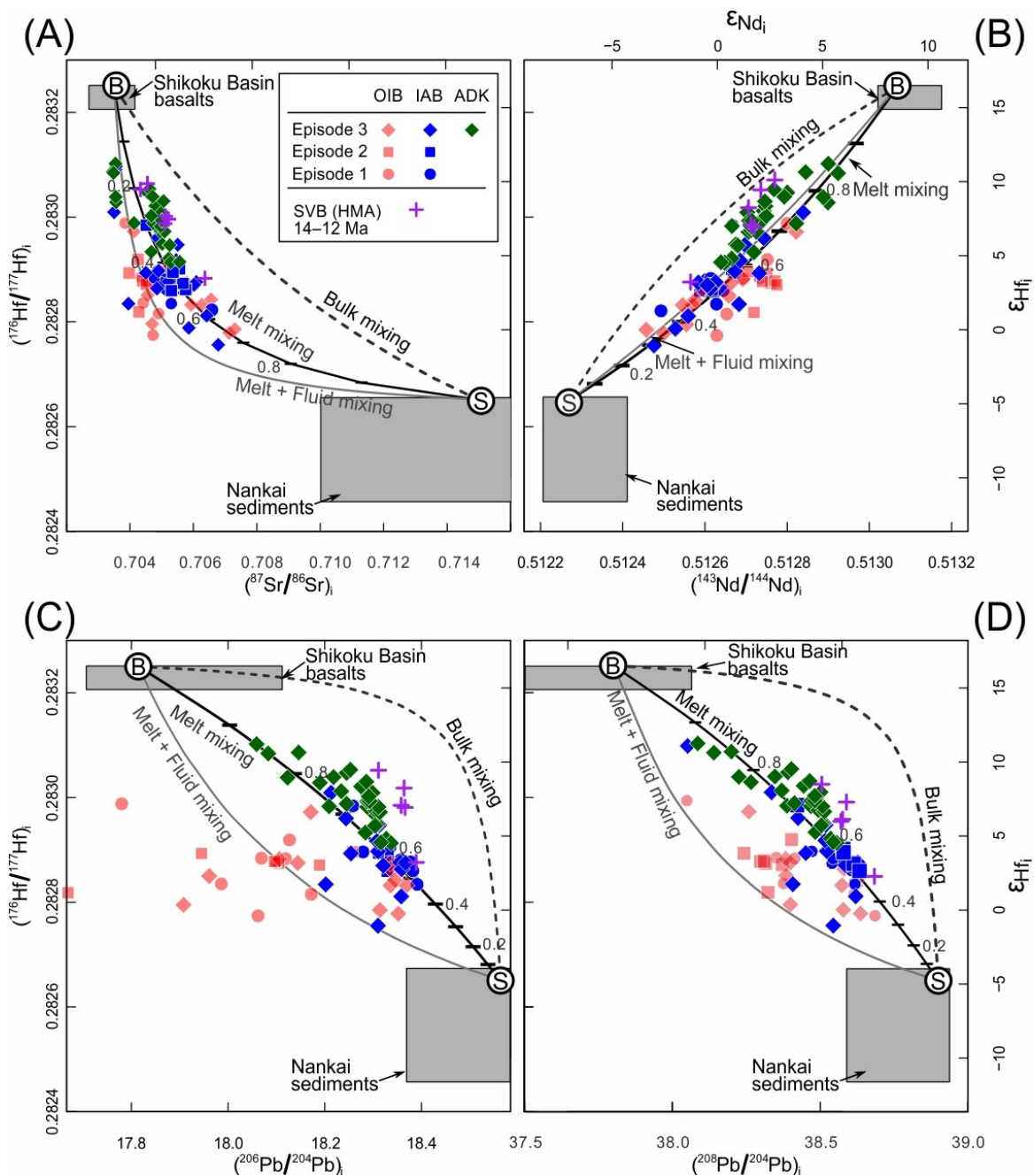


Figure 2-8. Mixing models between two components from oceanic crust basalts and sediments.

(A) $(^{87}\text{Sr}/^{86}\text{Sr})_i$, (B) $(^{143}\text{Nd}/^{144}\text{Nd})_i$, (C) $(^{206}\text{Pb}/^{204}\text{Pb})_i$, and (D) $(^{208}\text{Pb}/^{204}\text{Pb})_i$, plotted against $(^{176}\text{Hf}/^{177}\text{Hf})_i$. Data sources: Nankai sediment, [Ishikawa & Nakamura \(1994\)](#) and [Shimoda *et al.* \(1998\)](#); Shikoku basin basalts, [Hickey-Vargas \(1991, 1998\)](#), [Ishizuka *et al.* \(2009\)](#) and [Straub *et al.* \(2009, 2010\)](#). Solid and black lines indicate the compositions of hybrid melt of sediment- (“S”) and basalt- (“B”) derived melt. Dash lines indicate the compositions of bulk mélange of sediments and basalts. Gray lines indicate the compositions of hybrid component of sediment-derived melt and basalt-derived fluid.

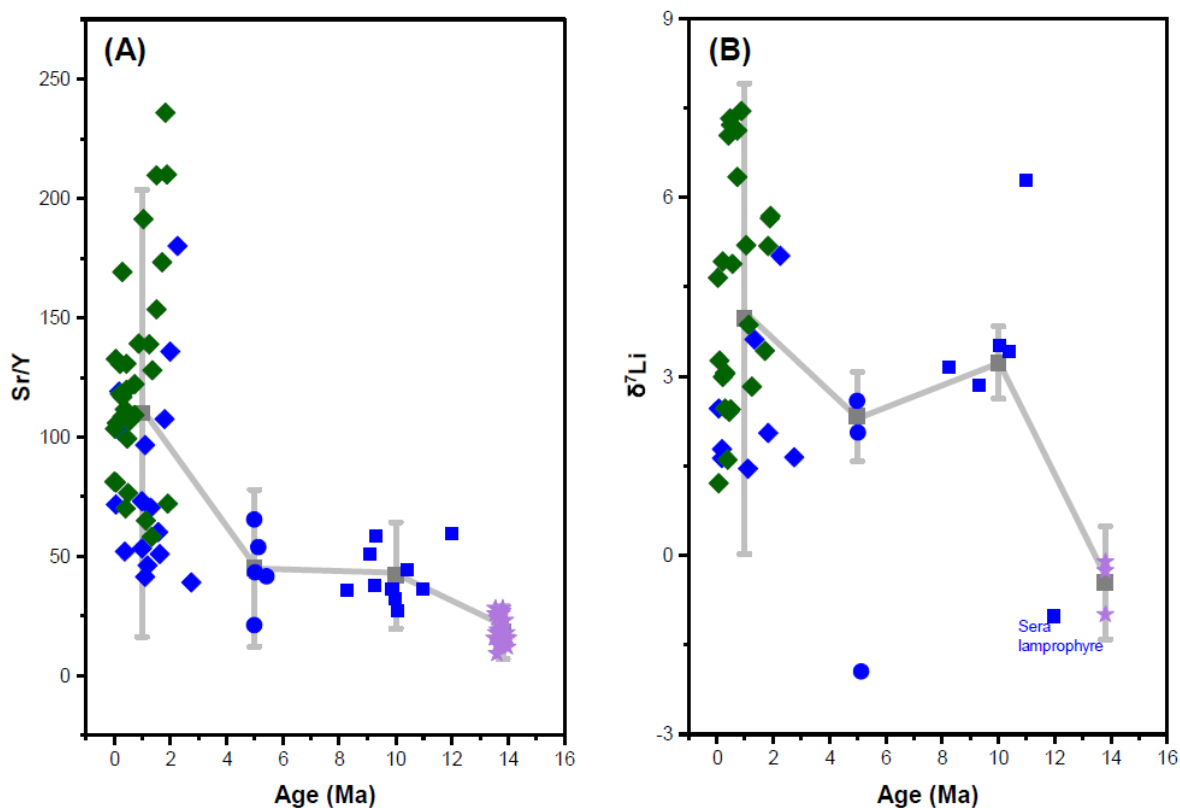


Figure 2-9. Temporal variations in (A) Sr/Y and (B) $\delta^7\text{Li}$ of volcanic rocks from Chugoku and Setouchi.

The mean values in each episode are connected by thick gray lines. The error bars on each mean indicate 2σ variation within each episode.

6.4 Temporal evolution of sediment contribution

Relative contributions of AOC- and sediment-derived components were examined by mass balance modeling using the calculated trace element concentrations and isotopic compositions. The AOC-Sediment mixing scenario extends between AOC melt and the sediment melt end member (**Figure 2-8**). Mixing of 10–60% sediment component with 40–90% basalt component can generally reproduce the Sr-Nd-Pb-Hf isotopic compositions of most Episode-3 ADK and IAB lavas (**Figure 2-8**). This result is consistent with the previous studies with models using Sr-Nd-Pb isotopes (Feineman et al., 2013; Pineda-Velasco et al., 2018). Mixing of 40–60% sediment component with 40–60% basalt component can generally reproduce the Sr-Nd-Pb-

Hf isotopic compositions of Episode-1 and -2 IAB lavas (**Figure 2-8**). This is also supported by the increase of Sr/Y ratio and $\delta^7\text{Li}$ values (**Figure 2-9**).

Our results of Hf isotope suggest the relative proportion of AOC component within slab melt gradually increased with time. The solidus of wet sediments is generally lower than wet basalts ([Johnson and Plank, 1999](#); [Kessel et al., 2005](#); [Schmidt and Poli, 2014](#)). The subduction dip may be steeper in 15-12 Ma than in younger episodes. Therefore, under higher pressures, the P-T path of SW Japan may cross over the sediment wet solidus at temperatures below 700°C but do not cross over the basalt wet solidus. As the subducted PHS plate become shallower, the P-T path of the subducted slab would migrate closer to the wet basalt solidus, also leading to the melting of basaltic crust. Even though some uncertainties of the specific physical conditions of magma generation remain, the overall geochemical data of the SW Japan magmas suggest the gradual transition from the melting of subducted sediments to the melting of oceanic crust in SW Japan.

6.5 Lateral structural variation in the subducting sediments

The Nankai Trough is a shallow trench, owing to subduction of the young and hot Shikoku Basin Plate and greater accumulation of sediments (>1000-m thickness; [Moore et al., 2001](#)). Seismic reflection survey revealed that the base of the accretionary complex has been eroded by the subducting Shikoku Basin Plate with topographic prominence (i.e., seamounts; [Bangs et al., 2006](#)). Eroded sedimentary rocks have been delivered to seismogenic zone, and a part of them probably subducted into deeper level. Since subduction erosion would have occurred for a prolonged period, significant quantity of sediments might have been carried into sub-lithospheric regions beneath SW Japan ([Stern, 2011](#)). Lateral variation in accumulated sediment ([Ike et al., 2008](#)) and slab morphology may lead to lateral variation in sediment contribution ([Park et al., 1999](#); [Bangs et al., 2006](#)). Below, we discuss the relationship between

the slab morphology and spatial variation in Hf isotopic composition of ADK in the episode 3 (**Figure 2-10**).

The Aonoyama and Wakurayama ADK have the most radiogenic Hf isotopic composition, whereas the Oe-Takayama ADK show the least radiogenic Hf among Quaternary ADK (**Figure 2-11A**). The Sambe and Daisen ADK have intermediate compositions between the two groups of ADK mentioned above. The Kurayoshi ADK have $^{176}\text{Hf}/^{177}\text{Hf}$ ratios which cover the range observed in Oe-Takayama, Sambe, Wakurayama and Daisen. The lateral pattern of Hf isotope variation is well similar to that of Nd isotope (**Figure 2-10B**). Given that they have significantly low $^{87}\text{Sr}/^{86}\text{Sr}$ and $^{206}\text{Pb}/^{204}\text{Pb}$ ratios, the Aonoyama ADK is recognized as the different isotopic subgroup in the Quaternary ADK in the Chugoku district (**Figure 2-10C and D**).

According to our modeling, sediment contribution varies among the volcanoes in Chugoku district; magmas erupted in Aonoyama region, located in the western part of Chugoku district, received a smaller contribution (10–20%) than those of the other volcanic regions (20–40%, **Figure 2-8**) in the central and eastern part of Chugoku district. Lateral variation in sediment contribution may be attributed to lateral variation in accumulated sediment (Ike et al., 2008) and slab morphology (Park et al., 1999; Bangs et al., 2006). Basement relief would facilitate drainage of turbidites and high rate of terrigenous sedimentation in the graben (Ike et al., 2008). Prominent basement reliefs are observed along the extinct spreading centers (Kinan Seamounts) in the central and eastern Shikoku basin (**Figure 2-1**). By contrast, the western Shikoku basin have the smooth basement relief (**Figure 2-1**). Ike et al. (2008) revealed that the amount of sediment along Nankai Trough decreases from the central and eastern regions of Shikoku basin with thickness of 1200–2000 m to the western regions with thickness of 600 m (**Figure 2-1**). Given the location of adakite volcanoes (**Figure 2-1**), it is reasonable to expect that adakite magma in the central and eastern Chugoku district (e.g., Daisen, Oe-takayama) could have a

greater contribution from sediment than those formed in the western Chugoku district (Aonoyama). In summary, Hf-isotope variation among adakite magmas in SW Japan can be attributed to lateral variation of sediment input into magma sources in relation to slab morphology.

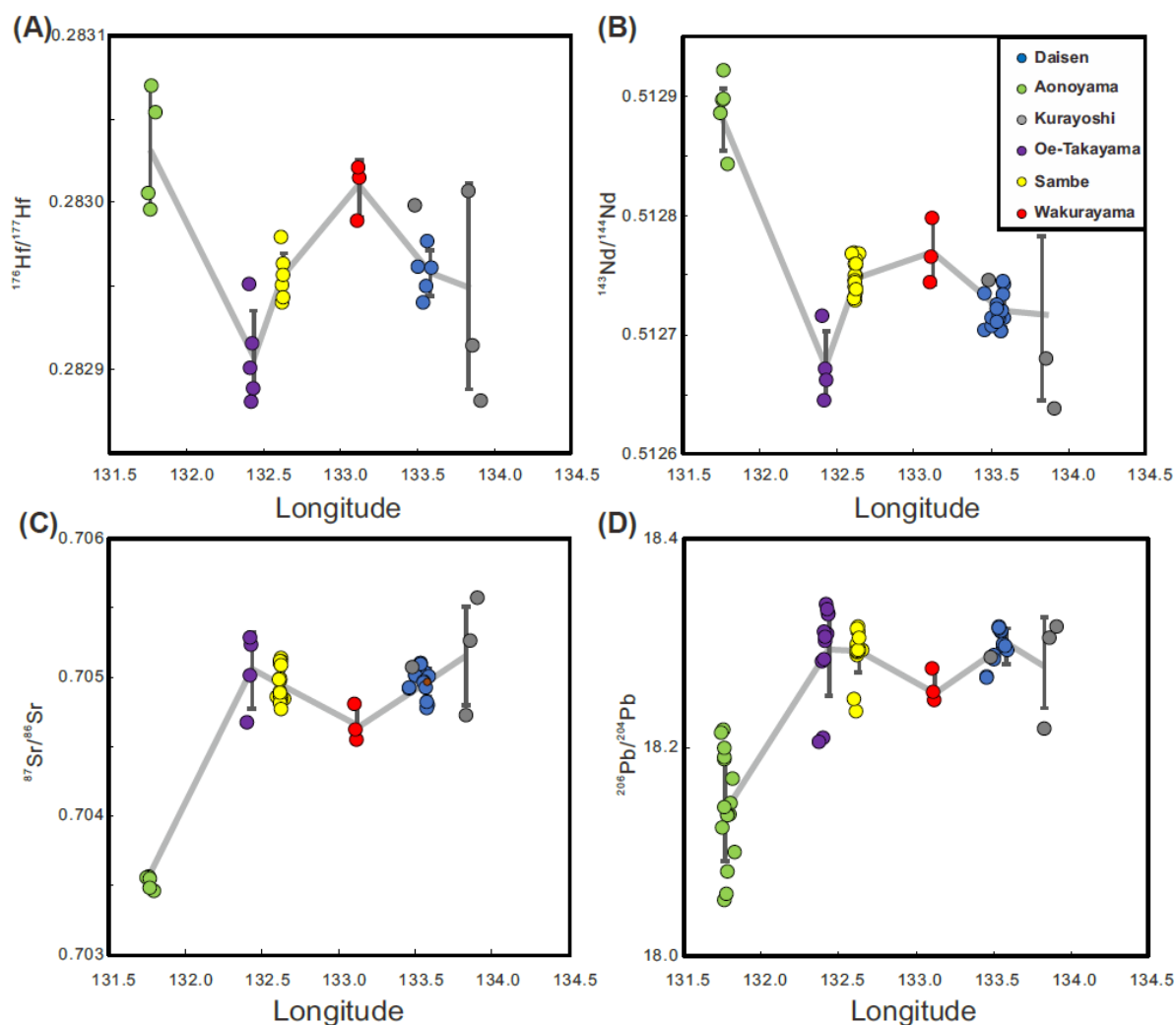


Figure 2-10. Longitudinal variations in Sr-Nd-Pb-Hf isotopic compositions of high-Sr andesites and dacites in the Chugoku district, southwest Japan.

Longitudinal variations in (A) ($^{176}\text{Hf}/^{177}\text{Hf}$)_i, (B) ($^{143}\text{Nd}/^{144}\text{Nd}$)_i, (C) ($^{87}\text{Sr}/^{86}\text{Sr}$)_i, and (D) ($^{206}\text{Pb}/^{204}\text{Pb}$)_i of high-Sr andesites and dacites in the Chugoku district, southwest Japan. The mean values in each volcanic field are connected by thick gray lines. The error bars on each mean indicate 1σ variation within each volcanic field.

6.6 Implication for the evolution of the subducting lithosphere and island-arc volcanism in Southwest Japan

Therefore, the thermal regime operating within wedge mantle beneath Chugoku (Syracuse et al., 2010) is compatible with a scenario in which slab released supercritical liquid or melt throughout the last 12 Myr (Kawamoto et al., 2012). Based on the above discussion, we revised the model by Nguyen et al (2020) for the volcanic evolution in Chugoku (**Figure 2-11**). In Episode 1 (12–8 Ma; **Figure 2-11A**), PHS slab continued to subduct steeply, and would have been located at 120 km beneath Sekiryō and Sanin. At that depth, the slab released supercritical fluid from basaltic crust (Mibe et al., 2011) and sediment melt and induced melting of wedge mantle. At around 5 Ma (in middle of Episode 2; **Figure 2-11B**), the leading edge of the slab was impinged by asthenospheric flow, resulting in slab tearing, dehydration of slab mantle, and melting of slab crust. Propagation of tears led to intensive slab melting and production of voluminous ADK magmas (**Figure 2-11C**).

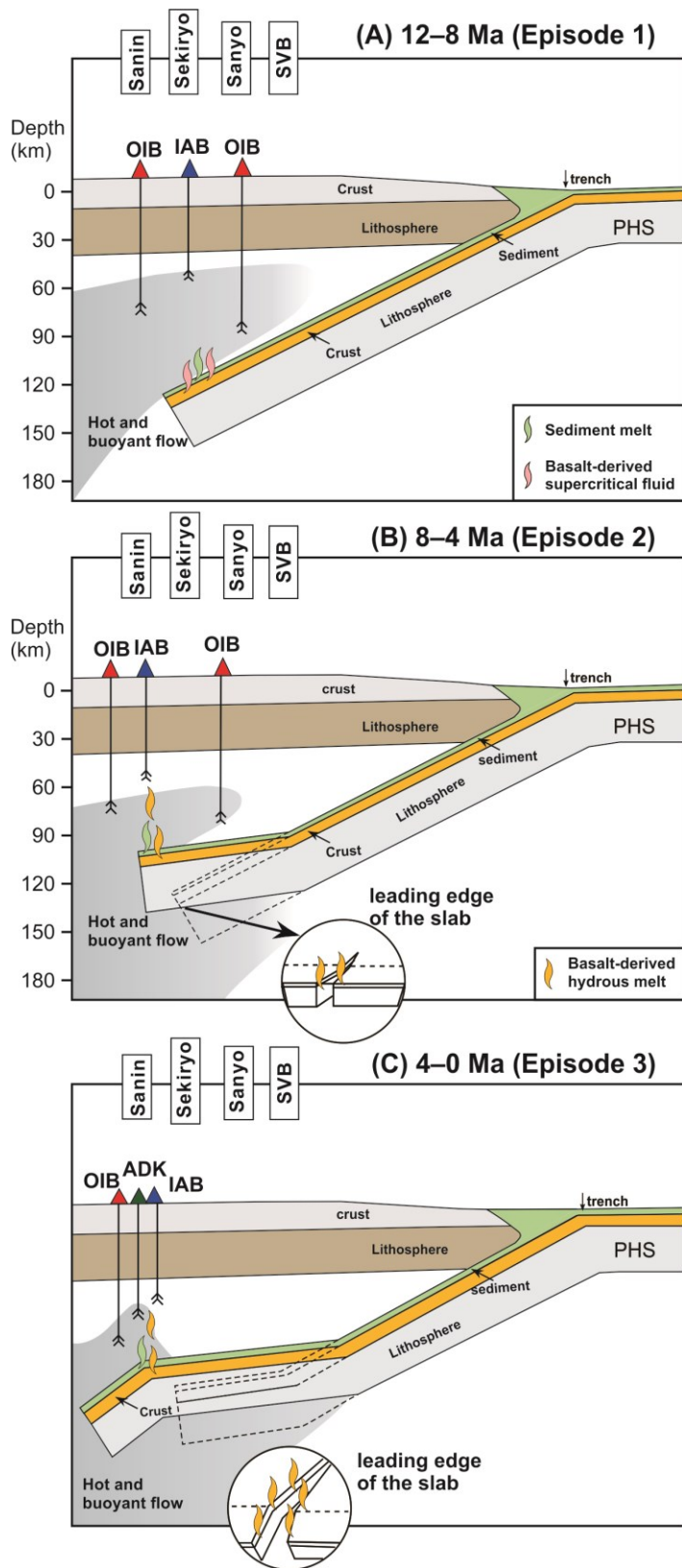


Figure 2-11. A conceptual model for the evolution of the Chugoku volcanism.

See text for details.

7. Conclusions

Hf isotope compositions of volcanic rocks from the Chugoku district in SW Japan show a clear temporal variation, from lower ($\epsilon_{\text{Hf}} = +2.0$ to $+5.0$) values in early-stage [12–5 million years (Myr) ago] samples to higher and more variable values (-0.6 to $+12.5$) in late-stage samples, suggesting the relative proportion of AOC component within slab melt gradually increased with time. Our modeling also suggests subducted basalt-derived fluids changed from supercritical fluids to hydrous melt. The compositional transition of slab-derived fluids in the last 12 Myr may be attributed to the shallowing of subducted slab. Lateral variation in sediment contribution in Chugoku district may be attributed to lateral variation in accumulated sediment and slab morphology.

References

- Armstrong R. L. (1981) Radiogenic isotopes: the case for crustal recycling on a near-steady-state no-continental-growth Earth. *Philosophical Transactions of the Royal Society of London. Series A, Mathematical and Physical Sciences* **301**, 443-472.
- Audétat A. and Keppler H. (2004) Viscosity of fluids in subduction zones. *Science* **303**, 513-516.
- Bangs N. L., Gulick S. P. and Shipley T. H. (2006) Seamount subduction erosion in the Nankai Trough and its potential impact on the seismogenic zone. *Geology* **34**, 701-704.
- Begemann F., Ludwig K. R., Lugmair G. W., Min K., Nyquist L. E. and Patchett P. J., et al. (2001) Call for an improved set of decay constants for geochronological use. *Geochim. Cosmochim. Ac.* **65**, 111-121.
- Behn M. D., Kelemen P. B., Hirth G., Hacker B. R. and Massonne H. (2011) Diapirs as the source of the sediment signature in arc lavas. *Nat. Geosci.* **4**, 641-646.

- Blichert-Toft J. and Frei R. (2001) Complex Sm-Nd and Lu-Hf isotope systematics in metamorphic garnets from the Isua supracrustal belt, West Greenland. *Geochim. Cosmochim. Ac.* **65**, 3177-3189.
- Bouvier A., Vervoort J. D. and Patchett P. J. (2008) The Lu–Hf and Sm–Nd isotopic composition of CHUR: constraints from unequilibrated chondrites and implications for the bulk composition of terrestrial planets. *Earth Planet. Sc. Lett.* **273**, 48-57.
- Cai Y., Lagatta A., Goldstein S. L., Langmuir C. H., Gómez-Tuena A. and Martín-Del Pozzo A. L., et al. (2014) Hafnium isotope evidence for slab melt contributions in the Central Mexican Volcanic Belt and implications for slab melting in hot and cold slab arcs. *Chem. Geol.* **377**, 45-55.
- Chauvel C., Garçon M., Bureau S., Besnault A., Jahn B. and Ding Z. (2014) Constraints from loess on the Hf–Nd isotopic composition of the upper continental crust. *Earth Planet. Sc. Lett.* **388**, 48-58.
- Chauvel C., Lewin E., Carpentier M., Arndt N. T. and Marini J. (2008) Role of recycled oceanic basalt and sediment in generating the Hf–Nd mantle array. *Nat. Geosci.* **1**, 64-67.
- Choi H., Choi S. H. and Yu Y. (2014) Isotope geochemistry of Jeongok basalts, northernmost South Korea: implications for the enriched mantle end-member component. *J. Asian Earth Sci.* **91**, 56-68.
- Choi S. H., Mukasa S. B., Kwon S. and Andronikov A. V. (2006) Sr, Nd, Pb and Hf isotopic compositions of late Cenozoic alkali basalts in South Korea: Evidence for mixing between the two dominant asthenospheric mantle domains beneath East Asia. *Chem. Geol.* **232**, 134-151.
- Choi S. H., Mukasa S. B., Zhou X., Xian X. H. and Andronikov A. V. (2008) Mantle dynamics beneath East Asia constrained by Sr, Nd, Pb and Hf isotopic systematics of ultramafic

- xenoliths and their host basalts from Hannuoba, North China. *Chem. Geol.* **248**, 40-61.
- Cooper G. F., Macpherson C. G., Blundy J. D., Maunder B., Allen R. W. and Goes S., et al. (2020) Variable water input controls evolution of the Lesser Antilles volcanic arc. *Nature* **582**, 525-529.
- Cruz-Uribe A. M., Marschall H. R., Gaetani G. A. and Le Roux V. (2018) Generation of alkaline magmas in subduction zones by partial melting of mélange diapirs—An experimental study. *Geology* **46**, 343-346.
- Currie C. A., Beaumont C. and Huisman R. S. (2007) The fate of subducted sediments: A case for backarc intrusion and underplating. *Geology* **35**, 1111.
- Defant M. J. and Drummond M. S. (1990) Derivation of some modern arc magmas by melting of young subducted lithosphere. *Nature (London)* **347**, 662-665.
- Delavault H., Chauvel C., Sobolev A. and Batanova V. (2015) Combined petrological, geochemical and isotopic modeling of a plume source: Example of Gambier Island, Pitcairn chain. *Earth Planet. Sc. Lett.* **426**, 23-35.
- Eisele J., Sharma M., Galer S. J. G., Blichert-Toft J., Devey C. W. and Hofmann A. W. (2002) The role of sediment recycling in EM-1 inferred from Os, Pb, Hf, Nd, Sr isotope and trace element systematics of the Pitcairn hotspot. *Earth Planet. Sc. Lett.* **196**, 197-212.
- Elliott T., Plank T., Zindler A., White W. and Bourdon B. (1997) Element transport from slab to volcanic front at the Mariana arc. *Journal of Geophysical Research: Solid Earth* **102**, 14991-15019.
- Feineman M., Moriguti T., Yokoyama T., Terui S. and Nakamura E. (2013) Sediment-enriched adakitic magmas from the Daisen volcanic field, Southwest Japan. *Geochemistry, Geophysics, Geosystems* **14**, 3009-3031.
- Gale A., Dalton C. A., Langmuir C. H., Su Y. and Schilling J. G. (2013) The mean composition

- of ocean ridge basalts. *Geochemistry, Geophysics, Geosystems* **14**, 489-518.
- Guo P., Niu Y., Sun P., Ye L., Liu J. and Zhang Y., et al. (2016) The origin of Cenozoic basalts from central Inner Mongolia, East China: The consequence of recent mantle metasomatism genetically associated with seismically observed paleo-Pacific slab in the mantle transition zone. *Lithos* **240**, 104-118.
- Hack A. C. and Thompson A. B. (2011) Density and viscosity of hydrous magmas and related fluids and their role in subduction zone processes. *J. Petrol.* **52**, 1333-1362.
- Hack A. C., Thompson A. B. and Aerts M. (2007) Phase relations involving hydrous silicate melts, aqueous fluids, and minerals. *Reviews in Mineralogy and Geochemistry* **65**, 129-185.
- Hacker B. R., Kelemen P. B. and Behn M. D. (2011) Differentiation of the continental crust by relamination. *Earth Planet. Sc. Lett.* **307**, 501-516.
- Hanyu T., Tatsumi Y. and Nakai S. (2002) A contribution of slab-melts to the formation of high-Mg andesite magmas; Hf isotopic evidence from SW Japan. *Geophys. Res. Lett.* **29**, 1-8.
- Hanyu T., Tatsumi Y., Nakai S., Chang Q., Miyazaki T. and Sato K., et al. (2006) Contribution of slab melting and slab dehydration to magmatism in the NE Japan arc for the last 25 Myr: Constraints from geochemistry. *Geochemistry, Geophysics, Geosystems* **7**, Q8002.
- Hart S. R. (1984) A large-scale isotope anomaly in the Southern Hemisphere mantle. *Nature* **309**, 753-757.
- Hickey-Vargas R. (1998) Origin of the Indian Ocean-type isotopic signature in basalts from Philippine Sea plate spreading centers: An assessment of local versus large-scale processes. *Journal of Geophysical Research: Solid Earth* **103**, 20963-20979.
- Hickey-Vargas R. (1991) Isotope characteristics of submarine lavas from the Philippine Sea: implications for the origin of arc and basin magmas of the Philippine tectonic plate. *Earth Planet. Sc. Lett.* **107**, 290-304.

- Ike T., Moore G. F., Kuramoto S., Park J. O., Kaneda Y. and Taira A. (2008) Variations in sediment thickness and type along the northern Philippine Sea Plate at the Nankai Trough. *Isl. Arc* **17**, 342-357.
- Irvine T. N. and Baragar W. (1971) A guide to the chemical classification of the common volcanic rocks. *Can. J. Earth Sci.* **8**, 523-548.
- Ishikawa T. and Nakamura E. (1994) Origin of the slab component in arc lavas from across-arc variation of B and Pb isotopes. *Nature* **370**, 205-208.
- Ishizuka O., Yuasa M., Taylor R. N. and Sakamoto I. (2009) Two contrasting magmatic types coexist after the cessation of back-arc spreading. *Chem. Geol.* **266**, 274-296.
- Iwamori H. (1991) Zonal structure of Cenozoic basalts related to mantle upwelling in southwest Japan. *Journal of Geophysical Research: Solid Earth* **96**, 6157-6170.
- Johnston S. T. and Thorkelson D. J. (1997) Cocos-Nazca slab window beneath Central America. *Earth Planet. Sc. Lett.* **146**, 465-474.
- Kay R. W. (1978) Aleutian magnesian andesites: Melts from subducted Pacific ocean crust. *J. Volcanol. Geoth. Res.* **4**, 117-132.
- Kelemen P. B. (1995) Genesis of high Mg# andesites and the continental crust. *Contrib. Mineral. Petr.* **120**, 1-19.
- Kelemen P. B. and Behn M. D. (2016) Formation of lower continental crust by relamination of buoyant arc lavas and plutons. *Nat. Geosci.* **9**, 197-205.
- Kelemen P. B., Shimizu N. and Dunn T. (1993) Relative depletion of niobium in some arc magmas and the continental crust: partitioning of K, Nb, La and Ce during melt/rock reaction in the upper mantle. *Earth Planet. Sc. Lett.* **120**, 111-134.
- Keppler H. (1996) Constraints from partitioning experiments on the composition of subduction-zone fluids. *Nature* **380**, 237-240.

- Kessel R., Schmidt M. W., Ulmer P. and Pettke T. (2005) Trace element signature of subduction-zone fluids, melts and supercritical liquids at 120–180 km depth. *Nature* **437**, 724-727.
- Kimura J. I., Stern R. J. and Yoshida T. (2005) Reinitiation of subduction and magmatic responses in SW Japan during Neogene time. *Geol. Soc. Am. Bull.* **117**, 969-986.
- Kimura J. I., Kunikiyo T., Osaka I., Nagao T., Yamauchi S. and Kakubuchi S., et al. (2003) Late Cenozoic volcanic activity in the Chugoku area, southwest Japan arc during back-arc basin opening and reinitiation of subduction. *Isl. Arc* **12**, 22-45.
- Kimura J., Gill J. B., Kunikiyo T., Osaka I., Shimoshioiri Y. and Katakuse M., et al. (2014) Diverse magmatic effects of subducting a hot slab in SW Japan: Results from forward modeling. *Geochemistry, Geophysics, Geosystems* **15**, 691-739.
- Kogiso T., Omori S. and Maruyama S. (2009) Magma genesis beneath Northeast Japan arc: a new perspective on subduction zone magmatism. *Gondwana Res.* **16**, 446-457.
- Kuritani T., Kimura J., Ohtani E., Miyamoto H. and Furuyama K. (2013) Transition zone origin of potassic basalts from Wudalianchi volcano, northeast China. *Lithos* **156**, 1-12.
- Kuritani T., Ohtani E. and Kimura J. (2011) Intensive hydration of the mantle transition zone beneath China caused by ancient slab stagnation. *Nat. Geosci.* **4**, 713-716.
- Kuritani T., Yokoyama T., Kobayashi K. and Nakamura E. (2003) Shift and rotation of composition trends by magma mixing: 1983 eruption at Miyake-jima Volcano, Japan. *J. Petrol.* **44**, 1895-1916.
- Langmuir C. H., Vocke R. D., Hanson G. N. and Hart S. R. (1978) A general mixing equation with applications to Icelandic basalts. *Earth Planet. Sc. Lett.* **37**, 380-392.
- Le Bas M., Maitre R. L., Streckeisen A., Zanettin B. and Rocks I. S. O. T. (1986) A chemical classification of volcanic rocks based on the total alkali-silica diagram. *J. Petrol.* **27**, 745-

750.

- Lu Y. H., Makishima A. and Nakamura E. (2007) Purification of Hf in silicate materials using extraction chromatographic resin, and its application to precise determination of $^{176}\text{Hf}/^{177}\text{Hf}$ by MC-ICP-MS with ^{179}Hf spike. *J. Anal. Atom. Spectrom.* **22**, 69.
- Makishima A., Nath B. N. and Nakamura E. (2008) New sequential separation procedure for Sr, Nd and Pb isotope ratio measurement in geological material using MC-ICP-MS and TIMS. *Geochem. J.* **42**, 237-246.
- Manning C. E. (2004) The chemistry of subduction-zone fluids. *Earth Planet. Sc. Lett.* **223**, 1-16.
- Marschall H. R. and Schumacher J. C. (2012) Arc magmas sourced from mélange diapirs in subduction zones. *Nat. Geosci.* **5**, 862-867.
- Mcculloch M. T. and Wasserburg G. J. (1978) Sm-Nd and Rb-Sr Chronology of Continental Crust Formation: Times of addition to continents of chemically fractionated mantle-derived materials are determined. *Science* **200**, 1003-1011.
- Mcdonough W. F. and Sun S. (1995) The composition of the Earth. *Chem. Geol.* **120**, 223-253.
- Mibe K., Kawamoto T., Matsukage K. N., Fei Y. and Ono S. (2011) Slab melting versus slab dehydration in subduction-zone magmatism. *Proceedings of the National Academy of Sciences* **108**, 8177-8182.
- Millot R., Allègre C., Gaillardet J. and Roy S. (2004) Lead isotopic systematics of major river sediments: a new estimate of the Pb isotopic composition of the Upper Continental Crust. *Chem. Geol.* **203**, 75-90.
- Moore G. F., Taira A., Klaus A., Becker L., Boeckel B. and Cragg B. A., et al. (2001) New insights into deformation and fluid flow processes in the Nankai Trough accretionary prism: Results of Ocean Drilling Program Leg 190. *Geochemistry, Geophysics, Geosystems* **2**.

- Moriguti T., Shibata T. and Nakamura E. (2004) Lithium, boron and lead isotope and trace element systematics of Quaternary basaltic volcanic rocks in northeastern Japan: mineralogical controls on slab-derived fluid composition. *Chem. Geol.* **212**, 81-100.
- Nebel O., Scherer E. E. and Mezger K. (2011) Evaluation of the ^{87}Rb decay constant by age comparison against the U–Pb system. *Earth Planet. Sc. Lett.* **301**, 1-8.
- Nguyen T. T., Kitagawa H., Pineda Velasco I. and Nakamura E. (2020) Feedback of Slab Distortion on Volcanic Arc Evolution: Geochemical Perspective From Late Cenozoic Volcanism in SW Japan. *Journal of Geophysical Research: Solid Earth* **125**.
- Nielsen S. G. and Marschall H. R. (2017) Geochemical evidence for mélangé melting in global arcs. *Science advances* **3**, e1602402.
- Park J. O., Tsuru T., Kaneda Y., Kono Y., Kodaira S. and Takahashi N., et al. (1999) A subducting seamount beneath the Nankai accretionary prism off Shikoku, southwestern Japan. *Geophys. Res. Lett.* **26**, 931-934.
- Patchett P. J., White W. M., Feldmann H., Kielinczuk S. and Hofmann A. W. (1984) Hafnium/rare earth element fractionation in the sedimentary system and crustal recycling into the Earth's mantle. *Earth Planet. Sc. Lett.* **69**, 365-378.
- Peacock S. M. and Wang K. (1999) Seismic Consequences of Warm versus Cool Subduction Metamorphism: Examples from Southwest and Northeast Japan. *Science* **286**, 937-939.
- Pineda Velasco I., Nguyen T. T., Kitagawa H. and Nakamura E. (2015) Comment on “Diverse magmatic effects of subducting a hot slab in SW Japan: Results from forward modeling” by J.-I. Kimura et al. *Geochemistry, Geophysics, Geosystems* **16**, 2848-2852.
- Pineda-Velasco I., Kitagawa H., Nguyen T. T., Kobayashi K. and Nakamura E. (2018) Production of High-Sr Andesite and Dacite Magmas by Melting of Subducting Oceanic Lithosphere at Propagating Slab Tears. *Journal of Geophysical Research: Solid Earth* **123**,

3698-3728.

- Plank T. and Langmuir C. H. (1998) La composition chimique des sédiments en subduction et ses conséquences pour la croûte et le Manteau. *Chem. Geol.* **145**, 325-394.
- Ryan J. G. and Chauvel C. (2014) The subduction-zone filter and the impact of recycled materials on the evolution of the mantle.
- Sakuyama T., Tian W., Kimura J., Fukao Y., Hirahara Y. and Takahashi T., et al. (2013) Melting of dehydrated oceanic crust from the stagnant slab and of the hydrated mantle transition zone: Constraints from Cenozoic alkaline basalts in eastern China. *Chem. Geol.* **359**, 32-48.
- Sanchez-Valle C. (2013) Structure and thermodynamics of subduction zone fluids from spectroscopic studies. *Reviews in Mineralogy and Geochemistry* **76**, 265-309.
- Schmidt M. W., Poli S., Holland H. D. and Turekian K. K. (2014) Treatise on geochemistry. *The Crust*, 567-591.
- Shibata T. and Nakamura E. (1997) Across-arc variations of isotope and trace element compositions from Quaternary basaltic volcanic rocks in northeastern Japan: Implications for interaction between subducted oceanic slab and mantle wedge. *Journal of Geophysical Research: Solid Earth* **102**, 8051-8064.
- Shimoda G., Tatsumi Y., Nohda S., Ishizaka K. and Jahn B. M. (1998) Setouchi high-Mg andesites revisited: geochemical evidence for melting of subducting sediments. *Earth Planet. Sc. Lett.* **160**, 479-492.
- Shu Y., Nielsen S. G., Zeng Z., Shinjo R., Blusztajn J. and Wang X., et al. (2017) Tracing subducted sediment inputs to the Ryukyu arc-Okinawa Trough system: Evidence from thallium isotopes. *Geochim. Cosmochim. Ac.* **217**, 462-491.
- Söderlund U., Patchett P. J., Vervoort J. D. and Isachsen C. E. (2004) The ^{176}Lu decay constant determined by Lu–Hf and U–Pb isotope systematics of Precambrian mafic intrusions. *Earth*

- Planet. Sc. Lett.* **219**, 311-324.
- Steiger R. H. and Jäger E. (1977) Subcommittee on geochronology: convention on the use of decay constants in geo- and cosmochronology. *Earth Planet. Sc. Lett.* **36**, 359-362.
- Stern C. R. and Kilian R. (1996) Role of the subducted slab, mantle wedge and continental crust in the generation of adakites from the Andean Austral Volcanic Zone. *Contrib. Mineral. Petr.* **123**, 263-281.
- Straub S. M., Goldstein S. L., Class C., Schmidt A. and Gomez-Tuena A. (2010) Slab and Mantle Controls on the Sr–Nd–Pb–Hf Isotope Evolution of the Post 42 Ma Izu–Bonin Volcanic Arc. *J. Petrol.* **51**, 993-1026.
- Sun Y., Ying J., Zhou X., Chu Z. and Su B. (2014) Geochemistry of ultrapotassic volcanic rocks in Xiaogulihe NE China: Implications for the role of ancient subducted sediments. *Lithos* **208**, 53-66.
- Syracuse E. M., van Keken P. E. and Abers G. A. (2010) The global range of subduction zone thermal models. *Phys. Earth Planet. In.* **183**, 73-90.
- Tamura Y., Yuhara M., Ishii T., Irino N. and Shukuno H. (2003) Andesites and dacites from Daisen volcano, Japan: partial-to-total remelting of an andesite magma body. *J. Petrol.* **44**, 2243-2260.
- Tatsumi Y. (2006) High-Mg Andesites in the Setouchi Volcanic Belt, Southwestern Japan: Analogy to Archean Magmatism and Continental Crust Formation? *Annu. Rev. Earth Pl. Sc.* **34**, 467-499.
- Terakado Y., Shimizu H. and Masuda A. (1988) Nd and Sr isotopic variations in acidic rocks formed under a peculiar tectonic environment in Miocene Southwest Japan. *Contrib. Mineral. Petr.* **99**, 1-10.
- Tollstrup D. L. and Gill J. B. (2005) Hafnium systematics of the Mariana arc: Evidence for

- sediment melt and residual phases. *Geology* **33**, 737-740.
- Walowski K. J., Wallace P. J., Hauri E. H., Wada I. and Clynne M. A. (2015) Slab melting beneath the Cascade Arc driven by dehydration of altered oceanic peridotite. *Nat. Geosci.* **8**, 404-408.
- Wang X., Chen L., Hofmann A. W., Mao F., Liu J. and Zhong Y., et al. (2017) Mantle transition zone-derived EM1 component beneath NE China: Geochemical evidence from Cenozoic potassic basalts. *Earth Planet. Sc. Lett.* **465**, 16-28.
- Widiyantoro S. and Rob V. D. H. (1996) Structure and Evolution of Lithospheric Slab Beneath the Sunda Arc, Indonesia. *Science* **271**, 1566-1570.
- Willig M., Stracke A., Beier C. and Salters V. J. M. (2020) Constraints on mantle evolution from Ce-Nd-Hf isotope systematics. *Geochim. Cosmochim. Ac.* **272**, 36-53.
- Woodhead J. D., Hergt J. M., Davidson J. P. and Eggins S. M. (2001) Hafnium isotope evidence for ‘conservative’ element mobility during subduction zone processes. *Earth Planet. Sc. Lett.* **192**, 331-346.
- Woodhead J., Stern R. J., Pearce J., Hergt J. and Vervoort J. (2012) Hf-Nd isotope variation in Mariana Trough basalts: The importance of “ambient mantle” in the interpretation of subduction zone magmas. *Geology (Boulder)* **40**, 539-542.
- Yogodzinski G. M., Kay R. W., Volynets O. N., Koloskov A. V. and Kay S. M. (1995) Magnesian andesite in the western Aleutian Komandorsky region: implications for slab melting and processes in the mantle wedge. *Geol. Soc. Am. Bull.* **107**, 505-519.
- Yokoyama T., Kobayashi K., Kuritani T. and Nakamura E. (2003) Mantle metasomatism and rapid ascent of slab components beneath island arcs: Evidence from ^{238}U - ^{230}Th disequilibria of Miyakejima volcano, Izu arc, Japan. *Journal of Geophysical Research: Solid Earth* **108**.

- Yokoyama T., Kuritani T., Kobayashi K. and Nakamura E. (2006) Geochemical evolution of a shallow magma plumbing system during the last 500 years, Miyakejima volcano, Japan: constraints from ^{238}U – ^{230}Th – ^{226}Ra systematics. *Geochim. Cosmochim. Ac.* **70**, 2885-2901.
- Yokoyama T., Makishima A. and Nakamura E. (1999) Evaluation of the coprecipitation of incompatible trace elements with fluoride during silicate rock dissolution by acid digestion. *Chem. Geol.* **157**, 175-187.
- Yoshikawa M. and Nakamura E. (1993) Precise isotope determination of trace amounts of Sr in magnesium-rich samples. *Journal of Mineralogy, Petrology and Economic Geology* **88**, 548-561.
- Zeng G., Chen L. H., Hu S. L., Xu X. S. and Yang L. F. (2013) Genesis of Cenozoic low-Ca alkaline basalts in the Nanjing basaltic field, eastern China: The case for mantle xenolith-magma interaction. *Geochemistry, Geophysics, Geosystems* **14**, 1660-1677.
- Zhang J., Zheng Y. and Zhao Z. (2009) Geochemical evidence for interaction between oceanic crust and lithospheric mantle in the origin of Cenozoic continental basalts in east-central China. *Lithos* **110**, 305-326.
- Zhang W., Zhang H., Fan W., Han B. and Zhou M. (2012) The genesis of Cenozoic basalts from the Jining area, northern China: Sr–Nd–Pb–Hf isotope evidence. *J. Asian Earth Sci.* **61**, 128-142.
- Zindler A. and Hart S. (1986) Chemical geodynamics. *Annu. Rev. Earth Pl. Sc.* **14**, 493-571.

Tables

Table 2-1: Hf, Sr, Nd and Pb isotopic compositions of late Cenozoic volcanic rocks in the Chugoku district, SW Japan.

Sample name	Region	Latitude (°N)	Longitude (°E)	Age (Ma)	Episode*	Type	Hf (ppm)	$(^{176}\text{Hf}/^{177}\text{Hf})_t$	$\epsilon_{\text{Hf}}(t)^\S$	$(^{143}\text{Nd}/^{144}\text{Nd})_t$	$\epsilon_{\text{Nd}}(t)^\#$	$(^{87}\text{Sr}/^{86}\text{Sr})_t$	$(^{206}\text{Pb}/^{204}\text{Pb})_t$	$(^{207}\text{Pb}/^{204}\text{Pb})_t$	$(^{208}\text{Pb}/^{204}\text{Pb})_t$
<u>OIB type</u>															
ABU-28	Mishima	35.47	134.79	11.0	1	OIB	3.26	0.282988	7.42	0.512800	3.59	0.703843	17.780	15.498	37.971
KAN-01	Kanmuri	34.44	132.08	11.0	1	OIB	6.41	0.282815	1.30	0.512653	0.72	0.704904	18.172	15.563	38.614
KAN-03	Kanmuri	35.10	133.91	8.88	1	OIB	6.54	0.282774	-0.20	0.512629	0.20	0.704727	18.062	15.552	38.686
SER-05	Sera	34.67	133.09	9.38	1	OIB	8.30	0.282835	1.98	0.512679	1.19	0.704420	17.986	15.539	38.376
SER-09	Sera	34.85	132.83	9.15	1	OIB	4.58	0.282883	3.68	0.512694	1.48	0.704838	18.119	15.547	38.415
KIB-02	Kibi	34.74	133.38	8.57	1	OIB	4.16	0.282884	3.71	0.512734	2.25	0.704346	18.069	15.525	38.350
KIB-05	Kibi	34.91	133.35	6.14	2	OIB	4.89	0.282893	3.94	0.512751	2.51	0.703970	17.945	15.484	38.243
KIB-08	Kibi	34.64	132.90	8.0	2	OIB	4.83	0.282919	4.91	0.512752	2.57	0.704258	18.127	15.538	38.404
SAM-01**	Hamada	34.79	132.02	6.13	2	OIB	7.38	0.282896	4.07	0.512704	1.60	0.705188	18.257	15.579	38.538
HAM-03	Hamada	35.05	134.11	7.0	2	OIB	5.93	0.282818	1.32	0.512719	1.91	0.704281	17.669	15.501	38.324
MY-01	Tsuyama	35.10	133.91	5.9	2	OIB	3.75	0.282874	3.27	0.512760	2.67	0.704831	18.105	15.525	38.316
MY-02	Tsuyama	35.10	133.91	5.9	2	OIB	3.78	0.282877	3.38	0.512740	2.29	0.704562	18.099	15.519	38.299
MY-03	Tsuyama	35.10	133.94	5.89	2	OIB	3.77	0.282878	3.41	0.512770	2.89	0.704394	18.096	15.517	38.311
OY-01	Tsuyama	35.49	134.53	4.4	2	OIB	3.90	0.282871	3.14	0.512775	2.94	0.704513	18.189	15.532	38.372
TSU-04	Tsuyama	34.75	133.32	6.64	2	OIB	3.20	0.282892	3.94						
ABU-16	Abu	35.04	132.56	0.31	3	OIB	3.28	0.282972	6.62	0.512822	3.76	0.704126	18.171	15.518	38.259
KUR-09	Kurayoshi (young)	35.44	133.82	2.13	3	OIB	4.59	0.282874	3.18	0.512627	-0.01	0.705809	18.335	15.592	38.586
KURA-01	Kurayoshi (young)	35.44	133.84	1.3	3	OIB	3.98	0.282832	1.68	0.512570	-1.14	0.705930	18.336	15.588	38.574
KURA-03	Kurayoshi (young)	35.44	133.84	1.34	3	OIB	4.32	0.282863	2.78	0.512594	-0.66	0.705901	18.336	15.590	38.581
KURA-04	Kurayoshi (young)	35.49	133.18	1.3	3	OIB	4.10	0.282832	1.68	0.512546	-1.60	0.706267	18.369	15.595	38.619
DAIK-02	Daikonjima	35.51	133.19	0.1	3	OIB	3.10	0.282850	2.30	0.512658	0.55	0.704557	17.961	15.536	38.385
DAIK-03	Daikonjima	34.44	131.58	0.10	3	OIB	2.81	0.282795	0.36	0.512555	-1.47	0.704708	17.908	15.548	38.399
OGI-12	N. Hyogo	35.49	133.83	1.09	3	OIB	4.12	0.282778	-0.23	0.512500	-2.52	0.707136	18.352	15.597	38.637

HYO-09	N. Hyogo	35.49	134.70	0.14	3	OIB	3.46	0.282882	3.43	0.512692	1.22	0.704781	18.106	15.554	38.383
HYO-11	N. Hyogo	35.58	134.78	0.09	3	OIB	3.84	0.282875	3.18	0.512664	0.67	0.705001	18.144	15.552	38.400
HYO-14	N. Hyogo	35.49	134.45	1.52	3	OIB	4.61	0.282842	2.04	0.512576	-1.01	0.706565	18.345	15.594	38.624
Yakuno	N. Hyogo	34.79	131.15	0.4	3	OIB	4.64	0.282785	0.01	0.512457	-3.36	0.707316	18.314	15.583	38.578
<u>IAB type</u>															
OTS-01	Otsu	34.35	130.84	9.10	1	IAB	5.82	0.282834	1.94	0.512628	0.18	0.705305	18.391	15.607	38.618
OTS-05	Otsu	34.34	130.95	8.29	1	IAB	4.11	0.282877	3.42	0.512612	-0.15	0.705271	18.377	15.602	38.595
OTS-06	Otsu	34.39	130.94	9.31	1	IAB	4.61	0.282860	2.86	0.512644	0.51	0.705159	18.382	15.609	38.606
OTS-10	Otsu	34.41	131.13	9.25	1	IAB	3.91	0.282896	4.15	0.512675	1.11	0.704882	18.279	15.587	38.472
SER-11	Sera	34.39	132.09	12.0	1	IAB	14.6	0.282821	1.55	0.512493	-2.38	0.706591	N.D.**	N.D.**	N.D.**
HIB-01	Hiba	34.99	132.90	10	1	IAB	4.36	0.282905	4.47	N.D.**	N.D.**		18.335	15.593	38.531
HIB-04	Hiba	35.06	133.04	10.4	1	IAB	5.49	0.282881	3.62	0.512605	-0.22	0.705097	18.357	15.593	38.557
HIB-06	Hiba	35.05	133.07	9.90	1	IAB	5.18	0.282874	3.35	0.512609	-0.16	0.705005	18.338	15.589	38.540
HIB-07	Hiba	34.99	133.08	10.1	1	IAB	4.48	0.282883	3.70	0.512614	-0.06	0.704768	18.331	15.588	38.543
MAT-04	Matsue	35.45	133.07	11.0	1	IAB	5.43	0.282984	7.29	0.512667	1.00	0.704509	18.258	15.576	38.422
MKM-01	Kurayoshi (old)	35.49	134.10	5.03	2	IAB	2.37	0.282900	4.20	0.512665	0.82	0.705568	18.331	15.586	38.579
KUR-16	Kurayoshi (old)	35.44	133.86	5	2	IAB	2.90	0.282861	2.80	0.512617	-0.13	0.705760	N.D.**	N.D.**	N.D.**
KUR-17	Kurayoshi (old)	35.44	133.86	5.15	2	IAB	2.85	0.282873	3.22	0.512621	-0.05	0.705671	18.351	15.594	38.614
KRW-02	Kurayoshi (old)	35.26	134.10	4.99	2	IAB	2.02	0.282859	2.72	0.512587	-0.71	0.705310	18.329	15.578	38.633
KRW-03	Kurayoshi (old)	35.26	134.14	5.43	2	IAB	2.25	0.282894	3.99	0.512670	0.92	0.705356	18.311	15.578	38.580
KAW-03	Kawamoto	34.99	132.51	2.26	3	IAB	2.25	0.282787	0.13	0.512528	-1.93	0.705861	N.D.**	N.D.**	N.D.**
MEN-02	Mengame	34.94	132.72	1.11	3	IAB	2.70	0.282897	3.97	0.512673	0.86	0.704906	18.310	15.581	38.523
ABU-06	Abu	34.44	131.50	1.57	3	IAB	4.47	0.282876	3.25	0.512626	-0.03	0.705215	18.356	15.590	38.600
ABU-11	Abu	34.48	131.44	0.06	3	IAB	2.70	0.283009	7.92	0.512839	4.09	0.703502	18.213	15.537	38.336
ABU-17	Abu	34.48	131.61	0.39	3	IAB	4.02	0.282893	3.83	0.512732	2.00	0.704504	18.254	15.553	38.451
ABU-21	Abu	34.49	131.63	0.18	3	IAB (SHO)	9.51	0.283091	10.82	0.512907	5.40	0.703546	N.D.**	N.D.**	N.D.**
ABU-23	Abu	34.49	131.65	0.18	3	IAB (SHO)	9.16	0.283097	11.04	0.512913	5.53	0.703562	18.036	15.512	38.052
ABU-26	Abu	34.60	131.69	2.01	3	IAB	4.61	0.282863	2.80	0.512613	-0.28	0.704858	18.359	15.603	38.614
MAT-02	Yokota	35.42	133.19	1.2	3	IAB	2.80	0.282960	6.20	0.512743	2.23	0.704882	18.244	15.564	38.425

YOK-01	Yokota	35.19	133.09	1.1	3	IAB	2.67	0.282917	4.68	0.512686	1.11	0.705458	18.308	15.580	38.517
YOK-05	Yokota	35.16	133.21	1.32	3	IAB	2.34	0.282947	5.75	0.512697	1.35	0.705512	18.313	15.582	38.519
US-01	Kurayoshi (young)	35.45	133.92	1.00	3	IAB	3.45	0.282755	-1.04	0.512476	-2.99	0.706789	18.310	15.578	38.544
OGI-03	N. Hyogo	35.48	134.42	0.98	3	IAB	4.40	0.282811	0.94	0.512559	-1.37	0.706422	18.358	15.593	38.621
INA-01	N. Hyogo	35.50	134.30	2.74	3	IAB	2.68	0.282875	3.25	0.512584	-0.82	0.706099	18.367	15.599	38.627
HYO-03	N. Hyogo	35.49	134.53	1.62	3	IAB	4.50	0.282870	3.03	0.512606	-0.42	0.706028	18.321	15.586	38.586
HYO-15	N. Hyogo	35.59	134.81	1.81	3	IAB	6.86	0.282834	1.77	0.512683	1.09	0.703953	18.202	15.556	38.408

ADK type

AON-03	Aonoyama	34.49	131.82	0.29	3	ADK	3.24		N.D. ^{††}	0.512851	4.32	0.703442	18.170	15.533	38.241
AON-04	Aonoyama	34.47	131.80	0.09	3	ADK	3.31	0.283086	10.65	0.512845	4.20	0.703460	18.146	15.527	38.200
AON-09	Aonoyama	34.45	131.77	0.30	3	ADK	3.64	0.283028	8.60	0.512899	5.26	0.703562	18.190	15.534	38.266
AON-17	Aonoyama	34.08	131.75	0.3	3	ADK	3.69	0.283038	8.95	0.512888	5.05	0.703550	18.123	15.532	38.225
AON-21	Aonoyama	34.25	131.77	0.38	3	ADK	3.80	0.283102	11.22	0.512900	5.28	0.703545	18.059	15.507	38.086
AON-22	Aonoyama	34.19	131.76	0.5	3	ADK	4.17	0.283084	10.58	0.512924	5.75	0.703481	18.083	15.521	38.140
OE-01	Oe-Takayama	35.07	132.43	1.52	3	ADK	2.64	0.282948	5.79	0.512675	0.91	0.705015	18.309	15.584	38.510
OE-02	Oe-Takayama	35.09	132.44	1.5	3	ADK	2.73		N.D. ^{††}	0.512662	0.66	0.705236	18.328	15.590	38.538
OE-03	Oe-Takayama	35.09	132.44	1.70	3	ADK	2.68	0.282921	4.84	0.512665	0.73	0.705236	18.327	15.589	38.536
OE-09	Oe-Takayama	35.12	132.41	1.05	3	ADK	2.46	0.282983	7.02	0.512666	0.72	0.705040	18.209	15.555	38.388
OE-10	Oe-Takayama	35.10	132.41	1.87	3	ADK	2.67	0.282933	5.27	0.512719	1.78	0.704677	18.284	15.580	38.484
OE-11	Oe-Takayama	35.11	132.42	1.83	3	ADK	2.78	0.282913	4.56	0.512648	0.40	0.705284	18.337	15.595	38.556
SAM-01**	Sambe	35.16	132.62	1.36	3	ADK	2.99	0.283012	8.05	0.512743	2.24	0.704832	18.234	15.550	38.370
SAM-06	Sambe	35.14	132.63	0.07	3	ADK	2.74	0.282995	7.43	0.512737	2.09	0.704832	18.293	15.571	38.484
SAM-14	Sambe	35.13	132.62	0.43	3	ADK	2.30	0.282972	6.62	0.512706	1.49	0.704957	18.299	15.576	38.504
SAM-16	Sambe	35.14	132.62	0.3	3	ADK	2.61	0.282982	6.97	0.512719	1.74	0.704832	18.288	15.566	38.469
SAM-20	Sambe	35.15	132.63	0.22	3	ADK	2.67	0.282988	7.18	0.512733	2.01	0.704738	18.293	15.572	38.484
SAM-21	Sambe	35.11	132.63	0.2	3	ADK	2.24	0.282975	6.72	0.512712	1.60	0.705057	18.305	15.575	38.493
WAK-01	Wakurayama	35.47	133.11	0.86	3	ADK	2.58	0.283021	8.36	0.512747	2.31	0.704807	18.275	15.569	38.444
WAK-02	Wakurayama	35.49	133.12	0.72	3	ADK	2.50	0.283047	9.28	0.512800	3.34	0.704552	18.245	15.558	38.391
WAK-03	Wakurayama	35.49	133.12	0.73	3	ADK	2.76	0.283053	9.49	0.512768	2.71	0.704620	18.253	15.561	38.403
2060707	Daisen	35.36	133.54	0.02	3	ADK	2.11	0.282972	6.61	0.512725	1.85	0.705097	18.314	15.579	38.514

3052002	Daisen	35.36	133.56	0.06	3	ADK	2.05	0.282982	6.97	0.512713	1.62	0.704969	18.311	15.578	38.508
3053003	Daisen	35.33	133.57	0.51	3	ADK	2.62	0.283009	7.93	0.512703	1.44	0.705004	18.299	15.578	38.502
3060102	Daisen	35.36	133.51	0.46	3	ADK	2.40	0.282993	7.36	0.512707	1.51	0.705013	18.288	15.575	38.470
3060604	Daisen	35.40	133.59	0.41	3	ADK	1.90	0.282993	7.36	0.512714	1.65	0.705005	18.293	15.575	38.482
SAN2	Daisen	35.38	133.57	0.05	3	ADK	2.27	0.283002	7.67	0.512749	2.32	0.704676	18.291	15.574	38.482
YOK-11	Daisen	35.36	133.49	0.55	3	ADK	2.44	0.283030	8.67	0.512746	2.28	0.705065	18.286	15.573	38.465
TG-01	Kurayoshi (young)	35.48	133.91	1.34	3	ADK	3.67	0.282914	4.59	0.512639	0.20	0.705568	18.316	15.586	38.545
KUR-01	Kurayoshi (young)	35.47	133.83	1.90	3	ADK	2.77	0.283039	9.02	0.512793	3.23	0.704720	18.218	15.550	38.347
KUR-05	Kurayoshi (young)	35.46	133.86	1.13	3	ADK	3.30	0.282946	5.71	0.512680	1.00	0.705261	18.304	15.576	38.504
KUR-11	Kurayoshi (young)	35.47	133.80	1.24	3	ADK	3.30	0.282988	7.20	0.512822	3.77	0.704130	18.245	15.558	38.413

Note: Sample locality (latitude and longitude), age, classification of rock type, Lu and Hf abundance, and Sr-Nd-Pb isotope data are from Feineman et al. (2013), Pineda-Velasco et al. (2018), Nguyen et al. (2020 in revision) and this study.

Type: OIB, ocean-island-basalt type; IAB, island-arc-basalt type (SHO, shoshonite); ADK, adakite type (high-Sr andesite and dacite)

††N.D. = not determined.

Table 2-2: Hf, Sr, Nd and Pb isotopic composition of hot and cold subduction zones in Pacific margins. (Reference therein)

Sample name	Arc	$(^{87}\text{Sr}/^{86}\text{Sr})_i$	$(^{143}\text{Nd}/^{144}\text{Nd})_i$	$(^{176}\text{Hf}/^{177}\text{Hf})_i$	$(^{206}\text{Pb}/^{204}\text{Pb})_i$	$(^{207}\text{Pb}/^{204}\text{Pb})_i$	$(^{208}\text{Pb}/^{204}\text{Pb})_i$	Reference
<u>Cold subduction zones</u>								
TYO 101	NE Japan	0.704266	0.512806	0.283037	18.323	15.565	38.422	Hanyu et al. (2006)
TYO 102	NE Japan	0.704957	0.512773	0.283055	18.379	15.580	38.483	Hanyu et al. (2006)
TYO 103	NE Japan	0.704974	0.512772	0.283008	18.383	15.582	38.489	Hanyu et al. (2006)
TYO 104	NE Japan	0.704600	0.512745	0.283040	18.377	15.577	38.482	Hanyu et al. (2006)
RZ-1	NE Japan	0.704478	0.512784	0.283056	18.297	15.553	38.309	Hanyu et al. (2006)

RZ-4	NE Japan	0.704563	0.512836	0.283136	18.330	15.561	38.361	Hanyu et al. (2006)
RZ-5	NE Japan	0.704792	0.512778	0.283054	18.383	15.569	38.426	Hanyu et al. (2006)
RZ-6	NE Japan	0.704824	0.512798	0.283129	18.396	15.582	38.468	Hanyu et al. (2006)
RZ-13	NE Japan	0.704342	0.512826	0.283075	18.271	15.547	38.267	Hanyu et al. (2006)
RZ-16	NE Japan	0.704776	0.512731	0.283066	18.417	15.583	38.478	Hanyu et al. (2006)
1908	NE Japan	N.D.	N.D.	0.283096	N.D.	N.D.	N.D.	Hanyu et al. (2006)
1909	NE Japan	0.704342	0.512798	0.283130	18.406	15.588	38.493	Hanyu et al. (2006)
1910	NE Japan	0.704176	0.512814	0.283144	18.369	15.599	38.481	Hanyu et al. (2006)
1911	NE Japan	N.D.	N.D.	0.283143	N.D.	N.D.	N.D.	Hanyu et al. (2006)
1912	NE Japan	0.704173	0.512823	0.283117	18.388	15.586	38.453	Hanyu et al. (2006)
TM-0	NE Japan	0.704709	0.512706	0.283120	18.427	15.586	38.523	Hanyu et al. (2006)
TM-1	NE Japan	0.704244	0.512791	0.283131	18.393	15.570	38.459	Hanyu et al. (2006)
TM-2	NE Japan	0.704210	0.512788	0.283140	18.401	15.578	38.482	Hanyu et al. (2006)
TM-3	NE Japan	N.D.	N.D.	0.283133	N.D.	N.D.	N.D.	Hanyu et al. (2006)
SKD-1	NE Japan	N.D.	N.D.	0.283125	N.D.	N.D.	N.D.	Hanyu et al. (2006)
1903	NE Japan	N.D.	N.D.	0.283158	N.D.	N.D.	N.D.	Hanyu et al. (2006)
1904	NE Japan	0.704367	0.512841	0.283185	18.453	15.591	38.545	Hanyu et al. (2006)
1905	NE Japan	0.704377	0.512875	0.283173	18.453	15.589	38.539	Hanyu et al. (2006)
1906	NE Japan	0.704468	0.512857	0.283167	18.456	15.592	38.561	Hanyu et al. (2006)
1907	NE Japan	N.D.	N.D.	0.283138	N.D.	N.D.	N.D.	Hanyu et al. (2006)
95072606	NE Japan	0.704301	0.512845	0.283149	18.561	15.601	38.637	Hanyu et al. (2006)
95073105	NE Japan	0.704216	0.512830	0.283164	18.558	15.605	38.656	Hanyu et al. (2006)
02082708	NE Japan	0.704242	0.512826	0.283168	18.550	15.590	38.593	Hanyu et al. (2006)
02082709	NE Japan	N.D.	N.D.	0.283169	N.D.	N.D.	N.D.	Hanyu et al. (2006)
GAM-07	Kamchatka	N.D.	0.513074	0.283220	N.D.	N.D.	N.D.	Münker et al. (2004)
GAM-14	Kamchatka	N.D.	0.512991	0.283212	N.D.	N.D.	N.D.	Münker et al. (2004)
GAM-26	Kamchatka	N.D.	0.513085	0.283255	N.D.	N.D.	N.D.	Münker et al. (2004)
GAM-28	Kamchatka	0.703341	0.513046	0.283235	18.341	15.518	38.093	Churikova et al. (2001), Münker et al. (2004)
KIZ-01	Kamchatka	0.703347	0.513107	0.283272	N.D.	N.D.	N.D.	Churikova et al. (2001), Münker et al. (2004)

KIZ-19	Kamchatka	N.D.	0.513118	0.283235	N.D.	N.D.	N.D.	Münker et al. (2004)
KIZ-24	Kamchatka	0.703342	0.513061	0.283247	N.D.	N.D.	N.D.	Churikova et al. (2001), Münker et al. (2004)
KIZ-24/1	Kamchatka	0.703365	0.513060	0.283251	18.326	15.510	38.056	Churikova et al. (2001), Münker et al. (2004)
SHM-01	Kamchatka	0.703339	0.513083	0.283262	18.312	15.503	37.983	Churikova et al. (2001), Münker et al. (2004)
SHM-03	Kamchatka	N.D.	0.513137	0.283292	N.D.	N.D.	N.D.	Münker et al. (2004)
SHM-04	Kamchatka	0.703378	0.513045	0.283262	N.D.	N.D.	N.D.	Churikova et al. (2001), Münker et al. (2004)
KOM-02/2	Kamchatka	0.703477	0.513036	0.283231	N.D.	N.D.	N.D.	Münker et al. (2004)
KOM-06	Kamchatka	0.703381	0.513044	0.283211	N.D.	N.D.	N.D.	Churikova et al. (2001), Münker et al. (2004)
KLU-03	Kamchatka	0.703580	0.513104	0.283244	18.287	15.508	37.994	Churikova et al. (2001), Münker et al. (2004)
KLU-06	Kamchatka	0.703600	0.513070	0.283275	N.D.	N.D.	N.D.	Münker et al. (2004)
KLU-12	Kamchatka	0.703659	0.513115	0.283276	18.309	15.517	38.020	Churikova et al. (2001), Münker et al. (2004)
KLU-15	Kamchatka	0.703504	0.513103	0.283226	18.306	15.496	37.964	Churikova et al. (2001), Münker et al. (2004)
2330	Kamchatka	0.703374	0.513091	0.283236	18.248	15.481	37.908	Churikova et al. (2001), Münker et al. (2004)
3-90	Kamchatka	0.703394	0.513982	0.283224	18.273	15.516	38.038	Churikova et al. (2001), Münker et al. (2004)
TOL-96-01	Kamchatka	N.D.	0.513141	0.283267	N.D.	N.D.	N.D.	Münker et al. (2004)
TOL-96-03	Kamchatka	0.703351	0.513094	0.283271	18.191	15.479	37.873	Churikova et al. (2001), Münker et al. (2004)
8840	Kamchatka	N.D.	0.513095	0.283255	N.D.	N.D.	N.D.	Münker et al. (2004)
90093	Kamchatka	0.703467	0.513125	0.283253	N.D.	N.D.	N.D.	Churikova et al. (2001), Münker et al. (2004)
2569	Kamchatka	0.703365	0.513127	0.283257	N.D.	N.D.	N.D.	Churikova et al. (2001), Münker et al. (2004)
2577	Kamchatka	N.D.	0.513138	0.283258	N.D.	N.D.	N.D.	Münker et al. (2004)
2581	Kamchatka	0.703390	0.513058	0.283246	18.328	15.481	37.908	Kepezhinskas et al., 1997, Münker et al. (2004)
2585	Kamchatka	0.703384	0.513137	0.283248	18.363	15.490	37.941	Churikova et al. (2001), Münker et al. (2004)
5734	Kamchatka	N.D.	0.513059	0.283231	N.D.	N.D.	N.D.	Münker et al. (2004)
SHIV-01-01	Kamchatka	N.D.	0.513157	0.283259	N.D.	N.D.	N.D.	Münker et al. (2004)
SHIV-01-05	Kamchatka	N.D.	0.513138	0.283254	N.D.	N.D.	N.D.	Münker et al. (2004)
SHIV-01-12	Kamchatka	N.D.	0.513142	0.283259	N.D.	N.D.	N.D.	Münker et al. (2004)
ACH-01	Kamchatka	N.D.	0.513039	0.283184	N.D.	N.D.	N.D.	Münker et al. (2004)
ESO-08	Kamchatka	0.703350	0.513105	0.283248	18.255	15.493	37.939	Churikova et al. (2001), Münker et al. (2004)
ICH-02	Kamchatka	0.703374	0.513059	0.283256	N.D.	N.D.	N.D.	Churikova et al. (2001), Münker et al. (2004)
ICH-05	Kamchatka	0.703390	0.513000	0.283110	18.063	15.483	37.975	Churikova et al. (2001), Münker et al. (2004)

ICH-10	Kamchatka	0.703400	0.512987	0.283152	N.D.	N.D.	N.D.	Churikova et al. (2001), Münker et al. (2004)
ICH-69	Kamchatka	N.D.	0.513021	0.283192	N.D.	N.D.	N.D.	Münker et al. (2004)
8-4-78	Aleutians	0.703012	0.513113	0.283211	17.889	15.402	37.271	Yogodzinski et al. (1995), Münker et al. (2004)
8-6-78	Aleutians	0.703092	0.513093	0.283225	17.928	15.411	37.362	Yogodzinski et al. (1995), Münker et al. (2004)
KCP-Y1	Aleutians	0.702912	0.513079	0.283212	17.778	15.384	37.191	Yogodzinski et al. (1995), Münker et al. (2004)
ADK-53	Aleutians	0.702842	0.513089	0.283205	18.365	15.478	37.840	Kay et al. (1978), Münker et al. (2004)
V38-42Y3	Aleutians	0.702812	0.513087	0.283235	17.883	15.406	37.324	Yogodzinski et al. (1995), Münker et al. (2004)
CB 3	Aleutians	0.703200	0.513006	0.283118	18.806	15.569	38.345	Morris and Hart (1983), Yogodzinski et al. (2010)
CB 5	Aleutians	0.703200	0.512998	0.283115	N.D.	N.D.	N.D.	Morris and Hart (1983), Yogodzinski et al. (2010)
CB 7	Aleutians	0.703510	0.512988	0.283114	18.909	15.579	38.457	Morris and Hart (1983), Yogodzinski et al. (2010)
CB 12	Aleutians	0.703360	0.512994	0.283119	N.D.	N.D.	N.D.	Morris and Hart (1983), Yogodzinski et al. (2010)
CB 44	Aleutians	N.D.	0.512975	0.283138	18.872	15.577	38.412	Morris and Hart (1983), Yogodzinski et al. (2010)
AMK 1	Aleutians	0.703100	0.513011	0.283120	N.D.	N.D.	N.D.	Morris and Hart (1983), Yogodzinski et al. (2010)
AMK 3	Aleutians	0.703080	0.513024	0.283126	N.D.	N.D.	N.D.	Morris and Hart (1983), Yogodzinski et al. (2010)
AMK 4	Aleutians	0.703050	0.513010	0.283127	18.814	15.570	38.369	Morris and Hart (1983), Yogodzinski et al. (2010)
AMK 5	Aleutians	0.703150	0.513009	0.283128	N.D.	N.D.	N.D.	Morris and Hart (1983), Yogodzinski et al. (2010)
AMK 7	Aleutians	0.703230	0.513004	0.283125	N.D.	N.D.	N.D.	Morris and Hart (1983), Yogodzinski et al. (2010)
SAR 11	Aleutians	N.D.	0.513074	0.283154	N.D.	N.D.	N.D.	Yogodzinski et al. (2010)
SAR 4	Aleutians	N.D.	0.513077	0.283148	N.D.	N.D.	N.D.	Yogodzinski et al. (2010)
UM 10	Aleutians	N.D.	0.513033	0.283153	N.D.	N.D.	N.D.	Yogodzinski et al. (2010)
UM 4	Aleutians	N.D.	0.513055	0.283149	N.D.	N.D.	N.D.	Yogodzinski et al. (2010)
UM 22	Aleutians	N.D.	0.513047	0.283154	N.D.	N.D.	N.D.	Yogodzinski et al. (2010)
UM 5	Aleutians	N.D.	0.513043	0.283142	N.D.	N.D.	N.D.	Yogodzinski et al. (2010)
UM 16	Aleutians	N.D.	0.513062	0.283151	N.D.	N.D.	N.D.	Yogodzinski et al. (2010)
UM 11	Aleutians	N.D.	0.513038	0.283153	N.D.	N.D.	N.D.	Yogodzinski et al. (2010)
BOG-3	Aleutians	N.D.	0.513041	0.283124	N.D.	N.D.	N.D.	Yogodzinski et al. (2010)
C1927	Aleutians	N.D.	0.513046	0.283108	N.D.	N.D.	N.D.	Yogodzinski et al. (2010)
47ABy103	Aleutians	N.D.	0.512985	0.283093	N.D.	N.D.	N.D.	Yogodzinski et al. (2010)
FMI 7	Aleutians	N.D.	0.513059	0.283169	N.D.	N.D.	N.D.	Yogodzinski et al. (2010)

FMI 8	Aleutians	N.D.	0.513064	0.283159	N.D.	N.D.	N.D.	Yogodzinski et al. (2010)
FMI 5	Aleutians	N.D.	0.513004	0.283128	N.D.	N.D.	N.D.	Yogodzinski et al. (2010)
FMI 6	Aleutians	N.D.	0.513037	0.283148	N.D.	N.D.	N.D.	Yogodzinski et al. (2010)
FMI 2	Aleutians	N.D.	0.513024	0.283141	N.D.	N.D.	N.D.	Yogodzinski et al. (2010)
KR01-37	Aleutians	N.D.	0.513011	0.283172	N.D.	N.D.	N.D.	Yogodzinski et al. (2010)
KR01-6	Aleutians	N.D.	0.513036	0.283176	N.D.	N.D.	N.D.	Yogodzinski et al. (2010)
KR02-74	Aleutians	N.D.	0.513013	0.283154	N.D.	N.D.	N.D.	Yogodzinski et al. (2010)
KR02-55	Aleutians	N.D.	0.513027	0.283171	N.D.	N.D.	N.D.	Yogodzinski et al. (2010)
KR02-20	Aleutians	N.D.	0.513018	0.283176	N.D.	N.D.	N.D.	Yogodzinski et al. (2010)
KR01-33	Aleutians	N.D.	0.513017	0.283167	N.D.	N.D.	N.D.	Yogodzinski et al. (2010)
KR01-9	Aleutians	N.D.	0.513026	0.283166	N.D.	N.D.	N.D.	Yogodzinski et al. (2010)
KR01-24	Aleutians	N.D.	0.513019	0.283174	N.D.	N.D.	N.D.	Yogodzinski et al. (2010)
K-7	Aleutians	N.D.	0.513006	0.283151	N.D.	N.D.	N.D.	Yogodzinski et al. (2010)
SIT80-5	Aleutians	N.D.	0.513057	0.283197	N.D.	N.D.	N.D.	Yogodzinski et al. (2010)
GS 727	Aleutians	N.D.	0.513051	0.283175	N.D.	N.D.	N.D.	Yogodzinski et al. (2010)
GS723	Aleutians	N.D.	0.513043	0.283192	N.D.	N.D.	N.D.	Yogodzinski et al. (2010)
GS725-B	Aleutians	N.D.	0.513052	0.283187	N.D.	N.D.	N.D.	Yogodzinski et al. (2010)
GS721B	Aleutians	N.D.	0.513049	0.283187	N.D.	N.D.	N.D.	Yogodzinski et al. (2010)
SIT-RK4	Aleutians	N.D.	0.513024	0.283155	N.D.	N.D.	N.D.	Yogodzinski et al. (2010)
MOF81-56A	Aleutians	N.D.	0.513027	0.283167	N.D.	N.D.	N.D.	Yogodzinski et al. (2010)
MOF81-54	Aleutians	0.702982	0.513019	0.283146	N.D.	N.D.	N.D.	Kay and Kay (1994), Yogodzinski et al. (2010)
MOF81-44	Aleutians	N.D.	0.513020	0.283171	N.D.	N.D.	N.D.	Yogodzinski et al. (2010)
MOF81-17	Aleutians	N.D.	0.513009	0.283161	N.D.	N.D.	N.D.	Yogodzinski et al. (2010)
MOF81-15	Aleutians	N.D.	0.512999	0.283150	N.D.	N.D.	N.D.	Yogodzinski et al. (2010)
MOF81-18	Aleutians	N.D.	0.513011	0.283149	N.D.	N.D.	N.D.	Yogodzinski et al. (2010)
MOF81-7	Aleutians	N.D.	0.512993	0.283139	N.D.	N.D.	N.D.	Yogodzinski et al. (2010)
BO9-6A	Aleutians	N.D.	0.513044	0.283172	N.D.	N.D.	N.D.	Yogodzinski et al. (2010)
BO9-8A	Aleutians	N.D.	0.513048	0.283182	N.D.	N.D.	N.D.	Yogodzinski et al. (2010)
LSIT04L21	Aleutians	N.D.	0.513051	0.283194	N.D.	N.D.	N.D.	Yogodzinski et al. (2010)
LSIT04L11	Aleutians	N.D.	0.513039	0.283184	N.D.	N.D.	N.D.	Yogodzinski et al. (2010)

LSIT04L32	Aleutians	N.D.	0.513046	0.283187	N.D.	N.D.	N.D.	Yogodzinski et al. (2010)
LSIT04L33	Aleutians	N.D.	0.513053	0.283189	N.D.	N.D.	N.D.	Yogodzinski et al. (2010)
LSIT04L3	Aleutians	N.D.	0.513058	0.283186	N.D.	N.D.	N.D.	Yogodzinski et al. (2010)
LSIT04L18	Aleutians	N.D.	0.513059	0.283182	N.D.	N.D.	N.D.	Yogodzinski et al. (2010)
LSIT04L7	Aleutians	N.D.	0.513067	0.283190	N.D.	N.D.	N.D.	Yogodzinski et al. (2010)
LSIT04L39	Aleutians	N.D.	0.513038	0.283185	N.D.	N.D.	N.D.	Yogodzinski et al. (2010)
LSIT04L10	Aleutians	N.D.	0.513063	0.283190	N.D.	N.D.	N.D.	Yogodzinski et al. (2010)
LSIT04L49	Aleutians	N.D.	0.513053	0.283216	N.D.	N.D.	N.D.	Yogodzinski et al. (2010)
LSIT04L55	Aleutians	N.D.	0.513055	0.283191	N.D.	N.D.	N.D.	Yogodzinski et al. (2010)
B19-6B (BUL6B)	Aleutians	N.D.	0.513090	0.283192	18.573	15.497	38.057	Kelemen et al. (1993), Yogodzinski et al. (2010)
B19-4D (BUL4D)	Aleutians	N.D.	0.513060	0.283173	18.619	15.491	38.083	Kelemen et al. (1993), Yogodzinski et al. (2010)
B19-6A (BUL6A)	Aleutians	N.D.	0.513082	0.283182	18.649	15.525	38.159	Kelemen et al. (1993), Yogodzinski et al. (2010)
70B29-1A (70-B29)	Aleutians	N.D.	0.513082	0.283202	18.485	15.495	37.970	Kelemen et al. (1993), Yogodzinski et al. (2010)
V35-G5A	Aleutians	0.702662	0.513154	0.283211	18.088	15.437	37.563	Yogodzinski et al. (1994), Yogodzinski et al. (2010)
V35-G4X1	Aleutians	0.702702	0.513170	0.283216	18.069	15.429	37.511	Yogodzinski et al. (1994), Yogodzinski et al. (2010)
V35-G1D	Aleutians	N.D.	0.513151	0.283197	N.D.	N.D.	N.D.	Yogodzinski et al. (2010)
V35-G1A	Aleutians	0.702632	0.513156	0.283212	18.106	15.441	37.549	Yogodzinski et al. (1994), Yogodzinski et al. (2010)
V35-G2A	Aleutians	0.702672	0.513164	0.283200	18.105	15.434	37.533	Yogodzinski et al. (1994), Yogodzinski et al. (2010)
V35-G4A2	Aleutians	0.702792	0.513153	0.283206	18.080	15.436	37.527	Yogodzinski et al. (1994), Yogodzinski et al. (2010)
CB-3	Aleutians	N.D.	0.513002	0.283118	18.803	15.564	38.344	Yogodzinski et al. (2015)
CB-5	Aleutians	N.D.	0.513001	0.283115	18.883	15.577	38.440	Yogodzinski et al. (2015)
CB-12	Aleutians	N.D.	0.512997	0.283119	18.944	15.594	38.535	Yogodzinski et al. (2015)
CB-44	Aleutians	N.D.	0.513006	0.283138	18.869	15.572	38.411	Yogodzinski et al. (2015)
CB-7	Aleutians	N.D.	0.512991	0.283114	18.906	15.574	38.456	Yogodzinski et al. (2015)
AMK-1	Aleutians	N.D.	0.513014	0.283120	18.823	15.558	38.348	Yogodzinski et al. (2015)
AMK-2	Aleutians	N.D.	0.513012	N.D.	18.785	15.574	38.379	Yogodzinski et al. (2015)
AMK-3	Aleutians	N.D.	0.513027	0.283126	18.797	15.553	38.315	Yogodzinski et al. (2015)
AMK-4	Aleutians	N.D.	0.513013	0.283127	18.811	15.565	38.368	Yogodzinski et al. (2015)
AMK-5	Aleutians	N.D.	0.513012	0.283128	18.798	15.553	38.317	Yogodzinski et al. (2015)
AMK-7	Aleutians	N.D.	0.513007	0.283125	18.804	15.551	38.312	Yogodzinski et al. (2015)

SAR11	Aleutians	N.D.	0.513074	0.283154	18.903	15.577	38.370	Yogodzinski et al. (2015)
SAR4	Aleutians	N.D.	0.513077	0.283148	N.D.	N.D.	N.D.	Yogodzinski et al. (2015)
47ABy103 (B1796)	Aleutians	N.D.	0.512985	0.283093	18.835	15.570	38.336	Yogodzinski et al. (2015)
C1927 (Bogoslov-1927)	Aleutians	N.D.	0.513046	0.283108	18.751	15.556	38.236	Yogodzinski et al. (2015)
BOG-3	Aleutians	N.D.	0.513041	0.283124	18.735	15.549	38.244	Yogodzinski et al. (2015)
UM10	Aleutians	N.D.	0.513033	0.283153	N.D.	N.D.	N.D.	Yogodzinski et al. (2015)
UM16	Aleutians	N.D.	0.513062	0.283151	18.909	15.596	38.496	Yogodzinski et al. (2015)
UM22	Aleutians	N.D.	0.513047	0.283154	18.919	15.606	38.520	Yogodzinski et al. (2015)
UM4	Aleutians	N.D.	0.513055	0.283149	18.662	15.519	38.134	Yogodzinski et al. (2015)
UM5	Aleutians	N.D.	0.513043	0.283142	18.915	15.602	38.492	Yogodzinski et al. (2015)
UM11	Aleutians	N.D.	0.513038	0.283153	N.D.	N.D.	N.D.	Yogodzinski et al. (2015)
FMI 8	Aleutians	N.D.	0.513004	0.283153	18.647	15.537	38.162	Yogodzinski et al. (2015)
FMI 6	Aleutians	N.D.	0.513037	0.283148	18.889	15.585	38.462	Yogodzinski et al. (2015)
FMI 7	Aleutians	N.D.	0.513059	0.283169	N.D.	N.D.	N.D.	Yogodzinski et al. (2015)
FMI 5	Aleutians	N.D.	0.513004	0.283128	18.964	15.594	38.543	Yogodzinski et al. (2015)
FMI2	Aleutians	N.D.	0.513024	0.283141	18.889	15.580	38.451	Yogodzinski et al. (2015)
KR02-74	Aleutians	N.D.	0.513013	0.283154	18.849	15.579	38.426	Yogodzinski et al. (2015)
KR02-55	Aleutians	N.D.	0.513027	0.283171	18.828	15.574	38.398	Yogodzinski et al. (2015)
KR01-09	Aleutians	N.D.	0.513026	0.283166	18.852	15.580	38.430	Yogodzinski et al. (2015)
KR01-37	Aleutians	N.D.	0.513022	0.283172	18.846	15.581	38.428	Yogodzinski et al. (2015)
KR01-33	Aleutians	N.D.	0.513017	0.283167	18.828	15.574	38.398	Yogodzinski et al. (2015)
KR01-20	Aleutians	N.D.	0.513018	0.283176	18.841	15.577	38.416	Yogodzinski et al. (2015)
KR01-06	Aleutians	N.D.	0.513036	0.283176	18.795	15.563	38.354	Yogodzinski et al. (2015)
KR01-24	Aleutians	N.D.	0.513019	0.283174	18.848	15.578	38.423	Yogodzinski et al. (2015)
KAS7-1	Aleutians	N.D.	0.513003	0.283161	18.922	15.590	38.508	Yogodzinski et al. (2015)
GS721B	Aleutians	N.D.	0.513049	0.283187	18.862	15.581	38.443	Yogodzinski et al. (2015)
GS723	Aleutians	N.D.	0.513043	0.283192	N.D.	N.D.	N.D.	Yogodzinski et al. (2015)
GS725B	Aleutians	N.D.	0.513052	0.283187	18.829	15.573	38.400	Yogodzinski et al. (2015)
GS727	Aleutians	N.D.	0.513051	0.283175	18.743	15.557	38.295	Yogodzinski et al. (2015)

SIT81-RK4	Aleutians	N.D.	0.513024	0.283173	18.851	15.582	38.439	Yogodzinski et al. (2015)
SIT80-5B	Aleutians	N.D.	0.513057	0.283197	18.829	15.574	38.402	Yogodzinski et al. (2015)
MOF80-GL5	Aleutians	N.D.	0.513009	N.D.	18.794	15.566	38.358	Yogodzinski et al. (2015)
MOF81-15	Aleutians	N.D.	0.512999	0.283150	N.D.	N.D.	N.D.	Yogodzinski et al. (2015)
MOF81-17	Aleutians	N.D.	0.513009	0.283161	N.D.	N.D.	N.D.	Yogodzinski et al. (2015)
MOF81-18	Aleutians	N.D.	0.513011	0.283149	N.D.	N.D.	N.D.	Yogodzinski et al. (2015)
MOF81-38	Aleutians	N.D.	N.D.	0.283149	18.781	15.566	38.342	Yogodzinski et al. (2015)
MOF81-44	Aleutians	N.D.	0.513020	0.283171	18.815	15.576	38.401	Yogodzinski et al. (2015)
MOF81-54 (ADK54)	Aleutians	N.D.	0.513019	0.283146	18.770	15.594	38.380	Yogodzinski et al. (2015)
MOF81-56A	Aleutians	N.D.	0.513027	0.283167	N.D.	N.D.	N.D.	Yogodzinski et al. (2015)
MOF81-7	Aleutians	N.D.	0.512993	0.283139	18.713	15.545	38.234	Yogodzinski et al. (2015)
BO9-8A	Aleutians	N.D.	0.513048	0.283182	18.804	15.569	38.374	Yogodzinski et al. (2015)
BO9-6A	Aleutians	N.D.	0.513044	0.283172	18.780	15.566	38.348	Yogodzinski et al. (2015)
LSIT04L21	Aleutians	N.D.	0.513051	0.283194	18.740	15.558	38.319	Yogodzinski et al. (2015)
LSIT04L11	Aleutians	N.D.	0.513039	0.283184	N.D.	N.D.	N.D.	Yogodzinski et al. (2015)
LSIT04L32	Aleutians	N.D.	0.513046	0.283187	18.788	15.565	38.373	Yogodzinski et al. (2015)
LSIT04L33	Aleutians	N.D.	0.513053	0.283189	18.787	15.568	38.377	Yogodzinski et al. (2015)
LSIT04L03	Aleutians	N.D.	0.513048	0.283186	18.781	15.565	38.366	Yogodzinski et al. (2015)
LSIT04L18	Aleutians	N.D.	0.513059	0.283182	18.765	15.558	38.335	Yogodzinski et al. (2015)
LSIT04L07	Aleutians	N.D.	0.513067	0.283190	18.763	15.555	38.328	Yogodzinski et al. (2015)
LSIT04L39	Aleutians	N.D.	0.513038	0.283185	18.761	15.561	38.343	Yogodzinski et al. (2015)
LSIT04L10	Aleutians	N.D.	0.513063	0.283190	18.769	15.560	38.344	Yogodzinski et al. (2015)
LSIT04L49	Aleutians	N.D.	0.513053	0.283216	18.762	15.565	38.348	Yogodzinski et al. (2015)
LSIT04L55	Aleutians	N.D.	0.513055	0.283191	18.748	15.559	38.330	Yogodzinski et al. (2015)
BUL4D	Aleutians	N.D.	0.513060	0.283173	18.614	15.484	38.061	Yogodzinski et al. (2015)
BUL6A	Aleutians	N.D.	0.513082	0.283182	18.644	15.518	38.139	Yogodzinski et al. (2015)
BUL6B	Aleutians	N.D.	0.513090	0.283192	18.568	15.490	38.035	Yogodzinski et al. (2015)
AT8032	Aleutians	N.D.	0.513116	0.283196	18.374	15.483	37.861	Yogodzinski et al. (2015)
AT83	Aleutians	N.D.	0.513118	0.283205	18.381	15.475	37.865	Yogodzinski et al. (2015)
V35-G2A	Aleutians	N.D.	0.513164	0.283200	18.102	15.434	37.517	Yogodzinski et al. (2015)

V35-G1A	Aleutians	N.D.	0.513156	0.283212	18.102	15.434	37.527	Yogodzinski et al. (2015)
V35-G1D	Aleutians	N.D.	0.513151	0.283197	18.098	15.434	37.564	Yogodzinski et al. (2015)
V35-G4A2	Aleutians	N.D.	0.513153	0.283206	18.072	15.434	37.507	Yogodzinski et al. (2015)
V35-G4X1	Aleutians	N.D.	0.513170	0.283216	18.062	15.424	37.497	Yogodzinski et al. (2015)
V35-G5A	Aleutians	N.D.	0.513154	0.283211	18.082	15.434	37.547	Yogodzinski et al. (2015)
V35-G5B	Aleutians	N.D.	0.513117	N.D.	18.092	15.434	37.547	Yogodzinski et al. (2015)
CB-3	Aleutians	N.D.	0.513002	0.283118	18.803	15.564	38.344	Yogodzinski et al. (2015)
CB-5	Aleutians	N.D.	0.513001	0.283115	18.883	15.577	38.440	Yogodzinski et al. (2015)
CB-12	Aleutians	N.D.	0.512997	0.283119	18.944	15.594	38.535	Yogodzinski et al. (2015)
CB-44	Aleutians	N.D.	0.513006	0.283138	18.869	15.572	38.411	Yogodzinski et al. (2015)
CB-7	Aleutians	N.D.	0.512991	0.283114	18.906	15.574	38.456	Yogodzinski et al. (2015)
AMK-1	Aleutians	N.D.	0.513014	0.283120	18.823	15.558	38.348	Yogodzinski et al. (2015)
AMK-2	Aleutians	N.D.	0.513012	N.D.	18.785	15.574	38.379	Yogodzinski et al. (2015)
AMK-3	Aleutians	N.D.	0.513027	0.283126	18.797	15.553	38.315	Yogodzinski et al. (2015)
AMK-4	Aleutians	N.D.	0.513013	0.283127	18.811	15.565	38.368	Yogodzinski et al. (2015)
AMK-5	Aleutians	N.D.	0.513012	0.283128	18.798	15.553	38.317	Yogodzinski et al. (2015)
AMK-7	Aleutians	N.D.	0.513007	0.283125	18.804	15.551	38.312	Yogodzinski et al. (2015)
SAR11	Aleutians	N.D.	0.513074	0.283154	18.903	15.577	38.370	Yogodzinski et al. (2015)
SAR4	Aleutians	N.D.	0.513077	0.283148	N.D.	N.D.	N.D.	Yogodzinski et al. (2015)
47ABy103 (B1796)	Aleutians	N.D.	0.512985	0.283093	18.835	15.570	38.336	Yogodzinski et al. (2015)
C1927 (Bogoslov-1927)	Aleutians	N.D.	0.513046	0.283108	18.751	15.556	38.236	Yogodzinski et al. (2015)
BOG-3	Aleutians	N.D.	0.513041	0.283124	18.735	15.549	38.244	Yogodzinski et al. (2015)
UM10	Aleutians	N.D.	0.513033	0.283153	N.D.	N.D.	N.D.	Yogodzinski et al. (2015)
UM16	Aleutians	N.D.	0.513062	0.283151	18.909	15.596	38.496	Yogodzinski et al. (2015)
UM22	Aleutians	N.D.	0.513047	0.283154	18.919	15.606	38.520	Yogodzinski et al. (2015)
UM4	Aleutians	N.D.	0.513055	0.283149	18.662	15.519	38.134	Yogodzinski et al. (2015)
UM5	Aleutians	N.D.	0.513043	0.283142	18.915	15.602	38.492	Yogodzinski et al. (2015)
UM11	Aleutians	N.D.	0.513038	0.283153	N.D.	N.D.	N.D.	Yogodzinski et al. (2015)
FMI 8	Aleutians	N.D.	0.513004	0.283153	18.647	15.537	38.162	Yogodzinski et al. (2015)

FMI 6	Aleutians	N.D.	0.513037	0.283148	18.889	15.585	38.462	Yogodzinski et al. (2015)
FMI 7	Aleutians	N.D.	0.513059	0.283169	N.D.	N.D.	N.D.	Yogodzinski et al. (2015)
FMI 5	Aleutians	N.D.	0.513004	0.283128	18.964	15.594	38.543	Yogodzinski et al. (2015)
FMI2	Aleutians	N.D.	0.513024	0.283141	18.889	15.580	38.451	Yogodzinski et al. (2015)
KR02-74	Aleutians	N.D.	0.513013	0.283154	18.849	15.579	38.426	Yogodzinski et al. (2015)
KR02-55	Aleutians	N.D.	0.513027	0.283171	18.828	15.574	38.398	Yogodzinski et al. (2015)
KR01-09	Aleutians	N.D.	0.513026	0.283166	18.852	15.580	38.430	Yogodzinski et al. (2015)
KR01-37	Aleutians	N.D.	0.513022	0.283172	18.846	15.581	38.428	Yogodzinski et al. (2015)
KR01-33	Aleutians	N.D.	0.513017	0.283167	18.828	15.574	38.398	Yogodzinski et al. (2015)
KR01-20	Aleutians	N.D.	0.513018	0.283176	18.841	15.577	38.416	Yogodzinski et al. (2015)
KR01-06	Aleutians	N.D.	0.513036	0.283176	18.795	15.563	38.354	Yogodzinski et al. (2015)
KR01-24	Aleutians	N.D.	0.513019	0.283174	18.848	15.578	38.423	Yogodzinski et al. (2015)
KAS7-1	Aleutians	N.D.	0.513003	0.283161	18.922	15.590	38.508	Yogodzinski et al. (2015)
GS721B	Aleutians	N.D.	0.513049	0.283187	18.862	15.581	38.443	Yogodzinski et al. (2015)
GS723	Aleutians	N.D.	0.513043	0.283192	N.D.	N.D.	N.D.	Yogodzinski et al. (2015)
GS725B	Aleutians	N.D.	0.513052	0.283187	18.829	15.573	38.400	Yogodzinski et al. (2015)
GS727	Aleutians	N.D.	0.513051	0.283175	18.743	15.557	38.295	Yogodzinski et al. (2015)
SIT81-RK4	Aleutians	N.D.	0.513024	0.283173	18.851	15.582	38.439	Yogodzinski et al. (2015)
SIT80-5B	Aleutians	N.D.	0.513057	0.283197	18.829	15.574	38.402	Yogodzinski et al. (2015)
MOF80-GL5	Aleutians	N.D.	0.513009	N.D.	18.794	15.566	38.358	Yogodzinski et al. (2015)
MOF81-15	Aleutians	N.D.	0.512999	0.283150	N.D.	N.D.	N.D.	Yogodzinski et al. (2015)
MOF-81-17	Aleutians	N.D.	0.513009	0.283161	N.D.	N.D.	N.D.	Yogodzinski et al. (2015)
MOF81-18	Aleutians	N.D.	0.513011	0.283149	N.D.	N.D.	N.D.	Yogodzinski et al. (2015)
MOF81-38	Aleutians	N.D.	N.D.	0.283149	18.781	15.566	38.342	Yogodzinski et al. (2015)
MOF81-44	Aleutians	N.D.	0.513020	0.283171	18.815	15.576	38.401	Yogodzinski et al. (2015)
MOF81-54 (ADK54)	Aleutians	N.D.	0.513019	0.283146	18.770	15.594	38.380	Yogodzinski et al. (2015)
MOF81-56A	Aleutians	N.D.	0.513027	0.283167	N.D.	N.D.	N.D.	Yogodzinski et al. (2015)
MOF81-7	Aleutians	N.D.	0.512993	0.283139	18.713	15.545	38.234	Yogodzinski et al. (2015)
BO9-8A	Aleutians	N.D.	0.513048	0.283182	18.804	15.569	38.374	Yogodzinski et al. (2015)
BO9-6A	Aleutians	N.D.	0.513044	0.283172	18.780	15.566	38.348	Yogodzinski et al. (2015)

LSIT04L21	Aleutians	N.D.	0.513051	0.283194	18.740	15.558	38.319	Yogodzinski et al. (2015)
LSIT04L44	Aleutians	N.D.	0.513066	0.283217	18.693	15.547	38.257	Yogodzinski et al. (2015)
LSIT04L3	Aleutians	N.D.	0.513048	0.283186	18.781	15.565	38.366	Yogodzinski et al. (2015)
LSIT04L33	Aleutians	N.D.	0.513053	0.283189	18.787	15.568	38.377	Yogodzinski et al. (2015)
LSIT04L32	Aleutians	N.D.	0.513046	0.283187	18.788	15.565	38.373	Yogodzinski et al. (2015)
LSIT04L11	Aleutians	N.D.	0.513039	0.283184	N.D.	N.D.	N.D.	Yogodzinski et al. (2015)
LSIT04E57	Aleutians	N.D.	N.D.	N.D.	18.881	15.588	38.486	Yogodzinski et al. (2015)
LSIT04L29	Aleutians	N.D.	0.513038	0.283222	18.793	15.570	38.385	Yogodzinski et al. (2015)
LSIT04L02	Aleutians	N.D.	0.513048	0.283233	18.771	15.563	38.354	Yogodzinski et al. (2015)
LSIT04L07	Aleutians	N.D.	0.513067	0.283190	18.763	15.555	38.328	Yogodzinski et al. (2015)
LSIT04L18	Aleutians	N.D.	0.513059	0.283182	18.765	15.558	38.335	Yogodzinski et al. (2015)
LSIT04L39	Aleutians	N.D.	0.513038	0.283185	18.761	15.561	38.343	Yogodzinski et al. (2015)
LSIT04L10	Aleutians	N.D.	0.513063	0.283190	18.769	15.560	38.344	Yogodzinski et al. (2015)
LSIT04L49	Aleutians	N.D.	0.513053	0.283216	18.762	15.565	38.348	Yogodzinski et al. (2015)
LSIT04L55	Aleutians	N.D.	0.513055	0.283191	18.748	15.559	38.330	Yogodzinski et al. (2015)
BUL4D	Aleutians	N.D.	0.513060	0.283173	18.614	15.484	38.061	Yogodzinski et al. (2015)
BUL6A	Aleutians	N.D.	0.513082	0.283182	18.644	15.518	38.139	Yogodzinski et al. (2015)
BUL6B	Aleutians	N.D.	0.513090	0.283192	18.568	15.490	38.035	Yogodzinski et al. (2015)
AT8032	Aleutians	N.D.	0.513116	0.283196	18.374	15.483	37.861	Yogodzinski et al. (2015)
AT83	Aleutians	N.D.	0.513118	0.283205	18.381	15.475	37.865	Yogodzinski et al. (2015)
V35-G2A	Aleutians	N.D.	0.513164	0.283200	18.102	15.434	37.517	Yogodzinski et al. (2015)
V35-G1A	Aleutians	N.D.	0.513156	0.283212	18.102	15.434	37.527	Yogodzinski et al. (2015)
V35-G1D	Aleutians	N.D.	0.513151	0.283197	18.098	15.434	37.564	Yogodzinski et al. (2015)
V35-G4A2	Aleutians	N.D.	0.513153	0.283206	18.072	15.434	37.507	Yogodzinski et al. (2015)
V35-G4X1	Aleutians	N.D.	0.513170	0.283216	18.062	15.424	37.497	Yogodzinski et al. (2015)
V35-G5A	Aleutians	N.D.	0.513165	0.283211	18.082	15.434	37.547	Yogodzinski et al. (2015)
TN182-21-002	Aleutians	N.D.	0.512970	0.283151	18.819	15.573	38.409	Yogodzinski et al. (2015)
TN182-29-001	Aleutians	N.D.	0.513035	0.283206	18.740	15.556	38.306	Yogodzinski et al. (2015)
TN182-29-002	Aleutians	N.D.	0.513056	0.283158	18.753	15.557	38.319	Yogodzinski et al. (2015)
TN182-16-002	Aleutians	N.D.	N.D.	0.283137	18.783	15.559	38.349	Yogodzinski et al. (2015)

TN182-20-001	Aleutians	N.D.	0.513135	0.283199	18.511	15.507	38.026	Yogodzinski et al. (2015)
TN182-20-003	Aleutians	N.D.	0.513077	0.283176	18.627	15.533	38.184	Yogodzinski et al. (2015)
TN182-19-003	Aleutians	N.D.	0.513082	N.D.	18.594	15.531	38.158	Yogodzinski et al. (2015)
TN182-22-001	Aleutians	N.D.	0.513051	0.283162	18.748	15.556	38.315	Yogodzinski et al. (2015)
TN182-22-002	Aleutians	N.D.	0.513029	N.D.	18.746	15.555	38.313	Yogodzinski et al. (2015)
TN182-28-004	Aleutians	N.D.	0.513077	0.283202	18.597	15.530	38.151	Yogodzinski et al. (2015)
TN182-09-001	Aleutians	0.703194	0.513083	0.283291	18.569	15.522	38.110	Yogodzinski et al. (2015), Yogodzinski et al. (2017)
SO201-1b-14-007	Aleutians	0.703126	N.D.	N.D.	18.522	15.509	38.045	Yogodzinski et al. (2015), Yogodzinski et al. (2017)
SO201-1b-14-008	Aleutians	0.703118	N.D.	N.D.	18.480	15.502	37.994	Yogodzinski et al. (2015), Yogodzinski et al. (2017)
SO201-1b-15-001	Aleutians	0.703120	N.D.	N.D.	18.484	15.503	37.998	Yogodzinski et al. (2015), Yogodzinski et al. (2017)
TN182-08-003	Aleutians	0.703225	0.513074	0.283214	18.569	15.524	38.120	Yogodzinski et al. (2015), Yogodzinski et al. (2017)
SO201-1b-16-007	Aleutians	0.703127	N.D.	N.D.	18.495	15.504	38.120	Yogodzinski et al. (2015), Yogodzinski et al. (2017)
TN182-08-013	Aleutians	0.703091	0.513080	0.283179	18.561	15.515	38.089	Yogodzinski et al. (2015), Yogodzinski et al. (2017)
TN182-07-002	Aleutians	0.703173	0.513079	0.283201	18.542	15.513	38.072	Yogodzinski et al. (2015), Yogodzinski et al. (2017)
TN182-08-014	Aleutians	0.703182	0.513097	0.283216	18.569	15.522	38.110	Yogodzinski et al. (2015), Yogodzinski et al. (2017)
SO201-1b-14-006	Aleutians	0.703122	N.D.	N.D.	18.502	15.503	38.013	Yogodzinski et al. (2015), Yogodzinski et al. (2017)
SO201-1b-09-002	Aleutians	0.702702	N.D.	N.D.	18.384	15.478	37.858	Yogodzinski et al. (2015), Yogodzinski et al. (2017)
TN182-13-001	Aleutians	0.703317	0.513093	0.283200	18.565	15.520	38.104	Yogodzinski et al. (2015), Yogodzinski et al. (2017)
SO201-1b-09-001	Aleutians	0.702705	N.D.	N.D.	18.381	15.475	37.851	Yogodzinski et al. (2015), Yogodzinski et al. (2017)
SO201-1b-09-005	Aleutians	0.702705	N.D.	N.D.	18.373	15.478	37.850	Yogodzinski et al. (2015), Yogodzinski et al. (2017)
SO201-1b-10-003	Aleutians	0.702712	N.D.	N.D.	18.393	15.478	37.865	Yogodzinski et al. (2015), Yogodzinski et al. (2017)
SO201-1b-10-005	Aleutians	0.702724	N.D.	N.D.	18.392	15.479	37.867	Yogodzinski et al. (2015), Yogodzinski et al. (2017)
TN182-05-001	Aleutians	0.702937	0.513109	0.283212	18.536	15.514	38.066	Yogodzinski et al. (2015), Yogodzinski et al. (2017)
SO201-1b-09-007	Aleutians	0.702774	N.D.	N.D.	18.405	15.482	37.885	Yogodzinski et al. (2015), Yogodzinski et al. (2017)
TN182-11-004	Aleutians	0.703118	0.513110	0.283186	18.534	15.512	38.057	Yogodzinski et al. (2015), Yogodzinski et al. (2017)
TN182-10-003	Aleutians	0.702829	0.513108	0.283288	18.476	15.493	37.955	Yogodzinski et al. (2015), Yogodzinski et al. (2017)
TN182-10-002	Aleutians	0.702881	0.513059	N.D.	18.474	15.492	37.955	Yogodzinski et al. (2015), Yogodzinski et al. (2017)
TN182-10-001	Aleutians	0.702872	0.513072	0.283191	18.474	15.492	37.975	Yogodzinski et al. (2015), Yogodzinski et al. (2017)
SO201-1b-09-008	Aleutians	0.702816	N.D.	N.D.	18.395	15.480	37.861	Yogodzinski et al. (2015), Yogodzinski et al. (2017)
TN182-11-003	Aleutians	0.702718	0.513087	0.283195	18.484	15.490	37.962	Yogodzinski et al. (2015), Yogodzinski et al. (2017)

TN182-11-001	Aleutians	0.702735	0.513106	0.283191	18.488	15.495	37.977	Yogodzinski et al. (2015), Yogodzinski et al. (2017)
TN182-11-005	Aleutians	0.702705	0.513083	0.283172	18.493	15.497	37.982	Yogodzinski et al. (2015), Yogodzinski et al. (2017)
TN182-10-004	Aleutians	0.702717	0.513091	0.283240	18.443	15.488	37.918	Yogodzinski et al. (2015), Yogodzinski et al. (2017)
SO201-1b-09-010	Aleutians	0.703111	N.D.	N.D.	18.468	15.500	37.974	Yogodzinski et al. (2015), Yogodzinski et al. (2017)
SO201-1b-10-010	Aleutians	0.702830	N.D.	N.D.	18.417	15.489	37.903	Yogodzinski et al. (2015), Yogodzinski et al. (2017)
SO201-1b-10-011	Aleutians	0.702960	N.D.	N.D.	18.486	15.501	37.988	Yogodzinski et al. (2015), Yogodzinski et al. (2017)
SO201-1b-09-011	Aleutians	0.703013	N.D.	N.D.	18.479	15.501	37.982	Yogodzinski et al. (2015), Yogodzinski et al. (2017)
SO201-1b-20-005	Aleutians	0.702627	N.D.	N.D.	18.353	15.467	37.807	Yogodzinski et al. (2015), Yogodzinski et al. (2017)
TN182-01-004	Aleutians	0.702821	0.513102	0.283192	18.491	15.501	37.995	Yogodzinski et al. (2015), Yogodzinski et al. (2017)
SO201-1b-09-014	Aleutians	0.702750	N.D.	N.D.	18.427	15.492	37.928	Yogodzinski et al. (2015), Yogodzinski et al. (2017)
TN182-03-004	Aleutians	0.702916	0.513083	0.283242	18.492	15.500	37.991	Yogodzinski et al. (2015), Yogodzinski et al. (2017)
TN182-03-005	Aleutians	0.702780	0.513084	N.D.	18.450	15.483	37.922	Yogodzinski et al. (2015), Yogodzinski et al. (2017)
TN182-03-008	Aleutians	0.702761	0.513093	0.283194	18.466	15.492	37.951	Yogodzinski et al. (2015), Yogodzinski et al. (2017)
TN182-03-002	Aleutians	0.702942	0.513098	N.D.	18.457	15.488	37.937	Yogodzinski et al. (2015), Yogodzinski et al. (2017)
TN182-03-009	Aleutians	0.702783	0.513110	0.283176	18.462	15.488	37.941	Yogodzinski et al. (2015), Yogodzinski et al. (2017)
TN182-07-009	Aleutians	0.702743	0.513123	0.283210	18.423	15.482	37.900	Yogodzinski et al. (2015), Yogodzinski et al. (2017)
TN182-07-004	Aleutians	0.702774	N.D.	0.283201	18.424	15.482	37.899	Yogodzinski et al. (2015), Yogodzinski et al. (2017)
TN182-07-005	Aleutians	0.702672	0.513108	0.283187	18.423	15.479	37.893	Yogodzinski et al. (2015), Yogodzinski et al. (2017)
TN182-04-004	Aleutians	0.702689	N.D.	N.D.	18.384	15.474	37.844	Yogodzinski et al. (2015), Yogodzinski et al. (2017)
TN182-01-006	Aleutians	0.702772	0.513115	0.283176	18.426	15.479	37.891	Yogodzinski et al. (2015), Yogodzinski et al. (2017)
TN182-01-001	Aleutians	0.702824	0.513088	0.283186	18.447	15.495	37.937	Yogodzinski et al. (2015), Yogodzinski et al. (2017)
TN182-01-003	Aleutians	0.702795	N.D.	0.283168	18.427	15.481	37.895	Yogodzinski et al. (2015), Yogodzinski et al. (2017)
TN182-04-003	Aleutians	0.702620	0.513132	0.283192	18.383	15.470	37.836	Yogodzinski et al. (2015), Yogodzinski et al. (2017)
TN182-01-007	Aleutians	0.702767	0.513097	0.283178	18.427	15.483	37.899	Yogodzinski et al. (2015), Yogodzinski et al. (2017)
SO201-1b-33-001	Aleutians	0.702640	0.513123	N.D.	18.340	15.457	37.756	Yogodzinski et al. (2015), Yogodzinski et al. (2017)
SO201-1b-36-003	Aleutians	0.702657	0.513094	N.D.	18.490	15.502	38.011	Yogodzinski et al. (2015), Yogodzinski et al. (2017)
SO201-1b-35-004	Aleutians	0.702620	0.513114	N.D.	18.344	15.458	37.765	Yogodzinski et al. (2015), Yogodzinski et al. (2017)
V3842Y3	Aleutians	N.D.	0.513101	0.283188	17.897	15.421	37.376	Yogodzinski et al. (2015)
V3842Y REP	Aleutians	N.D.	0.513076	0.283186	N.D.	N.D.	N.D.	Yogodzinski et al. (2015)
ADK04L7	Aleutians	N.D.	0.513101	0.283183	18.338	15.473	37.795	Yogodzinski et al. (2015)

1986A-1	Izu	0.703679	0.513114	0.283290	N.D.	N.D.	N.D.	Freymuth et al. (2016)
S2-1	Izu	0.703629	0.513114	0.283286	N.D.	N.D.	N.D.	Freymuth et al. (2016)
N4-1	Izu	0.703654	0.513114	0.283289	N.D.	N.D.	N.D.	Freymuth et al. (2016)
1469	Izu	0.703445	0.513113	0.283262	N.D.	N.D.	N.D.	Freymuth et al. (2016)
1983-2903	Izu	0.703471	0.513115	0.283263	N.D.	N.D.	N.D.	Freymuth et al. (2016)
MJ-12-02	Izu	0.703434	0.513112	0.283261	N.D.	N.D.	N.D.	Freymuth et al. (2016)
MJ-12-05	Izu	0.703466	0.513112	0.283256	N.D.	N.D.	N.D.	Freymuth et al. (2016)
3102804	Izu	0.703556	0.513109	0.283234	N.D.	N.D.	N.D.	Freymuth et al. (2016)
0302812A	Izu	0.703556	0.513108	0.283236	N.D.	N.D.	N.D.	Freymuth et al. (2016)
3103009	Izu	0.703513	0.513103	0.283226	N.D.	N.D.	N.D.	Freymuth et al. (2016)
881105-2 lava	Izu	0.703395	0.513088	0.283218	N.D.	N.D.	N.D.	Freymuth et al. (2016)
T87071906	Izu	0.703421	0.513087	0.283219	N.D.	N.D.	N.D.	Freymuth et al. (2016)
1	Izu	0.703462	0.513125	0.283277	N.D.	N.D.	N.D.	Freymuth et al. (2016)
11	Izu	0.703467	0.513127	0.283273	N.D.	N.D.	N.D.	Freymuth et al. (2016)
24	Izu	0.703454	0.513118	0.283272	N.D.	N.D.	N.D.	Freymuth et al. (2016)
37	Izu	0.703570	0.513124	0.283266	N.D.	N.D.	N.D.	Freymuth et al. (2016)
NJ-2	Izu	0.703326	0.513075	0.283229	N.D.	N.D.	N.D.	Freymuth et al. (2016)
NJ-1	Izu	0.703361	0.513067	0.283230	N.D.	N.D.	N.D.	Freymuth et al. (2016)
JB-2-std	Izu	0.703662	0.513067	0.283252	N.D.	N.D.	N.D.	Freymuth et al. (2016)
IO-5	Izu	0.703665	0.513079	0.283290	18.360	15.530	38.308	Kimura et al. (2010)
IO-6	Izu	0.703681	0.513057	N.D.	18.355	15.527	38.301	Kimura et al. (2010)
IO-9	Izu	0.703628	0.513093	N.D.	18.377	15.528	38.343	Kimura et al. (2010)
JB-2	Izu	0.703668	0.513069	0.283272	18.299	15.540	38.260	Kimura et al. (2010)
TS-5	Izu	0.703420	0.513098	0.283294	18.228	15.508	38.207	Kimura et al. (2010)
TS-10	Izu	0.703410	0.512999	N.D.	18.216	15.509	38.188	Kimura et al. (2010)
TS-12	Izu	0.703393	0.513046	N.D.	18.211	15.510	38.191	Kimura et al. (2010)
TS-13	Izu	0.703391	0.512990	N.D.	18.197	15.478	38.188	Kimura et al. (2010)
UJ-2	Izu	0.703239	0.513019	0.283209	18.168	15.514	38.139	Kimura et al. (2010)
UJ-8	Izu	0.703236	0.513094	N.D.	18.169	15.506	38.139	Kimura et al. (2010)

UJ-9	Izu	0.703265	0.513077	0.283209	18.175	15.495	38.120	Kimura et al. (2010)
UJ-10a	Izu	0.703275	0.513073	N.D.	18.143	15.516	38.109	Kimura et al. (2010)
UJ-10b	Izu	0.703264	0.513081	N.D.	18.115	15.513	38.060	Kimura et al. (2010)
NJ-1	Izu	0.703286	0.513137	N.D.	18.260	15.513	38.218	Kimura et al. (2010)
NJ-2	Izu	0.703343	0.513019	0.283213	18.244	15.509	38.214	Kimura et al. (2010)
NJ-5	Izu	0.703298	0.513055	N.D.	18.266	15.508	38.223	Kimura et al. (2010)
NJ-6a	Izu	0.703382	0.513089	N.D.	18.123	15.538	38.096	Kimura et al. (2010)
10182E	Izu	N.D.	0.513063	0.283248	N.D.	N.D.	N.D.	Pearce et al. (1999)
F-864	Izu	N.D.	0.513024	0.283230	N.D.	N.D.	N.D.	Pearce et al. (1999)
IZU-2	Izu	N.D.	0.513049	0.283280	N.D.	N.D.	N.D.	Pearce et al. (1999)
IZU-3	Izu	N.D.	0.513056	0.283190	N.D.	N.D.	N.D.	Pearce et al. (1999)
AN-1	Mariana	N.D.	N.D.	0.283211	N.D.	N.D.	N.D.	Woodhead et al. (2001)
AN-12B	Mariana	0.703385	0.512977	0.283208	18.747	15.541	38.309	Woodhead et al. (2001)
SA-2	Mariana	0.703365	0.512950	0.283186	18.908	15.578	38.411	Woodhead et al. (2001)
SA-P	Mariana	0.703355	0.512956	0.283194	18.877	15.609	38.468	Woodhead et al. (2001)
SA-B	Mariana	0.703355	0.512948	0.283176	18.904	15.560	38.368	Woodhead et al. (2001)
GU-6	Mariana	0.703365	0.512988	0.283236	18.713	15.548	38.275	Woodhead et al. (2001)
GU-9	Mariana	0.703415	0.513028	0.283223	18.727	15.573	38.368	Woodhead et al. (2001)
GU-10	Mariana	0.703385	0.513034	0.283226	18.710	15.563	38.335	Woodhead et al. (2001)
GU-20	Mariana	0.703475	0.513043	0.283230	18.649	15.558	38.269	Woodhead et al. (2001)
GU-21	Mariana	0.703485	0.513034	0.283240	18.829	15.582	38.432	Woodhead et al. (2001)
ALA-1	Mariana	0.703525	0.513000	0.283226	18.674	15.550	38.290	Woodhead et al. (2001)
PA-4	Mariana	0.703455	0.513018	0.283230	18.788	15.574	38.401	Woodhead et al. (2001)
PA-5	Mariana	0.703405	N.D.	0.283223	18.781	15.577	38.420	Woodhead et al. (2001)
PA-F3B	Mariana	0.703435	0.512998	0.283210	18.728	15.580	38.387	Woodhead et al. (2001)
AG-1A	Mariana	0.703305	0.512981	0.283203	18.644	15.563	38.265	Woodhead et al. (2001)
AG-6	Mariana	0.703405	0.512981	0.283193	18.739	15.578	38.415	Woodhead et al. (2001)
AS-2	Mariana	0.703375	0.513043	0.283247	N.D.	N.D.	N.D.	Woodhead et al. (2001)
M-1	Mariana	0.703495	0.513027	0.283223	N.D.	N.D.	N.D.	Woodhead et al. (2001)

U1	Mariana	0.703465	0.512993	0.283219	18.824	15.597	38.523	Woodhead et al. (2001)
U2	Mariana	0.703495	0.513004	0.283232	18.788	15.576	38.459	Woodhead et al. (2001)
U4	Mariana	0.703585	0.513017	0.283228	18.738	15.552	38.371	Woodhead et al. (2001)
U7	Mariana	0.703435	0.512977	0.283199	18.814	15.585	38.480	Woodhead et al. (2001)
AN4	Mariana	0.703430	0.512988	0.283273	18.789	15.591	38.486	Woodhed et al. (1989)
SAB	Mariana	0.703370	0.512959	0.283225	18.904	15.560	38.368	Woodhed et al. (1989)
SAP	Mariana	0.703370	0.512967	0.283217	18.877	15.609	38.468	Woodhed et al. (1989)
GUN	Mariana	0.703490	0.513013	0.283172	18.743	15.542	38.262	Woodhed et al. (1989)
ALA1	Mariana	0.703540	0.513011	0.283246	18.674	15.550	38.290	Woodhed et al. (1989)
AG1	Mariana	0.703320	0.512992	0.283180	18.644	15.553	38.265	Woodhed et al. (1989)
M3	Mariana	0.703530	0.513053	0.283305	18.686	15.535	38.297	Woodhed et al. (1989)
U1	Mariana	0.703480	0.513004	0.283229	18.824	15.597	38.523	Woodhed et al. (1989)
AN.D.t10	Mariana	0.703456	0.512981	0.283200	18.816	15.579	38.442	Wade et al. (2005)
D50-1-1	Mariana	0.703469	0.513038	N.D.	18.804	15.577	38.410	Stern et al. (2006)
D50-1-2	Mariana	0.703469	0.513070	N.D.	18.766	15.546	38.307	Stern et al. (2006)
D50-1-3	Mariana	0.703528	0.512987	0.283193	18.767	15.552	38.318	Stern et al. (2006)
D49-1-1	Mariana	0.703192	0.513020	0.283229	18.687	15.539	38.296	Stern et al. (2006)
D49-1-2	Mariana	0.703178	0.512979	N.D.	18.691	15.540	38.295	Stern et al. (2006)
D49-1-3	Mariana	0.703200	0.512989	N.D.	18.684	15.547	38.326	Stern et al. (2006)
D48-1-1	Mariana	0.703112	0.512957	0.283172	18.866	15.587	38.496	Stern et al. (2006)
D48-1-2	Mariana	0.703105	0.512992	N.D.	18.827	15.553	38.374	Stern et al. (2006)
D48-1-3	Mariana	0.703192	0.512956	N.D.	18.826	15.556	38.377	Stern et al. (2006)
D48-1-4	Mariana	0.703368	0.512948	N.D.	18.911	15.575	38.450	Stern et al. (2006)
D48-2-1	Mariana	0.703150	0.513004	N.D.	18.836	15.554	38.381	Stern et al. (2006)
D48-2-2	Mariana	0.703156	0.512978	N.D.	18.830	15.550	38.363	Stern et al. (2006)
D48-3-1	Mariana	0.703170	0.512999	N.D.	18.835	15.553	38.380	Stern et al. (2006)
D48-3-2	Mariana	0.703159	0.512967	N.D.	18.822	15.558	38.318	Stern et al. (2006)
D48-3-3	Mariana	0.703126	0.512953	0.283229	18.849	15.570	38.418	Stern et al. (2006)
D48-4-1	Mariana	0.703142	0.512966	N.D.	18.834	15.557	38.404	Stern et al. (2006)
D46-1-1	Mariana	0.703060	0.512945	0.283173	18.672	15.545	38.295	Stern et al. (2006)

D46-1-2	Mariana	0.703081	0.512934	0.283171	18.707	15.573	38.402	Stern et al. (2006)
D46-1-5	Mariana	0.703095	0.512944	N.D.	18.697	15.544	38.321	Stern et al. (2006)
D30/6	Mariana	N.D.	0.512862	0.283241	N.D.	N.D.	N.D.	Pearce et al. (1999)
P5	Mariana	N.D.	0.512989	0.283170	N.D.	N.D.	N.D.	Pearce et al. (1999)
P8	Mariana	N.D.	0.512992	0.283170	N.D.	N.D.	N.D.	Pearce et al. (1999)
AG-1	Mariana	N.D.	0.512984	0.283181	N.D.	N.D.	N.D.	Pearce et al. (1999)
AG-4	Mariana	N.D.	0.512984	0.283220	N.D.	N.D.	N.D.	Pearce et al. (1999)
115263	Mariana	N.D.	0.512997	0.283235	N.D.	N.D.	N.D.	Pearce et al. (1999)
AL-7	Mariana	N.D.	0.513038	0.283220	N.D.	N.D.	N.D.	Pearce et al. (1999)
AL-1	Mariana	N.D.	0.513011	0.283246	N.D.	N.D.	N.D.	Pearce et al. (1999)
SA-B	Mariana	N.D.	0.512959	0.283225	N.D.	N.D.	N.D.	Pearce et al. (1999)
SA-P	Mariana	N.D.	0.512967	0.283217	N.D.	N.D.	N.D.	Pearce et al. (1999)
AN-4	Mariana	N.D.	0.512988	0.283270	N.D.	N.D.	N.D.	Pearce et al. (1999)
GU-N	Mariana	N.D.	0.513013	0.283172	N.D.	N.D.	N.D.	Pearce et al. (1999)
M-3	Mariana	N.D.	0.513053	0.283305	N.D.	N.D.	N.D.	Pearce et al. (1999)
U-1	Mariana	N.D.	0.513004	0.283229	N.D.	N.D.	N.D.	Pearce et al. (1999)
TN273-24D-01-01	Mariana	0.703312	0.513064	0.283187	19.036	15.581	38.563	Ribeiro et al. (2017)
TN273-42D-01-01	Mariana	0.703126	0.513016	0.283164	19.052	15.577	38.565	Ribeiro et al. (2017)
TN273-44D-01-01	Mariana	0.703243	0.513070	0.283178	18.997	15.580	38.551	Ribeiro et al. (2017)
HPD1147R01	Mariana	0.703417	0.513137	0.283225	18.878	15.566	38.428	Tamura et al. (2014)
HPD1147R04	Mariana	0.703419	0.513133	0.283212	18.874	15.563	38.419	Tamura et al. (2014)
HPD1147R09	Mariana	0.703437	0.513120	0.283219	18.863	15.572	38.440	Tamura et al. (2014)
HPD1147R11	Mariana	0.703440	0.513122	0.283209	18.865	15.568	38.422	Tamura et al. (2014)
HPD1147R13	Mariana	0.703372	0.513112	0.283198	18.867	15.570	38.429	Tamura et al. (2014)
HPD1147R15	Mariana	0.703439	0.513111	0.283208	18.899	15.573	38.466	Tamura et al. (2014)
HPD1147R16	Mariana	0.703440	0.513105	0.283206	18.901	15.573	38.471	Tamura et al. (2014)
HPD1147R17	Mariana	0.703443	0.513114	0.283198	18.900	15.571	38.469	Tamura et al. (2014)
HPD1147R19	Mariana	0.703441	0.513108	0.283202	18.896	15.568	38.458	Tamura et al. (2014)
HPD1147R23	Mariana	0.703399	0.513061	0.283190	18.831	15.568	38.434	Tamura et al. (2014)
HPD1148R01	Mariana	0.703313	0.513062	0.283158	18.891	15.572	38.472	Tamura et al. (2014)

HPD1148R08	Mariana	0.703446	0.513083	N.D.	18.836	15.571	38.438	Tamura et al. (2014)
HPD1148R14	Mariana	0.703404	0.513108	N.D.	18.828	15.571	38.434	Tamura et al. (2014)
7088.0	Tonga-Kermadec	0.703495	0.513114	0.283141	18.642	15.564	38.318	Woodhead et al. (2001)
10378	Tonga-Kermadec	0.703325	N.D.	0.283108	18.664	15.597	38.392	Woodhead et al. (2001)
10415	Tonga-Kermadec	0.703469	0.513037	0.283102	18.678	15.596	38.437	Woodhead et al. (2001)
14840	Tonga-Kermadec	0.704358	0.512984	0.283126	18.723	15.625	38.605	Woodhead et al. (2001)
HH basal	Tonga-Kermadec	0.703678	0.513028	0.283197	18.666	15.575	38.317	Hergt and Woodhead (2007)
HH upper	Tonga-Kermadec	0.703812	0.512949	0.283176	18.598	15.563	38.262	Hergt and Woodhead (2007)
F30-69	Tonga-Kermadec	0.703735	0.512943	0.283174	18.599	15.563	38.263	Hergt and Woodhead (2007)
F39-69	Tonga-Kermadec	0.703802	0.512949	0.283180	18.599	15.563	38.265	Hergt and Woodhead (2007)
Metis	Tonga-Kermadec	0.703551	0.512992	0.283180	18.613	15.572	38.285	Hergt and Woodhead (2007)
Late 13	Tonga-Kermadec	0.703636	0.512967	0.283281	18.583	15.567	38.240	Hergt and Woodhead (2007)
Late 7-69	Tonga-Kermadec	0.703617	0.512966	0.283191	18.586	15.566	38.242	Hergt and Woodhead (2007)
Late 21-69	Tonga-Kermadec	0.703653	0.512975	0.283192	18.583	15.565	38.238	Hergt and Woodhead (2007)
T102	Tonga-Kermadec	0.703302	0.513038	0.283176	18.622	15.566	38.246	Hergt and Woodhead (2007)
T103C	Tonga-Kermadec	0.703329	0.513041	0.283184	18.623	15.566	38.249	Hergt and Woodhead (2007)
64T6	Tonga-Kermadec	0.703280	0.513040	0.283172	18.613	15.562	38.231	Hergt and Woodhead (2007)
T113	Tonga-Kermadec	0.703916	0.512917	0.283227	19.329	15.625	38.980	Hergt and Woodhead (2007)
NT64-T2	Tonga-Kermadec	0.703983	0.512891	0.283219	18.994	15.601	38.748	Hergt and Woodhead (2007)
NT64-T8	Tonga-Kermadec	0.704010	0.512885	0.283223	18.990	15.599	38.741	Hergt and Woodhead (2007)
X161	Tonga-Kermadec	0.703641	0.513051	0.283151	18.708	15.577	38.476	Todd et al. (2010)
C/8 (V445)	Tonga-Kermadec	0.704264	0.512975	0.283106	18.778	15.609	38.643	Todd et al. (2010)
7088.0	Tonga-Kermadec	0.703533	0.512972	0.283108	18.638	15.559	38.295	Pearce et al. (2007)
7005.0	Tonga-Kermadec	N.D.	0.513053	0.283102	N.D.	N.D.	N.D.	Pearce et al. (2007)
7005.0	Tonga-Kermadec	0.703513	0.512972	0.283126	18.635	15.561	38.320	Pearce et al. (2007)
10378	Tonga-Kermadec	0.703363	0.513047	0.283138	18.659	15.592	38.369	Pearce et al. (2007)
10380.0	Tonga-Kermadec	0.703473	0.513047	0.283153	18.620	15.571	38.323	Pearce et al. (2007)
10415.0	Tonga-Kermadec	0.703507	0.513130	0.283141	18.673	15.591	38.414	Pearce et al. (2007)
14840	Tonga-Kermadec	0.704396	0.513000	0.283126	18.718	15.620	38.582	Pearce et al. (2007)

14831.0	Tonga-Kermadec	0.704163	0.512974	0.283126	18.729	15.590	38.480	Pearce et al. (2007)
ATA8-8	Tonga-Kermadec	0.703357	0.513061	0.283184	18.716	15.555	38.336	Pearce et al. (2007)
23208.0	Tonga-Kermadec	0.703561	0.513001	0.283185	18.647	15.578	38.281	Pearce et al. (2007)
111550-1	Tonga-Kermadec	0.703672	0.513032	0.283198	18.665	15.584	38.311	Pearce et al. (2007)
LATE 13	Tonga-Kermadec	0.703693	0.512935	0.283195	18.520	15.555	38.132	Pearce et al. (2007)
FON8	Tonga-Kermadec	0.703791	0.512970	0.283190	18.593	15.551	38.215	Pearce et al. (2007)
NTT28/2	Tonga-Kermadec	0.704022	0.512891	0.283215	19.015	15.570	38.669	Pearce et al. (2007)
NTT26/1	Tonga-Kermadec	0.704020	0.512896	0.283223	19.027	15.578	38.704	Pearce et al. (2007)
NT64-T8	Tonga-Kermadec	0.703993	0.512895	0.283233	18.920	15.578	38.640	Pearce et al. (2007)
TAF3/2	Tonga-Kermadec	0.703899	0.512941	0.283227	19.238	15.582	38.791	Pearce et al. (2007)
TAF40	Tonga-Kermadec	0.703930	0.512955	0.283220	18.988	15.582	38.608	Pearce et al. (2007)
D7-17	Tonga-Kermadec	N.D.	N.D.	0.282979	N.D.	N.D.	N.D.	Turner et al. (2009)
T116	Tonga-Kermadec	N.D.	N.D.	0.283239	N.D.	N.D.	N.D.	Turner et al. (2009)
NTT25/4	Tonga-Kermadec	0.703990	0.512956	0.283375	19.032	15.595	38.765	Turner et al. (2009), Turner et al. (1997)
Fon11	Tonga-Kermadec	N.D.	N.D.	0.283183	N.D.	N.D.	N.D.	Turner et al. (2009)
Fon39	Tonga-Kermadec	0.703780	0.513074	0.283162	18.545	15.575	38.185	Turner et al. (2009), Turner et al. (1997)
Late2	Tonga-Kermadec	N.D.	N.D.	0.283103	N.D.	N.D.	N.D.	Turner et al. (2009)
26821.0	Tonga-Kermadec	N.D.	N.D.	0.283186	N.D.	N.D.	N.D.	Turner et al. (2009)
HHTop (HHHTOP)	Tonga-Kermadec	0.703700	0.513132	0.283192	18.520	15.557	38.109	Turner et al. (2009), Turner et al. (1997)
482-8-12	Tonga-Kermadec	0.703460	0.513169	0.283171	18.698	15.547	38.285	Turner et al. (2009), Turner et al. (1997)
14807.0	Tonga-Kermadec	N.D.	N.D.	0.283149	N.D.	N.D.	N.D.	Turner et al. (2009)
45653.0	Tonga-Kermadec	0.703450	0.513106	0.283124	18.687	15.569	38.351	Turner et al. (2009), Turner et al. (1997)
14868.0	Tonga-Kermadec	N.D.	N.D.	0.283132	N.D.	N.D.	N.D.	Turner et al. (2009)
37486.0	Tonga-Kermadec	0.703920	0.512960	0.283117	18.697	15.588	38.483	Turner et al. (2009), Turner et al. (1997)
<u>Hot subduction zones</u>								
TW 36	Luzon-Philippine	0.706010	0.512298	0.282920	18.425	15.648	38.843	Defant et al. (1990), McDermott et al. (1993), Marini et al. (2005)
TW 40	Luzon-Philippine	0.706098	0.512319	0.282937	18.429	15.646	38.828	Defant et al. (1990), McDermott et al. (1993), Marini et al. (2005)
TW 41	Luzon-Philippine	0.704827	0.512606	0.282995	18.414	15.620	38.982	McDermott et al. (1993), Marini et al. (2005)
TW 31	Luzon-Philippine	0.704307	0.512736	0.283058	18.295	15.582	38.557	Defant et al. (1990), McDermott et al. (1993), Marini et al. (2005)

TW 32	Luzon-Philippine	0.705433	0.512640	0.283067	18.393	15.631	38.780	Defant et al. (1990), McDermott et al. (1993), Marini et al. (2005)
B 3m	Luzon-Philippine	0.704759	0.512484	0.282799	18.432	15.598	38.500	Defant et al. (1990), McDermott et al. (1993), Marini et al. (2005)
B10	Luzon-Philippine	0.704455	0.512568	0.282793	18.406	15.590	38.640	McDermott et al. (1993), Marini et al. (2005)
B42	Luzon-Philippine	0.703933	0.512527	0.282781	18.364	15.567	38.522	McDermott et al. (1993), Marini et al. (2005)
B80	Luzon-Philippine	0.703954	0.512554	0.282889	N.D.	N.D.	N.D.	Defant et al. (1990), Marini et al. (2005)
B88	Luzon-Philippine	0.705443	0.512394	0.282688	18.382	15.603	38.664	Defant et al. (1990), McDermott et al. (1993), Marini et al. (2005)
B15	Luzon-Philippine	N.D.	0.512627	N.D.	N.D.	N.D.	N.D.	Marini et al. (2005)
Bb20	Luzon-Philippine	0.704556	0.512563	0.283079	18.536	15.623	38.843	Defant et al. (1990), McDermott et al. (1993), Marini et al. (2005)
Bb39	Luzon-Philippine	0.704483	0.512597	0.283139	18.520	15.630	38.789	McDermott et al. (1993), Marini et al. (2005)
Cm 5	Luzon-Philippine	0.703274	0.513038	0.283221	18.375	15.552	38.431	McDermott et al. (1993), Marini et al. (2005)
Cm 54	Luzon-Philippine	0.704043	0.512796	0.283181	18.505	15.618	38.737	McDermott et al. (1993), Marini et al. (2005)
Ca 9	Luzon-Philippine	0.703864	0.512658	0.283173	18.508	15.583	38.652	McDermott et al. (1993), Marini et al. (2005)
Ca 26	Luzon-Philippine	0.703955	0.512888	0.283165	18.575	15.624	38.812	McDermott et al. (1993), Marini et al. (2005)
47 A	Luzon-Philippine	0.703769	0.512939	0.283183	18.349	15.541	38.346	Defant et al. (1990), McDermott et al. (1993), Marini et al. (2005)
7414	Sunda-Banda	0.704345	0.512724	0.283095	18.661	15.649	38.884	Woodhead et al. (2001)
11498	Sunda-Banda	0.704353	0.512695	0.283085	18.664	15.648	38.888	Woodhead et al. (2001)
7421	Sunda-Banda	0.705672	0.512665	0.283124	18.770	15.703	39.181	Woodhead et al. (2001)
7678	Sunda-Banda	0.704766	0.512681	0.283043	18.608	15.616	38.651	Woodhead et al. (2001)
7422	Sunda-Banda	0.704665	0.512745	0.283119	18.636	15.649	38.906	Woodhead et al. (2001)
7423	Sunda-Banda	0.704190	0.512815	0.283133	18.571	15.626	38.759	Woodhead et al. (2001)
9047	Sunda-Banda	0.704352	0.512729	0.283149	18.780	15.689	39.137	Woodhead et al. (2001)
71-1002	Sunda-Banda	0.704555	0.512748	0.283108	18.704	15.675	39.031	Woodhead et al. (2001)
13672	Sunda-Banda	0.703972	0.512827	0.283144	18.572	15.616	38.766	Woodhead et al. (2001)
71-969	Sunda-Banda	0.704416	0.512572	0.282915	18.687	15.609	39.139	Woodhead et al. (2001)
71-970	Sunda-Banda	0.704593	0.512549	0.282923	18.679	15.607	39.113	Woodhead et al. (2001)
71-979	Sunda-Banda	0.705098	0.512595	0.283079	18.808	15.690	39.144	Woodhead et al. (2001)
71-982	Sunda-Banda	0.704860	0.512611	0.283033	18.885	15.698	39.197	Woodhead et al. (2001)
71-985	Sunda-Banda	0.705886	0.512447	0.282822	18.911	15.726	39.363	Woodhead et al. (2001)
71-989	Sunda-Banda	0.705833	0.512459	0.282853	18.919	15.732	39.395	Woodhead et al. (2001)

G01A	Sunda-Banda	N.D.	0.512647	0.282977	N.D.	N.D.	N.D.	Handley et al. (2011)
G01B	Sunda-Banda	N.D.	0.512653	0.282951	N.D.	N.D.	N.D.	Handley et al. (2011)
G10	Sunda-Banda	N.D.	0.512700	0.282975	N.D.	N.D.	N.D.	Handley et al. (2011)
G16	Sunda-Banda	N.D.	0.512629	0.282952	N.D.	N.D.	N.D.	Handley et al. (2011)
G17	Sunda-Banda	N.D.	0.512681	0.282976	N.D.	N.D.	N.D.	Handley et al. (2011), Handley et al. (2014)
G18	Sunda-Banda	N.D.	0.512660	0.282963	N.D.	N.D.	N.D.	Handley et al. (2011)
G19	Sunda-Banda	N.D.	0.512701	0.282988	N.D.	N.D.	N.D.	Handley et al. (2011)
G20	Sunda-Banda	N.D.	0.512675	0.282975	N.D.	N.D.	N.D.	Handley et al. (2011), Handley et al. (2014)
G21	Sunda-Banda	N.D.	0.512678	0.282972	N.D.	N.D.	N.D.	Handley et al. (2011)
G22	Sunda-Banda	N.D.	0.512664	0.282968	N.D.	N.D.	N.D.	Handley et al. (2011)
G23	Sunda-Banda	N.D.	0.512656	0.282957	N.D.	N.D.	N.D.	Handley et al. (2011), Handley et al. (2014)
G25	Sunda-Banda	N.D.	0.512677	0.282975	N.D.	N.D.	N.D.	Handley et al. (2011), Handley et al. (2014)
G26	Sunda-Banda	N.D.	0.512694	0.282997	N.D.	N.D.	N.D.	Handley et al. (2011)
G28	Sunda-Banda	N.D.	0.512683	0.282974	N.D.	N.D.	N.D.	Handley et al. (2011)
G30	Sunda-Banda	N.D.	0.512646	0.282956	N.D.	N.D.	N.D.	Handley et al. (2011)
G33	Sunda-Banda	N.D.	0.512699	0.282990	N.D.	N.D.	N.D.	Handley et al. (2011)
G35	Sunda-Banda	N.D.	0.512646	0.282939	N.D.	N.D.	N.D.	Handley et al. (2011), Handley et al. (2014)
G36A	Sunda-Banda	N.D.	0.512654	0.282955	N.D.	N.D.	N.D.	Handley et al. (2011), Handley et al. (2014)
G40	Sunda-Banda	N.D.	0.512679	0.282972	N.D.	N.D.	N.D.	Handley et al. (2011), Handley et al. (2014)
G42	Sunda-Banda	N.D.	0.512660	0.282967	N.D.	N.D.	N.D.	Handley et al. (2011)
G44	Sunda-Banda	N.D.	0.512702	0.282994	N.D.	N.D.	N.D.	Handley et al. (2011)
G46	Sunda-Banda	N.D.	0.512682	0.282982	N.D.	N.D.	N.D.	Handley et al. (2011), Handley et al. (2014)
G49	Sunda-Banda	N.D.	0.512722	0.283058	N.D.	N.D.	N.D.	Handley et al. (2011)
G51	Sunda-Banda	N.D.	0.512656	0.282951	N.D.	N.D.	N.D.	Handley et al. (2011)
G52	Sunda-Banda	N.D.	0.512737	0.283067	N.D.	N.D.	N.D.	Handley et al. (2011), Handley et al. (2014)
G55	Sunda-Banda	N.D.	0.512687	0.282978	N.D.	N.D.	N.D.	Handley et al. (2011)
GU1/T	Sunda-Banda	N.D.	0.512982	0.283157	N.D.	N.D.	N.D.	Handley et al. (2011)
GU5/T	Sunda-Banda	N.D.	0.512907	0.283147	N.D.	N.D.	N.D.	Handley et al. (2011)
GU7/T	Sunda-Banda	N.D.	0.512917	0.283134	N.D.	N.D.	N.D.	Handley et al. (2011)
GU9/T	Sunda-Banda	N.D.	0.512904	0.283142	N.D.	N.D.	N.D.	Handley et al. (2011)

GU15/T	Sunda-Banda	N.D.	0.512882	0.283137	N.D.	N.D.	N.D.	Handley et al. (2011)
GU16/T	Sunda-Banda	N.D.	0.512893	0.283142	N.D.	N.D.	N.D.	Handley et al. (2011)
M95-026	Sunda-Banda	0.705252	0.512738	0.283146	18.769	15.693	39.130	Handley et al. (2011), Handley et al. (2014)
M95-028	Sunda-Banda	0.705793	0.512729	0.283146	N.D.	N.D.	N.D.	Handley et al. (2011)
M96-050	Sunda-Banda	0.705539	0.512742	0.283160	N.D.	N.D.	N.D.	Handley et al. (2011)
M96-056	Sunda-Banda	N.D.	0.512776	0.283131	N.D.	N.D.	N.D.	Handley et al. (2011), Gertisser and Keller (2003)
M96-073	Sunda-Banda	0.705384	0.512785	0.283157	18.759	15.695	309.139	Handley et al. (2011), Handley et al. (2014)
M96-102	Sunda-Banda	0.705515	0.512753	N.D.	N.D.	N.D.	N.D.	Handley et al. (2011)
M96-137	Sunda-Banda	0.705269	0.512769	0.283148	18.759	15.695	39.139	Handley et al. (2011), Handley et al. (2014)
M96-142	Sunda-Banda	N.D.	0.512734	0.283128	N.D.	N.D.	N.D.	Handley et al. (2011), Gertisser and Keller (2003)
M96-175	Sunda-Banda	0.705105	0.512752	0.283185	N.D.	N.D.	N.D.	Handley et al. (2011)
M97-021	Sunda-Banda	N.D.	0.512723	0.283138	N.D.	N.D.	N.D.	Handley et al. (2011), Gertisser and Keller (2003)
M97-031	Sunda-Banda	N.D.	0.512712	0.283141	N.D.	N.D.	N.D.	Handley et al. (2011), Gertisser and Keller (2003)
M97-0392	Sunda-Banda	N.D.	0.512725	0.283137	N.D.	N.D.	N.D.	Handley et al. (2011), Gertisser and Keller (2003)
M97-068	Sunda-Banda	0.705703	0.512682	0.283128	18.763	15.694	39.141	Handley et al. (2011), Handley et al. (2014)
M98-107	Sunda-Banda	N.D.	0.512733	0.283144	N.D.	N.D.	N.D.	Handley et al. (2011), Gertisser and Keller (2003)
M98-031	Sunda-Banda	0.705540	0.512746	0.283141	N.D.	N.D.	N.D.	Handley et al. (2011), Gertisser and Keller (2003)
M98-047	Sunda-Banda	N.D.	0.512723	0.283144	N.D.	N.D.	N.D.	Handley et al. (2011), Gertisser and Keller (2003)
M98-0532	Sunda-Banda	N.D.	0.512770	0.283160	N.D.	N.D.	N.D.	Handley et al. (2011), Gertisser and Keller (2003)
M98-096	Sunda-Banda	0.705635	0.512697	0.283147	18.771	15.697	39.156	Handley et al. (2011), Handley et al. (2014)
BA11A2	Sunda-Banda	0.704783	0.512880	0.283139	18.697	15.646	38.935	Nebel et al. (2011), Vroon et al. (1993)
BN3A2	Sunda-Banda	0.704775	0.512873	0.283101	N.D.	N.D.	N.D.	Nebel et al. (2011), Vroon et al. (1993)
BN4A1	Sunda-Banda	0.704772	0.512877	0.283114	18.686	15.634	38.879	Nebel et al. (2011), Vroon et al. (1993)
MA2D	Sunda-Banda	N.D.	N.D.	0.283057	N.D.	N.D.	N.D.	Nebel et al. (2011)
MA5A	Sunda-Banda	0.705225	0.512750	0.283058	18.750	15.643	38.946	Nebel et al. (2011), Vroon et al. (1993)
MA6A1	Sunda-Banda	N.D.	N.D.	0.283050	N.D.	N.D.	N.D.	Nebel et al. (2011)
SE9A3	Sunda-Banda	0.708323	0.512500	0.282802	19.025	15.691	39.215	Nebel et al. (2011), Vroon et al. (1993)
SE21A	Sunda-Banda	0.708984	0.512444	0.282755	19.045	15.702	39.256	Nebel et al. (2011), Vroon et al. (1993)
SE25A	Sunda-Banda	0.709489	0.512410	0.282689	19.026	15.701	39.251	Nebel et al. (2011), Vroon et al. (1993)
NI1A1	Sunda-Banda	0.707699	0.512636	0.282997	19.374	15.740	39.599	Nebel et al. (2011), Vroon et al. (1993)

NI9A	Sunda-Banda	N.D.	N.D.	0.282996	N.D.	N.D.	N.D.	Nebel et al. (2011)
NI17A	Sunda-Banda	N.D.	N.D.	0.282993	N.D.	N.D.	N.D.	Nebel et al. (2011)
NI18A1	Sunda-Banda	0.706434	0.512696	0.283010	19.389	15.736	39.605	Nebel et al. (2011), Vroon et al. (1993)
TE1C	Sunda-Banda	0.707938	0.512522	0.282812	19.423	15.733	39.652	Nebel et al. (2011), Vroon et al. (1993)
TE2B2	Sunda-Banda	N.D.	N.D.	0.282899	N.D.	N.D.	N.D.	Nebel et al. (2011)
TE4B	Sunda-Banda	N.D.	N.D.	0.282877	N.D.	N.D.	N.D.	Nebel et al. (2011)
TE15	Sunda-Banda	0.707315	0.512585	0.282904	19.426	15.734	39.638	Nebel et al. (2011), Vroon et al. (1993)
DA1	Sunda-Banda	0.706698	0.512580	0.282895	19.367	15.736	39.729	Nebel et al. (2011), Vroon et al. (1993)
DA9B	Sunda-Banda	N.D.	N.D.	0.282908	N.D.	N.D.	N.D.	Nebel et al. (2011)
RO2	Sunda-Banda	0.708491	0.512461	0.282685	19.154	15.695	39.577	Nebel et al. (2011), Vroon et al. (1993)
RO8C6	Sunda-Banda	0.709166	0.512439	0.282676	19.192	15.707	39.578	Nebel et al. (2011), Vroon et al. (1993)
TG1 (TGI-5)	Setouchi	0.705127	0.512576	N.D.	18.446	15.606	38.672	Ishizaka and Carlson (1983), Shimoda et al. (1998)
NBY-11 (NBY-5)	Setouchi	0.705353	0.512541	N.D.	18.421	15.598	38.635	Ishizaka and Carlson (1983), Shimoda et al. (1998)
SNM-8c	Setouchi	0.705242	0.512555	N.D.	N.D.	N.D.	N.D.	Ishizaka and Carlson (1983)
SG-1	Setouchi	0.704664	0.512723	N.D.	N.D.	N.D.	N.D.	Ishizaka and Carlson (1983)
SD407	Setouchi	0.705017	0.512712	0.282985	18.358	15.583	38.558	Ishizaka and Carlson (1983), Shimoda et al. (1998)
SD265 (SD-261)	Setouchi	0.704895	0.512689	N.D.	18.366	15.599	38.586	Ishizaka and Carlson (1983), Shimoda et al. (1998)
SD264 (MDYB-2)	Setouchi	0.704861	0.512720	0.282981	18.366	15.594	38.552	Ishizaka and Carlson (1983), Shimoda et al. (1998)
SD411	Setouchi	0.704909	0.512706	0.283018	18.364	15.592	38.572	Ishizaka and Carlson (1983), Shimoda et al. (1998)
CH0	Setouchi	0.705380	0.512662	N.D.	N.D.	N.D.	N.D.	Ishizaka and Carlson (1983)
SD504	Setouchi	0.704975	0.512687	N.D.	N.D.	N.D.	N.D.	Ishizaka and Carlson (1983)
UDY	Setouchi	0.705164	0.512634	N.D.	N.D.	N.D.	N.D.	Ishizaka and Carlson (1983)
SD512	Setouchi	0.704993	0.512633	N.D.	18.343	15.594	38.555	Ishizaka and Carlson (1983), Tatsumi et al. (2002)
SD516	Setouchi	0.705281	0.512658	N.D.	N.D.	N.D.	N.D.	Ishizaka and Carlson (1983)
EHJ	Setouchi	0.705325	0.512669	N.D.	18.368	15.607	38.612	Ishizaka and Carlson (1983), Tatsumi et al. (2002)
SD438 (SDSYB)	Setouchi	0.704382	0.512736	0.283052	18.311	15.578	38.482	Ishizaka and Carlson (1983), Shimoda et al. (1998), Hanyu et al. (2002)
SD424	Setouchi	0.704561	0.512770	0.283071	N.D.	N.D.	N.D.	Ishizaka and Carlson (1983), Hanyu et al. (2002)
TK-17	Setouchi	0.704335	0.512730	N.D.	N.D.	N.D.	N.D.	Ishizaka and Carlson (1983)

TK-101	Setouchi	0.704071	0.512819	N.D.	18.294	15.568	38.469	Ishizaka and Carlson (1983), Shimoda et al. (1998)
Hg130	Setouchi	0.705181	0.512498	N.D.	N.D.	N.D.	N.D.	Ishizaka and Carlson (1983)
OS-5	Setouchi	0.704925	0.512665	N.D.	N.D.	N.D.	N.D.	Ishizaka and Carlson (1983)
Hg44	Setouchi	0.704903	0.512681	N.D.	N.D.	N.D.	N.D.	Ishizaka and Carlson (1983)
72032312	Setouchi	0.704209	0.512680	N.D.	N.D.	N.D.	N.D.	Ishizaka and Carlson (1983)
OS-24	Setouchi	0.704234	0.512684	N.D.	N.D.	N.D.	N.D.	Ishizaka and Carlson (1983)
SD812	Setouchi	N.D.	N.D.	N.D.	18.362	15.594	38.552	Shimoda et al. (1998)
SH7201	Setouchi	0.706030	0.512518	N.D.	18.388	15.606	38.654	Shimoda et al. (1998)
JA-2	Setouchi	0.706252	0.512565	0.282876	18.389	15.610	38.674	Shimoda et al. (1998), Hanyu et al. (2002)
TGI-6	Setouchi	0.705095	0.512577	N.D.	18.439	15.596	38.622	Shimoda et al. (1998)
NJSB	Setouchi	N.D.	N.D.	N.D.	18.408	15.584	38.587	Shimoda et al. (1998)
NJIB	Setouchi	N.D.	N.D.	N.D.	18.434	15.605	38.654	Shimoda et al. (1998)
SD249	Setouchi	N.D.	N.D.	0.282950	N.D.	N.D.	N.D.	Hanyu et al. (2002)
SD261	Setouchi	N.D.	N.D.	0.282950	N.D.	N.D.	N.D.	Hanyu et al. (2002)
AN160	Central Mexico	N.D.	0.512906	0.283046	N.D.	N.D.	N.D.	Cai et al. (2014)
AN179	Central Mexico	N.D.	0.512863	0.283037	N.D.	N.D.	N.D.	Cai et al. (2014)
AN182	Central Mexico	N.D.	0.512875	0.283088	N.D.	N.D.	N.D.	Cai et al. (2014)
AN81	Central Mexico	N.D.	0.512913	0.283044	N.D.	N.D.	N.D.	Cai et al. (2014)
M32	Central Mexico	N.D.	0.512898	0.283047	N.D.	N.D.	N.D.	Cai et al. (2014)
M34	Central Mexico	N.D.	0.512945	0.283058	N.D.	N.D.	N.D.	Cai et al. (2014)
M69	Central Mexico	N.D.	0.512886	0.283026	N.D.	N.D.	N.D.	Cai et al. (2014)
RAM101	Central Mexico	N.D.	0.512869	0.283032	N.D.	N.D.	N.D.	Cai et al. (2014)
RAM215	Central Mexico	N.D.	0.512915	0.283066	N.D.	N.D.	N.D.	Cai et al. (2014)
RAM22	Central Mexico	N.D.	0.512932	0.283065	N.D.	N.D.	N.D.	Cai et al. (2014)
RAM452	Central Mexico	N.D.	0.512927	0.283062	N.D.	N.D.	N.D.	Cai et al. (2014)
RAM453	Central Mexico	N.D.	0.512940	0.283067	N.D.	N.D.	N.D.	Cai et al. (2014)
RAM592	Central Mexico	N.D.	0.512963	0.283050	N.D.	N.D.	N.D.	Cai et al. (2014)
ASC-1	Central Mexico	N.D.	0.512746	0.282868	N.D.	N.D.	N.D.	Cai et al. (2014)
ASC43B	Central Mexico	N.D.	0.512900	0.283030	N.D.	N.D.	N.D.	Cai et al. (2014)

ASC44B	Central Mexico	N.D.	0.512930	0.283017	N.D.	N.D.	N.D.	Cai et al. (2014)
ASC45B	Central Mexico	N.D.	0.512922	0.283007	N.D.	N.D.	N.D.	Cai et al. (2014)
ASC47	Central Mexico	N.D.	0.512761	0.282920	N.D.	N.D.	N.D.	Cai et al. (2014)
SX1	Central Mexico	N.D.	0.512810	0.282931	N.D.	N.D.	N.D.	Cai et al. (2014)
CP22	Central Mexico	N.D.	0.512759	0.282899	N.D.	N.D.	N.D.	Cai et al. (2014)
CP35	Central Mexico	N.D.	0.512912	0.283003	N.D.	N.D.	N.D.	Cai et al. (2014)
CP40A	Central Mexico	N.D.	0.512780	0.282933	N.D.	N.D.	N.D.	Cai et al. (2014)
C46	Central Mexico	N.D.	0.512657	0.282860	N.D.	N.D.	N.D.	Cai et al. (2014)
SCI30	Central Mexico	N.D.	0.512567	0.282779	N.D.	N.D.	N.D.	Cai et al. (2014)
SCI32	Central Mexico	N.D.	0.512700	0.282890	N.D.	N.D.	N.D.	Cai et al. (2014)
SCI33	Central Mexico	N.D.	0.512680	0.282870	N.D.	N.D.	N.D.	Cai et al. (2014)
SCI34	Central Mexico	N.D.	0.512663	0.282857	N.D.	N.D.	N.D.	Cai et al. (2014)
SCI35	Central Mexico	N.D.	0.512586	0.282771	N.D.	N.D.	N.D.	Cai et al. (2014)
SCI42	Central Mexico	N.D.	0.512635	0.282835	N.D.	N.D.	N.D.	Cai et al. (2014)
SCI43	Central Mexico	N.D.	0.512582	0.282755	N.D.	N.D.	N.D.	Cai et al. (2014)
C64	Central Mexico	N.D.	0.512767	0.282878	N.D.	N.D.	N.D.	Cai et al. (2014)
ASC24C	Central Mexico	N.D.	0.512818	0.282995	N.D.	N.D.	N.D.	Cai et al. (2014)
SPO53	Central Mexico	N.D.	0.512880	0.282991	N.D.	N.D.	N.D.	Cai et al. (2014)
SPO55	Central Mexico	N.D.	0.512833	0.283028	N.D.	N.D.	N.D.	Cai et al. (2014)
SPO56	Central Mexico	N.D.	0.512828	0.283040	N.D.	N.D.	N.D.	Cai et al. (2014)
SPO57	Central Mexico	N.D.	0.512920	0.283023	N.D.	N.D.	N.D.	Cai et al. (2014)
SPO58B	Central Mexico	N.D.	0.512800	0.282954	N.D.	N.D.	N.D.	Cai et al. (2014)
LPO18	Central Mexico	N.D.	0.512879	0.283032	N.D.	N.D.	N.D.	Cai et al. (2014)
LPO2	Central Mexico	N.D.	0.512817	0.282964	N.D.	N.D.	N.D.	Cai et al. (2014)
SPO34	Central Mexico	N.D.	0.512885	0.283011	N.D.	N.D.	N.D.	Cai et al. (2014)
TP10C	Central Mexico	N.D.	0.512940	0.283058	N.D.	N.D.	N.D.	Cai et al. (2014)
TP13	Central Mexico	N.D.	0.512851	0.283015	N.D.	N.D.	N.D.	Cai et al. (2014)
LPO7	Central Mexico	N.D.	0.512787	0.282901	N.D.	N.D.	N.D.	Cai et al. (2014)
PW115	Central Mexico	N.D.	0.512990	0.283086	N.D.	N.D.	N.D.	Cai et al. (2014)
PW293	Central Mexico	N.D.	0.512914	0.283093	N.D.	N.D.	N.D.	Cai et al. (2014)

PW141	Central Mexico	N.D.	0.512951	0.283030	N.D.	N.D.	N.D.	Cai et al. (2014)
PW296	Central Mexico	N.D.	0.512967	0.283066	N.D.	N.D.	N.D.	Cai et al. (2014)
ASC6B	Central Mexico	N.D.	0.512872	0.283011	N.D.	N.D.	N.D.	Cai et al. (2014)
ASC7C	Central Mexico	N.D.	0.512907	0.283015	N.D.	N.D.	N.D.	Cai et al. (2014)
ASWA5	Central Mexico	N.D.	0.512878	0.283001	N.D.	N.D.	N.D.	Cai et al. (2014)
ASWA9	Central Mexico	N.D.	0.512876	0.282996	N.D.	N.D.	N.D.	Cai et al. (2014)
ASC1-S	Central Mexico	0.704378	0.512757	N.D.	N.D.	N.D.	N.D.	Straub et al. (2015)
CH-05-1	Central Mexico	0.703566	0.512945	N.D.	N.D.	N.D.	N.D.	Straub et al. (2015)
CH-05-11	Central Mexico	0.703760	0.512943	N.D.	18.642	15.584	38.369	Straub et al. (2015)
CH-05-12	Central Mexico	0.703811	0.512818	0.282914	18.778	15.621	38.586	Straub et al. (2015)
CH-05-14	Central Mexico	0.703837	0.512938	N.D.	N.D.	N.D.	N.D.	Straub et al. (2015)
CH-05-16	Central Mexico	0.703805	0.512824	0.282918	18.780	15.619	38.582	Straub et al. (2015)
CH-05-17	Central Mexico	0.704222	0.512858	0.283014	N.D.	N.D.	N.D.	Straub et al. (2015)
CH-05-2	Central Mexico	0.703630	0.512967	N.D.	N.D.	N.D.	N.D.	Straub et al. (2015)
CH-05-6	Central Mexico	0.704430	0.512898	0.283031	18.648	15.589	38.393	Straub et al. (2015)
CH-07-1	Central Mexico	0.703596	0.512942	0.283019	N.D.	N.D.	N.D.	Straub et al. (2015)
CH-07-12	Central Mexico	0.704106	0.512948	0.283050	18.635	15.587	38.379	Straub et al. (2015)
CH-07-14	Central Mexico	0.704182	0.512916	0.283029	18.651	15.593	38.409	Straub et al. (2015)
CH-07-15	Central Mexico	0.704100	0.512795	N.D.	N.D.	N.D.	N.D.	Straub et al. (2015)
CH-07-16	Central Mexico	0.704057	0.512799	0.282923	18.741	15.610	38.528	Straub et al. (2015)
CH-07-18	Central Mexico	0.704506	0.512733	N.D.	N.D.	N.D.	N.D.	Straub et al. (2015)
CH-07-19	Central Mexico	0.704544	0.512964	0.283006	18.716	15.604	38.504	Straub et al. (2015)
CH-07-2	Central Mexico	0.703410	0.512923	0.283012	18.689	15.589	38.410	Straub et al. (2015)
CH-07-5	Central Mexico	0.703661	0.512949	N.D.	N.D.	N.D.	N.D.	Straub et al. (2015)
CH-07-6	Central Mexico	0.704147	0.512925	0.283030	18.623	15.581	38.353	Straub et al. (2015)
CH-07-7	Central Mexico	0.704140	0.512925	N.D.	18.621	15.583	38.351	Straub et al. (2015)
CH-07-8	Central Mexico	0.704192	0.512927	N.D.	N.D.	N.D.	N.D.	Straub et al. (2015)
CH-07-9	Central Mexico	0.704170	0.512922	0.283020	18.635	15.585	38.374	Straub et al. (2015)
CH-08-10	Central Mexico	0.703421	0.512940	N.D.	N.D.	N.D.	N.D.	Straub et al. (2015)
CH-08-11	Central Mexico	0.703371	0.512942	0.282985	18.722	15.595	38.446	Straub et al. (2015)

CH-08-15	Central Mexico	0.704295	0.512934	0.282981	18.682	15.598	38.446	Straub et al. (2015)
CH-08-17	Central Mexico	0.703455	0.512910	0.282979	18.784	15.608	38.531	Straub et al. (2015)
CH-08-19	Central Mexico	0.703061	0.512992	0.283043	18.722	15.591	38.431	Straub et al. (2015)
CH-08-3	Central Mexico	0.704416	0.512823	0.282958	18.682	15.607	38.475	Straub et al. (2015)
CH-08-4	Central Mexico	0.703592	0.512884	0.282969	N.D.	N.D.	N.D.	Straub et al. (2015)
CH-08-5	Central Mexico	N.D.	N.D.	0.282876	N.D.	N.D.	N.D.	Straub et al. (2015)
CH-08-6	Central Mexico	0.703601	0.512946	0.283037	18.649	15.584	38.373	Straub et al. (2015)
CH-08-7	Central Mexico	0.703601	0.512946	0.283002	N.D.	N.D.	N.D.	Straub et al. (2015)
CH-08-8	Central Mexico	0.703652	0.512958	0.283038	18.644	15.583	38.365	Straub et al. (2015)
CH-09-11	Central Mexico	0.703053	0.512994	0.283056	18.708	15.594	38.433	Straub et al. (2015)
CH-09-16	Central Mexico	0.704501	0.512837	0.282976	18.674	15.596	38.433	Straub et al. (2015)
CH-09-19	Central Mexico	0.704582	0.512774	0.282951	18.687	15.606	38.498	Straub et al. (2015)
CH-09-2	Central Mexico	0.703811	0.512936	0.283043	N.D.	N.D.	N.D.	Straub et al. (2015)
CH-09-20	Central Mexico	0.704291	0.512864	0.282999	18.648	15.590	38.397	Straub et al. (2015)
CH05-11	Central Mexico	N.D.	N.D.	N.D.	18.642	15.584	38.369	Straub et al. (2015)
CH05-12	Central Mexico	N.D.	N.D.	0.282910	18.778	15.621	38.586	Straub et al. (2015)
CH05-16	Central Mexico	N.D.	N.D.	0.282920	18.780	15.619	38.582	Straub et al. (2015)
CH05-6	Central Mexico	N.D.	N.D.	0.283030	18.648	15.589	38.393	Straub et al. (2015)
CH07-12	Central Mexico	N.D.	N.D.	0.283050	18.635	15.587	38.379	Straub et al. (2015)
CH07-14	Central Mexico	N.D.	N.D.	0.283030	18.651	15.593	38.409	Straub et al. (2015)
CH07-16	Central Mexico	N.D.	N.D.	0.282920	18.741	15.610	38.528	Straub et al. (2015)
CH07-19	Central Mexico	N.D.	N.D.	0.283006	18.716	15.604	38.504	Straub et al. (2015)
CH07-2	Central Mexico	N.D.	N.D.	0.283010	18.689	15.589	38.410	Straub et al. (2015)
CH07-6	Central Mexico	N.D.	N.D.	0.283030	18.623	15.581	38.353	Straub et al. (2015)
CH07-7	Central Mexico	N.D.	N.D.	N.D.	18.621	15.583	38.351	Straub et al. (2015)
CH07-9	Central Mexico	N.D.	N.D.	0.283020	18.635	15.585	38.374	Straub et al. (2015)
CH08-11	Central Mexico	N.D.	N.D.	0.282990	18.722	15.595	38.446	Straub et al. (2015)
CH08-15	Central Mexico	N.D.	N.D.	0.282981	18.682	15.598	38.446	Straub et al. (2015)
CH08-17	Central Mexico	N.D.	N.D.	0.282980	18.784	15.608	38.531	Straub et al. (2015)
CH08-19	Central Mexico	N.D.	N.D.	0.283040	18.722	15.591	38.431	Straub et al. (2015)

CH08-3	Central Mexico	N.D.	N.D.	0.282960	18.682	15.607	38.475	Straub et al. (2015)
CH08-6	Central Mexico	N.D.	N.D.	0.283040	18.649	15.584	38.373	Straub et al. (2015)
CH08-8	Central Mexico	N.D.	N.D.	0.283040	18.644	15.583	38.365	Straub et al. (2015)
CH09-11	Central Mexico	N.D.	N.D.	0.283060	18.708	15.594	38.433	Straub et al. (2015)
CH09-16	Central Mexico	N.D.	N.D.	0.282980	18.674	15.596	38.433	Straub et al. (2015)
CH09-19	Central Mexico	N.D.	N.D.	0.282950	18.687	15.606	38.498	Straub et al. (2015)
CH09-20	Central Mexico	N.D.	N.D.	0.283000	18.648	15.590	38.397	Straub et al. (2015)
MCH-06-1	Central Mexico	0.704353	0.512749	N.D.	N.D.	N.D.	N.D.	Straub et al. (2015)
MCH-06-11	Central Mexico	0.703607	0.512866	0.282949	18.783	15.615	38.556	Straub et al. (2015)
MCH-06-12	Central Mexico	0.703087	0.512987	0.283059	18.724	15.594	38.443	Straub et al. (2015)
MCH-06-3	Central Mexico	0.704203	0.512775	N.D.	18.805	15.628	38.628	Straub et al. (2015)
MCH-06-5	Central Mexico	0.704208	0.512757	0.282876	18.808	15.628	38.633	Straub et al. (2015)
MCH-06-8	Central Mexico	0.703629	0.512916	N.D.	N.D.	N.D.	N.D.	Straub et al. (2015)
MCH-06-9	Central Mexico	0.703632	0.512928	0.282994	18.694	15.594	38.433	Straub et al. (2015)
MCH06-11	Central Mexico	N.D.	N.D.	0.282950	18.783	15.615	38.556	Straub et al. (2015)
MCH06-12	Central Mexico	N.D.	N.D.	0.283060	18.724	15.594	38.443	Straub et al. (2015)
MCH06-3	Central Mexico	N.D.	N.D.	N.D.	18.805	15.628	38.628	Straub et al. (2015)
MCH06-5	Central Mexico	N.D.	N.D.	0.282880	18.808	15.628	38.633	Straub et al. (2015)
MCH06-9	Central Mexico	N.D.	N.D.	0.282990	18.694	15.594	38.433	Straub et al. (2015)
POS-1	Central Mexico	0.704519	0.512816	0.283013	18.673	15.600	38.458	Straub et al. (2015)
POS-10	Central Mexico	0.704368	0.512846	0.282966	18.676	15.596	38.444	Straub et al. (2015)
POS-2	Central Mexico	0.704512	0.512820	0.282999	18.676	15.600	38.462	Straub et al. (2015)
POS-3	Central Mexico	0.704533	0.512815	0.282998	18.679	15.600	38.464	Straub et al. (2015)
POS-4	Central Mexico	0.704060	0.512909	0.283043	18.636	15.586	38.377	Straub et al. (2015)
POS-5	Central Mexico	0.704697	0.512785	0.282959	18.659	15.593	38.410	Straub et al. (2015)
POS-6	Central Mexico	0.704371	0.512785	0.283001	18.656	15.593	38.427	Straub et al. (2015)
POS-7	Central Mexico	0.704430	0.512792	0.282969	18.674	15.600	38.475	Straub et al. (2015)
POS-8	Central Mexico	0.704319	0.512877	0.282981	18.669	15.594	38.424	Straub et al. (2015)
POS-9	Central Mexico	0.704308	0.512882	0.282978	18.662	15.591	38.413	Straub et al. (2015)
S1	Central Mexico	0.704055	0.512801	0.282931	18.741	15.611	38.529	Straub et al. (2015)

S10	Central Mexico	N.D.	N.D.	0.282868	18.820	15.634	38.660	Straub et al. (2015)
S11	Central Mexico	0.704490	0.512754	N.D.	N.D.	N.D.	N.D.	Straub et al. (2015)
S12A	Central Mexico	0.703826	0.512938	N.D.	N.D.	N.D.	N.D.	Straub et al. (2015)
S2	Central Mexico	0.704475	0.512743	N.D.	N.D.	N.D.	N.D.	Straub et al. (2015)
S3	Central Mexico	0.704399	0.512745	N.D.	N.D.	N.D.	N.D.	Straub et al. (2015)
S4	Central Mexico	0.704392	0.512746	0.282872	18.811	15.632	38.648	Straub et al. (2015)
S5	Central Mexico	0.704386	0.512751	N.D.	N.D.	N.D.	N.D.	Straub et al. (2015)
S7	Central Mexico	0.704489	0.512734	N.D.	N.D.	N.D.	N.D.	Straub et al. (2015)
S8	Central Mexico	0.704528	0.512743	0.282879	18.819	15.634	38.662	Straub et al. (2015)
S9	Central Mexico	0.704493	0.512733	0.282868	18.820	15.634	38.660	Straub et al. (2015)
SPO38	Central Mexico	N.D.	N.D.	0.282990	N.D.	N.D.	N.D.	Straub et al. (2015)
SPO56a	Central Mexico	N.D.	N.D.	0.282980	N.D.	N.D.	N.D.	Straub et al. (2015)
SPO60	Central Mexico	0.704419	0.512836	0.282988	18.671	15.597	38.442	Straub et al. (2015)
T-11	Central Mexico	0.703700	0.512874	0.282981	18.608	15.582	38.329	Straub et al. (2015)
T-16	Central Mexico	0.703807	0.512850	0.282973	18.606	15.584	38.339	Straub et al. (2015)
T-17	Central Mexico	0.704199	0.512854	0.282973	18.594	15.577	38.309	Straub et al. (2015)
T-21	Central Mexico	0.704186	0.512856	0.282970	18.599	15.577	38.313	Straub et al. (2015)
BRC01-3	Cascade	0.703204	N.D.	0.283067	18.790	15.565	38.251	Mullen and Weis (2013)
BRC02	Cascade	N.D.	N.D.	N.D.	18.751	15.559	38.197	Mullen and Weis (2013)
BRC03-4	Cascade	0.703211	0.512968	0.283052	18.836	15.562	38.274	Mullen and Weis (2013)
BRC04	Cascade	0.703176	N.D.	0.283026	18.740	15.566	38.203	Mullen and Weis (2013)
BRC05-1	Cascade	0.703111	N.D.	0.283040	18.762	15.552	38.135	Mullen and Weis (2013)
BRC06	Cascade	0.703167	N.D.	0.283018	18.749	15.557	38.190	Mullen and Weis (2013)
BRC07-2	Cascade	0.703090	0.513014	0.283027	18.765	15.549	38.129	Mullen and Weis (2013)
BRC09-3	Cascade	0.702977	0.513026	0.283007	18.737	15.550	38.132	Mullen and Weis (2013)
BRC10	Cascade	0.703044	0.513033	0.283025	18.776	15.560	38.157	Mullen and Weis (2013)
SG01-2	Cascade	0.703132	0.513023	0.283017	18.749	15.546	38.116	Mullen and Weis (2013)
SG02-3	Cascade	0.703135	0.513003	0.283021	18.756	15.545	38.116	Mullen and Weis (2013)
SG10	Cascade	0.703114	N.D.	0.283012	18.739	15.553	38.136	Mullen and Weis (2013)

SG12	Cascade	0.703057	0.513015	N.D.	18.776	15.556	38.179	Mullen and Weis (2013)
SG16	Cascade	0.703093	N.D.	0.283023	18.762	15.557	38.166	Mullen and Weis (2013)
MM01-1	Cascade	0.703756	0.512932	0.283063	18.806	15.573	38.274	Mullen and Weis (2013)
MM02	Cascade	0.703124	0.512938	0.283050	18.706	15.551	38.108	Mullen and Weis (2013)
MM04	Cascade	0.703136	0.513032	0.283056	18.711	15.551	38.112	Mullen and Weis (2013)
MM08	Cascade	0.703156	N.D.	0.283022	18.692	15.559	38.082	Mullen and Weis (2013)
LIB-21	Cascade	0.703956	0.512836	0.283084	18.926	15.589	38.478	Mullen and Weis (2013)
02-MB-05	Cascade	0.703101	0.513003	0.283100	18.800	15.554	38.257	Mullen and Weis (2013)
07-MB-112	Cascade	0.703232	0.513036	0.283114	18.841	15.561	38.315	Mullen and Weis (2013)
02-MB-1	Cascade	0.703505	0.512901	N.D.	18.854	15.568	38.367	Mullen and Weis (2013)
06-MB-82	Cascade	0.703148	0.512988	N.D.	18.831	15.556	38.273	Mullen and Weis (2013)
07-MB-114	Cascade	0.703205	0.513039	N.D.	18.849	15.560	38.282	Mullen and Weis (2013)
06-MB-97	Cascade	0.703165	0.512995	N.D.	18.838	15.557	38.267	Mullen and Weis (2013)
BRC05-1	Cascade	0.703111	0.513005	0.283040	18.762	15.552	38.135	Mullen and Weis (2015)
BRC06	Cascade	0.703167	0.512996	0.283018	18.749	15.557	38.190	Mullen and Weis (2015)
BRC07-2	Cascade	0.703090	0.513014	0.283027	18.765	15.549	38.129	Mullen and Weis (2015)
BRC09-3	Cascade	0.702977	0.513027	0.283007	18.746	15.550	38.132	Mullen and Weis (2015)
BRC10	Cascade	0.703046	0.513032	0.283025	18.776	15.560	38.157	Mullen and Weis (2015)
THEC-1	Cascade	0.703034	0.513007	0.283043	18.739	15.546	38.117	Mullen and Weis (2015)
SG01-1	Cascade	N.D.	0.513007	N.D.	18.772	15.550	38.160	Mullen and Weis (2015)
SG01-2	Cascade	0.703132	0.513023	0.283017	18.749	15.546	38.116	Mullen and Weis (2015)
SG01-3	Cascade	0.703135	0.513002	0.283021	18.756	15.544	38.116	Mullen and Weis (2015)
SG10	Cascade	0.703114	0.512992	0.283012	18.739	15.553	38.136	Mullen and Weis (2015)
SG12	Cascade	0.703059	0.513000	N.D.	18.702	15.566	38.156	Mullen and Weis (2015)
SG16	Cascade	0.703093	0.513000	0.283023	18.762	15.557	38.166	Mullen and Weis (2015)
MM02	Cascade	0.703131	0.513032	0.283056	18.706	15.551	38.108	Mullen and Weis (2015)
MM04	Cascade	0.703136	0.513031	0.283056	18.711	15.551	38.112	Mullen and Weis (2015)
MM08	Cascade	0.703173	0.513025	0.283026	18.700	15.550	38.066	Mullen and Weis (2015)
EV01-1	Cascade	0.703357	0.512988	0.283053	18.757	15.558	38.185	Mullen and Weis (2015)
EV01-2	Cascade	0.703360	0.512997	0.283047	18.755	15.558	38.184	Mullen and Weis (2015)

MG11-8	Cascade	N.D.	N.D.	N.D.	N.D.	N.D.	N.D.	Mullen and Weis (2015)
MG28-4	Cascade	0.703155	0.513006	0.283017	18.709	15.550	38.107	Mullen and Weis (2015)
MG36-4	Cascade	N.D.	N.D.	N.D.	N.D.	N.D.	N.D.	Mullen and Weis (2015)
MG198-1	Cascade	0.703162	0.512994	0.283029	18.704	15.552	38.119	Mullen and Weis (2015)
MG71-1	Cascade	N.D.	N.D.	N.D.	N.D.	N.D.	N.D.	Mullen and Weis (2015)
MG435	Cascade	0.703241	0.512994	0.283051	18.692	15.553	38.152	Mullen and Weis (2015)
206-2	Cascade	N.D.	N.D.	N.D.	N.D.	N.D.	N.D.	Mullen and Weis (2015)
126-41	Cascade	N.D.	N.D.	N.D.	N.D.	N.D.	N.D.	Mullen and Weis (2015)
HC-454	Cascade	0.703805	0.512883	0.283047	18.779	15.570	38.294	Mullen and Weis (2015)
HC-456	Cascade	0.703784	0.512877	0.283054	18.807	15.568	38.332	Mullen and Weis (2015)
HC-460	Cascade	0.703801	0.512893	N.D.	18.780	15.575	38.301	Mullen and Weis (2015)
06-MB-97	Cascade	0.703165	0.512995	N.D.	18.838	15.557	38.267	Mullen and Weis (2015)
02-MB-5	Cascade	0.703101	0.513003	0.283100	18.800	15.554	38.257	Mullen and Weis (2015)
06-MB-82	Cascade	0.703148	0.512989	N.D.	18.837	15.556	38.279	Mullen and Weis (2015)
07-MB-112	Cascade	0.703232	0.513035	0.283114	18.841	15.561	38.315	Mullen and Weis (2015)
07-MB-114	Cascade	0.703205	0.513039	N.D.	18.849	15.560	38.282	Mullen and Weis (2015)
08-MB-122	Cascade	0.703240	0.513030	N.D.	N.D.	N.D.	N.D.	Mullen and Weis (2015)
DG-02-1	Cascade	0.703367	0.512981	0.283131	18.819	15.577	38.407	Mullen and Weis (2015)
DG-03-1	Cascade	0.703344	0.512982	0.283109	18.821	15.577	38.405	Mullen and Weis (2015)
DG-04	Cascade	N.D.	0.512981	N.D.	18.820	15.574	38.401	Mullen and Weis (2015)
WC01-3	Cascade	0.703176	0.513077	0.283143	18.674	15.540	38.188	Mullen and Weis (2015)
WC01-5	Cascade	0.703194	0.513071	0.283148	18.659	15.536	38.161	Mullen and Weis (2015)
IP01-2	Cascade	0.703542	0.512982	0.283140	18.835	15.577	38.428	Mullen and Weis (2015)
GP11-01	Cascade	N.D.	0.512949	N.D.	18.843	15.579	38.450	Mullen and Weis (2015)
MA-120	Cascade	0.702859	0.513018	0.283088	18.866	15.552	38.397	Mullen et al. (2017)
MA-953	Cascade	0.703635	0.512920	0.283062	18.982	15.598	38.669	Mullen et al. (2017)
75SV-3	Cascade	0.703668	0.512890	0.283049	18.949	15.613	38.614	Mullen et al. (2017)
75SH-268	Cascade	0.703448	0.512899	0.283049	18.952	15.606	38.596	Mullen et al. (2017)
81C621	Cascade	0.703491	0.512924	0.283073	18.896	15.584	38.516	Mullen et al. (2017)
82C894 (40 cycles d)	Cascade	0.703390	0.512942	0.283087	18.844	15.563	38.426	Mullen et al. (2017)

88C1521	Cascade	0.703615	0.512886	0.283041	18.907	15.594	38.541	Mullen et al. (2017)
88C1523	Cascade	0.703699	0.512885	0.283039	18.929	15.598	38.569	Mullen et al. (2017)
88C1557	Cascade	0.703469	0.512938	0.283042	18.871	15.588	38.488	Mullen et al. (2017)
80C354	Cascade	0.703696	0.512889	0.283044	18.909	15.602	38.556	Mullen et al. (2017)
LC86-855	Cascade	0.703962	0.512839	0.283031	18.979	15.619	38.646	Mullen et al. (2017)
LC85-671	Cascade	0.703886	0.512843	0.283027	18.967	15.617	38.634	Mullen et al. (2017)
LC86-1009	Cascade	0.703092	0.512888	0.283045	18.821	15.584	38.395	Mullen et al. (2017)
82-72f	Cascade	0.703398	0.512962	0.283100	18.815	15.564	38.450	Mullen et al. (2017)
767M	Cascade	0.703394	0.512964	0.283108	18.883	15.571	38.490	Mullen et al. (2017)
851M	Cascade	0.703394	0.512967	0.283115	18.879	15.575	38.491	Mullen et al. (2017)
881M	Cascade	0.703353	0.512958	0.283101	18.859	15.564	38.475	Mullen et al. (2017)
1161M	Cascade	0.703422	0.512918	0.283081	18.912	15.590	38.561	Mullen et al. (2017)
NS-01-16	Cascade	0.703512	0.512923	0.283061	18.839	15.583	38.461	Mullen et al. (2017)
NS-02-101	Cascade	0.703496	0.512913	0.283070	18.840	15.586	38.467	Mullen et al. (2017)
NS-03-132	Cascade	0.703490	0.512923	0.283065	18.837	15.584	38.463	Mullen et al. (2017)
NS-02-29	Cascade	0.703497	0.512915	0.283054	18.836	15.581	38.457	Mullen et al. (2017)
NS-02-38	Cascade	0.703520	0.512897	0.283068	18.851	15.584	38.476	Mullen et al. (2017)
NS-02-66	Cascade	0.703635	0.512905	0.283062	18.916	15.595	38.554	Mullen et al. (2017)
NS-03-164	Cascade	0.703483	0.512902	0.283064	18.840	15.579	38.457	Mullen et al. (2017)
NS-03-165	Cascade	0.703525	0.512899	0.283051	18.884	15.594	38.518	Mullen et al. (2017)
KliN.D.klini	Cascade	0.703335	0.512934	0.283009	18.874	15.560	38.304	Mullen et al. (2017)
Nichols Valley	Cascade	0.703044	0.512999	0.283042	18.742	15.544	38.112	Mullen et al. (2017)
PJA-2009-1	Cascade	0.703669	0.512947	0.283104	18.775	15.571	38.291	Mullen et al. (2017)
CC07-3	Cascade	0.703368	0.512973	0.283118	18.663	15.545	38.154	Mullen et al. (2017)
MA-767	Cascade	0.702818	0.513006	0.283053	19.029	15.577	38.565	Mullen et al. (2017)
MA-696	Cascade	0.702861	0.513009	0.283070	18.940	15.562	38.457	Mullen et al. (2017)
MA-120	Cascade	0.702859	0.513018	0.283088	18.866	15.552	38.397	Mullen et al. (2017)
MA-953	Cascade	0.703635	0.512920	0.283062	18.982	15.598	38.669	Mullen et al. (2017)
MA-332	Cascade	0.703264	0.512965	0.283094	18.886	15.573	38.512	Mullen et al. (2017)
SM-27	Cascade	0.703032	0.512894	0.282979	18.687	15.532	38.290	Mullen et al. (2017)

75SH-270	Cascade	0.704090	0.512829	0.283017	19.082	15.634	38.798	Mullen et al. (2017)
75SV-3	Cascade	0.703668	0.512890	0.283049	18.949	15.613	38.614	Mullen et al. (2017)
75SH-317	Cascade	0.703603	0.512889	0.283078	18.924	15.603	38.563	Mullen et al. (2017)
75SH-268	Cascade	0.703448	0.512899	0.283049	18.952	15.606	38.596	Mullen et al. (2017)
81C621	Cascade	0.703490	0.512924	0.283073	18.896	15.584	38.516	Mullen et al. (2017)
82C894	Cascade	0.703390	0.512942	0.283087	18.844	15.563	38.426	Mullen et al. (2017)
84C1143	Cascade	0.703507	0.512897	0.283079	18.901	15.578	38.517	Mullen et al. (2017)
88C1540	Cascade	0.703480	0.512916	0.283039	18.931	15.597	38.573	Mullen et al. (2017)
88C1530	Cascade	0.703548	0.512925	0.283057	18.913	15.599	38.562	Mullen et al. (2017)
88C1521	Cascade	0.703615	0.512976	0.283041	18.907	15.594	38.541	Mullen et al. (2017)
88C1523	Cascade	0.703699	0.512885	0.283039	18.929	15.598	38.569	Mullen et al. (2017)
88C1557	Cascade	0.703469	0.512938	0.283042	18.871	15.588	38.488	Mullen et al. (2017)
80C354	Cascade	0.703695	0.512889	0.283044	18.909	15.602	38.556	Mullen et al. (2017)
LC88-1398	Cascade	0.704143	0.512864	0.283035	18.963	15.617	38.631	Mullen et al. (2017)
LC86-1046	Cascade	0.703772	0.512879	0.283064	18.973	15.621	38.655	Mullen et al. (2017)
LC82-970	Cascade	0.703745	0.512886	0.283058	18.974	15.619	38.653	Mullen et al. (2017)
LC88-1311	Cascade	0.703807	0.512885	0.283073	18.978	15.625	38.667	Mullen et al. (2017)
LM87-1384	Cascade	0.704039	0.512837	0.283018	18.937	15.617	38.621	Mullen et al. (2017)
LC88-1312	Cascade	0.703136	0.512947	0.283056	18.818	15.589	38.427	Mullen et al. (2017)
LC82-905	Cascade	0.703941	0.512805	0.283004	18.974	15.621	38.651	Mullen et al. (2017)
LC86-855	Cascade	0.703961	0.512839	0.283031	18.979	15.619	38.646	Mullen et al. (2017)
LC85-671	Cascade	0.703886	0.512843	0.283027	18.967	15.617	38.634	Mullen et al. (2017)
LC86-1009	Cascade	0.703092	0.512888	0.283045	18.821	15.584	38.396	Mullen et al. (2017)
82-72-f	Cascade	0.703398	0.512962	0.283100	18.815	15.564	38.450	Mullen et al. (2017)
767M	Cascade	0.703394	0.512964	0.283108	18.883	15.571	38.490	Mullen et al. (2017)
1085M	Cascade	0.703395	0.512962	0.283114	18.885	15.575	38.500	Mullen et al. (2017)
851M	Cascade	0.703394	0.512967	0.283115	18.879	15.575	38.491	Mullen et al. (2017)
1376M	Cascade	0.703480	0.512949	0.283096	18.887	15.591	38.539	Mullen et al. (2017)
881M	Cascade	0.703352	0.512958	0.283101	18.859	15.564	38.475	Mullen et al. (2017)
1161M	Cascade	0.703422	0.512918	0.283081	18.912	15.590	38.561	Mullen et al. (2017)

NS-01-16	Cascade	0.703512	0.512923	0.283061	18.839	15.583	38.461	Mullen et al. (2017)
NS-02-101	Cascade	0.703496	0.512913	0.283070	18.840	15.586	38.467	Mullen et al. (2017)
NS-03-132	Cascade	0.703490	0.512923	0.283065	18.837	15.584	38.463	Mullen et al. (2017)
NS-02-29	Cascade	0.703497	0.512915	0.283054	18.836	15.581	38.457	Mullen et al. (2017)
NS-02-38	Cascade	0.703520	0.512897	0.283068	18.851	15.584	38.476	Mullen et al. (2017)
NS-02-46	Cascade	0.703486	0.512906	0.283080	18.820	15.577	38.434	Mullen et al. (2017)
NS-02-65	Cascade	0.703634	0.512905	0.283062	18.916	15.595	38.554	Mullen et al. (2017)
NS-02-75	Cascade	0.703524	0.512902	0.283058	18.867	15.583	38.499	Mullen et al. (2017)
NS-02-92	Cascade	0.703490	0.512918	0.283063	18.813	15.573	38.418	Mullen et al. (2017)
NS-02-135	Cascade	0.703502	0.512915	0.283068	18.835	15.580	39.448	Mullen et al. (2017)
NS-03-153	Cascade	0.703482	0.512903	0.283056	18.850	15.583	38.473	Mullen et al. (2017)
NS-03-164	Cascade	0.703483	0.512902	0.283064	18.840	15.579	38.457	Mullen et al. (2017)
NS-03-165	Cascade	0.703525	0.512899	0.283051	18.884	15.594	38.518	Mullen et al. (2017)
BPCB-1	Cascade	0.703388	0.512928	0.283052	18.845	15.594	38.471	Walowski et al. (2016)
BORG-1	Cascade	0.703805	0.512866	0.283055	18.901	15.605	38.546	Walowski et al. (2016)
BPB-1	Cascade	0.703869	0.512829	0.283059	18.957	15.617	38.620	Walowski et al. (2016)
BBL-05	Cascade	0.703931	0.512861	0.283057	18.967	15.622	38.658	Walowski et al. (2016)
BAS-44-01	Cascade	0.703521	0.512950	0.283094	18.924	15.610	38.571	Walowski et al. (2016)
BRVB-1	Cascade	0.703977	0.512835	0.283035	18.980	15.620	38.653	Walowski et al. (2016)
S 7	New Georgia	0.703788	0.512979	0.283118	18.519	15.573	38.435	Schuth et al. (2004), Schuth et al. (2009)
S 13	New Georgia	0.703889	0.513049	0.283177	18.496	15.552	38.415	Schuth et al. (2004), Schuth et al. (2009)
S 14	New Georgia	0.703830	0.513039	0.283177	N.D.	N.D.	N.D.	Schuth et al. (2004)
S 15	New Georgia	0.703667	0.513025	0.283182	18.474	15.546	38.385	Schuth et al. (2004), Schuth et al. (2009)
S 17	New Georgia	0.703878	0.513020	0.283130	18.542	15.532	38.323	Schuth et al. (2004), Schuth et al. (2009)
S 33	New Georgia	0.704298	0.512966	0.283161	18.552	15.575	38.434	Schuth et al. (2004), Schuth et al. (2009)
S 43	New Georgia	0.703559	0.513015	0.283158	18.588	15.521	38.307	Schuth et al. (2004), Schuth et al. (2009)
S 47	New Georgia	0.703563	0.513010	0.283159	N.D.	N.D.	N.D.	Schuth et al. (2004)
S 49	New Georgia	0.703632	0.513052	0.283155	18.579	15.523	38.324	Schuth et al. (2004), Schuth et al. (2009)
S 52	New Georgia	0.703390	0.513003	0.283167	18.592	15.531	38.301	Schuth et al. (2004), Schuth et al. (2009)

S 58	New Georgia	0.703576	0.513012	0.283173	18.595	15.533	38.344	Schuth et al. (2004), Schuth et al. (2009)
S 66	New Georgia	0.703500	0.513013	0.283172	N.D.	N.D.	N.D.	Schuth et al. (2004)
S 67	New Georgia	0.703575	0.513018	0.283172	18.615	15.538	38.363	Schuth et al. (2004), Schuth et al. (2009)
S 70	New Georgia	0.703541	0.513018	0.283184	18.593	15.545	38.390	Schuth et al. (2004), Schuth et al. (2009)
S 72	New Georgia	0.703542	0.513015	0.283186	18.596	15.534	38.343	Schuth et al. (2004), Schuth et al. (2009)
S 76	New Georgia	0.703755	0.513006	0.283136	18.459	15.527	38.329	Schuth et al. (2004), Schuth et al. (2009)
S E 3	New Georgia	0.703280	0.513025	0.283148	18.536	15.542	38.306	Schuth et al. (2004), Schuth et al. (2009)
S E 16	New Georgia	0.704031	0.512937	0.283139	18.470	15.539	38.313	Schuth et al. (2004), Schuth et al. (2009)
S S 1	New Georgia	0.703581	0.513026	0.283172	N.D.	N.D.	N.D.	Schuth et al. (2004)
VL 102	New Georgia	0.703454	0.513025	0.283154	18.438	15.551	38.189	König et al. (2007)
VL 103	New Georgia	0.703804	0.513035	0.283170	18.438	15.511	38.169	König et al. (2007)
VL 110	New Georgia	0.703513	0.513033	0.283154	18.478	15.521	38.269	König et al. (2007)
VL 111	New Georgia	0.703740	0.513029	0.283145	N.D.	N.D.	N.D.	König et al. (2007)
RG 113	New Georgia	0.703500	0.513056	0.283161	18.528	15.521	38.279	König et al. (2007)
RG 117	New Georgia	0.704024	0.512981	0.283147	18.548	15.521	38.309	König et al. (2007)
RG 118	New Georgia	0.703635	0.513026	0.283168	18.558	15.571	38.450	König et al. (2007)
RG 119	New Georgia	0.703543	0.513010	0.283179	18.518	15.511	38.249	König et al. (2007)
SB 121	New Georgia	0.703500	0.513049	0.283112	18.528	15.511	38.179	König et al. (2007)
SB 123	New Georgia	0.703547	0.513037	0.283110	18.548	15.541	38.279	König et al. (2007)
SB 125	New Georgia	0.703532	0.513006	0.283137	18.438	15.501	38.159	König et al. (2007)
SB 126	New Georgia	0.703513	0.512995	0.283132	18.438	15.541	38.249	König et al. (2007)
SB 128	New Georgia	0.703548	0.513028	0.283125	18.498	15.561	38.369	König et al. (2007)
SB 129	New Georgia	0.703478	0.512987	0.283133	18.478	15.541	38.319	König et al. (2007)
RG 131	New Georgia	0.703649	0.513010	0.283172	18.518	15.551	38.389	König et al. (2007)
SB 132	New Georgia	0.703505	0.513010	0.283134	18.478	15.531	38.249	König et al. (2007)
SB 133b	New Georgia	0.703583	0.512991	0.283122	18.438	15.501	38.179	König et al. (2007)
S 3	New Georgia	0.703201	0.513063	0.283139	N.D.	N.D.	N.D.	Schuth et al. (2009)
S 4	New Georgia	0.703831	0.512985	0.283171	18.566	15.557	38.435	Schuth et al. (2009)
S 5	New Georgia	0.703843	0.512961	0.283105	N.D.	N.D.	N.D.	Schuth et al. (2009)
S 9	New Georgia	0.703858	0.512992	0.283126	N.D.	N.D.	N.D.	Schuth et al. (2009)

S 18	New Georgia	0.703361	0.512971	0.283140	N.D.	N.D.	N.D.	Schuth et al. (2009)
S 20	New Georgia	0.703622	0.512999	0.283161	18.628	15.537	38.375	Schuth et al. (2009)
S 23	New Georgia	0.703438	0.513029	0.283135	18.507	15.528	38.262	Schuth et al. (2009)
S 27	New Georgia	0.703666	0.513006	0.283158	N.D.	N.D.	N.D.	Schuth et al. (2009)
S 28	New Georgia	0.703687	0.513011	0.283152	N.D.	N.D.	N.D.	Schuth et al. (2009)
S E 15	New Georgia	0.704212	0.512992	0.283141	N.D.	N.D.	N.D.	Schuth et al. (2009)
S 31	New Georgia	0.704199	0.512995	0.283146	N.D.	N.D.	N.D.	Schuth et al. (2009)
S 35	New Georgia	0.703826	0.512987	0.283084	N.D.	N.D.	N.D.	Schuth et al. (2009)
S 36 b	New Georgia	0.703566	0.513010	0.283166	N.D.	N.D.	N.D.	Schuth et al. (2009)
S 37	New Georgia	0.703551	0.512993	0.283189	N.D.	N.D.	N.D.	Schuth et al. (2009)
S 44	New Georgia	0.703620	0.513008	0.283173	N.D.	N.D.	N.D.	Schuth et al. (2009)
S 46	New Georgia	0.703613	0.512989	0.283169	N.D.	N.D.	N.D.	Schuth et al. (2009)
S 53	New Georgia	0.703673	0.513040	0.283123	N.D.	N.D.	N.D.	Schuth et al. (2009)
S 54	New Georgia	0.703529	0.513013	0.283144	N.D.	N.D.	N.D.	Schuth et al. (2009)
S 74	New Georgia	0.703669	0.513012	0.283191	N.D.	N.D.	N.D.	Schuth et al. (2009)
S 75	New Georgia	0.704149	0.513031	0.283169	N.D.	N.D.	N.D.	Schuth et al. (2009)
S 78	New Georgia	0.703604	0.512997	0.283180	N.D.	N.D.	N.D.	Schuth et al. (2009)
S N 2	New Georgia	0.703881	0.513041	0.283150	18.469	15.536	38.326	Schuth et al. (2009)
S 84 Ghi	New Georgia	0.703738	0.512976	0.283103	N.D.	N.D.	N.D.	Schuth et al. (2009)
S 87 VL	New Georgia	0.703556	0.512999	0.283130	N.D.	N.D.	N.D.	Schuth et al. (2009)
S 88 A+ Fau	New Georgia	0.703756	0.513070	0.283137	18.588	15.551	38.409	Schuth et al. (2009)
S 90 Fau	New Georgia	0.703750	0.512976	0.283069	18.523	15.491	38.256	Schuth et al. (2009)
S 95 Sho	New Georgia	0.705201	0.513133	0.283157	N.D.	N.D.	N.D.	Schuth et al. (2009)
S 98 Fau	New Georgia	0.703872	0.513035	0.283086	18.578	15.531	38.379	Schuth et al. (2009)
S 100 VL	New Georgia	0.703576	0.512991	0.283151	18.468	15.541	38.259	Schuth et al. (2009)
S 107 VL	New Georgia	0.704075	0.513015	0.283137	N.D.	N.D.	N.D.	Schuth et al. (2009)
S 108 VL	New Georgia	0.703747	0.513060	0.283160	N.D.	N.D.	N.D.	Schuth et al. (2009)
S 134 Ren	New Georgia	0.704044	0.512989	0.283148	N.D.	N.D.	N.D.	Schuth et al. (2009)
S 137 Ren	New Georgia	0.703930	0.513009	0.283144	18.477	15.537	38.284	Schuth et al. (2009)
S 142 NG	New Georgia	0.703662	0.513009	0.283109	N.D.	N.D.	N.D.	Schuth et al. (2009)

S 143 NG	New Georgia	0.703569	0.513061	0.283116	18.510	15.500	38.238	Schuth et al. (2009)	
S 149 Kol	New Georgia	0.704213	0.512953	0.283131	N.D.	N.D.	N.D.	Schuth et al. (2009)	
S 152 Kol	New Georgia	0.703825	0.512991	0.283171	18.448	15.511	38.179	Schuth et al. (2009)	
S 153 Mbo	New Georgia	0.703792	0.513023	0.283159	N.D.	N.D.	N.D.	Schuth et al. (2009)	
S 158 Pav	New Georgia	0.703663	0.513014	0.283161	N.D.	N.D.	N.D.	Schuth et al. (2009)	
S 160 Mba	New Georgia	0.703748	0.512970	0.283156	18.428	15.521	38.259	Schuth et al. (2009)	
S 162 Mak	New Georgia	0.703155	0.513045	0.283105	N.D.	N.D.	N.D.	Schuth et al. (2009)	
S 163 Mak	New Georgia	0.702868	0.513096	0.283139	18.625	15.500	38.134	Schuth et al. (2009)	
S 164 Mak	New Georgia	0.702896	0.513071	0.283135	N.D.	N.D.	N.D.	Schuth et al. (2009)	
SV 78	New Georgia	0.704078	0.513014	0.283144	18.480	15.551	38.377	Schuth et al. (2009)	
S 171 Sav	New Georgia	0.704026	0.512932	0.283127	18.498	15.541	38.379	Schuth et al. (2009)	
S 176 Sav	New Georgia	0.704137	0.512935	0.283115	18.478	15.541	38.339	Schuth et al. (2009)	
S 178 Sav	New Georgia	0.704025	0.513060	0.283116	N.D.	N.D.	N.D.	Schuth et al. (2009)	
S 179 Gua	New Georgia	0.703664	0.513006	0.283133	N.D.	N.D.	N.D.	Schuth et al. (2009)	
S 182 Gua	New Georgia	0.703639	0.513033	0.283148	N.D.	N.D.	N.D.	Schuth et al. (2009)	
S 185 Gua	New Georgia	0.703987	0.512971	0.283127	18.423	15.512	38.244	Schuth et al. (2009)	
S 187 Van	New Georgia	0.703606	0.513047	0.283159	18.668	15.531	38.339	Schuth et al. (2009)	
S 193 Van	New Georgia	0.703545	0.513046	0.283192	N.D.	N.D.	N.D.	Schuth et al. (2009)	
S 194 Van	New Georgia	0.703699	0.513055	0.283188	18.631	15.541	38.366	Schuth et al. (2009)	
S 200 Utu	New Georgia	0.703605	0.513058	0.283141	18.734	15.575	38.491	Schuth et al. (2009)	
S 204 Utu	New Georgia	0.703284	0.513045	0.283171	18.678	15.541	38.349	Schuth et al. (2009)	
S 206 Utu	New Georgia	0.703479	0.513006	0.283123	N.D.	N.D.	N.D.	Schuth et al. (2009)	
S 207 Tin	New Georgia	0.702969	0.513057	0.283157	18.619	15.507	38.177	Schuth et al. (2009)	
S 210 Tin	New Georgia	0.702961	0.513089	0.283160	N.D.	N.D.	N.D.	Schuth et al. (2009)	
S 215 Tin	New Georgia	0.703096	0.513066	0.283128	18.620	15.509	38.182	Schuth et al. (2009)	
S 217 SC	New Georgia	0.704514	0.513000	0.283129	18.529	15.499	38.160	Schuth et al. (2009)	
S 220 SC	New Georgia	0.703696	0.512974	0.283115	18.589	15.527	38.298	Schuth et al. (2009)	
IRAO-05	Chugoku, Japan	SW	0.704537	0.512726	0.282970	18.227	15.555	38.464	Kimura et al. (2014)

sugi-01	Chugoku, Japan	SW	0.705182	0.512612	0.283013	18.381	15.604	38.637	Kimura et al. (2014)
UYAMA-01	Chugoku, Japan	SW	0.703590	0.512790	0.282973	18.239	15.550	38.383	Kimura et al. (2014)
KAN-02	Chugoku, Japan	SW	0.703991	0.512862	0.282975	18.168	15.521	38.146	Kimura et al. (2014)
KATA-02	Chugoku, Japan	SW	0.703532	0.512904	0.283133	18.032	15.509	38.042	Kimura et al. (2014)
KATA-04	Chugoku, Japan	SW	0.703619	0.512926	0.283159	18.034	15.510	38.047	Kimura et al. (2014)
KA-02	Chugoku, Japan	SW	0.704348	0.512771	0.282937	18.219	15.587	38.387	Kimura et al. (2014)
KA-03	Chugoku, Japan	SW	0.704388	0.512771	0.282973	18.317	15.578	38.494	Kimura et al. (2014)
KASA-01	Chugoku, Japan	SW	0.704211	0.512781	0.282974	18.345	15.573	38.494	Kimura et al. (2014)
NAB-01	Chugoku, Japan	SW	0.704158	0.512769	0.283090	18.330	15.574	38.498	Kimura et al. (2014)
NG-09	Chugoku, Japan	SW	0.704165	0.512761	0.283017	18.332	15.559	38.411	Kimura et al. (2014)
DAI-03	Chugoku, Japan	SW	0.703737	0.512913	0.283017	18.268	15.556	38.357	Kimura et al. (2014)
HG-1	Chugoku, Japan	SW	0.703527	0.512896	N.D.	N.D.	N.D.	N.D.	Kimura et al. (2014)
HG-25	Chugoku, Japan	SW	0.704020	0.512805	N.D.	N.D.	N.D.	N.D.	Kimura et al. (2014)
HIRA-01	Chugoku, Japan	SW	0.704494	0.512722	0.282923	18.322	15.565	38.462	Kimura et al. (2014)
HORI-01	Chugoku, Japan	SW	0.706025	0.512624	N.D.	18.542	15.605	38.672	Kimura et al. (2014)
IRAO-05	Chugoku, Japan	SW	0.704537	0.512726	0.282970	18.227	15.555	38.464	Kimura et al. (2014)
K-01	Chugoku, Japan	SW	0.707142	0.512747	N.D.	18.797	15.600	38.717	Kimura et al. (2014)
KA-02	Chugoku, Japan	SW	0.704348	0.512771	0.282937	18.219	15.587	38.387	Kimura et al. (2014)
KA-03	Chugoku, Japan	SW	0.704388	0.512771	0.282973	18.317	15.578	38.494	Kimura et al. (2014)
KAN-02	Chugoku, Japan	SW	0.703991	0.512862	0.282975	18.168	15.521	38.146	Kimura et al. (2014)
KASA-01	Chugoku, Japan	SW	0.704211	0.512781	0.282974	18.345	15.573	38.494	Kimura et al. (2014)
KATA-01	Chugoku, Japan	SW	0.703557	0.512888	0.283128	18.038	15.512	38.055	Kimura et al. (2014)

KATA-02	Chugoku, Japan	SW	0.703532	0.512904	0.283133	18.032	15.509	38.042	Kimura et al. (2014)
KATA-04	Chugoku, Japan	SW	0.703619	0.512926	0.283159	18.034	15.510	38.047	Kimura et al. (2014)
NAB-01	Chugoku, Japan	SW	0.704158	0.512769	0.283090	18.330	15.574	38.498	Kimura et al. (2014)
NG-09	Chugoku, Japan	SW	0.704165	0.512761	0.283017	18.332	15.559	38.411	Kimura et al. (2014)
NKO-01	Chugoku, Japan	SW	0.705167	0.512819	N.D.	18.280	15.557	38.274	Kimura et al. (2014)
OG-03	Chugoku, Japan	SW	0.703920	0.512837	0.283047	18.230	15.545	38.310	Kimura et al. (2014)
Sugi-01	Chugoku, Japan	SW	0.705182	0.512612	0.283013	18.381	15.604	38.637	Kimura et al. (2014)
TATA-03	Chugoku, Japan	SW	0.704565	0.512708	0.282925	18.242	15.562	38.485	Kimura et al. (2014)
TATA-05	Chugoku, Japan	SW	0.703822	0.512849	0.283043	18.203	15.539	38.259	Kimura et al. (2014)
UYAMA-01	Chugoku, Japan	SW	0.703590	0.512790	0.282973	18.239	15.550	38.383	Kimura et al. (2014)
AO-1	Chugoku, Japan	SW	0.703475	0.512838	N.D.	N.D.	N.D.	N.D.	Kimura et al. (2014)
AO-2	Chugoku, Japan	SW	0.703444	0.512865	N.D.	N.D.	N.D.	N.D.	Kimura et al. (2014)
AO-3	Chugoku, Japan	SW	0.703433	0.512841	0.283104	18.152	15.534	38.223	Kimura et al. (2014), Kimura et al. (2015)
AO-4	Chugoku, Japan	SW	0.703462	0.512874	N.D.	N.D.	N.D.	N.D.	Kimura et al. (2014)
AN-1	Chugoku, Japan	SW	0.703590	0.512890	N.D.	N.D.	N.D.	N.D.	Kimura et al. (2014)
SI-1	Chugoku, Japan	SW	0.703461	0.512884	0.283096	N.D.	N.D.	N.D.	Kimura et al. (2014)
SI-2	Chugoku, Japan	SW	0.703514	0.512904	N.D.	N.D.	N.D.	N.D.	Kimura et al. (2014)
SI-3	Chugoku, Japan	SW	0.703475	0.512885	N.D.	N.D.	N.D.	N.D.	Kimura et al. (2014)
SE-1	Chugoku, Japan	SW	0.703469	0.512867	0.283057	18.084	15.519	38.131	Kimura et al. (2014), Kimura et al. (2015)
SE-2	Chugoku, Japan	SW	0.703510	0.512877	N.D.	N.D.	N.D.	N.D.	Kimura et al. (2014)
MI-1	Chugoku, Japan	SW	0.703509	0.512930	0.283104	18.104	15.510	38.094	Kimura et al. (2014), Kimura et al. (2015)
MI-2	Chugoku, Japan	SW	0.703423	0.512951	N.D.	N.D.	N.D.	N.D.	Kimura et al. (2014)

TA-1	Chugoku, Japan	SW	0.703486	0.512873	N.D.	N.D.	N.D.	N.D.	Kimura et al. (2014)
TA-2	Chugoku, Japan	SW	0.703443	0.512863	0.283109	18.116	15.530	38.211	Kimura et al. (2014), Kimura et al. (2015)
DS-3	Chugoku, Japan	SW	0.704853	0.512760	N.D.	N.D.	N.D.	N.D.	Kimura et al. (2014)
DS-4	Chugoku, Japan	SW	0.704740	0.512698	N.D.	N.D.	N.D.	N.D.	Kimura et al. (2014)
DS-5	Chugoku, Japan	SW	0.704979	0.512759	N.D.	N.D.	N.D.	N.D.	Kimura et al. (2014)
DS-2	Chugoku, Japan	SW	0.704065	0.512806	N.D.	N.D.	N.D.	N.D.	Kimura et al. (2014)
DS99-1	Chugoku, Japan	SW	0.704089	0.512806	N.D.	N.D.	N.D.	N.D.	Kimura et al. (2014)
K5090802	Chugoku, Japan	SW	0.704130	0.512821	0.283038	N.D.	N.D.	N.D.	Kimura et al. (2014)
K5090804	Chugoku, Japan	SW	0.704196	0.512803	0.283101	N.D.	N.D.	N.D.	Kimura et al. (2014)
DS-6	Chugoku, Japan	SW	0.704765	0.512769	0.282869	N.D.	N.D.	N.D.	Kimura et al. (2014)
DS-7	Chugoku, Japan	SW	0.704909	0.512724	N.D.	N.D.	N.D.	N.D.	Kimura et al. (2014)
DS-8	Chugoku, Japan	SW	0.705016	0.512722	N.D.	N.D.	N.D.	N.D.	Kimura et al. (2014)
DS-9	Chugoku, Japan	SW	0.705101	0.512731	N.D.	N.D.	N.D.	N.D.	Kimura et al. (2014)
DS-10	Chugoku, Japan	SW	0.704964	0.512717	N.D.	N.D.	N.D.	N.D.	Kimura et al. (2014)
DS-11	Chugoku, Japan	SW	0.704791	0.512739	N.D.	N.D.	N.D.	N.D.	Kimura et al. (2014)
DS-12	Chugoku, Japan	SW	0.704952	0.512730	N.D.	N.D.	N.D.	N.D.	Kimura et al. (2014)
DS-13	Chugoku, Japan	SW	0.704595	N.D.	N.D.	N.D.	N.D.	N.D.	Kimura et al. (2014)
DS-14	Chugoku, Japan	SW	0.704802	0.512790	N.D.	N.D.	N.D.	N.D.	Kimura et al. (2014)
DS-15	Chugoku, Japan	SW	0.704776	0.512765	0.282948	18.297	15.574	38.493	Kimura et al. (2014), Kimura et al. (2015)
DS99-2	Chugoku, Japan	SW	0.704799	0.512758	N.D.	18.283	15.570	38.459	Kimura et al. (2014), Kimura et al. (2015)
DS99-3	Chugoku, Japan	SW	0.704932	0.512743	0.282962	18.292	15.573	38.468	Kimura et al. (2014), Kimura et al. (2015)
DS99-4	Chugoku, Japan	SW	0.704506	N.D.	N.D.	N.D.	N.D.	N.D.	Kimura et al. (2014)

DS99-5	Chugoku, Japan	SW	0.704895	0.512750	N.D.	N.D.	N.D.	N.D.	Kimura et al. (2014)
DS99-6	Chugoku, Japan	SW	0.705012	0.000000	N.D.	N.D.	N.D.	N.D.	Kimura et al. (2014)
DS99-7	Chugoku, Japan	SW	0.704868	0.512784	N.D.	N.D.	N.D.	N.D.	Kimura et al. (2014)
HZ-1	Chugoku, Japan	SW	0.704738	0.512765	N.D.	N.D.	N.D.	N.D.	Kimura et al. (2014)
HZ-2	Chugoku, Japan	SW	0.704708	0.512749	N.D.	N.D.	N.D.	N.D.	Kimura et al. (2014)
HZ-3	Chugoku, Japan	SW	0.704995	0.512721	N.D.	N.D.	N.D.	N.D.	Kimura et al. (2014)
HZ99-1	Chugoku, Japan	SW	0.704781	N.D.	N.D.	N.D.	N.D.	N.D.	Kimura et al. (2014)
HZ99-2	Chugoku, Japan	SW	0.704856	0.512761	N.D.	N.D.	N.D.	N.D.	Kimura et al. (2014)
HZ99-3	Chugoku, Japan	SW	0.704795	0.512776	N.D.	N.D.	N.D.	N.D.	Kimura et al. (2014)
HZ00-4	Chugoku, Japan	SW	0.704750	0.512770	N.D.	N.D.	N.D.	N.D.	Kimura et al. (2014)
HZ00-5	Chugoku, Japan	SW	0.704697	0.512755	N.D.	N.D.	N.D.	N.D.	Kimura et al. (2014)
HZ00-9	Chugoku, Japan	SW	0.704694	0.512795	N.D.	N.D.	N.D.	N.D.	Kimura et al. (2014)
HZ00-12	Chugoku, Japan	SW	0.705065	0.512739	N.D.	N.D.	N.D.	N.D.	Kimura et al. (2014)
HZ00-14	Chugoku, Japan	SW	0.704851	0.512747	N.D.	N.D.	N.D.	N.D.	Kimura et al. (2014)
HZ00-19	Chugoku, Japan	SW	0.704860	0.512736	N.D.	N.D.	N.D.	N.D.	Kimura et al. (2014)
HZ00-20	Chugoku, Japan	SW	0.704445	0.512784	0.282969	N.D.	N.D.	N.D.	Kimura et al. (2014)
033002-1	Chugoku, Japan	SW	0.704710	0.512749	N.D.	18.305	15.576	38.498	Kimura et al. (2014), Kimura et al. (2015)
1-2	Chugoku, Japan	SW	0.704753	N.D.	N.D.	N.D.	N.D.	N.D.	Kimura et al. (2014)
2-2	Chugoku, Japan	SW	0.704773	0.512710	N.D.	18.298	15.575	38.495	Kimura et al. (2014), Kimura et al. (2015)
3-1	Chugoku, Japan	SW	0.704746	N.D.	N.D.	N.D.	N.D.	N.D.	Kimura et al. (2014)
5-1'	Chugoku, Japan	SW	0.704762	0.512738	0.283071	N.D.	N.D.	N.D.	Kimura et al. (2014)
5-2	Chugoku, Japan	SW	0.704761	0.512735	N.D.	N.D.	N.D.	N.D.	Kimura et al. (2014)

6-2	Chugoku, Japan	SW	0.704784	0.512733	N.D.	18.297	15.575	38.497	Kimura et al. (2014), Kimura et al. (2015)
7-1	Chugoku, Japan	SW	0.704720	0.512729	N.D.	18.298	15.576	38.500	Kimura et al. (2014), Kimura et al. (2015)
8-1	Chugoku, Japan	SW	0.704769	0.512686	0.282834	18.298	15.574	38.492	Kimura et al. (2014), Kimura et al. (2015)
1-FKNHD	Chugoku, Japan	SW	0.704982	0.512653	0.282999	N.D.	N.D.	N.D.	Kimura et al. (2014)
7-FKNTB2	Chugoku, Japan	SW	0.705249	0.512649	0.282879	N.D.	N.D.	N.D.	Kimura et al. (2014)
19-FMDR	Chugoku, Japan	SW	0.707966	0.512394	0.282753	N.D.	N.D.	N.D.	Kimura et al. (2014)
9-FKNOT	Chugoku, Japan	SW	0.707942	0.512372	0.282860	N.D.	N.D.	N.D.	Kimura et al. (2014)
17-FTKN	Chugoku, Japan	SW	0.706656	0.512495	0.282924	N.D.	N.D.	N.D.	Kimura et al. (2014)
14-FGGB	Chugoku, Japan	SW	0.707576	0.512392	0.282873	N.D.	N.D.	N.D.	Kimura et al. (2014)
2-FKNAK	Chugoku, Japan	SW	0.704924	0.512662	N.D.	N.D.	N.D.	N.D.	Kimura et al. (2014)
5-FKNSF	Chugoku, Japan	SW	0.704959	0.512664	N.D.	N.D.	N.D.	N.D.	Kimura et al. (2014)
4-FKNHT	Chugoku, Japan	SW	0.704978	0.512651	N.D.	N.D.	N.D.	N.D.	Kimura et al. (2014)
3-FKNJG	Chugoku, Japan	SW	0.705048	0.512672	N.D.	N.D.	N.D.	N.D.	Kimura et al. (2014)
6-FKNTC13	Chugoku, Japan	SW	0.705217	0.512674	0.282985	N.D.	N.D.	N.D.	Kimura et al. (2014)
10-FKNKB1	Chugoku, Japan	SW	0.705281	0.512655	0.282913	N.D.	N.D.	N.D.	Kimura et al. (2014)
11-FKNNK	Chugoku, Japan	SW	0.706456	0.512525	N.D.	N.D.	N.D.	N.D.	Kimura et al. (2014)
16-FTTK	Chugoku, Japan	SW	0.706460	0.512578	0.282875	N.D.	N.D.	N.D.	Kimura et al. (2014)
15-FMSK	Chugoku, Japan	SW	0.706657	0.512523	0.282955	N.D.	N.D.	N.D.	Kimura et al. (2014)
13-FKMS	Chugoku, Japan	SW	0.706690	0.512505	N.D.	N.D.	N.D.	N.D.	Kimura et al. (2014)
18-FTOG	Chugoku, Japan	SW	0.706712	0.512507	0.282802	N.D.	N.D.	N.D.	Kimura et al. (2014)
8-FKNBR	Chugoku, Japan	SW	0.706954	0.512476	0.282794	N.D.	N.D.	N.D.	Kimura et al. (2014)
12-FKNMG	Chugoku, Japan	SW	0.707261	0.512460	0.282779	N.D.	N.D.	N.D.	Kimura et al. (2014)

K5090301	Chugoku, Japan	SW	0.706000	0.512585	0.282783	18.326	15.586	38.560	Kimura et al. (2014)
K5091904	Chugoku, Japan	SW	0.706296	0.512554	0.282868	18.364	15.596	38.620	Kimura et al. (2014)
IWT-5	Chugoku, Japan	SW	0.703770	0.512826	0.282960	18.181	15.545	38.335	Kimura et al. (2014)
IWT-6	Chugoku, Japan	SW	0.704074	0.512748	N.D.	N.D.	N.D.	N.D.	Kimura et al. (2014)
TRD-1	Chugoku, Japan	SW	0.703849	0.512784	0.282884	N.D.	N.D.	N.D.	Kimura et al. (2014)
KSB-5	Chugoku, Japan	SW	0.705190	0.512711	N.D.	N.D.	N.D.	N.D.	Kimura et al. (2014)
KSB-7-1	Chugoku, Japan	SW	0.705023	0.512693	0.282918	N.D.	N.D.	N.D.	Kimura et al. (2014)
KSB-8	Chugoku, Japan	SW	0.705084	0.512692	N.D.	N.D.	N.D.	N.D.	Kimura et al. (2014)
KSB-10	Chugoku, Japan	SW	0.704962	0.512698	N.D.	N.D.	N.D.	N.D.	Kimura et al. (2014)
KSB-12	Chugoku, Japan	SW	0.704908	0.512724	0.282916	N.D.	N.D.	N.D.	Kimura et al. (2014)
KSB-15	Chugoku, Japan	SW	0.705153	0.512674	0.282939	N.D.	N.D.	N.D.	Kimura et al. (2014)
KHM-1	Chugoku, Japan	SW	0.705079	0.512698	N.D.	N.D.	N.D.	N.D.	Kimura et al. (2014)
KHM-3	Chugoku, Japan	SW	0.705065	0.512718	N.D.	N.D.	N.D.	N.D.	Kimura et al. (2014)
NEU-1	Chugoku, Japan	SW	0.704352	0.512844	0.283007	18.241	15.563	38.420	Kimura et al. (2014)
NEU-2	Chugoku, Japan	SW	0.704546	0.512803	0.283009	N.D.	N.D.	N.D.	Kimura et al. (2014)
OKD-3	Chugoku, Japan	SW	0.704322	0.512635	0.282976	N.D.	N.D.	N.D.	Kimura et al. (2014)
NTD-2	Chugoku, Japan	SW	0.704264	0.512674	0.282977	18.242	15.562	38.435	Kimura et al. (2014)
NRO-3	Chugoku, Japan	SW	0.704853	0.512744	0.282964	18.278	15.561	38.450	Kimura et al. (2014)
UND-1	Chugoku, Japan	SW	0.704462	0.512665	N.D.	N.D.	N.D.	N.D.	Kimura et al. (2014)
UND-6	Chugoku, Japan	SW	0.703877	0.512715	0.283006	18.298	15.580	38.511	Kimura et al. (2014)
SMN-1	Chugoku, Japan	SW	0.705454	0.512662	N.D.	N.D.	N.D.	N.D.	Kimura et al. (2014)
IID-2	Chugoku, Japan	SW	0.705068	0.512712	N.D.	N.D.	N.D.	N.D.	Kimura et al. (2014)

IID-5	Chugoku, Japan	SW	0.705474	0.512672	N.D.	N.D.	N.D.	N.D.	Kimura et al. (2014)
KND-1	Chugoku, Japan	SW	0.703419	0.512870	0.283002	N.D.	N.D.	N.D.	Kimura et al. (2014)
TDN-4	Chugoku, Japan	SW	0.703333	0.512878	0.282975	18.077	15.519	38.177	Kimura et al. (2014)
KBH-2	Chugoku, Japan	SW	0.704392	0.512669	N.D.	N.D.	N.D.	N.D.	Kimura et al. (2014)
KBH-4	Chugoku, Japan	SW	0.704506	0.512663	N.D.	N.D.	N.D.	N.D.	Kimura et al. (2014)
KRB-1	Chugoku, Japan	SW	0.704124	0.512715	0.282947	18.238	15.559	38.412	Kimura et al. (2014)
KRB-2	Chugoku, Japan	SW	0.704117	0.512693	N.D.	N.D.	N.D.	N.D.	Kimura et al. (2014)
ONG-1	Chugoku, Japan	SW	0.704630	0.512634	0.282903	18.158	15.531	38.280	Kimura et al. (2014)
MSK-2	Chugoku, Japan	SW	0.704877	0.512705	N.D.	N.D.	N.D.	N.D.	Kimura et al. (2014)
MSK-3	Chugoku, Japan	SW	0.704882	0.512737	N.D.	N.D.	N.D.	N.D.	Kimura et al. (2014)
KSG-1	Chugoku, Japan	SW	0.705128	0.512701	N.D.	N.D.	N.D.	N.D.	Kimura et al. (2014)
SMA-2	Chugoku, Japan	SW	0.704510	0.512674	N.D.	N.D.	N.D.	N.D.	Kimura et al. (2014)
SMA-6	Chugoku, Japan	SW	0.704223	0.512671	N.D.	N.D.	N.D.	N.D.	Kimura et al. (2014)
URD-3	Chugoku, Japan	SW	0.704149	0.512686	N.D.	N.D.	N.D.	N.D.	Kimura et al. (2014)
KMA-3	Chugoku, Japan	SW	0.705659	0.512636	0.282915	18.330	15.580	38.525	Kimura et al. (2014)
KMA-4	Chugoku, Japan	SW	0.705303	0.512691	N.D.	N.D.	N.D.	N.D.	Kimura et al. (2014)
BJD-2	Chugoku, Japan	SW	0.704895	0.512723	N.D.	N.D.	N.D.	N.D.	Kimura et al. (2014)
BJD-4	Chugoku, Japan	SW	0.705657	0.512643	N.D.	N.D.	N.D.	N.D.	Kimura et al. (2014)
NMR-2	Chugoku, Japan	SW	0.705011	0.512707	N.D.	N.D.	N.D.	N.D.	Kimura et al. (2014)
NMR-5	Chugoku, Japan	SW	0.705468	0.512691	0.282918	N.D.	N.D.	N.D.	Kimura et al. (2014)
NMR-24	Chugoku, Japan	SW	0.705464	0.512682	N.D.	N.D.	N.D.	N.D.	Kimura et al. (2014)
NMR-27'	Chugoku, Japan	SW	0.705514	0.512665	N.D.	N.D.	N.D.	N.D.	Kimura et al. (2014)

YKT-4	Chugoku, Japan	SW	0.705367	0.512686	0.282899	18.289	15.554	38.434	Kimura et al. (2014)
-------	-------------------	----	----------	----------	----------	--------	--------	--------	----------------------

Note: Isotopic compositions are time corrected if age and parent-daughter element abundance are available (thus these are denoted in parentheses with subscript i). Isotopic compositions are renormalized relative to the reference standard materials with the following values: $^{87}\text{Sr}/^{86}\text{Sr} = 0.710240$ for NIST SRM 987 ($^{87}\text{Sr}/^{86}\text{Sr} = 0.707990$ for Eimer & Amend SrCO₃), $^{143}\text{Nd}/^{144}\text{Nd} = 0.511860$ for La Jolla ($^{143}\text{Nd}/^{144}\text{Nd} = 0.511973$ for Renne Nd, 0.512648 for BCR-1, 0.512117 for JNdi-1), $^{176}\text{Hf}/^{177}\text{Hf} = 0.282160$ for JMC 475 ($^{176}\text{Hf}/^{177}\text{Hf} = 0.282192$ for JMC 14745), $^{206}\text{Pb}/^{204}\text{Pb} = 16.943$, $^{207}\text{Pb}/^{204}\text{Pb} = 15.500$, and $^{208}\text{Pb}/^{204}\text{Pb} = 36.729$ for NIST SRM 981 ($^{206}\text{Pb}/^{204}\text{Pb} = 18.299$, $^{207}\text{Pb}/^{204}\text{Pb} = 15.541$, and $^{208}\text{Pb}/^{204}\text{Pb} = 38.258$ for GSJ JB-3); N.D. = data not available or data not included as erroneous analysis

Table 2-3. Parameters used for the two-component mixing model

Input elemental concentrations ¹				
	Sr	Nd	Hf	Pb
AOC	203	12	2.79	1.18
SED	165	31	4.29	33.4
Input isotopic ratios ²				
	$(^{87}\text{Sr}/^{86}\text{Sr})_t$	$(^{143}\text{Nd}/^{144}\text{Nd})_t$	$(^{176}\text{Hf}/^{177}\text{Hf})_t$	$(^{206}\text{Pb}/^{204}\text{Pb})_t$
AOC	0.70330	0.51310	0.28325	17.78
SED	0.71300	0.51238	0.28265	18.45
Input partition coefficients between solid and fluid during melting ³				
D	Sr	Nd	Hf	Pb
AOC	0.05	0.66	1.93	0.03
SED	0.51	1.53	1.60	1.29
Input mobilities of fluids during dehydration ⁴				
M	Sr	Nd	Hf	Pb
AOC	30	3.20	1.42	81

¹Data are from Ishizuka et al. (2009) and Plank and Langmuir (1998) for AOC and SED, respectively

²Data are from Pineda-Velasco et al. (2018) and Plank and Langmuir (1998) for AOC and SED, respectively

³Data are from Kessel et al. (2005) and Johnson and Plank (1999) for AOC and SED, respectively

⁴Data are from Kessel et al. (2005)

Table 2-4: Hf, Sr, Nd and Pb isotopic composition of OIB lavas from eastern China, the Korean Peninsula. (Reference therein)

Region	⁸⁷ Sr/ ⁸⁶ Sr	¹⁴³ Nd/ ¹⁴⁴ Nd	¹⁷⁶ Hf/ ¹⁷⁷ Hf	²⁰⁶ Pb/ ²⁰⁴ Pb	²⁰⁷ Pb/ ²⁰⁴ Pb	²⁰⁸ Pb/ ²⁰⁴ Pb	Division	Reference
Wudalianchi	0.705640	0.512360	0.282615	16.47	15.43	36.44	NE China	Sun et al. (2014)
Wudalianchi	0.705540	0.512378	0.282615	16.47	15.40	36.38	NE China	Sun et al. (2014)
Wudalianchi	0.705713	0.512315	0.282609	16.50	15.40	36.41	NE China	Sun et al. (2014)
Wudalianchi	0.705418	0.512376	0.282633	16.51	15.40	36.41	NE China	Sun et al. (2014)
Wudalianchi	0.705458	0.512355	0.282625	16.52	15.42	36.49	NE China	Sun et al. (2014)
Wudalianchi	0.705516	0.512386	0.282621	16.47	15.41	36.40	NE China	Sun et al. (2014)
Wudalianchi	0.705436	0.512388	0.282633	16.54	15.47	36.60	NE China	Sun et al. (2014)
Wudalianchi	0.705459	0.512402	0.282634	16.55	15.45	36.58	NE China	Sun et al. (2014)
Wudalianchi	0.705503	0.512383	0.282628	16.48	15.42	36.45	NE China	Sun et al. (2014)
Wudalianchi	0.705465	0.512409	0.282633	16.50	15.41	36.44	NE China	Sun et al. (2014)
Wudalianchi	0.705532	0.512396	0.282629	16.50	15.42	36.46	NE China	Sun et al. (2014)
Wudalianchi	0.705520	0.512372	0.282629	16.49	15.44	36.50	NE China	Sun et al. (2014)
Wudalianchi	0.705330	0.512423	0.282638	16.50	15.44	36.49	NE China	Sun et al. (2014)
Wudalianchi	0.705625	0.512371	0.282610	16.49	15.46	36.55	NE China	Sun et al. (2014)
Jining	0.704999	0.512581	0.282860	17.40	15.48	37.75	CE China	Zhang et al. (2012)
Jining	0.705144	0.512583	0.282861				CE China	Zhang et al. (2012)
Jining	0.705036	0.512575	0.282854	17.37	15.46	37.69	CE China	Zhang et al. (2012)
Jining	0.705039	0.512630	0.282857	17.42	15.50	37.93	CE China	Zhang et al. (2012)
Jining	0.705028	0.512560	0.282856	17.40	15.50	37.82	CE China	Zhang et al. (2012)
Jining	0.704932	0.512646	0.282859				CE China	Zhang et al. (2012)
Jining	0.704933	0.512656	0.282862	17.43	15.50	37.93	CE China	Zhang et al. (2012)
Jining	0.704811	0.512723	0.282948	17.16	15.44	37.51	CE China	Zhang et al. (2012)

Jining	0.703993	0.512843	0.282987	17.66	15.48	37.86	CE China	Zhang et al. (2012)
Jining	0.705206	0.512688	0.282897	17.08	15.45	37.31	CE China	Zhang et al. (2012)
Jining	0.705152	0.512673	0.282907	17.06	15.45	37.31	CE China	Zhang et al. (2012)
Jining	0.704680	0.512728	0.282939	17.27	15.47	37.51	CE China	Zhang et al. (2012)
Jining	0.705285	0.512690	0.282938	17.46	15.48	38.03	CE China	Zhang et al. (2012)
Jining	0.705187	0.512700	0.282938	17.50	15.49	38.04	CE China	Zhang et al. (2012)
Jining	0.705176	0.512642	0.282887	17.43	15.48	37.81	CE China	Zhang et al. (2012)
Jining	0.704768	0.512681	0.282921	17.53	15.54	38.26	CE China	Zhang et al. (2012)
Jining	0.704803	0.512562	0.282909	17.41	15.42	37.77	CE China	Zhang et al. (2012)
Jining	0.705084	0.512549	0.282872	17.20	15.42	37.52	CE China	Zhang et al. (2012)
Jining	0.705146	0.512646	0.282884	17.10	15.42	37.33	CE China	Zhang et al. (2012)
Jining	0.705347	0.512578	0.282864	17.05	15.42	37.27	CE China	Zhang et al. (2012)
Jining	0.705233	0.512450	0.282851	16.95	15.41	37.82	CE China	Zhang et al. (2012)
Jining	0.705159	0.512578	0.282847	16.94	15.40	37.20	CE China	Zhang et al. (2012)
Jining	0.704205	0.512729	0.282935				CE China	Guo et al. (2014)
Jining	0.704406	0.512796	0.282881				CE China	Guo et al. (2014)
Jining	0.704064	0.512862	0.282942				CE China	Guo et al. (2014)
Jining	0.704104	0.512843	0.282932				CE China	Guo et al. (2014)
Jining	0.704119	0.513008	0.282970				CE China	Guo et al. (2016)
Jining	0.704644	0.512775	0.282935				CE China	Guo et al. (2016)
Jining	0.704071	0.512913	0.282972				CE China	Guo et al. (2016)
Jining	0.705357	0.512475	0.282767				CE China	Guo et al. (2016)
Jining	0.704981	0.512727	0.282866				CE China	Guo et al. (2016)
Jining	0.705107	0.512806	0.282949				CE China	Guo et al. (2016)
Jining	0.704222	0.512799	0.282978				CE China	Guo et al. (2016)
Jining	0.705358	0.512501	0.282795				CE China	Guo et al. (2016)
Jining	0.704706	0.512699	0.282886				CE China	Guo et al. (2016)
Abaga	0.703804	0.512967	0.283079				NE China	Guo et al. (2016)
Abaga	0.704041	0.512933	0.283037				NE China	Guo et al. (2016)
Abaga	0.704062	0.512932	0.283026				NE China	Guo et al. (2016)

Abaga	0.705284	0.512980	0.283030				NE China	Guo et al. (2016)
Abaga	0.705136	0.512912	0.283045				NE China	Guo et al. (2016)
Abaga	0.705265	0.512901	0.283042				NE China	Guo et al. (2016)
Abaga	0.704105	0.512941	0.283064				NE China	Guo et al. (2016)
Abaga	0.704313	0.512896	0.283017				NE China	Guo et al. (2016)
Abaga	0.704329	0.512943	0.283040				NE China	Guo et al. (2016)
Weichang	0.704343	0.512772	0.282924				CE China	Guo et al. (2016)
Weichang	0.704331	0.512762	0.282922				CE China	Guo et al. (2016)
Weichang	0.704805	0.512821	0.282951				CE China	Guo et al. (2016)
Weichang	0.704386	0.512830	0.282974				CE China	Guo et al. (2016)
Weichang	0.704447	0.512769	0.282934				CE China	Guo et al. (2016)
Weichang	0.704379	0.512894	0.283011				CE China	Guo et al. (2016)
Weichang	0.703956	0.512815	0.282948				CE China	Guo et al. (2016)
Weichang	0.703864	0.512865	0.283006				CE China	Guo et al. (2016)
Weichang	0.703829	0.512875	0.282998				CE China	Guo et al. (2016)
Weichang	0.703988	0.512821	0.282940				CE China	Guo et al. (2016)
Weichang	0.703905	0.512863	0.282996				CE China	Guo et al. (2016)
Weichang	0.703859	0.512859	0.282976				CE China	Guo et al. (2016)
Weichang	0.703905	0.512762	0.282926				CE China	Guo et al. (2016)
Weichang	0.704540	0.512721	0.282903				CE China	Guo et al. (2016)
Weichang	0.704211	0.512893	0.282979				CE China	Guo et al. (2016)
Weichang	0.704338	0.512834	0.282948				CE China	Guo et al. (2016)
Shandong	0.703296	0.512931	0.283040	18.10	15.51	38.22	CE China	Sakuyama et al. (2013)
Shandong	0.703277	0.512928	0.283066	18.13	15.51	38.24	CE China	Sakuyama et al. (2013)
Shandong	0.703300	0.512917	0.283027	18.09	15.51	38.22	CE China	Sakuyama et al. (2013)
Shandong	0.703281	0.512947	0.283054	18.15	15.51	38.26	CE China	Sakuyama et al. (2013)
Shandong	0.703152	0.512903	0.283052	18.14	15.49	38.13	CE China	Sakuyama et al. (2013)
Ulleung-Liancourt	0.704867	0.512541	0.282711	17.98	15.47	38.68	Japan Sea	Choi et al. (2006)
Ulleung-Liancourt	0.704724	0.512536	0.282735	17.97	15.46	38.58	Japan Sea	Choi et al. (2006)
Ulleung-Liancourt	0.704976	0.512530	0.282724	18.09	15.50	38.67	Japan Sea	Choi et al. (2006)

Ulleung-Liancourt	0.704474	0.512608	0.282773	17.88	15.40	38.30	Japan Sea	Choi et al. (2006)
Wan-Su	0.704070	0.512651	0.282863				CE China	Zhang et al. (2009)
Wan-Su	0.704063	0.512663	0.282886				CE China	Zhang et al. (2009)
Wan-Su	0.704235	0.512538	0.282802				CE China	Zhang et al. (2009)
Wan-Su	0.703975	0.512655	0.282853				CE China	Zhang et al. (2009)
Wan-Su	0.703892	0.512706	0.282868				CE China	Zhang et al. (2009)
Wan-Su	0.703545	0.512871	0.282929				CE China	Zhang et al. (2009)
Wan-Su	0.703632	0.512885	0.282850				CE China	Zhang et al. (2009)
Wan-Su	0.704093	0.512826	0.282941				CE China	Zhang et al. (2009)
Wan-Su	0.704445	0.512515	0.282689				CE China	Zhang et al. (2009)
Wan-Su	0.703465	0.512925	0.283015				CE China	Zhang et al. (2009)
Wan-Su	0.703258	0.512968	0.283078				CE China	Zhang et al. (2009)
Wan-Su	0.703427	0.512950	0.283060				CE China	Zhang et al. (2009)
Wan-Su	0.704053	0.512735	0.282861				CE China	Zhang et al. (2009)
Wan-Su	0.704035	0.512732	0.282866				CE China	Zhang et al. (2009)
Wan-Su	0.703609	0.512882	0.282968				CE China	Zhang et al. (2009)
Wan-Su	0.703567	0.512881	0.282975				CE China	Zhang et al. (2009)
Wan-Su	0.704105	0.512641	0.282862				CE China	Zhang et al. (2009)
Wan-Su	0.703906	0.512806	0.282927				CE China	Zhang et al. (2009)
Wan-Su	0.704285	0.512631	0.282782				CE China	Zhang et al. (2009)
Wan-Su	0.703742	0.512899	0.282964				CE China	Zhang et al. (2009)
Wan-Su	0.704982	0.512222	0.282732				CE China	Zhang et al. (2009)
Wan-Su	0.704956	0.512458	0.282595				CE China	Zhang et al. (2009)
Wan-Su	0.704866	0.512403	0.282611				CE China	Zhang et al. (2009)
Wan-Su	0.704465	0.512508	0.282614				CE China	Zhang et al. (2009)
Wan-Su	0.704218	0.512727	0.282823				CE China	Zhang et al. (2009)
Wan-Su	0.704689	0.512540	0.282791				CE China	Zhang et al. (2009)
Wan-Su	0.704365	0.512597	0.282815				CE China	Zhang et al. (2009)
Baengnyeong	0.703406	0.512978	0.283060	17.84	15.42	37.76	Japan Sea	Choi et al. (2006)
Baengnyeong	0.704385	0.512769	0.282971	17.74	15.48	38.18	Japan Sea	Choi et al. (2006)

Ganseong	0.705265	0.512687	0.282921	17.83	15.50	38.16	Japan Sea	Choi et al. (2006)
Ganseong	0.705053	0.512695	0.282873	17.84	15.51	38.19	Japan Sea	Choi et al. (2006)
Ganseong	0.705109	0.512789	0.282911	17.85	15.49	38.16	Japan Sea	Choi et al. (2006)
Ganseong	0.704559	0.512766	0.282981	17.91	15.50	38.17	Japan Sea	Choi et al. (2006)
Jeju	0.705014	0.512847	0.282938	18.89	15.65	39.49	Japan Sea	Choi et al. (2006)
Jeju	0.704141	0.512859	0.282935	19.11	15.65	39.70	Japan Sea	Choi et al. (2006)
Jogokri	0.704541	0.512893	0.283010				Japan Sea	Choi et al. (2006)
Jeongok	0.704505	0.512752	0.282947	17.82	15.55	38.42	Japan Sea	Choi et al. (2014)
Jeongok	0.704810	0.512662	0.282954	17.77	15.55	38.39	Japan Sea	Choi et al. (2014)
Jeongok	0.704574	0.512727	0.282949	17.81	15.53	38.34	Japan Sea	Choi et al. (2014)
Jeongok	0.704523	0.512718	0.282944	17.81	15.54	38.41	Japan Sea	Choi et al. (2014)
Hannuoba	0.703939	0.512902	0.283041				CE China	Choi et al. (2008)
Hannuoba	0.704743	0.512919	0.283035				CE China	Choi et al. (2008)
Hannuoba	0.704186	0.512906	0.282984				CE China	Choi et al. (2008)
Nushan-Tashan	0.703262	0.513016	0.283133				SE China	Zeng et al. (2013)
Nushan-Tashan	0.703186	0.513000	0.283125				SE China	Zeng et al. (2013)
Nushan-Tashan	0.703207	0.513016	0.283112				SE China	Zeng et al. (2013)
Nushan-Tashan	0.703173	0.513004	0.283131				SE China	Zeng et al. (2013)
Nushan-Tashan	0.703194	0.513005	0.283117				SE China	Zeng et al. (2013)
Nushan-Tashan	0.703203	0.513002	0.283126				SE China	Zeng et al. (2013)
Nushan-Tashan	0.703234	0.513003	0.283122				SE China	Zeng et al. (2013)
Nushan-Tashan	0.703186	0.513013	0.283123				SE China	Zeng et al. (2013)
Nushan-Tashan	0.703268	0.512992	0.283034				SE China	Zeng et al. (2013)
Nushan-Tashan	0.703236	0.512981	0.283063				SE China	Zeng et al. (2013)
Nuominhe	0.704789	0.512497	0.282803	17.36	15.46	37.48	NE China	Wang et al. (2017)
Nuominhe	0.704833	0.512475	0.282777	17.07	15.42	37.12	NE China	Wang et al. (2017)
Nuominhe	0.704733	0.512497	0.282774	17.14	15.43	37.26	NE China	Wang et al. (2017)
Nuominhe	0.704742	0.512461	0.282785	17.12	15.43	37.18	NE China	Wang et al. (2017)
Nuominhe	0.704768	0.512526	0.282810	17.17	15.43	37.29	NE China	Wang et al. (2017)
Nuominhe	0.704671	0.512534	0.282830	17.10	15.43	37.13	NE China	Wang et al. (2017)

Erkeshan	0.705589	0.512362	0.282522				NE China	Wang et al. (2017)
Erkeshan	0.705637	0.512344	0.282524				NE China	Wang et al. (2017)
Erkeshan	0.705626	0.512347	0.282521				NE China	Wang et al. (2017)
Wudalianchi	0.705371	0.512408	0.282564				NE China	Wang et al. (2017)
Wudalianchi	0.705412	0.512414	0.282549				NE China	Wang et al. (2017)
Wudalianchi	0.705370	0.512429	0.282574				NE China	Wang et al. (2017)
Wudalianchi	0.705383	0.512428	0.282572				NE China	Wang et al. (2017)
Wudalianchi	0.705439	0.512423	0.282570				NE China	Wang et al. (2017)
Wudalianchi	0.705420	0.512439	0.282569				NE China	Wang et al. (2017)
Wudalianchi	0.705410	0.512407	0.282563				NE China	Wang et al. (2017)
Wudalianchi	0.705414	0.512399	0.282553				NE China	Wang et al. (2017)
Wudalianchi	0.705579	0.512400	0.282512				NE China	Wang et al. (2017)
Wudalianchi	0.705133	0.512464	0.282661				NE China	Wang et al. (2017)
Wudalianchi	0.705184	0.512474	0.282659				NE China	Wang et al. (2017)
Wudalianchi	0.705130	0.512453	0.282657				NE China	Wang et al. (2017)
Wudalianchi	0.705273	0.512432	0.282616				NE China	Wang et al. (2017)
Wudalianchi	0.705241	0.512418	0.282617				NE China	Wang et al. (2017)
Xiaogulihe	0.705646	0.512360	0.282608	16.47	15.42	36.45	NE China	Wang et al. (2017)
Xiaogulihe	0.705546	0.512378	0.282608	16.47	15.39	36.38	NE China	Wang et al. (2017)
Xiaogulihe	0.705719	0.512315	0.282602	16.50	15.40	36.41	NE China	Wang et al. (2017)
Xiaogulihe	0.705424	0.512376	0.282626	16.51	15.40	36.41	NE China	Wang et al. (2017)
Xiaogulihe	0.705464	0.512355	0.282618	16.52	15.42	36.49	NE China	Wang et al. (2017)
Xiaogulihe	0.705522	0.512386	0.282614	16.47	15.40	36.40	NE China	Wang et al. (2017)
Xiaogulihe	0.705442	0.512388	0.282626	16.54	15.46	36.61	NE China	Wang et al. (2017)
Xiaogulihe	0.705465	0.512402	0.282627	16.55	15.45	36.58	NE China	Wang et al. (2017)
Xiaogulihe	0.705509	0.512383	0.282621	16.48	15.42	36.46	NE China	Wang et al. (2017)
Xiaogulihe	0.705471	0.512409	0.282626	16.50	15.41	36.45	NE China	Wang et al. (2017)
Xiaogulihe	0.705538	0.512396	0.282622	16.50	15.42	36.47	NE China	Wang et al. (2017)
Xiaogulihe	0.705526	0.512372	0.282622	16.49	15.44	36.51	NE China	Wang et al. (2017)
Xiaogulihe	0.705336	0.512423	0.282631	16.50	15.44	36.50	NE China	Wang et al. (2017)

Xiaogulihe	0.705631	0.512371	0.282603	16.49	15.46	36.56	NE China	Wang et al. (2017)
Wudalianchi	0.705147	0.512439	0.282642	17.05	15.43	37.14	NE China	Wang et al. (2017)
Wudalianchi	0.705277	0.512408	0.282597	16.94	15.45	36.97	NE China	Wang et al. (2017)
Wudalianchi	0.705171	0.512418	0.282640	17.04	15.44	37.11	NE China	Wang et al. (2017)
Wudalianchi	0.705181	0.512337	0.282611	16.93	15.44	36.96	NE China	Wang et al. (2017)
Wudalianchi	0.705176	0.512412	0.282642	17.01	15.44	37.09	NE China	Wang et al. (2017)
Wudalianchi	0.705299	0.512418	0.282594	17.10	15.44	37.10	NE China	Wang et al. (2017)
Wudalianchi	0.705393	0.512360	0.282555	16.83	15.43	36.79	NE China	Wang et al. (2017)
Wudalianchi	0.705413	0.512349	0.282548	16.85	15.44	36.80	NE China	Wang et al. (2017)

Chapter 3. Slab melting beneath the Southwest Japan Arc driven by dehydration of altered oceanic serpentinite: Evidence from Boron isotopes

Abstract

The mechanism that drives slab melting beneath the Southwest Japan arc and other warm-slab subduction zones have been debated because oceanic crust beneath the volcanic front is predicted to be largely dehydrated so that hardly initiates its melting. Andesitic and dacitic lavas with high Sr/Y and La/Yb ratios (i.e., adakites) from subduction zones are interpreted to be the products of slab melting under hydrous conditions, and hence may shed insight into the source of fluids to facilitate slab melting. In this study, we first report the B isotope data of high-Sr andesites and dacites (adakites) from a modern subduction zone, the Chugoku district in the Southwest Japan Arc. The adakitic lavas have $\delta^{11}\text{B}$ values of -7.2‰ to $+0.3\text{‰}$, which are higher than unaltered MORB range ($-7.1 \pm 0.9\text{‰}$), and show a clear along-arc variation; the highest $\delta^{11}\text{B}$ values are found in the western part of the arc (-2.2 to $+0.3\text{‰}$) and decrease toward the eastern ends (-7.2 to -3.3‰). Such a change in B isotope composition is similar to the along-arc variations in Sr, Nd and Pb isotope compositions found in these lavas. Accordingly, the $\delta^{11}\text{B}$ values are correlated with $^{143}\text{Nd}/^{144}\text{Nd}$ ratios, $^{87}\text{Sr}/^{86}\text{Sr}$ ratios, $^{206}\text{Pb}/^{204}\text{Pb}$, and $^{207}\text{Pb}/^{204}\text{Pb}$ ratios (correlation factor $r = 0.71\sim 0.77$). Results from slab dehydration modeling and mixing calculations suggest that the B isotopic compositions of the SW Japan adakites are not consistent with melts derived from altered oceanic crust (AOC) and sediments, or fluids from wedge serpentinites (formed in the mantle wedge). Instead, the heavy B-isotope signature in these adakites can be best explained by melting of AOC and sediments

with fluids from a slab mantle serpentinite. These correlations between $\delta^{11}\text{B}$ values and radiogenic isotopes point toward the mixing of two compositions: (1) a high- $\delta^{11}\text{B}$ hybrid component (60–80%), which is composed of a serpentinite fluid from slab mantle serpentinite (20%–40%) and a melt from dehydrated oceanic crust (60%–80%); (2) a low- $\delta^{11}\text{B}$ melt from the progressive dehydration of subducted sediments (20–40%). Our modelling shows that, in the hotter subduction zone, fluids were released from the deeper plate interior and migrate into the upper crust of the subducting slab, which was dehydrated at shallower depths, causing those to melt.

1. Introduction

In subduction zone, oceanic lithosphere sinks into the mantle and the crustal layer of subducting oceanic lithosphere (slab) progressively metamorphoses with increasing depth. Fluids released from the slab lead to hydration and melting of the overlying mantle and formation of volcanic arcs (Ishikawa and Nakamura, 1994; Nakamura et al., 1985; Sakuyama and Nesbitt, 1986).

When a young (<25 Myr) and hot slab subducts, the oceanic crust can partially melt and produce magmas of intermediate to felsic compositions. Defant and Drummond (1990) noted peculiar geochemical characteristics of these magmas such as high-Sr abundance and referred to such magma as adakite, in reference to its first documented occurrence on the island of Adak in the Aleutians (Kay, 1978). There is geochemical evidence for melting of the oceanic crust beneath some warm-slab endmembers such Mexico (Cai et al., 2014), the Cascades (Walowski et al., 2016), and SW Japan (Kimura et al., 2014; Pineda-Velasco et al., 2018; Nguyen et al., 2020). However, slab melting has proved to be a challenge to our current understanding of arc magmatism. Because the hotter nature of the young, subducted plate causes most dehydration of the oceanic crust to occur beneath the forearc rather than the arc (Rondenay et al., 2008;

Aber et al., 2009; Walowski et al., 2015), little H₂O may reach sub-arc depths to initiate the melting of anhydrous MORB-like basalts (> 1100 °C under 1-3 GPa; Bouilhol et al., 2015), unless there is an extra water supplier.

The hydrated upper mantle portion of the subducted plate is able to carry H₂O to greater depths in the form of antigorite and chlorite until the slab top reaches ~80–100 km depth, which corresponds to volcanic fronts in the subduction zones (Spandler et al., 2008; van Keken et al. 2011; Walowski et al., 2015). As a result, dehydration of the serpentinized peridotite in the slab mantle portion have great potential to provide H₂O for the partial melting of the oceanic crust (Freymuth et al., 2016; Spandler and Pirard, 2013).

Boron (B) isotopes ($\delta^{11}\text{B} = [({}^{11}\text{B}/{}^{10}\text{B})_{\text{Sample}}/({}^{11}\text{B}/{}^{10}\text{B})_{\text{SRM951}} - 1] \times 1,000$) are a powerful tool for tracing subducted serpentinites (e.g., Cannaò et al., 2016; De Hoog and Savov, 2018; Harvey, Garrido, et al., 2014; Martin et al., 2016, 2020; Yamada et al., 2019). First, B is enriched in serpentinites ([B] up to 100 ppm, where brackets indicate concentration) but is extremely depleted in the pristine mantle ([B] < 0.1 ppm) (Figure 3-1; Leeman, 1996; Marschall, 2018). Second, large differences in $\delta^{11}\text{B}$ exist among the slab serpentinites (+5.5‰ to +40.5‰; Martin et al., 2020), mantle wedge serpentinites (−14‰ to +10‰; Martin et al., 2020), sediments (mostly negative; Ishikawa and Nakamura, 1993), AOC (mostly 0 to +5‰; Marschall, 2018), and mantle ($-7.1 \pm 0.9\text{‰}$; Marschall et al., 2017) (Figure 3-1). Thus, B isotopes have been employed to identify the presence of recycled serpentinites in arc magmas (e.g., Bouvier et al., 2019; Cooper et al., 2020; Jones et al., 2014; Leeman et al., 2017; Tonarini et al., 2007, 2011; Zhang et al., 2021).

Although serpentinites and the fluids released from their dehydration are implicated in slab melting, little B isotope studies exist to explore that link due to the lack of B isotope data for slab melts ('true' adakites; De Hoog and Savov, 2017). The southwest (SW) Japan arc is an

example of a volcanic field in which high-Sr andesites and dacites (“adakites” and ADK) occur (Feineman et al., 2013; Kimura et al., 2014; Morris, 1995). It is generally accepted that these andesites and dacites in SW Japan are attributed to melting of the young, subducted plate (Shikoku Basin Plate) in late Cenozoic time (Feineman et al., 2013; Kimura et al., 2014; Morris, 1995; Shibata et al., 2014). In this study, we analyzed the B isotopes and B concentrations of the andesites and dacites from the Chugoku district of SW Japan to explore that link between fluids released from serpentinites and slab melting.

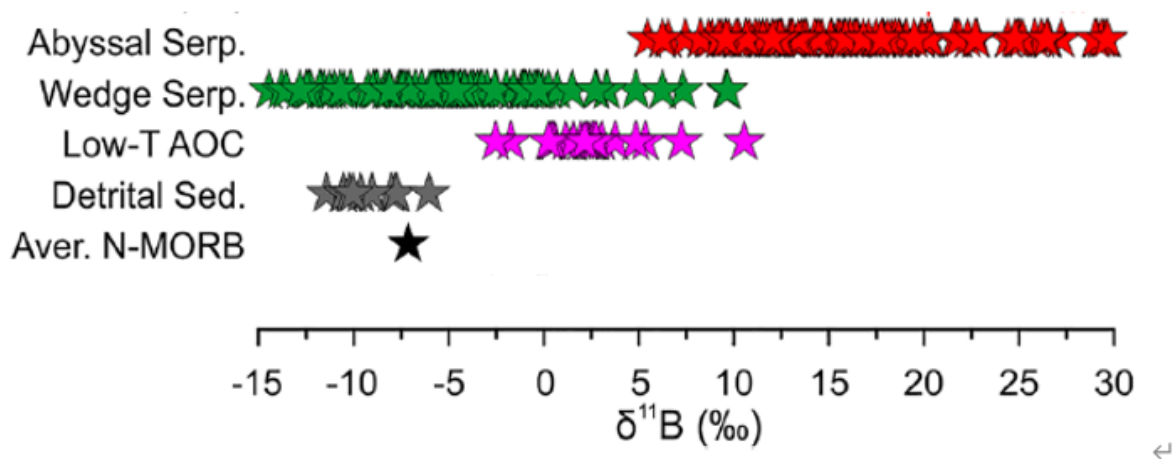


Figure 3-1. Boron isotope ($\delta^{11}\text{B}$) compositions of some arc volcanic rocks, back-arc volcanic rocks, serpentinite (Serp.), altered oceanic crust (AOC), mid-ocean ridge basalts (MORB), and sediment. The figure is cited from (Zhang et al., 2019). Data sources: Abyssal serpentinite (Boschi et al., 2008, 2013; Harvey et al., 2014; Martin et al., 2016, 2020; Vils et al., 2009), Mantle wedge serpentinite (Martin et al., 2016, 2020), Low-temperature AOC (Ishikawa & Nakamura, 1992; Smith et al., 1995), Detrital sediment (Chetelat et al., 2009), and Average (Aver.) N-MORB (Marschall, 2018).

2. Analytical methods

Boron isotopic compositions ($^{11}\text{B}/^{10}\text{B}$) were analyzed for 19 ADK samples at the Pheasant Laboratory for Geochemistry and Cosmochemistry, Institute for Planetary Materials, Okayama University at Misasa (Nakamura et al., 2003). Isotopic measurements were performed by a thermal ionization mass spectrometry using a Thermo Fisher Scientific TRITON Plus following the procedure described in Nakamura et al. (1992). The B-isotopic compositions

of samples are presented as deviation in parts per thousand (‰) from the standard (NIST NBS951); $\delta^{11}\text{B} = ([^{11}\text{B}/^{10}\text{B}]_{\text{sample}}/[^{11}\text{B}/^{10}\text{B}]_{\text{standard}} - 1) \times 1000$ where $[^{11}\text{B}/^{10}\text{B}]_{\text{standard}} = 4.0545 \pm 0.0007$, 2σ , $n=8$). The analytical reproducibility for natural samples in B isotopic analyses are better than 0.2‰ (2σ), respectively.

3. Results

New $\delta^{11}\text{B}$ data for the selected ADK samples from the Chugoku district are reported in **Table 3-1**. The $\delta^{11}\text{B}$ values of high-Mg andesites (HMA) from Setouchi reported in [Ishikawa and Nakamura \(1994\)](#) are also present. Major and trace element compositions, and Sr-Nd-Hf-Pb isotopes data of the studied samples are reported in the literature ([Ishizaka and Carlson, 1983](#); [Ishikawa and Nakamura, 1994](#); [Moriguti and Nakamura, 1998](#); [Feineman et al., 2013](#); [Pineda-Velasco et al., 2018](#); [Nguyen et al., 2020](#)). Boron concentrations of ADK range from 3.5 to 9.6 ppm and the $\delta^{11}\text{B}$ values range from -7.2 ‰ to $+0.3$ ‰ (**Figure 3-2A**). The observed $\delta^{11}\text{B}$ are larger than that in unaltered MORB ($-7.1\text{‰} \pm 0.9\text{‰}$; [Marschall et al., 2017](#)). The $\delta^{11}\text{B}$ values of HMA show a smaller variation (-6.3 to -6.8‰ , [Ishikawa and Nakamura, 1994](#)) and overlap with those of unaltered MORB (**Figure 3-2**). It should also be noted that the $\delta^{11}\text{B}$ values of HMA are also close to those of subducted sediments (-6 to -8‰ ; [Ishikawa and Nakamura, 1994](#)).

Among ADK samples, those from Aonoyama volcanic field, located in the western section of Chugoku district, have higher $\delta^{11}\text{B}$ values (-2.2 to $+0.3\text{‰}$) than other regions (-7.2 to -3.3‰) (**Figure 3-3**). The lowest values among ADK (-7.2‰) occur in Daisen ADK (KARA1) from central region.

Overall, $\delta^{11}\text{B}$ values of AKD and HMA are not correlated with mobile/immobile incompatible element ratios, such as B/Nb (**Figure 3-2B**). However, broad positive correlations are found between $\delta^{11}\text{B}$ values and $^{143}\text{Nd}/^{144}\text{Nd}$ ratios, while roughly negative correlations are

found between $\delta^{11}\text{B}$ values and $^{87}\text{Sr}/^{86}\text{Sr}$ ratios, $^{206}\text{Pb}/^{204}\text{Pb}$, and $^{207}\text{Pb}/^{204}\text{Pb}$ ratios (**Figure 3-4**).

To evaluate the possibility of magma differentiation affecting B-isotope signatures, $\delta^{11}\text{B}$ values of the Chugoku ADK are plotted against SiO_2 and MgO contents (**Figure 3-5**). There is no observable correlation between $\delta^{11}\text{B}$ values and SiO_2 or MgO , suggesting that magma differentiation has a negligible effect on the $^{11}\text{B}/^{10}\text{B}$ ratios. This inference is supported by the variations in Sr, Nd, Hf and Pb isotopic compositions ([Pineda-Velasco et al., 2018](#); [Nguyen et al., 2020](#)). Post-emplacement weathering is also considered to alter $^{11}\text{B}/^{10}\text{B}$ ratio in volcanic rocks, mainly due to uptake of B into clay minerals formed by alteration of primary silicates ([Tanaka and Nakamura, 2005](#)). The loss on ignition (LOI) is considered to represent the extents of H_2O addition during weathering. Most samples have LOI lower than 1.5 wt. % and the $\delta^{11}\text{B}$ and LOI of our samples does not show a clear correlation (**Figure 3-6**), supporting that $\delta^{11}\text{B}$ of our samples have not been largely modified by secondary alteration.

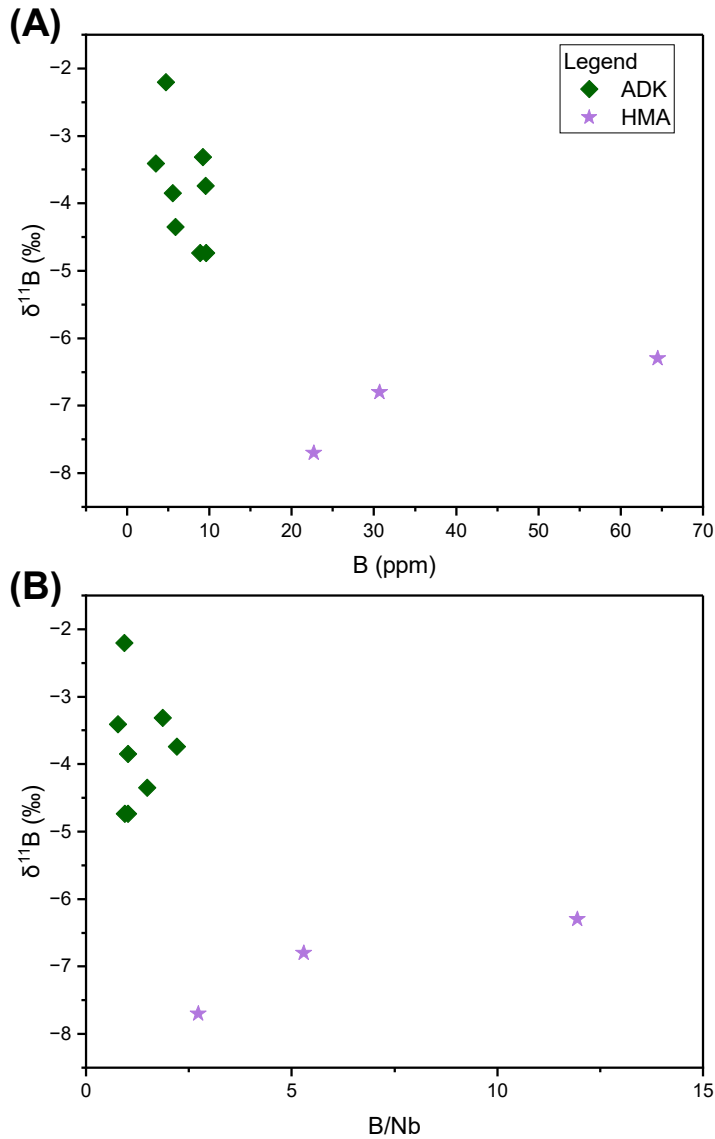


Figure 3-2. $\delta^{11}\text{B}$ (‰) versus boron concentrations and B/Nb ratios obtained for ADK from the Chugoku district and HMA from the Setouchi district in SW Japan

$\delta^{11}\text{B}$ (‰) plotted against (A) boron concentrations (ppm) and (B) B/Nb ratios obtained for ADK from the Chugoku district and HMA from the Setouchi district in SW Japan. Error bars on the values represent propagated analytical uncertainties at the 2σ level.

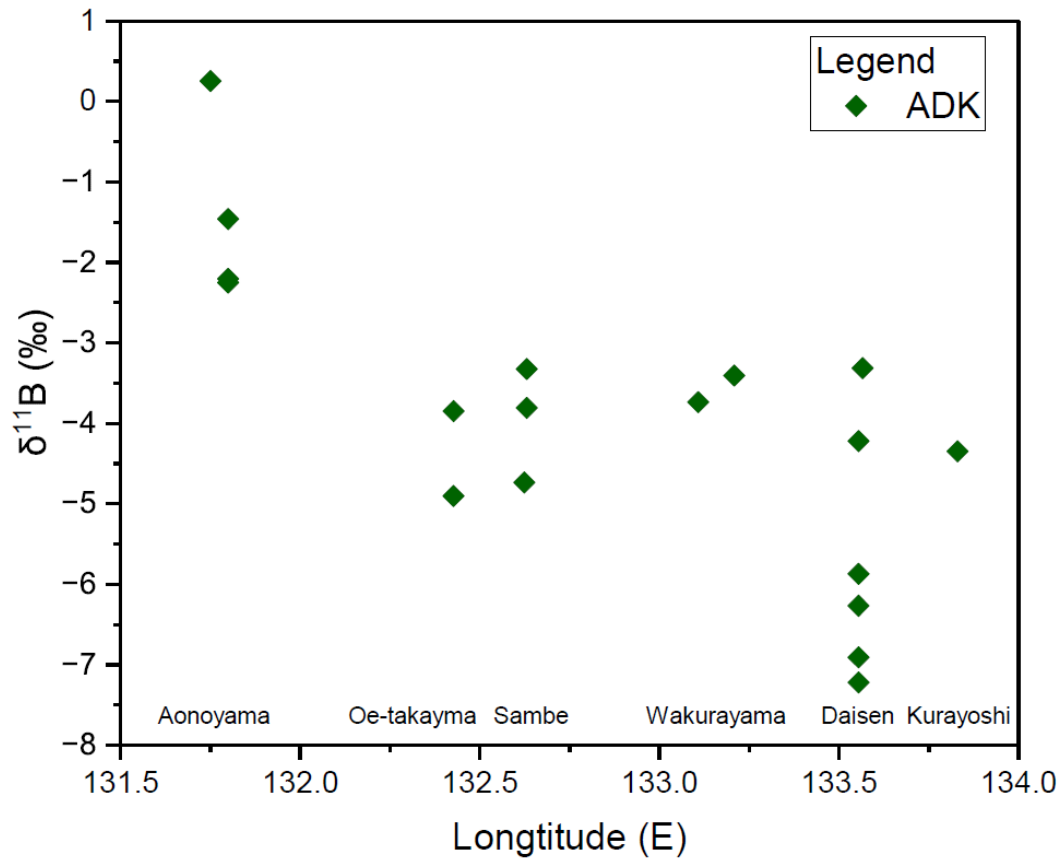


Figure 3-3. $\delta^{11}\text{B}$ (‰) plotted against longitudes of collection sites of the volcanic rocks from the Chugoku district in SW Japan.

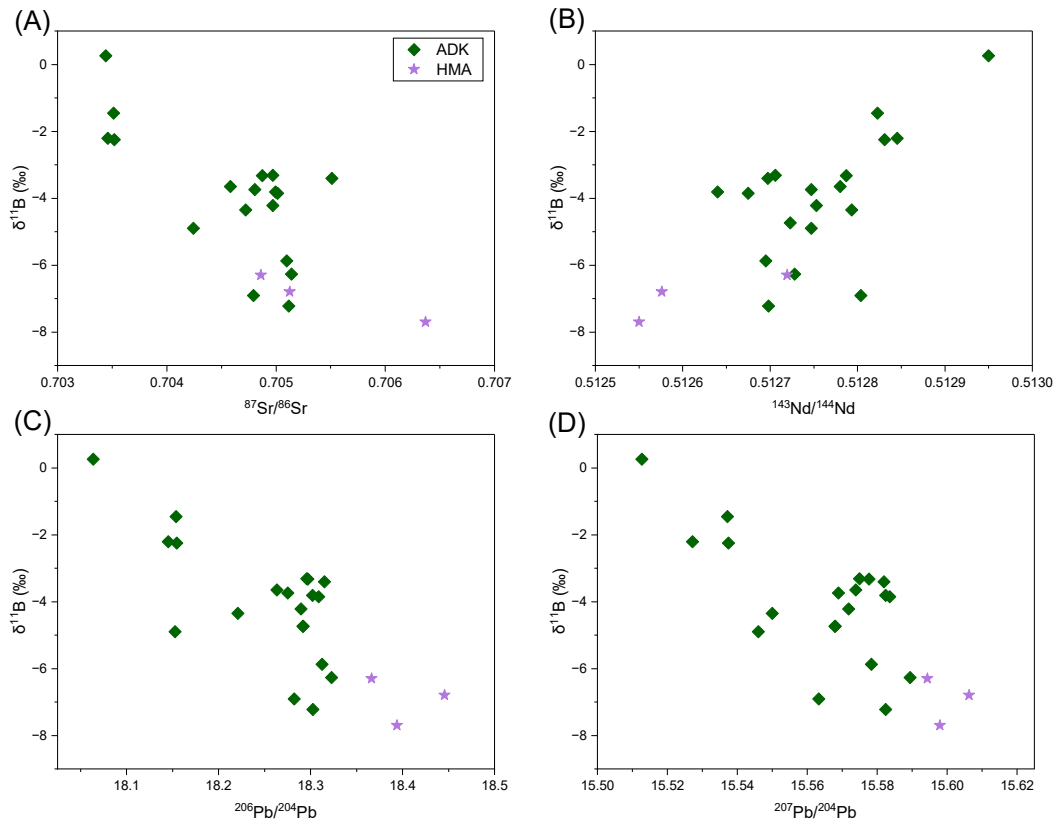


Figure 3-4. Plots of $\delta^{11}\text{B}$ values versus Sr-Nd-Pb isotopic compositions of the Chugoku ADK and the Setouchi HMA.

Plots of $\delta^{11}\text{B}$ values versus (A) $(^{87}\text{Sr}/^{86}\text{Sr})_t$, (B) $(^{143}\text{Nd}/^{144}\text{Nd})_t$, (C) $(^{206}\text{Pb}/^{204}\text{Pb})_t$, and (D) $(^{207}\text{Pb}/^{204}\text{Pb})_t$ of the Chugoku ADK and the Setouchi HMA.

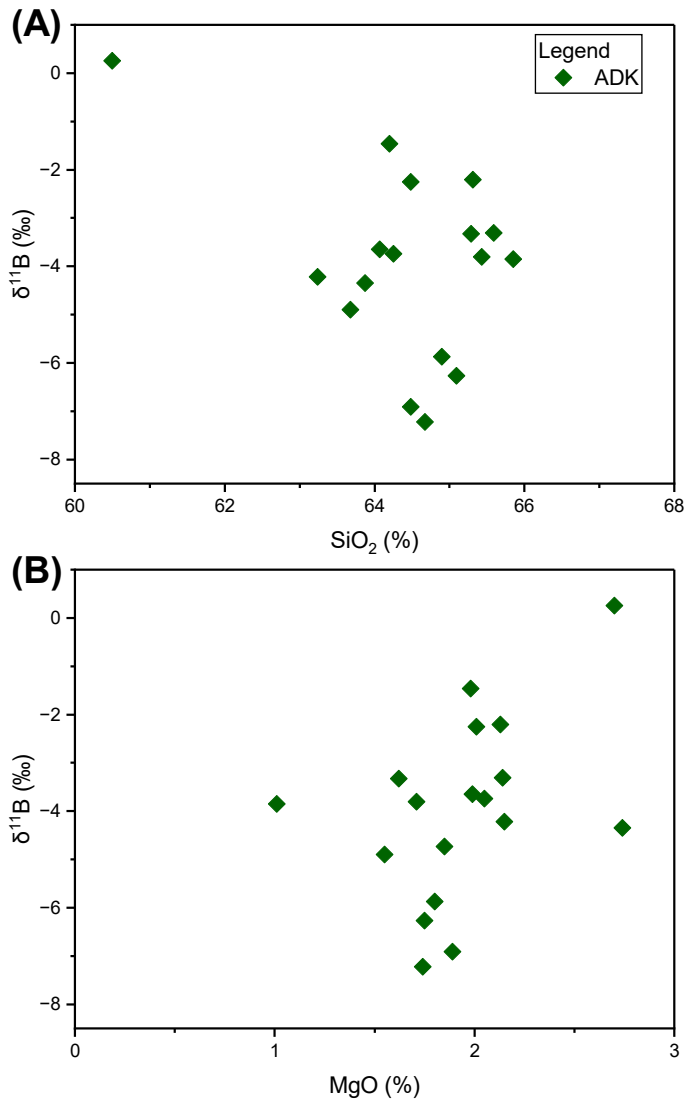


Figure 3-5. Plots of $\delta^{11}\text{B}$ values against (A) SiO_2 abundance and (B) MgO abundance of ADK. Uncertainty (2σ) of $\delta^{11}\text{B}$ value ($\pm 0.2\text{‰}$) is shown as an error bar in the corner of each plot.

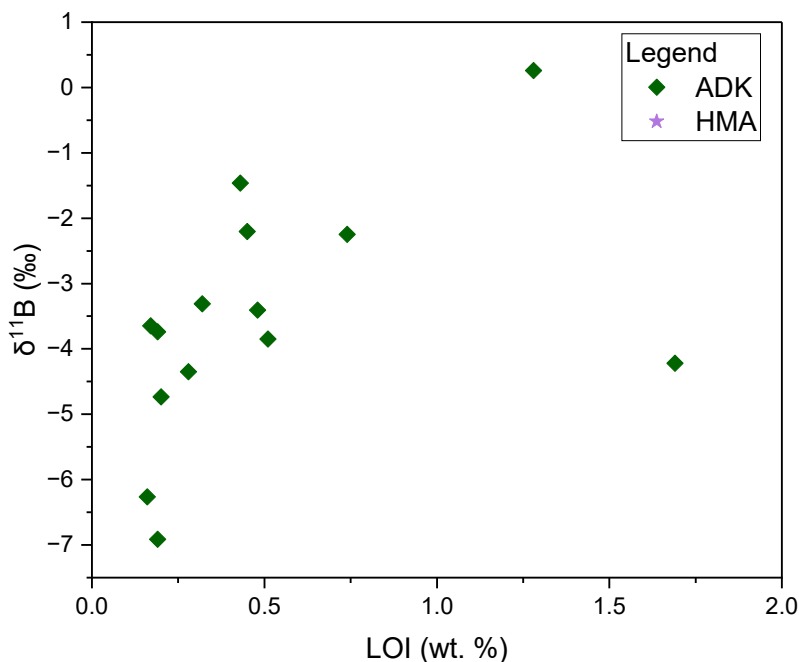


Figure 3-6. Plots of $\delta^{11}\text{B}$ in ADK of the Chugoku district in SW Japan versus LOI (Loss on ignition).

2σ error of $\delta^{11}\text{B}$ for the Chugoku district samples is $\pm 0.2\%$.

4. Discussion

Given that the subducted slabs experienced heating and dehydration, the mechanism and rate of slab-derived fluid will depend on the thermal structure of the subduction zone and slab depth. The upper slab (i.e., sediment and AOC) may be much higher temperature than the mantle portion of the subducted plate, and such a strong thermal gradient may cause diverse metamorphism and dehydration processes (e.g., [Leeman et al., 1996](#), [Syracuse et al., 2010](#)). The AOC and sediment portions of the slab are likely to be significantly dehydrated and may even reach the melting condition in hot conditions, while slab mantle can preserve significant water content. As a result, dehydration of the serpentinized peridotite in the slab mantle portion have potential to provide H_2O for the partial melting of the oceanic crust ([Freyruth et al., 2016](#); [Spandler and Pirard, 2013](#)). Below, we evaluate several reservoirs/processes that potentially

could facilitate the formation of slab melt using B isotopic data of adakites from SW Japan.

4.1. Potential sources of boron in arc magmas

Boron sources which may contribute to arc magmas include the depleted mantle wedge, altered oceanic crust (AOC), the subducted sediments and serpentinized peridotite from oceanic lithosphere or mantle wedge, all of which have varied boron contents and boron isotope compositions.

The formation of adakites have little contribution from mantle peridotite, but HMA have more source contribution from mantle component. SW Japan mantle wedge has been considered a depleted or PUM mantle (e.g., [Kimura et al., 2014](#); [Pineda-Velasco et al, 2018](#); [Nguyen et al., 2020](#)). In any case, the mantle (both depleted and enriched) is characterized by very low boron content. Therefore, melting of the mantle wedge contributes negligible boron to primary arc magmas and has little impact upon their $\delta^{11}\text{B}$ compositions for HMA samples ([Pineda-Velasco et al., 2018](#))

Mafic portions of the oceanic crust have low B contents when formed, but due to hydrothermal interaction with seawater (~ 4.5 ppm B with $\delta^{11}\text{B} = +39.5\%$; [Spivack and Edmond, 1987](#)), altered oceanic crust has considerably higher B concentrations (>1 to 69 ppm) and $\delta^{11}\text{B}$ values ($\sim 0\%$ to $+5\%$) ([Smith et al., 1995](#), [Spivack and Edmond, 1987](#), [Yamaoka et al., 2011](#), [Yamaoka et al., 2012](#)). Subducting sediments are also a potentially important reservoir, although sediments have highly variable boron concentrations and isotope ratios ([Ishikawa and Nakamura, 1993](#)), reflecting variable proportions of continental detritus with negative $\delta^{11}\text{B}$ values (30–100ppm B and $\delta^{11}\text{B} = -8\%$ to -13%), and pelagic sediments with positive $\delta^{11}\text{B}$ values (1–150 ppm B and $\delta^{11}\text{B} = +2.1\%$ to $+26.2\%$).

A final potential source of B in subduction zones is serpentinized peridotite. Serpentine can form in the subducted oceanic lithosphere at intermediate and fast spreading centers as a

result of seawater penetration through the slab bending faults outboard of subduction zones (Alt et al., 2012). An alternative serpentinite may form in the forearc by dehydration fluids and dragged down by subduction-induced mantle flow [e.g., Hattori and Guillot, 2003]. During serpentinization, boron and preferentially ^{11}B is added to peridotite, resulting in positive $\delta^{11}\text{B}$ values ($\delta^{11}\text{B}=+5.5\text{‰}$ to $+40.5\text{‰}$; Martin et al., 2020) and high boron concentrations (50–81 ppm) (Spivack and Edmond, 1987). As serpentinite can contain >13 wt% H_2O , its breakdown has the potential to release large quantities of water into the mantle wedge (e.g., Rüpke et al., 2004, Spandler and Pirard, 2013).

In order to define the geochemical features of the subduction-related components and their relative contributions to magma genesis, we modeled the Sr, Nd, Pb and B isotopic composition of fluids from the different reservoirs beneath the volcanic front and their subsequent mixing processes.

4.2. Parameters for B isotopic fractionation during the dehydration modeling

Progressive metamorphic dehydration of the slab during subduction releases boron, and preferentially ^{11}B , into slab-derived fluids (King et al., 2007, Moran et al., 1992, Peacock and Hervig, 1999). Therefore, fluids released from the slab become isotopically lighter in B and contain less boron as the slab is subducted to greater depths. A significant fraction ($> \sim 75\%$; Leeman and Sisson, 1996) of the initial B inventory in subducting slabs is contained in the uppermost few km, consisting of sediments and altered oceanic crust.

Marschall et al. (2006b) developed a stepwise mass balance-based dehydration model which predicted water loss in combination with B depletions. Prograde metamorphism can be modeled as small steps of batch dehydration. This approach was adopted in several B isotope studies aimed at identifying fluid sources in subduction zones, such as in S. Sandwich and Salvador Arc (Tonarini et al. 2007, 2011; Scambelluri and Tonarini 2012). The model was

refined further by [Jones et al. \(2014\)](#), who incorporated the thermal regime of the subduction zone in their dehydration scenarios in order to calculate more realistic water and B fluxes from different segments of the subducting slab. In order to account for the reduction in both $\delta^{11}\text{B}$ values and the boron contents in slab-derived fluids with progressive heating and dehydration of the slab, dehydration of the subducting slab has been modelled in 10 km intervals. The modeling applied the equations of [Marschall et al. \(2006\)](#) to simulate boron release linked to water content and boron isotopic fractionation calculated using the temperature-dependent B fractionation factor according to [Hervig et al. \(2002\)](#) and a partition coefficient of Boron (D_B) between hydrous fluids and restite slab. The slab surface temperature from thermal parameters for the SW Japan (Chugoku) arc section ([Syracuse et al., 2010](#); [Kimura et al., 2014](#)) are combined with the dehydration depths estimated from [Kimura et al. \(2014\)](#) to calculate the $\delta^{11}\text{B}$ values and B contents in each step (**Figure 3-7**; [Syracuse et al., 2010](#)).

Boron isotopic fractionation in previous studies was normally calculated using a bulk partition coefficient of B between hydrous fluids and restite slab of 0.1 ([Brenan et al., 1998](#)). However, [Brenan et al. \(1998\)](#) presented the partition coefficients for Boron between aqueous fluid and different minerals (cpx, opx, grt, mica etc.) in the basaltic portion of the downgoing slab. Since mica (or phengite) has relatively large partition coefficients (0.2 for mica, 0.7 for phengite) compared to other minerals (<0.1), the bulk partition coefficients of eclogite would be largely controlled by the proportion of mica or phengite ([Marschall et al., 2006](#)). A partition coefficient of B of 0.1 would require the proportion of phengite more than 10%, which is unlikely in the eclogite system and thus overestimated. On the other hand, previous study suggested that $>80\%$ and 60–80% of the subducted B in the subducted sediment ([You et al. 1995, 1996](#); [Savov et al. 2007](#)) and slab serpentinites ([Scambelluri et al. 2004](#); [Deschamps et al. 2011](#); [Kodolanyi and Pettke 2011](#); [Vils et al. 2011](#); [Debret et al. 2013](#)) are recycled in the

fore-arc, as B strongly partitions into such fluids. AOC at about 20–40 km depth is considered to be much lower than the average AOC value of $\delta^{11}\text{B} = +3.4\text{‰}$, due to the loss of heavy B to the forearc at shallow depth (Pabst et al. 2012). Using the partition coefficient of B of 0.1 will require > 15 wt.% and >30 wt.% of water to be lost in the forearc to achieve the Boron loss of 60% and 80%, respectively, which are highly unlikely to occur in the forearc (Rupke et al., 2004).

The selection of bulk partition coefficient of B would be highly uncertain and of challenge, because of the variation of mineral assemblage. Nevertheless, Adakites are special samples, because the composition is dominated by slab contribution, rather than mantle component. Therefore, the mixing modeling of Boron isotope do not involve mantle peridotite, which has extremely low Boron content (0.06 ppm). For adakites, the boron from only AOC melt and sediment melt could constrain the minimal value of slab-derived Boron, when the additional contribution from serpentinite is not considered. ADK from Chugoku district have Boron content ranging from 5 ppm to 10 ppm. If we apply a simple calculation following the model in Pineda-Velasco et al. (2018), the [B] of AOC and sediment protolith before melting should be less than 2 ppm and 4 ppm, respectively. However, Shikoku basin basalts (AOC) and Nankai sediments have average boron concentration of 32 ppm (Shu et al., 2017) and ~80 ppm (You et al., 1995), respectively. Therefore, more than 90% of boron are required to be lost by the dehydration processes beneath the Chugoku district, hence a bulk partition coefficient of B should be lower than 0.01 to fit the scenario. Using a bulk partition coefficient of 0.01 would be feasible, because using it can cause the loss of 80% boron in the forearc in the condition of water loss of ~3% in the forearc (Rupke et al., 2004).

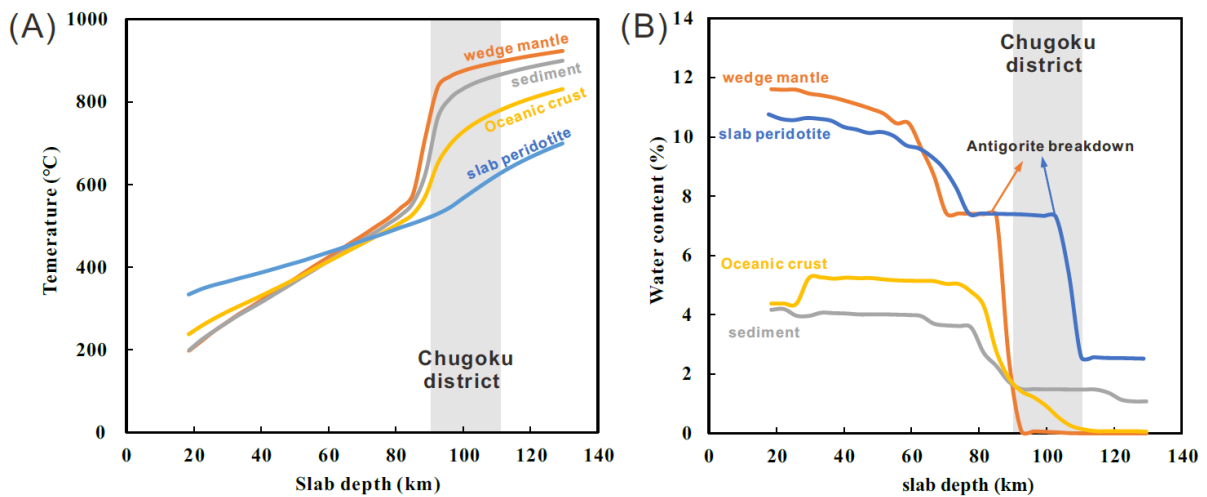


Figure 3-7. (A) Slab temperature change (°C) and (B) dehydration water loss (wt. %) as a function of slab depth (km) of the slab sediment, oceanic crust (AOC), mantle wedge peridotite and slab lithosphere peridotite in the Chugoku subduction zone,

Data are from [Kimura et al. \(2014\)](#) and [Syracuse et al. \(2010\)](#). The gray shadows indicate the P-T conditions of the slab beneath the the Chugoku district in SW Japan (90-110 km; [Zhao et al., 2012](#)).

4.3 Dehydration of the upper slab (AOC + sediments)

The Sr, Nd and Pb concentration and isotopic compositions of AOC and sediments are from [Pineda-Velasco et al. \(2018\)](#) and are assumed to be constant during the metamorphic dehydration. The composition of the endmembers and the model results are reported in **Table 3-2 and 3-3** and plotted in **Figures 3-8 and 3-9**.

Boron content and $\delta^{11}\text{B}$ values of sediment components are from sediments subducting into Nankai Trough (80 ppm and -3‰ ; [You et al., 1995](#)). Much of the pore waters and weakly bound water in clays are lost during compaction and diagenesis at shallow depths. We assume that adsorbed, interstitial and pore waters (~ 3 wt. % water) was expelled prior to ~ 20 km depth) (**Figure 3-8**; [Brown et al., 2001](#); [Toki et al., 2014](#); [Hüpers et al., 2016](#)). The dehydration in the forearc cause the loss of $\sim 80\%$ of the subducted B recycled to wedge mantle, which is consistent with previous studies ([You et al. 1995, 1996](#); [Savov et al. 2007](#)). After water contents were reduced from 4.2% to 0.9% in the sediments from 20 km to 100 km depth (gray lines in

Figure 3-7B; Rupke, 2004; Kimura et al., 2014), the sediment residue in the model evolves to -32‰ at ~ 100 km depth directly underneath the volcanic front (**Figure 3-8**).

Boron content of altered oceanic crust (AOC) are from Shikoku basin basalts (32 ppm; Shu et al., 2017) and their $\delta^{11}\text{B}$ values are represented by the average of global altered oceanic crust ($+5\text{‰}$; Smith et al., 1995; Leeman et al., 2004). The B isotopic composition of AOC through dehydration is difficult to be estimated because of the uncertainties involved with shallow fluid release (Jones et al., 2014; Zhang et al., 2019). We estimated the boron isotopic composition of AOC at 30 km depth was reduced to -6‰ from $+5\text{‰}$ after the shallow fluid release (1 wt. %; **Figure 3-8**). This value is in good agreement with the blueschist clasts in the Mariana forearc (average $\delta^{11}\text{B}$ value: -6‰), which represent material from a slab-derived mafic material that metamorphosed at about 20–40 km depth and thus were the closest equivalent material (Pabst et al. 2012). After water contents were reduced from 5.2% to 0.05% in the AOC from 20 km to 100 km depth (yellow lines in **Figure 3-7B**; Kimura et al., 2014), the AOC residue in the model evolves to $\sim -19\text{‰}$ at ~ 100 km depth due to the continuous release of ^{11}B into slab-derived fluids (**Figure 3-8**).

A basic outcome of the modeling is that the release of shallow fluid takes a large proportion of the initial B, and strongly fractionates $\delta^{11}\text{B}$. Water released from the uppermost slab become depleted at Benioff zone depths ($\geq \sim 80$ km) beneath the arc proper (Van Keken et al. 2011), therefore residual slabs and their melt are predicted to have very low $\delta^{11}\text{B}$ (i.e., $-19\text{‰} \sim -32\text{‰}$; **Figure 3-8, Table 3-2**), which was demonstrated by many studies (Tonarini et al., 2007, 2011; Jones et al., 2014; Zhang et al., 2019; Cooper et al., 2020). Thus, the simple mixing between an AOC melt and a sediment melt at depths directly beneath the volcanic front, cannot reasonably account for the $\delta^{11}\text{B}$ ratios in SW Japan ADK lavas.

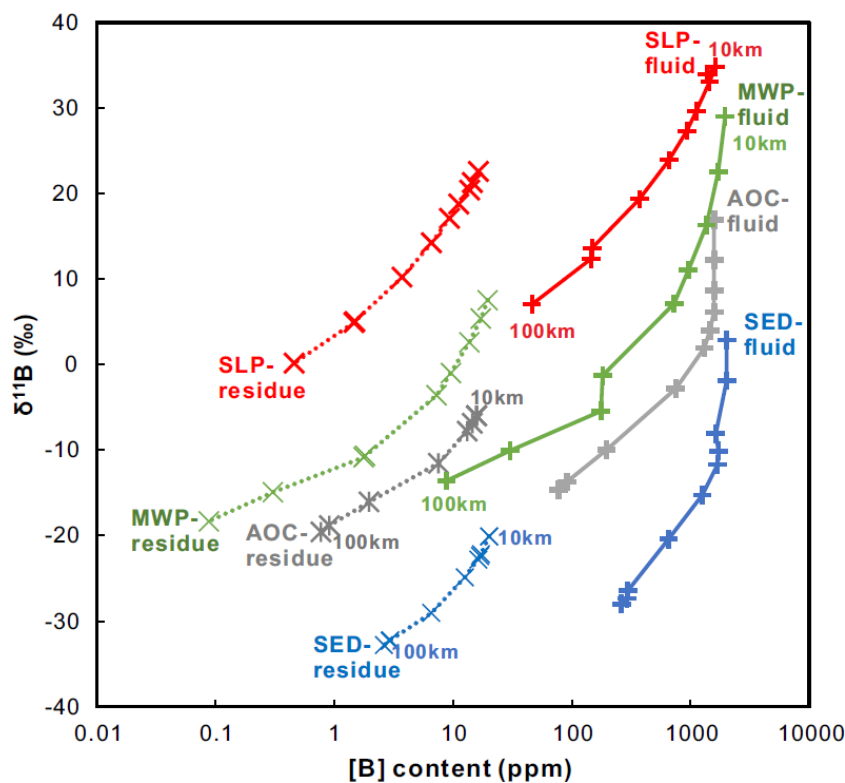


Figure 3-8. Dehydration model showing the variation of $\delta^{11}\text{B}$ and B concentrations of the slab sediment (SED), oceanic crust (AOC), mantle wedge peridotite (MWP) and slab lithosphere peridotite (SLP) as well as their dehydration fluids with subduction depth from 30 km until 110 km with 10 km intervals.

The initial water contents of the slab sediment, oceanic crust, mantle wedge peridotite and slab lithosphere peridotite were assumed to be 7.2 %, 6.3 %, 13.0 % and 13.0 %, respectively. The dehydration of different proportion of slab was based on P-T parameters in **Figure 3-7**. Thus, the compositions of the AOC (B = 32 ppm; $\delta^{11}\text{B}$ = 5.5‰; [Leeman et al., 2004](#), [Smith et al., 1995](#)) and the sediments (B = 80 ppm; $\delta^{11}\text{B}$ = -3‰; [You et al., 1998](#)), mantle wedge peridotite (B = 46.7 ppm; $\delta^{11}\text{B}$ = 30‰; [Scambelluri et al. 2004](#); [Boschi et al., 2008](#); [Jones et al., 2014](#)) and slab lithosphere peridotite (B = 46.7 ppm; $\delta^{11}\text{B}$ = 30‰; [Scambelluri et al. 2004](#); [Boschi et al., 2008](#); [Jones et al., 2014](#)) were used as the starting values. The model used a temperature-dependent B fractionation factor from [Hervig et al. \(2002\)](#) and a rock/fluid B partition coefficient of 0.01.

4.4 Dehydration of the serpentinized peridotite

The serpentinites formed in the mantle wedge are a potential fluid source for arc magmas ([Martin et al., 2016, 2020](#)). However, since the subducting Shikoku basin Plate is relatively young and warm, the antigorite near the slab surface would totally breakdown at 600 °C to

650 °C before reaching the depth (< 75 km depth) before the arc front (orange line in **Figure 3-7**; [Syracuse et al., 2010](#)). Although H₂O can be carried to sub-arc depths beneath the Chugoku region by chlorite in the wedge serpentinite ([Van Keken et al., 2011](#); [Walowski et al., 2015](#)). Because nearly all B is released from hydrated peridotite beneath the forearc during antigorite breakdown, chlorite-derived fluids is thought to be poor in B ([Marschall et al. 2006a](#)) and contribute little B to the subduction component ([Spandler et al., 2014](#)). Modelled $\delta^{11}\text{B}$ value and B concentration in the fluids released from slab serpentinites were calculated in the same way as the dehydration of the upper slab. Our calculation suggests that after the multi-stage dehydration, the fluid released from wedge serpentinite in the model decrease from 30‰ to -4 ‰ at ~100 km depth (**Figure 3-8**), which can hardly explain the $\delta^{11}\text{B}$ values of ADK.

Furthermore, the initial $\delta^{11}\text{B}$ composition of wedge serpentinite may be overestimated because recent studies have shown that the mantle wedge serpentinites have relatively light and variable B isotopes ($\delta^{11}\text{B} = -14.5\text{‰}$ to $+10\text{‰}$), as the slab-derived metamorphic fluids have decreasing $\delta^{11}\text{B}$ values with increasing depth ([Martin et al., 2016, 2020](#); [Yamada et al., 2019](#)). On the other hand, a roughly linear correlation between B isotopes and other radiogenic isotopes (Sr, Nd and Pb) can be observed in our samples (**Figure 3-6**). This correlation can be explained by simple binary mixing between a low- $\delta^{11}\text{B}$ endmember (with low $^{143}\text{Nd}/^{144}\text{Nd}$, and high $^{87}\text{Sr}/^{86}\text{Sr}$, $^{206}\text{Pb}/^{204}\text{Pb}$ and $^{207}\text{Pb}/^{204}\text{Pb}$) and a high- $\delta^{11}\text{B}$ endmember (with high $^{143}\text{Nd}/^{144}\text{Nd}$, and low $^{87}\text{Sr}/^{86}\text{Sr}$, $^{206}\text{Pb}/^{204}\text{Pb}$ and $^{207}\text{Pb}/^{204}\text{Pb}$). If serpentinite-derived fluids are from wedge mantle, mixing of sediment melt and AOC melt should occur prior to the contribution of fluid from wedge serpentinite. However, a mixing between a hybrid AOC+Sediment component with lower $\delta^{11}\text{B}$ and Boron and a serpentinite-derived fluid (such as wedge serpentine) with higher $\delta^{11}\text{B}$ and Boron is unlikely, because the large differences in their B/Sr (or B/Nd, B/Pb) ratios would not produce a line, but instead a strongly convex hyperbolic curve. Therefore, the

low- $\delta^{11}\text{B}$ endmember represent sediment melt, and the high- $\delta^{11}\text{B}$ endmember may be a composite of components derived from AOC melt and the dehydration of ocean lithospheric mantle.

In comparison, slab serpentinites can be insulated within the subducting slab and dehydrate at greater depth (Rüpke et al., 2004). The serpentine minerals within the slab are at P-T conditions of the antigorite-chlorite transition beneath the Chugoku district (600 °C to 700 °C at 90 km to 110 km; blue lines in **Figure 3-7**), and antigorite breakdown can release significant amounts of ^{11}B -rich fluid (Harvey et al., 2014; Scambelluri et al., 2004). On the other hand, the fluids from slab serpentinites underlying the oceanic crust also have more potential to ascend and facilitate the slab melting than mantle wedge serpentinites, which are above the slab. Shallow hydrothermal metasomatism at mid-oceanic ridges can produce serpentinitized peridotites with $\delta^{11}\text{B}$ as high as 30 to 40‰ (Vils et al., 2009). Therefore, we assume Boron content and $\delta^{11}\text{B}$ values of the slab serpentinites to be 46.7 ppm (Scambelluri et al. 2004) and +30‰ (Boschi et al., 2008; Jones et al., 2014), respectively (**Table 3-2**). The Sr, Nd and Pb concentrations of the slab serpentinites are from Tonarini et al. (2007) and their isotopic compositions are assumed to be the same as that of AOC (Pineda-Velasco et al., 2018) (**Table 3-3**).

Modelled $\delta^{11}\text{B}$ value and B concentration in the fluids released from slab serpentinites were calculated in the same way as the dehydration of the upper slab. The Moho temperature for the SW Japan arc (Chugoku section) are from Syracuse et al. (2010) and the dehydration depths are estimated from Kimura et al. (2014) (blue lines in **Figure 3-7**). Initial water content was assumed to be 13% in the abyssal serpentinites. Upon subduction, lizardite and chrysotile break down at about 250–300 °C and will lose 1–2% water and a large amount of B of ~ 70% (**Figure 3-8**; Scambelluri et al. 2004; Deschamps et al. 2011; Vils et al. 2011). Fluid was also

release during the breakdown of brucite to olivine (at ca. 450 °C; [Kimura et al., 2014](#)). Despite the sizeable shallow loss, considerable amounts of B carrying their original heavy isotope signature are retained in antigorite serpentinite ([Deschamps et al. 2011](#); [Scambelluri and Tonarini 2012](#)) until extensive dehydration during antigorite breakdown occurs at ca. 650–700 °C. The breakdown of antigorite in the slab serpentinites occurs at 100–120 km depth underneath the volcanic arc front in the Chugoku district (**Figure 3-7**; [Syracuse et al., 2010](#)). The serpentinites-derived fluids in the model evolves to ~7 ‰ at ~100 km depth (**Figure 3-8**).

We calculated the mixing of sediment melt and a composite component derived from AOC melt and slab serpentinite-derived fluid in different proportions based on the composition of modelled Sr-Nd-Pb and B isotopic compositions of slab serpentinite-derived fluid and slab melt (**Figure 3-9**). The mixing of sediment melt (~16 ‰) was mixed with a composite component derived from AOC melt and slab serpentinite-derived fluid (~+3.5 ‰) can well explain the B isotopic composition of ADK samples from SW Japan (**Figure 3-9**). The composite component of Boron is composed of 20–40% serpentinite-derived fluid and 60–80% AOC melt (**Figure 3-9**). This scenario is feasible, because the water from the serpentinites enters upward to the oceanic crust before the overlying sediments and serpentinite-derived fluid will mix with AOC melt and later mix with sediment melt.

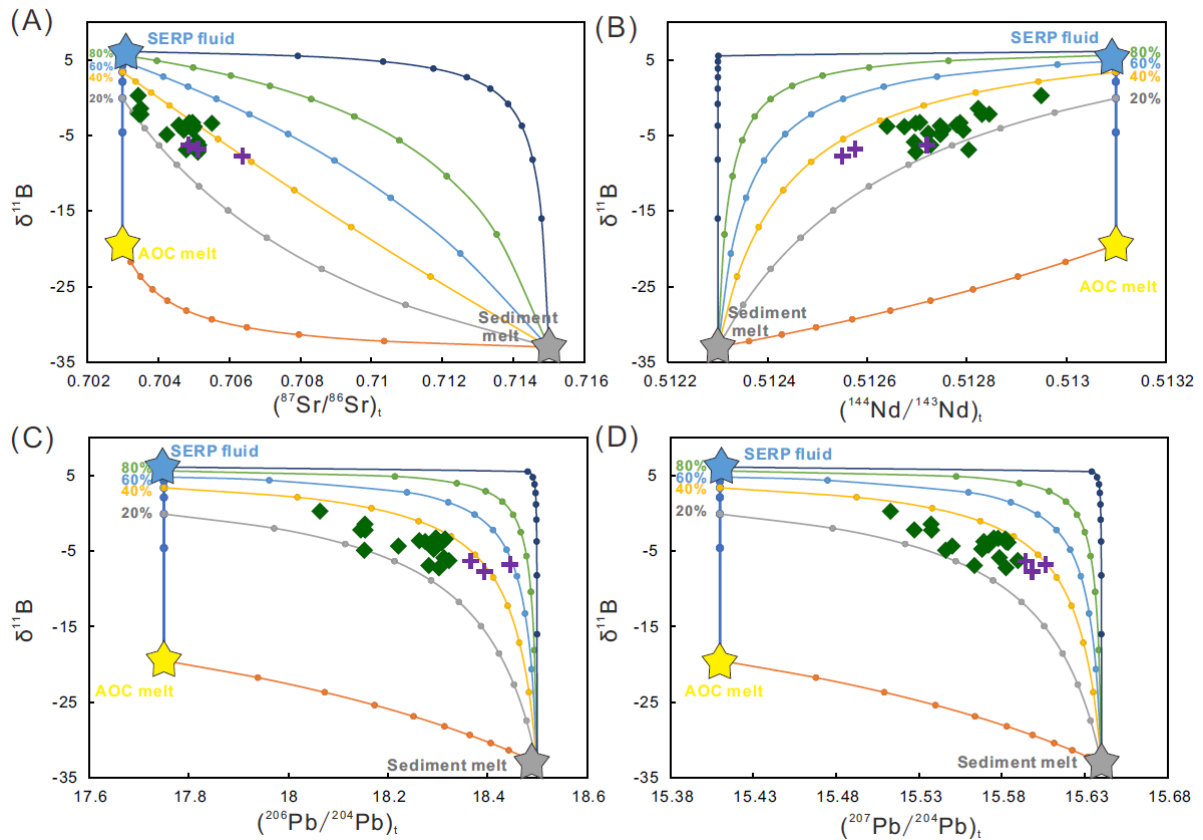


Figure 3-9. Plot of $\delta^{11}\text{B}$ in volcanic rocks from the Chugoku district in SW Japan versus (A) $(^{87}\text{Sr}/^{86}\text{Sr})_t$, (B) $(^{143}\text{Nd}/^{144}\text{Nd})_t$, (C) $(^{206}\text{Pb}/^{204}\text{Pb})_t$, and (D) $(^{207}\text{Pb}/^{204}\text{Pb})_t$.

References include melts from Nankai sediment (gray star symbols), melts from Shikoku basin basalts (yellow star symbols) and fluids from slab lithosphere serpentinite (blue star symbols). Sr-Nd-Pb radiogenic isotopic data of the Chugoku district lavas are from [Pineda-Velasco et al. \(2018\)](#) and [Nguyen et al. \(2020\)](#). [B] contents and $\delta^{11}\text{B}$ values of input dehydrated components of slab are from the calculated results in the modeling (shown in [Figure 3-8](#) and [Table 3-2](#)). Sr-Nd-Pb concentrations and radiogenic isotopes of Nankai sediments and Shikoku basin basalts are from [Pineda-Velasco et al. \(2018\)](#) ([Table 3-3](#)). The Sr, Nd and Pb concentrations of the slab serpentinites are from [Tonarini et al. \(2007\)](#) and their isotopic compositions are assumed to be the same as that of AOC ([Pineda-Velasco et al., 2018](#)) ([Table 3-3](#)). 2σ error of $\delta^{11}\text{B}$ for the Chugoku district samples is $\pm 0.2\%$.

4.5 Implications for slab melting

Because melting of the upper oceanic crust takes place in the garnet stability field, a hallmark of slab melting is the geochemical signature imposed by garnet, such as high Sr/Y and La/Yb. Lavas from the Chugoku district, and other relatively hot-slab subduction zones

such as Cascades and Mexico (Cai et al., 2014; Kimura et al., 2014; Walowski et al., 2016), have values of these ratios that are higher than most other arc magmas, and are interpreted to be slab melts. However, during subduction, the sediment, oceanic crust, and uppermost mantle of the subducting plate undergo progressive metamorphism accompanied with dehydration reactions (Poli and Schmidt, 2002). The depth of dehydration reactions varies with temperature of the subducting slabs (Peacock, 2009). The crustal section of young and hot plate, such as the Shikoku Basin Plate, releases most water at shallow depth (50–80 km) with transformation to dry eclogite-facies rocks (Figure 3-7; Kimura, 2017; Kimura et al., 2014; Peacock and Wang, 1999).

Melting temperatures for subducting slabs are largely affected by the presence of water. Experimental studies have demonstrated that solidus temperatures of dry basaltic rocks are higher by 500–700 °C at depths for slab melting than that of wet basaltic rocks (Kessel et al., 2005; Yasuda et al., 1994). The temperatures of subducted Shikoku Basin Plate, predicted by a numerical model (Syracuse et al., 2010), surpass wet basalt solidus at 90–110 km, indicating the likelihood of slab melting if it is hydrated. The occurrence of hornblende in high-Sr andesites and dacites is consistent with melt production under hydrous condition (2 wt % or more water in melts; Green, 1972). Therefore, beneath the Chugoku district, the upper, upper portions of the plate are likely to intersect with the MORB + H₂O and sediment + H₂O solidi (Figure 3-7).

Fluids released from serpentinite in the mantle section of the subducting slab are most potential reservoirs to provide water to upper slab (Kimura et al., 2014; Poli and Schmidt, 2002; Portnyagin et al., 2007; Walowski et al., 2015). However, sediment melt normally dominates the trace-element and radiogenic isotopic signature (Sr-Nd-Pb isotopes) on arc magma, including ADK in the Chugoku district (Pineda-Velasco et al., 2018), and mutes the signals

from the subducted lithosphere peridotite. Our modeling results by B isotopes suggest sediment + AOC signals are subordinate to contributions from the subducted lithosphere peridotite from the perspective of Boron isotopic systematics. Our results provide strong evidence for melting of sediments and basalt in the upper part of the subducted oceanic plate fluxed by the fluids rising from deeper parts of the slab beneath Chugoku district. Our work in the Chugoku segment of Southwest Japan predict that H₂O-rich fluids are released from the slab interior during serpentine breakdown at sub-arc depths, providing H₂O that could cause partial melting of the slab top in the hot subduction zone.

5. Conclusions

The mechanism of melt generation in warm-slab subduction zones, such as Southwest Japan, has been debated due to the high slab surface temperatures lead to most dehydration of upper slab beneath the forearc rather than the arc. We report the B isotopic compositions of adakitic lavas (ADK) from the Chugoku section of Southwestern Japan in order to constrain the influence of subduction components (AOC, sediments, and serpentinites) on the fluid source of the slab melt beneath the Southwestern Japan. The ADK lavas have the $\delta^{11}\text{B}$ values from -6.6‰ to 0.3‰. Dehydration models suggest that composite fluids/melts derived from AOC, sediments, and wedge serpentinites fail to explain the $\delta^{11}\text{B}$ values of the ADK lavas. Rather, we infer that they may be produced from sources that were influenced by slab-serpentine-derived fluids, as has been proposed for the origin of heavy B isotopes in some other arc lavas (e.g., Mariana, Tonga, and South Sandwich). Our results provide strong evidence that hydrous slab melt in the Chugoku section of SW Japan arc is driven by fluid addition from the slab mantle peridotite.

References

Abers G. A., Mackenzie L. S., Rondenay S., Zhang Z., Wech A. G. and Creager K. C. (2009)

- Imaging the source region of Cascadia tremor and intermediate-depth earthquakes. *Geology* **37**, 1119-1122.
- Alt J. C., Garrido C. J., Shanks Iii W. C., Turchyn A., Padrón-Navarta J. A. and Sánchez-Vizcaíno V. L., et al. (2012) Recycling of water, carbon, and sulfur during subduction of serpentinites: A stable isotope study of Cerro del Almiraz, Spain. *Earth Planet. Sc. Lett.* **327**, 50-60.
- Asamori K. and Zhao D. (2015) Teleseismic shear wave tomography of the Japan subduction zone. *Geophysical Supplements to the Monthly Notices of the Royal Astronomical Society* **203**, 1752-1772.
- Boschi C., Dini A., Früh-Green G. L. and Kelley D. S. (2008) Isotopic and element exchange during serpentinization and metasomatism at the Atlantis Massif (MAR 30 N): insights from B and Sr isotope data. *Geochim. Cosmochim. Ac.* **72**, 1801-1823.
- Bouvier A., Manzini M., Rose-Koga E. F., Nichols A. R. and Baumgartner L. P. (2019) Tracing of Cl input into the sub-arc mantle through the combined analysis of B, O and Cl isotopes in melt inclusions. *Earth Planet. Sc. Lett.* **507**, 30-39.
- Brenan J. M., Neroda E., Lundstrom C. C., Shaw H. F., Ryerson F. J. and Phinney D. L. (1998) Behaviour of boron, beryllium, and lithium during melting and crystallization: constraints from mineral-melt partitioning experiments. *Geochim. Cosmochim. Ac.* **62**, 2129-2141.
- Brenan J. M., Ryerson F. J. and Shaw H. F. (1998) The role of aqueous fluids in the slab-to-mantle transfer of boron, beryllium, and lithium during subduction; experiments and models. *Geochim. Cosmochim. Ac.* **62**, 3337-3347.
- Brown K. M., Saffer D. M. and Bekins B. A. (2001) Smectite diagenesis, pore-water freshening, and fluid flow at the toe of the Nankai wedge. *Earth Planet. Sc. Lett.* **194**, 97-109.
- Cai Y., Lagatta A., Goldstein S. L., Langmuir C. H., Gómez-Tuena A. and Martín-Del Pozzo

- A. L., et al. (2014) Hafnium isotope evidence for slab melt contributions in the Central Mexican Volcanic Belt and implications for slab melting in hot and cold slab arcs. *Chem. Geol.* **377**, 45-55.
- Cannaò E., Scambelluri M., Agostini S., Tonarini S. and Godard M. (2016) Linking serpentinite geochemistry with tectonic evolution at the subduction plate-interface: The Voltri Massif case study (Ligurian Western Alps, Italy). *Geochim. Cosmochim. Ac.* **190**, 115-133.
- Chaussidon M. and Jambon A. (1994) Boron content and isotopic composition of oceanic basalts: geochemical and cosmochemical implications. *Earth Planet. Sc. Lett.* **121**, 277-291.
- Chaussidon M. and Marty B. (1995) Primitive boron isotope composition of the mantle. *Science* **269**, 383-386.
- Chetelat B., Liu C., Gaillardet J., Wang Q. L., Zhao Z. Q. and Liang C. S., et al. (2009) Boron isotopes geochemistry of the Changjiang basin rivers. *Geochim. Cosmochim. Ac.* **73**, 6084-6097.
- Cooper G. F., Macpherson C. G., Blundy J. D., Maunder B., Allen R. W. and Goes S., et al. (2020) Variable water input controls evolution of the Lesser Antilles volcanic arc. *Nature* **582**, 525-529.
- De Hoog J. C. M. and Savov I. P. (2017) Boron Isotopes as a Tracer of Subduction Zone Processes. Springer International Publishing, Cham. pp. 217-247.
- Debret B., Nicollet C., Andreani M., Schwartz S. and Godard M. (2013) Three steps of serpentinitization in an eclogitized oceanic serpentinitization front (Lanzo Massif–Western Alps). *J. Metamorph. Geol.* **31**, 165-186.
- Defant M. J. and Drummond M. S. (1990) Derivation of some modern arc magmas by melting of young subducted lithosphere. *Nature (London)* **347**, 662-665.
- Deschamps F., Guillot S., Godard M., Andreani M. and Hattori K. (2011) Serpentinites act as

- sponges for fluid-mobile elements in abyssal and subduction zone environments. *Terra Nova* **23**, 171-178.
- Feineman M., Moriguti T., Yokoyama T., Terui S. and Nakamura E. (2013) Sediment-enriched adakitic magmas from the Daisen volcanic field, Southwest Japan. *Geochemistry, Geophysics, Geosystems* **14**, 3009-3031.
- Freytmuth H., Ivko B., Gill J. B., Tamura Y. and Elliott T. (2016) Thorium isotope evidence for melting of the mafic oceanic crust beneath the Izu arc. *Geochim. Cosmochim. Ac.* **186**, 49-70.
- Green T. H. (1972) Crystallization of calc-alkaline andesite under controlled high-pressure hydrous conditions. *Contrib. Mineral. Petr.* **34**, 150-166.
- Harvey J., Garrido C. J., Savov I., Agostini S., Padrón-Navarta J. A. and Marchesi C., et al. (2014) 11B-rich fluids in subduction zones: The role of antigorite dehydration in subducting slabs and boron isotope heterogeneity in the mantle. *Chem. Geol.* **376**, 20-30.
- Hattori K. H. and Guillot S. (2003) Volcanic fronts form as a consequence of serpentinite dehydration in the forearc mantle wedge. *Geology* **31**, 525-528.
- Hervig R. L., Moore G. M., Williams L. B., Peacock S. M., Holloway J. R. and Roggensack K. (2002) Isotopic and elemental partitioning of boron between hydrous fluid and silicate melt. *Am. Mineral.* **87**, 769-774.
- Hüpers A., Kasemann S. A., Kopf A. J., Meixner A., Toki T. and Shinjo R., et al. (2016) Fluid flow and water–rock interaction across the active Nankai Trough subduction zone forearc revealed by boron isotope geochemistry. *Geochim. Cosmochim. Ac.* **193**, 100-118.
- Ishikawa T. and Nakamura E. (1994) Origin of the slab component in arc lavas from across-arc variation of B and Pb isotopes. *Nature* **370**, 205-208.
- Ishikawa T. and Nakamura E. (1993) Boron isotope systematics of marine sediments. *Earth*

- Planet. Sc. Lett.* **117**, 567-580.
- Ishizaka K. and Carlson R. W. (1983) Nd-Sr systematics of the Setouchi volcanic rocks, southwest Japan: a clue to the origin of orogenic andesite. *Earth Planet. Sc. Lett.* **64**, 327-340.
- Iwamori H. (1991) Zonal structure of Cenozoic basalts related to mantle upwelling in southwest Japan. *Journal of Geophysical Research: Solid Earth* **96**, 6157-6170.
- Jones R. E., De Hoog J. C. M., Kirstein L. A., Kasemann S. A., Hinton R. and Elliott T., et al. (2014) Temporal variations in the influence of the subducting slab on Central Andean arc magmas: Evidence from boron isotope systematics. *Earth Planet. Sc. Lett.* **408**, 390-401.
- Kay R. W. (1978) Aleutian magnesian andesites: Melts from subducted Pacific ocean crust. *J. Volcanol. Geoth. Res.* **4**, 117-132.
- Kessel R., Ulmer P., Pettke T., Schmidt M. W. and Thompson A. B. (2005) The water–basalt system at 4 to 6 GPa: Phase relations and second critical endpoint in a K-free eclogite at 700 to 1400 C. *Earth Planet. Sc. Lett.* **237**, 873-892.
- Kimura J. I., Stern R. J. and Yoshida T. (2005) Reinitiation of subduction and magmatic responses in SW Japan during Neogene time. *Geol. Soc. Am. Bull.* **117**, 969-986.
- Kimura J. (2017) Modeling chemical geodynamics of subduction zones using the Arc Basalt Simulator version 5. *Geosphere* **13**, 992-1025.
- Kimura J., Gill J. B., Kunikiyo T., Osaka I., Shimoshioiri Y. and Katakuse M., et al. (2014) Diverse magmatic effects of subducting a hot slab in SW Japan: Results from forward modeling. *Geochemistry, Geophysics, Geosystems* **15**, 691-739.
- King R. L., Bebout G. E., Grove M., Moriguti T. and Nakamura E. (2007) Boron and lead isotope signatures of subduction-zone mélange formation: hybridization and fractionation along the slab–mantle interface beneath volcanic arcs. *Chem. Geol.* **239**, 305-322.

- Kodolányi J., Pettke T., Spandler C., Kamber B. S. and Gméling K. (2012) Geochemistry of ocean floor and fore-arc serpentinites: constraints on the ultramafic input to subduction zones. *J. Petrol.* **53**, 235-270.
- Konrad-Schmolke M. and Halama R. (2014) Combined thermodynamic–geochemical modeling in metamorphic geology: Boron as tracer of fluid–rock interaction. *Lithos* **208-209**, 393-414.
- Konrad-Schmolke M., Halama R. and Manea V. C. (2016) Slab mantle dehydrates beneath Kamchatka–Yet recycles water into the deep mantle. *Geochemistry, Geophysics, Geosystems* **17**, 2987-3007.
- Leeman W. P. (1996) Implications for Subduction Processes. *Subduction Top to Bottom* **96**, 269.
- Leeman W. P. and Sisson V. B. (2018) Geochemistry of boron and its implications for crustal and mantle processes. In *Boron*. De Gruyter. pp. 645-708.
- Leeman W. P., Tonarini S., Chan L. H. and Borg L. E. (2004) Boron and lithium isotopic variations in a hot subduction zone—the southern Washington Cascades. *Chem. Geol.* **212**, 101-124.
- Leeman W. P., Tonarini S. and Turner S. (2017) Boron isotope variations in Tonga-Kermadec-New Zealand arc lavas: Implications for the origin of subduction components and mantle influences. *Geochemistry, Geophysics, Geosystems* **18**, 1126-1162.
- Li H., Li X., Ryan J. G., Zhang C. and Xu Y. (2022) Boron isotopes in boninites document rapid changes in slab inputs during subduction initiation. *Nat. Commun.* **13**.
- Mahony S. H., Wallace L. M., Miyoshi M., Villamor P., Sparks R. S. J. and Hasenaka T. (2011) Volcano-tectonic interactions during rapid plate-boundary evolution in the Kyushu region, SW Japan. *Geol. Soc. Am. Bull.* **123**, 2201-2223.

- Marschall H. R. (2006) Syros Metasomatic Tourmaline: Evidence for Very High- 11B Fluids in Subduction Zones. *J. Petrol.* **47**, 1915-1942.
- Marschall H. R., Altherr R., Ludwig T., Kalt A., Gméling K. and Kasztovszky Z. (2006) Partitioning and budget of Li, Be and B in high-pressure metamorphic rocks. *Geochim. Cosmochim. Ac.* **70**, 4750-4769.
- Marschall H. R., Altherr R. and Rüpke L. (2007) Squeezing out the slab — modelling the release of Li, Be and B during progressive high-pressure metamorphism. *Chem. Geol.* **239**, 323-335.
- Marschall H. R., Wanless V. D., Shimizu N., Pogge Von Strandmann P. A. E., Elliott T. and Monteleone B. D. (2017) The boron and lithium isotopic composition of mid-ocean ridge basalts and the mantle. *Geochim. Cosmochim. Ac.* **207**, 102-138.
- Marschall H. and Foster G. (2018) *Boron isotopes*. Springer.
- Martin C., Flores K. E. and Harlow G. E. (2016) Boron isotopic discrimination for subduction-related serpentinites. *Geology* **44**, 899-902.
- Martin C., Flores K. E., Vitale-Brovarone A., Angiboust S. and Harlow G. E. (2020) Deep mantle serpentinitization in subduction zones: Insight from in situ B isotopes in slab and mantle wedge serpentinites. *Chem. Geol.* **545**, 119637.
- Mccaig A. M., Titarenko S. S., Savov I. P., Cliff R. A., Banks D. and Boyce A., et al. (2018) No significant boron in the hydrated mantle of most subducting slabs. *Nat. Commun.* **9**.
- Moran A. E., Sisson V. B. and Leeman W. P. (1992) Boron depletion during progressive metamorphism: implications for subduction processes. *Earth Planet. Sc. Lett.* **111**, 331-349.
- Moriguti T. and Nakamura E. (1998) Across-arc variation of Li isotopes in lavas and implications for crust/mantle recycling at subduction zones. *Earth Planet. Sc. Lett.* **163**, 167-174.

- Morris P. A. (1995) Slab melting as an explanation of Quaternary volcanism and aseismicity in southwest Japan. *Geology* **23**, 395.
- Nakamura E., Campbell I. H. and Sun S. (1985) The influence of subduction processes on the geochemistry of Japanese alkaline basalts. *Nature* **316**, 55-58.
- Nakamura E., Ishikawa T., Birck J. and Allègre C. J. (1992) Precise boron isotopic analysis of natural rock samples using a boron-mannitol complex. *Chem. Geol.* **94**, 193-204.
- Nakamura E., Makishima A., Moriguti T., Kobayashi K., Sakaguchi C. and Yokoyama T., et al. (2003) Comprehensive geochemical analyses of small amounts (< 100 mg) of extraterrestrial samples for the analytical competition related to the sample return mission MUSES-C. *Inst. Space Astronaut. Sci. Rep. SP.* **16**, 49-101.
- Nguyen T. T., Kitagawa H., Pineda Velasco I. and Nakamura E. (2020) Feedback of Slab Distortion on Volcanic Arc Evolution: Geochemical Perspective From Late Cenozoic Volcanism in SW Japan. *Journal of Geophysical Research: Solid Earth* **125**.
- Noguchi M., Kamei A., Suzuki H. and Kobayashi N. (2021) Igneous activity of the Daito granodiorite in Un-nan area, San'in zone, Southwest Japan. *Journal of Geological Society of Japan* **127**, 461-478.
- Pabst S., Zack T., Savov I. P., Ludwig T., Rost D. and Tonarini S., et al. (2012) The fate of subducted oceanic slabs in the shallow mantle: Insights from boron isotopes and light element composition of metasomatized blueschists from the Mariana forearc. *Lithos* **132**, 162-179.
- Peacock S. M. (2009) Thermal and metamorphic environment of subduction zone episodic tremor and slip. *Journal of Geophysical Research: Solid Earth* **114**.
- Peacock S. M. and Hervig R. L. (1999) Boron isotopic composition of subduction-zone metamorphic rocks. *Chem. Geol.* **160**, 281-290.

- Peacock S. M. and Wang K. (1999) Seismic Consequences of Warm versus Cool Subduction Metamorphism: Examples from Southwest and Northeast Japan. *Science* **286**, 937-939.
- Pi J., You C. and Wang K. (2016) The influence of Ryukyu subduction on magma genesis in the Northern Taiwan Volcanic Zone and Middle Okinawa Trough — Evidence from boron isotopes. *Lithos* **260**, 242-252.
- Pineda-Velasco I., Kitagawa H., Nguyen T. T., Kobayashi K. and Nakamura E. (2018) Production of High-Sr Andesite and Dacite Magmas by Melting of Subducting Oceanic Lithosphere at Propagating Slab Tears. *Journal of Geophysical Research: Solid Earth* **123**, 3698-3728.
- Poli S. and Schmidt M. W. (2002) Petrology of subducted slabs. *Annu. Rev. Earth Pl. Sc.* **30**, 207-235.
- Portnyagin M., Hoernle K., Plechov P., Mironov N. and Khubunaya S. (2007) Constraints on mantle melting and composition and nature of slab components in volcanic arcs from volatiles (H₂O, S, Cl, F) and trace elements in melt inclusions from the Kamchatka Arc. *Earth Planet. Sc. Lett.* **255**, 53-69.
- Rondenay S., Abers G. A. and Van Keken P. E. (2008) Seismic imaging of subduction zone metamorphism. *Geology* **36**, 275-278.
- Rosner M., Erzinger J., Franz G. and Trumbull R. B. (2003) Slab-derived boron isotope signatures in arc volcanic rocks from the Central Andes and evidence for boron isotope fractionation during progressive slab dehydration. *Geochemistry, Geophysics, Geosystems* **4**.
- Rupke L. (2004) Serpentine and the subduction zone water cycle. *Earth Planet. Sc. Lett.* **223**, 17-34.
- Sakuyama M. and Nesbitt R. W. (1986) Geochemistry of the Quaternary volcanic rocks of the

- northeast Japan arc. *J. Volcanol. Geoth. Res.* **29**, 413-450.
- Savov I. P., Ryan J. G., D'Antonio M. and Fryer P. (2007) Shallow slab fluid release across and along the Mariana arc-basin system: Insights from geochemistry of serpentinized peridotites from the Mariana fore arc. *Journal of Geophysical Research* **112**.
- Scambelluri M., Müntener O., Ottolini L., Pettke T. T. and Vannucci R. (2004) The fate of B, Cl and Li in the subducted oceanic mantle and in the antigorite breakdown fluids. *Earth Planet. Sc. Lett.* **222**, 217-234.
- Scambelluri M. and Tonarini S. (2012) Boron isotope evidence for shallow fluid transfer across subduction zones by serpentinized mantle. *Geology* **40**, 907-910.
- Schmidt M. and Poli S. (2013) Devolatilization during subduction, 669-701.
- Shibata T. Y. M. I. (2014) Along-arc geochemical variations in Quaternary magmas of northern Kyushu Island, Japan. *Geological Society, London, Special Publications* **385**, 15-29.
- Shimoda G., Tatsumi Y., Nohda S., Ishizaka K. and Jahn B. M. (1998) Setouchi high-Mg andesites revisited: geochemical evidence for melting of subducting sediments. *Earth Planet. Sc. Lett.* **160**, 479-492.
- Shu Y., Nielsen S. G., Zeng Z., Shinjo R., Blusztajn J. and Wang X., et al. (2017) Tracing subducted sediment inputs to the Ryukyu arc-Okinawa Trough system: Evidence from thallium isotopes. *Geochim. Cosmochim. Ac.* **217**, 462-491.
- Smith H. J., Spivack A. J., Staudigel H. and Hart S. R. (1995) The boron isotopic composition of altered oceanic crust. *Chem. Geol.* **126**, 119-135.
- Spandler C., Hermann J., Faure K., Mavrogenes J. A. and Arculus R. J. (2008) The importance of talc and chlorite “hybrid” rocks for volatile recycling through subduction zones; evidence from the high-pressure subduction mélange of New Caledonia. *Contrib. Mineral. Petr.* **155**, 181-198.

- Spandler C. and Pirard C. (2013) Element recycling from subducting slabs to arc crust: A review. *Lithos* **170**, 208-223.
- Spivack A. J. and Edmond J. M. (1987) Boron isotope exchange between seawater and the oceanic crust. *Geochim. Cosmochim. Ac.* **51**, 1033-1043.
- Straub S. M. and Layne G. D. (2002) The systematics of boron isotopes in Izu arc front volcanic rocks. *Earth Planet. Sc. Lett.* **198**, 25-39.
- Sugden P. J., Savov I. P., Agostini S., Wilson M., Halama R. and Meliksetian K. (2020) Boron isotope insights into the origin of subduction signatures in continent-continent collision zone volcanism. *Earth Planet. Sc. Lett.* **538**, 116207.
- Syracuse E. M., van Keken P. E. and Abers G. A. (2010) The global range of subduction zone thermal models. *Phys. Earth Planet. In.* **183**, 73-90.
- Tanaka R. and Nakamura E. (2005) Boron isotopic constraints on the source of Hawaiian shield lavas. *Geochim. Cosmochim. Ac.* **69**, 3385-3399.
- Tatsumi Y. and Hanyu T. (2003) Geochemical modeling of dehydration and partial melting of subducting lithosphere: Toward a comprehensive understanding of high-Mg andesite formation in the Setouchi volcanic belt, SW Japan. *Geochemistry, Geophysics, Geosystems* **4**, 1081.
- Toki T., Higa R., Ijiri A., Tsunogai U. and Ashi J. (2014) Origin and transport of pore fluids in the Nankai accretionary prism inferred from chemical and isotopic compositions of pore water at cold seep sites off Kumano. *Earth, Planets and Space* **66**, 1-14.
- Tonarini S., Leeman W. P. and Ferrara G. (2001) Boron isotopic variations in lavas of the Aeolian volcanic arc, South Italy. *J. Volcanol. Geoth. Res.* **110**, 155-170.
- Tonarini S., Agostini S., Doglioni C., Innocenti F. and Manetti P. (2007) Evidence for serpentinite fluid in convergent margin systems: The example of El Salvador (Central

- America) arc lavas. *Geochemistry, Geophysics, Geosystems* **8**, Q09014.
- Tonarini S., Agostini S., Innocenti F. and Manetti P. (2005) $\delta^{11}\text{B}$ as tracer of slab dehydration and mantle evolution in Western Anatolia Cenozoic Magmatism. *Terra Nova* **17**, 259-264.
- Tonarini S., Leeman W. P. and Leat P. T. (2011) Subduction erosion of forearc mantle wedge implicated in the genesis of the South Sandwich Island (SSI) arc: Evidence from boron isotope systematics. *Earth Planet. Sc. Lett.* **301**, 275-284.
- Tsuyoshi Ishikawa A B. F. T. (1997) Source, composition and distribution of the fluid in the Kurile mantle wedge: Constraints from across-arc variations of Br/Nb and B isotopes. *Earth Planet. Sc. Lett.* **152**, 123-138.
- Tsuyoshi I., Tera F. and Nakazawa T. (2001) Boron isotope and trace element systematics of the three volcanic zones in the Kamchatka arc. *Geochim. Cosmochim. Ac.* **65**, 423-4537.
- van Keken P. E., Hacker B. R., Syracuse E. M. and Abers G. A. (2011) Subduction factory: 4. Depth-dependent flux of H_2O from subducting slabs worldwide. *Journal of Geophysical Research* **116**.
- Vils F., Müntener O., Kalt A. and Ludwig T. (2011) Implications of the serpentine phase transition on the behaviour of beryllium and lithium–boron of subducted ultramafic rocks. *Geochim. Cosmochim. Ac.* **75**, 1249-1271.
- Walowski K. J., Wallace P. J., Clynne M. A., Rasmussen D. J. and Weis D. (2016) Slab melting and magma formation beneath the southern Cascade arc. *Earth Planet. Sc. Lett.* **446**, 100-112.
- Walowski K. J., Wallace P. J., Hauri E. H., Wada I. and Clynne M. A. (2015) Slab melting beneath the Cascade Arc driven by dehydration of altered oceanic peridotite. *Nat. Geosci.* **8**, 404-408.

- Wu F., Turner S. and Schaefer B. F. (2020) Mélange versus fluid and melt enrichment of subarc mantle: A novel test using barium isotopes in the Tonga-Kermadec arc. *Geology* **48**, 1053-1057.
- Yamada C., Tsujimori T., Chang Q. and Kimura J. (2019) Boron isotope variations of Franciscan serpentinites, northern California. *Lithos* **334**, 180-189.
- Yamaoka K., Matsukura S., Ishikawa T., Kawahata H. and Anonymous (2011) Boron contents and isotope compositions of oceanic crusts from the Oman and Troodos Ophiolites **2011**, S11B-S1484B.
- Yamaoka K., Ishikawa T., Matsubaya O., Ishiyama D., Nagaishi K. and Hiroyasu Y., et al. (2012) Boron and oxygen isotope systematics for a complete section of oceanic crustal rocks in the Oman ophiolite. *Geochim. Cosmochim. Ac.* **84**, 543-559.
- Yasuda A., Fujii T. and Kurita K. (1994) Melting phase relations of an anhydrous mid-ocean ridge basalt from 3 to 20 GPa: Implications for the behavior of subducted oceanic crust in the mantle. *Journal of Geophysical Research: Solid Earth* **99**, 9401-9414.
- You C. F., Chan L. H., Spivack A. J. and Gieskes J. M. (1995) Lithium, boron, and their isotopes in sediments and pore waters of Ocean Drilling Program Site 808, Nankai Trough; implications for fluid expulsion in accretionary prisms. *Geology (Boulder)* **23**, 37-40.
- Zhang X., Zhai S., Yu Z., Guo K. and Wang S. (2019) Subduction contribution to the magma source of the Okinawa Trough-Evidence from boron isotopes. *Geol. J.* **54**, 605-613.
- Zhang Y., Gaetani G., Zeng Z., Monteleone B., Yin X. and Wang X., et al. (2021) Halogen (F, Cl) Concentrations and Sr-Nd-Pb-B Isotopes of the Basaltic Andesites From the Southern Okinawa Trough: Implications for the Recycling of Subducted Serpentinites. *Journal of Geophysical Research: Solid Earth* **126**.
- Zhao D., Yanada T., Hasegawa A., Umino N. and Wei W. (2012) Imaging the subducting slabs

and mantle upwelling under the Japan Islands. *Geophys. J. Int.* **190**, 816-828.

Zhao X., Mao J., Liu K., Li Z., Ye H. and Zhou J., et al. (2018) Petrogenesis of the Jurassic adakitic rocks in Gan-Hang Belt South China: Response to the Palaeo-Pacific Plate oblique subduction. *Geol. J.* **53**, 2019-2044.

Tables

Table 3-1. [B] and $\delta^{11}\text{B}$ data of studied samples from the Chugoku district of Southwest Japan

Sample name	Region	Age (Ma)	$\delta^{11}\text{B}$ (‰)	B (ppm)	Nb (ppm)	B/Nb	SiO ₂	MgO	LOI
KARA1	Daisen		-7.2		15		64.67	1.74	
KOR1	Daisen		-4.2		9.26		63.24	2.15	1.69
MISEN1	Daisen		-6.3		13.28		65.09	1.75	0.16
MISEN4	Daisen		-5.9		11		64.9	1.8	
SAN3	Daisen		-6.9		13.14		64.48	1.89	0.19
OS4	Sambe		-3.3		16.67		65.29	1.62	
SAM3	Sambe		-3.8		11		65.43	1.71	
OET1	Oe-takayama		-4.9		8.95		63.68	1.55	
SHIK1	Aonoyama		0.3		10.06		60.5	2.7	1.28
AON4	Aonoyama		-2.2		9		64.48	2.01	0.74
AON2	Aonoyama		-1.5		10		64.2	1.98	0.43
DAKE1	Wakurayama		-3.6		5.45		64.07	1.99	0.17
AON-04	Aonoyama	0.1	-2.2	4.7	5.05	0.93	65.31	2.13	0.45
OE-1	Oe-takayama	1.5	-3.9	5.6	5.46	1.02	65.85	1.01	0.51
WAK-1	Wakurayama	0.9	-3.7	9.5	4.32	2.21	64.25	2.05	0.19
KUR-1	Kurayoshi	1.9	-4.3	5.9	3.96	1.48	63.87	2.74	0.28
YOK-05	Yokota	1.3	-3.4	3.5	4.49	0.78	51.19	9.47	0.48
3053002	Daisen	0.1	-3.3	9.2	4.93	1.86	65.59	2.14	0.32
SAM-19	Sambe		-4.7	9.6	9.36	1.02		1.85	0.2
JA-2	Setouchi	13.4	-7.7	22.7	8.31	2.73	56.4	6.8	
TG1	Setouchi	14.0	-6.8	30.7	5.8	5.29	58.5	9.45	
SD264 (MDYB-2)	Setouchi	12.8	-6.3	64.5	5.4	11.94	58.42	6.05	

Table 3-2. [B] and $\delta^{11}\text{B}$ of different endmembers for the mixing model in Figure 3-9

Endmember	B (ppm)	$\delta^{11}\text{B}$
<i>AOC [a]</i>		
Starting comp.	32	5.5
Fluid (at 100 km depth)	77.4	-14.7

Residue (at 100 km depth)	0.8	-19.5
<i>Sediment [b]</i>		
Starting comp.	80	-3
Fluid (at 100 km depth)	263	-28
Residue (at 100 km depth)	2.6	-32.8
<i>Ultramafic slab ± serpentine [c]</i>		
Starting comp.	46.7	30
Fluid (at 100 km depth)	46	7
Residue (at 100 km depth)	0.5	0.2
<i>Recycled forearc serpentinites [d]</i>		
Starting comp.	46.7	30
Fluid (at 100 km depth)	9	-3.6
Residue (at 100 km depth)	0.1	-8.3
<i>Mantle</i>	0.06	-5

Data source

a: [B] content is from Shu et al. (2017), and $\delta^{11}\text{B}$ value is from the average value of global AOC by Smith et al. (1995);

b: [B] content and $\delta^{11}\text{B}$ value are from You et al. (1997);

c: [B] content is from Scambelluri et al. (2004), and $\delta^{11}\text{B}$ value is from Vils et al. (2009) (abyssal serpentinites);

d: [B] content and $\delta^{11}\text{B}$ value are from Benton et al., 2001 (Mariana forearc serpentinites)

Table 3-3. Parameters of Sr-Nd-Pb contents and isotopic ratios for mixing models

	$\frac{87\text{Sr}}{86\text{Sr}}$	Sr (ppm)	$\frac{143\text{Nd}}{144\text{Nd}}$	Nd (ppm)	$\frac{206\text{Pb}}{204\text{Pb}}$	$\frac{207\text{Pb}}{204\text{Pb}}$	Pb (ppm)
AOC ^a	0.703	203	0.5131	12	17.75	15.41	1.18
Sediment ^a	0.715	165	0.5123	30.9	18.5	15.64	33.4
Serpentinite ^b	0.703	40	0.5131	0.004	17.75	15.41	0.08

^a From Pineda-velasco et al. (2018).

^b The Sr, Nd and Pb concentrations of the slab serpentinites are from Tonarini et al. (2007) and their isotopic compositions are assumed to be the same as that of AOC (Pineda-Velasco et al., 2018).

Chapter 4. A rapid method of simultaneous chromatographic purification of Li and Mg for isotopic analyses using MC-ICP-MS

Abstract

Lithium (Li) and Magnesium (Mg) isotopes have been widely used as valuable tracers to study geological processes. In general, several column separation procedures have been used to separate Li and Mg. In this study, we present an optimized protocol for the rapid and simultaneous purification of Li and Mg, which significantly reduces the separation time, required reagent volume, and procedural blanks compared to previous methods. Samples with small amounts of Li (generally 5 ng Li yielding Mg masses of 1–1200 μg) were separated, with the corresponding yields of Li and Mg being nearly 100%. Lithium and Mg isotope analyses were performed using an MC-ICP-MS (Thermo Scientific NEPTUNE Plus) and only <0.2 ng Li and <150 ng Mg were consumed for each analysis. Matrix-doping experiments reveal that the matrix effect is negligible for the determination of Li and Mg isotopes from a wide array of geological samples using our protocol. The robustness of the protocol has been validated by replicated analyses of standard solutions and geological standards, which yield long-term external 2σ precision better than $\pm 0.6\text{‰}$ for $\delta^7\text{Li}$ and $\pm 0.08\text{‰}$ for $\delta^{26}\text{Mg}$. Lithium and Mg isotopic ratios of all reference materials measured in this study agreed well with previous data within uncertainties. The method developed in this study allows for the rapid and high-purity separation of Li and Mg and subsequent high-precision isotopic analyses of these elements.

Keywords: Li isotope; Mg isotope; Single-step separation; Rapid separation; MC-ICP-MS; Matrix effect

1. Introduction

Lithium and Magnesium are moderate to highly soluble and mobile elements. Their isotopic ratios (i.e., ${}^7\text{Li}/{}^6\text{Li}$, ${}^{25}\text{Mg}/{}^{24}\text{Mg}$, and ${}^{26}\text{Mg}/{}^{24}\text{Mg}$) are significantly fractionated, in particular under low-temperature geological conditions due to their large relative differences in mass. Considering the differences in elemental partitioning and fluid mobility, combinations of Li and Mg isotopic variability in oceanic island basalts, arc lavas, and seafloor serpentinites provide valuable constraints for investigating crustal assimilation, fluid sources, and the nature of water–rock interactions (e.g., [Moriguti and Nakamura, 1998](#); [Teng, 2017](#); [Penniston-Dorland and Liu, 2017](#)).

Generally, a multi-collector inductively coupled plasma mass spectrometry (MC-ICP-MS) has been used for the high-precision determination of Li and Mg isotopes. To eliminate potential isobaric interferences and the matrix effect for Li and Mg masses, it is necessary to analyze purified mono-elemental solutions for the isotopic measurements. Accordingly, a multi-step sample preparation procedure is required, including separating Li and Mg from the sample matrices through cation-exchange chromatography. In general, the purification of Li from geological samples requires one to four separate column step(s) (e.g., [Moriguti and Nakamura, 1998](#); [Tomascak et al., 1999](#); [James and Palmer, 2000](#); [Misra et al., 2009](#)) and of Mg two to three steps (e.g., [Chang et al., 2003](#); [Tipper et al., 2006](#); [Wiechert and Halliday, 2007](#)). Thus, separating both Li and Mg from the geological samples generally requires more than three steps of ion-exchange chromatography to achieve sufficient purification. Recently, a single column separation method was used to separate Li and Mg from geological samples ([Bohlin et al., 2018](#)), but this method still used a relatively large volume of reagents (60 mL) and a relatively long time for separation of both elements (~24 h).

In this study, we present a rapid method for the purification of Li and Mg based on a single-

step separation method (Bohlin et al., 2018), and the volume of resin and reagents are reduced to 1.5 mL and ~22 mL, respectively. As a result, the blanks of Li and Mg are reduced to <2 pg and <0.8 ng, respectively, and the separation time is reduced to about 4.5 h (< 2 h to collect the Li fraction). Li and Mg isotopic measurements were performed using a multi-collector inductively coupled plasma mass spectrometer (MC-ICP-MS). Li isotopic analyses were performed using 10^{13} Ω amplifiers, which allows the measurement of sub-nanogram samples of Li with a high precision of $\pm 0.6\%$ (2σ) and consumes less than 0.2 ng of sample per an analysis. Mg isotopic analyses were performed using 10^{11} Ω amplifiers and consumed less than 150 ng of sample per analysis with a high precision of $\pm 0.08\%$ (2σ). To verify the reliability of the analytical protocol, the Li and Mg isotopic compositions of nine geological reference standards (PCC-1, JP-1, DTS-1, BHVO-2, BCR-1, JB-2, AGV-1, G-2, and SGR-1) are also presented.

2. Experimental Methods

2.1 Reagents and materials

Sample digestion, chemical separation, and mass spectrometric analyses were carried out at the Pheasant Memorial Laboratory for Geochemistry and Cosmochemistry (PML), Institute for Planetary Materials, Okayama University at Misasa (Nakamura et al., 2003). All experiments were carried out on the clean bench of a class 100 all-fresh-type clean room, and the temperature was maintained at 21 ± 1 °C.

Reagents and resins. High purity water (>18.2 M Ω cm $^{-1}$) was prepared using a Milli-Q system (Merck Millipore, France). Guaranteed-grade 46% HF (FUJIFILM Wako Pure Chemical Co.), electronics industry (EL)-grade 70% HNO $_3$ (Kanto Chemical Co., Inc.), and EL-grade 36% HCl (Kanto Chemical Co. Inc.) that is diluted to 6 mol L $^{-1}$ HCl were distilled once using a PFA sub-boiling distillation apparatus. These once-distilled reagents are referred

as 1D-grade. The HCl, HF, and HNO₃ used in the experiments were prepared by diluting 1D-grade HCl, HF, and HNO₃ with water, respectively. The molarities of HCl (0.70 and 1.50 mol L⁻¹) and HF (0.35 mol L⁻¹) used for column separation were conditioned within a 1% uncertainty by titration.

Li and Mg isotopic reference materials. The NIST SRM 8545 standard (LSVEC, Li₂CO₃) dissolved in 0.5 mol L⁻¹ HNO₃ was used as a bracketing calibrator for Li isotopic measurements. The DSM-3 standard (pure magnesium metal from Dead Sea Magnesium Ltd., Israel; (Galy et al., 2003)) dissolved in 0.5 mol L⁻¹ HNO₃ was used as a bracketing calibrator for Mg isotopes. The Li and Mg isotopic compositions of the unknown samples are expressed with the δ notation (‰) relative to the standards as: $\delta^7\text{Li} = ({}^7\text{Li}/{}^6\text{Li})_{\text{sample}}/({}^7\text{Li}/{}^6\text{Li})_{\text{LSVEC}} - 1$ and $\delta^{25 \text{ or } 26}\text{Mg} = ({}^{25 \text{ or } 26}\text{Mg}/{}^{24}\text{Mg})_{\text{sample}}/({}^{25 \text{ or } 26}\text{Mg}/{}^{24}\text{Mg})_{\text{DSM-3}} - 1$, respectively.

The Cambridge-1 standard (Romil Ltd., Waterbeach, Cambridge, UK; (Galy et al., 2003)) was measured as a secondary standard for Mg during the Mg isotope analysis. In addition, the PML-Li1 standard (an in-house Li standard prepared from 1000 $\mu\text{g mL}^{-1}$ standard solution, KANTO Chemical Co., Inc.), PML-Mg1 (an in-house Mg standard prepared from 1000 $\mu\text{g mL}^{-1}$ magnesium solution, FUJIFILM Wako Pure Chemical Co.), and PML-Mg2 (an in-house Mg standard prepared from 10000 $\mu\text{g mL}^{-1}$, Thermo Fisher Scientific Spectrum® 14430 magnesium solution) were also prepared as secondary standards.

Geological samples. The applicability and effectiveness of the developed separation procedure were evaluated by analyzing nine reference materials. These included three peridotites (JP-1 (GSJ), PCC-1 (USGS), DTS-1 (USGS)), three basalts (JB-2 (GSJ), BCR-1 (USGS), BHVO-2 (USGS)), an andesite (AGV-1 (USGS)), a shale (SGR-1 (USGS)) and a granite (G-2 (USGS)).

2.2 Sample and standard preparation

Approximately 20–100 mg powdered samples were weighed in a 7 mL Savillex® Teflon™ PFA screw jar and mixed with 0.6 mL of 30 mol L⁻¹ HF and 0.3 mL of 7 mol L⁻¹ HClO₄. Subsequently, the samples were digested into HF-HClO₄ solutions by the agitation using an ultrasonic bath for three days. Afterward, the samples were dried following the method of Yokoyama et al. (1999) to decompose fluorides. To ensure effective fluoride decomposition, a further step involving the addition of 0.3 mL of 7 mol L⁻¹ HClO₄ was undertaken, followed by sample drying. Subsequently, 0.3 mL of 6 mol L⁻¹ HCl was added, and the sample was dried up at 90 °C. Finally, the decomposed samples were redissolved into 0.7 mol L⁻¹ HCl. Aliquots of sample solutions containing ~5 ng of Li were used for chromatographic separations. The masses of the matrix elements in the loading solution of each sample aliquot, adjusted to Li = 5 ng, are presented in **Table 4-1**.

A synthetic Li-Mg mixed solution (18.2 µg mL⁻¹ for both Li and Mg dissolved in 0.7 mol L⁻¹ HCl) was used to examine the recoveries and elution curves of Li and Mg through chromatographic separation. The Li-Mg mixed solution was prepared by mixing LSVEC and in-house PML-Mg2 standard solutions.

Table 4-1. Loaded masses on column for calibration seen in Figure 4-1.

Element	unit	Peridotite			Basalt			Andesite	Granite	Shale
		JP-1	DTS-1	PCC-1	BHVO-2	BCR-1	JB-2	AGV-1	G-2	SGR-1
Na	ng	441	113	935	17374	9509	9407	16444	4466	755
Al	ng	9998	2524	14948	75949	27653	47778	47228	12061	1174
P	ng	14	15	17	1059	613	240	1038	84	43
K	ng	26	28	31	2013	1165	457	1973	159	82
Ca	ng	10959	2221	16837	85895	19205	43439	18211	2030	2036
Mn	ng	2678	2348	4101	1389	548	999	370	35	11
Fe	ng	17521	16339	272648	90725	36175	61637	24627	2751	721
Mg	ng	77657	70259	122016	45380	8043	16407	4348	670	898
		1	1	8						

Li	ng	5	5	5	5	5	5	5	5	5
Li/Mg	ng/n g	6.4×10^{-6}	7.1×10^{-6}	4.1×10^{-6}	1.1×10^{-4}	6.2×10^{-4}	3.0×10^{-4}	1.1×10^{-3}	7.5×10^{-3}	5.6×10^{-3}
Li/Total cation	ng/n g	5.1×10^{-6}	5.7×10^{-6}	3.3×10^{-6}	1.6×10^{-5}	4.9×10^{-5}	2.8×10^{-5}	4.4×10^{-5}	2.2×10^{-4}	8.7×10^{-4}

2.3 Column chromatography

Bohlin et al. (2018) developed a single cation-exchange chromatography procedure to separate Li and Mg from geological samples using a cation-exchange resin (AGMP-50, BioRad™, Hercules, CA, USA). The method used a column with an aspect ratio of *c.* 60:1 (25 cm height and 4 mm diameter) packed with 3 mL of cation-exchange resin. The use of such a long column resulted in a relatively long time needed for separation of both Li and Mg (~24h) and the method required 60 mL of reagents. In this study, the same cation-exchange resin (AGMP-50) was used, but the column was prepared with 1/2 the aspect ratio (12.5 cm height, 4 mm diameter) and resin volume (1.5 mL) compared to that used by Bohlin et al. (2018), for the separation of Li and Mg from matrix elements. Information concerning the elution protocol, including the pretreatment and volume of each eluate, is presented in **Table 4-2**.

Before sample loading, the resin was cleaned with 7.5 mL of 6 mol L⁻¹ HCl and 7.5 mL of water, then conditioned with 4.5 mL of 0.7 mol L⁻¹ HCl. After loading a sample solution dissolved in 0.1 mL of 0.7 mol L⁻¹ HCl, Al and Ti were extracted with 1.5 mL of 0.35 mol L⁻¹ HF and 1 mL of 0.7 mol L⁻¹ HCl (denoted as E0 in **Table 4-2**). Lithium was then eluted in 0.7 mol L⁻¹ HCl and collected as a 4.5 mL cut (E2 in **Table 4-2**). Pre- and post-E2 cuts (denoted as E1 and E3 in **Table 4-2**, both with 1 mL) were collected to ensure that there was no breakthrough of Li or matrix elements (**Figure 4-1**). Following the collection of Li, Na was washed with 6 mL of 0.7 mol L⁻¹ HCl (E4). The Mg cut was then collected in 5.5 mL of 1.5 mol L⁻¹ HCl (E6), with a pre- and post-Mg cut of 0.5 mL (E5) and 1 mL (E7), respectively. The

total volume of reagent used after sample loading was ~22 mL. All cuts collected were dried at 90 °C, then heated with concentrated HNO₃ at 90 °C. The treatment with HNO₃ transformed the samples into nitrate salts and decomposed any organic matter derived from the resin. The samples were heated at 90 °C till dryness, then dissolved in 0.5 mol L⁻¹ HNO₃. To re-use the resin, the retained elements, divalent and trivalent cations such as Ca, Ba, and REE, were washed out using 15 mL of 6 mol L⁻¹ HCl, then preconditioned using 15 mL of water and conditioned using 4.5 mL of 0.7 mol L⁻¹ HCl before loading the next sample solution.

The volume of resin and reagents used in this study were reduced to 0.5 and 0.4 times those used in Bohlin et al. (2018), respectively. As a result, the duration of the ion-exchange chromatography from the sample loading to the collection of the post-Mg cut was about 4.5 h, which is about 20% of that used in Bohlin et al. (2018).

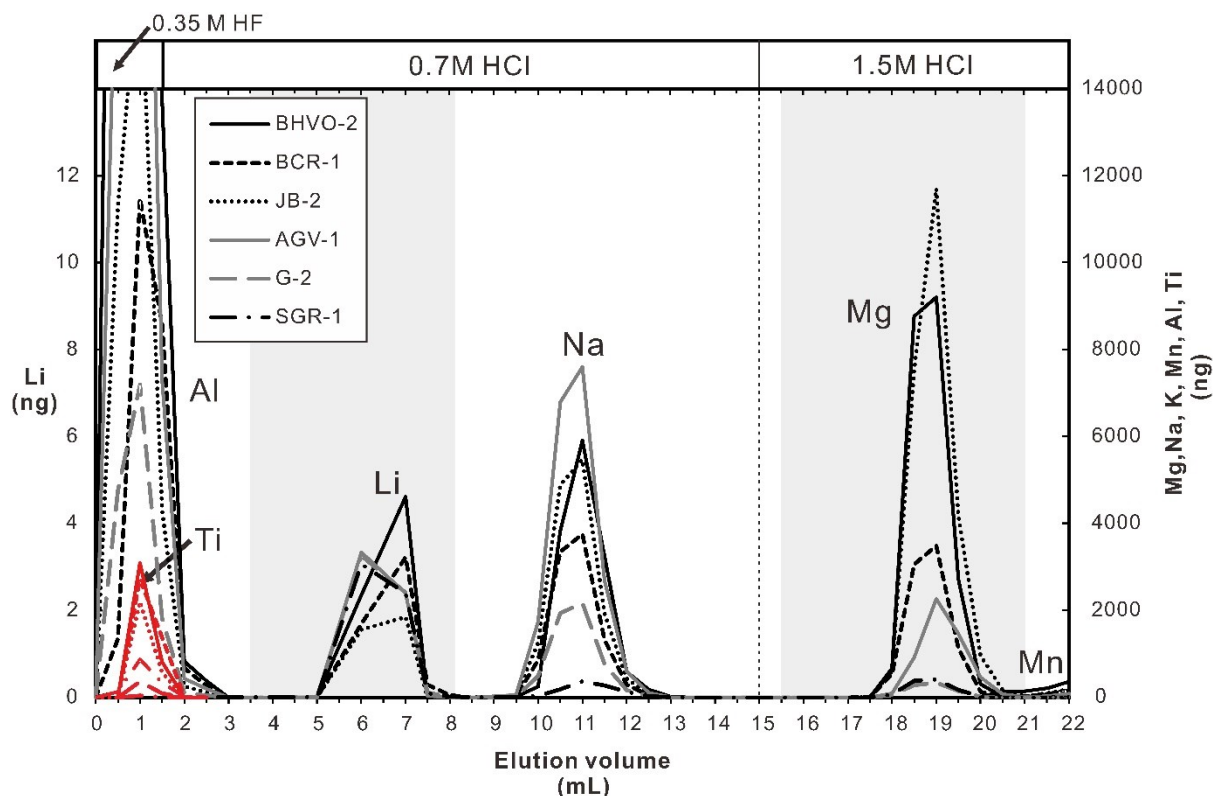


Figure 4-1. Elution curves for separation of Li and Mg from various sample matrices (reference standard silicate rocks).

The calibration was carried out by a collection of every 1 mL eluate fractions. Red lines indicate the Ti fraction to distinguish it from the Al fraction. Fractions of Li and Mg are collected when eluent passes through the column at 3.5–8 mL (in 4.5 mL eluate) and at 15.5–21 mL (in 5.5 mL eluate), respectively. The grey-colored regions indicate the fractions which are collected for Li and Mg isotope analyses. Fe and K are eluted about 2 mL after the Mg fraction (1.5 mol L⁻¹ HCl). For sample composition, see **Table 4-1**.

Table 4-2. Elution protocol for single-step separation of Li and Mg from sample matrices.

Elution cut	Volume	Reagent
Resin cleaning	7.5 mL	6 mol L ⁻¹ HCl
	7.5 mL	Milli-Q
Conditioning	4.5 mL	0.7 mol L ⁻¹ HCl
Load sample	0.1 mL	0.7 mol L ⁻¹ HCl
E0 Al and Ti washout	1.5 mL	0.35 mol L ⁻¹ HF
	1 mL	0.7 mol L ⁻¹ HCl
E1 Pre-Li	1 mL	0.7 mol L ⁻¹ HCl
E2 Li fraction	4.5 mL	0.7 mol L ⁻¹ HCl
E3 Post-Li	1 mL	0.7 mol L ⁻¹ HCl
E4 Na removal	6 mL	0.7 mol L ⁻¹ HCl
E5 Pre-Mg	0.5 mL	1.5 mol L ⁻¹ HCl
E6 Mg fraction	5.5 mL	1.5 mol L ⁻¹ HCl
E7 Post-Mg	1 mL	1.5 mol L ⁻¹ HCl

2.4 Mass spectrometry

The mass fractions of Li, Mg, and matrix elements in the solutions during the ion chromatographic calibrations were measured using a quadrupole ICP-MS (Thermo Scientific iCAP-TQ), with wet plasma conditions. High-precision isotopic determination of both Li (⁷Li/⁶Li) and Mg (²⁵Mg/²⁴Mg and ²⁶Mg/²⁴Mg) was performed by MC-ICP-MS (Thermo Scientific NEPTUNE Plus). We adopted a standard-sample bracketing technique to correct the instrumental drift and mass bias. Concentrations of Li and Mg in both the samples and the standards were typically 0.3 and 200 ng mL⁻¹, respectively, and the concentration of the sample and standard solutions matched within 10%. An instrumental background measurement was

performed by analyzing 0.5 mol L⁻¹ HNO₃ before analyzing each standard and sample solution. Standard and sample measurements were bracketed by background measurements. Thus, background correction was performed by subtracting an average of the background values measured before and after each sample and standard. A secondary standard (PML-Li1 and Cambridge-1 for Li and Mg, respectively) was measured every six samples to determine the external precision of isotope ratios. A gain calibration and electronic baseline measurement were performed at the beginning of a given analytical session.

Li isotopic measurements: The sample introduction system consists of a self-aspirating PFA nebulizer (50 μL/min, Elemental Scientific, USA) and an ARIDUS II (Cetac Technology, USA) desolvation system. The measurement was performed using the combination of a Ni “normal-type” sample cone and a “X-type” skimmer cone and in low-resolution mode. Detection of Li ions was employed using Faraday cups (L5 and H4 cups for ⁶Li and ⁷Li, respectively) equipped with 10¹³ Ω amplifiers. The sensitivity of ⁷Li was 0.35 V per 0.3 ng mL⁻¹ Li. The advantage of using the 10¹³ Ω amplifiers is the better baseline reproducibility (±1.0 μV, 1σ, n = 300, normalized to 10¹¹ Ω) relative to that of 10¹¹ Ω amplifiers (±4.5 μV, 1σ, n = 300), resulting in a 4.5-fold improvement in signal-to noise ratio (S/N) at a ⁶Li⁺ beam intensity of 10–35 mV (normalized to 10¹¹ Ω). Such ultra-low electronic noise allows precise determination of the ⁷Li/⁶Li ratios with ⁶Li⁺ and ⁷Li⁺ beam sizes of ≤35 mV and ≤0.51 V. Additional details of the instrumental setup are presented in **Table 4-3**.

Mg isotopic measurements: The sample introduction system consists of a self-aspirating PFA nebulizer (50 μL min⁻¹, Elemental Scientific, USA) and an APEX-IR desolvation system (Elemental Scientific Inc., USA). The temperatures of the spray chamber and the Peltier cooling coil of the desolvating system were set at 100°C and -3°C, respectively. The measurement was performed using the combination of a Ni “normal-type” sample cone and a

“X-type” skimmer cone and in medium resolution mode. Detection of Mg ions was employed using a Faraday cup (L3, C, and H3 cups for $^{24}\text{Mg}^+$, $^{25}\text{Mg}^+$, and $^{26}\text{Mg}^+$, respectively) equipped with $10^{11} \Omega$ amplifiers. N_2 gas was mixed with the sample aerosol within the desolvator. Although the introduction of N_2 gas increases $^{12}\text{C}^{14}\text{N}^+$ interference on $^{26}\text{Mg}^+$, the $^{12}\text{C}^{14}\text{N}^+$ can be resolved by an offset of the H3 cup ($^{26}\text{Mg}^+$) towards a higher mass in medium resolution mode (**Figure 4-2A** and B). Beyond this drawback, the introduction of N_2 gas improved the signal intensity and stability (**Figure 4-2C** and D) and thus has the advantage of improving the S/N by a factor of 30 to 40 compared to not using N_2 gas. The sensitivity of ^{24}Mg was 20 V per 200 ng mL^{-1} Mg solution. Additional details of the instrumental setup are presented in **Table 4-3**.

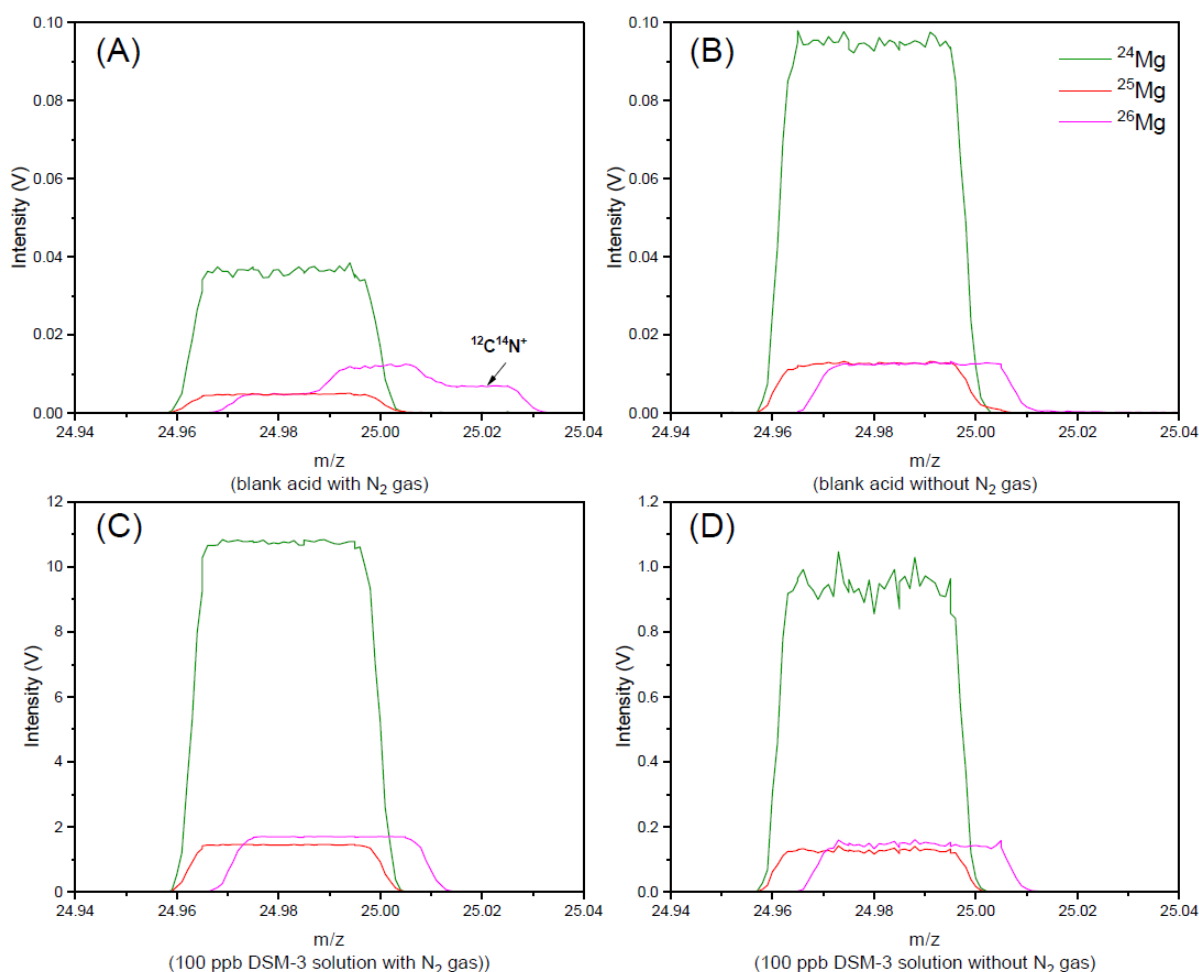


Figure 4-2. Mass scan across $m/z = 25$ amu on the center cup in (A) blank acid ($0.5 \text{ mol L}^{-1} \text{ HNO}_3$) with N_2 gas. (B) blank acid without N_2 gas; (C) 100 ppb DSM-3 solution with N_2 gas; and (D) 100 ppb DSM-3 solution without N_2 gas.

$^{12}\text{C}^{14}\text{N}^+$ interference ($\sim 7.5 \text{ mV}$) is located on the right-hand shoulder of the ^{26}Mg peak and an offset of the H3 cup towards a higher mass quantitatively avoids the CN interference on ^{26}Mg in Figure 4-2B.

Table 4-3. Instrumental parameters for the analysis of Li and Mg isotopes on the NEPTUNE Plus.

	Li	Mg
Preferred concentration	analyte 0.3 ppb (0.35 V on ^7Li)	200 ppb (20 V on ^{24}Mg)
RF-power	1200 W	1200 W
Guard electrode	On	On
Inlet system	Aridus	APEX-IR
Nebulizer aspiration rate	50 $\mu\text{L}/\text{min}$	50 $\mu\text{L}/\text{min}$
Injector	1.8 mm (Platinum)	1.8 mm (Platinum)
Sample cone	Normal (Nickel)	Normal (Nickel)

Skimmer cone	X (Nickel)	X (Nickel)
Faraday cups	L5 (⁶ Li), H4 (⁷ Li)	L3 (²⁴ Mg), C (²⁵ Mg), H3 (²⁶ Mg)
Amplifiers	10 ¹³ Ω	10 ¹¹ Ω
Resolution	Low	Medium
Uptake time	200 s	100 s
Wash time	90 s	90 s
Blocks	1	1
Cycles	56	50
Integration time	4.2 s	4.2 s
Total analysis time per sample	470.4 s	420 s
Sample consumption	<0.2 ng	<150 ng
Matrix	0.5 mol L ⁻¹ HNO ₃	0.5 mol L ⁻¹ HNO ₃
Bracketing standard	LSVEC	DSM-3
Secondary standard	PML-Li1	Cambridge-1

3. Results and discussion

3.1 Sample-standard concentration matching

Several studies have shown the importance of matching the concentrations between the samples and bracketing standards for accurate isotopic analyses (e.g., [Magna et al., 2004](#); [An et al., 2014](#); [Teng et al., 2014](#); [Bohlin et al., 2018](#)). Instrumental backgrounds with very low $\delta^7\text{Li}$ values ($\sim -200\text{‰}$) have been shown to affect measured $^7\text{Li}/^6\text{Li}$ when the concentrations of the bracketing standard and sample have differed by more than 50% ([Huang et al., 2010](#); [Magna et al., 2004](#); [Bohlin et al., 2018](#)). To examine the concentration-dependent mass fractionation, $^7\text{Li}/^6\text{Li}$ of the LSVEC was measured at varying concentrations against the bracketing LSVEC standard (**Figure 4-3A**). The $\delta^7\text{Li}$ values were within the range of analytical uncertainty ($0 \pm 0.6\text{‰}$) for all tested sample/standard concentration ratios from 20% to 160%.

The concentration-dependent Mg isotope fractionation between samples and standards has also been evaluated in previous studies (e.g., [Huang et al., 2009](#); [Wang et al., 201](#)). For example, [Huang et al. \(2009\)](#) observed that the $\delta^{26}\text{Mg}$ value of the sample does not depend on the concentration when the concentrations of Mg in the samples and standards are matched to within 50% for 'dry' plasma conditions. We evaluated the effects of concentration mismatch

between the standards and samples on Mg isotope analysis by measuring DSM-3 with variable concentrations (**Figure 4-3B**). The measured $\delta^{26}\text{Mg}$ values were within the range of analytical uncertainty ($0 \pm 0.08\text{‰}$) when the sample/standard concentration ratios were between 80% and 180% (**Figure 4-3B**).

To avoid the analytical artifact caused by the difference in Li or Mg concentrations between samples and bracketing standards, the concentrations of samples were measured against the bracketing standard (LSVEC and DSM-3) before isotopic analysis. In this study, concentrations of Li and Mg for samples and standards were matched within $\pm 10\%$.

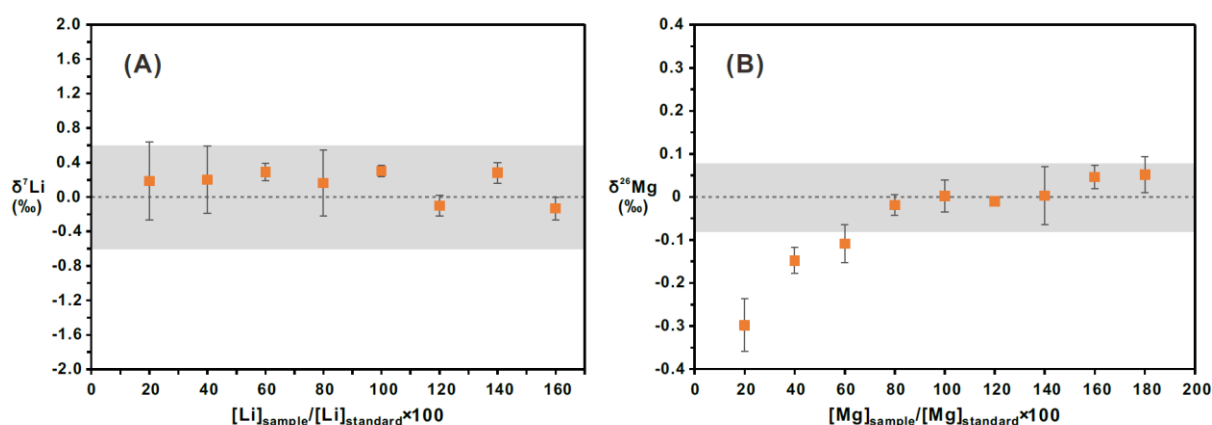


Figure 4-3. $\delta^7\text{Li}$ values of LSVEC (A) and $\delta^{26}\text{Mg}$ values of DSM-3 (B) at varying sample/standard concentration ratios.

The concentrations of Li and Mg of standards were fixed as 0.3 ppb and 200 ppb, respectively. The grey field marks the 2SD external reproducibility in this study ($\pm 0.6\text{‰}$ for LSVEC and $\pm 0.08\text{‰}$ for DSM-3).

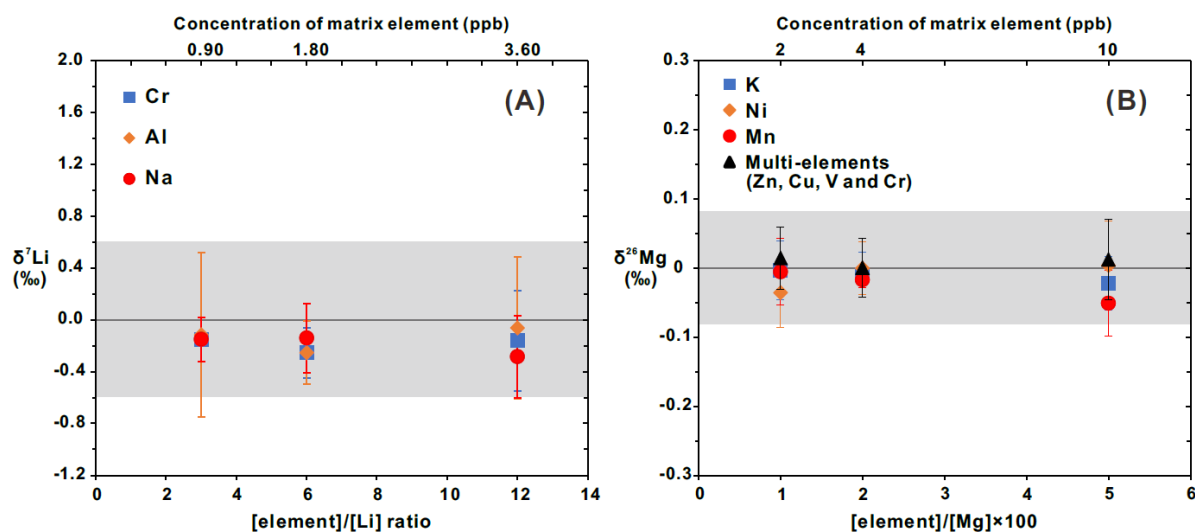


Figure 4-4. Effect of contaminant matrix elements on (A) $\delta^7\text{Li}$ values of LSVEC and (B) $\delta^{26}\text{Mg}$ values of DSM-3.

The concentrations of Li and Mg were fixed as 0.3 ppb and 200 ppb, respectively. The grey fields mark the 2SD external reproducibility in this study ($\pm 0.6\text{‰}$ for $\delta^7\text{Li}$ measurements and $\pm 0.08\text{‰}$ for $\delta^{26}\text{Mg}$ measurements). In the mixture of Mg and multi-element solution, the ratio of each element (Zn, Cu, V and Cr) over Mg was fixed as 0.01, 0.02, and 0.05.

3.2 Recovery yields and blanks of lithium and magnesium

The ion exchange method employed in this study achieved a recovery for Li of $100 \pm 3\%$ and for Mg of $103 \pm 4\%$ ($n = 3$) from the synthetic solution. The recovery yield of Li and Mg from the geological samples was $>99.4\%$ and $>99.8\%$, respectively ($n = 9$). The Li and Mg abundances in the pre-cut (E1 and E5) and post-cut (E3 and E7) of the Li and Mg fractions using geological samples were $<0.2\%$ of the loaded sample masses ($n = 9$), confirming the quantitative recovery of the analytes. Total procedural blanks of Li and Mg were <2 pg and <0.8 ng, respectively ($n = 4$), which are $<1\%$ of the loaded sample masses. Thus, the effect of the total procedural blanks was negligible for the measured Li and Mg isotopic ratios.

3.3 Evaluation of the interfering elements removal procedure

Impurities that were not separated from Li, during column chromatography, could

significantly change the plasma condition and further affect the isotopic ratio of samples (Magna et al., 2004; Huang et al., 2010; Bohlin et al., 2018; Liu et al., 2018; Zhu et al., 2019). Previous studies have reported that the use of a membrane-containing desolvation system (such as Aridus) may result in large instrumental mass bias as a function of the Na/Li, Mg/Li, and Al/Li ratio in the sample solution (Nishio and Nakai, 2002; Magna et al., 2004). The concentrations of Na, Mg, Al, P, K, Ca, Ti, V, Cr, Mn, and Fe in the Li cuts from all nine geological reference samples were measured. All the examined elements, except for Cr in five samples, were below the detection limits (e.g., Na < 0.5 ng, Al < 1.3 ng, and Ti < 0.3 ng). The Cr/Li mass ratio yielded 3.2 for JP-1, 4.3 for DTS-1, 9.7 for BHVO-2, 0.6 for BCR-1, and 1.1 for JB-2.

To evaluate the possible matrix effects, the Li isotopic composition of the LSVEC standard was measured by doping variable amounts of Cr (mass ratios of Cr/Li = 3, 6, and 12). Doping experiments were also performed for Al and Na, which are eluted before and after the Li cut, respectively, using the same Al/Li or Na/Li mass ratios as Cr/Li mass ratios (**Figure 4-4A**). The $\delta^7\text{Li}$ values of the Na, Al, or Cr-doped Li solution are within the external precision of our method in the examined solutions (**Figure 4-4A**). Therefore, the presence of Cr in the Li fraction does not modify the measured isotopic compositions.

For Mg isotopic measurements, it has been reported that matrix elements present in the analyzed solutions could affect the precision and accuracy (e.g., Galy et al., 2001; Huang et al., 2009; Wang et al., 2011; An et al., 2014; Teng et al., 2014), because they not only suppress the ionization and throughput of Mg in the plasma and interface region, but also produce “isobaric interference” on the Mg isotopes. Polyatomic species such as $^{12}\text{C}^{12}\text{C}^+$, $^{12}\text{C}^{13}\text{C}^+$, $^{40}\text{Ar}^{12}\text{C}^{2+}$, $^{12}\text{C}^{14}\text{N}^+$, $^{12}\text{C}^{13}\text{CH}^+$, $^{23}\text{NaH}^+$ and doubly charged species such as $^{48}\text{Ti}^{2+}$, $^{48}\text{Ca}^{2+}$, $^{50}\text{Ti}^{2+}$, $^{50}\text{Cr}^{2+}$, $^{52}\text{Cr}^{2+}$ are the main isobaric interferences for ^{24}Mg , ^{25}Mg , and ^{26}Mg . The presence of matrix

elements, such as Na, Al, Ca, Mn, Ni, Fe, and Cu, in Mg isotopic analysis has been evaluated previously and the general consensus is that an element/Mg ratio <0.05 does not affect the accuracy of isotopic analyses (Galy et al., 2001; Huang et al., 2009; Wang et al., 2011; Teng et al., 2010; Pogge von Strandmann et al., 2011). Concentrations of Na, Al, K, Ca, V, Cr, Mn, Fe, Ni, Cu, Zn, and Ti in the Mg cuts from all nine geological reference samples were measured. Among the examined elements, Na, Al, K, Ca, Fe, and Ti were below the detection limits for all samples, but impurities of V, Cr, Mn, Ni, Cu, and Zn were detected. The recoveries of these transition metal impurities in the Mg cut were V $<30\%$, Cr $<20\%$, Mn $<7\%$, Ni $>90\%$, Cu $>95\%$ and Zn $>95\%$. Although these elements were not fully separated from Mg, the mass ratios of these elements relative to Mg were small: V/Mg <0.003 , Cr/Mg <0.003 , Mn/Mg <0.003 , Ni/Mg <0.011 , Cu/Mg <0.007 , and Zn/Mg <0.016 and the total matrix cations in the Mg cut are $<2\%$.

To evaluate the matrix effect for the Mg isotopic measurements, doping experiments were performed for 200 ppb of Mg solution (DSM-3) by adding 2, 4, and 10 ppb of Mn, Ni, K, or a Zn-Cu-V-Cr mixed solution (i.e., mass ratio of each doped element to Mg was 0.01, 0.02, and 0.05) (**Figure 4-4B**). We observed that the measured Mg isotope ratios were within the external precision of the instrument and remained constant with increasing concentrations of the contaminant elements (**Figure 4-3B**). Although $\sim 30\%$ of V and $\sim 90\text{-}95\%$ of Ni, Cu, and Zn were recovered in the Mg cut, mass fractions of these elements relative to Mg in the silicate rock samples is typically <0.05 (GeoReM database: <http://georem.mpch-mainz.gwdg.de/>). Thus, the proposed separation protocol is applicable for high-precision Mg isotopic analysis of most geological samples. If a sample with significantly high concentrations of these transition metal elements (Ni, Cu, Zn, V and Cr) relative to Mg needs to be analysed, Mg can be further purified using additional column chromatography (e.g., Marechal et al., 1999; Zhu et al., 2002;

Schiller et al., 2014; Wu et al., 2016; Ratnayake et al., 2021).

3.4 Li and Mg isotopic compositions of reference materials

The long-term (24 months) mean $\delta^7\text{Li}$ values of PML-Li1 was $0.0 \pm 0.6\text{‰}$ (2SD, $n = 25$). Mg secondary standard Cambridge-1 yields a long-term (12 months) average $\delta^{26}\text{Mg}$ value of $-2.60 \pm 0.08\text{‰}$ (2SD, $n = 8$), which was identical to published values (Tipper et al., 2006; Teng et al., 2014; Bohlin et al., 2018). The long-term (6 months) mean values of PML-Mg1 and PML-Mg2 were $-0.91 \pm 0.06\text{‰}$ (2SD, $n = 45$) and $-3.90 \pm 0.08\text{‰}$ (2SD, $n = 60$).

To demonstrate the applicability of our technique to various sample matrices and to contribute to the Li and Mg isotope database of the reference standards, Li and Mg isotopic compositions for nine geological reference standards (PCC-1, JP-1, DTS-1, BHVO-2, BCR-1, JB-2, AGV-1, G-2, and SGR-1) were measured (**Figures 4-5 and 4-6**). Our measured Li and Mg isotopic values, in general, are within the uncertainty of the previously published values, validating the effectiveness of the proposed purification and analytical procedure.

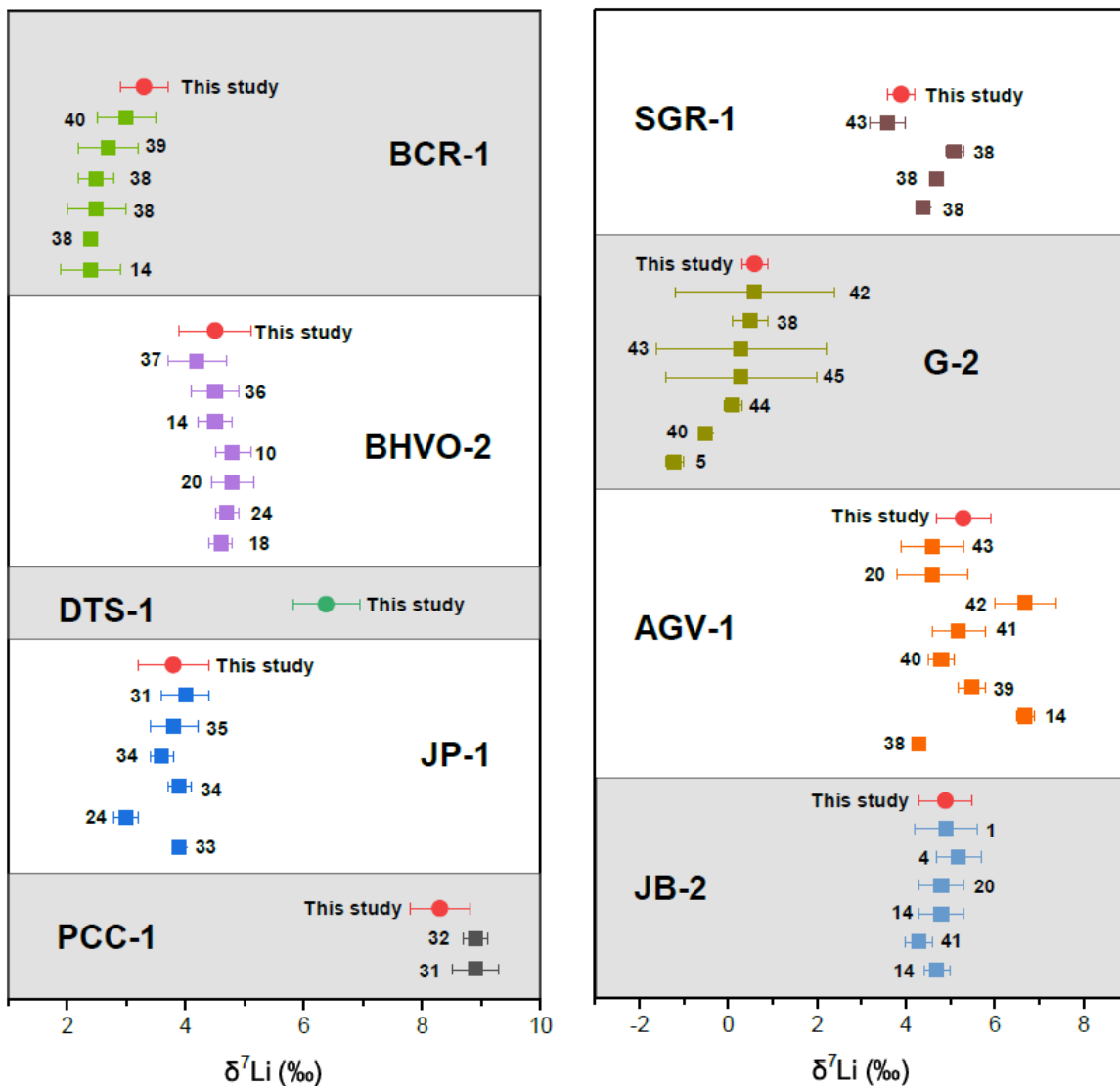


Figure 4-5. $\delta^7\text{Li}$ values for the reference geological samples analyzed in this study in comparison with literature data.

Numbers indicate the data sources, which are listed in **Table 4-4**. Error bars in this figure represent 2SD.

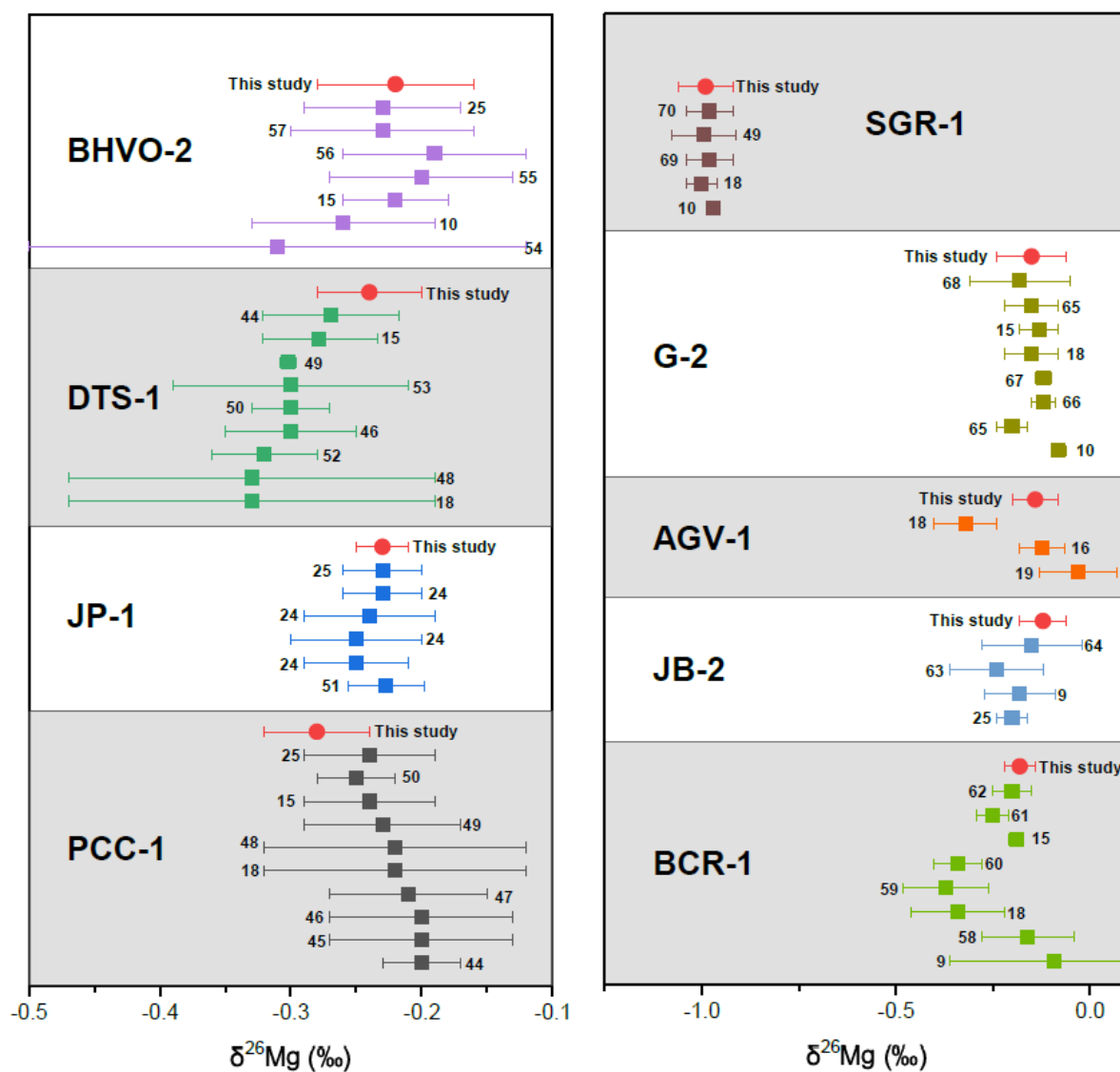


Figure 4-6. $\delta^{26}\text{Mg}$ values for the reference geological samples analyzed in this study in comparison with literature data.

Numbers indicate the data sources, which are listed in **Table 4-5**. Error bars in this figure represent 2SD.

Table 4-4. $\delta^7\text{Li}$ values of reference standards.

	$\delta^7\text{Li}$ (‰)	2σ (‰)	Reference	Reference
PCC-1	8.9	0.4	Magna et al., 2006	31
	8.9	0.2	Seitz et al., 2004	32
	8.3	0.5	This study	
JP-1	3.9	0.1	Magna et al., 2008	33
	3	0.2	Pogge von Strandmann et al., 2011	24

	3.9	0.2	Magna et al., 2015	34
	3.6	0.2	Magna et al., 2015	34
	3.8	0.4	Ackerman et al., 2013	35
	4	0.4	Magna et al., 2006	31
	3.8	0.6	This study	
DTS-1	6.4	0.6	This study	
BHVO-2	4.6	0.2	Huang et al., 2009	18
	4.7	0.2	Pogge von Strandmann et al., 2011	24
	4.8	0.35	Liu et al., 2018	20
	4.8	0.3	Bohlin et al., 2018	10
	4.5	0.3	Magna et al., 2004	14
	4.5	0.4	Choi et al., 2013	36
	4.2	0.5	Vlastélic et al., 2014	37
	4.5	0.5	This study	
BCR-1	2.4	0.5	Magna et al., 2004	14
	2.4	0.1	Phan et al., 2016	38
	2.5	0.5	Phan et al., 2016	38
	2.5	0.3	Phan et al., 2016	38
	2.7	0.5	Rudnick et al., 2004	39
	3	0.5	Aulbach et al., 2009	40
	3.3	0.4	This study	
JB-2	4.7	0.3	Magna et al., 2004	14
	4.3	0.3	Jeffcoate et al., 2004	41
	4.8	0.5	Magna et al., 2004	14
	4.7	0.5	Liu et al., 2018	20
	5.2	0.5	Tomascak et al., 1999	4
	4.9	0.7	Moriguti and Nakamura, 1998	1
	4.9	0.6	This study	
AGV-1	4.3	0.1	Phan et al., 2016	38
	6.7	0.2	Magna et al., 2004	14
	5.5	0.3	Lin et al., 2016	39
	4.8	0.3	Li et al., 2016	40
	5.2	0.6	Liu et al., 2015	41
	6.7	0.7	Sauzeat et al., 2015	42
	4.6	0.8	Liu et al., 2018	20
	4.6	0.7	Liu et al., 2010	43
	5.3	0.6	This study	
G-2	-1.2	0.2	James and Palmer, 2000	5
	-0.5	0.1	Li et al., 2016	40
	0.1	0.2	Pogge von Strandmann, 2019	44

	0.3	1.7	Barnes et al., 2012	45
	0.3	1.9	Liu et al., 2010	43
	0.5	0.4	Phan et al., 2016	38
	0.6	1.8	Sauzeat et al., 2015	42
	0.6	0.3	This study	
SGR-1	4.4	0.1	Phan et al., 2016	38
	4.7	0.1	Phan et al., 2016	38
	5.1	0.2	Phan et al., 2016	38
	3.6	0.4	Pogge von Strandmann et al., 2017	43
	3.9	0.3	This study	

Table 4-5. $\delta^{25}\text{Mg}$ and $\delta^{26}\text{Mg}$ values of reference standards.

	$\delta^{25}\text{Mg}$ (‰)	2σ (‰)	$\delta^{26}\text{Mg}$ (‰)	2σ (‰)	Reference	Reference
PCC-1	-0.10	0.03	-0.20	0.03	An et al., 2017	44
	-0.10	0.04	-0.20	0.07	Su et al., 2015	45
	-0.10	0.05	-0.20	0.07	Hu et al., 2016	46
	-0.13	0.02	-0.21	0.06	Gao et al., 2018	47
	-0.13	0.07	-0.22	0.10	Huang et al., 2009	18
	-0.13	0.07	-0.22	0.10	Huang et al., 2011	48
	-0.10	0.01	-0.23	0.06	Teng et al., 2015	49
	-0.12	0.03	-0.24	0.05	An et al., 2014	15
	-0.13	0.03	-0.25	0.03	Chen et al., 2018	50
	-0.13	0.02	-0.24	0.05	Gao et al., 2019	25
	-0.10	0.01	-0.28	0.04	This study	
JP-1	-0.12	0.02	-0.23	0.03	Handler et al., 2009	51
	-0.12	0.04	-0.25	0.04	Pogge von Strandmann et al., 2011	24
	-0.13	0.05	-0.25	0.05	Pogge von Strandmann et al., 2011	24
	-0.12	0.04	-0.24	0.05	Pogge von Strandmann et al., 2011	24
	-0.12	0.02	-0.23	0.03	Pogge von Strandmann et al., 2011	24
	-0.13	0.04	-0.26	0.06	Gao et al., 2019	25
	-0.13	0.02	-0.23	0.02	This study	
DTS-1	-0.14	0.03	-0.33	0.14	Huang et al., 2009	18
	-0.14	0.03	-0.33	0.14	Huang et al., 2011	48
	-0.16	0.04	-0.32	0.04	Ke et al., 2016	52
	-0.14	0.04	-0.30	0.05	Hu et al., 2016	46
	-0.13	0.03	-0.30	0.03	Chen et al., 2018	50
	-0.13	0.05	-0.30	0.09	Teng et al., 2010	53
	-0.13	0.01	-0.30	0.01	Teng et al., 2015	49
	-0.15	0.00	-0.28	0.04	An et al., 2014	15
	-0.13	0.04	-0.27	0.05	An et al., 2017	44
	-0.12	0.02	-0.24	0.04	This study	

BHVO-2	-0.16	0.11	-0.31	0.19	Opfergelt et al., 2012	54
	-0.14	0.04	-0.26	0.07	Bohlin et al., 2018	10
	-0.10	0.03	-0.22	0.04	An et al., 2014	15
	-0.10	0.05	-0.20	0.07	Lee et al., 2014	55
	-0.10	0.03	-0.19	0.07	Bizzarro et al., 2011	56
	-0.12	0.05	-0.23	0.07	Ryu et al., 2016	57
	-0.12	0.04	-0.25	0.06	Gao et al., 2019	25
	-0.10	0.05	-0.22	0.06	This study	
BCR-1	-0.06	0.06	-0.09	0.27	Wiecher and Halliday, 2007	9
	-0.13	0.05	-0.16	0.12	Bourdon et al., 2010	58
	-0.17	0.08	-0.34	0.12	Huang et al., 2009	18
	-0.19	0.07	-0.37	0.11	Young and Galy, 2004	59
	-0.18	0.04	-0.34	0.06	Teng et al., 2007	60
	-0.10	0.01	-0.19	0.02	An et al., 2014	15
	-0.13	0.02	-0.25	0.04	Fan et al., 2016	61
	-0.12	0.02	-0.20	0.05	Tao et al., 2018	62
-0.07	0.03	-0.18	0.04	This study		
JB-2	-0.09	0.04	-0.20	0.04	Gao et al., 2019	25
	-0.09	0.02	-0.18	0.09	Wiecher and Halliday, 2007	9
	-0.11	0.03	-0.24	0.12	Pogge von Strandmann et al., 2008	63
	-0.08	0.02	-0.15	0.13	Bizzarro et al., 2005	64
	-0.05	0.04	-0.12	0.06	This study	
AGV-1	-0.01	0.01	-0.03	0.10	Wang et al., 2011	19
	-0.06	0.04	-0.12	0.06	Teng et al., 2014	16
	-0.16	0.05	-0.32	0.08	Huang et al., 2009	18
	-0.06	0.03	-0.14	0.06	This study	
G-2	-0.03	0.04	-0.08	0.02	Bohlin et al., 2018	10
	-0.10	0.03	-0.20	0.04	Bao et al., 2019	65
	-0.07	0.05	-0.12	0.03	Liu et al., 2014	66
	-0.06	0.02	-0.12	0.02	Dai et al., 2017	67
	-0.07	0.14	-0.15	0.07	Huang et al., 2009	18
	-0.07	0.04	-0.13	0.05	An et al., 2014	15
	-0.08	0.06	-0.15	0.07	Teng et al., 2014	65
	-0.11	0.08	-0.18	0.13	Bao et al., 2020	68
	-0.06	0.04	-0.15	0.08	This study	
SGR-1	-0.52	0.03	-0.97	0.02	Bohlin et al., 2018	10
			-1.00	0.04	Huang et al., 2009	18
	-0.50	0.06	-0.98	0.06	Wombacher et al., 2009	69
	-0.51	0.03	-1.00	0.08	Teng et al., 2015	49
	-0.51	0.03	-0.98	0.06	Hu et al., 2017	70

4. Conclusions

We developed a rapid chemical separation procedure for the simultaneous purification of Li and Mg with short separation time (~4.5 h), small amounts of reagent (~22 mL), and low blank level (<2 pg and <0.8 ng for Li and Mg, respectively). During Li and Mg isotopic analyses, the matrix effect and effect of concentration-dependent isotopic fractionation between the samples and the standards were evaluated using the NEPTUNE Plus MC-ICP-MS with a dry plasma condition. The matrix effects are negligible both for Li and Mg isotopic ratios for a wide array of geological samples. Based on repeated measurements of standard solutions and geological reference materials, the external reproducibility of $\delta^7\text{Li}$ and $\delta^{26}\text{Mg}$ was better than 0.6 ‰ and 0.08 ‰ (2SD), respectively. The $\delta^7\text{Li}$ of the geological reference materials lies in a range from 0.6 to 8.3‰, whereas the $\delta^{26}\text{Mg}$ ranges from -0.99 to -0.12‰. The $\delta^7\text{Li}$ and $\delta^{26}\text{Mg}$ ratios of geological reference materials are consistent with previously published data, validating that the methods presented here can provide highly accurate and precise measurements of the Li and Mg isotopic ratios in samples with a low Li or Mg concentration.

References

- Ackerman L., Apaček P., Magna T., Ulrych J., Svojtka M. and Hegner E., et al. (2013) Alkaline and carbonate-rich melt metasomatism and melting of subcontinental lithospheric mantle: evidence from mantle xenoliths, NE Bavaria, Bohemian Massif. *J. Petrol.* **54**, 2597-2633.
- An Y., Huang J., Griffin W. L., Liu C. and Huang F. (2017) Isotopic composition of Mg and Fe in garnet peridotites from the Kaapvaal and Siberian cratons. *Geochim. Cosmochim. Acta.* **200**, 167-185.

- An Y., Wu F., Xiang Y., Nan X., Yu X. and Yang J., et al. (2014) High-precision Mg isotope analyses of low-Mg rocks by MC-ICP-MS. *Chem. Geol.* **390**, 9-21.
- Aulbach S. and Rudnick R. L. (2009) Origins of non-equilibrium lithium isotopic fractionation in xenolithic peridotite minerals: examples from Tanzania. *Chem. Geol.* **258**, 17-27.
- Bao Z., Huang K., Huang T., Shen B., Zong C. and Chen K., et al. (2019) Precise magnesium isotope analyses of high-K and low-Mg rocks by MC-ICP-MS. *J. Anal. Atom. Spectrom.* **34**, 940-953.
- Bao Z., Huang K., Xu J., Deng L., Yang S. and Zhang P., et al. (2020) Preparation and characterization of a new reference standard GSB-Mg for Mg isotopic analysis. *J. Anal. Atom. Spectrom.* **35**, 1080-1086.
- Bizzarro M., Baker J. A., Haack H. and Lundgaard K. L. (2005) Rapid timescales for accretion and melting of differentiated planetesimals inferred from ^{26}Al - ^{26}Mg chronometry. *The Astrophysical Journal Letters* **632**, L41.
- Bizzarro M., Paton C., Larsen K., Schiller M., Trinquier A. and Ulfbeck D. (2011) High-precision Mg-isotope measurements of terrestrial and extraterrestrial material by HR-MC-ICPMS—implications for the relative and absolute Mg-isotope composition of the bulk silicate Earth. *J. Anal. Atom. Spectrom.* **26**, 565-577.
- Bohlin M. S., Misra S., Lloyd N., Elderfield H. and Bickle M. J. (2017) High-precision determination of lithium and magnesium isotopes utilising single column separation and multi-collector inductively coupled plasma mass spectrometry. *Rapid Commun. Mass Sp.* **32**, 93-104.
- Bourdon B., Tipper E. T., Fitoussi C. and Stracke A. (2010) Chondritic Mg isotope composition of the Earth. *Geochim. Cosmochim. Ac.* **74**, 5069-5083.
- Chang V. T., Makishima A., Belshaw N. S. and O'Nions R. K. (2003) Purification of Mg from

- low-Mg biogenic carbonates for isotope ratio determination using multiple collector ICP-MS. *J. Anal. Atom. Spectrom.* **18**, 296-301.
- Chen L., Teng F., Song X., Hu R., Yu S. and Zhu D., et al. (2018) Magnesium isotopic evidence for chemical disequilibrium among cumulus minerals in layered mafic intrusion. *Earth Planet. Sc. Lett.* **487**, 74-83.
- Choi M. S., Ryu J., Park H. Y., Lee K., Kil Y. and Shin H. S. (2013) Precise determination of the lithium isotope ratio in geological samples using MC-ICP-MS with cool plasma. *J. Anal. Atom. Spectrom.* **28**, 505-509.
- Dai L., Zhao Z., Zheng Y., An Y. and Zheng F. (2017) Geochemical distinction between carbonate and silicate metasomatism in generating the mantle sources of alkali basalts. *J. Petrol.* **58**, 863-884.
- Fan B., Zhao Z., Tao F., Li X., Tao Z. and Gao S., et al. (2016) The geochemical behavior of Mg isotopes in the Huanghe basin, China. *Chem. Geol.* **426**, 19-27.
- Galy A., Belshaw N. S., Halicz L. and O Nions R. K. (2001) High-precision measurement of magnesium isotopes by multiple-collector inductively coupled plasma mass spectrometry. *Int. J. Mass Spectrom.* **208**, 89-98.
- Galy A., Yoffe O., Janney P. E., Williams R. W., Cloquet C. and Alard O., et al. (2003) Magnesium isotope heterogeneity of the isotopic standard SRM980 and new reference materials for magnesium-isotope-ratio measurements. *J. Anal. Atom. Spectrom.* **18**, 1352-1356.
- Gao T., Ke S., Li R., Meng X., He Y. and Liu C., et al. (2019) High-precision magnesium isotope analysis of geological and environmental reference materials by multiple-collector inductively coupled plasma mass spectrometry. *Rapid Commun Mass Spectrom* **33**, 767-777.

- Gao T., Ke S., Wang S., Li F., Liu C. and Lei J., et al. (2018) Contrasting Mg isotopic compositions between Fe-Mn nodules and surrounding soils: Accumulation of light Mg isotopes by Mg-depleted clay minerals and Fe oxides. *Geochim. Cosmochim. Ac.* **237**, 205-222.
- Handler M. R., Baker J. A., Schiller M., Bennett V. C. and Yaxley G. M. (2009) Magnesium stable isotope composition of Earth's upper mantle. *Earth Planet. Sc. Lett.* **282**, 306-313.
- Hu Y., Teng F., Plank T. and Huang K. (2017) Magnesium isotopic composition of subducting marine sediments. *Chem. Geol.* **466**, 15-31.
- Hu Y., Teng F., Zhang H., Xiao Y. and Su B. (2016) Metasomatism-induced mantle magnesium isotopic heterogeneity: evidence from pyroxenites. *Geochim. Cosmochim. Ac.* **185**, 88-111.
- Huang F., Glessner J., Ianno A., Lundstrom C. and Zhang Z. (2009) Magnesium isotopic composition of igneous rock standards measured by MC-ICP-MS. *Chem. Geol.* **268**, 15-23.
- Huang F., Zhang Z., Lundstrom C. C. and Zhi X. (2011) Iron and magnesium isotopic compositions of peridotite xenoliths from Eastern China. *Geochim. Cosmochim. Ac.* **75**, 3318-3334.
- Huang K., You C., Liu Y., Wang R., Lin P. and Chung C. (2010) Low-memory, small sample size, accurate and high-precision determinations of lithium isotopic ratios in natural materials by MC-ICP-MS. *J. Anal. Atom. Spectrom.* **25**, 1019.
- James R. H. and Palmer M. R. (2000) The lithium isotope composition of international rock standards. *Chem. Geol.* **166**, 319-326.
- Jeffcoate A. B., Elliott T., Thomas A. and Bouman C. (2004) Precise/small sample size determinations of lithium isotopic compositions of geological reference materials and modern seawater by MC-ICP-MS. *Geostand. Geoanal. Res.* **28**, 161-172.

- Ke S., Teng F., Li S., Gao T., Liu S. and He Y., et al. (2016) Mg, Sr, and O isotope geochemistry of syenites from northwest Xinjiang, China: Tracing carbonate recycling during Tethyan oceanic subduction. *Chem. Geol.* **437**, 109-119.
- Lee S., Ryu J. and Lee K. (2014) Magnesium isotope geochemistry in the Han River, South Korea. *Chem. Geol.* **364**, 9-19.
- Liu X., Teng F., Rudnick R. L., McDonough W. F. and Cummings M. L. (2014) Massive magnesium depletion and isotope fractionation in weathered basalts. *Geochim. Cosmochim. Ac.* **135**, 336-349.
- Liu Y., Huang K. and Lee D. (2018) Precise and accurate boron and lithium isotopic determinations for small sample-size geological materials by MC-ICP-MS. *J. Anal. Atom. Spectrom.* **33**, 846-855.
- Magna T., Day J. M., Mezger K., Fehr M. A., Dohmen R. and Aoudjehane H. C., et al. (2015) Lithium isotope constraints on crust–mantle interactions and surface processes on Mars. *Geochim. Cosmochim. Ac.* **162**, 46-65.
- Magna T., Ionov D. A., Oberli F. and Wiechert U. (2008) Links between mantle metasomatism and lithium isotopes: Evidence from glass-bearing and cryptically metasomatized xenoliths from Mongolia. *Earth Planet. Sc. Lett.* **276**, 214-222.
- Magna T., Wiechert U. H. and Halliday A. N. (2004) Low-blank isotope ratio measurement of small samples of lithium using multiple-collector ICPMS. *Int. J. Mass Spectrom.* **239**, 67-76.
- Magna T., Wiechert U. and Halliday A. N. (2006) New constraints on the lithium isotope compositions of the Moon and terrestrial planets. *Earth Planet. Sc. Lett.* **243**, 336-353.
- Marechal C. N., Telouk P. and Albarede F. (1999) Precise analysis of copper and zinc isotopic compositions by plasma-source mass spectrometry. *Chem. Geol.* **156**, 251-273.

- Misra S. and Froelich P. N. (2009) Measurement of lithium isotope ratios by quadrupole-ICP-MS: application to seawater and natural carbonates. *J. Anal. Atom. Spectrom.* **24**, 1524.
- Moriguti T. and Nakamura E. (1998) High-yield lithium separation and the precise isotopic analysis for natural rock and aqueous samples. *Chem. Geol.* **145**, 91-104.
- Nakamura E., Makishima A., Moriguti T., Kobayashi K., Sakaguchi C. and Yokoyama T., et al. (2003) Comprehensive geochemical analyses of small amounts (< 100 mg) of extraterrestrial samples for the analytical competition related to the sample return mission MUSES-C. *Inst. Space Astronaut. Sci. Rep. SP.* **16**, 49-101.
- Nishio Y. and Nakai S. I. (2002) Accurate and precise lithium isotopic determinations of igneous rock samples using multi-collector inductively coupled plasma mass spectrometry. *Anal. Chim. Acta* **456**, 271-281.
- Opfergelt S., Georg R. B., Delvaux B., Cabidoche Y., Burton K. W. and Halliday A. N. (2012) Mechanisms of magnesium isotope fractionation in volcanic soil weathering sequences, Guadeloupe. *Earth Planet. Sc. Lett.* **341**, 176-185.
- Penniston-Dorland S., Liu X. and Rudnick R. L. (2017) Lithium Isotope Geochemistry. *Reviews in Mineralogy and Geochemistry* **82**, 165-217.
- Phan T. T., Capo R. C., Stewart B. W., Macpherson G. L., Rowan E. L. and Hammack R. W. (2016) Factors controlling Li concentration and isotopic composition in formation waters and host rocks of Marcellus Shale, Appalachian Basin. *Chem. Geol.* **420**, 162-179.
- Pogge Von Strandmann P. A., Elliott T., Marschall H. R., Coath C., Lai Y. and Jeffcoate A. B., et al. (2011) Variations of Li and Mg isotope ratios in bulk chondrites and mantle xenoliths. *Geochim. Cosmochim. Ac.* **75**, 5247-5268.
- Pogge Von Strandmann P. A., James R. H., van Calsteren P., Gíslason S. R. and Burton K. W. (2008) Lithium, magnesium and uranium isotope behaviour in the estuarine environment of

- basaltic islands. *Earth Planet. Sc. Lett.* **274**, 462-471.
- Pogge Von Strandmann P. A., Vaks A., Bar-Matthews M., Ayalon A., Jacob E. and Henderson G. M. (2017) Lithium isotopes in speleothems: Temperature-controlled variation in silicate weathering during glacial cycles. *Earth Planet. Sc. Lett.* **469**, 64-74.
- Ratnayake D. M., Tanaka R. and Nakamura E. (2021) Novel nickel isolation procedure for a wide range of sample matrices without using dimethylglyoxime for isotope measurements using MC-ICP-MS. *Anal. Chim. Acta* **1181**, 338934.
- Rudnick R. L., Tomascak P. B., Njo H. B. and Gardner L. R. (2004) Extreme lithium isotopic fractionation during continental weathering revealed in saprolites from South Carolina. *Chem. Geol.* **212**, 45-57.
- Ryu J., Vigier N., Decarreau A., Lee S., Lee K. and Song H., et al. (2016) Experimental investigation of Mg isotope fractionation during mineral dissolution and clay formation. *Chem. Geol.* **445**, 135-145.
- Sauzéat L., Rudnick R. L., Chauvel C., Garçon M. and Tang M. (2015) New perspectives on the Li isotopic composition of the upper continental crust and its weathering signature. *Earth Planet. Sc. Lett.* **428**, 181-192.
- Schiller M., Van Kooten E., Holst J. C., Olsen M. B. and Bizzarro M. (2014) Precise measurement of chromium isotopes by MC-ICPMS. *J Anal At Spectrom* **29**, 1406-1416.
- Seitz H., Brey G. P., Lahaye Y., Durali S. and Weyer S. (2004) Lithium isotopic signatures of peridotite xenoliths and isotopic fractionation at high temperature between olivine and pyroxenes. *Chem. Geol.* **212**, 163-177.
- Su B., Teng F., Hu Y., Shi R., Zhou M. and Zhu B., et al. (2015) Iron and magnesium isotope fractionation in oceanic lithosphere and sub-arc mantle: Perspectives from ophiolites. *Earth Planet. Sc. Lett.* **430**, 523-532.

- Tao R., Zhang L., Li S., Zhu J. and Ke S. (2018) Significant contrast in the Mg-C-O isotopes of carbonate between carbonated eclogite and marble from the S.W. Tianshan UHP subduction zone: Evidence for two sources of recycled carbon. *Chem. Geol.* **483**, 65-77.
- Teng F. Z., Li W. Y., Ke S., Yang W., Liu S. A. and Sedaghatpour F., et al. (2015) Magnesium isotopic compositions of international geological reference materials. *Geostand. Geoanal. Res.* **39**, 329-339.
- Teng F. (2017) Magnesium Isotope Geochemistry. *Reviews in Mineralogy and Geochemistry* **82**, 219-287.
- Teng F., Li W., Rudnick R. L. and Gardner L. R. (2010) Contrasting lithium and magnesium isotope fractionation during continental weathering. *Earth Planet. Sc. Lett.* **300**, 63-71.
- Teng F., Wadhwa M. and Helz R. T. (2007) Investigation of magnesium isotope fractionation during basalt differentiation: implications for a chondritic composition of the terrestrial mantle. *Earth Planet. Sc. Lett.* **261**, 84-92.
- Teng F. and Yang W. (2014) Comparison of factors affecting the accuracy of high-precision magnesium isotope analysis by multi-collector inductively coupled plasma mass spectrometry. *Rapid Commun. Mass Sp.* **28**, 19-24.
- Tipper E. T., Galy A., Gaillardet J., Bickle M. J., Elderfield H. and Carder E. A. (2006) The magnesium isotope budget of the modern ocean: constraints from riverine magnesium isotope ratios. *Earth Planet. Sc. Lett.* **250**, 241-253.
- Tomascak P. B., Tera F., Helz R. T. and Walker R. J. (1999) The absence of lithium isotope fractionation during basalt differentiation: new measurements by multicollector sector ICP-MS. *Geochim. Cosmochim. Ac.* **63**, 907-910.
- Vlastélic I., Staudacher T., Bachèlery P., Télouk P., Neuville D. and Benbakkar M. (2011) Lithium isotope fractionation during magma degassing: constraints from silicic

- differentiates and natural gas condensates from Piton de la Fournaise volcano (Réunion Island). *Chem. Geol.* **284**, 26-34.
- Wang G., Lin Y., Liang X., Liu Y., Xie L. and Yang Y., et al. (2011) Separation of magnesium from meteorites and terrestrial silicate rocks for high-precision isotopic analysis using multiple collector-inductively coupled plasma-mass spectrometry. *J. Anal. Atom. Spectrom.* **26**, 1878-1886.
- Wiechert U. and Halliday A. N. (2007) Non-chondritic magnesium and the origins of the inner terrestrial planets. *Earth Planet. Sc. Lett.* **256**, 360-371.
- Wombacher F., Eisenhauer A., Heuser A. and Weyer S. (2009) Separation of Mg, Ca and Fe from geological reference materials for stable isotope ratio analyses by MC-ICP-MS and double-spike TIMS. *J. Anal. Atom. Spectrom.* **24**, 627-636.
- Wu F., Qi Y., Yu H., Tian S., Hou Z. and Huang F. (2016) Vanadium isotope measurement by MC-ICP-MS. *Chem. Geol.* **421**, 17-25.
- Yokoyama T., Makishima A. and Nakamura E. (1999) Evaluation of the coprecipitation of incompatible trace elements with fluoride during silicate rock dissolution by acid digestion. *Chem. Geol.* **157**, 175-187.
- Young E. D. and Galy A. (2004) The isotope geochemistry and cosmochemistry of magnesium. *Reviews in Mineralogy and Geochemistry* **55**, 197-230.
- Zhu X. K., Guo Y., Williams R. J. P., O'Nions R. K., Matthews A. and Belshaw N. S., et al. (2002) Mass fractionation processes of transition metal isotopes. *Earth Planet. Sc. Lett.* **200**, 47-62.
- Zhu Z., Yang T. and Zhu X. (2019) Achieving rapid analysis of Li isotopes in high-matrix and low-Li samples with MC-ICP-MS: new developments in sample preparation and mass bias behavior of Li in ICPMS. *J. Anal. Atom. Spectrom.* **34**, 1503-1513.

Chapter 5. Lithium isotope constraints on slab and mantle contribution to arc magmas in SW Japan

Abstract

Dehydration of subducting oceanic lithosphere (slab) induces Li-isotope fractionation between the fluid and the slab, suggested by the $\delta^7\text{Li}$ variation ($\sim 10\%$) in exhumed subduction complexes. Given that arc magmas represent melt of the supraslab mantle, a large $\delta^7\text{Li}$ variation is anticipated for arc volcanic rocks. However, the $\delta^7\text{Li}$ values in these rocks are mostly homogeneous within the range of mid-ocean ridge basalts ($+1.6$ to $+5.6\%$). The lack of a subduction-related $\delta^7\text{Li}$ signature has been explained by (1) homogenization by mixing of different magma sources, (2) loss of Li from the slab via dehydration, or (3) homogenization by diffusive exchange of slab-derived Li and the mantle. The Chugoku district in SW Japan is an ideal place to study the process responsible for Li-isotope variation in arc magmas, since the Chugoku volcanic rocks show large $\delta^7\text{Li}$ variation (-1.9 to $+7.4\%$). High $\delta^7\text{Li}$ values ($+6.3$ to $+7.4\%$) are found in some high-Sr andesites and dacites (adakites) whereas low $\delta^7\text{Li}$ values (-1.0 to -0.1%) are found in high-Mg andesites. The parental magmas of these rocks have been sourced from subducted oceanic crust and sediments, respectively, with various extents of the interaction with wedge mantle. The limited extents of Li isotope modification are indicated by the similarity of the $\delta^7\text{Li}$ values of these rocks and their supposed sources. The models for a slab dehydration and a diffusive exchange between slab-derived melt and mantle demonstrate that the $\delta^7\text{Li}$ signatures of the sources can be preserved in the adakites if they ascent rapidly in mantle.

1. Introduction

It is generally accepted that fluids play a critical role in the production of arc magmas (Ishikawa & Nakamura, 1994; Nakamura et al., 1985; Perfit et al., 1980; Sakuyama & Nesbitt, 1986). Fluids lower the solidi of magma sources, thus inducing melting without the need for mantle with an anomalously high temperature. Fluids are considered to be expelled from oceanic lithospheric rocks during their subduction beneath an arc. Fluids also transport elements via dissolution of materials in subducted oceanic lithosphere (slab), resulting in elemental enrichments in arc magmas. The extents of the enrichments are related to the elemental solubility of a given element or group. For example, alkali metals and alkaline earth metals are highly soluble in fluids and thus are enriched in arc magmas (Kessel et al., 2005).

Lithium represents an element with a high solubility in fluids (Kessel et al., 2005). It has two isotopes (${}^7\text{Li}$ and ${}^6\text{Li}$) that fractionate during element partitioning between two substances; e.g., fluid and rock or vapor and melt (Penniston-Dorland et al., 2017; Tomascak et al., 2016). In general, ${}^7\text{Li}$ are preferentially transferred into fluids (Caciagli et al., 2011; Wunder et al., 2006), and as a result, arc volcanic rocks are expected to record high $\delta^7\text{Li}$ values from their hydrated sources. However, $\delta^7\text{Li}$ values of most arc rocks fall within the range of unaltered mid-ocean ridge basalts (MORB with $\delta^7\text{Li} = +1.6$ to $+5.6\text{‰}$; Marschall et al., 2017; Tomascak et al., 2008). Given that MORB likely represent a well-averaged melt extracted from the upper mantle (Langmuir et al., 1992), the $\delta^7\text{Li}$ value of MORB well approximates the $\delta^7\text{Li}$ value of the upper mantle ($+1.4$ to $+5.2\text{‰}$), postulated by the analyses of pristine mantle rocks (Jeffcoate et al., 2007; Lai et al., 2015; Magna et al., 2006a; Pogge von Strandmann et al., 2011; Seitz et al., 2004). Accordingly, the similarity of $\delta^7\text{Li}$ between MORB and arc volcanic rocks has been interpreted to reflect the prevalence of the upper mantle as a source of Li in arc magmas (Tomascak et al., 2002). The apparent similarity in $\delta^7\text{Li}$ values of arc magmas and MORB has been explained by the three scenarios: (1) homogenization by mixing of different magma

sources, (2) loss of Li from the slab via dehydration, or (3) homogenization by diffusive exchange of slab-derived Li and the mantle.

Scenario 1 explains the lack of a subduction-related $\delta^7\text{Li}$ signal by the contributions of Li from various materials of the subducting oceanic lithosphere, including sediments (silicate/carbonate), basalts and serpentinites. Sediments have high [Li] ($>10 \text{ mg}\cdot\text{g}^{-1}$ except for specific types such as foram ooze, marl and diatom, or volcano clastics; [Bouman et al., 2004](#); [Brens et al., 2019](#); [Chan et al., 2006](#); [Plank, 2014](#); [Tang et al., 2014](#); [You et al., 1995](#)), hence fluids or melts from sediments could represent a significant Li budget in arc magma sources. Some serpentinitized abyssal peridotites have $\delta^7\text{Li}$ values as high as +20‰ ([Brant et al., 2012](#); [Decitre et al., 2002](#); [Vils et al., 2008](#)), and hence could be another potential reservoir. Previous studies found that $\delta^7\text{Li}$ values of sediments subducting in some trenches [$+3.9 \pm 2.3\%$ (1σ); [Plank, 2014](#); [Tang et al., 2014](#)] are similar to that of the mantle (i.e., $\delta^7\text{Li}$ of MORB, +1.6 to +5.6‰). Thus, if sediment dominates subduction Li inputs, the arc magmas should have $\delta^7\text{Li}$ values indistinguishable from MORB.

Scenario 2 explains the lack of subduction-related $\delta^7\text{Li}$ signal by extensive dehydration of the oceanic lithosphere ([Leeman et al., 2004](#); [Magna et al., 2006b](#); [Moriguti et al. 2004](#)). The dehydration was proposed to substantially lower [Li] and $\delta^7\text{Li}$ values before the slab reaches the depth (70–170 km; [Syracuse & Abers, 2006](#)) beneath arc volcanoes ([Moriguti and Nakamura, 1998](#); [Zack et al., 2003](#)). In particular, dehydration occurs at shallower depths in relatively warm subduction zones ([Abers et al., 2017](#)). Accordingly, the sources of magmas in warm subduction zones are considered to contain little slab-derived Li. Instead, the Li in the magma source is dominated by that from the mantle, which should have a $\delta^7\text{Li}$ value similar to MORB. This inference is consistent with across-arc variations in [Li] and $\delta^7\text{Li}$ value of some arc lavas which include low-[Li] rocks with MORB-like $\delta^7\text{Li}$ value from back-arc regions (e.g.,

central America; [Tomascak et al., 2000](#)).

Scenario 3 explains the lack of subduction-related $\delta^7\text{Li}$ signal by re-equilibration of Li between slab-derived fluids and the overlying mantle. When fluids ascend through the mantle, they should react with the mantle. The abundance of Li in the mantle ($\sim 1 \text{ mg}\cdot\text{g}^{-1}$; [Marschall et al., 2017](#)) appears to be high enough to alter Li isotope composition of fluids to be similar to that of the mantle ([Caciagli et al., 2011](#); [Halama et al. 2009](#); [Magna et al., 2006b](#); [Parkinson et al. 2007](#); [Tomascak et al. 2000, 2002](#)).

In this study, Li isotopic compositions of the late Cenozoic volcanic rocks from the Chugoku district in Southwest (SW) Japan arc are investigated. This district hosts various types of volcanic rocks which represent melts derived from subducted sediments (high-Mg andesite; [Shimoda et al., 1998](#)) and oceanic crust [high-Sr andesites and dacite (adakite); [Feineman et al., 2013](#); [Pineda-Velasco et al., 2018](#)]. We find that these rocks show $\delta^7\text{Li}$ values beyond the range of MORB, probably due to contributions from subducted sediments and oceanic crust. This in turn allows us to examine the role of slab contribution in Li isotopic systematics of the arc. We also investigate Li-isotope analyses of other types of volcanic rocks (basalts) and integrate Sr-Nd-Hf-Pb isotope analyses in order to examine the role of slab-mantle interaction in the Li isotopic systematics of the arc.

2. Results

New $^7\text{Li}/^6\text{Li}$ data for the selected samples of volcanic rocks from the Chugoku district are reported in **Table 5-1**. The $\delta^7\text{Li}$ values of the Chugoku volcanic rocks range from -1.9‰ to $+7.4\text{‰}$. The observed $\delta^7\text{Li}$ variation is far larger than the range found in unaltered MORB ($+1.6\text{‰}$ to $+5.6\text{‰}$; [Marschall et al., 2017](#); [Tomascak et al., 2008](#)) and that of most other arcs (**Figure 5-1**). HMA in the Setouchi district shows a lower-than-MORB $\delta^7\text{Li}$ signature with smaller variation (-1.0 to -0.1‰ , this study), compared with IAB and ADK in the Chugoku

district (**Figure 5-1**). The $\delta^7\text{Li}$ values of most IAB show a variation as small as 2‰ ($\delta^7\text{Li} = +1.5$ to $+3.6$ ‰) and fall within the range of MORB. Three IAB samples have $\delta^7\text{Li}$ values outside the range of MORB. Among these samples, the sample MAT-04 (Matsue), erupted in Episode 1, has a $\delta^7\text{Li}$ value ($+6.29$ ‰) higher than $\delta^7\text{Li}$ values of unaltered MORB, whereas KUR-17 (Kurayoshi), erupted in Episode 2, has a $\delta^7\text{Li}$ value (-1.95 ‰) lower than $\delta^7\text{Li}$ values of unaltered MORB. The second lowest $\delta^7\text{Li}$ value (-1.02 ‰) among IAB is found in an ultrapotassic lamprophyre, SER-11 (Sera), erupted in Episode 1, whereas the second highest $\delta^7\text{Li}$ value ($+5.02$ ‰) is found in an ultrapotassic lamprophyre, KAW-03 (Kawamoto), erupted in Episode 3. These lamprophyres also have Sr, Nd, or Hf isotopic compositions which define the lowest or highest values among IAB or are close to these extreme values. SER-11 has the highest $(^{87}\text{Sr}/^{86}\text{Sr})_t$ (subscript t denotes age-corrected composition), the lowest $(^{143}\text{Nd}/^{144}\text{Nd})_t$, and the second lowest $(^{176}\text{Hf}/^{177}\text{Hf})_t$ among IAB, whereas KAW-03 has the third highest $(^{87}\text{Sr}/^{86}\text{Sr})_t$, the second lowest $(^{143}\text{Nd}/^{144}\text{Nd})_t$, and the lowest $(^{176}\text{Hf}/^{177}\text{Hf})_t$ among IAB (**Figure 5-2**).

The $\delta^7\text{Li}$ values of ADK ($\delta^7\text{Li} = +1.2$ to $+7.4$ ‰) largely overlap with those of IAB, and some ADK have $\delta^7\text{Li}$ values ($+6.3$ ‰ to $+7.4$ ‰) significantly higher than $\delta^7\text{Li}$ values of unaltered MORB. Such ADK are from the volcanic fields in the central Chugoku district, consisting of Wakurayama and Daisen. The eruption ages of the high- $\delta^7\text{Li}$ Daisen samples are older (0.4–0.5 Ma) than those of the other Daisen samples (<0.4 Ma) ([Feineman et al., 2013](#)). No samples with $\delta^7\text{Li}$ values lower than MORB were found among the ADK samples, when the analytical uncertainty was taken into consideration.

IAB samples do not exhibit a clear temporal variation in $\delta^7\text{Li}$ values, rather their $\delta^7\text{Li}$ are mostly falling within the range of $\delta^7\text{Li}$ values for unaltered MORB irrespective of their eruption ages (**Figure 5-3**). ADK samples also do not show a clear correlation between $\delta^7\text{Li}$ value and

eruption age (2 Ma to <0.1 Ma; Pineda-Velasco et al., 2018; Nguyen et al., 2020; and reference therein) (Figure 5-3). It is however noted that high $\delta^7\text{Li}$ values ($> +5.6\%$) found in some ADK samples are consistent with increased influence of the contribution from oceanic crust melt, as Sr/Nd and Th/U show (Nguyen et al., 2020).

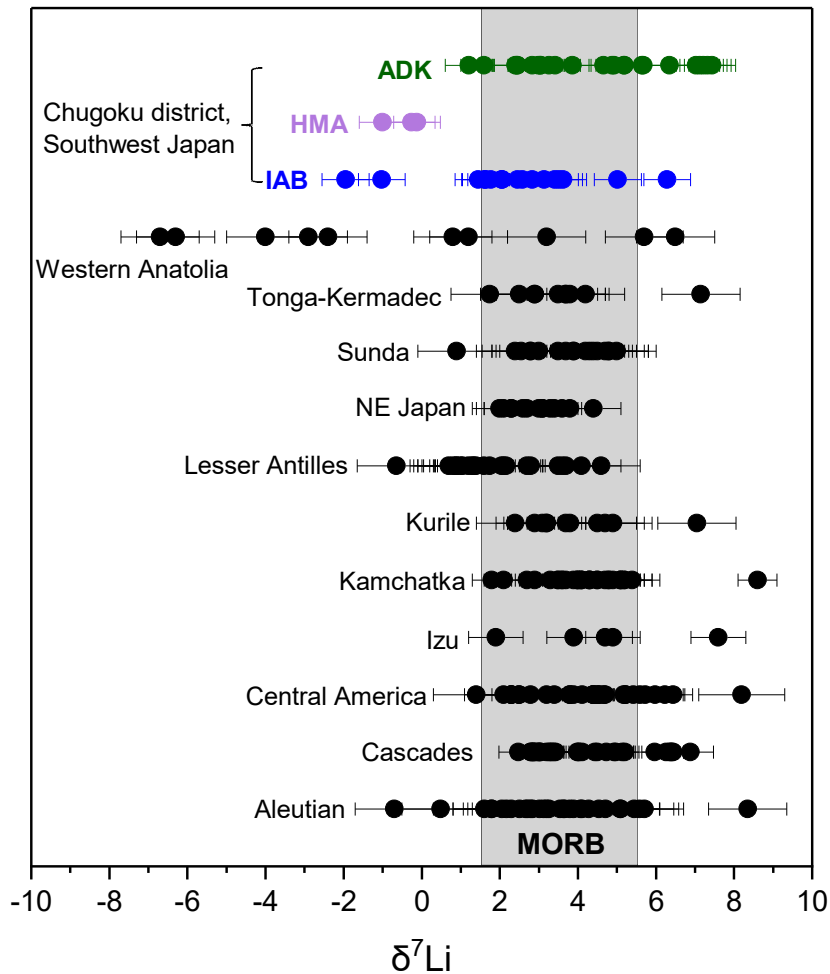


Figure 5-1. $\delta^7\text{Li}$ values in volcanic rocks from the Chugoku district in SW Japan (ADK: green dots; IAB: blue dots; HMA: purple dots) compared to published values for mafic-intermediate volcanic rocks ($\text{SiO}_2 \leq 63$ wt%, except for rocks classified as ‘adakite’) in other arcs.

Note that the data for altered rocks or atypical arc rocks are screened out; those include rocks with high LOI (loss on ignition) or high CIA (chemical index of alteration), highly alkaline rocks (e.g., shoshonite),

and intraplate-type mafic rocks (similar to our OIB). The range of $\delta^7\text{Li}$ values of unaltered MORB is shown as a gray band ($+1.6\text{‰} \leq \delta^7\text{Li} \leq +5.6\text{‰}$; Marschall et al., 2017; Tomascak et al., 2008). Data sources of the $\delta^7\text{Li}$ values of other arc volcanic rocks are as follows; Aleutians (Hanna et al., 2020; Tomascak et al., 2002), Cascades (Magna et al., 2006b; Leeman et al., 2004), Central America (Chan et al., 2002; Tomascak et al., 2000; Walker et al., 2009), Izu (Moriguti & Nakamura, 1998), Kamchatka (Halama et al., 2009; Liu et al., 2020), Kurile (Tomascak et al., 2002), Lesser Antilles (Tang et al., 2014), NE Japan (Moriguti et al., 2004), Sunda (Tomascak et al., 2002), Tonga-Kermadec (Brens Jr. et al., 2019), Western Anatolia (Agostini et al., 2008). Analytical uncertainties of $\delta^7\text{Li}$ values (as 2σ external reproducibility or $2\sigma_m$ within-run precision) are shown as error bars (0.6‰ for our study, and 0.07–1.2‰ for the literature data).

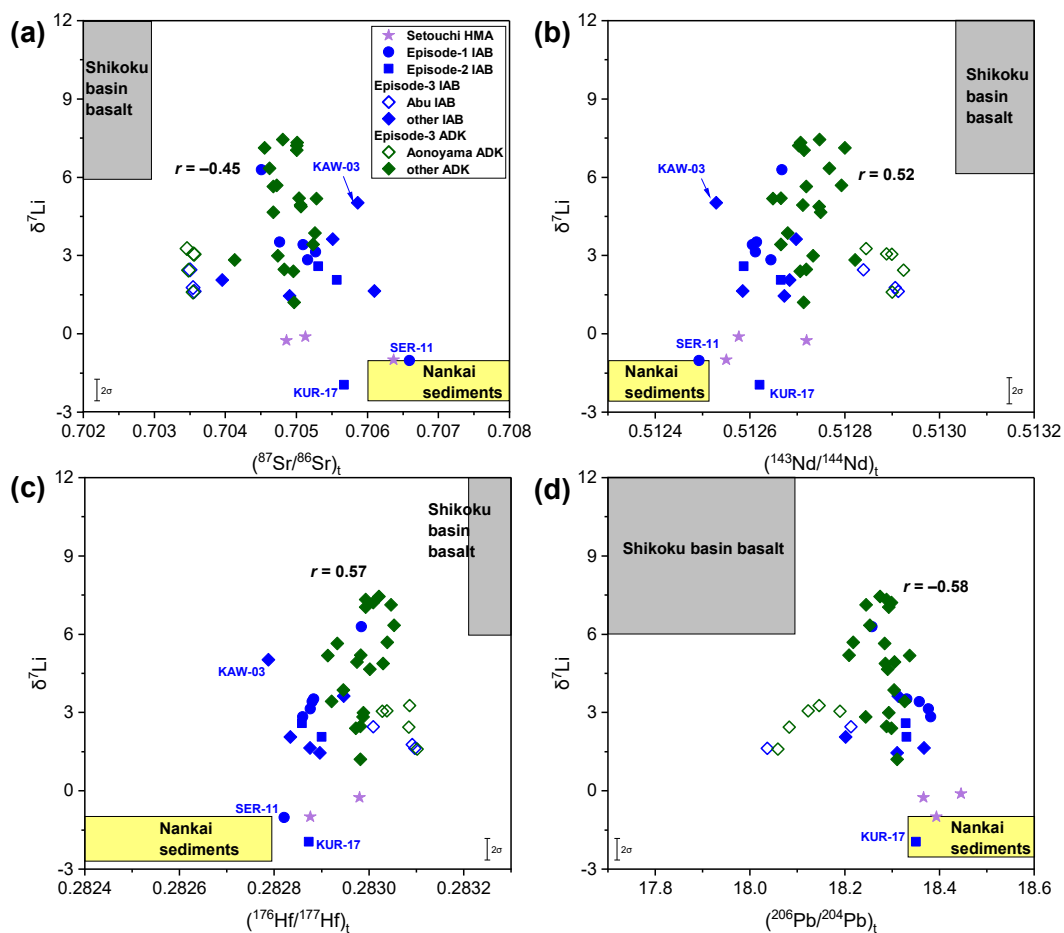


Figure 5-2. Plot of $\delta^7\text{Li}$ in volcanic rocks from the Chugoku district in SW Japan versus (a) $(^{87}\text{Sr}/^{86}\text{Sr})_t$, (b) $(^{143}\text{Nd}/^{144}\text{Nd})_t$, (c) $(^{176}\text{Hf}/^{177}\text{Hf})_t$, and (d) $(^{206}\text{Pb}/^{204}\text{Pb})_t$.

Correlation coefficients (r) for $\delta^7\text{Li}$ values and Sr-Nd-Hf-Pb isotopic compositions are shown in each plot (note that r is calculated for IAB and ADK shown by filled symbols). Sr-Nd-Pb-Hf radiogenic isotopic data of the Chugoku volcanic rocks are from [Pineda-Velasco et al. \(2018\)](#) and [Nguyen et al. \(2020\)](#). $\delta^7\text{Li}$ values of subducted sediments are taken from the $\delta^7\text{Li}$ values measured by [Moriguti and Nakamura \(1998\)](#) for metasedimentary rocks (shales) in the accretionary complex (Shimanto Belt). The Sr-Nd-Pb-Hf isotopic compositions of sediments are from published data for the Shimanto shales/sandstones or terrigenous sediments in Nankai Trough/Shikoku Basin ([Ishikawa & Nakamura, 1994](#); [Plank & Langmuir, 1998](#); [Shimoda et al., 1998](#); [Shu et al., 2017](#); [Terakado et al., 1988](#)). Sr-Nd-Pb-Hf radiogenic isotopes of Shikoku basin basalts are from [Hickey-Vargas \(1991, 1998\)](#), [Ishizuka et al. \(2009\)](#), [Shu et al. \(2017\)](#), and [Straub et al. \(2010\)](#). The range of $\delta^7\text{Li}$ values in Shikoku Basin basalts is assumed to be the same as the variation in global seafloor basalts (i.e., altered oceanic crusts) presented in [Penniston-Dorland et al. \(2017\)](#). The $\delta^7\text{Li}$ value of mantle wedge is assumed to be $+3.5 \pm 0.5\text{‰}$, which is the mean $\delta^7\text{Li}$ value of pristine peridotites ([Jeffcoate et al., 2007](#); [Lai et al., 2015](#); [Magna et al., 2006a](#); [Pogge von Strandmann et al., 2011](#); [Seitz et al., 2004](#)). Uncertainty of $\delta^7\text{Li}$ values for the Chugoku district samples is $\pm 0.6\text{‰}$ (2σ external reproducibility).

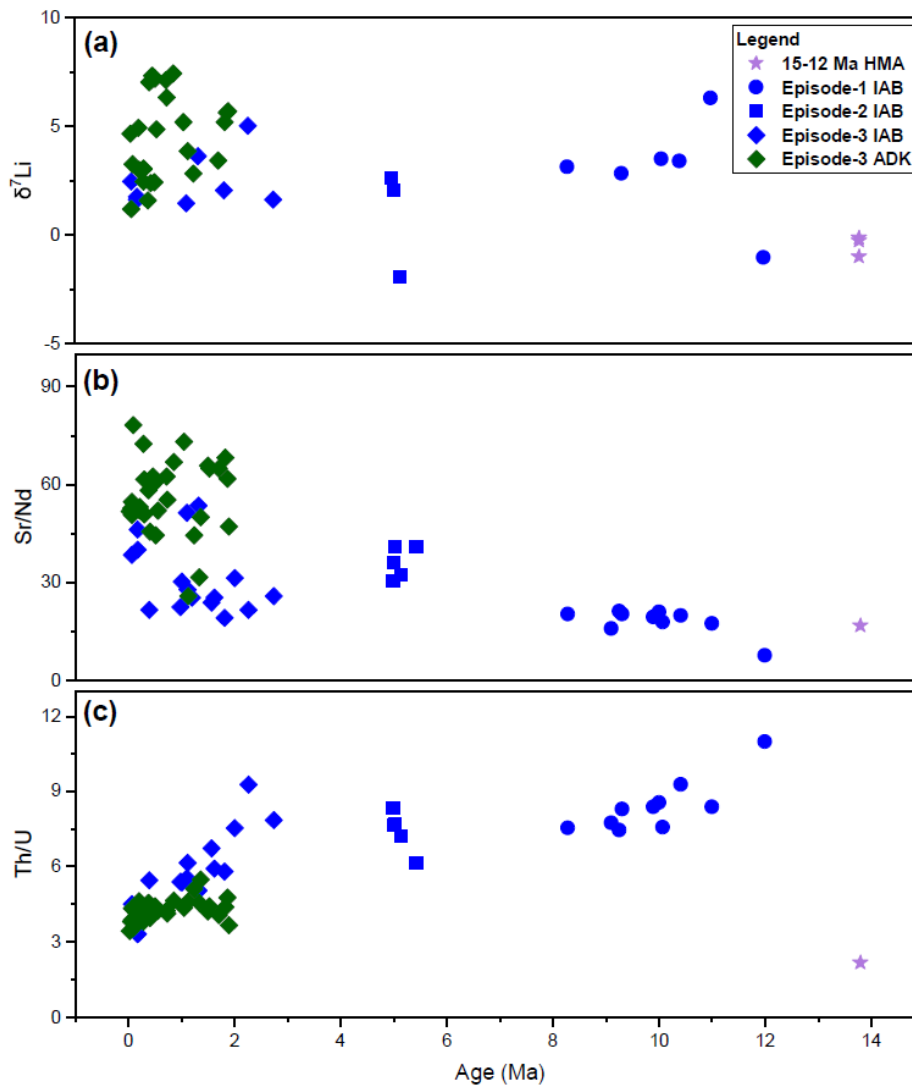


Figure 5-3. Temporal variations in (a) $\delta^7\text{Li}$ value, (b) Sr/Nd ratio, and (c) Th/U ratios of the Chugoku volcanic rocks.

Data sources are from [Nguyen et al., \(2020\)](#) and this study.

3. Discussion

Volcanic rocks from the Chugoku district in SW Japan show a significant variation in $\delta^7\text{Li}$ (-1.9 to $+7.4\text{‰}$), far beyond the $\delta^7\text{Li}$ range found in unaltered MORB. The overall $\delta^7\text{Li}$ variation is the largest among the volcanic rocks from global arcs (**Figure 5-1**). An exception is the Western Anatolia-Aegean arc that contains Cenozoic mafic-intermediate volcanic rocks with extremely low and high $\delta^7\text{Li}$ values (-7.0‰ to $+8.2\text{‰}$; [Agostini et al., 2008](#)). In the arc,

the difference in $\delta^7\text{Li}$ value among samples is related to rock suites. The low- $\delta^7\text{Li}$ volcanic rocks (-7.0‰ to $+3.2\text{‰}$) are from the ultrapotassic suite, while the high- $\delta^7\text{Li}$ volcanic rocks ($+5.7$ to $+8.2\text{‰}$) are from the sub-alkaline andesitic suite. Therefore, SW Japan lavas may provide a vital opportunity to examine the role of slab contribution and slab-mantle interaction in Li isotopic systematics.

We first discuss whether the processes responsible for the large variation in $\delta^7\text{Li}$ of the Chugoku volcanic rocks occurred at a shallow level (e.g., intracrustal) or deep level (e.g., mantle) (Section 5.1). Then, we discuss the $\delta^7\text{Li}$ variation via (1) sediment and altered oceanic crust (AOC) contributions (Section 5.2), and (2) Li-isotope fractionation during subduction (Section 5.3). Then, we address the interaction of slab-derived components and the mantle (Section 5.4) Finally, we provide the implication of $\delta^7\text{Li}$ variation in global arc magmas (Section 5.5).

3.1 Processes responsible for $^7\text{Li}/^6\text{Li}$ variation

3.1.1 Post-emplacement processes

Fractionation of ^6Li and ^7Li could occur by degassing of magmas during their emplacements (Neukampf et al., 2022; Schiavi et al., 2010). During degassing of felsic melts, Li is partitioned into a vapor (fluid) phase (Webster et al., 1989). Fractionation of ^6Li and ^7Li via degassing also results in the depletion of ^7Li in a residual melt, and thus the $[\text{Li}]$ and $\delta^7\text{Li}$ values of co-magmatic samples show a positive correlation (e.g., Neukampf et al., 2022). Such a positive correlation is not observed in IAB or ADK rocks from each volcanic field (Figure 5-4). Thus, the $\delta^7\text{Li}$ variations in these rocks are dominantly controlled by processes other than degassing.

Post-emplacement weathering is also considered to alter the $\delta^7\text{Li}$ values of volcanic rocks by the uptake of Li into clay minerals formed by alteration of primary silicates (e.g., Vigier et

al., 2008). Between clay minerals and a fluid, isotope fractionation occurs, resulting in enrichment of ^6Li in altered silicate rocks containing clay minerals (Vigier et al., 2008). Clay minerals form from primary volcanic constituents, and their formations accompany a net loss of the mobile elements, including Mg, Ca, Na and K (Babechuk et al., 2014). By contrast, Al and Fe are preferentially retained in weathered rocks (Babechuk et al., 2014). Accordingly, relative proportions of major element oxides show the variations among rocks with different extents of weathering and alteration. The chemical index of alteration (CIA), given as molar fractions of major oxides $\text{Al}_2\text{O}_3/(\text{Al}_2\text{O}_3 + \text{CaO}^* + \text{Na}_2\text{O} + \text{K}_2\text{O}) \times 100$ (where CaO^* refers to Ca in silicates) represents a good measure of the extent of weathering/alteration (Nesbitt & Young, 1982; McLennan 1993). The $\delta^7\text{Li}$ and CIA values of ADK and IAB samples in each volcanic field do not show a clear correlation (Figures 5-5a and 5-6). Secondary alteration could also result in elemental fractionation, resulting in variations in Cs/Rb and Li/Y, owing to different susceptibility or resistivity against secondary alteration (Palmer & Edmond, 1989; Seyfried Jr. et al., 1998). These element ratios are not correlated with $\delta^7\text{Li}$ (Figure 5-7), providing further support for an insignificant effect of secondary alteration on $\delta^7\text{Li}$ variations in IAB and ADK. In summary, the observed variation in $\delta^7\text{Li}$ of the volcanic rocks in the Chugoku district is largely attributed to the processes that occurred prior to the eruption of their parent magmas.

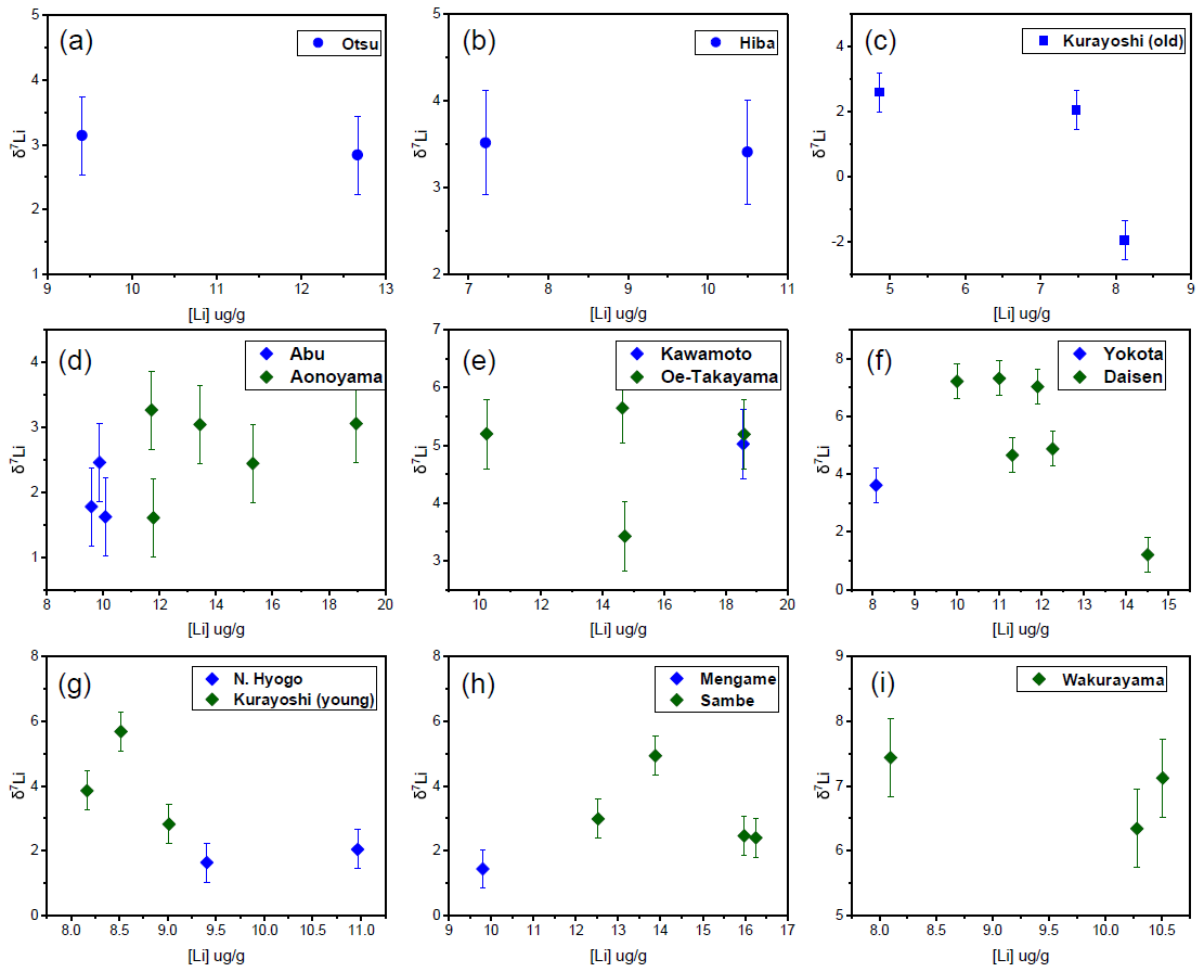


Figure 5-4. Comparison of Li contents ($[Li]$ in $\mu\text{g}\cdot\text{g}^{-1}$) and $\delta^7\text{Li}$ values of volcanic rocks in each volcanic field of the Chugoku district in SW Japan.

Comparison of Li contents ($[Li]$ in $\mu\text{g}\cdot\text{g}^{-1}$) and $\delta^7\text{Li}$ values of volcanic rocks in each volcanic field (if data are available for more than two samples) of the Chugoku district in SW Japan. The IAB samples are shown by blue squares and the ADK samples are shown by green squares, respectively. Error bar denotes analytical uncertainty ($\pm 0.6\text{‰}$ in $2\sigma_m$).

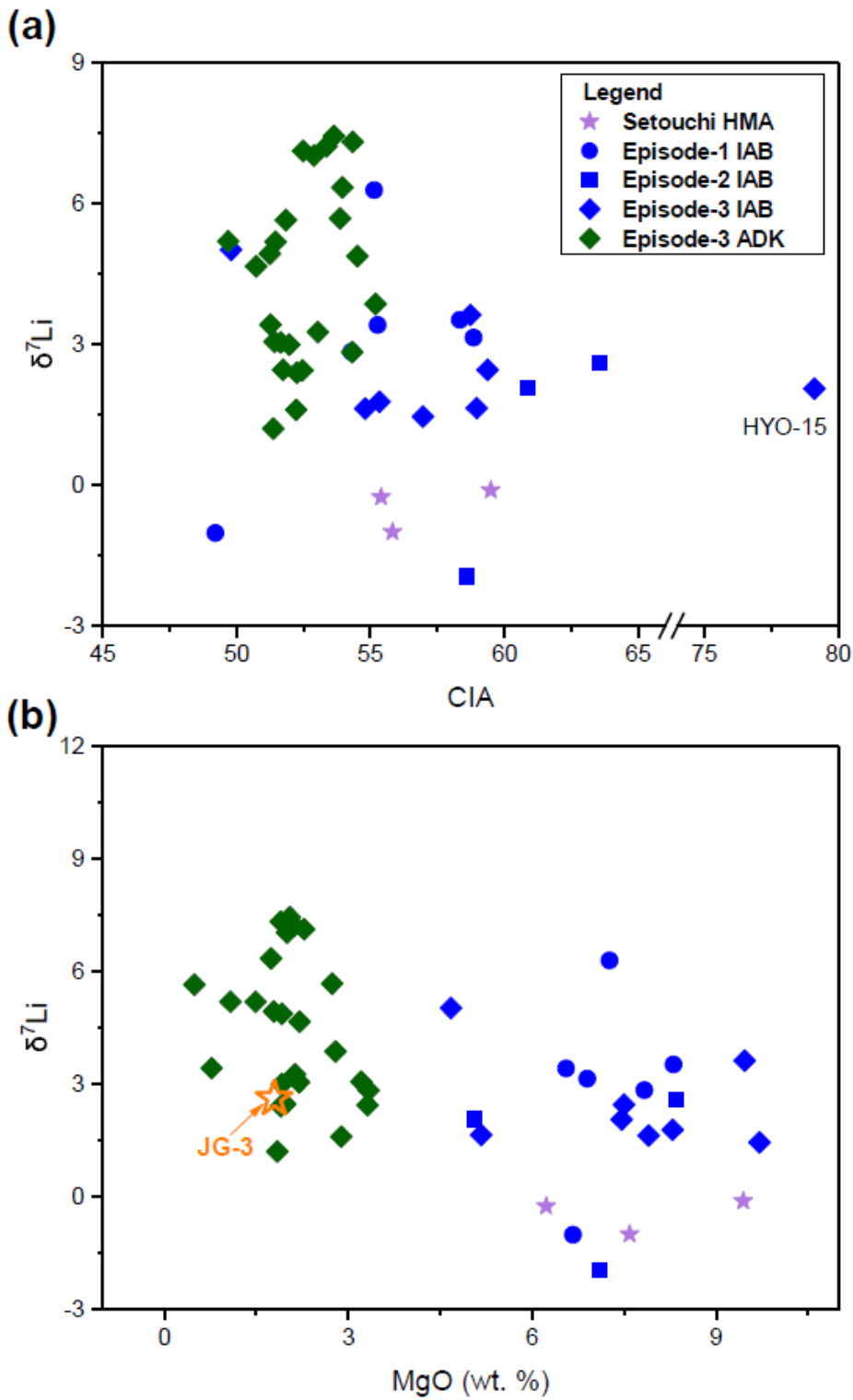


Figure 5-5. Plots of $\delta^7\text{Li}$ in ADK and IAB of the Chugoku district in SW Japan against (a) CIA and (b) MgO.

Plots of $\delta^7\text{Li}$ in ADK and IAB of the Chugoku district in SW Japan against (a) CIA [chemical index of

alteration; $\text{Al}_2\text{O}_3/(\text{Al}_2\text{O}_3 + \text{CaO}^* + \text{Na}_2\text{O} + \text{K}_2\text{O}) \times 100$, where CaO^* refers to Ca in silicates (Nesbitt & Young, 1982; McLennan, 1993)] and (b) MgO. The composition of JG-3, an upper-crustal granitic rock in the Chugoku district, is from Imai et al. (1995) and Magna et al. (2010). Uncertainty of $\delta^7\text{Li}$ values of the Chugoku district samples is $\pm 0.6\text{‰}$ (2σ external reproducibility).

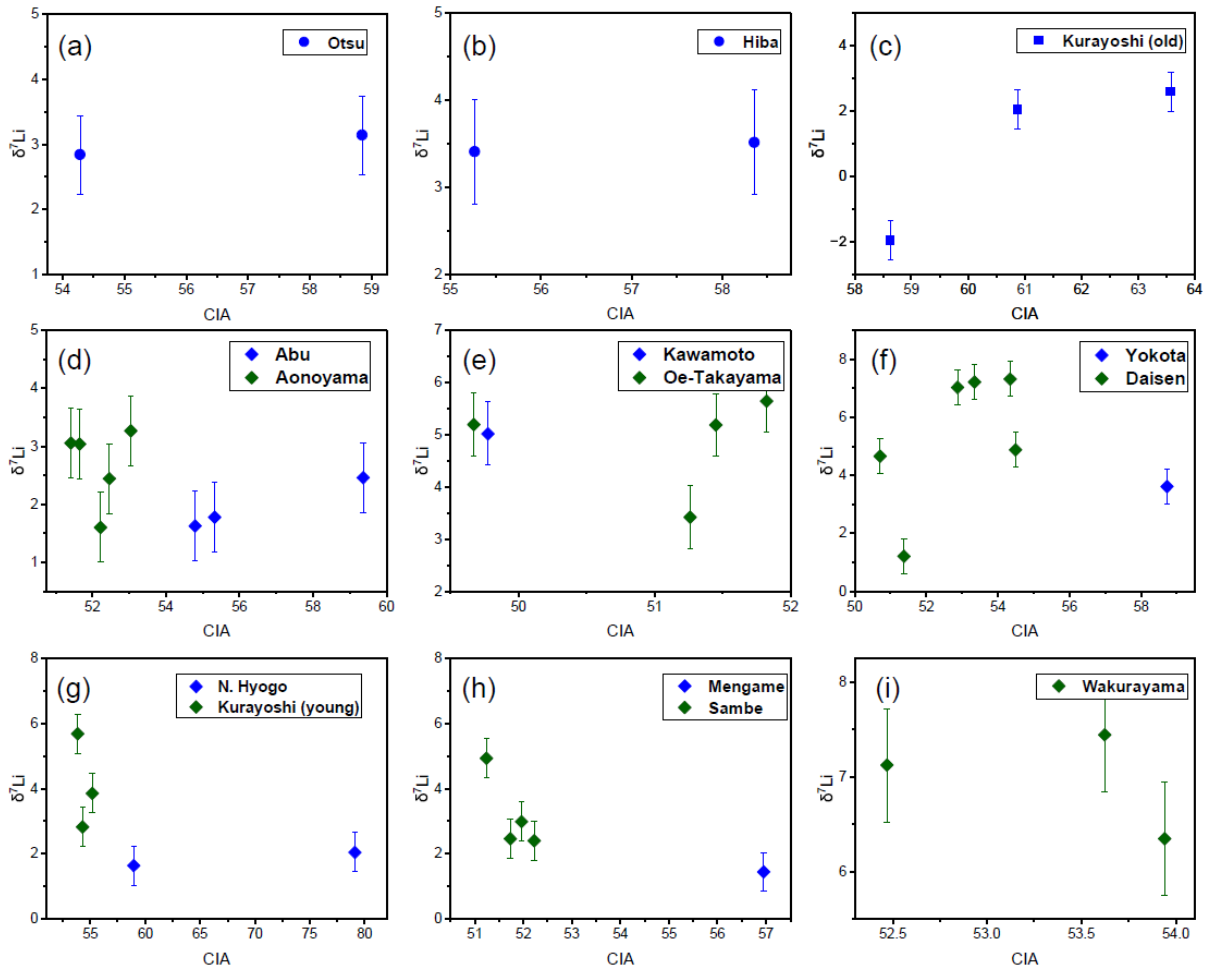


Figure 5-6. Comparison of CIA (chemical index of alteration) and $\delta^7\text{Li}$ values of volcanic rocks in each volcanic field of the Chugoku district in SW Japan.

The symbols are the same as in Figure 5-4. Error bar denotes analytical uncertainty ($\pm 0.6\text{‰}$ $2\sigma_m$).

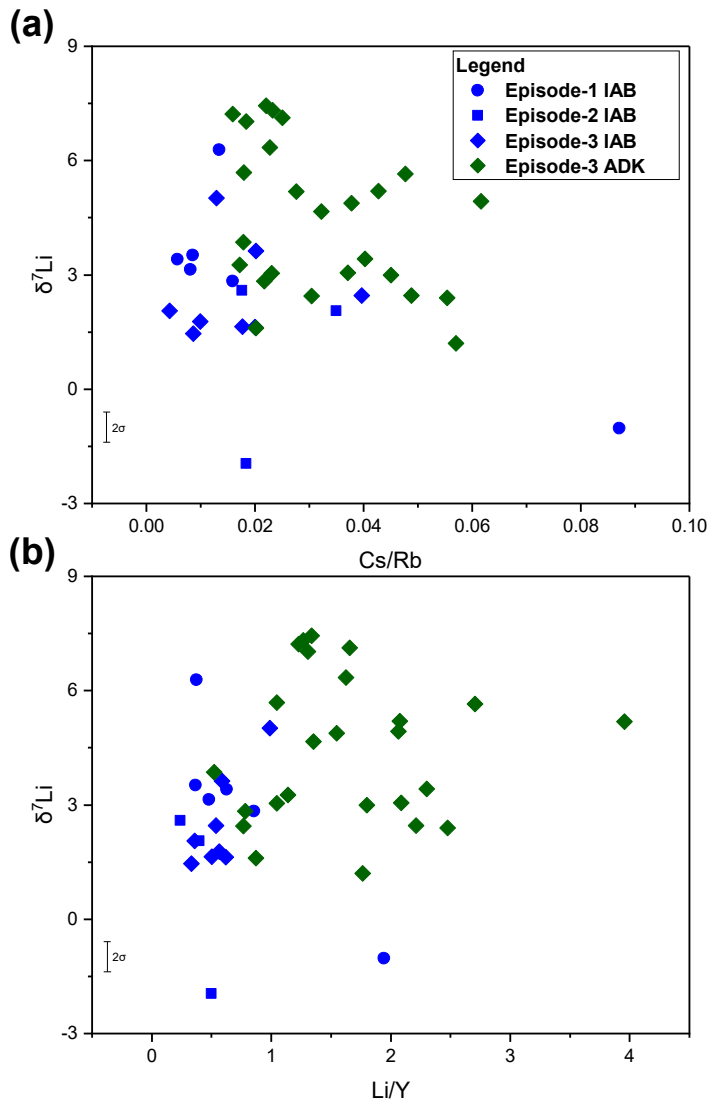


Figure 5-7. Comparison of $\delta^7\text{Li}$ values with (a) Cs/Rb ratio and (b) Li/Y ratios of volcanic rocks of IAB and ADK types.

Error bar denotes analytical uncertainty ($\pm 0.6\text{‰}$ in $2\sigma_m$).

3.1.1 Pre-emplacment processes

It is generally considered that fractionation of $^7\text{Li}/^6\text{Li}$ occurs to a limited extent in magmatic systems, owing to a high diffusion rate at high temperatures ($\sim 1000\text{ }^\circ\text{C}$) (Schuessler

et al., 2009; Tomascak et al., 1999). During differentiation of a magma, Li exchanges between crystallized phases (e.g., olivine and clinopyroxene) and a residual magma. Owing to kinetic effects, the light isotope (i.e., ${}^6\text{Li}$) preferentially diffuses into these phases. Numerical experiments or *in-situ* analyses of Li-isotope compositions demonstrated that the $\delta^7\text{Li}$ values of these phases could decrease by 10‰ or more relative to a coexisting melt (Parkinson et al., 2007; Weyer & Seitz, 2012). If these phases are mechanically separated, residual magma becomes to be enriched in ${}^7\text{Li}$. However, such a process is unlikely to significantly affect the $\delta^7\text{Li}$ values of volcanic rocks because the faster diffusion of Li resulted in isotopic re-equilibration between crystallized phases and a magma prior to eruptions. Thus, it is unlikely that magmatic differentiation is responsible for production of the entire $\delta^7\text{Li}$ variation (>9‰) in the Chugoku volcanic rocks. This inference is supported by covariation of $\delta^7\text{Li}$ values with the Sr, Nd, Hf and Pb isotopic compositions of these rocks. Nevertheless, we examine the feasibility of Li isotope fractionation via magmatic processes.

In **Figure 5-5b**, the $\delta^7\text{Li}$ values of IAB and ADK are plotted against their MgO contents, as indices of differentiation. Although our samples were collected from volcanoes in different fields in the Chugoku district, an overall correlation between the $\delta^7\text{Li}$ value and MgO content is anticipated if the variation in $\delta^7\text{Li}$ is dominated by fractional crystallization. However, these rocks do not show a significant correlation ($r = -0.057$ for ADK and -0.016 for IAB) between $\delta^7\text{Li}$ and MgO, even among samples from the same volcanic fields (**Figures 5-5b and 5-8**). We thus consider that the variation in $\delta^7\text{Li}$ of the Chugoku volcanic rocks was produced by processes other than fractional crystallization, consistent with the conclusion of previous studies (Schuessler et al., 2009; Tomascak et al., 1999).

The $\delta^7\text{Li}$ value of a magma could also be altered via ingestion of crustal materials with distinct $\delta^7\text{Li}$ values. Crustal materials in the Chugoku district mainly consist of felsic plutonic

rocks in its upper part and mafic plutonic rocks in its lower part (Yamane et al., 2012). Felsic plutonic rocks are considered to be a major assimilant since they have solidus temperatures lower than those of mafic magmas. A reference silicate rock, JG-3, provided by the Geological Survey of Japan, is a Paleogene (58–56 Ma) granodiorite from the Chugoku district (Ishihara & Tani, 2013; Noguchi et al., 2021). This rock could represent a felsic member of the upper crustal rock in the Chugoku district. The [Li] of 20.9 and 24.5 $\mu\text{g}\cdot\text{g}^{-1}$ and the $\delta^7\text{Li}$ value of +2.40 and +2.56‰ are reported for JG-3 (Magna et al., 2010; Figure 5-5b). The $\delta^7\text{Li}$ values of the JG-3 aliquots are well within the range of $\delta^7\text{Li}$ values of the volcanic rocks from the Chugoku district as well as that of unaltered MORB. Accordingly, assimilation of upper crustal rock in mafic magmas could not produce intermediate to felsic magmas with the $\delta^7\text{Li}$ values significantly different from MORB. The ADK-type andesites and dacites dominate intermediate and felsic volcanic rocks erupted in Episode 3 (Kimura et al., 2005), and their $\delta^7\text{Li}$ values (–2.0 to +6.3‰) significantly overlap with the $\delta^7\text{Li}$ values of IAB in the same episode (+1.5 to +5.0‰). Thus, one may anticipate that ADK could have been derived by fractional crystallization of mafic parental magmas with or without the assimilation of upper crustal rocks. Previous studies, however, suggest that ADK magmas were derived by melting of the subducted oceanic lithosphere (Feineman et al., 2013; Kimura et al., 2014; Pineda-Velasco et al., 2018). We thus consider that crustal assimilation did not play a major role in the production of $\delta^7\text{Li}$ variation among different types of volcanic rocks in the Chugoku district.

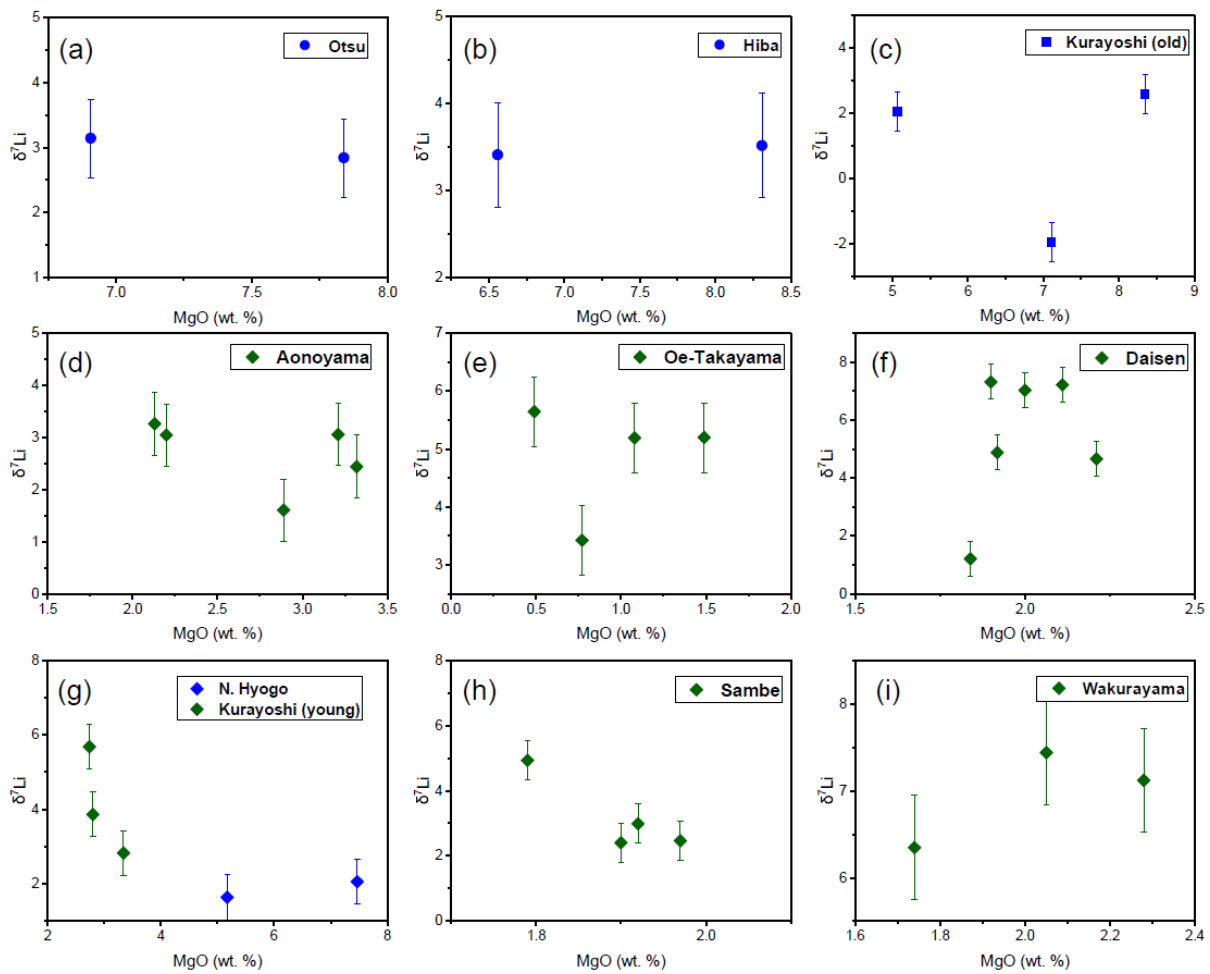


Figure 5-8. Comparison of MgO contents (wt. %) and $\delta^7\text{Li}$ values of volcanic rocks in each volcanic field of the Chugoku district in SW Japan.

The symbols are the same as in Figure 5-4. Error bar denotes analytical uncertainty ($\pm 0.6\text{‰}$ in $2\sigma_m$).

3.1.2 Subduction inputs to the magma sources

Neither post-emplacement alteration nor pre-emplacement magmatic processes account for the observed $\delta^7\text{Li}$ variations in the Chugoku volcanic rocks. We thus infer that $\delta^7\text{Li}$ variations reflect the characteristics of their magma sources or the processes of melt transport in the mantle. [Nguyen et al. \(2020\)](#) argued that polybaric melting of upwelling mantle resulted in the predominance of refractory peridotite in the wedge mantle. The $\delta^7\text{Li}$ value of the mantle would have varied little since peridotite represents a major source of Li in the mantle. The $\delta^7\text{Li}$ value of the mantle would have varied little since peridotite represents a major source of Li in

the mantle. We thus assume the $\delta^7\text{Li}$ value of the wedge mantle to be the same as the mean $\delta^7\text{Li}$ value ($+3.5 \pm 1.0\%$) of pristine peridotites (Jeffcoate et al., 2007; Lai et al., 2015; Magna et al., 2006a; Pogge von Strandmann et al., 2011; Seitz et al., 2004). It is noted that the $\delta^7\text{Li}$ value postulated for the wedge mantle is identical to the mean $\delta^7\text{Li}$ value of unaltered MORB ($+3.6 \pm 2.0\%$) within analytical uncertainty. The $\delta^7\text{Li}$ value of the Chugoku volcanic rocks extends beyond the postulated $\delta^7\text{Li}$ value of the mantle, implying the contribution of the other magma sources.

The other sources are likely derived from crustal or lithospheric materials introduced into melting regions via slab subduction (Feineman et al., 2013; Kimura et al., 2014; Nguyen et al., 2020; Pineda-Velasco et al., 2018). We considered that these sources include AOC, sediments, and/or serpentinite (e.g., Liu et al., 2020; Moriguti & Nakamura, 1998; Tang et al., 2014). The HMA and ADK provide key constraints to identify the contributions of these components. HMA is considered to have been mainly derived from subducted sediments (Hanyu et al., 2002; Kawamoto et al., 2012; Shimoda et al., 1998; Tatsumi & Hanyu, 2003), whereas ADK is suggested to have been largely derived from AOC (Feineman et al., 2013; Kimura et al., 2014; Pineda-Velasco et al., 2018). These volcanic rocks show significant variations in Sr-Nd-Hf-Pb isotope compositions, which are interpreted to have resulted from the changes in relative contributions of AOC and sediments to parental magmas (Feineman et al., 2013; Hanyu et al., 2002; Kimura et al., 2014; Pineda-Velasco et al., 2018; Shimoda et al., 1998; Tatsumi & Hanyu, 2003). Thus, the comparison of Li-isotope data with Sr-Nd-Hf-Pb isotope data for these samples may provide insights into the $\delta^7\text{Li}$ signatures of AOC and sediments subducted beneath the Chugoku district. For this purpose, $\delta^7\text{Li}$ values of the IAB, ADK and HMA are plotted against $^{87}\text{Sr}/^{86}\text{Sr}$, $^{143}\text{Nd}/^{144}\text{Nd}$, $^{176}\text{Hf}/^{177}\text{Hf}$, and $^{206}\text{Pb}/^{204}\text{Pb}$ ratios in **Figure 5-2**. In these plots, broad correlations are observed; positive correlations are found between $\delta^7\text{Li}$ values and

$^{143}\text{Nd}/^{144}\text{Nd}$ and $^{176}\text{Hf}/^{177}\text{Hf}$ ratios, while negative correlations are found between $\delta^7\text{Li}$ values and $^{87}\text{Sr}/^{86}\text{Sr}$ and $^{206}\text{Pb}/^{204}\text{Pb}$ ratios, respectively. If data for ADK from Aonoyama (6 out of 6 samples) and IAB from Abu (6 out of 6 samples) are excluded, the correlations are considered to be significant; absolute values of correlation coefficients for these pairs are 0.45–0.58 (**Figure 5-2**) and the statistic t for these coefficients are 2.99 to 4.13 which are greater than the critical t value at 5% significance level [$t_{\text{critical}} = 2.030\text{--}2.035$ for degree of freedom of $N_{\text{data}} - 2$ (35–37)]. These linear correlations point toward the compositions of AOC (Shikoku Basin basalts; Hickey-Vargas, 1991, 1998; Ishizuka et al., 2009; Shu et al., 2017; Straub et al., 2010) and sediments (Nankai sediments; Ishikawa & Nakamura, 1994; Moriguti & Nakamura, 1998; Plank & Langmuir, 1998; Shimoda et al., 1998; Shu et al., 2017; Terakado et al., 1988; You et al., 1995). The ADK and HMA samples plot close to these compositions. We thus consider that these two magma types preserve a slab-derived Li-isotope signature, although their parental magmas must have interacted with wedge mantle to different extents, inferred from large differences in MgO content or $\text{Mg}^{\#}$ [$\equiv 100 \times \text{Mg}/(\text{Mg} + \text{Fe}^{2+})$ in moles] between these two magma types; MgO = 0.36–3.3 wt% and $\text{Mg}^{\#} = 25\text{--}61$ for ADK, and MgO = 6.1–9.5 wt% and $\text{Mg}^{\#} = 70\text{--}76$ for HMA (**Table 5-1**; Pineda-Velasco et al., 2018; Tatsumi & Ishizaka, 1982).

It should be also noted that the samples excluded for the above evaluation show distinct geochemical features. Aonoyama ADK and Abu IAB show larger variations in $^{143}\text{Nd}/^{144}\text{Nd}$ and smaller variations in $^{87}\text{Sr}/^{86}\text{Sr}$ than other ADK and IAB (Kimura et al., 2014). Pineda-Velasco et al. (2018) interpreted that the difference in the $^{143}\text{Nd}/^{144}\text{Nd}$ - $^{87}\text{Sr}/^{86}\text{Sr}$ correlation between Aonoyama and other ADK samples is due to smaller extent of melting of AOC beneath Aonoyama (and adjacent Abu) region(s). The data for Aonoyama ADK and Abu IAB plot off the arrays formed by the other ADK and IAB to lower $^{87}\text{Sr}/^{86}\text{Sr}$ and $^{206}\text{Pb}/^{204}\text{Pb}$ and to higher $^{143}\text{Nd}/^{144}\text{Nd}$ and $^{176}\text{Hf}/^{177}\text{Hf}$. Possible causes of their derivations from the isotope-correlation

arrays are discussed in Section 5.4.

3.2 Processes responsible for heterogeneity of Li isotope compositions of the Chugoku magmas

Volcanic rocks (mafic to intermediate) in different arcs show different extents of the variations in $\delta^7\text{Li}$ values (**Figure 5-1**). The rocks in some arcs show the $\delta^7\text{Li}$ variation mostly falling within the $\delta^7\text{Li}$ range of unaltered MORB. The arcs dominated by volcanic rocks with $\delta^7\text{Li}$ values of 1.6–5.6‰ are Aleutian (Tomascak et al., 2002; Hanna et al., 2020), Kamchatka (Liu et al., 2020), NE Japan (Moriguti et al., 2004), Sunda (Tomascak et al., 2002), and Tonga-Kermadec (Brens Jr. et al., 2019). In these arcs, the $\delta^7\text{Li}$ data for 85% or more samples fall within the range of $\delta^7\text{Li}$ values of unaltered MORB. Volcanic rocks in some back-arc basins also yield mafic volcanic rocks with $\delta^7\text{Li}$ values mostly within the range of MORB [e.g., South Shetland (Ross Island; Košler et al., 2009), Ryukyu (Okinawa Trough; Zeng et al., 2021), and Tonga (Lau Basin; Brens Jr. et al., 2019)].

By contrast, some arcs contain certain amounts of volcanic rocks with $\delta^7\text{Li}$ values higher than that of unaltered MORB ($> +5.6\text{‰}$). These arcs include Cascades (7 out of 30; Leeman et al., 2004; Magna et al., 2006b), Izu (1 out of 5; Moriguti & Nakamura 1998), and Central America (6 out of 33; Chan et al. 2002; Tomascak et al., 2000; Walker et al., 2009). Also noted are the other two arcs which contain certain amounts of volcanic rocks with $\delta^7\text{Li}$ values lower than unaltered MORB ($< +1.6\text{‰}$). These arcs are Lesser Antilles (11 out of 23 samples; Tang et al., 2014) and Western Anatolia (7 out of 10 samples; Agostini et al., 2008). Such low- $\delta^7\text{Li}$ rocks are also found in the Chugoku district (HMA and a few IAB rocks). The Chugoku district is also characterized by the occurrence of certain amounts of volcanic rocks with $\delta^7\text{Li}$ values higher than unaltered MORB (8 out of 25 ADK samples and 1 of 17 IAB samples).

In general, volcanic rocks show across-arc variations in abundance ratios of key trace

elements (e.g., Li/Y, B/Be, B/Nb, Ce/Pb, Ba/La) and $^{87}\text{Sr}/^{86}\text{Sr}$, $^{143}\text{Nd}/^{144}\text{Nd}$, $^{176}\text{Hf}/^{177}\text{Hf}$ and $^{206, 207, 208}\text{Pb}/^{204}\text{Pb}$. The variations in these trace-element and isotopic ratios extend beyond the ranges found in MORB. Such large variations are interpreted as a result of the involvement of subducted materials (AOC and sediments) in magma sources (e.g., [Ishikawa & Nakamura, 1994](#); [Nakamura et al., 1985](#); [Perfit et al., 1980](#); [Sakuyama & Nesbitt, 1986](#); [Shibata & Nakamura, 1997](#); [Yogodzinski et al., 2015](#); [Yokoyama et al., 2003](#)). Hence, these trace-elements and isotopic ratios have been used as geochemical proxies of the subduction inputs. It is noted that the $\delta^7\text{Li}$ values of volcanic rocks in most arcs do not show clear correlations in the above trace-element and isotopic ratios (e.g., [Leeman et al. 2004](#); [Moriguti et al. 2004](#); [Tang et al., 2014](#)).

Apparent similarity of $\delta^7\text{Li}$ values between arc volcanic rocks and unaltered MORB has been attributed to (1) mixing of slab-derived components and mantle, both of which have similar $\delta^7\text{Li}$ values (i.e., sediments have $\delta^7\text{Li}$ values falling within the range of unaltered MORB; e.g., [Brens Jr. et al., 2019](#); [Tang et al., 2014](#)), (2) no or insignificant Li inputs from a subducting slab after intensive dehydration at shallower depths (it lost most of its Li; e.g., [Leeman et al., 2004](#); [Magna et al., 2006b](#)), (3) buffering of slab-derived Li via isotopic exchange with surrounding mantle (with $\delta^7\text{Li}$ value falling within the range of unaltered MORB; e.g., [Caciagli et al., 2011](#); [Halama et al., 2009](#)). These three scenarios could also explain the lack of clear correlations between $\delta^7\text{Li}$ values and trace-elements and Sr-Nd-Hf-Pb isotopic ratios.

Scenario 1 is suggested in the studies of the volcanic rocks in the Tonga-Kermadec arc ([Brens Jr. et al., 2019](#)) and Aleutian arc ([Hanna et al., 2020](#)). Considering their high [Li] ($\sim 100 \mu\text{g}\cdot\text{g}^{-1}$; [Brens Jr. et al., 2019](#); [Plank, 2014](#); [Tang et al., 2014](#)), subducted sediments could represent one of the major Li inputs in arc-magma sources. In the studies of volcanic rocks

from these arcs, the $\delta^7\text{Li}$ values of subducting sediments are directly measured (Brens Jr. et al., 2019; Chan et al., 2006). The $\delta^7\text{Li}$ values of these sediments show a variation of +1.2 to +8.0‰; i.e., most of them have $\delta^7\text{Li}$ values indistinguishable from unaltered MORB (+1.6 to +5.6‰; Marschall et al., 2017; Tomascak et al., 2008). The $\delta^7\text{Li}$ value of the global subducting sediment, given as a weighted mean of the analyses for 27 trench sediments, is $+2.4 \pm 0.2\text{‰}$ (Plank, 2014), being well within the range of $\delta^7\text{Li}$ of unaltered MORB ($+3.6 \pm 2.0$; Tomascak et al., 2008). Therefore, if Li inventory in arc magmas is dominated by subducting sediments, volcanic rocks in those arcs should have $\delta^7\text{Li}$ values indistinguishable from MORB.

Scenario 2 is suggested in the studies of volcanic rocks in NE Japan (Moriguti et al., 2004) and Cascadia arcs (Leeman et al., 2004; Magna et al., 2006b). These island arcs have subducting slabs with shallower dip angles or younger ages, thus intensive dehydration would have occurred at shallower depths due to a high T/P gradient via subduction. During dehydration, ^7Li should have been lost preferentially from subducted AOC or sediments. For AOC, progressive dehydration may have lowered its $\delta^7\text{Li}$, and eventually it could have $\delta^7\text{Li}$ values indistinguishable from the wedge mantle. Further dehydration of deeply subducted AOC could have $\delta^7\text{Li}$ values lower than that of unaltered MORB ($< +1.6\text{‰}$). The occurrence of low- $\delta^7\text{Li}$ metamorphic rocks in exhumed subduction complexes (Zack et al., 2003; Simons et al., 2010) or low- $\delta^7\text{Li}$ magmas (melt inclusions) in plume-related volcanic fields (Kobayashi et al., 2004) and ultra rear-arc regions (Schiavi et al., 2012) may support this inference.

Scenario 3 is suggested in the studies of volcanic rocks in Kurile, Sunda, Aleutians (Tomascak et al., 2002) and Kamchatka (Liu et al., 2020). In these arcs, significant contributions from subducted slabs are detected by various geochemical proxies (e.g., Li/Y, B/Be, B/Nb, Ba/La, Pb/Ce, Sb/Ce). In addition, these proxies show significant variations within each arc and often exhibit clear across-arc trends. Apparent decoupling of the $\delta^7\text{Li}$ values and

other trace-element ratios can be explained by buffering of isotopic differences between slab-derived Li and mantle Li via diffusive equilibration (Caciagli et al., 2011; Halama et al., 2009). This in turn suggests that travel time of slab-derived fluids to magma source regions is long enough to attain diffusive isotope equilibrium in most arcs.

The Chugoku volcanic rocks show variation in their $\delta^7\text{Li}$ value that extends beyond the range of MORB. Thus, the processes mentioned in Scenario 1 did not occur or occurred but did not affect the Li isotopic compositions of the magmas. The process mentioned in Scenario 2 (i.e., intensive dehydration) likely occurred, as the current PHS slab is subducting at a shallow angle. Isotope equilibration via fluid-mantle interaction, as proposed in Scenario 3, may also have occurred to some extent. However, neither Scenarios 2 nor 3 did completely attenuate slab-derived Li-isotope signatures found in the Chugoku volcanic rocks. The origin of the $\delta^7\text{Li}$ variation in the volcanic rocks is attributed to the involvement of multiple Li inventories. We discuss possible Li inventories in Sections 5.2.1 to 5.2.3 to examine Scenario 1. Then, Li-isotope fractionation during subduction is discussed in Section 5.3 to examine Scenario 2. Lastly, the effect of the process proposed in Scenario 3, i.e., mantle buffering, is discussed in Section 5.4.

3.2.1 Sediments

Sedimentary rocks in the Nankai Trough or fore-arc terrane have $\delta^7\text{Li}$ values of -4.5 to $+4.6\text{‰}$, and the majority have $\delta^7\text{Li} < +2\text{‰}$ (Moriguti & Nakamura, 1998; You et al., 1995). It has been argued that the Setouchi HMA was derived from a source largely affected by sediments (Hanyu et al., 2002; Kawamoto et al., 2012; Shimoda et al., 1998). Their $\delta^7\text{Li}$ values (-1.0 to -0.2‰) are significantly lower than those of unaltered MORB, while these values are well within the range of sediments. Thus, the sediment origin for this magma is supported by Li-isotopic compositions (Oi et al., 1997; this study). The eruption of the Sera lamprophyre

occurred shortly (~2 Myrs) after the eruption of HMA. The $\delta^7\text{Li}$ value of the rock (-1.0‰) is also lower than MORB (**Figure 5-2**). This peculiar high-K rock has geochemical features consistent with its derivation from a sediment-enriched source (e.g., strong enrichments in Ba, Th, Pb, REE and Li; [Nguyen et al., 2020](#)). We thus consider that sediments subducted beneath the Chugoku district have $\delta^7\text{Li}$ values significantly lower than those of unaltered MORB.

Previous studies proposed that ADK in the Chugoku district was produced by the melting of subducted oceanic crust with significant sediment contribution ([Feineman et al., 2013](#); [Kimura et al., 2014](#); [Pineda-Velasco et al., 2018](#)). However, ADK have $\delta^7\text{Li}$ values different from sediments. Rather, these are similar to the $\delta^7\text{Li}$ values of unaltered MORB or AOC (**Figure 5-2**). The apparent discrepancy of the sediment contribution to ADK will be examined in Section 5.4 using Li isotope data from this study and Sr-Nd-Pb isotope composition by [Feineman et al. \(2013\)](#) and [Pienda-Velasco et al. \(2018\)](#).

3.2.2 AOC

Previous studies have documented that IAB and ADK show broad linear correlations among their Sr, Nd, Hf and Pb isotope compositions and these linear or curvilinear arrays in a plot point toward the compositions of subducted basalts and sediments ([Feineman et al., 2013](#); [Kimura et al., 2014](#); [Nguyen et al., 2020](#); [Pineda-Velasco et al., 2018](#)). New $\delta^7\text{Li}$ data for IAB and ADK samples from this study are combined with Sr, Nd, Hf and Pb isotope data published in these previous studies (**Figure 5-2**). Broad linear correlations are also observed between $\delta^7\text{Li}$ values and $^{87}\text{Sr}/^{86}\text{Sr}$, $^{143}\text{Nd}/^{144}\text{Nd}$, $^{176}\text{Hf}/^{177}\text{Hf}$ or $^{206}\text{Pb}/^{204}\text{Pb}$ ratios. The lower $\delta^7\text{Li}$ ends of these linear arrays point toward the measured composition of Nankai sediments. Therefore, the higher $\delta^7\text{Li}$ ends of these arrays are interpreted to represent the compositions of AOC. This inference is consistent with the estimated Sr, Nd, Hf and Pb isotopic compositions (lower $^{87}\text{Sr}/^{86}\text{Sr}$ and $^{206}\text{Pb}/^{204}\text{Pb}$ ratios and higher $^{143}\text{Nd}/^{144}\text{Nd}$ and $^{176}\text{Hf}/^{177}\text{Hf}$ ratios) similar to the

observed compositions of the Shikoku-Basin basalts.

3.2.3 Serpentinized mantle

Some ADK have $\delta^7\text{Li}$ values significantly higher than unaltered MORB. This feature can also be explained if a high- $\delta^7\text{Li}$ source(s) other than AOC was involved. [Pineda-Velasco et al. \(2018\)](#) argued that the fluids that facilitated slab melting may have been supplied from sub-surface layers (mantle section) of the subducting lithosphere. Serpentinite, a major lithology of the slab mantle section, could retain fluids to a deeper level (~100 km or deeper) if it was not intensively heated (<700 °C; [Ulmer & Trommsdorff, 1995](#)). Thus, it can be a main fluid supplier other than AOC. [Pineda-Velasco et al. \(2018\)](#) noted that ADK volcanoes are located above aseismic slab discontinuities, interpreted as slab tears at, which the slab mantle section was exposed to ambient asthenospheric mantle. Exposure to asthenospheric mantle may have caused intensive dehydration of this layer and induced melting of the overlying AOC layer. Serpentinized abyssal peridotites have a greater variation in $\delta^7\text{Li}$ values (–28 to +14‰) than their unaltered protoliths, and higher $\delta^7\text{Li}$ values ($\delta^7\text{Li} > +5.6\text{‰}$) are found in rocks with higher [Li] (0.5–9 $\mu\text{g}\cdot\text{g}^{-1}$; [Decitre et al., 2002](#); [Vils et al., 2009](#)). If the subducted PHS plate contained a high- $\delta^7\text{Li}$ serpentinized section, then the breakdown of serpentines in the section could have resulted in the release of fluids that could facilitate the melting of AOC and elevate the $\delta^7\text{Li}$ values of AOC melts. It is however noted that [Li] in serpentinized abyssal peridotites are generally low [$3.3 \pm 3.0 \mu\text{g}\cdot\text{g}^{-1}$ ($n = 6$), calculated for rocks with $\delta^7\text{Li} > +5.6\text{‰}$ in [Decitre et al. \(2002\)](#) and [Vils et al. \(2009\)](#)], compared with [Li] of AOC [6–37 $\mu\text{g}\cdot\text{g}^{-1}$; [Chan et al. \(2002\)](#); [Bouman et al. \(2004\)](#)]. In addition, released Li is mostly redistributed in olivines in solid residues after the dehydration of serpentinite ([Scambelluri et al., 2004](#)). Accordingly, [Li] in fluids is buffered at a lower level. We thus conclude that serpentinite dehydration would have little affected the $\delta^7\text{Li}$ value of ADK. Instead, high $\delta^7\text{Li}$ values in ADK should be explained as

a result of limited or insignificant fractionation of ${}^7\text{Li}/{}^6\text{Li}$ in AOC during the metamorphic dehydration of the subducted slab.

3.3 Modeling of Li-isotope fractionation during subduction

3.3.1 Elemental and isotopic composition for modeling

Moriguti and Nakamura (1998) presented the [Li] and $\delta^7\text{Li}$ values of Shimanto shales. The protoliths of the shales are sedimentary rocks deposited in a marginal basin in the Miocene (Yamamoto, 1987). The [Li] and $\delta^7\text{Li}$ values of the two shale samples are 40 and 57 $\mu\text{g}\cdot\text{g}^{-1}$ and -2.7 and -1.5‰ , respectively. You et al. (1995) presented the [Li] and $\delta^7\text{Li}$ values of sediments currently deposited in Nankai Trough. Analyzed samples are separated from drilled cores of sediment piles with 1300-m thickness. The upper pile (< 550 m depth) consists of terrigenous sediment (turbidites) with [Li] = 40–50 $\mu\text{g}\cdot\text{g}^{-1}$ and $\delta^7\text{Li}$ of -2.5 to $+1.3\text{‰}$ [mean -1.1‰ , $n = 4$; Note that their “ $\delta^6\text{Li}$ values” are recalculated to be $\delta^7\text{Li}$ with the standard value of Moriguti and Nakamura (1998)]. These values largely overlap with the values for Shimanto shales by Moriguti and Nakamura (1998). The lower hemipelagic muds (> 620 m depth) show [Li] of 30 to 70 $\mu\text{g}\cdot\text{g}^{-1}$ and $\delta^7\text{Li}$ of -4.5 to $+4.6\text{‰}$ (mean $+0.6\text{‰}$, $n = 10$), which are largely overlapped with those of turbidites. The values of [Li] = 50 $\mu\text{g}\cdot\text{g}^{-1}$ and $\delta^7\text{Li} = -1.0\text{‰}$ are used in the modeling as the elemental and isotopic compositions of Li of the sediment prior to subduction.

The [Li] = 3.7–42 $\mu\text{g}\cdot\text{g}^{-1}$ (mean $\pm 1\sigma = 16 \pm 13$ $\mu\text{g}\cdot\text{g}^{-1}$, $n = 11$) was reported for the submarine basalts in the Shikoku Basin (Akizawa et al., 2021; Shu et al., 2017; Straub et al., 2010). The $\delta^7\text{Li}$ values of these basalts have not yet been reported. It has been documented that $\delta^7\text{Li}$ values of ocean floor basalts are correlated with their [Li] or H_2O abundances (Brant et al., 2012; Chan et al., 1992). The correlation of $\delta^7\text{Li}$ and $1/[\text{Li}]$ (in $\mu\text{g}\cdot\text{g}^{-1}$) of the data of hydrothermally altered basalts from Mid-Atlantic Ridge (23°N transect) by Chan et al. (1992)

is approximated as $\delta^7\text{Li} = -57.37/[\text{Li}] (\mu\text{g} \cdot \text{g}^{-1}) + 14.90$ ($r^2 = 0.934$). Using the equation with the mean $[\text{Li}]$ of Shikoku Basin basalts ($16 \mu\text{g} \cdot \text{g}^{-1}$), $\delta^7\text{Li} = +11.3\%$ is calculated. These values are used in the modeling.

3.3.2 The factor and the extent of Li isotope fractionation

The modeling of $\delta^7\text{Li}$ of AOC/sediment and their-derived fluids utilizes the Rayleigh equation which involves a fractionation factor (α). [Zack et al. \(2003\)](#) and [Marschall et al. \(2007a\)](#) examined the $\delta^7\text{Li}$ value of dehydrated AOC. Note that these two studies used different α . [Zack et al. \(2003\)](#) used α value defined as $\alpha \equiv \frac{(^7\text{Li}/^6\text{Li})_{\text{fluid}}}{(^7\text{Li}/^6\text{Li})_{\text{AOC}}}$, and the values are referred to [Chan et al. \(1992, 1993\)](#) who calculated α values using Li-isotope ratios of hydrothermal fluids and altered basalts from mid-ocean ridges. The α values of [Chan et al. \(1992, 1993\)](#) are 1.019 at $T = 2$ °C and 1.003–1.007 (1.005 as median) at $T = 350$ °C. [Zack et al. \(2003\)](#) may have assumed the linear relationship between α and T as $\alpha = -4.0230 \times 10^{-5}T$ (K) + 1.0300 (calculated by regression analysis in this study). We confirmed that α is 1.015 at 100 °C as was obtained by [Zack et al. \(2003\)](#). [Zack et al. \(2003\)](#) reproduced the observed $\delta^7\text{Li}$ value of natural eclogites (Trescolmen eclogites with $\delta^7\text{Li}$ as low as -10%) using the Rayleigh equation with $\alpha = 1.015$ and partition coefficient $K_{\text{dLi}} (\equiv [\text{Li}]_{\text{AOC}}/[\text{Li}]_{\text{fluid}}) = 0.05$. However, a later study has reexamined these model inputs. [Marschall et al. \(2007a\)](#) used $\alpha = 1.0106$, as they assumed metamorphic T of 300 °C. They mentioned that the temperature dependency of α is corrected using the experimental result by [Wunder et al. \(2006\)](#). [Marschall et al. \(2007a\)](#) also used the different K_{dLi} (0.15) which is estimated by considering its temperature dependency ([Berger et al., 1988](#)).

It is noted that [Wunder et al. \(2006\)](#) defined the fractionation factor as $\Delta^7\text{Li} =$

$\delta ^7\text{Li}_{\text{solid}} - \delta ^7\text{Li}_{\text{fluid}} (\equiv \delta ^7\text{Li}_{\text{AOC}} - \delta ^7\text{Li}_{\text{fluid}})$. The $\Delta^7\text{Li}$ values by [Wunder et al. \(2006\)](#) show temperature dependency, expressed as $\Delta^7\text{Li} = -4.61 \times \left(\frac{1000}{T[\text{K}]}\right) + 2.48$. The α and $\Delta^7\text{Li}$ at a given temperature can be converted from one to another. Below, the derivation for the conversion is shown.

The $\delta^7\text{Li}$ values of AOC ($\delta^7\text{Li}_{\text{AOC}}$) and fluid ($\delta^7\text{Li}_{\text{fluid}}$) are defined as

$$\delta ^7\text{Li}_{\text{AOC}} = \left[\frac{\left(\frac{{}^7\text{Li}}{{}^6\text{Li}}\right)_{\text{AOC}}}{\left(\frac{{}^7\text{Li}}{{}^6\text{Li}}\right)_{\text{std}}} - 1 \right] \times 10^3 \quad (1)$$

and

$$\delta ^7\text{Li}_{\text{fluid}} = \left[\frac{\left(\frac{{}^7\text{Li}}{{}^6\text{Li}}\right)_{\text{fluid}}}{\left(\frac{{}^7\text{Li}}{{}^6\text{Li}}\right)_{\text{std}}} - 1 \right] \times 10^3 \quad (2)$$

where $\left(\frac{{}^7\text{Li}}{{}^6\text{Li}}\right)_{\text{std}}$ denotes ${}^7\text{Li}/{}^6\text{Li}$ ratio of a standard with $\delta^7\text{Li} = 0$ (i.e., L-SVEC). Solving the equations 1 and 2 for $\left(\frac{{}^7\text{Li}}{{}^6\text{Li}}\right)_{\text{AOC}}$ and $\left(\frac{{}^7\text{Li}}{{}^6\text{Li}}\right)_{\text{fluid}}$, we get

$$\left(\frac{{}^7\text{Li}}{{}^6\text{Li}}\right)_{\text{AOC}} = (\delta ^7\text{Li}_{\text{AOC}} \times 10^{-3} + 1) \times \left(\frac{{}^7\text{Li}}{{}^6\text{Li}}\right)_{\text{std}} \quad (3)$$

and

$$\left(\frac{{}^7\text{Li}}{{}^6\text{Li}}\right)_{\text{fluid}} = (\delta ^7\text{Li}_{\text{fluid}} \times 10^{-3} + 1) \times \left(\frac{{}^7\text{Li}}{{}^6\text{Li}}\right)_{\text{std}} . \quad (4)$$

Using the equations 3 and 4, α is expressed as

$$\alpha = \frac{\left(\frac{{}^7\text{Li}}{{}^6\text{Li}}\right)_{\text{fluid}}}{\left(\frac{{}^7\text{Li}}{{}^6\text{Li}}\right)_{\text{AOC}}} = \frac{\delta ^7\text{Li}_{\text{fluid}} \times 10^{-3} + 1}{\delta ^7\text{Li}_{\text{AOC}} \times 10^{-3} + 1} . \quad (5)$$

From the definition of $\Delta^7\text{Li}$, $\delta^7\text{Li}_{\text{fluid}}$ is expressed as

$$\delta^7\text{Li}_{\text{fluid}} = \delta^7\text{Li}_{\text{AOC}} - \Delta^7\text{Li}. \quad (6)$$

Using the equations 5 and 6, α is expressed as

$$\alpha = \frac{(\delta^7\text{Li}_{\text{AOC}} - \Delta^7\text{Li}) \times 10^{-3} + 1}{\delta^7\text{Li}_{\text{AOC}} \times 10^{-3} + 1}. \quad (7)$$

The temperature-dependent equation of $\Delta^7\text{Li}$ by [Wunder et al. \(2006\)](#) is plugged into the equation 7 as

$$\alpha = \frac{\left\{ \delta^7\text{Li}_{\text{AOC}} + 4.61 \times \left(\frac{1000}{T[\text{K}]} \right) - 2.48 \right\} \times 10^{-3} + 1}{\delta^7\text{Li}_{\text{AOC}} \times 10^{-3} + 1}. \quad (8)$$

Using the equation 8, the validity of using different α is examined. The $\alpha = 1.0106$ used in [Marschall et al. \(2007a\)](#) corresponds to α at 75 °C. We thus consider that “ $T = 300$ °C” in Figure 3a of [Marschall et al. \(2007a\)](#) is the temperature to estimate K_{dLi} (0.15) from their Figure 2a. But this temperature is not feasible to attain $\alpha = 1.0106$. At $T = 300$ °C, α should be 1.0055. Hence, the K_{dLi} and α used in the same model are inconsistent in terms of their reference temperature.

For a better comparison of the models by [Zack et al. \(2003\)](#) and [Marschall et al. \(2007a\)](#), the same T should be used as a model input. We chose 100 °C as a common model input, resulting in $K_{\text{dLi}} = 0.05$ and $\alpha = 1.015$ for [Zack et al. \(2003\)](#) and $K_{\text{dLi}} = 1.17$ and $\alpha = 1.010$ for [Marschall et al. \(2007a\)](#). The K_{dLi} in the model for [Marschall et al. \(2007a\)](#) is estimated from the T - K_{dLi} relationship (for chlorite) in Figure 2a of their study (<400 °C). This plot includes the experimental data of [Berger et al. \(1988\)](#) and the data points yield the regression line $\log K_{\text{dLi}} = -3.268 \times 10^{-3} \cdot T$ (in °C) + 0.3937. Using these pairs of K_{dLi} and α , the $\delta^7\text{Li}$ values of dehydrated AOC are estimated. The options of H_2O content (1–8 wt%) and Li

abundance ($15\text{--}80 \mu\text{g}\cdot\text{g}^{-1}$) for AOC are the same as in Zack et al. (2003) and Marschall et al. (2007a). The result of the modeling is shown in Figure 5-9.

Owing to the difference in model inputs, the results by this study and by Marschall et al. (2007a) are different. Nevertheless, the results by Marschall et al. (2007a) and this study led to the same conclusion that the dehydration of AOC decreases the $\delta^7\text{Li}$ value by 5‰ or smaller. For the possible range in temperature ($50\text{--}900 \text{ }^\circ\text{C}$), the α varies from 1.0116 ($50 \text{ }^\circ\text{C}$) to 1.0014 ($900 \text{ }^\circ\text{C}$) (Equation 8), whereas the K_{dLi} varies from 1.70 ($50 \text{ }^\circ\text{C}$) to 0.05 ($>500 \text{ }^\circ\text{C}$) after Marschall et al. (2007a). The larger α and/or smaller K_{dLi} results in the greater extent of isotope fractionation. The maximum fractionation occurs at $600 \text{ }^\circ\text{C}$ and results in the decrease of $\delta^7\text{Li}$ by 3‰. In this study, we used K_{dLi} by Berger et al. (1988) at $< 400 \text{ }^\circ\text{C}$ and by Marschall et al. (2007a) at $> 400 \text{ }^\circ\text{C}$, and α (or $\Delta^7\text{Li}$) by Wunder et al. (2006) for AOC dehydration.

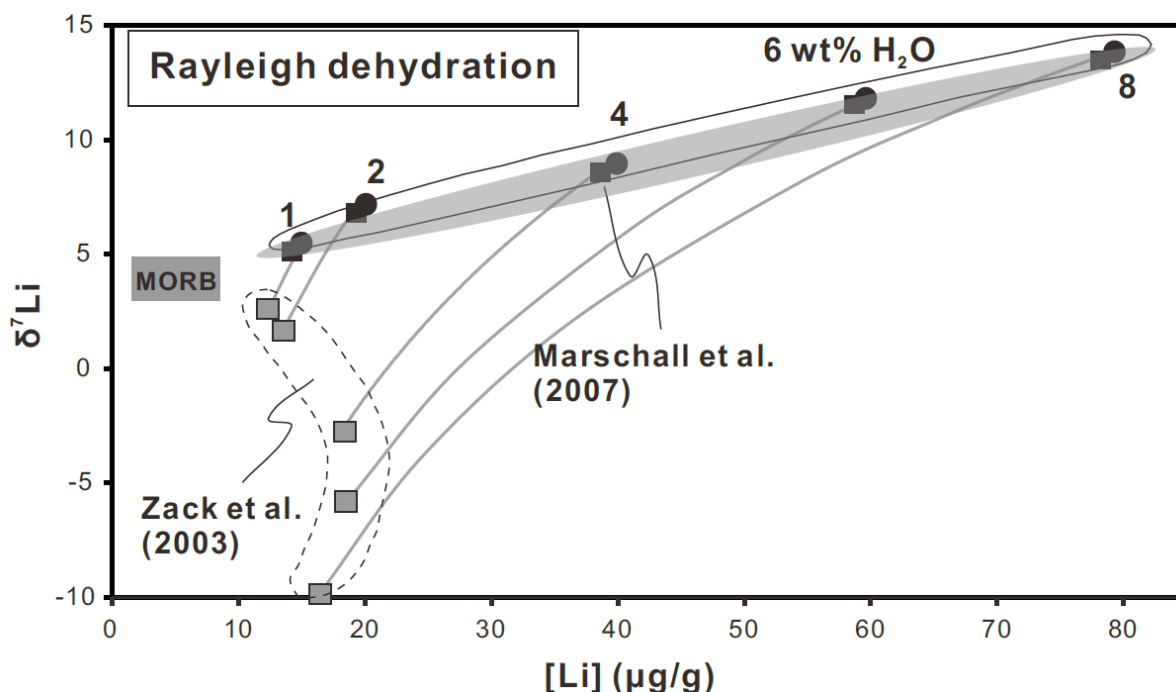


Figure 5-9. Results of the modeling of $[\text{Li}]$ and $\delta^7\text{Li}$ of subducting AOC using the Rayleigh distillation equation.

The models assume that isotope fractionation occurs at 100 °C. The black circles show the initial [Li] and $\delta^7\text{Li}$ of AOC with different H₂O contents (1, 2, 4, 6 and 8 wt%). The difference in the model results by [Zack et al. \(2003\)](#), shown by gray squares, and [Marschall et al. \(2007a\)](#), shown by black squares, are due to the use of different partition coefficients (K_{dLi}) and isotope fractionation factors (α) of Li between AOC and fluid. [Zack et al. \(2003\)](#) followed the temperature (T)– α relationship by [Chan et al. \(1992, 1993\)](#), while [Marschall et al. \(2007a\)](#) used the T– α relationship by [Wunder et al. \(2006\)](#). The difference in K_{dLi} between these two studies is from the presence of minor phases in the model AOC (K_{dLi} becomes larger if minor phases such as chlorite, smectite or zeolite are included in residual phases).

[Simons et al. \(2010\)](#) examined the $\delta^7\text{Li}$ value of dehydrated sediment. They assumed that the fractionation factor α for sediment is the same as that for AOC at given temperatures, i.e., they used the temperature-dependent factor by [Wunder et al. \(2006\)](#). It is however noted that [Wunder et al. \(2007\)](#) presented the temperature-dependent α better applicable to sediment, and these values are used in our modeling. [Simons et al. \(2010\)](#) consider the varying K_{dLi} for subducting sediments as its phase assemblage changes during subduction. Phase assemblages were calculated by the model of [Schmidt and Poli \(2003\)](#) and Li partition coefficients of each phase are taken from [Berger et al. \(1988\)](#). The T - K_{dLi} relationship by [Simons et al. \(2010\)](#) is expressed as $K_{\text{dLi}} = -2.87 \times T \text{ (in } ^\circ\text{C)} \times 10^{-3} + 1.252$ ($r^2 = 0.992$) at < 450 °C. At ≥ 450 °C, the K_{dLi} is constant at 0.14.

[Marschall et al. \(2007a\)](#) and [Simons et al. \(2010\)](#) considered the multi-stage stepwise dehydration. We also considered this model for the evolution of [Li] and $\delta^7\text{Li}$ values of subducted sediment and AOC. In the next section, the application of the stepwise dehydration model is outlined.

3.3.3 P-T path and water loss during progressive dehydration

The release of fluids (dominated by H₂O) results from diagenesis or metamorphism of AOC and sediment with increasing pressure and temperature via subduction. Phase relations in varying temperature and pressure conditions can be predicted by thermodynamic model (Connolly, 2005). Kimura et al. (2014) and Kimura (2017) implemented thermodynamic modeling of phase assemblage of AOC and sediment in their petrologic tool termed Arc Basalt Simulator (ABS). In the ABS model, mafic crustal section of the subducting oceanic lithosphere consists of layers of basalts, dikes (diabase), and gabbros, and it is overlain by sediment. Each layer of mafic crustal section is divided into upper and lower sublayers. The AOC corresponds to their “UBAS” (upper basalt sublayer) and “LBAS” (lower basalt sublayer). Different layers or sublayers have different temperatures and H₂O abundances. Hence, rocks in different layers show different release curves of H₂O along subduction *P-T* paths.

In the model, the initial H₂O abundance in AOC is 5.3 wt% [mean of H₂O abundances in UBAS and LBAS in ABS (Kimura et al., 2014; Kimura, 2017)]. The value is comparable to the maximum LOI values (~6 wt%) of Shikoku Basin basalts (Chen et al., 2020). The initial H₂O abundance of the subducted sediment is assumed to be 5.3 wt% in Kimura’s model. The value is comparable to the maximum H₂O⁺ (structural water) abundances in Shimanto shales (3.8 wt% after Yamamoto et al., 1997). Kimura’s model provides H₂O abundance in dehydrated AOC and sediment at the pressure range of 0.5 GPa (*c.* 19 km depth) to 6 GPa (*c.* 220 km depth) with a step of 0.1 GPa. We used the H₂O estimates for AOC and sediment (SED) at 0.5 to 3.5 GPa (*c.* 20–120 km depth). Temperatures of the AOC and SED layers, predicted by the ABS model, at certain depths were also used for the modeling (for calculation of temperature-dependent factors).

3.3.4 Li abundances of fluids and residual AOC or sediment during dehydration

Li abundances of fluid ($c_{\text{Li}}^{\text{fluid}}$) and AOC ($c_{\text{Li}}^{\text{AOC}}$) show the relationship as

$$c_{\text{Li}}^{\text{fluid}_n} = \frac{c_{\text{Li}}^{\text{AOC}_{n-1}}}{(K_{\text{dLi}}^n - 1) \frac{m_{\text{AOC}_n}}{m_{\text{AOC}_{n-1}}} + 1} \quad (9)$$

where subscript n or $n - 1$ denote dehydration steps, K_{dLi}^n is partition coefficients of Li between AOC and fluid ($c_{\text{Li}}^{\text{AOC}_n}/c_{\text{Li}}^{\text{fluid}_n}$), and m denotes the mass of AOC at each dehydration step. Temperature-dependent K_{dLi}^n is calculated from data by [Berger et al. \(1988\)](#) ($50^\circ\text{C} < T < 300^\circ\text{C}$) and [Marschall et al. \(2007b\)](#) ($T > 300^\circ\text{C}$). Derivation of the equation 9 is given below (c.f. [Marschall et al., 2006](#)).

The masses of fluids formed in dehydration steps $n-1$ and n are expressed as $m_{\text{fluid}_{n-1}}$ and m_{fluid_n} , and the mass of residual AOC in dehydration steps $n-1$ and n are expressed as $m_{\text{AOC}_{n-1}}$ and m_{AOC_n} . The mass balance among m_{fluid_n} , $m_{\text{AOC}_{n-1}}$ and m_{AOC_n} is expressed as

$$m_{\text{AOC}_{n-1}} = m_{\text{AOC}_n} + m_{\text{fluid}_n}. \quad (10)$$

Similarly, the mass balance of elemental Li is expressed as

$$m_{\text{Li}}^{\text{AOC}_{n-1}} = m_{\text{Li}}^{\text{AOC}_n} + m_{\text{Li}}^{\text{fluid}_n}. \quad (11)$$

Partition coefficients of Li between AOC and fluid is defined as

$$K_{\text{dLi}}^n \equiv \frac{c_{\text{Li}}^{\text{AOC}_n}}{c_{\text{Li}}^{\text{fluid}_n}}. \quad (12)$$

The concentration of Li (c_{Li}), mass of Li (m_{Li}), and mass of fluid (m_{fluid}) or AOC (m_{AOC}) should satisfy the following relationships.

$$c_{\text{Li}}^{\text{fluid}_n} = \frac{m_{\text{Li}}^{\text{fluid}_n}}{m_{\text{fluid}_n}} \quad (13)$$

and

$$c_{\text{Li}}^{\text{AOC}_n} = \frac{m_{\text{Li}}^{\text{AOC}_n}}{m_{\text{AOC}_n}}. \quad (14)$$

Partition coefficient (equation 12) can be written with the equations 13 and 14 as

$$K_{\text{dLi}}^n = \frac{m_{\text{Li}}^{\text{AOC}_n}}{m_{\text{Li}}^{\text{fluid}_n}} \cdot \frac{m_{\text{fluid}_n}}{m_{\text{AOC}_n}}. \quad (15)$$

The equation 15 is rearranged as

$$m_{\text{Li}}^{\text{fluid}_n} = \frac{m_{\text{Li}}^{\text{AOC}_n}}{K_{\text{dLi}}^n} \cdot \frac{m_{\text{fluid}_n}}{m_{\text{AOC}_n}}. \quad (16)$$

Combining the equations 10, 11 and 16, and then solving for $m_{\text{Li}}^{\text{fluid}_n}$, we get

$$m_{\text{Li}}^{\text{fluid}_n} = \frac{m_{\text{fluid}_n} m_{\text{Li}}^{\text{AOC}_{n-1}}}{K_{\text{dLi}}^n (m_{\text{AOC}_{n-1}} - m_{\text{fluid}_n}) + m_{\text{fluid}_n}}. \quad (17)$$

The equation 17 can also be expressed as

$$m_{\text{Li}}^{\text{fluid}_n} = \frac{m_{\text{Li}}^{\text{AOC}_{n-1}}}{K_{\text{dLi}}^n \left(\frac{m_{\text{AOC}_{n-1}}}{m_{\text{fluid}_n}} - 1 \right) + 1}. \quad (18)$$

Using the equations 13 and 14, the equation 18 can be rewritten as

$$c_{\text{Li}}^{\text{fluid}_n} m_{\text{fluid}_n} = c_{\text{Li}}^{\text{fluid}_n} (m_{\text{AOC}_{n-1}} - m_{\text{AOC}_n}) = \frac{c_{\text{Li}}^{\text{AOC}_{n-1}} m_{\text{AOC}_{n-1}}}{K_{\text{dLi}}^n \left(\frac{m_{\text{AOC}_{n-1}}}{m_{\text{AOC}_{n-1}} - m_{\text{AOC}_n}} - 1 \right) + 1}. \quad (19)$$

Solving the equation 19 for $c_{\text{Li}}^{\text{fluid}_n}$, we get

$$c_{\text{Li}}^{\text{fluid}_n} = \frac{c_{\text{Li}}^{\text{AOC}_{n-1}}}{(K_{\text{dLi}}^n - 1) \frac{m_{\text{AOC}_n}}{m_{\text{AOC}_{n-1}}} + 1}. \quad (20)$$

The same mass balance calculation can be applied to Li exchange between sediment and fluid. The K_{d} of Li between sediment and fluid is from data by [Simons et al. \(2010\)](#).

3.3.5 Li isotopic compositions of fluids and residual AOC or sediment during dehydration

The extent to which ${}^7\text{Li}/{}^6\text{Li}$ fractionate between fluid and AOC is expressed as

$$\Delta\delta {}^7\text{Li} = \delta {}^7\text{Li}_{\text{fluid}_n} - \delta {}^7\text{Li}_{\text{AOC}_n}. \quad (21)$$

The temperature (T)-dependent $\Delta\delta {}^7\text{Li}$ is given after [Wunder et al. \(2006\)](#) as

$$\Delta\delta {}^7\text{Li} = 4.61 \cdot \frac{1000}{T \text{ (K)}} - 2.48. \quad (22)$$

Note that [Wunder et al. \(2006\)](#) originally defined $\Delta\delta {}^7\text{Li}$ as $\delta {}^7\text{Li}_{\text{AOC}_n} - \delta {}^7\text{Li}_{\text{fluid}_n}$. The ${}^7\text{Li}/{}^6\text{Li}$ ratio or $\delta {}^7\text{Li}$ value is the expression in the molar unit. A molar ratio can be converted to a weight ratio of ${}^7\text{Li}/{}^6\text{Li}$ ($m_{7\text{Li}}/m_{6\text{Li}}$) as

$$\frac{{}^7\text{Li}}{{}^6\text{Li}} = \frac{\frac{m_{7\text{Li}}}{u_{7\text{Li}}}}{\frac{m_{6\text{Li}}}{u_{6\text{Li}}}} = \frac{m_{7\text{Li}}}{m_{6\text{Li}}} \times \frac{6.015122}{7.016004} = 0.857343012 \frac{m_{7\text{Li}}}{m_{6\text{Li}}} \quad (23)$$

where $u_{6\text{Li}}$ and $u_{7\text{Li}}$ denote unit masses of isotopes ${}^6\text{Li}$ (6.015122) and ${}^7\text{Li}$ (7.016004), respectively. $\delta {}^7\text{Li}_{\text{fluid}_n}$ and $\delta {}^7\text{Li}_{\text{AOC}_n}$ are defined as

$$\delta {}^7\text{Li}_{\text{fluid}_n} = \left\{ \frac{\left(\frac{{}^7\text{Li}}{{}^6\text{Li}} \right)_{\text{fluid}_n}}{\left(\frac{{}^7\text{Li}}{{}^6\text{Li}} \right)_{\text{L-SVEC}}} - 1 \right\} \cdot 10^3 \quad (24)$$

and

$$\delta {}^7\text{Li}_{\text{AOC}_n} = \left\{ \frac{\left(\frac{{}^7\text{Li}}{{}^6\text{Li}} \right)_{\text{AOC}_n}}{\left(\frac{{}^7\text{Li}}{{}^6\text{Li}} \right)_{\text{L-SVEC}}} - 1 \right\} \cdot 10^3 \quad (25)$$

where $\left(\frac{{}^7\text{Li}}{{}^6\text{Li}} \right)_{\text{L-SVEC}} = 12.1163$ is after [Moriguti and Nakamura \(1998\)](#). The equations 24 and

25 are rewritten as

$$\delta \text{}^7\text{Li}_{\text{fluid}_n} = \left\{ \frac{\left(\frac{m \text{}^7\text{Li}}{m \text{}^6\text{Li}} \right)_{\text{fluid}_n} - 1}{\left(\frac{m \text{}^7\text{Li}}{m \text{}^6\text{Li}} \right)_{\text{L-SVEC}}} \right\} \cdot 10^3 \quad (26)$$

and

$$\delta \text{}^7\text{Li}_{\text{AOC}_n} = \left\{ \frac{\left(\frac{m \text{}^7\text{Li}}{m \text{}^6\text{Li}} \right)_{\text{AOC}_n} - 1}{\left(\frac{m \text{}^7\text{Li}}{m \text{}^6\text{Li}} \right)_{\text{L-SVEC}}} \right\} \cdot 10^3. \quad (27)$$

Note that the conversion factor of isotope “molar” ratio to isotope “mass” ratio (0.857343012, see the equation 23) is canceled in the δ notation. The equations 26 and 27 are plugged into the equation 21 as

$$\Delta \delta \text{}^7\text{Li}_n = \left\{ \frac{\left(\frac{m \text{}^7\text{Li}}{m \text{}^6\text{Li}} \right)_{\text{fluid}_n} - 1}{\left(\frac{m \text{}^7\text{Li}}{m \text{}^6\text{Li}} \right)_{\text{L-SVEC}}} \right\} \cdot 10^3 - \left\{ \frac{\left(\frac{m \text{}^7\text{Li}}{m \text{}^6\text{Li}} \right)_{\text{AOC}_n} - 1}{\left(\frac{m \text{}^7\text{Li}}{m \text{}^6\text{Li}} \right)_{\text{L-SVEC}}} \right\} \cdot 10^3. \quad (28)$$

The equation 28 is rearranged as

$$\left(\frac{m \text{}^7\text{Li}}{m \text{}^6\text{Li}} \right)_{\text{fluid}_n} - \left(\frac{m \text{}^7\text{Li}}{m \text{}^6\text{Li}} \right)_{\text{AOC}_n} = \frac{\Delta \delta \text{}^7\text{Li}_n}{1000} \left(\frac{m \text{}^7\text{Li}}{m \text{}^6\text{Li}} \right)_{\text{L-SVEC}} = \frac{\Delta \delta \text{}^7\text{Li}_n}{1000} \left(\frac{\text{}^7\text{Li}}{\text{}^6\text{Li}} \right)_{\text{L-SVEC}} \times 1.166394298. \quad (29)$$

where a factor 1.166394298 is the ratio of the mass of ${}^7\text{Li}$ over the mass of ${}^6\text{Li}$.

Mass balance of ${}^6\text{Li}$ and ${}^7\text{Li}$ in fluid and AOC during dehydration can be described as

$$m \text{}^6\text{Li}^{\text{fluid}_n} + m \text{}^6\text{Li}^{\text{AOC}_n} = m \text{}^6\text{Li}^{\text{AOC}_{n-1}} \quad (30)$$

and

$$m_{7\text{Li}}^{\text{fluid}_n} + m_{7\text{Li}}^{\text{AOC}_n} = m_{7\text{Li}}^{\text{AOC}_{n-1}}. \quad (31)$$

Combining the equations 29, 30 and 31, we get

$$\left(\frac{m_{7\text{Li}}^{\text{AOC}_{n-1}} - m_{7\text{Li}}^{\text{AOC}_n}}{m_{6\text{Li}}^{\text{AOC}_{n-1}} - m_{6\text{Li}}^{\text{AOC}_n}} \right) - \left(\frac{m_{7\text{Li}}}{m_{6\text{Li}}} \right)_{\text{AOC}_n} = \frac{\Delta\delta_{7\text{Li}_n}}{1000} \left(\frac{7\text{Li}}{6\text{Li}} \right)_{\text{L-SVEC}} \times 1.166394298. \quad (32)$$

The term φ is defined as

$$\varphi = \frac{\Delta\delta_{7\text{Li}_n}}{1000} \left(\frac{7\text{Li}}{6\text{Li}} \right)_{\text{L-SVEC}} \times 1.166394298 = \frac{m_{6\text{Li}}^{\text{AOC}_n} \cdot m_{7\text{Li}}^{\text{AOC}_{n-1}} - m_{6\text{Li}}^{\text{AOC}_{n-1}} (m_{\text{Li}}^{\text{AOC}_n} - m_{6\text{Li}}^{\text{AOC}_n})}{m_{6\text{Li}}^{\text{AOC}_n} \cdot m_{6\text{Li}}^{\text{AOC}_{n-1}} - (m_{6\text{Li}}^{\text{AOC}_n})^2} \quad (33)$$

where $m_{\text{Li}}^{\text{AOC}_n}$ is the mass of Li in AOC at n -th dehydration step and expressed as

$$m_{\text{Li}}^{\text{AOC}_n} = m_{6\text{Li}}^{\text{AOC}_n} + m_{7\text{Li}}^{\text{AOC}_n}. \quad (34)$$

The equation 33 is rewritten with the equation 34 as

$$\left(m_{6\text{Li}}^{\text{AOC}_n} \right)^2 + \frac{(1-\varphi)m_{6\text{Li}}^{\text{AOC}_{n-1}} + m_{7\text{Li}}^{\text{AOC}_{n-1}}}{\varphi} m_{6\text{Li}}^{\text{AOC}_n} - \frac{m_{6\text{Li}}^{\text{AOC}_{n-1}} \cdot m_{\text{Li}}^{\text{AOC}_n}}{\varphi} = 0. \quad (35)$$

The equation 35 is a quadratic equation in the form of $ax^2 + bx + c = 0$ where $a = 1$, $b =$

$\frac{(1-\varphi)m_{6\text{Li}}^{\text{AOC}_{n-1}} + m_{7\text{Li}}^{\text{AOC}_{n-1}}}{\varphi}$, and $c = -\frac{m_{6\text{Li}}^{\text{AOC}_{n-1}} \cdot m_{\text{Li}}^{\text{AOC}_n}}{\varphi}$, respectively. The solution of the equation is

given as $x = \frac{-b \pm \sqrt{b^2 - 4ac}}{2a}$ or

$$m_{6\text{Li}}^{\text{AOC}_n} = \frac{1}{2} \left\{ \frac{(\varphi - 1)m_{6\text{Li}}^{\text{AOC}_{n-1}} - m_{7\text{Li}}^{\text{AOC}_{n-1}}}{\varphi} + \sqrt{\left[\frac{(\varphi - 1)m_{6\text{Li}}^{\text{AOC}_{n-1}} - m_{7\text{Li}}^{\text{AOC}_{n-1}}}{\varphi} \right]^2 + 4 \frac{m_{6\text{Li}}^{\text{AOC}_{n-1}} \cdot m_{\text{Li}}^{\text{AOC}_n}}{\varphi}} \right\}. \quad (36)$$

Then, $m_{7\text{Li}}^{\text{AOC}_n}$ is given as

$$m_{7\text{Li}}^{\text{AOC}_n} = m_{\text{Li}}^{\text{AOC}_n} - m_{6\text{Li}}^{\text{AOC}_n}. \quad (37)$$

Now, the $\delta^7\text{Li}$ value of residual AOC after n -th dehydration step can be calculated from $m_{6\text{Li}}^{\text{AOC}_n}$ and $m_{7\text{Li}}^{\text{AOC}_n}$ with the equation 27.

The equations 21–37 can be applied to Li isotope fractionation during the dehydration of sediment. It should be noted that the extent to which ^6Li and ^7Li fractionate during sediment dehydration is different from the case for AOC dehydration. We used the following equation to calculate the temperature-dependent isotope fractionation factor by [Wunder et al. \(2007\)](#)

$$\Delta\delta^7\text{Li} = 4.52 \cdot \frac{1000}{T \text{ (K)}} - 4.74 \text{ (< 500 }^\circ\text{C)} \quad (38)$$

and

$$\Delta\delta^7\text{Li} = -1.3 (\pm 0.2, > 500 \text{ }^\circ\text{C}). \quad (39)$$

3.3.6 Summary of results

SW Japan arc is a hot subduction zone where a young oceanic lithosphere is subducting ([Syracuse et al., 2010](#); [van Keken et al., 2011](#)). Therefore, intensive dehydration of AOC and sediment (SED) should have occurred during subduction ([Peacock & Wang, 1999](#); [Tatsumi et al., 2020](#)). Intensive dehydration should have induced Li isotope fractionation ([Marschall et al., 2007](#); [Simons et al., 2010](#); [Zack et al., 2003](#)). [Zack et al. \(2003\)](#) examined the evolution of $\delta^7\text{Li}$ in subducting AOC using a simple Rayleigh distillation model with a constant isotope fractionation factor and partition coefficient between rocks and fluids. However, such a simple model is probably not viable, as AOC and SED would have dehydrated continuously during subduction. Given that fractionation factor and partition coefficient would have varied, owing to changes in P - T condition via subduction ([Berger et al., 1988](#); [Marschall et al., 2007](#); [Wunder](#)

et al., 2006). Rather, it is more appropriate to apply the incremental dehydration model (Marschall et al., 2007; Simons et al., 2010). Recent studies provided the possible P - T paths of various lithologies within the subducting slab beneath the district (Kimura et al., 2014; Syracuse et al., 2010), which allow us to precisely examine the change in elemental and isotopic compositions of subducted Li sources. The results are summarized in **Tables 5-2 and 5-3**. It is noted that subducted sediments would have incongruently melted, having left solid residues possibly containing Li-rich phases (e.g., garnet). Johnson and Plank (1999) analyzed [Li] of melts and residues produced by melting experiments of sedimentary starting materials. Their results do not show preferential retention of Li in residues ($[\text{Li}]_{\text{residue}}/[\text{Li}]_{\text{starting material}} < 1$ for all experiments). We thus consider that significant isotope fractionation did not occur during the formation of fluids or melts from subducted sediments.

Results of the modeling are shown in **Figure 5-10** and **Tables 5-2 and 5-3**. The extents to which Li-isotope fractionation occur in AOC and SED largely depend on the amounts of fluids released from these lithologies. Then, the releases of fluids are governed by breakdowns of hydrous phases in AOC and SED. The models predicted that the [Li] and $\delta^7\text{Li}$ values of AOC and SED significantly decrease during subduction in the depth of > 70 km (**Figure 5-10**). This is because major hydrous phases in AOC and SED (amphibole, lawsonite, chlorite, prehnite, pumpellyite, and talc) are broken down, as postulated by the model for SW Japan (Kimura et al., 2014; Kimura, 2017) using thermodynamic algorithms (Connolly & Kerrick, 1987; Connolly & Petrini, 2002). Nevertheless, the predicted changes of $\delta^7\text{Li}$ values to the depth for melting (90 km) are relatively small; 2‰ (+ 11.5‰ to +9.7‰) for AOC and 0.5‰ (−1.0‰ to −1.5‰) for SED, respectively. These changes accompany a significant decrease in Li abundances ($[\text{Li}]/[\text{Li}]_0 = 56\%$ for AOC and 27% for SED, respectively, where [Li] and $[\text{Li}]_0$ are subducted and pre-subducted AOC or SED).

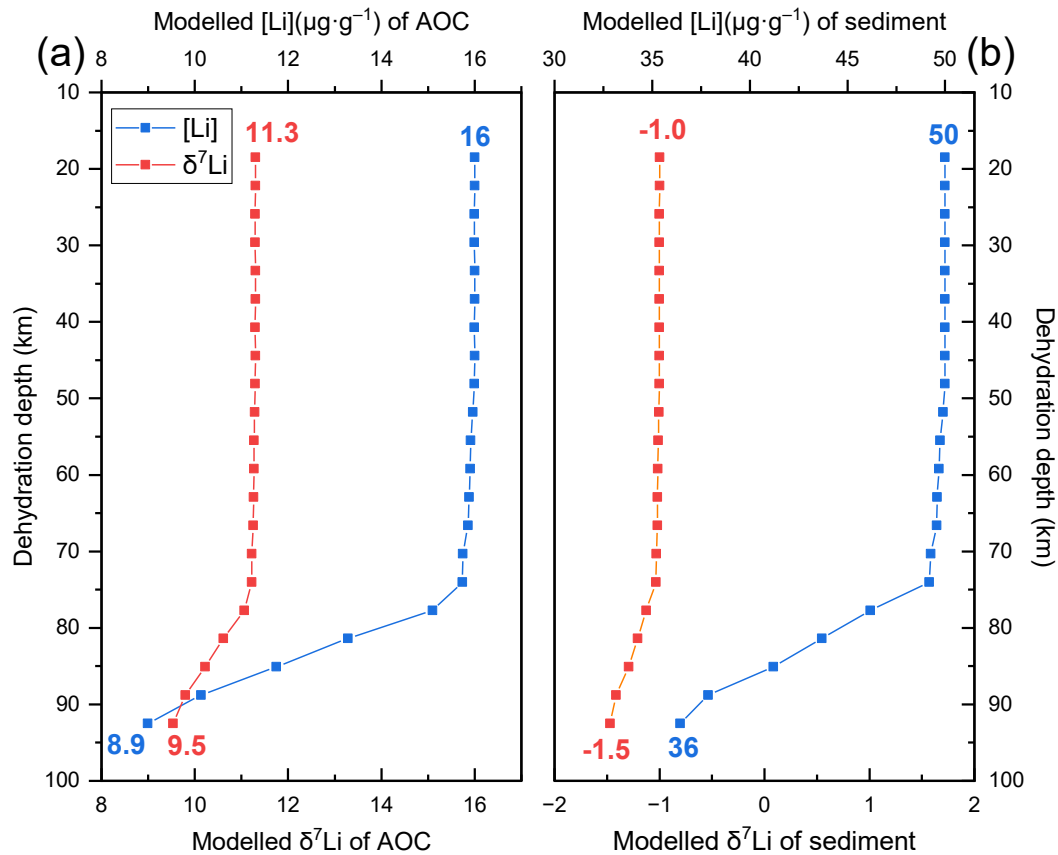


Figure 5-10. The changes in [Li] (blue lines) and $\delta^7\text{Li}$ values (red lines) of (a) AOC (Shikoku Basin basalt) and (b) sediment (Nankai sediment) in the subducted oceanic lithosphere at the depth from c. 20 km to 90 km beneath the Chugoku district.

Those data are calculated by the incremental dehydration model (Marschall et al., 2007; Simons et al., 2010). Significant drops in [Li] and $\delta^7\text{Li}$ values of AOC and SED in the depth of > 70 km are due to the breakdown of major hydrous phases in these materials (amphibole, lawsonite, chlorite, prehnite, pumpellyite, and talc).

3.4 Mantle buffering of the slab-derived Li-isotope signature

The IAB magmas are considered to have been derived by partial melting of mantle metasomatized by slab-derived fluids or melts (Kimura et al., 2014; Nguyen et al., 2020). Most IAB rocks have $\delta^7\text{Li}$ values within the range of MORB. Slab-derived fluids would be a mixture

of AOC- and SED-derived fluids or melts. The IAB source should have been heated to the temperature required for melting (1220–1380 °C; [Nguyen et al., 2020](#)). Under such a high-temperature condition, the slab-derived Li-isotope signature may have been attenuated by diffusive isotope equilibrium with the mantle. The inference is supported by the homogeneity of $\delta^7\text{Li}$ values, falling within the range of unaltered MORB, in the majority of mantle-derived rocks distributed over the globe through geologic time ([Halama et al., 2008](#); [Krienitz et al., 2012](#)).

Migration of slab-derived fluids or melts could have occurred in the form of (1) diffuse porous flow ([Mibe et al., 1999](#)), (2) fracture flow ([Davies, 1999](#)) or (3) diapir ([Hall & Kincaid, 2001](#)). Siliceous fluids or hydrous melts are highly viscous, resulting in low permeability. Thus, their transports likely occur in the form of either fracture flow ([Kepezhinskas et al., 1996](#)) or diapirs ([Yogodzinski et al., 2015](#)). Nevertheless, the likelihood of transport by diffuse porous flow is examined using the approach by [Caciagli et al. \(2011\)](#) using the chromatographic model of Navon and Stolper (1987). In the model, a mantle column consisting of mineral grains with interconnected pores is considered. Fluids or melts go upward through interconnected pore space in the mantle column of a finite length. The X_{melt} is the mass fraction of Li in the fluid/melt in the column defined as

$$X_{\text{melt}} \equiv \frac{\Phi \rho_{\text{melt}}}{\Phi \rho_{\text{melt}} + (1 - \Phi) \rho_{\text{mantle}} K_{\text{dLi}}} \quad (2)$$

where ϕ is fluid/melt fraction in the mantle column (porosity), ρ_{melt} and ρ_{mantle} are the densities of a fluid/melt and the solid mantle, and K_{dLi} is partition coefficient of Li between the solid mantle and a fluid/melt ($K_{\text{dLi}} \equiv [\text{Li}]_{\text{mantle}}/[\text{Li}]_{\text{melt}}$), respectively. The ϕ of 0.03 follows Navon and Stolper (1987), and ρ_{melt} and ρ_{mantle} are assumed to be 3 g/cm³ and 3.25 g/cm³ respectively ([Jull & Kelemen, 2001](#); [Pineda-Velasco et al., 2018](#)). The K_{d} is estimated to be 0.25 from

partitioning data for Li in mafic mineral phases (Adam & Green, 2006; Brenan et al., 1998; McDade et al., 2003; Ottolini et al., 2009) and the assumed mantle mineralogy [60 wt% olivine + 20 wt% clinopyroxene + 20wt% orthopyroxene for fertile peridotite after McDonough and Rudnick (1998)].

Using equation 3, the mass fraction of Li retained in transported fluids/melts is estimated to be 10% ($X_{\text{melt}} = 0.1$). The mass fraction of Li is proportional to the velocity of Li in the mantle relative to the velocity of fluid/melt (Navon & Stolper, 1987); i.e., Li moves 10 times slower than melt. Thus, the travel time of Li in the column is 10 times longer than the travel time of fluid/melt. The Daisen ADK samples have the $(^{230}\text{Th}/^{232}\text{Th})$ and $(^{238}\text{U}/^{232}\text{Th})$ activity ratios which indicate ^{238}U - ^{230}Th disequilibrium (Feineman et al., 2013; Tokunaga et al., 2010). Given that the half-life of ^{230}Th (c. 75000 years) and the melting depth (i.e., column length, c. 60 km; Pineda-Velasco et al., 2018), the fluid/melt velocity is estimated to be c. $1 \text{ m}\cdot\text{year}^{-1}$. Accordingly, the Li velocity is estimated to be c. $0.1 \text{ m}\cdot\text{year}^{-1}$ or $10 \text{ cm}\cdot\text{year}^{-1}$. The base of the wedge mantle would have been dragged by the underlying slab due to mechanical coupling (Wada & Wang, 2009). Thus, a large quantity of Li could not migrate upward through the wedge mantle when the Li velocity is comparable to the slab descent rate. The slab descent rate in SW Japan is estimated to be $4.3 \text{ cm}\cdot\text{year}^{-1}$ (Syracuse et al., 2010), which is comparable to the Li velocity. Thus, transport of slab-derived Li by percolation of fluids through the mantle is unlikely.

The other feasible styles of melt transport are fracture flow or diapiric rise. The velocity of melts by these flow styles is more rapid. Also, the surface area to volume ratios of melts in these flow styles is significantly lower than that for porous flow. Thus, lesser extents of melt-mantle interaction are anticipated during melt migration (Navon & Stolper, 1987). Pineda-Velasco et al. (2018) argued that slab-derived melts were transported in the form of diapirs. In

this case, Li isotope exchange occurs between a diapir and the surrounding mantle via diffusion at their contact. For modeling the change in Li isotope composition for this scenario, we applied the non-steady state radial diffusion model after Crank (1975) and Halama et al. (2008), expressed as

$$\frac{C - C_1}{C_0 - C_1} = 1 + \frac{2a}{\pi r} \sum_{n=1}^{\infty} \frac{(-1)^n}{n} \sin \frac{n\pi r}{a} \exp\left(\frac{-Dn^2\pi^2 t}{a^2}\right) \quad (3)$$

where C is [Li] at the distance r from the center of a spherical diapir (slab melt) with the radius a at time t , C_0 is the [Li] of the surface of a spherical diapir, C_1 is the initial [Li] (assumed to be homogeneous), D is the diffusion coefficient of Li, respectively. Note that r and a have the relationship of $0 \leq r \leq a$ or $0 \leq r/a \leq 1$. In the modeling, C_0 is [Li] of the mantle and C_1 is [Li] of the slab-derived melt.

The slab-derived melt, erupted as ADK magma, is considered to be a mixed melt of AOC and SED melts in an 8:2 ratio (Feineman et al., 2013; Pineda-Velasco et al., 2018). The [Li] in AOC melt is calculated to be $19 \mu\text{g}\cdot\text{g}^{-1}$ using [Li] = $8.9 \mu\text{g}\cdot\text{g}^{-1}$ in dehydrated AOC, melting stoichiometry (clinopyroxene : garnet : rutile = 0.46 : 0.53 : 0.01), the distribution coefficients between melt and clinopyroxene ($K_d^{\text{cpx/melt}} = 0.75$) and garnet ($K_d^{\text{garnet/melt}} = 0.12$) after Klemme et al. (2002) and that for rutile is assumed to be $K_d^{\text{rutile/melt}} = 0$ (yielding $K_d^{\text{AOC/melt}} = 0.41$), and the modal batch melting with melting degree of $F = 10\%$ after Pineda-Velasco et al. (2018). The [Li] in SED melt is calculated to be $55 \mu\text{g}\cdot\text{g}^{-1}$ using [Li] = $36 \mu\text{g}\cdot\text{g}^{-1}$ in dehydrated SED, bulk distribution coefficient ($K_d^{\text{sediment/melt}}$) of 0.44 (Johnson & Plank, 1999), and $F = 40\%$ (Pineda-Velasco et al., 2018). The [Li] and $\delta^7\text{Li}$ values of a mixed melt are calculated to be $26 \mu\text{g}\cdot\text{g}^{-1}$ and +4.9‰.

It is noted that the calculated $\delta^7\text{Li}$ value for the mixed melt is within the range of MORB and unable to explain the high- $\delta^7\text{Li}$ values in some ADK (up to +7.4‰). Possible reasons for

the discrepancy of the calculated and observed $\delta^7\text{Li}$ for ADK are the uncertainties of input parameters. Specifically, the $\delta^7\text{Li}$ value of pre-subduction AOC is uncertain as the $\delta^7\text{Li}$ values of Shikoku basin basalts have not been reported so far. If $\delta^7\text{Li}$ value of AOC is higher than +25‰ ($\delta^7\text{Li}$ value of +14‰ for dehydrated AOC), the AOC-SED mixed melt could have $\delta^7\text{Li}$ +7‰ or higher, consistent with the observed ADK. Such a high $\delta^7\text{Li}$ value is unlikely as most Shikoku Basin basalts are not highly altered by the reaction with seawater in relatively shorter period of time (<26 Myrs) from the age of its basin (Okino et al., 1994). The lower $^{87}\text{Sr}/^{86}\text{Sr}$ (< 0.7029) of the basalts supports this idea [Pineda-Velasco et al. (2018) and reference therein]. Alternatively, we speculate the uncertainty of [Li] or $\delta^7\text{Li}$ value of SED when its Li was mixed with AOC Li. Feineman et al. (2013) proposed that a significant quantity of sediments might have accumulated in the mantle or the base of crust beneath the Chugoku since the early Miocene. The accumulated sediments form a new chemical reservoir that has trace-element and Sr-Nd-Hf-Pb isotopic features inherited from sediment. When the AOC-derived melt upwelled to the surface, it could have reacted with this reservoir and gain “sediment-like” trace-element and isotopic features. If this is the case, sediment contribution to [Li] and $\delta^7\text{Li}$ of ADK would be reduced, as $\delta^7\text{Li}$ of sediments could be buffered to mantle-like $\delta^7\text{Li}$ range due to the diffusion for a prolonged period (>10 Myrs). Accordingly, Li in ADK is dominated by AOC-derived Li ($\delta^7\text{Li} > +7\text{‰}$). We selected [Li] = 20 $\mu\text{g}\cdot\text{g}^{-1}$ and $\delta^7\text{Li} = +7.0\text{‰}$ ($[^6\text{Li}] = 1.3 \mu\text{g}\cdot\text{g}^{-1}$ and $[^7\text{Li}] = 18.7 \mu\text{g}\cdot\text{g}^{-1}$) as a possible option for the initial element ($\equiv C_1$) and isotopic composition of a slab-derived melt in the diapir. The [Li] ($\equiv C_0$) and $\delta^7\text{Li}$ value of the mantle are assumed to be 1.3 $\mu\text{g}\cdot\text{g}^{-1}$ and +3.5‰ after Marschall et al. (2017).

The D in the equation 44 is calculated using the T - D relationship for ^7Li in a felsic melt by Holycross et al. (2018) as

$$D = D_0 \exp\left(\frac{-E_a}{RT}\right) \quad (45)$$

where D_0 is the pre-exponential reference diffusivity ($4.47 \times 10^{-8} \text{ m}^2 \cdot \text{s}^{-1}$), E_a is the activation energy of diffusion ($39.31 \text{ kJ} \cdot \text{mol}^{-1}$), R is the gas constant ($8.314 \text{ J} \cdot \text{K}^{-1} \cdot \text{mol}^{-1}$), and T is temperature in Kelvin (K). From the equation 45, D at $T = 800, 900, 1000, 1100, 1200, 1300$ and $1400 \text{ }^\circ\text{C}$ are calculated to be $5.45 \times 10^{-10}, 7.94 \times 10^{-10}, 1.09 \times 10^{-9}, 1.43 \times 10^{-9}, 1.80 \times 10^{-9}, 2.21 \times 10^{-9}$, and $2.65 \times 10^{-9} \text{ m}^2 \cdot \text{s}^{-1}$, respectively. The diffusion coefficient of ${}^6\text{Li}$ is calculated (e.g., [Richter et al., 2009](#)) as

$$D_{{}^6\text{Li}} = D_{{}^7\text{Li}} \left(\frac{m_{{}^7\text{Li}}}{m_{{}^6\text{Li}}}\right)^\beta = 1.031 D_{{}^7\text{Li}}. \quad (46)$$

where $D_{{}^6\text{Li}}$ and $D_{{}^7\text{Li}}$ are the diffusion coefficients of ${}^6\text{Li}$ and ${}^7\text{Li}$, $m_{{}^6\text{Li}}$ and $m_{{}^7\text{Li}}$ are the isotope masses of ${}^6\text{Li}$ ($6.015 \text{ g} \cdot \text{mol}^{-1}$) and ${}^7\text{Li}$ ($7.016 \text{ g} \cdot \text{mol}^{-1}$), and β is the empirical coefficient which is characteristic of a material that fills a spherical body. We used the coefficient β of 0.2; the value is experimentally determined for a hydrous felsic melt by [Spallanzani et al. \(2022\)](#).

The size of a diapir (a) and the duration time (t) of the diffusive reaction are essential input parameters for the modeling. The radius of a diapir is estimated to be 3–10 km from the size of each ADK volcano. The rising velocity is estimated to be $0.2\text{--}2 \text{ m} \cdot \text{year}^{-1}$ from the size and density of the diapir ([Pineda-Velasco et al. 2018](#); this study). The travel time of diapir through the mantle is estimated to be 29 to 320 kyrs. We assume that the travel time is the same as the duration time of a melt in the mantle.

The $[\text{Li}]$ and $\delta^7\text{Li}$ variations at a given distance from the center of the diapir and a given temperature are shown in **Figure 5-11**. For a diapir $> 3 \text{ km}$ in radius, the $[\text{Li}]$ and $\delta^7\text{Li}$ values of a melt do not change significantly over the time for transit ($< 320 \text{ kyrs}$) through the mantle. The model well explains the preservation of high $\delta^7\text{Li}$ values in some ADK. The low-Mg

feature of most ADK samples also suggested that slab-derived melts did not reach Fe/Mg equilibrium with the mantle during their ascent to the surface (Pineda-Velasco et al., 2018).

An exception is for Aonoyama ADK samples all of which have the $\delta^7\text{Li}$ values (+1.6 to +3.3‰) being well within the range of unaltered MORB. It should be noted that these ADK rocks (and IAB from the nearby region, Abu) plot off the arrays formed by the other ADK and IAB in **Figure 5-2** to lower $^{87}\text{Sr}/^{86}\text{Sr}$ and $^{206}\text{Pb}/^{204}\text{Pb}$ and to higher $^{143}\text{Nd}/^{144}\text{Nd}$ and $^{176}\text{Hf}/^{177}\text{Hf}$. Pineda-Velasco et al. (2018) argued that the melting degree of AOC for Aonoyama ADK is smaller than that for the other ADK, while the melting degree of SED is similar among all ADK. Accordingly, the mixing occurs in higher $(\text{Li}/\text{Sr})_{\text{SED}}/(\text{Li}/\text{Sr})_{\text{AOC}}$, $(\text{Li}/\text{Nd})_{\text{SED}}/(\text{Li}/\text{Nd})_{\text{AOC}}$, $(\text{Li}/\text{Hf})_{\text{SED}}/(\text{Li}/\text{Hf})_{\text{AOC}}$ and $(\text{Li}/\text{Pb})_{\text{SED}}/(\text{Li}/\text{Pb})_{\text{AOC}}$ for Aonoyama ADK than those for other ADK (**Figure 5-12**). To substantiate this inference, a general mixing equation is applied to Li-Sr, Li-Nd, Li-Pb and Li-Hf isotope mixing (**Figure 5-12**). The curvature function r is optimized to fit the data for Aonoyama and the other ADK lying along the hyperbolic lines. The Aonoyama data fit well with hyperbolic curves for Sr-Nd-Pb-Hf to Li isotope mixing with greater r , compared with other andesites and dacites, consistent with the inference for lower-degree of melting of AOC for Aonoyama ADK.

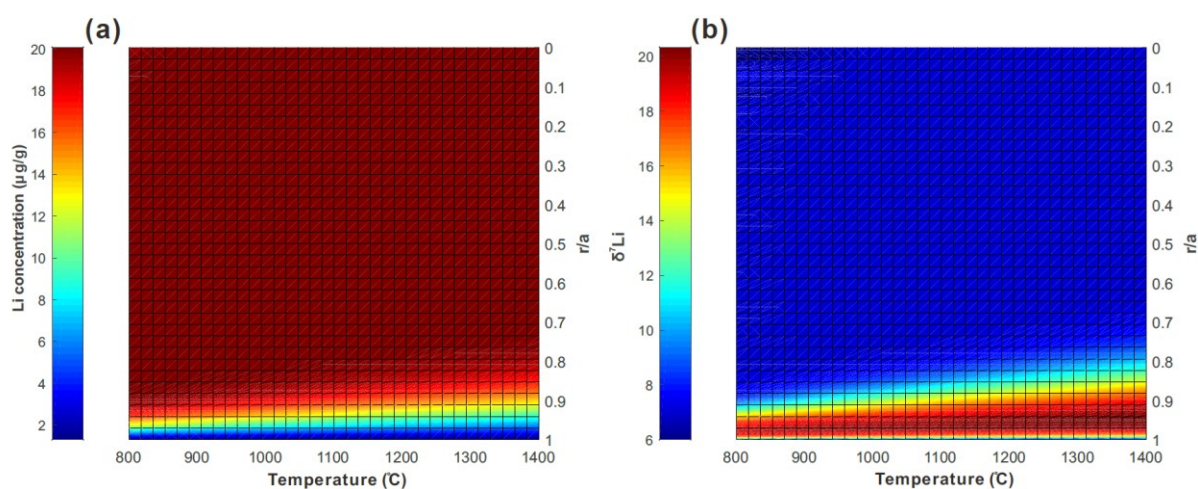


Figure 5-11. Diffusion modeling for temporal and spatial changes in Li concentration and $\delta^7\text{Li}$ values of a slab melt diapir with the radius of 3000 m (initial $[\text{Li}] = 20 \mu\text{g}\cdot\text{g}^{-1}$ and initial $\delta^7\text{Li} = +7\%$), having been preserved in the mantle ($[\text{Li}] = 1.3 \mu\text{g}\cdot\text{g}^{-1}$ and $\delta^7\text{Li} = +3.5\%$) during 320 kyrs. The changes in $[\text{Li}]$ concentration and $\delta^7\text{Li}$ values in the diffusion surfaces are calculated across the distance from the surface to the center of a diapir and over the temperature range from 800 °C (slab surface temperature at which slab melting occurred; Pineda-Velasco et al., 2018) to 1400 °C (maximum temperature of wedge mantle, estimated from primitive basalts; Nguyen et al., 2020). The r/a value is a dimensionless parameter based on the sphere's radius a and the distance from the sphere's center r , i.e., the surface of the sphere corresponds to a value of 1.

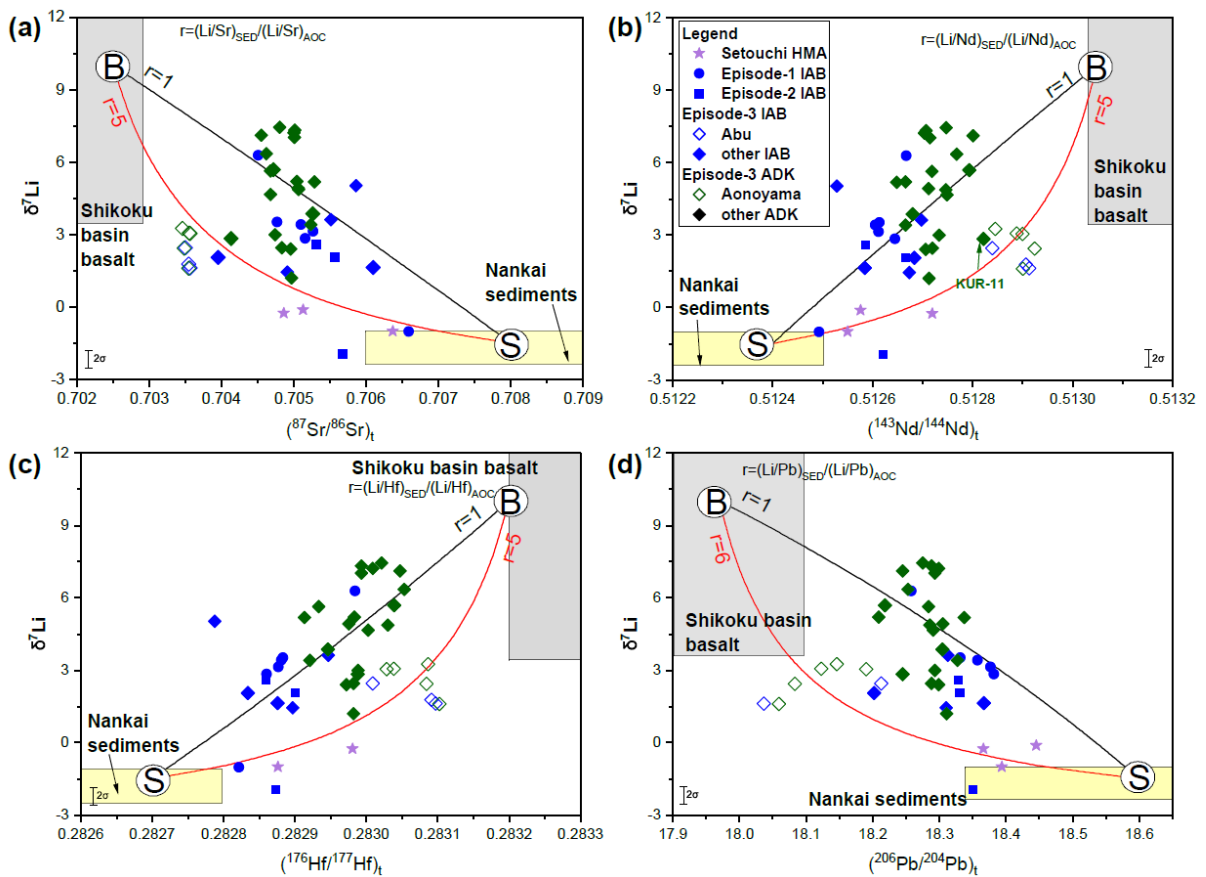


Figure 5-12. Plots of $\delta^7\text{Li}$ versus $(^{87}\text{Sr}/^{86}\text{Sr})_t$ (a), $(^{143}\text{Nd}/^{144}\text{Nd})_t$ (b), $(^{176}\text{Hf}/^{177}\text{Hf})_t$ (c), $(^{206}\text{Pb}/^{204}\text{Pb})_t$ (d) for the volcanic rocks in Chugoku district.

The hyperbolic curves shown are those for the mixing of components from subducting basalt (denoted as “B”, i.e., AOC) and sediment (“S”, i.e., SED) with various r . The definition of “ r ” is shown in each

figure. The references for the composition of Nankai sediment and Shikoku basin basalts are the same as that in **Figure 5-2**.

3.5 Implications for Li isotope variation in global arc magmas

Three scenarios have been proposed to explain the apparent similarity of $\delta^7\text{Li}$ values between island-arc rocks and MORB/mantle: (1) mixing of the mantle and subducted sediments, both of which have $\delta^7\text{Li}$ values indistinguishable from MORB (Plank, 2014; Tang et al., 2014), (2) contribution of the AOC-derived component with a MORB-like $\delta^7\text{Li}$ value by dehydration-induced isotopic fractionation (Leeman et al., 2004; Magna et al., 2006b), (3) buffering of slab-derived Li via diffusive isotopic exchange with surrounding mantle that has a MORB-like $\delta^7\text{Li}$ value (Caciagli et al., 2011; Halama et al., 2009; Tomascak et al., 2002). The feasibilities of these scenarios are examined using the results of this study.

The SW Japan arc provides a vital opportunity to examine Scenario 1, as the subducted sediments or the equivalents have $\delta^7\text{Li}$ values distinct from MORB (Moriguti & Nakamura, 1998; You et al., 1995) and yield magmas directly derived from sediments and AOC (Pineda-Velasco et al., 2018; Shimoda et al., 1998). We documented the Li-isotope compositions of these magmas akin to sediments or AOC. If AOC has the $\delta^7\text{Li}$ value significantly higher than unaltered MORB while sediments have the $\delta^7\text{Li}$ value significantly lower than unaltered MORB (or vice versa), then hybridization of these components can produce MORB-like $\delta^7\text{Li}$ values (Tomascak et al., 2016), as is found in SW Japan.

Scenario 2 requires the estimate of the extent to which Li isotopes fractionate during dehydration. SW Japan is an ideal field to examine the issue because the P - T path and metamorphic reaction of the subducting slab are well constrained (Kimura et al., 2014; van Keken et al., 2011) and the analysis of ADK offers us an opportunity to know the $\delta^7\text{Li}$ value of

the subducted AOC after intensive dehydration (Feineman et al., 2013; Kimura et al., 2014; Pineda-Velasco et al., 2018). We demonstrated, based on numerical models, that Li isotopes fractionate to a limited extent, as proposed by Marschall et al. (2007), and it well explains the high $\delta^7\text{Li}$ values of ADK. Thus, Scenario 2 is unlikely for SW Japan and probably for many other arcs.

Scenario 3 can also be examined in SW Japan, as the arc yielded magmas that reacted highly with the mantle (IAB and HMA). The effect of mantle buffering on Li isotope is inevitable, in particular, in the case of transport of fluids dominated by aqueous liquid (e.g., Caciagli et al., 2011; Halama et al., 2009; Marschall & Tang, 2020; Tomascak et al., 2002). In contrast, as our modeling suggested, if fluids are enriched in solute components, such as hydrous melt (ADK), they could move rapidly with larger masses in the forms of diapir (or fracture flow) and hence the slab-derived Li-isotope signature could be preserved. The scenario may explain the occurrence of volcanic rocks with higher-than-MORB $\delta^7\text{Li}$ values such as in the Cascades (Magna et al., 2006b) and lower-than-MORB $\delta^7\text{Li}$ values such as in the Lesser Antilles (Tang et al., 2014), where slab melt or sediment melt are proposed to be probable mechanisms to produce those arc magmas (Labanieh et al., 2012; Walowski et al., 2015, 2016).

Therefore, we suggest hybrid slab-derived components (from AOC and sediments), rather than subduction-induced dehydration or diffusive equilibrium with the mantle, would control the Li isotopic composition of arc magmas if the fluids/melts transport rapidly or voluminously, such as diapirs. Recent numerical models also predict the likelihood of incorporation of subducted materials as diapir (referred to as *mélange* diapir) into the wedge mantle (Marschall & Schumacher, 2012).

4. Conclusions

The main conclusions reached in this study are:

1. The late Cenozoic volcanic rocks in the Chugoku district show a large variation in $\delta^7\text{Li}$ values (-1.9 to $+7.4$ ‰), spanning beyond the entire range of MORB ($+1.6$ to $+5.6$ ‰), as a result of various extents of interaction among magma source components with different $\delta^7\text{Li}$, derived from subducted sediments, subducted oceanic crust, and wedge mantle.
2. The lower-than-MORB $\delta^7\text{Li}$ values of high-Mg andesites and the higher-than-MORB $\delta^7\text{Li}$ values of high-Sr andesites and dacites (adakites) in the Chugoku district suggest large contributions of sediment and subducted basalts, respectively, to their magma sources.
3. Modeling the dehydration of subducted sediment ($\delta^7\text{Li}$ of -1 ‰) and oceanic crust ($\delta^7\text{Li}$ of $+11$ to $+12$ ‰) shows that $\delta^7\text{Li}$ values of these subducted materials were not significantly changed (<2 ‰) by metamorphic dehydration and could produce the variation in $\delta^7\text{Li}$ values in the mantle beneath the district.
4. Modeling the diffusive isotope equilibrium indicates that the transport of melts from subducted sediments or oceanic crusts was fast ($\sim 1 \text{ m}\cdot\text{year}^{-1}$) enough to retain the $\delta^7\text{Li}$ values of when they were formed, and suggests the possible melt transport mechanism of diapiric rise or fracture flow.

References

- Abers G. A., Van Keken P. E. and Hacker B. R. (2017) The cold and relatively dry nature of mantle forearcs in subduction zones. *Nat. Geosci.* **10**, 333-337.
- Adam J. and Green T. (2006) Trace element partitioning between mica- and amphibole-bearing garnet lherzolite and hydrous basanitic melt; 1, Experimental results and the investigation of controls on partitioning behaviour. *Contrib. Mineral. Petr.* **152**, 1-17.
- Agostini S., Ryan J. G., Tonarini S. and Innocenti F. (2008) Drying and dying of a subducted slab: Coupled Li and B isotope variations in Western Anatolia Cenozoic Volcanism. *Earth Planet. Sc. Lett.* **272**, 139-147.

- Akizawa N., Ohara Y., Okino K., Ishizuka O., Yamashita H. and Machida S., et al. (2021) Geochemical characteristics of back-arc basin lower crust and upper mantle at final spreading stage of Shikoku Basin: an example of Mado Megamullion. *Progress in Earth and Planetary Science* **8**, 1-24.
- Babechuk M. G., Widdowson M. and Kamber B. S. (2014) Quantifying chemical weathering intensity and trace element release from two contrasting basalt profiles, Deccan Traps, India. *Chem. Geol.* **363**, 56-75.
- Benton L. D., Ryan J. G. and Savov I. P. (2004) Lithium abundance and isotope systematics of forearc serpentinites, Conical Seamount, Mariana forearc: Insights into the mechanics of slab-mantle exchange during subduction. *Geochemistry, Geophysics, Geosystems* **5**.
- Berger G., Schott J. and Guy C. (1988) Behavior of Li, Rb and Cs during basalt glass and olivine dissolution and chlorite, smectite and zeolite precipitation from seawater; experimental investigations and modelization between 50 degrees and 300 degrees C. *Chem. Geol.* **71**, 297-312.
- Bouman C., Elliott T. and Vroon P. Z. (2004) Lithium inputs to subduction zones. *Chem. Geol.* **212**, 59-79.
- Bouvier A. S., Métrich N. and Deloule E. (2008) Slab-Derived Fluids in the Magma Sources of St. Vincent (Lesser Antilles Arc): Volatile and Light Element Imprints. *J. Petrol.* **49**, 1427-1448.
- Brant C., Coogan L. A., Gillis K. M., Seyfried W. E., Pester N. J. and Spence J. (2012) Lithium and Li-isotopes in young altered upper oceanic crust from the East Pacific Rise. *Geochim. Cosmochim. Ac.* **96**, 272-293.
- Brenan J. M., Ryerson F. J. and Shaw H. F. (1998) The role of aqueous fluids in the slab-to-mantle transfer of boron, beryllium, and lithium during subduction; experiments and models.

- Geochim. Cosmochim. Ac.* **62**, 3337-3347.
- Brens R., Liu X. M., Turner S. and Rushmer T. (2019) Lithium isotope variations in Tonga–Kermadec arc-Lau back-arc lavas and Deep Sea Drilling Project (DSDP) Site 204 sediments. *Isl. Arc* **28**.
- Caciagli N., Brenan J. M., McDonough W. F. and Phinney D. (2011) Mineral–fluid partitioning of lithium and implications for slab–mantle interaction. *Chem. Geol.* **280**, 384-398.
- Chan L. H., Edmond J. M., Thompson G. and Gillis K. (1992) Lithium isotopic composition of submarine basalts; implications for the lithium cycle in the oceans. *Earth Planet. Sc. Lett.* **108**, 151-160.
- Chan L. H., Leeman W. P. and You C. F. (2002) Lithium isotopic composition of Central American volcanic arc lavas: implications for modification of subarc mantle by slab-derived fluids: correction. *Chem. Geol.* **182**, 293-300.
- Chan L. H., Leeman W. P. and Plank T. (2006) Lithium isotopic composition of marine sediments. *Geochemistry, Geophysics, Geosystems* **7**, Q6005.
- Chan L., Edmond J. M. and Thompson G. (1993) A lithium isotope study of hot springs and metabasalts from mid-ocean ridge hydrothermal systems. *Journal of Geophysical Research* **98**, 9653-9659.
- Chen S., Hou T., Liu J. and Zhang Z. (2020) Geochemical Variation of Miocene Basalts within Shikoku Basin: Magma Source Compositions and Geodynamic Implications. *Minerals (Basel)* **11**, 25.
- Connolly J. and Pettrini K. (2002) An automated strategy for calculation of phase diagram sections and retrieval of rock properties as a function of physical conditions. *J. Metamorph. Geol.* **20**, 697-708.
- Connolly J. A. (2005) Computation of phase equilibria by linear programming: a tool for

- geodynamic modeling and its application to subduction zone decarbonation. *Earth Planet. Sc. Lett.* **236**, 524-541.
- Crank J. (1975) *The mathematics of diffusion*. Clarendon Press, Oxford.
- Davies J. H. (1999) The role of hydraulic fractures and intermediate-depth earthquakes in generating subduction-zone magmatism. *Nature (London)* **398**, 142-145.
- Decitre S., Buatier M. and James R. (2004) Li and Li isotopic composition of hydrothermally altered sediments at Middle Valley, Juan De Fuca. *Chem. Geol.* **211**, 363-373.
- Decitre S., Deloule E., Reisberg L., James R., Agrinier P. and Mével C. (2002) Behavior of Li and its isotopes during serpentinization of oceanic peridotites. *Geochemistry, Geophysics, Geosystems* **3**, 1-20.
- Dunn T. and Sen C. (1994) Mineral/matrix partition coefficients for orthopyroxene, plagioclase, and olivine in basaltic to andesitic systems; a combined analytical and experimental study. *Geochim. Cosmochim. Ac.* **58**, 717-733.
- Feineman M., Moriguti T., Yokoyama T., Terui S. and Nakamura E. (2013) Sediment-enriched adakitic magmas from the Daisen volcanic field, Southwest Japan. *Geochemistry, Geophysics, Geosystems* **14**, 3009-3031.
- Halama R., Mcdonough W. F., Rudnick R. L. and Bell K. (2008) Tracking the lithium isotopic evolution of the mantle using carbonatites. *Earth Planet. Sc. Lett.* **265**, 726-742.
- Halama R., Savov I. P., Rudnick R. L. and Mcdonough W. F. (2009) Insights into Li and Li isotope cycling and sub-arc metasomatism from veined mantle xenoliths, Kamchatka. *Contrib. Mineral. Petr.* **158**, 197-222.
- Hall P. S. and Kincaid C. (2001) Diapiric flow at subduction zones: A recipe for rapid transport. *Science* **292**, 2472-2475.
- Hanna H. D., Liu X., Park Y., Kay S. M. and Rudnick R. L. (2020) Lithium isotopes may trace

- subducting slab signatures in Aleutian arc lavas and intrusions. *Geochim. Cosmochim. Ac.* **278**, 322-339.
- Hanyu T., Tatsumi Y. and Nakai S. (2002) A contribution of slab-melts to the formation of high-Mg andesite magmas; Hf isotopic evidence from SW Japan. *Geophys. Res. Lett.* **29**, 1-8.
- Hickey Vargas R. (1998) Origin of the Indian Ocean-type isotopic signature in basalts from Philippine Sea plate spreading centers: An assessment of local versus large-scale processes. *Journal of Geophysical Research: Solid Earth* **103**, 20963-20979.
- Hickey-Vargas R. (1991) Isotope characteristics of submarine lavas from the Philippine Sea: implications for the origin of arc and basin magmas of the Philippine tectonic plate. *Earth Planet. Sc. Lett.* **107**, 290-304.
- Holycross M. E., Watson E. B., Richter F. M. and Villeneuve J. (2018) Diffusive fractionation of Li isotopes in wet, highly silicic melts. *Geochemical Perspectives Letters* **6**, 39-42.
- Imai N., Terashima S., Itoh S. and Ando A. (1995) 1994 compilation values for GSJ reference samples, "igneous rock series". *Geochem. J.* **29**, 91-95.
- Ishihara S. and Tani K. (2013) Zircon age of granitoids hosting molybdenite-quartz vein deposits in the central Sanin Belt, Southwest Japan. *Shigen-Chishitsu* **63**, 11-14.
- Ishikawa T. and Nakamura E. (1994) Origin of the slab component in arc lavas from across-arc variation of B and Pb isotopes. *Nature* **370**, 205-208.
- Ishizuka O., Yuasa M., Taylor R. N. and Sakamoto I. (2009) Two contrasting magmatic types coexist after the cessation of back-arc spreading. *Chem. Geol.* **266**, 274-296.
- Jeffcoate A. B., Elliott T., Thomas A., Bouman C. and Anonymous (2004) Precise, small sample size determinations of lithium isotopic compositions of geological reference materials and modern seawater by MC-ICP-MS. *Geostand. Geoanal. Res.* **28**, 161-172.

- Johnson M. C. and Plank T. (2000) Dehydration and melting experiments constrain the fate of subducted sediments. *Geochemistry, Geophysics, Geosystems* **1**, 1007.
- Jull M. and Kelemen P. Á. (2001) On the conditions for lower crustal convective instability. *Journal of Geophysical Research: Solid Earth* **106**, 6423-6446.
- Kawamoto T., Kanzaki M., Mibe K., Matsukage K. N. and Ono S. (2012) Separation of supercritical slab-fluids to form aqueous fluid and melt components in subduction zone magmatism. *Proceedings of the National Academy of Sciences* **109**, 18695-18700.
- Kepezhinskas P., Defant M. J. and Drummond M. S. (1996) Progressive enrichment of island arc mantle by melt-peridotite interaction inferred from Kamchatka xenoliths. *Geochim. Cosmochim. Ac.* **60**, 1217-1229.
- Kessel R., Schmidt M. W., Ulmer P. and Pettke T. (2005) Trace element signature of subduction-zone fluids, melts and supercritical liquids at 120–180 km depth. *Nature* **437**, 724-727.
- Kimura J. I., Stern R. J. and Yoshida T. (2005) Reinitiation of subduction and magmatic responses in SW Japan during Neogene time. *Geol. Soc. Am. Bull.* **117**, 969-986.
- Kimura J. (2017) Modeling chemical geodynamics of subduction zones using the Arc Basalt Simulator version 5. *Geosphere (Boulder, Colo.)* **13**, 992-1025.
- Kimura J., Gill J. B., Kunikiyo T., Osaka I., Shimoshioiri Y. and Katakuse M., et al. (2014) Diverse magmatic effects of subducting a hot slab in SW Japan: Results from forward modeling. *Geochemistry, Geophysics, Geosystems* **15**, 691-739.
- Klemme S., Blundy J. D. and Wood B. J. (2002) Experimental constraints on major and trace element partitioning during partial melting of eclogite. *Geochim. Cosmochim. Ac.* **66**, 3109-3123.
- Kobayashi K., Tanaka R., Moriguti T., Shimizu K. and Nakamura E. (2004) Lithium, boron,

- and lead isotope systematics of glass inclusions in olivines from Hawaiian lavas: evidence for recycled components in the Hawaiian plume. *Chem. Geol.* **212**, 143-161.
- Košler J., Magna T., Mlčoch B., Mixa P., Nývlt D. and Holub F. V. (2009) Combined Sr, Nd, Pb and Li isotope geochemistry of alkaline lavas from northern James Ross Island (Antarctic Peninsula) and implications for back-arc magma formation. *Chem. Geol.* **258**, 207-218.
- Krienitz M., Garbe-Schönberg C., Romer R. L., Meixner A., Haase K. M. and Stroncik N. A. (2012) Lithium isotope variations in ocean island basalts—implications for the development of mantle heterogeneity. *J. Petrol.* **53**, 2333-2347.
- Labanieh S., Chauvel C., Germa A. and Quidelleur X. (2012) Martinique: a Clear Case for Sediment Melting and Slab Dehydration as a Function of Distance to the Trench. *J. Petrol.* **53**, 2441-2464.
- Lai Y., Pogge Von Strandmann P. A. E., Dohmen R., Takazawa E. and Elliott T. (2015) The influence of melt infiltration on the Li and Mg isotopic composition of the Horoman peridotite massif. *Geochim. Cosmochim. Ac.* **164**, 318-332.
- Langmuir C. H., Klein E. M. and Plank T. (1992) Petrological systematics of mid-ocean ridge basalts: constraints on melt generation beneath ocean ridges. *Mantle flow and melt generation at mid-ocean ridges*, 183-280.
- Leeman W. P., Tonarini S., Chan L. H. and Borg L. E. (2004) Boron and lithium isotopic variations in a hot subduction zone—the southern Washington Cascades. *Chem. Geol.* **212**, 101-124.
- Liu H., Xiao Y., Sun H., Tong F., Heuser A. and Churikova T., et al. (2020) Trace Elements and Li Isotope Compositions Across the Kamchatka Arc: Constraints on Slab-Derived Fluid Sources. *Journal of Geophysical Research: Solid Earth* **125**.
- Magna T., Janousek V., Kohut M., Oberli F. and Wiechert U. (2010) Fingerprinting sources of

- orogenic plutonic rocks from Variscan Belt with lithium isotopes and possible link to subduction-related origin of some A-type granites. *Chem. Geol.* **274**, 94-107.
- Magna T., Wiechert U., Grove T. L. and Halliday A. N. (2006) Lithium isotope fractionation in the southern Cascadia subduction zone. *Earth Planet. Sc. Lett.* **250**, 428-443.
- Magna T., Wiechert U. and Halliday A. N. (2006) New constraints on the lithium isotope compositions of the Moon and terrestrial planets. *Earth Planet. Sc. Lett.* **243**, 336-353.
- Mahony S. H., Wallace L. M., Miyoshi M., Villamor P., Sparks R. S. J. and Hasenaka T. (2011) Volcano-tectonic interactions during rapid plate-boundary evolution in the Kyushu region, SW Japan. *Geol. Soc. Am. Bull.* **123**, 2201-2223.
- Marschall H. R., Altherr R., Ludwig T., Kalt A., Gméling K. and Kasztovszky Z. (2006) Partitioning and budget of Li, Be and B in high-pressure metamorphic rocks. *Geochim. Cosmochim. Ac.* **70**, 4750-4769.
- Marschall H. R., Altherr R. and Rüpke L. (2007) Squeezing out the slab — modelling the release of Li, Be and B during progressive high-pressure metamorphism. *Chem. Geol.* **239**, 323-335.
- Marschall H. R., Pogge Von Strandmann P. A. E., Seitz H., Elliott T. and Niu Y. (2007) The lithium isotopic composition of orogenic eclogites and deep subducted slabs. *Earth Planet. Sc. Lett.* **262**, 563-580.
- Marschall H. R. and Tang M. (2020) High-temperature processes; is it time for lithium isotopes? *Elements (Quebec)* **16**, 247-252.
- Marschall H. R., Wanless V. D., Shimizu N., Pogge Von Strandmann P. A. E., Elliott T. and Monteleone B. D. (2017) The boron and lithium isotopic composition of mid-ocean ridge basalts and the mantle. *Geochim. Cosmochim. Ac.* **207**, 102-138.
- Marsh B. D. (1979) Island arc development: Some observations, experiments, and speculations.

- The Journal of Geology* **87**, 687-713.
- Mcdade P., Blundy J. D. and Wood B. J. (2003) Trace element partitioning on the Tinaquillo Lherzolite solidus at 1.5 GPa. *Phys. Earth Planet. In.* **139**, 129-147.
- Mcdonough W. F. and Rudnick R. L. (1998) Mineralogy and composition of the upper mantle. *Reviews in mineralogy* **37**, 139-164.
- Mclennan S. M. (1993) Weathering and global denudation. *The Journal of Geology* **101**, 295-303.
- Mibe K., Fujii T. and Yasuda A. (1999) Control of the location of the volcanic front in island arcs by aqueous fluid connectivity in the mantle wedge. *Nature (London)* **401**, 259-262.
- Moriguti T. and Nakamura E. (1998) Across-arc variation of Li isotopes in lavas and implications for crust/mantle recycling at subduction zones. *Earth Planet. Sc. Lett.* **163**, 167-174.
- Moriguti T., Shibata T. and Nakamura E. (2004) Lithium, boron and lead isotope and trace element systematics of Quaternary basaltic volcanic rocks in northeastern Japan: mineralogical controls on slab-derived fluid composition. *Chem. Geol.* **212**, 81-100.
- Nakamura E., Campbell I. H. and Sun S. (1985) The influence of subduction processes on the geochemistry of Japanese alkaline basalts. *Nature (London)* **316**, 55-58.
- Navon O. and Stolper E. (1987) Geochemical consequences of melt percolation; the upper mantle as a chromatographic column. *The Journal of geology* **95**, 285-307.
- Neukampf J., Laurent O., Tollan P., Bouvier A., Magna T. and Ulmer P., et al. (2022) Degassing from magma reservoir to eruption in silicic systems; the Li elemental and isotopic record from rhyolitic melt inclusions and host quartz in a Yellowstone rhyolite. *Geochim. Cosmochim. Ac.* **326**, 56-76.
- Nguyen T. T., Kitagawa H., Pineda Velasco I. and Nakamura E. (2020) Feedback of Slab

- Distortion on Volcanic Arc Evolution: Geochemical Perspective from Late Cenozoic Volcanism in SW Japan. *Journal of Geophysical Research: Solid Earth* **125**.
- Niu Y. (2004) Bulk-rock major and trace element compositions of abyssal peridotites; implications for mantle melting, melt extraction and post-melting processes beneath mid-ocean ridges. *J. Petrol.* **45**, 2423-2458.
- Noguchi M., Kamei A., Suzuki H. and Kobayashi N. (2021) Igneous activity of the Daito granodiorite in Un-nan area, San'in zone, Southwest Japan. *Journal of Geological Society of Japan* **127**, 461-478.
- Oi T., Odagiri T. and Nomura M. (1997) Extraction of lithium from GSJ rock reference samples and determination of their lithium isotopic compositions. *Anal. Chim. Acta* **340**, 221-225.
- Okino K., Shimakawa Y. and Nagaoka S. (1994) Evolution of the Shikoku basin. *Journal of geomagnetism and geoelectricity* **46**, 463-479.
- Ottolini L., Laporte D., Raffone N., Devidal J. and Le Fevre B. (2009) New experimental determination of Li and B partition coefficients during upper mantle partial melting. *Contrib. Mineral. Petr.* **157**, 313-325.
- Palmer M. R. and Edmond J. M. (1989) Cesium and rubidium in submarine hydrothermal fluids; evidence for recycling of alkali elements. *Earth Planet. Sc. Lett.* **95**, 8-14.
- Parkinson I., Hammond S., James R. and Rogers N. (2007) High-temperature lithium isotope fractionation: Insights from lithium isotope diffusion in magmatic systems. *Earth Planet. Sc. Lett.* **257**, 609-621.
- Peacock S. M. and Wang K. (1999) Seismic Consequences of Warm versus Cool Subduction Metamorphism: Examples from Southwest and Northeast Japan. *Science* **286**, 937-939.
- Penniston-Dorland S., Liu X. and Rudnick R. L. (2017) Lithium Isotope Geochemistry. *Reviews in Mineralogy and Geochemistry* **82**, 165-217.

- Perfit M. R., Gust D. A., Bence A. E., Arculus R. J. and Taylor S. R. (1980) Chemical characteristics of island-arc basalts: implications for mantle sources. *Chem. Geol.* **30**, 227-256.
- Pineda-Velasco I., Kitagawa H., Nguyen T. T., Kobayashi K. and Nakamura E. (2018) Production of High-Sr Andesite and Dacite Magmas by Melting of Subducting Oceanic Lithosphere at Propagating Slab Tears. *Journal of Geophysical Research: Solid Earth* **123**, 3698-3728.
- Pineda-Velasco I., Nguyen T. T., Kitagawa H. and Nakamura E. (2015) Comment on "Diverse magmatic effects of subducting a hot slab in SW Japan: Results from forward modeling" by J.-I. Kimura et al. *Geochemistry, geophysics, geosystems: G3* **16**, 2848-2852.
- Plank T. (2014) The chemical composition of subducting sediments. In *The Crust* (ed. R. L. Rudnick), Vol. 4 *Treatise on Geochemistry* (second ed.) (eds. H. D. Holland and K. K. Turekian). Elsevier Ltd, Oxford. pp. 607-629.
- Plank T. and Langmuir C. H. (1998) The chemical composition of subducting sediment and its consequences for the crust and mantle. *Chem. Geol.* **145**, 325-394.
- Richter F. M., Liang Y. and Davis A. M. (1999) Isotope fractionation by diffusion in molten oxides. *Geochim. Cosmochim. Ac.* **63**, 2853-2861.
- Sakuyama M. and Nesbitt R. W. (1986) Geochemistry of the Quaternary volcanic rocks of the northeast Japan arc. *J. Volcanol. Geoth. Res.* **29**, 413-450.
- Scambelluri M., Müntener O., Ottolini L., Pettke T. T. and Vannucci R. (2004) The fate of B, Cl and Li in the subducted oceanic mantle and in the antigorite breakdown fluids. *Earth Planet. Sc. Lett.* **222**, 217-234.
- Schiavi F., Kobayashi K., Moriguti T., Nakamura E., Pompilio M. and Tiepolo M., et al. (2010) Degassing, crystallization and eruption dynamics at Stromboli; trace element and lithium

- isotopic evidence from 2003 ashes. *Contrib. Mineral. Petr.* **159**, 541-561.
- Schiavi F., Kobayashi K., Nakamura E., Tiepolo M. and Vannucci R. (2012) Trace element and Pb–B–Li isotope systematics of olivine-hosted melt inclusions: insights into source metasomatism beneath Stromboli (southern Italy). *Contrib. Mineral. Petr.* **163**, 1011-1031.
- Schmidt M. W. and Poli S. (2003) Generation of mobile components during subduction of oceanic crust. *Treatise on geochemistry* **3**, 659.
- Schuessler J. A., Schoenberg R. and Sigmarsson O. (2009) Iron and lithium isotope systematics of the Hekla volcano, Iceland—evidence for Fe isotope fractionation during magma differentiation. *Chem. Geol.* **258**, 78-91.
- Seyfried Jr W. E., Chen X. and Chan L. (1998) Trace element mobility and lithium isotope exchange during hydrothermal alteration of seafloor weathered basalt: an experimental study at 350 C, 500 bars. *Geochim. Cosmochim. Ac.* **62**, 949-960.
- Shaw D. M. (1970) Trace element fractionation during anatexis. *Geochim. Cosmochim. Ac.* **34**, 237-243.
- Shibata T. and Nakamura E. (1997) Across-arc variations of isotope and trace element compositions from Quaternary basaltic volcanic rocks in northeastern Japan: Implications for interaction between subducted oceanic slab and mantle wedge. *Journal of Geophysical Research: Solid Earth* **102**, 8051-8064.
- Shimoda G., Tatsumi Y., Nohda S., Ishizaka K. and Jahn B. M. (1998) Setouchi high-Mg andesites revisited: geochemical evidence for melting of subducting sediments. *Earth Planet. Sc. Lett.* **160**, 479-492.
- Shu Y., Nielsen S. G., Zeng Z., Shinjo R., Blusztajn J. and Wang X., et al. (2017) Tracing subducted sediment inputs to the Ryukyu arc-Okinawa Trough system: Evidence from thallium isotopes. *Geochim. Cosmochim. Ac.* **217**, 462-491.

- Simons K. K., Harlow G. E., Brueckner H. K., Goldstein S. L., Sorensen S. S. and Hemming N. G., et al. (2010) Lithium isotopes in Guatemalan and Franciscan HP–LT rocks: Insights into the role of sediment-derived fluids during subduction. *Geochim. Cosmochim. Ac.* **74**, 3621-3641.
- Spallanzani R., Koga K. T., Cichy S. B., Wiedenbeck M., Schmidt B. C. and Oelze M., et al. (2022) Lithium and boron diffusivity and isotopic fractionation in hydrated rhyolitic melts. *Contrib. Mineral. Petr.* **177**, 1-17.
- Straub S. M., Goldstein S. L., Class C., Schmidt A. and Gomez-Tuena A. (2010) Slab and Mantle Controls on the Sr–Nd–Pb–Hf Isotope Evolution of the Post 42 Ma Izu–Bonin Volcanic Arc. *J. Petrol.* **51**, 993-1026.
- Syracuse E. M. and Abers G. A. (2006) Global compilation of variations in slab depth beneath arc volcanoes and implications. *Geochemistry, Geophysics, Geosystems* **7**.
- Syracuse E. M., van Keken P. E. and Abers G. A. (2010) The global range of subduction zone thermal models. *Phys. Earth Planet. In.* **183**, 73-90.
- Tang M., Rudnick R. L. and Chauvel C. (2014) Sedimentary input to the source of Lesser Antilles lavas: A Li perspective. *Geochim. Cosmochim. Ac.* **144**, 43-58.
- Tatsumi Y. and Hanyu T. (2003) Geochemical modeling of dehydration and partial melting of subducting lithosphere: Toward a comprehensive understanding of high-Mg andesite formation in the Setouchi volcanic belt, SW Japan. *Geochemistry, Geophysics, Geosystems* **4**, 1081.
- Tatsumi Y. and Ishizaka K. (1982) Origin of high-magnesian andesites in the Setouchi volcanic belt, Southwest Japan; I, Petrographical and chemical characteristics. *Earth Planet. Sc. Lett.* **60**, 293-404.
- Tatsumi Y., Suenaga N., Yoshioka S., Kaneko K. and Matsumoto T. (2020) Contrasting

- volcano spacing along SW Japan arc caused by difference in age of subducting lithosphere. *Sci. Rep.-Uk* **10**.
- Terakado Y., Shimizu H. and Masuda A. (1988) Nd and Sr isotopic variations in acidic rocks formed under a peculiar tectonic environment in Miocene Southwest Japan. *Contrib. Mineral. Petr.* **99**, 1-10.
- Tokunaga S., Nakai S. and Orihashi Y. (2010) Two types of adakites revealed by ^{238}U - ^{230}Th disequilibrium from Daisen Volcano, southwestern Japan. *Geochem. J.* **44**, 379-386.
- Tomascak P. B. (2000) Lithium isotope evidence for light element decoupling in the Panama subarc mantle. *Geology* **28**, 507-510.
- Tomascak P. B., Langmuir C. H., le Roux P. J. and Shirey S. B. (2008) Lithium isotopes in global mid-ocean ridge basalts. *Geochim. Cosmochim. Ac.* **72**, 1626-1637.
- Tomascak P. B., Tera F., Helz R. T. and Walker R. J. (1999) The absence of lithium isotope fractionation during basalt differentiation; new measurements by multicollector sector ICP-MS. *Geochim. Cosmochim. Ac.* **63**, 907-910.
- Tomascak P. B., Widom E., Benton L. D., Goldstein S. L. and Ryan J. G. (2002) The control of lithium budgets in island arcs. *Earth Planet. Sc. Lett.* **196**, 227-238.
- Tomascak P., Magna T. and Dohmen R. (2015) *Advances in Lithium Isotope Geochemistry*. Springer International Publishing AG, Cham, Switzerland.
- Ulmer P. and Trommsdorff V. (1995) Serpentine stability to mantle depths and subduction-related magmatism. *Science* **268**, 858-861.
- van Keken P. E., Hacker B. R., Syracuse E. M. and Abers G. A. (2011) Subduction factory: 4. Depth-dependent flux of H_2O from subducting slabs worldwide. *Journal of Geophysical Research* **116**.
- Vervoort J. D., Plank T. and Prytulak J. (2011) The Hf–Nd isotopic composition of marine

- sediments. *Geochim. Cosmochim. Ac.* **75**, 5903-5926.
- Vigier N., Decarreau A., Millot R., Carignan J., Petit S. and France-Lanord C. (2008) Quantifying Li isotope fractionation during smectite formation and implications for the Li cycle. *Geochim. Cosmochim. Ac.* **72**, 780-792.
- Vils F., Pelletier L., Kalt A., Müntener O. and Ludwig T. (2008) The Lithium, Boron and Beryllium content of serpentinized peridotites from ODP Leg 209 (Sites 1272A and 1274A): Implications for lithium and boron budgets of oceanic lithosphere. *Geochim. Cosmochim. Ac.* **72**, 5475-5504.
- Vils F., Tonarini S., Kalt A. and Seitz H. (2009) Boron, lithium and strontium isotopes as tracers of seawater–serpentinite interaction at Mid-Atlantic ridge, ODP Leg 209. *Earth Planet. Sc. Lett.* **286**, 414-425.
- Wada I. and Wang K. (2009) Common depth of slab-mantle decoupling: Reconciling diversity and uniformity of subduction zones. *Geochemistry, Geophysics, Geosystems* **10**, Q10009.
- Walker J. A., Teipel A. P., Ryan J. G. and Syracuse E. (2009) Light elements and Li isotopes across the northern portion of the Central American subduction zone. *Geochemistry, Geophysics, Geosystems* **10**, Q06S16.
- Walowski K. J., Wallace P. J., Clynne M. A., Rasmussen D. J. and Weis D. (2016) Slab melting and magma formation beneath the southern Cascade arc. *Earth Planet. Sc. Lett.* **446**, 100-112.
- Walowski K. J., Wallace P. J., Hauri E. H., Wada I. and Clynne M. A. (2015) Slab melting beneath the Cascade Arc driven by dehydration of altered oceanic peridotite. *Nat. Geosci.* **8**, 404-408.
- Webster J. D., Holloway J. R. and Hervig R. L. (1989) Partitioning of lithophile trace elements between H₂O and H₂O + CO₂ fluids and topaz rhyolite melt. *Economic geology and the*

- bulletin of the Society of Economic Geologists* **84**, 116-134.
- Weyer S. and Seitz H. M. (2012) Coupled lithium and iron isotope fractionation during magmatic differentiation. *Chem. Geol.* **294-295**, 42-50.
- Wunder B., Meixner A., Romer R. L., Feenstra A., Schettler G. and Heinrich W. (2007) Lithium isotope fractionation between Li-bearing staurolite, Li mica and aqueous fluids; an experimental study. *Chem. Geol.* **238**, 277-290.
- Wunder B., Meixner A., Romer R. L. and Heinrich W. (2006) Temperature-dependent isotopic fractionation of lithium between clinopyroxene and high-pressure hydrous fluids. *Contrib. Mineral. Petr.* **151**, 112-120.
- Yamamoto K., Nakamaru K. and Adachi M. (1997) Depositional environments of "accreted bedded cherts" in the Shimanto terrane, Southwest Japan, on the basis of major and minor element compositions. *The Journal of Earth and Planetary Sciences, Nagoya University* **44**, 1-19.
- Yamane N., Kanagawa K. and Ito T. (2012) Contrasting seismic reflectivity of the lower crust and uppermost mantle between NE Japan and SW Japan as illustrated by petrophysical analyses of mafic and ultramafic xenoliths. *Journal of Geophysical Research: Solid Earth* **117**.
- Chuang, Y., Lin, J., and Chang Y. A. (1987) A thermodynamic description and phase relationships of the Fe-Cr system: Part I the BCC phase and the sigma phase. *Calphad* **11**, 57-72.
- Yogodzinski G. M., Brown S. T., Kelemen P. B., Vervoort J. D., Portnyagin M. and Sims K. W. W., et al. (2015) The Role of Subducted Basalt in the Source of Island Arc Magmas: Evidence from Seafloor Lavas of the Western Aleutians. *J. Petrol.* **56**, 441-492.
- You C. F., Chan L. H., Spivack A. J. and Gieskes J. M. (1995) Lithium, boron, and their

isotopes in sediments and pore waters of Ocean Drilling Program Site 808, Nankai Trough; implications for fluid expulsion in accretionary prisms. *Geology (Boulder)* **23**, 37-40.

Zack T., Tomascak P. B., Rudnick R. L., Dalpé C. and McDonough W. F. (2003) Extremely light Li in orogenic eclogites: The role of isotope fractionation during dehydration in subducted oceanic crust. *Earth Planet. Sc. Lett.* **208**, 279-290.

Zeng Z., Li X., Zhang Y. and Qi H. (2021) Lithium, Oxygen and Magnesium Isotope Systematics of Volcanic Rocks in the Okinawa Trough: Implications for Plate Subduction Studies. *Journal of Marine Science and Engineering* **10**, 40.

Tables

Table 5-1. Li isotopic compositions of late Cenozoic volcanic rocks on the Chugoku district, SW Japan

Sample name	Region	Latitude (°N)	Longitude (°E)	Age (Ma)	Episode*	Li (ppm)	$\delta^7\text{Li}$	MgO (wt%)	LOI (wt%)	FeO*/MgO	Mg ^{#†}	CIA [‡]	Cs/Rb	Li/Y
<u>IAB type</u>														
OTS-01	Otsu	34.348	130.839	9.10	1	12.9		6.88	1.31	1.43	59.5	53	0.0148	0.72
OTS-05	Otsu	34.343	130.950	8.29	1	9.41	+3.14	6.91	0.24	1.13	65.0	59	0.0081	0.48
OTS-06	Otsu	34.392	130.938	9.31	1	12.7	+2.84	7.84	0.63	1.37	60.5	54	0.0159	0.86
OTS-10	Otsu	34.405	131.129	9.25	1	8.50		10.21	1.38	0.81	72.0	61	0.0162	0.53
SER-11	Sera	34.851	132.834	12.0	1	77.3	-1.02	6.67	1.94	1.14	64.8	49	0.0871	1.94
HIB-01	Hiba	34.991	132.900	10	1	7.62		6.88	0.45	1.07	66.2	59	0.0083	0.37
HIB-04	Hiba	35.059	133.035	10.4	1	10.5	+3.41	6.56	0.47	1.02	67.2	55	0.0057	0.62
HIB-06	Hiba	35.045	133.074	9.90	1	7.45		6.73	0.81	1.08	65.9	62	0.0138	0.41
HIB-07	Hiba	34.987	133.077	10.1	1	7.21	+3.51	8.31	0.19	0.93	69.3	58	0.0086	0.36
MAT-04	Matsue	35.452	133.069	11.0	1	8.53	+6.29	7.27	1.81	1.00	67.7	55	0.0134	0.38
MKM-01	Kurayoshi (old)	35.494	134.102	5.03	2	7.48	+2.06	5.07	-0.09	1.67	55.7	61	0.0350	0.40
KUR-16	Kurayoshi (old)	35.442	133.863	5	2	7.17		8.23	1.19	1.01	67.6	61	0.0140	0.47
KUR-17	Kurayoshi (old)	35.443	133.859	5.15	2	8.12	-1.95	7.11	0.50	1.23	63.0	59	0.0184	0.50
KRW-02	Kurayoshi (old)	35.258	134.100	4.99	2	4.86	+2.59	8.35	0.97	1.21	63.5	64	0.0176	0.24
KRW-03	Kurayoshi (old)	35.256	134.138	5.43	2	5.56		7.55	0.77	1.21	63.4	62	0.0082	0.33
KAW-03	Kawamoto	34.993	132.514	2.26	3	18.6	+5.02	4.68	1.60	1.47	58.8	50	0.0129	0.99
MEN-02	Mengame	34.938	132.724	1.11	3	9.80	+1.45	9.71	0.38	0.77	73.2	57	0.0086	0.33
ABU-06	Abu	34.442	131.498	1.57	3	10.0		6.05	0.11	2.13	49.6	51	0.0384	0.53
ABU-11	Abu	34.479	131.444	0.06	3	9.87	+2.46	7.51	0.46	1.16	64.3	59	0.0396	0.54
ABU-17	Abu	34.477	131.605	0.39	3	10.6		7.49	-0.19	1.17	64.3	55	0.0054	0.56
ABU-21	Abu	34.487	131.625	0.18	3	9.59	+1.78	8.30	-0.38	0.93	69.2	55	0.0100	0.57

ABU-23	Abu	34.493	131.645	0.18	3	10.1	+1.62	7.91	0.86	0.96	68.5	55	0.0200	0.62
ABU-26	Abu	34.603	131.688	2.01	3	12.0		4.39	0.16	1.76	54.4	52	0.0105	0.81
MAT-02	Yokota	35.418	133.185	1.2	3	8.85		7.18	2.69	0.95	68.8	63	0.0143	0.50
YOK-01	Yokota	35.191	133.086	1.1	3	7.84		7.48	0.19	0.84	71.5	56	0.0074	0.54
YOK-05	Yokota	35.160	133.209	1.32	3	8.09	+3.62	9.47	0.48	0.72	74.3	59	0.0202	0.59
US-01	Kurayoshi (young)	35.452	133.919	1.00	3	9.71		4.69	-0.17	1.65	56.0	59	0.0165	0.78
OGI-03	N. Hyogo	35.479	134.420	0.98	3	13.2		4.29	0.84	1.74	54.6	57	0.0202	0.80
INA-01	N. Hyogo	35.500	134.299	2.74	3	9.41	+1.65	5.17	0.63	1.75	54.5	59	0.0177	0.50
HYO-03	N. Hyogo	35.491	134.530	1.62	3	8.73		5.29	0.26	1.38	60.4	56	0.0097	0.42
HYO-15	N. Hyogo	35.592	134.811	1.81	3	11.0	+2.06	7.46	6.15	1.46	58.9	79	0.0043	0.36

ADK type

AON-03	Aonoyama	34.493	131.815	0.29	3	13.2		2.36	1.20	1.44	60.7	53	0.0185	1.51
AON-04	Aonoyama	34.473	131.800	0.09	3	11.7	+3.26	2.13	0.45	1.63	57.8	53	0.0173	1.14
AON-09	Aonoyama	34.448	131.765	0.30	3	13.4	+3.04	2.20	0.53	1.53	59.2	52	0.0231	1.05
AON-17	Aonoyama	34.076	131.751	0.3	3	19.0	+3.06	3.21	2.07	1.12	66.6	51	0.0371	2.09
AON-21	Aonoyama	34.254	131.774	0.38	3	11.8	+1.60	2.89	1.03	1.55	59.1	52	0.0203	0.87
AON-22	Aonoyama	34.188	131.764	0.5	3	15.3	+2.44	3.32	1.29	1.48	60.1	52	0.0304	0.77
OE-01	Oe-Takayama	35.070	132.427	1.52	3	10.4		1.01	0.51	2.94	43.2	51	0.0346	1.44
OE-02	Oe-Takayama	35.090	132.435	1.5	3	12.4		0.36	1.00	6.82	24.6	52	0.0293	2.49
OE-03	Oe-Takayama	35.089	132.436	1.70	3	14.7	+3.42	0.77	0.75	3.47	39.1	51	0.0403	2.30
OE-09	Oe-Takayama	35.115	132.409	1.05	3	10.2	+5.20	1.49	0.39	1.88	54.3	50	0.0428	2.08
OE-10	Oe-Takayama	35.102	132.413	1.87	3	14.6	+5.64	0.49	1.23	4.47	33.3	52	0.0477	2.71
OE-11	Oe-Takayama	35.107	132.424	1.83	3	18.6	+5.19	1.08	2.00	2.38	48.4	51	0.0276	3.96
SAM-01**	Sambe	35.162	132.616	1.36	3	10.1		1.78	1.20	2.33	48.9	57	0.0055	1.11
SAM-06	Sambe	35.135	132.631	0.07	3	11.7		1.94	0.23	1.80	55.3	52	0.0463	1.74
SAM-14	Sambe	35.129	132.620	0.43	3	16.3	+2.40	1.90	0.26	1.76	55.9	52	0.0554	2.47
SAM-16	Sambe	35.135	132.620	0.3	3	16.0	+2.46	1.97	0.47	1.80	55.3	52	0.0488	2.21
SAM-20	Sambe	35.154	132.626	0.22	3	12.5	+3.00	1.92	0.21	1.85	54.7	52	0.0450	1.80
SAM-21	Sambe	35.114	132.631	0.2	3	13.9	+4.93	1.79	0.36	1.67	57.1	51	0.0616	2.07
WAK-01	Wakurayama	35.467	133.108	0.86	3	8.10	+7.44	2.05	0.19	1.77	55.7	54	0.0222	1.34

WAK-02	Wakurayama	35.485	133.121	0.72	3	10.5	+7.12	2.28	0.23	1.63	57.8	52	0.0250	1.66
WAK-03	Wakurayama	35.492	133.116	0.73	3	10.3	+6.35	1.74	0.78	2.16	50.8	54	0.0229	1.63
2060707	Daisen	35.364	133.538	0.02	3	13.8		1.80	0.07	2.02	52.5	51	0.0533	1.69
3052002	Daisen	35.355	133.555	0.06	3	14.5	+1.21	1.84	0.38	2.05	52.1	51	0.0570	1.76
3053003	Daisen	35.328	133.566	0.51	3	10.0	+7.22	2.11	0.73	1.85	54.7	53	0.0159	1.23
3060102	Daisen	35.355	133.507	0.46	3	11.0	+7.32	1.90	0.32	2.12	51.3	54	0.0233	1.27
3060604	Daisen	35.403	133.589	0.41	3	11.9	+7.03	2.00	0.42	1.90	54.0	53	0.0184	1.30
SAN2	Daisen	35.377	133.572	0.05	3	11.3	+4.66	2.05	0.47	1.76	55.9	51	0.0323	1.35
YOK-11	Daisen	35.360	133.485	0.55	3	12.3	+4.88	1.92	0.37	2.24	49.8	54	0.0377	1.55
TG-01	Kurayoshi (young)	35.478	133.910	1.34	3	12.3		2.87	0.70	1.79	55.5	58	0.0155	1.04
KUR-01	Kurayoshi (young)	35.465	133.830	1.90	3	8.52	+5.68	2.74	-0.27	1.66	57.4	54	0.0180	1.05
KUR-05	Kurayoshi (young)	35.461	133.861	1.13	3	8.17	+3.86	2.80	0.93	2.18	50.6	55	0.0179	0.52
KUR-11	Kurayoshi (young)	35.470	133.802	1.24	3	9.01	+2.83	3.34	0.25	1.49	60.0	54	0.0217	0.78
<u>HMA type</u>														
JA-2	Setouchi	34.35	133.93	14.1		28.7	-1.00	7.60	1.96	0.74	73.9	56		
TG1	Setouchi	34.46	135.56	13.9			-0.12	9.47	1.15	0.65	76.2	59		
SD264 (MDYB-2)	Setouchi	34.50	134.19	13.3			-0.26	6.05	0.78	0.92	69.5	55		

Note: Analyses shown by boldface font were obtained in this study, and those shown by normal font were obtained by [Feineman et al. \(2013\)](#), [Imai et al. \(1995\)](#); [Ishikawa and Nakamura \(1994\)](#), [Ishizaka and Carlson \(1983\)](#), [Nguyen et al. \(2020\)](#), [Pineda-Velasco et al. \(2018\)](#), [Tatsumi and Ishizaka \(1982a, b\)](#), and [Shimoda et al. \(1998\)](#).

*Episode 1, 12–8 Ma; Episode 2, 8–4 Ma; Episode 3, 4 Ma to present ([Nguyen et al., 2020](#))

**The sample name of "SAM-01" is assigned to different rock specimens; one for ADK-type dacite from Sambe volcano and another is OIB-type basalt from the vicinity of Sambe volcano ([Pineda-Velasco et al., 2018](#); [Nguyen et al., 2020](#)).

†Mg# value is calculated as $100 \text{ Mg}/(\text{Mg} + \text{Fe}^{2+})$ where $\text{Fe}^{2+}/\text{Fe}_{\text{total}}$ is assumed to be 0.80 for ADK ([Pineda-Velasco et al., 2018](#)) and 0.85 for HMA, IAB and OIB ([Nguyen et al., 2020](#); this study).

‡CIA (chemical index of alteration) after [Nesbitt and Young \(1982\)](#) and [McLennan \(1993\)](#), defined as $[\text{Al}_2\text{O}_3/(\text{Al}_2\text{O}_3 + \text{CaO}^* + \text{Na}_2\text{O} + \text{K}_2\text{O})] \times 100$ where oxide abundances are given in molecular proportions and CaO* denotes CaO abundances in silicate fraction in a rock.

Table 5-2. Results of the incremental dehydration modeling for the altered oceanic crust beneath the Chugoku district, SW Japan

Step	Input parameters						Model outputs			
	T (°C)	P (GPa)	Depth (km)	H ₂ O (wt%)	D_{Li}^n	$D^7\text{Li}_n$	[Li] _{AOC} (μg·g ⁻¹)	[Li] _{fluid} (μg·g ⁻¹)	$\delta^7\text{Li}_{\text{AOC}}$	$\delta^7\text{Li}_{\text{fluid}}$
0	201	0.50	19	5.29	0.544	7.23	16.0		11.3	
1	225	0.60	22	5.29	0.456	6.78	16.0	35.1	11.3	18.1
2	246	0.70	26	5.27	0.388	6.40	16.0	41.2	11.3	17.7
3	266	0.80	30	5.27	0.335	6.07	16.0	47.8	11.3	17.4
4	283	0.90	33	5.28	0.293	5.80	16.0	54.5	11.3	17.1
5	300	1.00	37	5.28	0.260	5.57	16.0	61.6	11.3	16.9
6	317	1.10	41	5.27	0.229	5.34	16.0	70.0	11.3	16.6
7	334	1.20	44	5.28	0.201	5.12	16.0	79.6	11.3	16.4
8	351	1.30	48	5.27	0.176	4.91	16.0	90.7	11.3	16.2
9	368	1.40	52	5.24	0.155	4.71	16.0	103	11.3	16.0

10	388	1.50	56	5.19	0.134	4.50	15.9	119	11.3	15.8
11	406	1.60	59	5.18	0.129	4.31	15.9	123	11.3	15.6
12	424	1.70	63	5.16	0.129	4.14	15.9	123	11.3	15.4
13	442	1.80	67	5.14	0.129	3.97	15.9	123	11.3	15.2
14	460	1.90	70	5.03	0.129	3.81	15.7	122	11.2	15.0
15	478	2.00	74	5.02	0.129	3.66	15.7	122	11.2	14.9
16	496	2.10	78	4.48	0.115	3.51	15.1	131	11.1	14.6
17	516	2.20	81	3.04	0.096	3.36	13.3	138	10.6	14.0
18	540	2.30	85	2.08	0.070	3.19	11.8	168	10.2	13.4
19	593	2.40	89	0.97	0.067	2.84	10.1	151	9.8	12.6
20	715	2.50	93	0.08	0.068	2.18	8.99	132	9.5	11.7
21	772	2.60	96	0.08	0.068	1.93	8.99	132	9.5	11.5
22	801	2.70	100	0.08	0.068	1.81	8.99	132	9.5	11.3
23	820	2.80	104	0.08	0.068	1.74	8.99	132	9.5	11.3
24	834	2.90	107	0.08	0.068	1.68	8.99	132	9.5	11.2

25	845	3.00	111	0.04	0.068	1.64	8.94	131	9.5	11.2
26	854	3.10	115	0	0.068	1.61	8.89	131	9.5	11.1
27	863	3.20	118	0	0.068	1.58	8.89	131	9.5	11.1
28	870	3.30	122	0	0.068	1.55	8.89	131	9.5	11.1

T-P condition and H₂O abundance of a crustal layer of the subducting slab (Philippine Sea Plate with Shikoku Basin crust) are after [Kimura \(2017\)](#).

Depth (km) is calculated as P (GPa) \times 37.

$K_{dLi} = C_{Li}^{AOC}/C_{Li}^{fluid}$. Temperature dependency of K_{dLi} is corrected following [Berger et al. \(1988\)](#) at $T < 400$ °C and [Marschall et al. \(2007\)](#) at $T > 400$ °C.

$\Delta\delta^7Li \equiv \delta^7Li_{fluid} - \delta^7Li_{AOC} = 4.61 \times (1000/T) - 2.48$ after [Wunder et al. \(2006\)](#)

Table 5-3. Results of the incremental dehydration modeling for the sediment beneath the Chugoku district, SW Japan

Input parameters							Model outputs			
Step	T (°C)	P (GPa)	Depth (km)	H ₂ O (wt%)	K_{dLi}	$\Delta\delta^7Li_n$	[Li] _{sed} ($\mu\text{g}\cdot\text{g}^{-1}$)	[Li] _{fluid} ($\mu\text{g}\cdot\text{g}^{-1}$)	δ^7Li_{sed}	δ^7Li_{fluid}
0	198	0.50	19	5.29	0.681	4.85	50.0		-1.0	
1	224	0.60	22	5.29	0.609	4.36	50.0	82.2	-1.0	3.4
2	245	0.70	26	5.27	0.547	3.98	50.0	91.3	-1.0	3.0

3	265	0.80	30	5.27	0.491	3.66	50.0	101.9	-1.0	2.7
4	284	0.90	33	5.28	0.435	3.37	50.0	114.8	-1.0	2.4
5	301	1.00	37	5.28	0.386	3.13	50.0	129.5	-1.0	2.1
6	318	1.10	41	5.27	0.336	2.90	50.0	148.7	-1.0	1.9
7	337	1.20	44	5.28	0.283	2.67	50.0	176.5	-1.0	1.7
8	355	1.30	48	5.27	0.231	2.46	50.0	216.4	-1.0	1.5
9	374	1.40	52	5.24	0.176	2.24	49.9	283	-1.0	1.2
10	392	1.50	56	5.19	0.124	2.05	49.7	403	-1.0	1.0
11	411	1.60	59	5.17	0.140	1.86	49.7	355	-1.0	0.8
12	430	1.70	63	5.14	0.140	1.69	49.6	354	-1.0	0.7
13	448	1.80	67	5.14	0.140	1.53	49.6	354	-1.0	0.5
14	467	1.90	70	5.03	0.140	1.37	49.3	352	-1.0	0.3
15	485	2.00	74	5.01	0.140	1.30	49.2	351	-1.0	0.3
16	505	2.10	78	3.95	0.140	1.30	46.2	330	-1.1	0.2
17	525	2.20	81	3.04	0.140	1.30	43.7	312	-1.2	0.1

18	556	2.30	85	2.08	0.140	1.30	41.2	294	-1.3	0.0
19	626	2.40	89	0.69	0.140	1.30	37.9	270	-1.4	-0.1
20	762	2.50	93	0.08	0.140	1.30	36.4	260	-1.5	-0.2
21	809	2.60	96	0.08	0.140	1.30	36.4	260	-1.5	-0.2
22	831	2.70	100	0.08	0.140	1.30	36.4	260	-1.5	-0.2
23	846	2.80	104	0.08	0.140	1.30	36.4	260	-1.5	-0.2
24	857	2.90	107	0.08	0.140	1.30	36.4	260	-1.5	-0.2
25	866	3.00	111	0.00	0.140	1.30	36.3	259	-1.5	-0.2
26	874	3.10	115	0.00	0.140	1.30	36.3	259	-1.5	-0.2
27	881	3.20	118	0.00	0.140	1.30	36.3	259	-1.5	-0.2
28	888	3.30	122	0.00	0.140	1.30	36.3	259	-1.5	-0.2

T-P condition and H₂O abundance of a sediment layer of the subducting slab (Philippine Sea Plate with Shikoku Basin crust) are after [Kimura \(2017\)](#).

Depth (km) is calculated as P (GPa) \times 37.

$K_{dLi} = C_{Li}^{SED}/C_{Li}^{fluid}$. Temperature dependency of K_{dLi} is corrected following [Simons et al. \(2010\)](#).

$\Delta\delta^7Li \equiv \delta^7Li_{fluid} - \delta^7Li_{sediment} = 4.52 \times (1000/T) - 4.74$ (< 500 °C) and 1.30 (constant, > 500 °C) after [Wunder et al. \(2007\)](#)

Chapter 6. Mg isotope fractionation and modification of slab-derived melt: Perspective from Mg isotopic compositions of volcanic rocks from the Southwest Japan

Abstract

The magnesium isotope was regarded as a sensitive tracer to fluids from slab lithosphere serpentinites. However, the effect of the thermal structure of a subduction zone to the Mg isotope composition of fluids is yet not clear. Fluids from the subarc depth of warm subduction zones were predicted to have heavier slab $\delta^{26}\text{Mg}$ signatures. In order to investigate Mg isotope composition of volcanic rocks from warm subduction zones, we report Mg isotopic data of volcanic rocks from the Chugoku district of Southwest Japan. Except two lamprophyre samples from Sera and Kawamoto, those lavas display nearly homogeneous Mg isotopic compositions, with an average $\delta^{26}\text{Mg}$ of $-0.23 \pm 0.08\text{‰}$ (2SD, $N=43$), similar to that of mantle peridotite ($-0.25 \pm 0.06\text{‰}$). The lack of correlation between $\delta^{26}\text{Mg}$ and slab-component index indicates the absence of clear slab-derived components. However, our modelling suggests that partial melts derived from subducted oceanic crust (-0.17‰ to $+0.06\text{‰}$) and detrital sediments ($+0.3\text{‰}$ to $+0.6\text{‰}$) could have substantially heavier Mg isotopic compositions compared to those in sources and mantle. The mixing calculation suggests that only $> 3\%$ of Mg ingestion from the mantle peridotite to the slab melt may significantly buffer high $\delta^{26}\text{Mg}$ signature in slab-derived melts to mantle $\delta^{26}\text{Mg}$ values, which may explain the mantle-like Mg isotopic composition of Chugoku lavas.

1. Introduction

The magnesium isotope study of the subduction zone recently shows that it may be a

sensitive tracer for slab input and is particularly sensitive to tracking subduction carbonate rocks and serpentinites (Teng, 2017 and its references). In contrast to the uniform $\delta^{26}\text{Mg}$ values in global peridotites ($-0.25 \pm 0.06\text{‰}$, Teng et al., 2010), the subduction lithology has highly heterogeneous Mg isotope composition, and the carbonate facies has a low- $\delta^{26}\text{Mg}$ signature, and marine sediments, altered oceanic crust and ultramafic rocks usually show different high $\delta^{26}\text{Mg}$ value (Beinlich et al., 2014; Teng et al., 2016; Hu et al., 2017; Liu et al., 2017; Huang et al., 2018; Guo et al., 2019).

Magnesium isotope data of arc lavas are scarce but reveal significant variabilities between different arcs. The arc lavas from the arc front of the Kamchatka Peninsula and Costa Rica volcanoes have mantle-like Mg isotopic composition, while the arc lavas in the Lesser Antilles Islands and the Philippines are characterized by higher $\delta^{26}\text{Mg}$ values than mantle (Teng et al., 2016; Li et al., 2017). The higher $\delta^{26}\text{Mg}$ values were interpreted as reflecting the contribution from slab-derived fluid, especially from serpentinitized slab mantle (Teng et al., 2016; Li et al., 2017), although the lavas from Lesser Antilles show strong sediment signals, and other arc lavas primarily show contributions from slab-derived fluids. Recently, slightly heavier $\delta^{26}\text{Mg}$ values are also found in some of the Cascadia and Makran arc lavas, but are only confined to more evolved samples, which are mainly attributed to crustal assimilation and fractional crystallization (Brewer et al., 2018; Pang et al., 2020).

The thermal structure of a given subduction zone has a profound influence on the dehydration path of the subduction slab, the properties and fluxes of the slab-mantle mass transfer agents (fluids vs. melts), and ultimately on the composition of arc magmas. The mean $\delta^{26}\text{Mg}$ value of these arcs shows a general correlation with subduction parameters. For example, the increasing value of $\delta^{26}\text{Mg}$ is related to the increase of slab surface temperature and slab depth. These correlations indicate that the Mg isotopic characteristics of lavas beneath the

volcanic front may be controlled by dehydration reaction under the unique P-T conditions of each subduction zone. In the subarc depth of the cold subduction zone or the magma derived from relatively shallow depth, the main water sources in the oceanic crust are amphibole, chlorite, lawsonite, zoisite, and paragonite (Schmidt and Poli, 2014). These minerals either do not contain too much Mg (e.g., lawsonite, zoisite), or they may have Mg isotope compositions similar to those of mantle olivine and pyroxene owing to similar Mg-O bond strength (e.g., amphibole) (Hu et al., 2020). In contrast, fluids from the sub arc depth of the warm subduction zone or magmas from relatively deep depths may have heavier slab $\delta^{26}\text{Mg}$ signatures because these deeper fluids have stronger solubility and are more solute-rich (e.g., Manning, 2004) and the higher slab temperatures facilitate the release of fluid from the serpentinized slab mantle. Compared with oceanic crust, serpentinite has much higher water content and magnesium concentration. More importantly, serpentinized peridotites and constituent phyllosilicates usually have Mg isotopic compositions different from those of the normal mantle. For example, variable heavy magnesium isotopic compositions have been recorded in talc and antigorite (up to +0.30 ‰, Beinlich et al., 2014), altered abyssal peridotites (Liu et al., 2017), and exhumed whiteschists metasomatized by Mg-rich fluids derived from serpentinite dehydration (−0.07 to +0.72 ‰, Chen et al., 2016).

Although released fluids may have different $\delta^{26}\text{Mg}$ values from protolith, Magnesium isotope fractionation of whole silicate rock itself during metamorphic dehydration is limited. Li et al. (2014) analyzed a set of well-characterized metapelites from the Onawa contact aureole and found Mg isotopic compositions of metapelites do not change even though significant amounts of fluids was lost during prograde metamorphism. A similar conclusion is also reached for metamorphic dehydration of subduction zone rocks. Wang et al. (2014) systematically measured Mg isotopes for a set of genetically related prograde metamorphosed meta-basaltic

rocks from the Dabie orogen, with metamorphic grade ranging from greenschist, amphibolite to eclogite. All these samples have similar Mg isotopic composition, indicating limited Mg isotope fractionation during prograde metamorphism of mafic rocks. Overall, these studies suggest that metamorphic dehydration does not produce measurable Mg isotopic changes and metamorphic rocks still preserve Mg isotopic compositions of their protoliths. The lack of isotope fractionation during prograde metamorphism mainly results from the conservative behavior of Mg as Mg is always hosted in major rock-forming minerals during metamorphic reactions and little Mg was lost into fluids (<5%).

The southwest (SW) Japan arc is an example of a volcanic field in which high-Sr andesites and dacites (“adakites”) occur (Feineman et al., 2013; Kimura et al., 2014; Morris, 1995). It is generally accepted that these andesites and dacites in SW Japan are attributed to melting of the young, subducted plate (Shikoku Basin Plate) in late Cenozoic time (Feineman et al., 2013; Kimura et al., 2014; Morris, 1995; Shibata et al., 2014). However, the fluid source of slab melting remains a question. Because the hotter nature of the young, subducted plate causes most dehydration of the oceanic crust to occur beneath the forearc rather than the arc (Rondenay et al., 2008; Aber et al., 2009; Walowski et al., 2015), little H₂O may reach sub-arc depths. The hydrated upper mantle portion of the subducted plate is able to carry bound H₂O to greater depths in the form of antigorite and chlorite until the slab top reaches ~80–90 km depth (Van Keken et al. 2011; Walowski et al., 2015), hence, dehydration of the serpentinitized peridotite in the slab mantle portion have potential to provide H₂O for the partial melting of the oceanic crust (Freythuth et al., 2016; Spandler and Pirard, 2013). As we mentioned above, Mg isotopes are a powerful tool for tracing the fluids from subducted serpentinites and slab serpentinites from hot subduction zones may release fluids with different Mg isotopic signatures from mantle peridotite. Therefore, in this study, Mg isotopes is employed to identify

the fluid source which facilitating slab melting beneath the Chugoku district of SW Japan.

2. Results

New $^{26}\text{Mg}/^{24}\text{Mg}$ and $^{25}\text{Mg}/^{24}\text{Mg}$ data along with their MgO contents for the 43 samples of volcanic rocks from the Chugoku district are reported in **Table 6-1**. The Sr-Nd-Hf-Pb isotopic data for the same samples, analyzed by [Feineman et al. \(2013\)](#), [Ishizaka and Carlson \(1983\)](#), [Moriguti and Nakamura \(1998\)](#), [Nguyen et al. \(2020\)](#) and [Pineda-Velasco et al. \(2015, 2018\)](#) are presented in Table 2-1. Two shale samples from Shimanto Belt are also presented in **Table 6-1**.

2.1 Temporal variation

Arc magma in SW Japan do not show systematic temporal variation, regardless of their rock type (IAB, ADK and HMA) (**Figure 6-1**). Considering the analytical error, only two samples have $\delta^{26}\text{Mg}$ higher than fresh MORB, and are Sera lamprophyre from episode 1 and Kawamoto minette from episode 3.

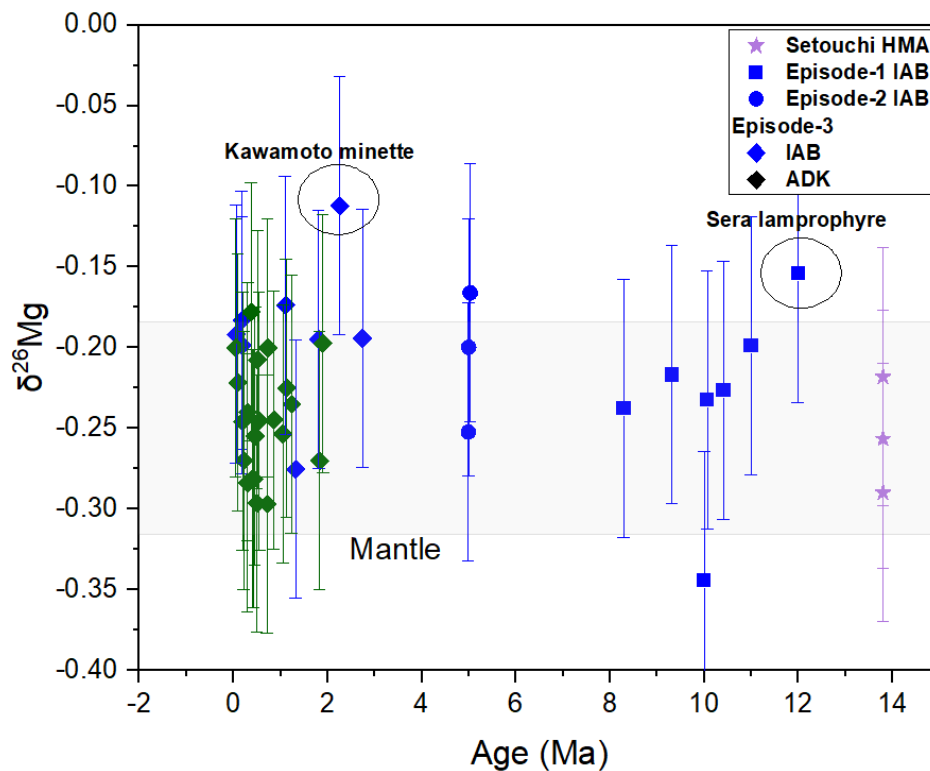


Figure 6-1. $\delta^{26}\text{Mg}$ (‰) plotted against sample age of volcanic rocks from the Chugoku district in SW Japan.

2.2 Spatial variation

Arc magma regardless of their rock type (IAB, ADK and HMA) in SW Japan do not show clear spatial variation (**Figure 6-2**). Two samples with $\delta^{26}\text{Mg}$ > fresh MORB (Sera lamprophyre and Kawamoto minette) are from central part of Chugoku district.

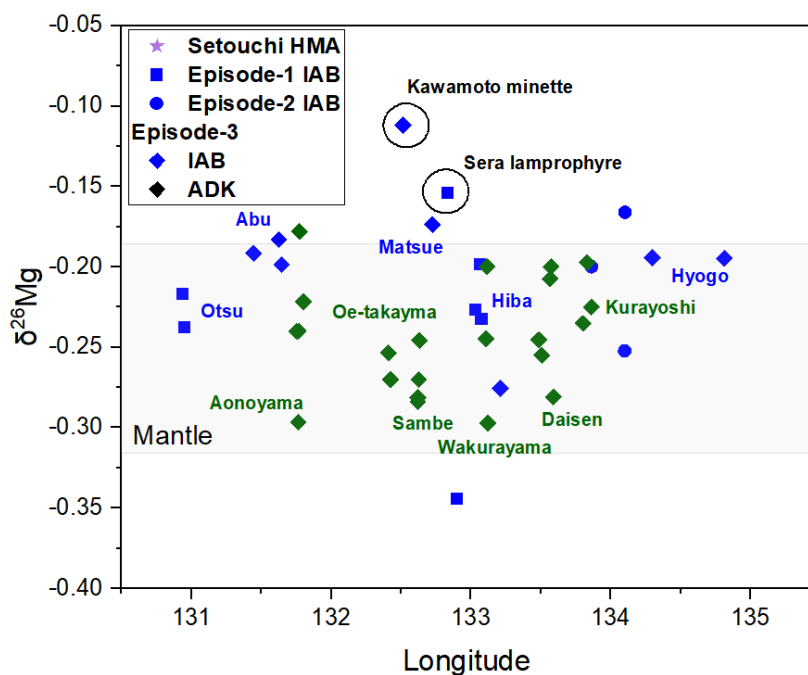


Figure 6-2. $\delta^{26}\text{Mg}$ (‰) plotted against Longitude of volcanic rocks from the Chugoku district in SW Japan.

2.3 Correlation of Mg isotope with $^{87}\text{Sr}/^{86}\text{Sr}$, $^{143}\text{Nd}/^{144}\text{Nd}$, $^{177}\text{Hf}/^{178}\text{Hf}$, and $^{206}\text{Pb}/^{204}\text{Pb}$

Arc magma in SW Japan do not show systematic variation with Sr, Nd, Pb and Hf isotopes, regardless of their rock type (IAB, ADK and HMA) (**Figure 6-3**). Two samples with $\delta^{26}\text{Mg}$ > fresh MORB (Sera lamprophyre and Kawamoto minette) have highest $^{87}\text{Sr}/^{86}\text{Sr}$, and lowest $^{143}\text{Nd}/^{144}\text{Nd}$ and $^{177}\text{Hf}/^{178}\text{Hf}$.

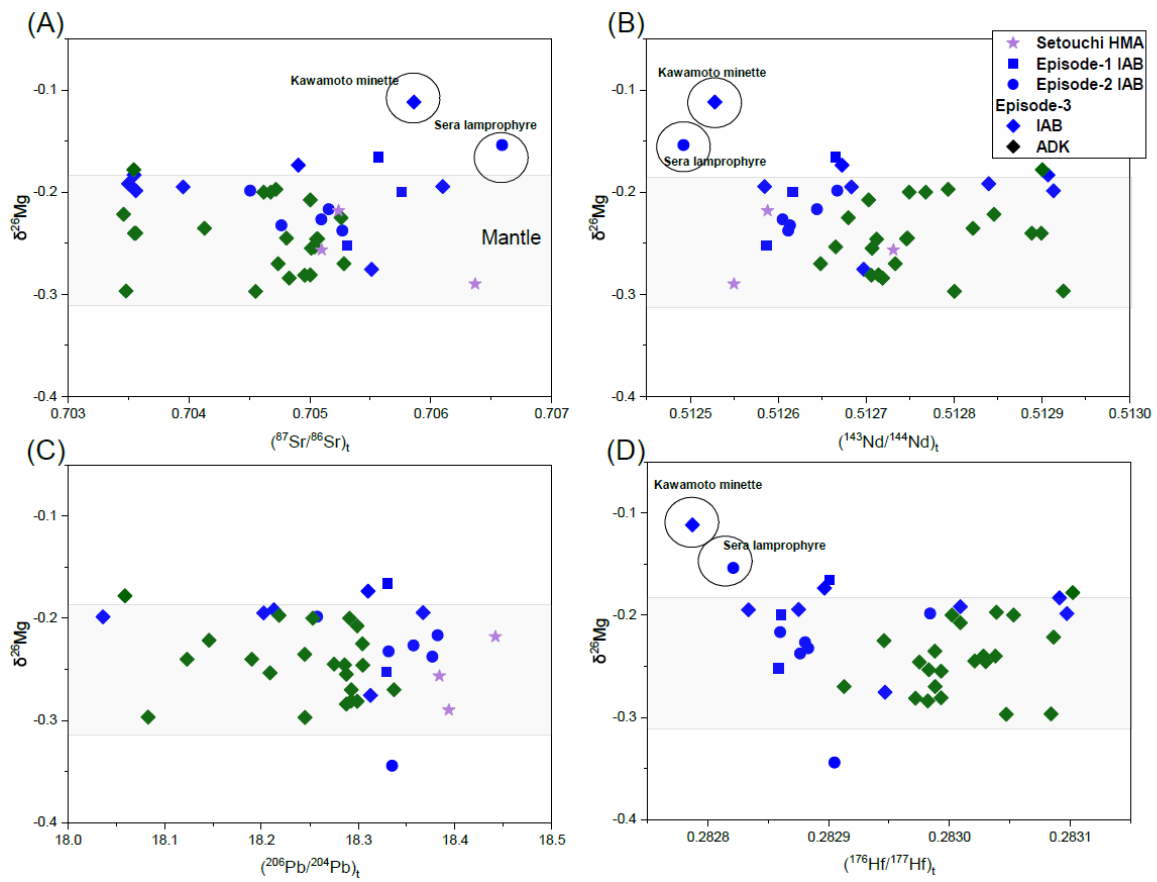


Figure 6-3. Plot of $\delta^{26}\text{Mg}$ in volcanic rocks from the Chugoku district in SW Japan versus (A) $(^{87}\text{Sr}/^{86}\text{Sr})_t$, (B) $(^{143}\text{Nd}/^{144}\text{Nd})_t$, (C) $(^{206}\text{Pb}/^{204}\text{Pb})_t$, and (D) $(^{176}\text{Hf}/^{177}\text{Hf})_t$.

2.4 Correlation of Mg isotope with trace element ratios

Arc magma in SW Japan do not show systematic variation with Sr/Nd, La/Yb, Th/U and Pb/Ce, which represent the contribution of altered oceanic crust (AOC), source garnet residue, subducted sediments, and aqueous fluids (**Figure 6-4**). Two samples with $\delta^{26}\text{Mg} > \text{fresh MORB}$ (Sera lamprophyre and Kawamoto minette) have highest La/Yb and Th/U, and lowest Sr/Nd and Pb/Ce.

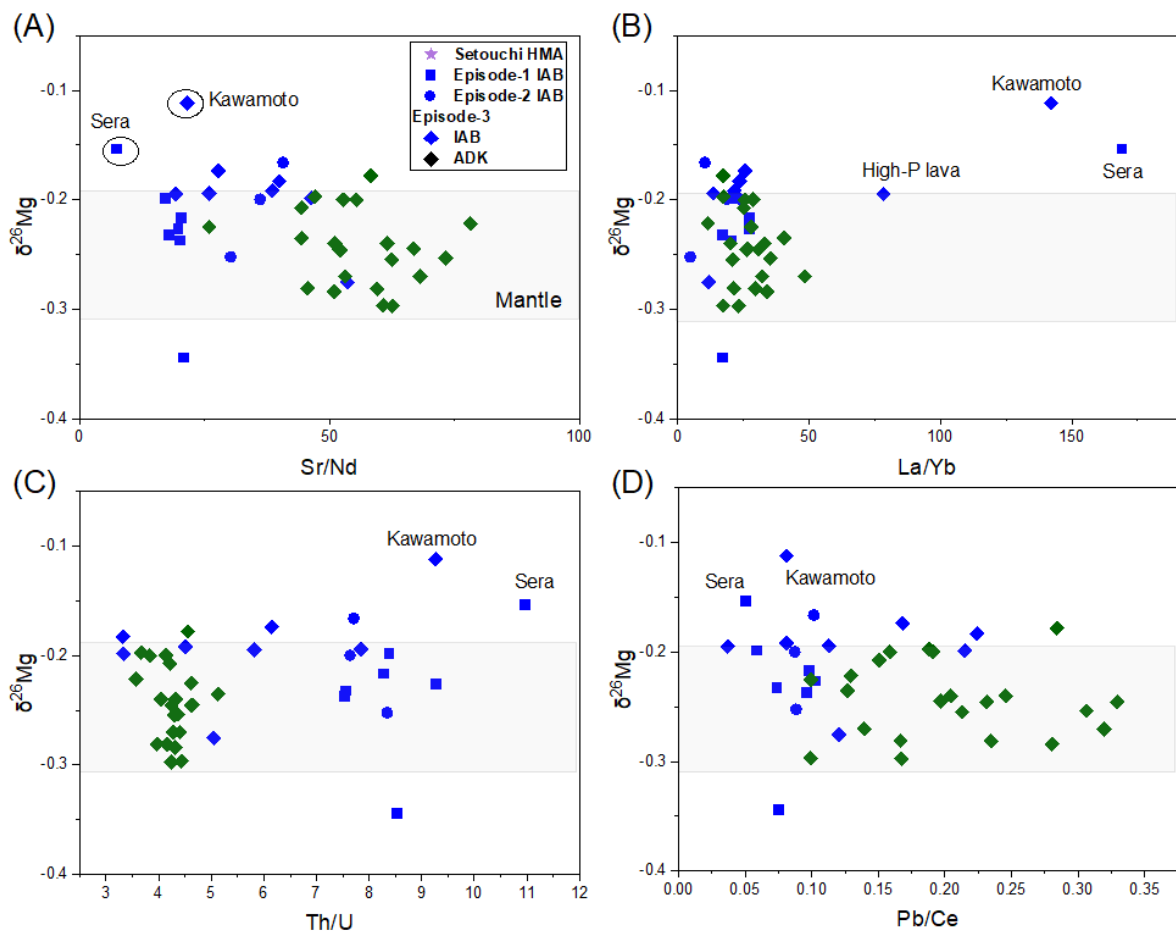


Figure 6-4. Plot of $\delta^{26}\text{Mg}$ in volcanic rocks from the Chugoku district in SW Japan versus (A) Sr/Nd, (B) La/Yb, (C) Th/U, and (D) Pb/Ce.

3. Discussion

The subducting lithosphere is composed of four units: sediment, basalt, gabbro and serpentinized peridotite, respectively from the top to the bottom. Recent studies summarized below suggest that marine sediments, altered oceanic crust (AOC) and abyssal peridotites have very heterogeneous Mg isotopic composition and subduction of the subducted slab thus can recycle isotopically distinct Mg into the mantle.

3.1 The contribution of altered oceanic basalts

3.1.1 The Magnesium isotopic composition of the altered oceanic basalts

Compared to serpentinites ($\text{MgO} > 40 \text{ wt.}\%$), the altered oceanic basalts are characterized

by low Mg concentrations (MgO=4~10 wt.%) and wide ranges of $\delta^{26}\text{Mg}$ values (Chen et al., 2016; Chen et al., 2020; Huang et al., 2015; Huang et al., 2018). Altered oceanic basalts have very heterogeneous Mg isotopic compositions (-1.2 ~ +0.2‰). Huang et al. (2018) suggested that formation of Mg-bearing minerals (saponite and calcite) during low-temperature alteration of the oceanic crust accounts for the highly variable $\delta^{26}\text{Mg}$ values of the altered oceanic crust. Early saponite formation leads to relatively high $\delta^{26}\text{Mg}$ and subsequent carbonate precipitation causes the dilution of Mg and tend to take up the light Mg isotopes. Other studies of AOC from Eastern Pacific Rise and Southern Pacific show similar or slightly higher $\delta^{26}\text{Mg}$ than fresh MORB (Huang et al., 2015; Zhong et al., 2017).

3.1.2 Behavior and fractionation of Mg isotopes during the melting of oceanic crust

Magnesium is a major element in the silicate Earth and is a major cation in all major mafic rock-forming minerals: olivine (Ol), orthopyroxene (Opx), clinopyroxene (Cpx), hornblende (Hbl) and biotite (Bt). Measurements of coexisting olivine, Opx and Cpx in mantle xenoliths (Handler et al. 2009; Yang et al. 2009; Liu et al. 2011; Pogge von Strandmann et al. 2011; Xiao et al. 2013; Lai et al. 2015; Hu et al. 2016; Wang et al. 2016), and coexisting hornblende and biotite in granitoids (Liu et al. 2011) suggest limited (<0.2‰) equilibrium inter-mineral fractionations. As these five minerals contain most Mg in the Earth and control Mg budget from ultramafic to felsic rocks, the limited inter-mineral fractionations among these minerals indicate small Mg isotope fractionation during magmatic differentiation, be it basaltic or granitic, as shown in previous studies (Teng et al. 2007, 2010; Liu et al. 2010).

The limited inter-mineral fractionations reflect the similar coordination of Mg in these minerals. Equilibrium isotope fractionation is qualitatively controlled by the coordination number of Mg in minerals, with heavy isotopes preferring minerals with high-bonding energy sites (i.e., low coordination sites) (Urey, 1947). The coordination number of Mg in Ol, Opx,

Cpx, Hbl and Bt is the same of 6. Therefore, limited equilibrium inter-mineral fractionation among these minerals is expected. However, the coordination of Mg is not 6 in two important rock-forming minerals as it is 4 in spinel (Spl) and 8 in garnet (Grt) (Howie et al. 1992). Thus, spinel is expected to be isotopically heavier whereas garnet is expected to be isotopically lighter than coexisting Ol, Opx, Cpx, Hbl or Bt.

Therefore, slab melting with residual garnets will produce heavy Mg isotopic components in slab melts, but the subsequent magmatic and crystallization processes will not fractionate Mg isotopic composition (Stracke et al., 2018; Wang et al., 2015). Mg isotope fractionation during slab melting varies with pressures, temperatures, H₂O involved or not. We modelled possible Mg isotope fractionation ($\Delta^{26}\text{Mg}_{\text{melt-source}}$) during the melting of oceanic crust beneath the Chugoku district following the approach of He et al. (2017) and Wang et al. (2015). Mg isotopic compositions for partial melts from oceanic crust at 90~100 km (~2.6 GPa) and 800°C are calculated based on phase relationship from representative melting experiments on MORB-like materials (Rapp and Watson, 1995; Sisson and Kelemen, 2018) and mass balance (Wang et al., 2020):

$$\delta^{26}\text{Mg}_{\text{melt}} = \delta^{26}\text{Mg}_{\text{source}} + \left(\sum f_{\text{Mg}, i} \times \Delta^{26}\text{Mg}_{\text{melt-}i} \right) \times \left(1 - F / \left(F + (1-F) \times \frac{\text{MgO}_{\text{residue}}}{\text{MgO}_{\text{melt}}} \right) \right)$$

, where F is the degree of partial melting, *i* represents MgO-rich mineral phase in the residua, $f_{\text{Mg}, i} = (\text{MgO}_i \times A_i) / (\sum \text{MgO}_i \times A_i)$, A_i represents the mineral *i* abundance in the residue, $\Delta^{26}\text{Mg}_{\text{melt-}i}$ represents the Mg isotope fractionation between melt and mineral *i* in the residual source, and $\text{MgO}_{\text{residue}}$ is estimated by a mineral-proportion weighted average.

The residual minerals during partial melting of subducted oceanic crust include garnet, clinopyroxene, ± hornblende, ± orthopyroxene, ± Fe-Ti oxide (magnetite and ilmenite), ± quartz, ± feldspar, ± rutile, ± titanite, ± apatite. Only four Mg-rich minerals (garnet,

clinopyroxene, hornblende, orthopyroxene) are considered to calculate $\delta^{26}\text{Mg}_{\text{melt}}$, because Quartz, feldspar, rutile, titanite, Fe-Ti oxide and apatite contain negligible MgO compared to the melt and other minerals and thus cannot cause Mg isotope fractionation during partial melting. The starting MgO composition of slab as well as phase proportion and MgO contents of four minerals in the residue are from [Rapp and Watson \(1995\)](#) and [Sisson and Kelemen \(2018\)](#), because the used MgO contents (6.1 to 8.4 wt. %) are similar to that of Shikoku basin basalts (1.7 to 8.4 wt. %). Based on statistic fractionation factors between garnet, hornblende, orthopyroxene and clinopyroxene (**Table 6-2**; e.g., [Handler et al., 2009](#); [Huang et al., 2013](#); [Liu et al., 2010](#); [Teng et al., 2017](#)), $\Delta^{26}\text{Mg}_{\text{residue-melt}}$ and $\delta^{26}\text{Mg}$ of oceanic crust melt are determined by $\Delta^{26}\text{Mg}_{\text{i-melt}}$ and the MgO fraction of these minerals in the residue. The $\delta^{26}\text{Mg}$ of the oceanic crust source is assumed to be -0.25‰, which is the average value of MORB. The calculation details are listed in **Table 6-2**.

Calculated $\delta^{26}\text{Mg}$ of oceanic crust melt ranges from -0.17‰ to +0.01‰ using parameters in [Rapp and Watson \(1995\)](#) and from +0.03 to +0.06‰ at 2.6 GPa using parameters in [Sisson and Kelemen \(2018\)](#) (**Table 6-2**). Therefore, partial melts derived from subducted oceanic crust could have substantially heavier Mg isotopic compositions compared to these sources and mantle, which is inconsistent with the mantle-like Mg isotopic composition of Chugoku lavas. Previous studies suggest that recycled sediments may have extremely low $\delta^{26}\text{Mg}$ isotopic compositions ([Li et al., 2017](#)). If it is the case, the melting of sediments with low $\delta^{26}\text{Mg}$ isotopic compositions may mix with oceanic crust melt with high $\delta^{26}\text{Mg}$ values and produce slab melt with mantle-like $\delta^{26}\text{Mg}$ composition, like that of Chugoku lavas. The scenario will be discussed below.

3.2 Sediment contribution

[Hu et al. \(2017\)](#) and [Teng et al. \(2016\)](#) systematically investigated Mg isotopic

compositions of 94 well-characterized marine sediments from 12 drill sites outboard of the world's major subduction zones. The $\delta^{26}\text{Mg}$ values in these subducting sediments vary greatly from -3.65 to $+0.52$. The detritus-dominated sediments have $\delta^{26}\text{Mg}$ (-0.57 to $+0.52$) comparable to the weathered crustal materials (e.g., -0.52 to $+0.92$) (Shen et al., 2009; Li et al., 2010; Liu et al., 2010; Huang et al., 2012, 2013; Ling et al., 2013; Wimpenny et al., 2014). By contrast, the calcareous oozes yield low $\delta^{26}\text{Mg}$ (-3.65 to -0.32), falling in the range of previous studies of marine carbonates. Furthermore, the $\delta^{26}\text{Mg}$ is negatively correlated with CaO/TiO_2 in these sediments, which is consistent with the fact that carbonate-rich sediments are generally enriched in light Mg isotopes and silicate-rich ones are enriched in heavy ones. Hence, incorporating different sediments into mantle source will generate magmas with different $\delta^{26}\text{Mg}$ features.

3.2.1 Detritus-dominated sediments contribution

Previous study has demonstrated that detritus sediment-derived components cannot significantly modify the Mg isotopic compositions of the subarc mantle wedge, because detritus-dominated sediments have low Mg concentration (2–3% for Nankai sediments), compared with carbonate minerals, such as dolomite (22%), magnesite (48%), and peridotite (48%). Moreover, detritus-rich sediments tend to have higher $\delta^{26}\text{Mg}$ than the mantle values. Shimanto shales, an equivalent to terrigenous sediments subducted into Nankai trench, have heavier $\delta^{26}\text{Mg}$ of -0.06 and -0.17 , which is consistent with this systematic (Table 6-1). Therefore, the bulk addition of recycled detritus-dominated sediments to oceanic crust melt are unlikely to explain the mantle-like Mg isotopes of Chugoku lavas.

If the sediments beneath the Chugoku district are transported as sediment melt (Feineman et al., 2013; Pineda-Velasco et al., 2018), the presence of residual garnet will cause even higher $\delta^{26}\text{Mg}$ of sediment-derived component. We modelled possible Mg isotope fractionation

($\Delta^{26}\text{Mg}_{\text{melt-source}}$) during the melting of subducted sediments beneath the Chugoku district, following the same modeling method for oceanic crust melt (**Table 6-3**). Mg isotopic compositions for partial melts from subducted sediments at ~ 3 GPa and 800-1000°C are calculated based on phase relationship from representative melting experiments on clay-like materials ([Skora and Blundy, 2010](#)) and mass balance (after [Wang et al., 2020](#)). The residual minerals during partial melting of subducted sediments mainly include garnet (MgO \sim 12 wt.%), clinopyroxene (MgO \sim 6 wt.%), kyanite (MgO $<$ 1 wt.%), phengite (MgO \sim 3 wt.%) \pm hornblende, \pm orthopyroxene. The calculated $\delta^{26}\text{Mg}$ and MgO of sediment melt ranges from +0.3‰ to +0.6‰ and from 0.5 wt.% to 1.2 wt.%, respectively. Therefore, the melt of detritus sediments cannot explain the scenario of Chugoku lavas and the possibility of carbonate sediment, which has much lower ^{26}Mg values, will be discussed below.

3.2.2 Carbonate sediments contribution

The Late Cretaceous and Cenozoic continental basalts (CBY) from eastern China have low $\delta^{26}\text{Mg}$ isotopic compositions ([Li et al., 2017](#)). The large-scale mantle low $\delta^{26}\text{Mg}$ anomaly in eastern China was attributed to recycled sedimentary carbonates, such as dolomite and magnesite, which have distinctly low $\delta^{26}\text{Mg}$ value compared to mantle. However, IAB (island-arc basalts) have mantle-like or heavy Mg isotopes ($\delta^{26}\text{Mg} = -0.35$ to 0.06), indicating that slab components with heavy Mg isotopes and only carbonates with limited Mg were dissolved into fluids during dehydration, otherwise, the IAB would exhibit a light Mg isotopic composition. Two reasons may be probable to explain insignificant role of carbonate recycle on Mg isotopic composition in the subarc regions.

First, dissolutions of carbonates could be preferential to Ca-rich carbonate because the solubility of calcite or aragonite is significantly higher than that of dolomite and magnesite at

high pressures based on molecular dynamics (Li et al., 2017). Calcite with low Mg content could be the major component in the carbonate carried by oceanic crust at the initial subduction stage. Chen et al., (2018) present the $\delta^{26}\text{Mg}$ value of Myanmar jadeitites and associated rocks, representing fluids from forearc subduction channel. The jadeite-forming fluids have low $\delta^{26}\text{Mg}$ values. The low $\delta^{26}\text{Mg}$ signature of the fluids is explained by the dissolution of Ca-rich carbonate in subducted sediments or altered oceanic crust. However, dehydrated fluid contains Ca, but little Mg, that has a limited influence on the Mg isotopic composition of the mantle wedge. This selective dissolution process of carbonates may result in the removal of most of the Ca-rich carbonates from, and leaving Mg-rich carbonates in, the subducting slabs.

Second, a high-pressure experimentation shows that calcite will be reacting with pyroxene and transformed into dolomite at high pressures between 23 and 45 kbars or magnesite at higher pressures (Li et al., 2017; Li et al., 2021). Tian et al. (2018) studied arc-like volcanic rocks from Tengchong, SW China, which exhibit homogeneous and lighter Mg isotopic compositions than the average mantle and island arc lavas, but similar to the <110 Ma intra-continental basalts from eastern China. This study suggested that Mg-rich carbonate-dolomite can be dissolved by supercritical liquids and subducted into a deep mantle wedge to depths of 120–300 km in the oceanic subduction zone. Thus, magmas with low $\delta^{26}\text{Mg}$ features sourced from the Mg-rich carbonate of subducted slabs will be formed in much deeper zones in the backarc regions, rather than subarc regions.

Therefore, neither oceanic crust nor sediments could explain the Mg isotopic composition of Chugoku lavas. In comparison, Hu et al. (2020) suggests that fluids derived from serpentinized peridotites of slab lithosphere are more effective metasomatic agents for Mg. The scenario will be discussed below.

3.3 The contribution of slab serpentinite

A final potential source of Mg from slab is slab serpentinitized peridotite. Due to the bending of the subducting slab, widespread extensional fractures will allow further hydration of the subducting oceanic lithosphere mantle as the oceanic slab is approaching the trench (Faccenna et al., 2009; Maruyama et al., 2009; Ranero et al., 2003). Compared to other rock units, serpentinitized rocks can contain up to 16% water (Deschamps et al., 2013; Kodolányi et al., 2012), and can be preserved well at relatively wide ranges of temperature-pressure conditions (Peters et al., 2017). Under high temperature-pressure conditions, a great quantity of fluids and elements are released from the serpentinites, and thus serpentinites are the carrier of fluids and mobile elements (e.g., Evans et al., 2013; Shen et al., 2020; Wunder and Schreyer, 1997). Compared to oceanic crust and sediments, serpentinites have much higher Mg concentrations, and serpentinitized peridotites and constituent phyllosilicates often have Mg isotopic compositions that are different from the normal mantle (Meng et al., 2021).

Magnesium isotopic compositions of abyssal peridotites reported so far are significantly heavier than the mantle because of the Mg isotope fractionation induced by hydrothermal processes during accretion and residence in the deep ocean (Wimpenny et al. 2012; Liu et al. 2017). Most of these abyssal peridotite samples from the Mid Atlantic Ridge, the Gakkel Ridge and Southwest Indian Ridge have been intensively altered, dominated by serpentinitization and/or weathering and have $\delta^{26}\text{Mg}$ varying from -0.24 to 0.03 , with an average value of -0.12 ± 0.13 (2SD, $n = 32$). In particular, $\delta^{26}\text{Mg}$ increases with increasing loss on ignition (LOI), suggesting that low-T seafloor weathering and the formation of clays are the main causes for the enrichment of heavy Mg isotopes in the abyssal peridotites.

Generally, deep-subducting oceanic ultramafic mélanges (slab lithosphere) will experience the following fluid-rock interactions: (a) peridotite serpentinitization; (2) replacement of

antigorite by talc and (3) replacement of talc by tremolite (Li et al., 2018). Similar $\delta^{26}\text{Mg}$ values of the partially serpentinized and completely serpentinized peridotites indicates small Mg isotopic fractionation during peridotite serpentinization. The higher $\delta^{26}\text{Mg}$ values of talc reflect the preferential loss of the light Mg isotopes into fluids when talc replaces serpentine. Tremolite, which completely replaced talc, have lighter Mg isotopic compositions. Thus, the breakdown of talc in serpentinite will release fluids with high $\delta^{26}\text{Mg}$.

However, calculations by Syracuse et al. (2010), indicate that the serpentinized oceanic lithospheric mantle under Chugoku district at sub-arc depths (90–110 km) has temperatures lower than 650°C, probably around 500–600°C, far below the talc breakdown temperature (~700–800°C (Spandler et al., 2008)). Hence, the fluids released from slab serpentinite have Mg isotopic compositions similar to those of mantle, making the expected signal of special serpentinite-derived $\delta^{26}\text{Mg}$ absent in the Chugoku lavas.

3.4 Mantle peridotite contribution

Partial melts derived from slab melting will penetrate and assimilate the mantle wedge peridotites en route to surface to form adakites (e.g., Rapp et al., 1999; Martin et al., 2005). Migration of slab-expelled melts in the mantle is likely accompanied by progressive re-equilibration of their Mg isotopic compositions with the ambient mantle.

The budget of Mg beneath the Chugoku district is controlled by the hybrid melt of AOC melts and sediment melts (detritus-dominated) with higher $\delta^{26}\text{Mg}$. Despite $\delta^{26}\text{Mg}$ is predicted to be higher than MORB for slab melts, the Chugoku lavas reveal uniform Mg isotopic compositions that fall within MORB and display no correlation with common indices of fluid or melt metasomatism, such as Ba/La and Pb/Ce, suggesting that slab melt from the Philippine plate may not preserve its Mg isotope composition through the infiltration in the mantle wedge. Given the strikingly different MgO contents between slab-derived melts

(oceanic crust and subducted sediments) and mantle wedge peridotites (mostly <1 wt% versus ~48 wt%), any $\delta^{26}\text{Mg}$ signal in the former created by isotope fractionation during slab melting may be erased by melt-mantle interaction. The binary mixing calculation also suggests that only > 3% of Mg ingestion from the mantle peridotite to the slab melt may significantly modify slab-derived melts with high $\delta^{26}\text{Mg}$ that were fractionated during slab melting and buffered those to mantle $\delta^{26}\text{Mg}$ values (**Figure 6-5**).

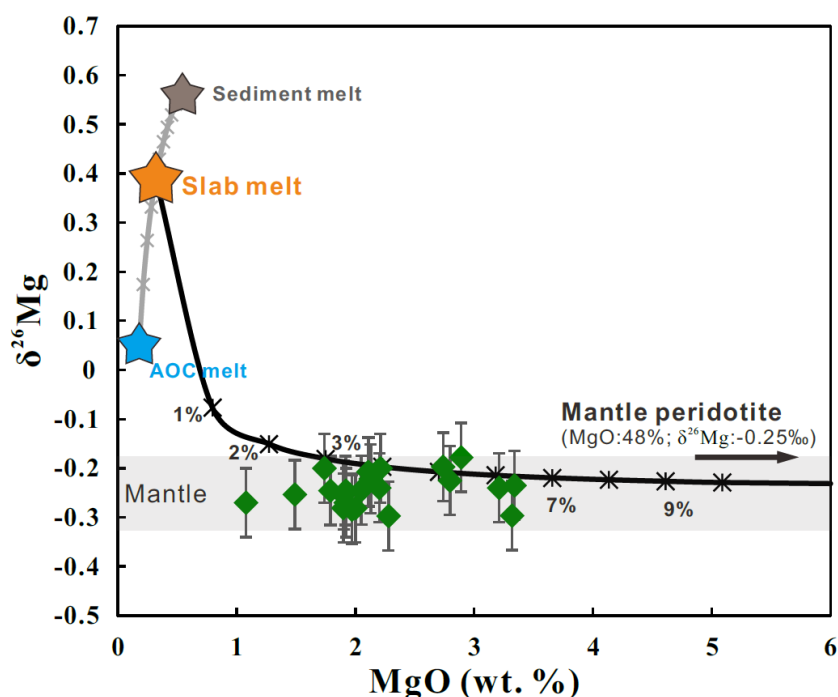


Figure 6-5. The diagram of $\delta^{26}\text{Mg}$ vs MgO for predicted pristine slab-derived melts.

Binary mixing curves between representative predicted slab-derived melts and the mantle wedge peridotite are also shown. Crosses denote 1% increments in panel.

4. Conclusions

Volcanic rocks (ADK, IAB and HMA) from the Chugoku district of Southwest Japan display nearly homogeneous Mg isotopic compositions, with an average $\delta^{26}\text{Mg}$ of $-0.23 \pm 0.08\text{‰}$ (2SD, $N = 43$), comparable to that of mantle peridotite. The lack of correlation between $\delta^{26}\text{Mg}$ and slab-component index indicates the absence of clear slab-derived components. Modelling suggests that Mg isotope fractionation between the melt and slab residue ($\Delta^{26}\text{Mg}_{\text{melt-residue}}$) is

large and much higher than mantle range. However, isotope fractionation can be easily erased by melt-mantle interaction in a slab melting scenario. In this regard, Mg isotopes of adakites may not be an effective tracer of recycled materials.

References

- Abers G. A., Mackenzie L. S., Rondenay S., Zhang Z., Wech A. G. and Creager K. C. (2009) Imaging the source region of Cascadia tremor and intermediate-depth earthquakes. *Geology* **37**, 1119-1122.
- Beinlich A., Mavromatis V., Austrheim H. and Oelkers E. H. (2014) Inter-mineral Mg isotope fractionation during hydrothermal ultramafic rock alteration – Implications for the global Mg-cycle. *Earth Planet. Sc. Lett.* **392**, 166-176.
- Brewer A. W., Teng F. and Mullen E. (2018) Magnesium Isotopes as a Tracer of Crustal Materials in Volcanic Arc Magmas in the Northern Cascade Arc. *Frontiers in Earth Science* **6**.
- Chen Y., Huang F., Shi G., Wu F., Chen X. and Jin Q., et al. (2018) Magnesium Isotope Composition of Subduction Zone Fluids as Constrained by Jadeitites from Myanmar. *Journal of Geophysical Research: Solid Earth* **123**, 7566-7585.
- Chen Y., Demény A., Schertl H., Zheng Y., Huang F. and Zhou K., et al. (2020) Tracing subduction zone fluids with distinct Mg isotope compositions: Insights from high-pressure metasomatic rocks (leucophyllites) from the Eastern Alps. *Geochim. Cosmochim. Ac.* **271**, 154-178.
- Chen Y., Schertl H., Zheng Y., Huang F., Zhou K. and Gong Y. (2016) Mg–O isotopes trace the origin of Mg-rich fluids in the deeply subducted continental crust of Western Alps. *Earth Planet. Sc. Lett.* **456**, 157-167.
- Deschamps F., Godard M., Guillot S. and Hattori K. (2013) Geochemistry of subduction zone

- serpentinites: A review. *Lithos* **178**, 96-127.
- Evans B. W., Hattori K. and Baronnet A. (2013) Serpentinite: what, why, where? *Elements* **9**, 99-106.
- Faccenna C., Di Giuseppe E., Funiciello F., Lallemand S. and van Hunen J. (2009) Control of seafloor aging on the migration of the Izu–Bonin–Mariana trench. *Earth Planet. Sc. Lett.* **288**, 386-398.
- Feineman M., Moriguti T., Yokoyama T., Terui S. and Nakamura E. (2013) Sediment-enriched adakitic magmas from the Daisen volcanic field, Southwest Japan. *Geochemistry, Geophysics, Geosystems* **14**, 3009-3031.
- Freyruth H., Ivko B., Gill J. B., Tamura Y. and Elliott T. (2016) Thorium isotope evidence for melting of the mafic oceanic crust beneath the Izu arc. *Geochim. Cosmochim. Ac.* **186**, 49-70.
- Guo B., Zhu X., Dong A., Yan B., Shi G. and Zhao Z. (2019) Mg isotopic systematics and geochemical applications; a critical review. *J. Asian Earth Sci.* **176**, 368-385.
- Handler M. R., Baker J. A., Schiller M., Bennett V. C. and Yaxley G. M. (2009) Magnesium stable isotope composition of Earth's upper mantle. *Earth Planet. Sc. Lett.* **282**, 306-313.
- Howie R. A., Zussman J. and Deer W. (1992) *An introduction to the rock-forming minerals*. Longman London, UK.
- Hu Y., Teng F. and Ionov D. A. (2020) Magnesium isotopic composition of metasomatized upper sub-arc mantle and its implications to Mg cycling in subduction zones. *Geochim. Cosmochim. Ac.* **278**, 219-234.
- Hu Y., Teng F., Plank T. and Huang K. (2017) Magnesium isotopic composition of subducting marine sediments. *Chem. Geol.* **466**, 15-31.
- Hu Y., Teng F., Zhang H., Xiao Y. and Su B. (2016) Metasomatism-induced mantle

- magnesium isotopic heterogeneity: evidence from pyroxenites. *Geochim. Cosmochim. Ac.* **185**, 88-111.
- Huang F., Chen L., Wu Z. and Wang W. (2013) First-principles calculations of equilibrium Mg isotope fractionations between garnet, clinopyroxene, orthopyroxene, and olivine: Implications for Mg isotope thermometry. *Earth Planet. Sc. Lett.* **367**, 61-70.
- Huang J., Guo S., Jin Q. and Huang F. (2020) Iron and magnesium isotopic compositions of subduction-zone fluids and implications for arc volcanism. *Geochim. Cosmochim. Ac.* **278**, 376-391.
- Huang J., Ke S., Gao Y., Xiao Y. and Li S. (2015) Magnesium isotopic compositions of altered oceanic basalts and gabbros from IODP site 1256 at the East Pacific Rise. *Lithos* **231**, 53-61.
- Huang J. and Xiao Y. (2016) Mg-Sr isotopes of low- $\delta^{26}\text{Mg}$ basalts tracing recycled carbonate species: Implication for the initial melting depth of the carbonated mantle in Eastern China. *Int. Geol. Rev.* **58**, 1350-1362.
- Huang K., Teng F., Plank T., Staudigel H., Hu Y. and Bao Z. (2018) Magnesium isotopic composition of altered oceanic crust and the global Mg cycle. *Geochim. Cosmochim. Ac.* **238**, 357-373.
- Huang K., Teng F., Wei G., Ma J. and Bao Z. (2012) Adsorption-and desorption-controlled magnesium isotope fractionation during extreme weathering of basalt in Hainan Island, China. *Earth Planet. Sc. Lett.* **359**, 73-83.
- Ishizaka K. and Carlson R. W. (1983) Nd-Sr systematics of the Setouchi volcanic rocks, southwest Japan: a clue to the origin of orogenic andesite. *Earth Planet. Sc. Lett.* **64**, 327-340.
- Kimura J., Gill J. B., Kunikiyo T., Osaka I., Shimoshioiri Y. and Katakuse M., et al. (2014)

- Diverse magmatic effects of subducting a hot slab in SW Japan: Results from forward modeling. *Geochemistry, Geophysics, Geosystems* **15**, 691-739.
- Kodolányi J., Pettke T., Spandler C., Kamber B. S. and Gméling K. (2012) Geochemistry of ocean floor and fore-arc serpentinites: constraints on the ultramafic input to subduction zones. *J. Petrol.* **53**, 235-270.
- Lai Y., Pogge Von Strandmann P. A. E., Dohmen R., Takazawa E. and Elliott T. (2015) The influence of melt infiltration on the Li and Mg isotopic composition of the Horoman peridotite massif. *Geochim. Cosmochim. Ac.* **164**, 318-332.
- Lee C. and Kim Y. (2021) Role of warm subduction in the seismological properties of the forearc mantle: An example from southwest Japan. *Sci Adv* **7**.
- Li M., Liu S., Lee H., Yang C. and Wang Z. (2021) Magnesium and zinc isotopic anomaly of Cenozoic lavas in central Myanmar: Origins and implications for deep carbon recycling. *Lithos* **386-387**, 106011.
- Li S., Yang W., Ke S., Meng X., Tian H. and Xu L., et al. (2017) Deep carbon cycles constrained by a large-scale mantle Mg isotope anomaly in eastern China. *National Science Review* **4**, 111-120.
- Li W. Y., Teng F. Z., Wing B. A. and Xiao Y. (2014) Limited magnesium isotope fractionation during metamorphic dehydration in metapelites from the Onawa contact aureole, Maine. *Geochemistry, Geophysics, Geosystems* **15**, 408-415.
- Li W., Teng F., Ke S., Rudnick R. L., Gao S. and Wu F., et al. (2010) Heterogeneous magnesium isotopic composition of the upper continental crust. *Geochim. Cosmochim. Ac.* **74**, 6867-6884.
- Li W., Teng F. and Xiao Y. (2018) Magnesium isotope record of fluid metasomatism along the slab-mantle interface in subduction zones. *Geochim. Cosmochim. Ac.* **237**, 312-319.

- Ling M., Liu Y., Williams I. S., Teng F., Yang X. and Ding X., et al. (2013) Formation of the world's largest REE deposit through protracted fluxing of carbonatite by subduction-derived fluids. *Sci. Rep.-Uk* **3**, 1-8.
- Liu D., Zhao Z., Zhu D., Niu Y., Widom E. and Teng F., et al. (2015) Identifying mantle carbonatite metasomatism through Os–Sr–Mg isotopes in Tibetan ultrapotassic rocks. *Earth Planet. Sc. Lett.* **430**, 458-469.
- Liu P., Teng F., Dick H. J., Zhou M. and Chung S. (2017) Magnesium isotopic composition of the oceanic mantle and oceanic Mg cycling. *Geochim. Cosmochim. Ac.* **206**, 151-165.
- Liu S. and Li S. (2019) Tracing the Deep Carbon Cycle Using Metal Stable Isotopes: Opportunities and Challenges. *Engineering* **5**, 448-457.
- Liu S., Teng F., He Y., Ke S. and Li S. (2010) Investigation of magnesium isotope fractionation during granite differentiation: implication for Mg isotopic composition of the continental crust. *Earth Planet. Sc. Lett.* **297**, 646-654.
- Liu S., Teng F., Yang W. and Wu F. (2011) High-temperature inter-mineral magnesium isotope fractionation in mantle xenoliths from the North China craton. *Earth Planet. Sc. Lett.* **308**, 131-140.
- Manning C. E. (2004) The chemistry of subduction-zone fluids. *Earth Planet. Sc. Lett.* **223**, 1-16.
- Martin H., Smithies R. H., Rapp R., Moyen J. and Champion D. (2005) An overview of adakite, tonalite–trondhjemite–granodiorite (TTG), and sanukitoid: relationships and some implications for crustal evolution. *Lithos* **79**, 1-24.
- Maruyama S., Hasegawa A., Santosh M., Kogiso T., Omori S. and Nakamura H., et al. (2009) The dynamics of big mantle wedge, magma factory, and metamorphic–metasomatic factory in subduction zones. *Gondwana Res.* **16**, 414-430.

- Meng Y., Yuan H., Santosh M., Mooney W. D. and Guo L. (2021) Heavy magnesium isotopes in the Gangdese Magmatic Belt: Implications for magmatism in the Mesozoic subduction system of southern Tibet. *Lithos* **390-391**, 106106.
- Moriguti T. and Nakamura E. (1998) Across-arc variation of Li isotopes in lavas and implications for crust/mantle recycling at subduction zones. *Earth Planet. Sc. Lett.* **163**, 167-174.
- Morris P. A. (1995) Slab melting as an explanation of Quaternary volcanism and aseismicity in southwest Japan. *Geology* **23**, 395.
- Nguyen T. T., Kitagawa H., Pineda Velasco I. and Nakamura E. (2020) Feedback of Slab Distortion on Volcanic Arc Evolution: Geochemical Perspective From Late Cenozoic Volcanism in SW Japan. *Journal of Geophysical Research: Solid Earth* **125**.
- Pang K., Teng F., Sun Y., Chung S. and Zarrinkoub M. H. (2020) Magnesium isotopic systematics of the Makran arc magmas, Iran: Implications for crust-mantle Mg isotopic balance. *Geochim. Cosmochim. Ac.* **278**, 110-121.
- Peters D., Bretscher A., John T., Scambelluri M. and Pettke T. (2017) Fluid-mobile elements in serpentinites: Constraints on serpentinisation environments and element cycling in subduction zones. *Chem. Geol.* **466**, 654-666.
- Pineda-Velasco I., Kitagawa H., Nguyen T. T., Kobayashi K. and Nakamura E. (2018) Production of High-Sr Andesite and Dacite Magmas by Melting of Subducting Oceanic Lithosphere at Propagating Slab Tears. *Journal of Geophysical Research: Solid Earth* **123**, 3698-3728.
- Pogge Von Strandmann P. A. E., Elliott T., Marschall H. R., Coath C., Lai Y. and Jeffcoate A. B., et al. (2011) Variations of Li and Mg isotope ratios in bulk chondrites and mantle xenoliths. *Geochim. Cosmochim. Ac.* **75**, 5247-5268.

- Ranero C. R., Phipps Morgan J., McIntosh K. and Reichert C. (2003) Bending-related faulting and mantle serpentinization at the Middle America trench. *Nature* **425**, 367-373.
- Rapp R. P. and Watson E. B. (1995) Dehydration melting of metabasalt at 8-32 kbar; implications for continental growth and crust-mantle recycling. *J. Petrol.* **36**, 891-931.
- Rondenay S., Abers G. A. and Van Keken P. E. (2008) Seismic imaging of subduction zone metamorphism. *Geology* **36**, 275-278.
- Schmidt M. and Poli S. (2013) Devolatilization during subduction.
- Shen B., Jacobsen B., Lee C. A., Yin Q. and Morton D. M. (2009) The Mg isotopic systematics of granitoids in continental arcs and implications for the role of chemical weathering in crust formation. *Proceedings of the National Academy of Sciences* **106**, 20652-20657.
- Shen T., Zhang C., Chen J., Hermann J., Zhang L. and Padrón-Navarta J. A., et al. (2020) Changes in the cell parameters of antigorite close to its dehydration reaction at subduction zone conditions. *American Mineralogist: Journal of Earth and Planetary Materials* **105**, 569-582.
- Shibata T. Y. M. I. (2014) Along-arc geochemical variations in Quaternary magmas of northern Kyushu Island, Japan. *Geological Society, London, Special Publications* **385**, 15-29.
- Sisson T. W. and Kelemen P. B. (2018) Near-solidus melts of MORB+ 4 wt% H₂O at 0.8–2.8 GPa applied to issues of subduction magmatism and continent formation. *Contrib. Mineral. Petr.* **173**, 1-23.
- Skora S. and Blundy J. (2010) High-pressure Hydrous Phase Relations of Radiolarian Clay and Implications for the Involvement of Subducted Sediment in Arc Magmatism. *J. Petrol.* **51**, 2211-2243.
- Spandler C., Hermann J., Faure K., Mavrogenes J. A. and Arculus R. J. (2008) The importance of talc and chlorite “hybrid” rocks for volatile recycling through subduction zones; evidence

- from the high-pressure subduction mélange of New Caledonia. *Contrib. Mineral. Petr.* **155**, 181-198.
- Spandler C. and Pirard C. (2013) Element recycling from subducting slabs to arc crust: A review. *Lithos* **170**, 208-223.
- Stracke A., Tipper E. T., Klemme S. and Bizimis M. (2018) Mg isotope systematics during magmatic processes: Inter-mineral fractionation in mafic to ultramafic Hawaiian xenoliths. *Geochim. Cosmochim. Ac.* **226**, 192-205.
- Syracuse E. M., van Keken P. E. and Abers G. A. (2010) The global range of subduction zone thermal models. *Phys. Earth Planet. In.* **183**, 73-90.
- Teng F. (2017) Magnesium Isotope Geochemistry. *Reviews in Mineralogy and Geochemistry* **82**, 219-287.
- Teng F., Hu Y. and Chauvel C. (2016) Magnesium isotope geochemistry in arc volcanism. *Proceedings of the National Academy of Sciences* **113**, 7082-7087.
- Teng F., Li W., Ke S., Marty B., Dauphas N. and Huang S., et al. (2010) Magnesium isotopic composition of the Earth and chondrites. *Geochim. Cosmochim. Ac.* **74**, 4150-4166.
- Teng F., Wadhwa M. and Helz R. T. (2007) Investigation of magnesium isotope fractionation during basalt differentiation: implications for a chondritic composition of the terrestrial mantle. *Earth Planet. Sc. Lett.* **261**, 84-92.
- Teng F., Wang S. and Moynier F. (2019) Tracing the formation and differentiation of the Earth by non-traditional stable isotopes. *Science China Earth Sciences* **62**, 1702-1715.
- Tian H., Yang W., Li S., Ke S. and Duan X. (2018) Low $\delta^{26}\text{Mg}$ volcanic rocks of Tengchong in Southwestern China: A deep carbon cycle induced by supercritical liquids. *Geochim. Cosmochim. Ac.* **240**, 191-219.
- Urey H. C. (1947) The thermodynamic properties of isotopic substances. *Journal of the*

- Chemical Society (Resumed)*, 562-581.
- van Keken P. E., Hacker B. R., Syracuse E. M. and Abers G. A. (2011) Subduction factory: 4. Depth-dependent flux of H₂O from subducting slabs worldwide. *Journal of Geophysical Research* **116**.
- von Strandmann P. A. P., Elliott T., Marschall H. R., Coath C., Lai Y. and Jeffcoate A. B., et al. (2011) Variations of Li and Mg isotope ratios in bulk chondrites and mantle xenoliths. *Geochim. Cosmochim. Ac.* **75**, 5247-5268.
- Walowski K. J., Wallace P. J., Hauri E. H., Wada I. and Clynne M. A. (2015) Slab melting beneath the Cascade Arc driven by dehydration of altered oceanic peridotite. *Nat. Geosci.* **8**, 404-408.
- Wang S. J., Teng F. Z. and Bea F. (2015) Magnesium isotopic systematics of metapelite in the deep crust and implications for granite petrogenesis. *Geochem Perspect Lett* **1**, 75-83.
- Wang S., Teng F., Li S. and Hong J. (2014) Magnesium isotopic systematics of mafic rocks during continental subduction. *Geochim. Cosmochim. Ac.* **143**, 34-48.
- Wang S., Teng F. and Scott J. M. (2016) Tracing the origin of continental HIMU-like intraplate volcanism using magnesium isotope systematics. *Geochim. Cosmochim. Ac.* **185**, 78-87.
- Wang Y., He Y. and Ke S. (2020) Mg isotope fractionation during partial melting of garnet-bearing sources; an adakite perspective. *Chem. Geol.* **537**, 119478.
- Wimpenny J., Harvey J. and Yin Q. (2012) The effects of serpentinization on Mg isotopes in Mid-Atlantic ridge peridotite **2012**, S41A-S1700A.
- Wimpenny J., Colla C. A., Yin Q., Rustad J. R. and Casey W. H. (2014) Investigating the behaviour of Mg isotopes during the formation of clay minerals. *Geochim. Cosmochim. Ac.* **128**, 178-194.
- Wunder B. and Schreyer W. (1997) Antigorite: High-pressure stability in the system MgO□

SiO₂ □ H₂O (MSH). *Lithos* **41**, 213-227.

Xiao Y., Teng F., Zhang H. and Yang W. (2013) Large magnesium isotope fractionation in peridotite xenoliths from eastern North China craton: Product of melt–rock interaction. *Geochim. Cosmochim. Ac.* **115**, 241-261.

Yang W., Teng F. and Zhang H. (2009) Chondritic magnesium isotopic composition of the terrestrial mantle: a case study of peridotite xenoliths from the North China craton. *Earth Planet. Sc. Lett.* **288**, 475-482.

Zhong Y., Chen L., Wang X., Zhang G., Xie L. and Zeng G. (2017) Magnesium isotopic variation of oceanic island basalts generated by partial melting and crustal recycling. *Earth Planet. Sc. Lett.* **463**, 127-135.

Tables

Table 6-1. Mg isotopic compositions of Late Cenozoic volcanic rocks in the Chugoku district, SW Japan and metasedimentary rocks (shales) from Shimanto zone

Sample name	Region	Latitude (°N)	Longitude (°E)	Age (Ma)	Episode*	Type	MgO (wt%)	δ ²⁵ Mg	δ ²⁶ Mg
<u>IAB type</u>									
OTS-01	Otsu	34.348	130.839	9.10	1	IAB	6.88		
OTS-05	Otsu	34.343	130.950	8.29	1	IAB	6.91	-0.11	-0.24
OTS-06	Otsu	34.392	130.938	9.31	1	IAB	7.84	-0.10	-0.22
OTS-10	Otsu	34.405	131.129	9.25	1	IAB	10.21		
SER-11	Sera	34.851	132.834	12.0	1	IAB	6.67	-0.05	-0.15
HIB-01	Hiba	34.991	132.900	10	1	IAB	6.88	-0.17	-0.34
HIB-04	Hiba	35.059	133.035	10.4	1	IAB	6.56	-0.11	-0.23
HIB-06	Hiba	35.045	133.074	9.90	1	IAB	6.73		
HIB-07	Hiba	34.987	133.077	10.1	1	IAB	8.31	-0.12	-0.23
MAT-04	Matsue	35.452	133.069	11.0	1	IAB	7.27	-0.07	-0.20
MKM-01	Kurayoshi (old)	35.494	134.102	5.03	2	IAB	5.07	-0.08	-0.17
KUR-16	Kurayoshi (old)	35.442	133.863	5	2	IAB	8.23	-0.12	-0.20
KUR-17	Kurayoshi (old)	35.443	133.859	5.15	2	IAB	7.11		
KRW-02	Kurayoshi (old)	35.258	134.100	4.99	2	IAB	8.35	-0.12	-0.25
KRW-03	Kurayoshi (old)	35.256	134.138	5.43	2	IAB	7.55		
KAW-03	Kawamoto	34.993	132.514	2.26	3	IAB	4.68	-0.06	-0.11
MEN-02	Mengame	34.938	132.724	1.11	3	IAB	9.71	-0.09	-0.17
ABU-06	Abu	34.442	131.498	1.57	3	IAB	6.05		

ABU-11	Abu	34.479	131.444	0.06	3	IAB	7.51	-0.09	-0.19
ABU-17	Abu	34.477	131.605	0.39	3	IAB	7.49		
ABU-21	Abu	34.487	131.625	0.18	3	IAB (SHO)	8.30	-0.09	-0.18
ABU-23	Abu	34.493	131.645	0.18	3	IAB (SHO)	7.91	-0.06	-0.20
ABU-26	Abu	34.603	131.688	2.01	3	IAB	4.39		
MAT-02	Yokota	35.418	133.185	1.2	3	IAB	7.18		
YOK-01	Yokota	35.191	133.086	1.1	3	IAB	7.48		
YOK-05	Yokota	35.160	133.209	1.32	3	IAB	9.47	-0.13	-0.28
US-01	Kurayoshi (young)	35.452	133.919	1.00	3	IAB	4.69		
OGI-03	N. Hyogo	35.479	134.420	0.98	3	IAB	4.29		
INA-01	N. Hyogo	35.500	134.299	2.74	3	IAB	5.17	-0.04	-0.19
HYO-03	N. Hyogo	35.491	134.530	1.62	3	IAB	5.29		
HYO-15	N. Hyogo	35.592	134.811	1.81	3	IAB	7.46	-0.07	-0.19

ADK type

AON-03	Aonoyama	34.493	131.815	0.29	3	ADK	2.36		
AON-04	Aonoyama	34.473	131.800	0.09	3	ADK	2.13	-0.11	-0.22
AON-09	Aonoyama	34.448	131.765	0.30	3	ADK	2.20	-0.04	-0.24
AON-17	Aonoyama	34.076	131.751	0.3	3	ADK	3.21		
AON-21	Aonoyama	34.254	131.774	0.38	3	ADK	2.89	-0.19	-0.18
AON-22	Aonoyama	34.188	131.764	0.5	3	ADK	3.32	-0.13	-0.30
OE-01	Oe-Takayama	35.070	132.427	1.52	3	ADK	1.01		
OE-02	Oe-Takayama	35.090	132.435	1.5	3	ADK	0.36		
OE-03	Oe-Takayama	35.089	132.436	1.70	3	ADK	0.77		
OE-09	Oe-Takayama	35.115	132.409	1.05	3	ADK	1.49	-0.12	-0.25
OE-10	Oe-Takayama	35.102	132.413	1.87	3	ADK	0.49		
OE-11	Oe-Takayama	35.107	132.424	1.83	3	ADK	1.08	-0.06	-0.27
SAM-01**	Sambe	35.162	132.616	1.36	3	ADK	1.78		
SAM-06	Sambe	35.135	132.631	0.07	3	ADK	1.94		
SAM-14	Sambe	35.129	132.620	0.43	3	ADK	1.90	-0.14	-0.28
SAM-16	Sambe	35.135	132.620	0.3	3	ADK	1.97	-0.13	-0.28
SAM-20	Sambe	35.154	132.626	0.22	3	ADK	1.92	-0.09	-0.20
SAM-21	Sambe	35.114	132.631	0.2	3	ADK	1.79	-0.12	-0.25
WAK-01	Wakurayama	35.467	133.108	0.86	3	ADK	2.05	-0.12	-0.24
WAK-02	Wakurayama	35.485	133.121	0.72	3	ADK	2.28	-0.14	-0.30
WAK-03	Wakurayama	35.492	133.116	0.73	3	ADK	1.74	-0.06	-0.20
2060707	Daisen	35.364	133.538	0.02	3	ADK	1.80		
3052002	Daisen	35.355	133.555	0.06	3	ADK	1.84	-0.13	-0.27
3053003	Daisen	35.328	133.566	0.51	3	ADK	2.11	-0.10	-0.21
3060102	Daisen	35.355	133.507	0.46	3	ADK	1.90	-0.12	-0.25
3060604	Daisen	35.403	133.589	0.41	3	ADK	2.00	-0.14	-0.28
SAN2	Daisen	35.377	133.572	0.05	3	ADK	2.21	-0.05	-0.20
YOK-11	Daisen	35.360	133.485	0.55	3	ADK	1.92	-0.10	-0.25
TG-01	Kurayoshi (young)	35.478	133.910	1.34	3	ADK	2.87		
KUR-01	Kurayoshi (young)	35.465	133.830	1.90	3	ADK	2.74	-0.06	-0.20
KUR-05	Kurayoshi (young)	35.461	133.861	1.13	3	ADK	2.80	-0.11	-0.23
KUR-11	Kurayoshi (young)	35.470	133.802	1.24	3	ADK	3.34	-0.12	-0.24

<u>HMA type‡</u>									
JA-2	Setouchi	34.35	133.93	13.4	HMA	7.68	-0.15	-0.29	
TG1	Setouchi	34.46	135.56	14	HMA	9.47	-0.11	-0.22	
SD264	Setouchi	34.50	134.19	12.8	HMA	6.05	-0.10	-0.26	
<u>Sediments</u>									
605	Shimanto						-0.01	-0.06	
606	Shimanto						-0.08	-0.17	

Table 6-2. The calculated $\delta^{26}\text{Mg}$ of AOC melts and residue under P and T conditions beneath the Chugoku district.

Rock No.	2237	2242	3	3	2
Starting material	H ₂ O-saturated MORB	H ₂ O-saturated MORB	tholeiite	tholeiite	high-Al basalt
P	2.6	2.6	2.2	2.2	3.2
T	800	800	1050	1100	1125
Mineral assemblage					
grt	39.2	41.0	35.7	12.9	40.7
cpx	40.0	37.1	45.0	46.2	35.3
melt	19.1	18.7	19.3	31.5	23.5
Hbl					
opx					
qtz/cs/st	0.4	1.8			
feldspar				9.5	
rut	1.2	.1.1			
tit					
ap	0.4	0.4			
ox/ilm					
other	2.0	2.2	0.0	9.5	0.0
F	0.19	0.19	0.19	0.32	0.24
Mineral <i>i</i> abundance in the residue					
A_{grt}	48.28	51.06	44.24	18.80	53.55
A_{cpx}	49.26	46.20	55.76	67.35	46.45
A_{Hbl}					
A_{opx}					
A_{ox}					
MgO of different minerals					
MgO_{grt}	5.7	6.1	8.92	11.86	7.95
MgO_{cpx}	10.3	10.8	10.89	12.69	7.80

MgO_{melt}	0.18	0.17	1.07	3.87	0.77
MgO_{Hbl}					
MgO_{opx}					
MgO_{ox}					
MgO_{residue}	7.8	8.1	10.0	10.8	7.9
MgO_{source}	6.9	6.9	8.4	8.4	6.1
MgO_{residue}/MgO_{melt}	43.3	47.7	9.4	2.8	10.2
D(MgO)_{grt/cpx}	0.55	0.57	0.82	0.93	1.02
Mg isotope fractionation between melt and mineral i in the residual source					
Δ²⁶Mg_{grt-cpx}	-0.86	-0.86	-0.57	-0.53	-0.51
Δ²⁶Mg_{Hbl-cpx}	0.03	0.03	0.02	0.02	0.02
Δ²⁶Mg_{opx-cpx}	-0.03	-0.03	-0.02	-0.02	-0.02
f_{Mg, i} = [MgO_i × A_i] / [∑MgO_i × A_i]					
f_{Mg, grt}	0.35	0.39	39%	21%	54%
f_{Mg, cpx}	0.65	0.61	61%	79%	46%
f_{Mg, Hbl}					
f_{Mg, opx}					
f_{Mg, ox}					
Results					
δ²⁶Mg_{melt}	0.03	0.06	-0.05	-0.17	0.00
Δ²⁶Mg_{melt-source}	0.28	0.31	0.20	0.08	0.25
δ²⁶Mg_{residue}	-0.25	-0.25	-0.26	-0.26	-0.26
Reference	Sisson & Kelmen (2018)		Rapp and Watson (1995)		

Table 6-3. The calculated δ²⁶Mg of sediment melts and residue under P and T conditions beneath the Chugoku district, SW Japan.

Rock No.	c10	c23	c9	c7	c8	c17	c14	c22	c13	c21	c20
Starting material											
water	7	7	7	7	7	9	13	15	15	15	15
T	800	850	900	1000	1100	800	1000	750	800	900	1000
Mineral assemblage											
grt	23.0	30.0	28.0	31.0	23.0	23.0	29.0	20.0	30.0	36.0	31.0
cpx	12.0	1.2									
melt	25.0	44.0	49.0	58.0	70.0	40.0	65.0	23.0	45.0	55.0	60.0
ky	12.0	8.5	10.0	8.7	6.6	5.2	5.3		10.0	6.5	6.7
phen	8.5	1.5				18.0		11.0	5.0		

ru	0.3	0.3	0.2	0.2		0.1	0.2	0.4	0.7	0.1	0.2
ilm	1.7	1.4	3.0			3.4		0.5			
accessory	2.0	1.7	3.2	0.2	0.0	3.5	0.2	0.9	0.7	0.1	0.2
total	57.5	42.9	41.2	39.9	29.6	49.7	34.5	31.9	45.7	42.6	37.9
F	0.25	0.44	0.49	0.58	0.70	0.40	0.65	0.23	0.45	0.55	0.60
Mineral <i>i</i> abundance in the residue											
A_{grt}	40.0	69.9	68.0	77.7	77.7	46.3	84.1	62.7	65.6	84.5	81.8
A_{cpx}	20.9	2.8									
A_{ky}	20.9	19.8	24.3	21.8	22.3	10.5	15.4		21.9	15.3	17.7
A_{phen}	14.8	3.5				36.2		34.5	10.9		
A_{ox}											
MgO of different minerals											
MgO_{grt}	12.37	11.43	13.89	12.26	13.15	13.01	11.79	8.23	10.85	10.77	11.44
MgO_{cpx}	5.48										
MgO_{melt}	0.46	0.59	0.31	0.68	1.41	0.55	1.21	0.41	0.73	0.57	0.69
MgO_{ky}	0.21	0.20	0.28	0.42	0.42	0.20	0.30		0.21	0.06	0.50
MgO_{phen}	3.50	3.70				3.37		3.07	3.88		
MgO_{ox}											
MgO_{residue}	6.7	8.2	9.5	9.6	10.3	7.3	10.0	6.2	7.6	9.1	9.4
MgO_{source}	6.9	6.9	6.9	6.9	6.9	6.9	6.9	6.9	6.9	6.9	6.9
MgO_{residue}/MgO_{melt}	14.5	13.8	30.7	14.1	7.3	13.2	8.2	15.2	10.4	16.0	13.7
Mg isotope fractionation between melt and mineral <i>i</i> in the residual source											
$\Delta^{26}\text{Mg}_{\text{grt-cpx}}$	-0.86	-0.78	-0.72	-0.61	-0.53	-0.86	-0.61	-0.95	-0.86	-0.72	-0.61
$\Delta^{26}\text{Mg}_{\text{ky-cpx}}$											
$\Delta^{26}\text{Mg}_{\text{phen-cpx}}$											
$f_{\text{Mg}, i} = [\text{MgO}_i \times A_i] / [\sum \text{MgO}_i \times A_i]$											
$f_{\text{Mg}, \text{grt}}$	74.4 %	97.9 %	99.3 %	99.0 %	99.1 %	82.9 %	99.5 %	83.0 %	93.8 %	99.9 %	99.1 %
$f_{\text{Mg}, \text{cpx}}$	17.2 %										
$f_{\text{Mg}, \text{ky}}$	0.6%	0.5%	0.7%	1.0%	0.9%	0.3%	0.5%		0.6%	0.1%	0.9%
$f_{\text{Mg}, \text{phen}}$	7.8%	1.6%				16.8 %		17.0 %	5.6%		
$f_{\text{Mg}, \text{ox}}$											
Results											
$\delta^{26}\text{Mg}_{\text{melt}}$	0.49	0.59	0.55	0.41	0.26	0.54	0.36	0.63	0.61	0.53	0.41
$\Delta^{26}\text{Mg}_{\text{melt-source}}$	0.74	0.84	0.80	0.66	0.51	0.79	0.61	0.88	0.86	0.78	0.66
$\delta^{26}\text{Mg}_{\text{residue}}$	-0.13	-0.16	-0.14	-0.17	-0.24	-0.15	-0.23	-0.13	-0.18	-0.17	-0.18
Reference	Skora et al. (2010)										

Chapter 7. Summary and future vision

This dissertation investigates sources, properties and transfer of slab-derived fluids beneath the Chugoku section of Southwest Japan arc. I first developed the purification and analytical method of Li and Mg isotopes. Next, the properties and recycling of slab-derived fluids into the mantle is considered. Specifically, I approach this topic by studying the Hf-B-Li-Mg isotopic composition of volcanic rocks from the Chugoku district of Southwest Japan, exploring the source materials for metasomatic agents that may lead to distinct isotopic compositions from mantle, and investigating processes that can influence the isotopic distribution. The results from this dissertation contribute to the understanding of the role and behavior of slab-derived fluids. The main conclusions drawn from this dissertation along with future directions are discussed below:

(1) The first topic (Chapter 2) investigates the properties of slab-derived fluids in the Chugoku volcanic rocks by Hf isotopes. We attribute the temporal change in $^{176}\text{Hf}/^{177}\text{Hf}$ values to the transition of the slab-derived fluid component from a supercritical liquid to a hydrous melt in the last 12 million years (Myrs), owing to shallow subduction and morphological distortion of the oceanic lithosphere. Later work may couple Hf isotope systematics with other non-traditional stable isotopes, such as potassium (K) and Molybdenum (Mo), which behave differently from Hf isotopes during geological processes. The subduction lithologies (marine sediments, altered oceanic crust and ultramafic rocks) usually have highly heterogeneous K and Mo isotope composition, and hence may give a more complete picture of the working mechanism for slab-derived fluids in general.

(2) Chapter 3 focuses on B isotope variation in adakites, which points to the involvement of inputs from the fluid from slab mantle serpentinite. Our study finds that, in the hotter

subduction zone, fluids are released from the deeper serpentinites and facilitate the melting of the upper crustal section in the slab, which was dehydrated at shallower depths but re-hydrated by the addition of serpentinite-derived fluids. In the future, more detailed investigations on B isotopic compositions in adakites of Chugoku district, Kyushu district and High-Mg andesites from Setouchi are required to explore the temporal and spatial variation of B isotopic composition of SW Japan arc lavas and the fluid sources to facilitate the melting of slab.

(3) Chapter 4 presents an optimized protocol for the rapid and simultaneous purification of Li and Mg, which significantly reduces the separation time, required reagent volume, and procedural blanks compared to previous methods. This method still has the potential to separate other elements using an additional column, because Cu and Zn are eluted with Mg fractions, and many other elements, such as Fe, K and Ca, are eluted after the collection of Li and Mg fractions.

(4) Chapter 5 presents a Li isotope investigation on volcanic rocks in the Chugoku district in SW Japan which show a large $\delta^7\text{Li}$ variation (-1.9 to $+7.4\%$). High $\delta^7\text{Li}$ values ($+1.2$ to $+7.4\%$) are found in high-Sr andesites and dacites (adakites) whereas low $\delta^7\text{Li}$ values (-1.0 to -0.1%) are found in high-Mg andesites. Our study suggests that subduction-related $\delta^7\text{Li}$ features in arc magmas can be preserved if (1) slab-derived fluids/melts have distinct $\delta^7\text{Li}$ values from MORB and (2) rapid ascent of those fluids/melts allows the limited isotope exchange with mantle. Our study provides an example where Li isotopic composition from slab-released fluids is well preserved. However, more investigation needs to be done on the abilities of different types of fluids to survive the equilibrium processes with mantle, and which component finally dominates the budget of preserved Li, especially sediments.

(5) Chapter 6 presents a systematic investigation of the Mg isotope compositions in the Chugoku volcanic rocks, which have an average $\delta^{26}\text{Mg}$ of $-0.23 \pm 0.08\%$ (2SD, N = 41) and

are within the range of mantle peridotite. Our modeling suggests slab-derived melts may have $\delta^{26}\text{Mg}$ higher than their sources by up to +0.31‰, but the heavy Mg isotopic features can be easily buffered by later melt-mantle interaction. Therefore, Mg isotopes may be not a powerful tracer of slab melting. To further constrain the role of Mg isotopic composition in arc magma genesis, future studies on arc lavas derived from different slab-depths and subduction zones with contrasting thermal structures are needed, which permits inter-arc comparison on how dehydration of different hydrous phases at various pressure-temperature conditions affect the Mg isotopic compositions of arc magmas.